ABSTRACT

Title of Dissertation:	DESIGN AND SYNTHESIS OF POLYOLEFIN MATERIALS FOR NANOSTRUCTURED SELF-ASSEMBLY: BUILDING BLOCKS, COPOLYMERS, AND POLYMER CONJUGATES
	Charlotte Maria Wentz , Doctor of Philosophy, 2022
Dissertation directed by:	Professor Lawrence R. Sita Department of Chemistry and Biochemistry

Polyolefin based materials are essential to today's society in both simplistic commodity plastics to complex nanostructured materials and optoelectronic devices. In order to better understand these materials and make new impactful innovations, there is a barrier of fabrication, scalability, versatility, and programmability. The answer to the world's plastic waste problem lies not in removing our use of polymers but relies in better understanding their properties, utilizing them as building blocks in advanced materials, and creating a long-lasting advanced material.

Towards the goal of overcoming limitations in fabrication and scalability the work herein presents on utilizing a toolbox of living polymerization techniques such as living chain transfer polymerization (LCCTP) where new functionalities, stereochemical microstructures, optical properties, and physical properties of the polyolefin can be designed and systematically controlled. The polyolefins made through these techniques are scalable and versatile with end-group functionalization creating a seemingly endless choice of polymer building blocks and polymer

materials. In line with creating new technologies that are programable the polyolefin building blocks made herein are utilized in multiple conjugates to create and understand methods and mechanisms of solid-state nanostructured self-assembly and access rare nonclassical phases that are highly desirable for their properties and uses in a plethora of applications. The conjugates investigated involve either a sugar-based head group covalently bond to a polymer tail to access rare and misunderstood Frank Kasper phase order-order transitions, or a perylene chromophore core covalently bond on both sides of the core in a linear fashion to polymer domains to create highly florescent or optically active materials that are useful in organic technologies such as solar cells, light emitting diodes, or nanotechnology. These perylene based conjugates can self-assemble into unique columnar phases and single gyroid phase. These results with conjugates provide methods for reliable and programmable access to rich phase behavior through the design of the polyolefin domains.

DESIGN AND SYNTHESIS OF POLYOLEFIN MATERIALS FOR NANOSTRUCTURED SELF-ASSEMBLY: BUILDING BLOCKS, COPOLYMERS, AND POLYMER CONJUGATES

by

Charlotte Maria Wentz

Dissertation submitted to the Faculty of the Graduate School of the
University of Maryland, College Park, in partial fulfillment
of the requirements for the degree of
Doctor of Philosophy
2022

Advisory Committee:
Professor Lawrence R. Sita, Chair
Professor Daniel E. Falvey
Professor Efrain E. Rodriguez
Professor Mercedes K. Taylor
Professor Mohamad I. Al-Sheikhly

Dedication

This work is dedicated to the two people in my life that have taught me love, perseverance, and to believe in myself. To my mother, who is a woman of exceptional kindness, patience, and passion. She has nurtured and guided me every step of the way. To my partner, Morgan Kramer, who is a man of extraordinary intelligence, thoughtfulness, and strength. I am forever grateful you came into my life and saved it.

"I see now that the circumstances of one's birth are irrelevant. It is what you do with the gift of life that determines who you are." – Mewtwo, *Pokémon the First Movie*

Acknowledgements

To begin I must give my sincerest appreciation to my advisor Dr. Lawrence R. Sita for his guidance, mentorship, and support throughout my time here at UMD. Dr. Sita has influenced me into the scientist, educator, and critical thinker I am today. This work presented herein would not be present without his efforts. I am forever grateful.

My committee members: Dr. Falvey, Dr. Rodriguez, Dr. Taylor, and Dr. Al-Sheikhly, I would also like to thank for your help through the program and the wisdom you have pass on.

There are many people throughout my life who have influenced me to the point at which I am today. My advisors and professors from Lycoming College helped me find my passion for chemistry and education: Dr. Ramsey, Dr. McDonald, Dr. Bendorf, Dr. Mahler, Dr. Hanes, and Dr. Rogers. Your lessons and confidence in me pushed me to pursue my Ph.D. Thank you.

I am thankful to my family and friends who have been a part of this journey and offered support and encouragement. Especially my mother Patricia, and my brothers George, Tom, and Matthew. Thank you mom for all the late-night phone calls, words of guidance, and your never-ending love. To my colleagues at UMD thank you for your friendship. To my life-long friends, thank you for your support and companionship.

My mentors in the Sita group who have offered me their knowledge, patience, and encouragement, I thank you; Dr. Kätchen L. Lachmayr, Dr. Mark A. Wallace, Dr. Wonseok Hwang, and Dr. Leila Dunman. The truth of success is it is never done alone. Thank you all for helping me. I would also like to extend great thanks to the scientist

and staff at Brookhaven National Lab, who offered assistance and instruction, especially Dr. Esther Tsai and Dr. Kevin Yager.

To the current member of the Sita group thank you, Danyon, Brendan, Cole, Will, Kayla, and Katharina. Specifically, Danyon, thank you for being my best work friend and for always being someone I can talk to. To Will, Kayla, and Katharina thank you for letting me teach you synthetic techniques and reminding me of my passion for teaching. I wish you all great success.

To my fiancé, Morgan, there are no words to describe my thanks to you. You have been through this process every step of the way as we found love for each other in our first year here at UMD. You have been a sounding board for me and encourage me in my darkest times. You nurtured me back to health after brain surgery, showed me so much love and patience I never felt before, and believed in me when I couldn't believe in myself. Your love is priceless, thank you.

I am also thankful to the University of Maryland Graduate School, janitorial staff, administrative staff, NMR facility, and Department of Chemistry and Biochemistry for all the work, assistance, awards, support, and funding opportunities that have been provided to me.

Table of Contents

Dedication...……..ii

Acknowledgments ……...…iii

Table of Contents v

List of Tables ix

List of Figures x

List of Schemes xiii

List of abbreviations xiv

List of Publications xvii

Chapter 1: Introduction to Polymerizations and Polyolefin Materials 1

1.1 Introductuon to Polymerizations..... 1

1.1.1 Ziegler-Natta ……1

1.1.2 Homogeneous Metallocene Complexes ...…….....3

1.1.3 Living Polymerization ……..5

1.1.4 Living Coordinative Polymerization ……8

1.1.5 Living Coordinative Chain Transfer Polymerization ……..……11

1.2 Introduction to Polyolefin Building Blocks ……13

1.2.1 End-group Functionalization ……13

1.2.2 Characterization ……15

1.3 Introduction to Self-Assembly ……18

1.3.1 Surfactants ……..20

1.3.2 Model for Classical Phases in Block Copolymers ……..23

1.3.3 Frank Kasper Phases ……27

1.3.4 Liquid Crystals……30

1.3.5 π-π Stacking Chromophores ……..33

1.3.6 Characterizations ……...35

1.4 Goals and Scope of this work ……..38

Chapter 2:Stereomodulation of Poly(4-methyl-1-pentene)[PMP]: Adoption of Neglected and Misunderstoof Commercial Polyolefin 41

2.1 Introductions 41

2.2 Stereomodulation of PMP through Living Coordinative- and Living Coordinative Chain Transfer Polymerization [LCP, LCCTP] 47

2.3 Establishing *atactic* PMP 53

2.4 Two-State Degenerative Polymerization 57

2.5 Molecular Weight Dependency Effects on iPMP Microstructure and Physical Properties 61

2.6 Conclusions 66

2.7 Supporting Experimental Information 67

2.7.1 Synthetic Procedures 67

2.7.2 Characterization Parameters 73

2.7.3 Supporting Results 75

Chapter 3: Investigation into Synthesizing a Stereoblocky PMP Material…..……129

3.1 Brief History of 'Stereoblocky' Materials 129

3.2 Three-Component LCCTP System 131

3.3 Results of LCCTP with Two Stereo-influencing Catalysts in an One-Pot Polymerization 134

3.4 Conclusions 143

3.5 Supporting Experimental Information 144

3.5.1 Synthetic Procedures 144

3.5.2 Characterization Parameters 146

3.5.3 Supporting Results 147

Chapter 4: Engineering α, ω nonconjugated dienes 166

4.1 Background 166

4.2 Application of Optical Purity as a Programmable Variable for Stereomodulated LCCTP of 1,6-heptadiene and 1,5-hexadiene 170

4.3 Effects of Crystallinity Within PMCP-*co*-PMCH Materials 176

4.4 Conclusions 187

4.5 Supporting Experimental Information 189

4.5.1 Synthetic Procedures 189

4.5.2 Characterization Parameters 193

4.5.3 Supporting Results 195

Chapter 5: Block Copolymers [BCP] 234

5.1 Introduction 234

5.2 Crystallin-Amorphous BCP 238

5.3 Building Block Polymers 246

5.4 Conclusions 251

5.5 Supporting Experimental Information 252

5.5.1 Synthetic Procedures 252

5.5.2 Characterization Parameters 255

5.5.3 Supporting Results 258

Chapter 6: Sugar Polyolefin Conjugates 277

6.1 Background 277

6.2 Introduction 280

6.3 Exceptionally Stable One-Component FK A15 Phase 282

6.3.1 Mechanism 290

6.3.2 Conclusions 293

6.4 Background of Soft Matter Multi-Component FK Phases 294

6.5 Room temperature FK A15 297

6.6 Two- and Three-Component σ Phase 302

6.6.1 Mechanism 310

6.6.2 Conclusions 312

6.7 Overall Sugar Polyolefin Conjugate Conclusions 312

6.8 Supporting Experimental Information 314

6.8.1 Synthetic Procedures.....314

6.8.2 Characterization Parameters 321

6.8.3 Supporting Results 324

Chapter 7: Perylene Bisiimde-Polyolefin Conjugates 393

7.1 Background in Perylene Bisimides 393

7.2 Mesophase Engineering of Perylene Bisimide–Polyolefin Conjugates Introduction 396

7.3 Mesophase Engineering of Perylene Bisimide–Polyolefin Conjugates: From Columnar and Optically Active Single Gyroid Nanostructures of Neutral and Radical Anions to Luminous Liquids and Waxes 400

7.4 Blends 420

7.4.1 Poly(3-hexylthiophene) (P3HT) 420

7.4.2 *Dye 254 Conjugate*.....422

7.5 Conclusions 424

7.6 Supporting Experimental Information 426

7.6.1 Synthetic Procedures 426

7.6.2 Characterization Parameters 438

7.6.3 Supporting Results 444

Chapter 8: Conclusions and Future Work 523

References 525

List of Tables

Table 1.1 Summary of supramolecular interactions for macromolecular self-assemblies ……. ……...……19

Table 2.1 LCCTP and LCP of 4M1P …….....55

Table 2.2 Two-state degenerative LCP of 4M1P …….59

Table 3.1 LCCTP conditions and PMP results …….135

Table 3.2 Dynamic mechanical analysis results ……139

Table 4.1 LCP and LCCTP of 1,5-hexadiene and 1,6-heptadiene ……...…171

Table 4.2 LCCTP of copolymer materials …….180

Table 5.1 Di- and Triblock copolymers ……...240

Table 5.2 Diblock copolymers ……..……244

Table 5.3 Telechelic polyolefins and heterotelechelic polyolefins ……249

Table 6.1 Correlation between neat and two- and three-component materials with phase behavior observed ……307

Table 7.1 Summary of PBI polyolefin conjugates properties and behavior ……403

List of Figures

Figure 1.1 Stereochemical microstructures of polypropylene ……..…4

Figure 1.2 General structure of CpAM catalysts …….10

Figure 1.3 Synthetic routes for xPAOs from LCCTP ……..……...….14

Figure 1.4 Weight distribution curves for theoretical samples ……...16

Figure 1.5 DSC trace of theoretical amorphous and semicrystalline polymers……..17

Figure 1.6 Surfactant self-assemblies based on packing parameter ……21

Figure 1.7 Different molecular architectures for block copolymers …….. 24

Figure 1.8 Theoretical phase diagram for linear AB-type BCPs predicted by self-consistent mean-field theory ……26

Figure 1.9 Frank-Kasper polyhedron with CN 12, 14, 15, and 16 ……28

Figure 1.10 Schematic representation of different types of columnar mesophases….32

Figure 1.11 Schematic representation of a homeotropic alignment and planar alignment ……..……...33

Figure 1.12 Representative conformations of benzene pi-stacking …….34

Figure 1.13 Schematic layout of SAXS …….……36

Figure 1.14 Cartooned radio to represent all the gears in the toolbox that can be adjusted to change the stereomodulated PMP materials produced ……...39

Figure 2.1 ^{13}C NMR of isotactic and atactic PMP ……49

Figure 2.2 XRD profiles of stereoregular PMP …..……..51

Figure 2.3 XRD profiles of atactic PMP ……..53

Figure 2.4 Demonstration of the manufacture of optically transparent disks ……..…53

Figure 2.5 Partial DSC data for aPMP …….56

Figure 2.6 ^{13}C NMR, DSC traces, and plot of PMP samples …….60

Figure 2.7 Stacked ^{13}C NMR of PMP samples ……..63

Figure 2.8 Stacked DSC traces of PMP samples ……65

Figure 3.1 ^{13}C NMR of iPMP, aPMP, and homopolymer blend ……134

Figure 3.2 ^{13}C NMR, DSC, graphic plots of PMP samples ……..…136

Figure 3.3 Image of separated homopolymers from bulk material ……137

Figure 3.4 Image of iPMP, bulk homopolymer blends PMP materials, and aPMP 138

Figure 3.5 Stress-strain curves for PMP samples ……140

Figure 3.6 Images of DMA experiments ……..141

Figure 3.7 ^{13}C NMR spectra of blended iPMP and aPMP ……142

Figure 4.1 ^{13}C NMR of PMCH references ……..……..173

Figure 4.2 ^{13}C NMR of PMCH samples ……..174

Figure 4.3 ^{13}C NMR of PMCP references ……179

Figure 4.4 ^{13}C NMR of copolymers samples……182

Figure 4.5 Partial DSC traces of copolymer samples ……..……183

Figure 4.6 Whole series of copolymers samples *Tg* calculations ……186

Figure 5.1 Block copolymer PH-PMP-PH AFM phase map ……..……241

Figure 5.2 Block copolymer PH-PMP-PH AFM phase map ……242

Figure 5.3 Block copolymer PH-PMP AFM phase map ……..……243

Figure 5.4 SAXS of PD-PMCP sample ……245

Figure 5.5 AFM phase map of aPMP-PCL diblock copolymers ……..……250

Figure 6.1 Frank Kasper unit cell ……..…281

Figure 6.2 ^{1}H NMR of CB-aPMP conjugate ……285

Figure 6.3 Thermal heating stage at Brookhaven National Lab ……286

Figure 6.4 SAXS of CB-aPMP conjugate ……287

Figure 6.5 VT SAXS of CB-aPMP conjugate thermal ramp ……290

Figure 6.6 Proposed mechanism for solid-state epitaxial order-order transition …..292

Figure 6.7 Unit cell of FK σ phase ……295

Figure 6.8 Selected VT SACS for CB-aPH conjugate ……299

Figure 6.9 Selected VT SAXS for GAL-aPH conjugate ……..301

Figure 6.10 Model to produce chimeric and hybrid A15 structures ……303

Figure 6.11 Selected VT SAXS of GAL-aPMP conjugates ……305

Figure 6.12 Selected VT SACS of two component blends ……308

Figure 6.13 SAXS thermal ramp of two component blends ……309

Figure 6.14 Fitting model for SAXS thermal ramp …….……310

Figure 6.15 Transformation from the FK A15 to σ phase ……311

Figure 7.1 Partial electronic absorption and fluorescence for PBI conjugate ……404

Figure 7.2 Electronic circular dichroism ……..…406

Figure 7.3 AFM phase map of PBI polyolefin conjugates ……408

Figure 7.4 SAXS and GISAXS of PBI conjugates ……410

Figure 7.5 UV-vis spectra and EPR of cobaltocenium radial complexes ……....412

Figure 7.6 Selected SAXS of PBI conjugates and cobaltocenium radical complex . 416

Figure 7.7 Luminous liquid and molded wax PBI conjugate materials ……418

Figure 7.8 EPR and UV-vis of P3HT blends with PBI conjugates ……421

Figure 7.9 Pigment Red 254 …….……422

Figure 7.10 SAXS of blended aPP-DPP-aPP with aPP-PBI-aPP conjugate ……423

List of Schemes

Scheme 1.1. Cossee and Arlman mechanism for Siegler-Natta process ……..…2

Scheme 1.2 Examples of termination pathways from LCP ……..8

Scheme 1.3 Mechanism of two-state stereomodulated LCP ……11

Scheme 1.4 Mechanism of LCCTP ……..……...12

Scheme 2.1 Chemical microstructure and synthesis of poly(4-methyl-1-pentene) ..…44

Scheme 3.1 Summary of the reagents and methods that were employed in the one-pot LCCTP of 4M1P using a dual pre-initiator system ……132

Scheme 4.1 Stereomodulated living coordinative chain transfer of cyclopolymerization of 1,5 hexadiene and 1,g-heptadiene …….....168

Scheme 4.2 Stereoengineering of PMCH microstructure ……169

Scheme 4.3 LCCTP of copolymer materials ……181

Scheme 5.1 Summary of synthesis of di- and triblock polymers …….239

Scheme 5.2 Production of heterotelechelic polyolefins ……...247

Scheme 6.1 Chemical layout structure of sugar-polyolefin conjugates ……...…279

Scheme 6.2 List of structures of sugar-polyolefin conjugates ……...283

Scheme 6.3 Structure and synthesis of sugar-polyolefin conjugates ……...…284

Scheme 7.1 General structure of perylene bisimide derivatives ……..……..……395

Scheme 7.2 Synthesis of PBI-polyolefin conjugates ……...……..401

List of Abbreviations

$AlEt_3$ – Triethylaluminum

$AlMe_3$ – Trimethylaluminum

aPD – Atactic Poly(1-decene)

aPOD – Atactic Poly(1-octadecene)

aPH – Atactic Poly(1-hexene)

aPMP – Atactic Poly(4-methyl-1-pentene)

aPP – Atactic Polypropylene

BCP – Block Copolymer

BCC – Body Centered Cubic

C – Hexagonally Packed Cylinders

CAC – Critical Aggregation Concentration

CB – Cellobiose

CN – Coordination Number

Cp – cyclopentadienyl

Cp* - Pentamethylcyclopentadienyl

CpAM – Cyclopentadienyl Amidinate

CTA – Chain Transfer Agent

DDQC – Dodecagonal Quasicrystal Phase

DG – Double Gyroid

Đ – Dispersity

DPn - Number-average Degrees of Polymerization

DSC – Differential Scanning Calorimetry

DMA – Dynamic Mechanical Analysis

Eq. – Equivalents

FCC – Face Centered Cubic

FK – Frank-Kasper

GAL – Galactose

GISAXS – Grazing Incidents Small Angle X-ray Scattering

GYR - Gyroid

GPC – Gel Permeation Chromatography

HCP – Hexagonal Close Packed

HDPE – High Density Polyethylene

HIPG – Highly Ordered Pyrolytic Graphite

Hf – Hafnium

iPMP – Isotactic Poly(4-methyl-1-pentene)

LAM - Lamellar

LCP – Living Coordinative Polymerization

LCCTP – Living Coordinate Chain Transfer Polymerization

M_n - Number Average Molecular Weight

M_w – Weight Average Molecular Weight

NMR – Nuclear Magnetic Resonance

PE – Polyethylene

PMCP – Poly(1,3-methylene cyclopentane)

PMCH – Poly(1,3-methylene cyclohexane)

PP – Polypropene

PS – Polystyrene

RI – Refractive Index

SAXS – Small Angle X-ray Scattering

TCP – Topologically Close Packed

T_g – Glass Transition Temperature

TGA – Thermalgravimetric Analysis

T_m – Melting Temperature

T_c – Cold Crystallization temperature

T_{OD} – Order-Disorder Phase Transition

T_{OO} - Order-Order Phase Transition

VT – Variable Temperature

$ZnEt_2$ – Diethylzinc

$ZnPh_2$ – Diphenylzinc

Zr - Zirconium

4M1P – 4-methyl-1-pentene

List of Publications

1. **Wentz, C. M**.; Fischbach D. M.; Sita, L.R., Stereomodulation of Poly(4-methyl-1-pentene): Adoption of a Neglected and Misunderstood Commercial Polyolefin. *Angew. Chem. Int. Ed.* **2022**, e202211992.

2. Burkey, A. A.; Fischbach, D. M.; **Wentz, C. M**.; Beers, K. L.; Sita, L. R., Highly Versatile Strategy for the Production of Telechelic Polyolefins. *ACS Macro Lett*. **2022**, *11*, 402-409.

3. Wallace, M. A.; **Wentz, C. M**.; Sita, L. R., Optical Purity as a Programmable Variable for Controlling Polyolefin Tacticity in Living Coordinative Chain Transfer Polymerization: Application to the Stereomodulated LCCTP of α, ω-Nonconjugated Dienes. *ACS Catal.* **2021**, *11*, 4583-4592.

4. Lachmayr, K. K.; **Wentz, C. M**.; Sita, L.R., An exceptionally stable and scalable sugar-polyolefin Frank-Kasper A15 phase. *Angew. Chem. Int. Ed.* **2020**, *59*, 1521-1526.

5. **Wentz, C. M.**; Lachmayr, K. K.; Tsai, E. H. R.; Sita, L. R., Thermotropic Glycolipid Quasicrystal and Frank-Kasper Phases: Unique Mechanism for Rapid Phase Transitions, *(manuscript in preparation).*

6. **Wentz, C. M;** Tsai, E. H. R.; Yager, K. G.; Gonzalez-Lopez, L.; Diethrich, T. J.; Al-Sheikly, M. I.; Sita, L. R. Mesophase Engineering of Perylene Bisimide Polyolefin Conjugates: From Columnar & Optically Active Single Gyroid Nanostructures of Neutral & Radical Anions to Luminous Liquids & Waxes, (*manuscript in preparation*).

7. **Wentz, C. M.**; Burgenson, W. R.; Sita, L. R., Controlling Crystallinity Through Copolymerization of 1,5-Hexadiene and 1,6-Heptadiene, (*manuscript in preparation*).

8. Grosvenor, E. C.; Hughes J. C.; Stanfield, C. W.; Blanchard, R. L.; Fox, A. C.; Mihok, O.L.; Lee, K.; Brodsky, J. R.; Hoy, A.; Uniyal, A.; Whitaker, S. M.; Acha, C.; Gibson, K.; Ding, L.; Lewis, C. A.; Lopez, L. G.; **Wentz, C.M.**; Sita, L. R.; Al-Sheikly, M. On the Mechanism of Pulsed Electron Beam Radiation-Induced Modification of Poly(lactic Acid) for Applications in Biodegradable Food Packaging. **2021,** *12*, 1819.

Chapter 1: Introduction to Polymerization and Polyolefin Materials

1.1 Introduction to Polymerization

1.1.1 Ziegler-Natta

It is inarguable that most technological advancements of this 20th century have been the development of plastics. So much so that as a society we produce over 350 million metric tons annually.[1] There is no limit to how we utilize plastics in everyday life, from the more obvious packaging, toys, shipping, to the less obvious medical equipment, electronics, and textiles. It is this versatility that allows us to make new material developments and make new advancements. Though the plastic revolution began as early as 1920s we owe our thanks to Karl Ziegler and Giulio Natta who discovered group 4 transition-metal catalysis which made polymerizing ethene and propene industrialized. Their methods used milder conditions such as decreases temperatures and pressure restrictions. Ziegler and Natta's work has led to the design of a large variety of catalysts that have influenced the industrial scale production of commodity plastics such as high-density polyethene (HDPE) from a titanium-based catalyst.[2-4] In 1963 they were awarded the Nobel Prize in Chemistry for their efforts and discoveries that have made the world we live in today possible.

The first generation of Zeigler catalyst dates back to 1953 were titanium tetrachloride ($TiCl_4$) with diethyl aluminum chloride (Et_2AlCl) was utilized as a co-

catalyst for the production of polypropylene with a 90% isotactic microstructure.[2,4] The most widely accepted mechanism for the Ziegler-Natta process was proposed by Cossee and Arlman,[5,6] Scheme 1.1, were the insertion of a single ethylene monomer, into a growing polymer, is polymerized with $TiCl_4$ followed by the transfer of one of the ethyl groups from the $AlEt_3$. First, coordination to the π-conjugated olefin to the metal center occurs and forms a η2-olefin adduct. Next Migratory insertion of the olefin into a polymer chain through a four-membered transition state facilitates the chain growth and generates an open coordination site for the next ethylene unit. This process repeats until chain termination occurs by quenching or by another chain terminating process.

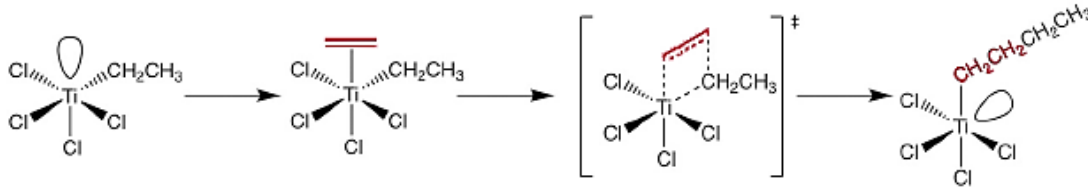

Scheme 1.1 Cossee and Arlman mechanism for the Zeigler-Natta process, showing the insertion of ethene monomer using heterogeneous $TiCl_4$ catalyst.

There were many generations of $TiCl_3$ based catalyst developed due to the wide success of Ziegler-Natta work. Such as catalyst were $MgCl_2$-supported were the $MgCl_2$ had improved activity, stereoselectivity, and allowed for reduction in the amount of titanium needed to do polymerizations thanks to its internal and external donors. While these heterogenous catalyst played an important role in the industrial production of polyolefins it was not until developments with group IV transition metals that the production of polymers of high yield, low polydispersity, and lowed by-products was achieved. Despite the success of heterogeneous catalysis there are many limitations:

(1) lack a defined active site, (2) tailored catalyst design is difficult, and (3) polymers produced often suffered broad molecular weight distribution and were difficult to characterize.[7]

1.1.2 Homogeneous Metallocene Complexes

In an effort to provide better control over polymer architectures and compositions the development of metallocene based catalysis began in the 1980s.[8] To start Sir Geoffrey and Wilkinson developed titanocene dibromide zirconocene dibromide (Cp_2Br_2), and since then the discoveries of metallocene for polymerization has been extensive.[7,9] Generally, metallocene catalysts have a formula of Cp_2MX_2, (Cp= cyclopentadienyl; M = metal often time Ti, Zr, of Hf based; X = can be either a methyl or a halide group). The catalyst is activated by an alkyl aluminum co-catalysts such as triethyl aluminum ($AlMe_3$) through the process of alkyl group abstraction. However, there was many issues when it came to polymerization with metallocene's including decreased rates, inability to polymerize propene, and failed polymerizations of any higher olefins.[12] It was not until Sinn and Kaminsky work with metallocene/$AlMe_3$ systems and small amounts of water that there was increased activity.[7,10] The breakthrough with water allowed the formation of methyaluminozane (MAO) to assist with polymerizations and while the exact structure and role of MAO is not yet fully understood one function of the MAO is hydrolysis of $AlMe_3$.[7,11]

As olefins monomers branched beyond ethene, they began to have the attractive feature of pendant chains whose orientation along the polymer backbone lead to

different stereochemical configuration (tacticity) to occur and with that came a change in overall property of the polymer material. Figure 1.1 presents different microstructures for polypropylene (PP) and the corresponding characteristics of isotactic and atactic PP.[13-17]

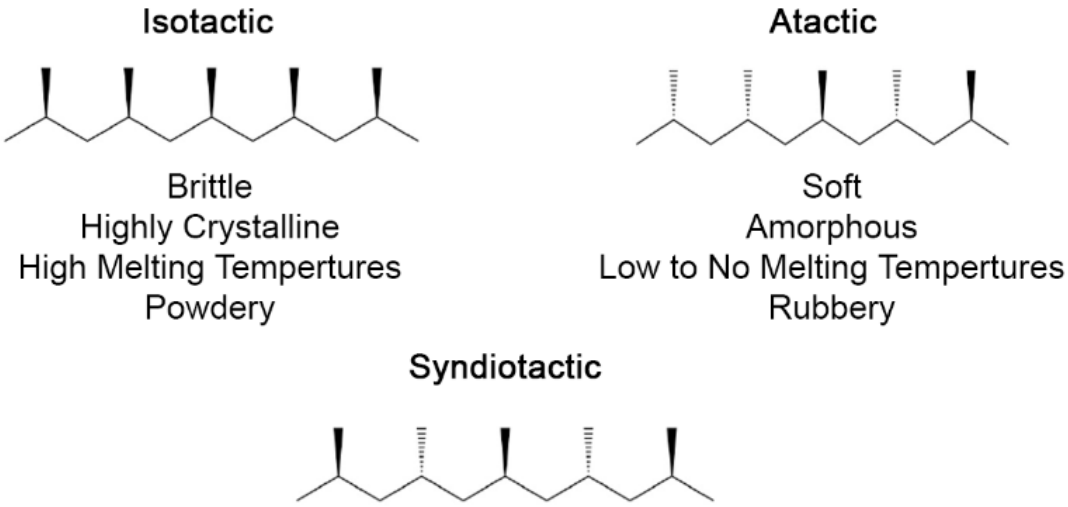

Figure 1.1 Stereochemical microstructures of polypropylene.

While metallocene systems were groundbreaking they had problems controlling the stereoregularity within the polymer thus limiting the scope of properties a single monomer type can possess. However, two major developments in stereoselective catalysts changed the field of metallocene chemistry and offered control over the tailoring of the polyolefin microstructure: (1) incorporating different alkyl groups into a cyclopentadienyl ligand allowed for higher levels of enantiomorphic site control to produce stereoselective polymer, (2) metallocene symmetry such as chiral or stereo-rigid nature gave the greatest control over the olefins insertion.[18-21] De Rosa and coworkers are a great example of *ansa*-bridging metallocene catalysts that

stereocontrol the insertion of the olefin through the *ansa*-bridging moiety effect on locking the rotation of the configuration thus making it C_1-symmetric. Consequently, this allowed for isotactic PP to be yielded free from regioerrors thus creating a range of stiff-plastics with high melting points and thermoplastics with flexible behaviors, as well as thermoplastic elastomers with high tensile strength.[7,12,22] While these *ansa*-bridged metallocene's do offer a range of polyolefin materials, they lack usefulness on an industrial scale due to complex synthesis of the catalyst itself and expense of the ligand structure. Furthermore, the biggest limitation lies in the 'one catalyst, one material' motif where one would have to make multiple expensive synthetically difficult catalysis to create stereogradient of materials.

1.1.3 Living Polymerizations

Modern synthetic polymer chemistry is contingent upon living polymerizations. Description of living polymerization are those where chain growth occurs at the same rate for all polymer chains and will continue without irreversible chain transfer or termination pathways. When these conditions are met it allows for precise control over the molecular weight of the polymer and introduces the possibility of end-group functionalities to be added through quenching methods. The earliest description of polymerization described as living date to Flory's polymerizations of ethylene oxides and since then has been applied to a wide range of different polymerization techniques.[23-29] Within the current work living coordinative polymerizations will be discussed and are categorized as such through seven criteria. It is important to note that

if these criteria are met polymer materials resulting will contain narrow molecular weight distributions where the dispersity, $Đ$, approaches but never can reach 1.00.[25]

1. Rate of initiation (k_i) must be greater than rate of propagation (k_p) thus polymerization will proceed until all monomer is consumed, and the addition of subsequent monomer will result in further chain growth.
2. The number average molecular weight (M_n) increases linearly as a function of monomer consumption.
3. The number of active sites present remains consistent for the length of the polymerization.
4. Molecular weight can be precisely controlled stoichiometrically.
5. Polymers yielded have narrow molecular weight distributions where $M_w/M_n \sim 1.00$
6. Block copolymers can be polymerized through sequential monomer addition.
7. End-group functionalization is attainable.

The ability to have polymers with narrow dispersity is the most defining attribute of living polymerizations. The number average molecular weight is described as the total weight of the sample divided by the number of molecules within the sample, Equation 1.1. Where the ordinary arithmetic mean is labeled as $N_{i,}$ and polymer chains molar mass is labeled M_i.[30] The weight-average molecular weights is described as the weighted mass fraction of each molecule relative the whole sample, Equation 1.2. Dispersity is defined by the ratio of the weight average molecular weight and number average molecular weight, Equation 1.3.[31]

Equation 1.1 $$\boldsymbol{M_n = \sum_i \frac{\sum_i N_i M_i}{\sum_i N_i}}$$

Equation 1.2 $$\boldsymbol{M_w = \sum_i \frac{\sum_i N_i M_i^2}{\sum_i N_i}}$$

Equation 1.3 $$Đ = {}^{M_w}/_{M_n}$$

The overall molecular weight and dispersity withing the polymer strongly influences the physical properties of the material, such as melting point (T_m), glass transition temperature (T_g), solubility, viscosity, chain entanglement, radius of gyration, and mechanical strength.[32,33] Therefore, it is important when considering a polymerization method to consider the system/ property relationship. Tying it back to heterogeneous Ziegler-Natta catalysts they generally had *Đ* values that ranged from 3 - 20.Whereas, stereoselective metallocene catalysts accessed materials with *Đ* values closer to 3.00. While 'living' systems have been able to target *Đ* closer to 1.00.

It is important to note that the rate of chain transfer will always be greater than the rate of propagation but as the reaction proceeds with time the rate of propagation will change. Specifically, the rate of propagation will slow down toward the end of the reaction thus generally speaking the dispersity of the material also changes as a function of time. Even at incredibly low degrees of polymerization one can achieve low monodispersity. Furthermore, the dispersity will become even more narrow as propagation slows.

1.1.4 Living Coordinative Polymerization

Living coordinative polymerization (LCP) is distinguished by the ability to control the polymer in terms of dispersity, molecular weight, microstructures, and molecular architecture of the polymer. Difficulties in LCP development arose from early termination pathways.[34,35] Scheme 1.2 presents several chain termination pathways from the LCP of ethylene. To begin,

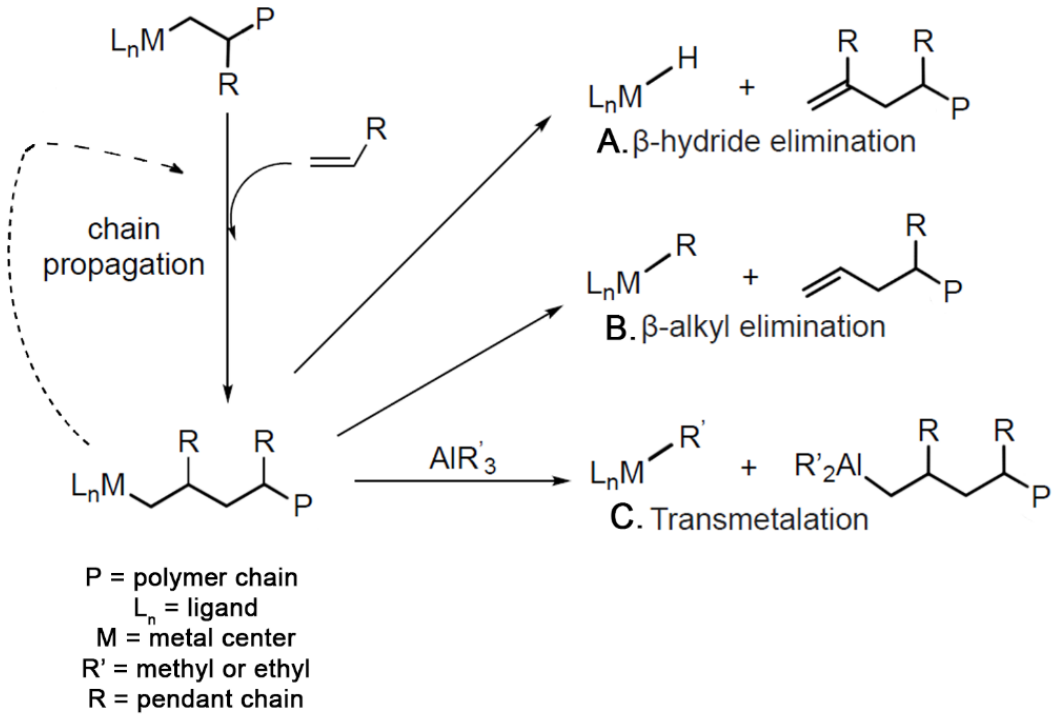

Scheme 1.2 Examples of termination pathways from LCP.

(A) and (B) in Scheme 1.2 depicts β-hydrogen elimination that process either through transfer to the metal (A) or direct transfer to monomer (B). Presented in (C) is the pathway for chain termination through σ-bond metathesis called transmetalation.[34,35,36]

To utilize LCP without these early termination pathways the use of borate co-catalyst in place of alkyl aluminum has proven successful.[37]

In 1979 Doi and co-workers reported the first LCP from group IV vanadium catalysts with a general form of [V(acetylacetonate)$_3$] activated through Et_2AlCl and produced syndiotactic PP with narrow molecular weight distribution.[38,39] Limitations in this study were that living character was only achievable below -65 °C, had very few monomer insertions, and only 4% of vanadium centers were active.[38,39] More recently, the development of group VI transition metal catalysts with LCP has been reported for a number of α-olefins, α,ω-nonconjugated dienes, and cyclic monomers.[37] Such as systems developed by McVonville,[40,41] Kol,[42] Schrock,[43] Coates,[44] and Sita.[45] The Sita group present not only LCP systems but also utilize ethene, propene, higher carbon number linear and branch chain α-olefins, and also α,ω-nonconjugated dienes through a family of group VI cyclopentadienyl amidinate complexes (CpAM). These CpAM catalyst act as initiators for LCP to produce high yielding, one-pot synthesis, that provides narrow dispersity, tunable degrees of polymerization (DP_n), and targeted molecular weights. With such a system employed it offers considerable control over tailoring stereochemical microstructures of the polyolefin materials.

Within the Sita Group the general structure for CpAM catalysts is presented in Figure 1.2A where these initiators are activated by a borate co-initiator

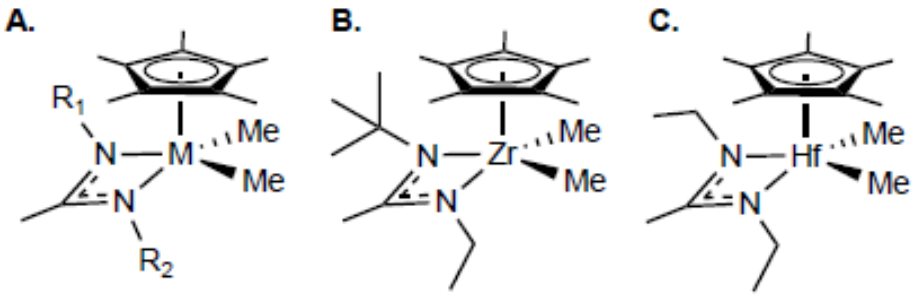

Figure 1.2 General structure of CpAM catalysts.

[PhNMe$_2$H][B(C$_6$F$_5$)$_4$] (B1) at ambient and sub-ambient conditions. The design of the *C$_1$*-symmetric Zr pre-initiator, [Cp*ZrMe$_2${*N*-(*t*Bu)C(Me)N(et)}], in Figure 1.2B, preforms stereoselective LCP to produce isotactic polymers.[45-47] This pre-initiator with LCP technique has led to not only a number of homopolymers but also di- and tri-block copolymers.[48,49] LCP technique with Zr pre-initiator only lead to stereoregular polyolefins and it was of interest to modulate that stereoerrors in the polyolefin microstructure to generate a range of polyolefins with different stereochemical grades. Thus two-state stereomodulated LCP was developed.[46,50-57] These techniques of stereomodulated LCP is a degenerative group transfer process where a fast reversible methyl or chloro group transfer occurs between a population of *x* active propagators and a population of *1-x* dormant species that are created due to sub-stoichiometric activation of the pre-initiator species, Scheme 1.3. The dormant species metal-center

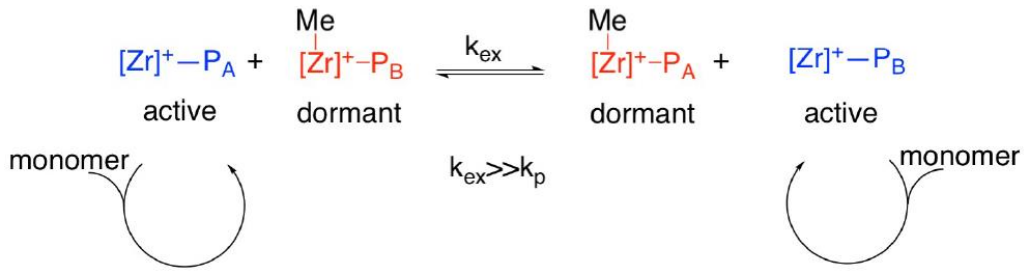

Scheme 1.3 Mechanism of two-state stereomodulated LCP.

can epimerize and therefore change stereo-directive control and inserts stereoerrors into the polymer chain.[50-57] When utilizing this system, it has been shown to produce stereoblock polyolefin materials with tunable block length.

1.1.5 Living Coordinative Chain Transfer Polymerization

Despite all that LCP and living degenerative group-transfer offers, there is still a limitation and dependence on expensive transition metal catalysts and 'one chain per active site' motif. When the addition of a chain transfer agent (CTA), such as diethyl zinc ($ZnEt_2$), is added to the polymerization system it increases the number of polymer chains a single cite can produce, thus acting as a surrogate metal to the catalyst. This process is known as living coordinative chain transfer polymerization (LCCTP), Scheme 1.4. LCCTP allows for much larger quantities of narrow dispersity, tunable molecular weight, polymers to be synthesized. In 2008, Sita and co-workers demonstrated that LCCTP with C_s-symmetric hafnium catalyst [Cp*$HfMe_2$[N(Et)C(Me)N(Et)], Figure 1.2C, activated by the borate co-initiator with

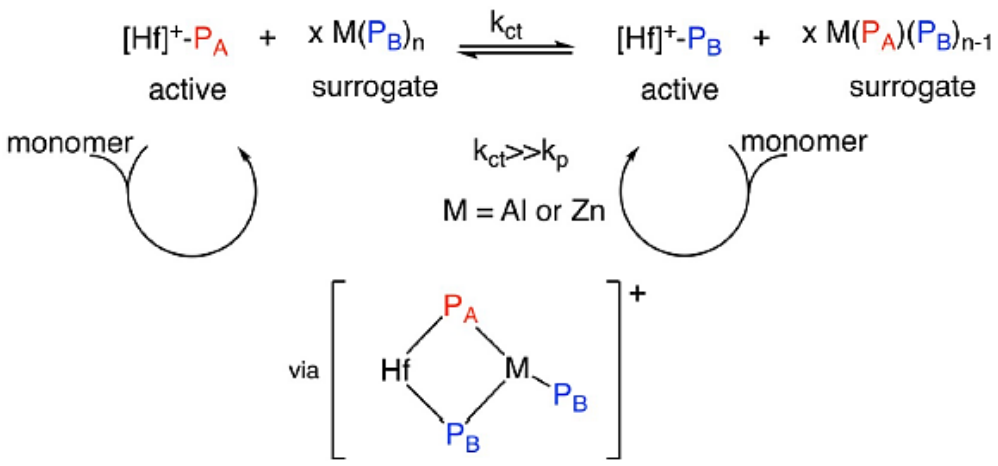

Scheme 1.4 Mechanism of LCCTP

$ZnEt_2$ produced completely atactic amorphous polypropylene.[58,59] The success of the LCCTP process relies on the fast and reversible polymeryl group transfer between active Hf center and the CTA. The rate of chain transfer (k_{ct}) is much greater than the rate of chain propagation (k_p). In order to target a molecular weight for the polymer (M_w) Equation 1.4 can be used where equivalents (eq.) of monomer and CTA, and M monomer molecular weight, and n_i number of chain sites on CTA are important.

One of the most useful aspect of LCCTP is the ability to produce end-group functionalized poly(α-olefinate) (xPAOs) through various X-Y reagents talked about in in detail the next section.

Equation 1.4 $$M_w = \frac{(Eq.monomer)(M\ monomer)}{(Eq.CTA)(n_i)}$$

1.2 Introduction to Polyolefin Building Blocks

The precise polyolefins made through LCCTP can act as non-polar building blocks to be utilized in molecular conjugate systems, to create a larger recyclable polymer, or as unique homopolymer materials. In general, end-group functionalization is of great importance because they offer further opportunities to create unique molecules with a wider range of applications. Within the work herein polyolefins synthesized through LCP and LCCTP are utilized as building blocks, if functionalized, or unique polyolefin materials if not functionalized.

1.2.1 End-Group Functionalization

In this work the most common end-group functionalization involves termination with elemental iodine (I_2) for further substitutions to azido-termination, and reduction to amino termination, see Figure 1.3. More specifically, the azido-terminated polyolefins were utilized with sugar head-groups to establish the sugar polyolefin conjugates. While the amino terminated polyolefins were used with perylene chromophore cores to establish the perylene bisimide conjugates. Each aspect of the polyolefin is tuned for specific properties and treated as a building block that can be used with another molecular component.

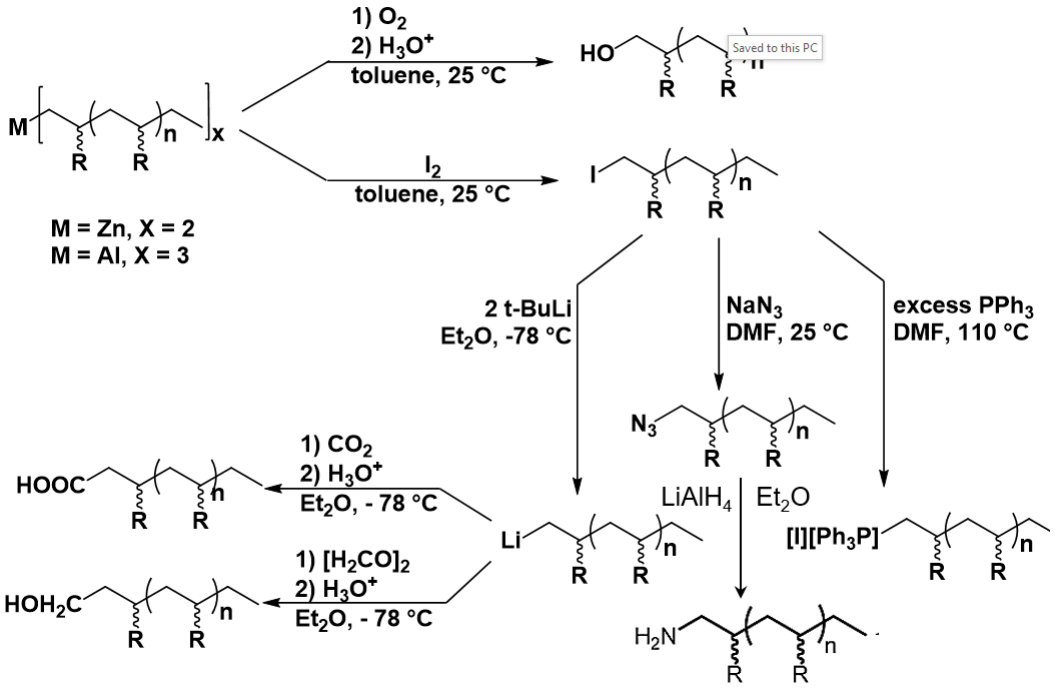

Figure 1.3 Synthetic routes for xPAOs from LCCTP.

Proven here, and in previous studies done by this group, the xPAOs can function as non-polar building blocks for a variety of conjugate systems. These materials have shown to undergo microphase segregation to several classical and nonclassical phases discussed herein. [60-65] More recently, these xPAOs have been synthetically engineered to contain bifunctionality meaning that there are functional groups on both end of the polyolefin domain.[66] This was accomplished through utilizing diphenyl zinc ($ZnPh_2$) CTA while iodo quenching the reaction. This allowed for a phenyl group to end cap one end of the chain and an iodine the other. From there simple synthetic modifications allowed for an alcohol group to take the place of the iodine, more information in Chapter 5. These telechelic polyolefins can also act as non-polar building blocks and have been investigated for the purpose of creating reversible/ recyclable polymers that

break back down into the telechelic polymers rather than all the way to the monomer unit. This allows for a faster and more energy efficient recyclability where the polymerization step can be skipped.

1.2.2 Characterization

The key factors to determine physical properties within polymers are: (1) chemical composition which can be elucidated through nuclear magnetic resonance (NMR), (2) molecular weight and dispersity which can be understood through gel permeation chromatography (GPC), and (3) glass transition temperature or melting temperature which can be observed through differential scanning calorimetry (DSC). NMR is used frequently throughout the investigation in this work to explain the microstructure of the polymer chain. Since the goal of many studies is to influence the stereoregularity of the polymer it is important to note that not all carbon NMR studies can do so quantitatively and sometimes can only offer a qualitative analysis. When it comes to functionality of the polymer NMR offers the ability to track the change in functionality due to the shift of the alpha protons peak located next to the functionality, see SI for each chapter for peak shifts and peak profile changes. Lastly, NMR offers a rough estimate of the molecular weight of the polymer using the alpha peak integrated against the broad peaks for the rest of the polymer chain. This is extremely useful for polymers that are insoluble in solvents and unable to be characterized by GPC.

When it comes to a more accurate measurement of molecular weight of the polymer GPC is useful not only in telling the length of the polymer chain but the

dispersity of the polymer material itself. Take Figure 1.4 for example, despite having the same number-average molecular weight, red line and black line, the high molecular weight chains in the broad sample (red line) have a higher dispersity and effect the polymers overall physical properties such as viscosity, chain-entanglement, and can limit its use in certain applications or as a xPAO building block.[67] The green line represents a bimodal profile which even more so represents completely two

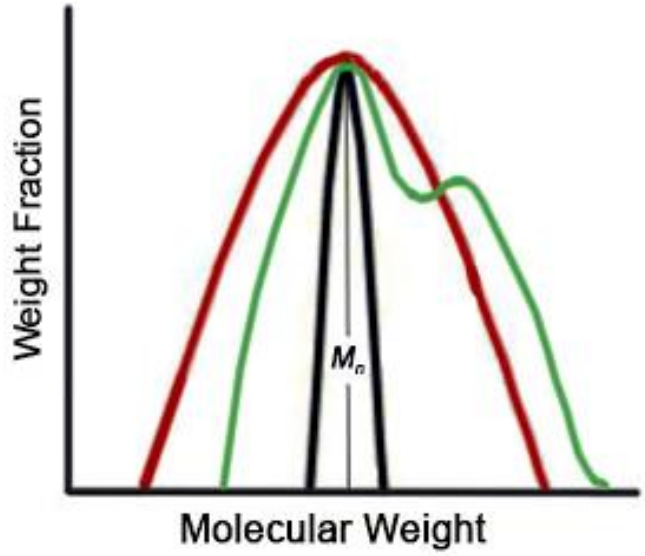

Figure 1.4 Weight distribution curves for three theroetical samples. Red and black lines represent samples of equivalent number-average molecular weight but different dispersities while green lines represents a bimodal separate species.

different species of polymer existing within the material. Other than molecular weight and dispersity of the polymer GPC can also help understand the polymerization conditions and if anything is incorrect. For example, if the molecular weight does not match the targeted molecular weight for the reaction this can mean several things including that the polymerization did not go to completion, that the catalysts system was not fully activated, or the monomer feedstock was not properly added to the reaction mixture. If the dispersity of the materials is large this could be due to improper

activation or inhomogeneous reaction mixing. It is important to note that the disparities of lower molecular weight polyolefins are higher since the rate or propagation is at its fastest at the beginning of the polymerization. Even though the rate of chain transfer will be greater than propagation the ratio is larger due to the speed of propagation. Lastly, if the polyolefin has difficulty with solubility the dispersity can also be incorrectly measured by the GPC to be larger than it is. High temperature GPC can be utilized instead from materials that are insoluble at room temperature.

The mechanical properties, processability, and phase separation of the polymers and conjugates have a strong dependency on the temperature transitions within the polymer. For example, within hard-soft block copolymers if the hard domain has a low melting temperature (T_m) and the soft domain has a high glass transition temperature (T_g) there might not be enough dissimilarity between the two domains to phase separate. Additionally, cold crystallization temperature (T_c) can be observed in semicrystalline to crystalline polymers, Figure 1.5.

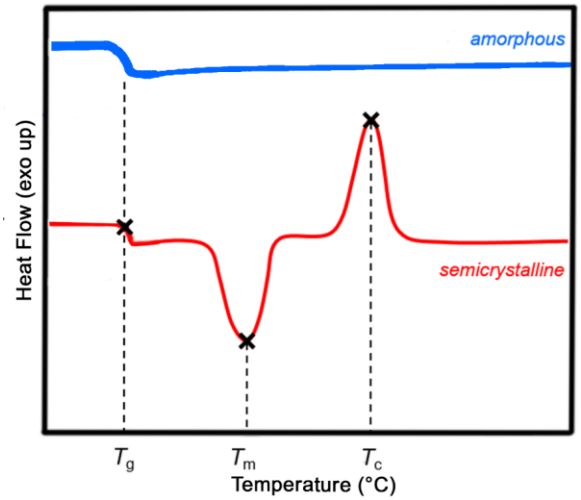

Figure 1.5 DSC trace of theroetical amorphous (blue) and semicrystaline (red) polymers with glass transition temperture (T_g), melting temperture (T_m), and cold crystallization temperture (T_c) labeled, where exo is up.

All three of these characterization techniques are utilized to understand the physical characteristics of the polymers made and are employed as a way to design the physical properties or phase behavior of the materials. These techniques help problem shoot the design of the polymers themselves as well as the synthesis.

1.3 Introduction to Self-Assembly

All living creatures are depended on the self-assembly and complex folding of proteins and DNA. Furthermore, advancements in supramolecular chemistry are reliant on self-assembly of the material as a multitude of applications rely on this behavior: technology, catalysis, medicine, biomedical engineering, nanopatterning, and much more.[68-74] This being known the structure and function of a material are heavily intertwined with the self-assembly on a molecular or macromolecular scale. Understanding and observing self-assembly within a material is not a trivial pursuit. Even the smallest of differences within the structure or properties of a compound can result in drastically different microphase separations. In order to design new self-assembling materials, it is important to understand what governs self-assembly and be able to utilize that knowledge to apply it to a designable motif.

This introduction will present briefly different types of packing systems and models for ‘classical’ and ‘non-classical’ phases. The polyolefin-based conjugates and materials made within the body of this work are classified as thermotropic solid-state soft matter materials and systems described within this introduction will focus on materials of the same or similar classification. It is important to note that many past

investigations into phase separation have relied upon 'shooting in the dark and hoping to hit a target' method to formulate predictions or theories and it is of importance to understand the rules and requirements of self-assembly in a more systematic way to help advance technologies among many other applications.

Molecular self-assembly is reliant upon spontaneous association of molecules through noncovalent interactions, without external driving force, to result in stable phase separated 'aggregates'.[71] Some of those non-covalent interactions could be forces such as hydrogen bonding, hydrophobic interactions, electrostatic interactions, $\pi - \pi$ interactions, van der Waals forces, and others, Table 1.1.[75,76] The fundamental thermodynamic principle of self-assembly is the presence of favorable enthalpic driving force that is strong enough to overcome an unfavorable

Table 1.1 Summary of supramolecular interactions for macromolecular self-assemblies. Adapted with permission from Su, Z. B. *et al.* The role of architectural engineering in macromolecular self-assemblies via non-covalent interactions: A Molecular LEGO approach. *Prog. Polym. Sci.* **2020**, *103*. Copyright 2020 Elsevier.

Interactions	Length Scale	Energy (kJ/mol)
Van der Walls	Several Å	< 5
Hydrogen Bonding	1.5 – 2.5 Å	40 – 60
Halogen Bonding	2.6 – 3.6 Å	10 – 150
Ion-Ion interactions	1 – 100 Å	100 – 350
Ion-dipole interactions	1 – 100 Å	50 – 200
Dipole-Dipole Interactions	1 – 100 Å	5 – 50
$\pi - \pi$ Interactions	3 – 4.5 Å	0 – 50
Hydrophobic Effect	N/A	N/A

entropic contribution from the increase in organization, leaving the structure existing at a thermodynamic minimum at equilibrium.[75] This ultimately lowers the free energy of the arrangement compared to the unordered system.[76,77]

1.3.1 Surfactants

Surfactants are a class of amphiphilic molecules that readily self-assemble and are one of the most common and simplest examples of self-assembled systems. The term amphiphile comes from the concept that *amphi-* means 'both' in Greek, and -phile from *philia* means 'love'. Amphiphiles contain both hydrophilic and lipophilic parts meaning a portion of the compound is 'loves' water and the other portion of the compound 'loves' organic solvents.[78] Within this body of work sugar polyolefin conjugates closely resemble surfactants as the polar sugar head covalently bound to a non-polar polyolefin building block domains creates an amphiphilic material that phase separates in the solid-state.

To begin most surfactants, tend to be small organic molecules that contain a polar head-group that can be zwitterionic, cationic, anionic, or nonionic.[79] Self-assembly studies of surfactants often take place in solution to help induce the phase separation due to the incompatibility between a hydrophobic region and polar solvent. When above the critical aggregation concentration (CAC) these surfactants will reversibly and dynamically adopt different conformations in order to minimize unfavorable interactions. For example, in aqueous solutions the polar head-group of the surfactant will orient itself on the exterior and self-assemble so that the interior of the structure, made up of the hydrophobic region, avoids interaction with that solution. This dispersal of the cohesive energy is favored during this self-assembly.[79] There are many shapes these aggregates can form, Figure 1.6, and the shape is strongly influenced by the environmental parameters such as temperature, concentration of solution, and pH.[80] Because of the behavior and ability to reduce interfacial tension within liquids is

why they are called surfactants, 'surface active agents' and are often utilized in cleaning products, personal-care products, detergents, emulsifiers, and drug delivery systems.[81,82]

Today, the self-assembly of surfactants proposed methodology has been headed by two groups, first being Tanford and the second being Israelachvii and co-workers Mitchell, and Nanham. Tanford proposed the concept of opposite forces in order to formulate a quantitative expression for the free energy change during aggregation.[83-85]

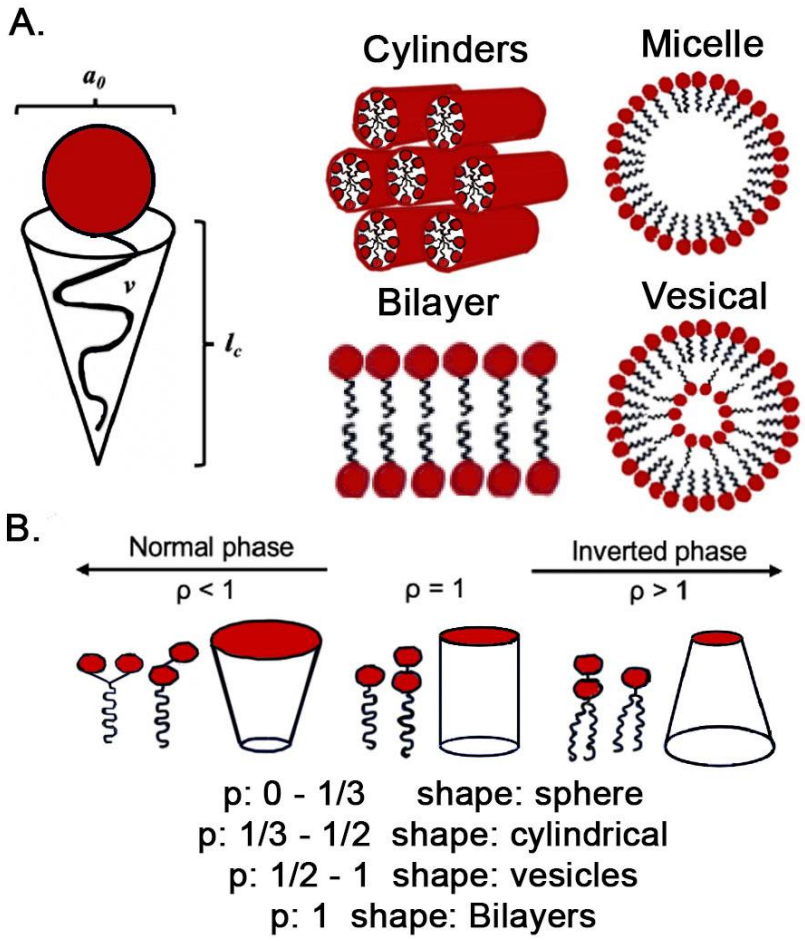

Figure 1.6 (A) Surfactant self-assemblies based on packing parameter *p*. (B) General structures of glycolipides where red represents the polar head group and the black represents the non-polar polymer chains.

While Israelachvii *et al.* clarified how the molecular structure of surfactants control the shape and size of the aggregates observed.[86] This proposal relied on a geometry-based molecular packing parameter, and allowed one to predict the size and shape off the aggregate from a combination of the molecular packing parameters and thermodynamic principles.[75] This parameter is known as the packing parameter *p*, which is equal to the volume of the tail (v) divided by the product of area of the polar head group (a_o) times the length of the tail (l_c). Therefore, $p = v/a_o l_c$ and the ratios between these variables predict the corresponding self-assemblies, Figure 1.6. Each self-assembled structure contains a different way in which the material can be utilized. For example, micelle and vesical aggregates are particularly useful in drug delivery systems. Relevant to today's continued pandemic with Covid-19 one of the major limitations to getting the vaccine to be distributed world-wide was its stability at room temperature. The vaccination had to be delivered in specific packaging and kept cold even when transportation would take it through all different outdoor climates. A surfactant that is safe for the human body that could encapsulate the vaccination for Covid-19 could propose as a helpful tool in the overall stability and handling of the vaccination. This is just one relevant example of how surfactants and the self-assembly of the materials can affect our society.

There are cases were amphiphiles (other than surfactants) can self-assemble without solvent known as amphitropic. Regardless, these types of amphiphiles that are amphitropic follow similar packing parameters proposed by Israelachvii and co-workers.[87] For a lyotropic system, as amphiphile concentration increases the phases observed can change from micellar ($Pm\bar{3}n$, $Im\bar{3}m$, $Fm\bar{3}m$, and $Fd\bar{3}m$), to columnar, to

lamellar, then cubic (Ia$\bar{3}$d, Pn3m, and Im$\bar{3}$m). When it comes to thermotropic amphiphiles there is less understood, and no proposed phase diagram has been documented. In general, for liquid crystal amphiphiles there is a suggested correlation with the increase in interfacial curvature. The proposed relationship follows that a smectic A phase will be first observed, then bicontinuous cubic phase, followed by a columnar phase, and ends with a micellar cubic phase.[88] However, there are many factors that change the mesophase for a thermotropic systems such as chemical composition and temperature of the material.

1.3.2 Model for Classical Phases in Block Copolymers

Block copolymers (BCP) make up a large classification of molecules with the general definition being, made up of two or more immiscible or chemically distinct blocks covalently linked together. Figure 1.7 displays the wide array of structures BCPs can possess. The structural covalent bond that links the immiscible or chemically distinct domain together prevents macrophase separation and instead microphase separates into many unique morphologies. The simplest and comprehensible study of AB-type BCP allows one to predict and understand what ‘classical’ morphologies a material can obtain. For BCP that contain hydrophilic and hydrophobic blocks that

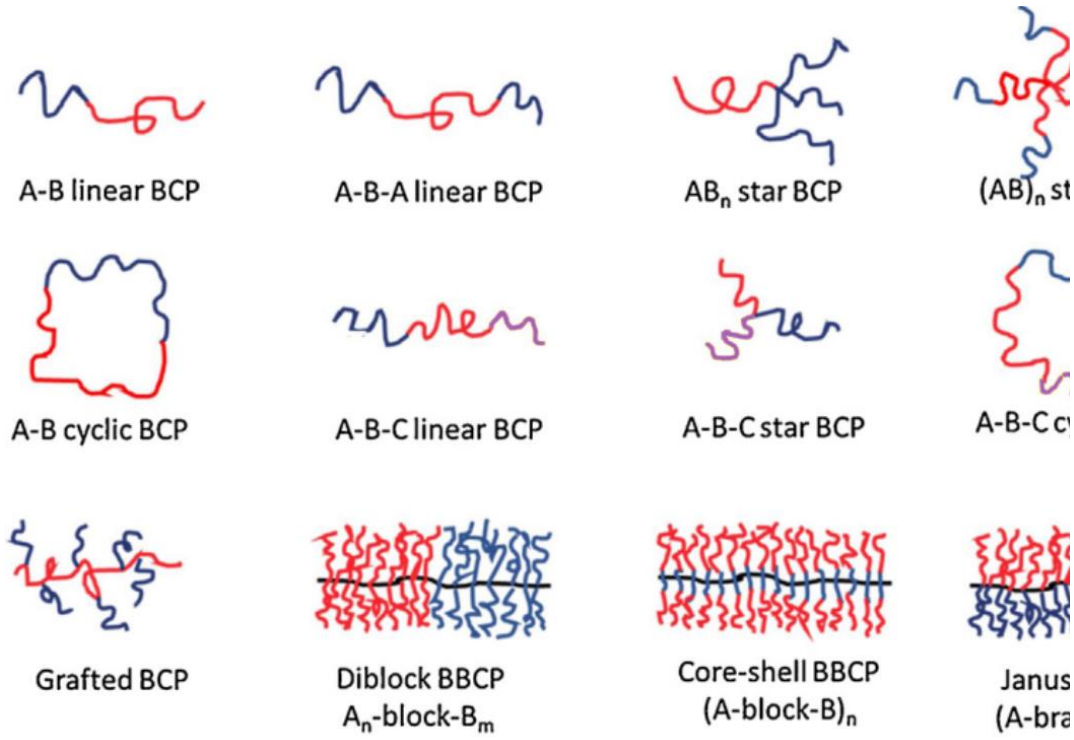

Figure 1.7 Different molecular architectures for block copolymers. Adapted with permission from Su, Z. B. *et al.* The role of architectural engineering in macromolecular self-assemblies via non-covalent interactions: A Molecular LEGO approach. *Prog. Polym. Sci.* **2020**, *103*. Copyright 2020 Elsevier.

repel one-another, without solution, one can see the formation of block-selective separation and self-assemblies as a result of this unfavorable mixing enthalpy and small mixing entropy.[89] Flory-Huggin's theory explains coil-coil binary polymer mixtures to model and describe the mixing and de-mixing of polymers through the Flory-Huggins interaction parameter, χ, Equation 1.5. This parameter describes the nonideal mixing free energy or in other words the degree of incompatibilty between blocks within a BCP by the free energy cost of the contact between disimilar blocks, A and B.[30,90,91] Where z represents the number of nearest-neighboring monomers. The symbols ε_{AB}, ε_{AA}, ε_{BB} are the interaction energies between the differeing monomer types, while k_BT

is the Boltzmann constant and T is the temperture. The value of χ is usually very small and positive and inversly related to temperture of the system since increases tempertures promotes the mixing of the system.

Equation 1.5 $$\chi_{AB} = \left(\frac{z}{k_{BT}}\right)\left[\varepsilon_{AB} - \left(\frac{1}{2}\right)(\varepsilon_{AA} + \varepsilon_{BB})\right]$$

Leibler in 1980s proposed a new model for coil-coil BCPs and it was based on three main factors. Leibler utilized the parameters χN and volume fractions for each block to generate a phase diagram that predicts the morphologies of BCPs.[92]

1. The sum of the degree of polymerization of the blocks (N) is equal to the degrees of polymerization for each repeating monomer unit within each block where A and B are different blocks : $N = N_A + N_B$.

2. Flory-Huggin's interaction parameter, χ.

3. The volume fraction for each block adds up to 1: $f_A + f_B = 1$

To describe additional morphologies that can be observed with BCP self-consistent mean field theory provides a more complete depiction of diblock copolymer phase behavior where bicontinuous gyroid phase is now included.[93,94] Masen *et al.* developed the phase diagram adapted in Figure 1.8, which includes a graphical representation of the competition between interfacial energy of incompatible block interactions and resulting mesophases observed. These phases are driven by both enthalpically effects and entropy loss due to chain stretching and organization during

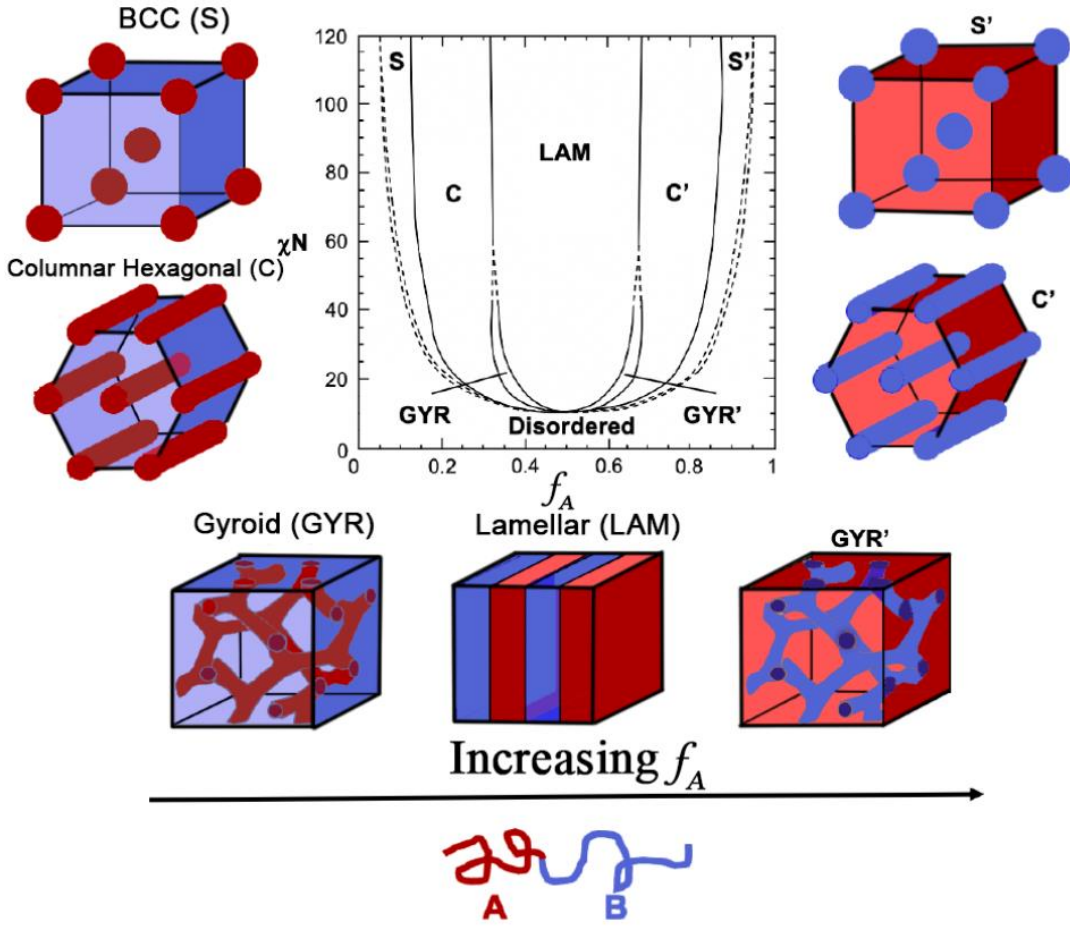

Figure 1.8 Theoretical phase digram for linear AB-type BCPs predicted by self-consistent mean-field theory. Surronding the graph is the classical morphologies: body centered cubic (S), columnar hexagonal or hexagonaly packed cylinders (*C*), bicontinous gyroid (GYR), and lamellar (LAM) as a function of volume fraction of block A in the AB-BCP.

phase separation process.[95] Because the χ value tends to be so small Leibler proposed that the total χN needs to be greater than 10.5 for phase separation to occur.[92] That being said, the smaller the polymer chains the smaller the feature size of the morphological pattern is. Therefore, specifically morphologies with sub-10nm domain spacing have been found to be useful in microelectronics with few examples in the literature able to achieve such small spacing.[96]

Within this body of work many materials, including BCPs, are explored for their self-assembly were the careful design of non-polar polyolefin building blocks are utilized to tune the phases observed. The self-assembly of the materials takes up two main goals of this work were (1) is to show the versatility of our scalable functionalized polyolefin (xPAOs) building blocks to systematic effect on phase separation, and (2) utilize the xPAOs with sugar-based conjugates and perylene-based conjugates to access rare and rich phase behavior while creating a methodology to access the phases observed.

1.3.3 Frank Kasper Phases

There are many types of materials that self-assemble and amongst those are metal alloys or other 'hard' matter systems. These types of systems can self-assemble into 'non-classical' phases such as Frank-Kasper (FK) phases.[97] These FK phases are classified as topologically close packing of atoms with different atomic radii, electronic states, shapes, or sizes. Frank and Kasper as early as 1950's studied these systems solely in 'hard' sphere phases where they discovered that these spheres most efficiently sort and pack into a coordinate number (CN) of 12 with three possible arrangements. The first being face-centered cubic (FCC) which is a cuboctahedra shape. The second involving a twinned cuboctahedra shapes for hexagonal close packing (HCP). The third being a topologically close packing (TPC) phase with icosahedron shape which comes from a distortion of the central atom in CN 12 to give a free energy minimum. This 12-coordination distorted icosahedra occurs when a polyhedra of larger coordination

number is grouped with it. These larger polyhedra have triangular faces and basic intersections of tetrahedral arrangement with slight distortions of atomic positions giving rise to CN of 14, 15, and 16, Figure 1.9. The FK phases contain a minimum of two of the four possible polyhedra, as the CN 12 distorted icosahedra alone does not have 6-fold symmetry. Within these polyhedra there are two types of bonds, or contact points, labeled as either a 6-fold or 5-fold vertices, Figure 1.9.[97,98]

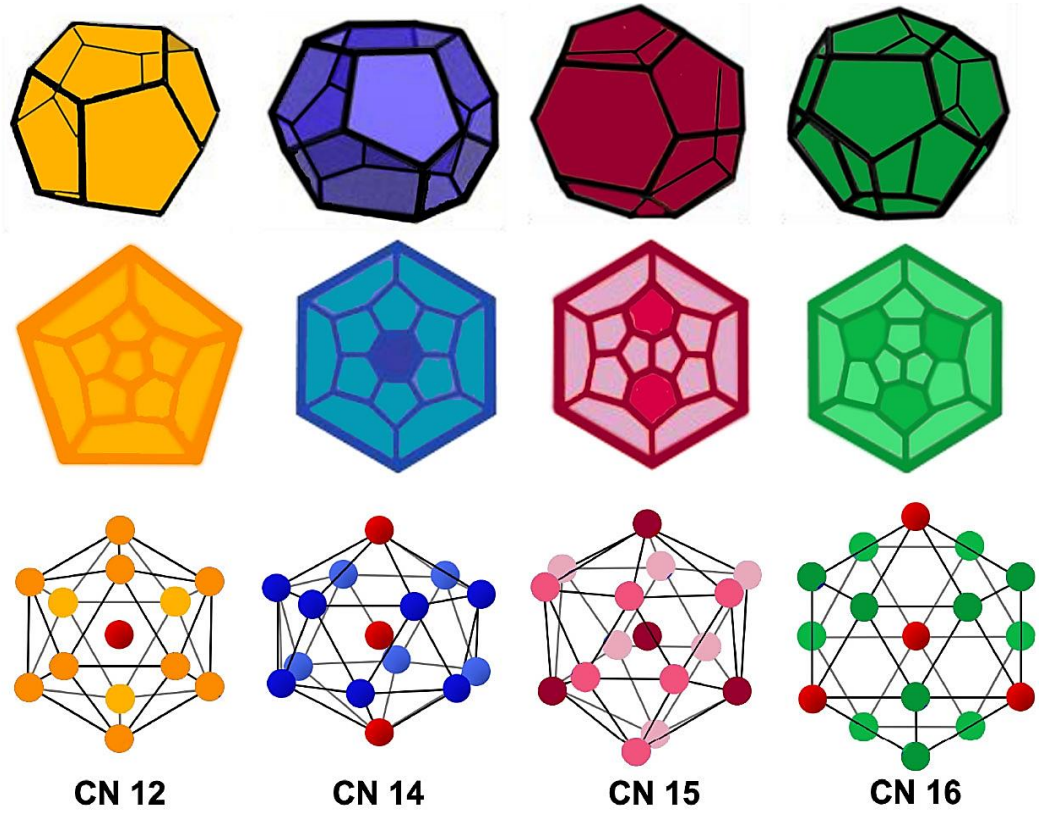

Figure 1.9 Frank-Kasper polyhedras (top) with CN 12, 14, 15, and 16. The 6-folg close connection are between the red spheres and neighboring atoms, and the 5-fold close connections are bewteen the red spheres and other colored spheres. The CN 12 icosahedron (middle) has 20 faces with no 6-fold connections. CN 14 (middle) has 24 faces with two 6-fold connections. CN15 has 26 faces (middle) and theww 6-fold connections. CN16 has 28 faces (middle) with four 6-fold connections.

Frank Kasper original metal alloys were found to have 27 known phases. For example, the cubic FK A15 phase contains the CN 12 and CN 14 polyhedra comprised of 8 atoms grouped into two sets, A_3B (Nb_3Sn). Other phases such as Laves C14 and C15 contain the CN 12 and CN 16 with general stoichiometry of AB_2, such as $MgZn_2$ and $MgCu_2$. When it comes to the tetragonal σ phase there are 30 atoms grouped into five sets with CN 12 and CN 14, and the other set is CN 15 polyhedra, (CrFe).[99] These metallic alloy phases are of important interest due to their useful properties in use in superconducting materials, such as in the FK A15 of Nb_3Sn material.[100]

Branching away from metallic alloys FK phases also have been observed in soft matter systems where the spheres are now comprised of deformable/ squishable cells that can form these complex phases, Voronoi or Wigner Seitz micelles. Overall, FK phases are thought to result from subtle competitions between thermodynamic enthalpic and entropic driving forces and molecular shape. FK phases in soft matter materials remain relatively rare with a difficulty resting in one's ability to systematically target phases and have those phases be long lasting. That being said FK phases such as A15, σ, C14 and C15 Laves, and Z phase are reportedly found in liquid crystals[101,102], dendrons[103], 'giant' molecules[104,105], block copolymers[106], small-molecule surfactants[107-109], and colloidal nanoparticles.[110] Within soft matter materials the most common FK phases to be observed include FK A15 and σ phase. These two phases both come from periodic approximations of different quasicrystals with rotational symmetry but no long-range translational periodicity.[111,112]

Within this body of work sugar polyolefins are observed to self-assemble into FK A15, σ, and dodecaquasicrystalline (DDQC) phases. The methodology behind the

phases observed within sugar polyolefin conjugates set new presidents for order-order transitions hypothesis. Dendritic liquid crystals provide a method for how materials can transition into hexagonal cylindrical phases then into spheres for the FK A15 phase. Generally, the molecular shape of the dendrimer or dendron controls the resulting supramolecular assembly which in-turn changes the yielding phases. For example, dendrons that have an overall wedge-shape generally assemble into columnar phases, whereas other form conical shapes.[113] An example of an early thermotropic dendritic liquid crystal, in 1997, was of a crown-ether tapped molecules that formed wedge shapes into columnar phases, and conical monodendrons formed spheres into FK A15 phase.[114,115] Since then, it has been widely excepted that having a material that has flexibility to both adopt a wedge and conical shape allows for FK phases to emerge.

While many soft matter materials can access FK phases and pieces of their methodology can be parallel the sugar polyolefin conjugates discussed herein. The sugar polyolefin conjugates represent the first soft matter thermotropic material with both remarkable stability and accessibility to many classical and non-classical morphologies such as FK phases .

1.3.4. Liquid Crystals

Liquid crystals belong to a unique group of soft materials because they exhibit a molecular organization that resembles aspects of both the solid state and the liquid state. To further understand this difference, in crystalline solids the molecules will display a long-range ordering at fixed positions at regular distances with a very specific

orientation. However, liquid crystalline materials demonstrate a unique intermediate state between anisotropic solids and isotropic liquids were the molecular shape of the material plays a significant role in the ordering and behavior of the materials.[116,117] It was believed that only rod-like molecules could display liquid crystalline mesomorphism, but in 1977 Chandrasekhar and co-workers reported a thermotropic single-component disc-like molecule.[118] This discovery opened up new understandings behind liquid crystal research. Disc-like molecules with polyaromatic molecules as a centered rigid cored that are surrounded by flexible tails often yield discotic phases, such as triphenylenes, hexabenzocoronene, and carboxyldiimido-perylenes. Materials with a perylene core are talked about in the investigations herein and fall under the category of disc-like liquid crystals. The morphology of these materials is due to the microphase segregation of the central rigid cores and the flexible tails. There are two main mesophases that are observed within these disc-like molecules: (1) nematic discotic (N_D), and (2) columnar phases (Col). In nematic ordering the molecules exhibit only orientational ordering whereas in columnar phases the molecules display both orientational and positional ordering. These columnar phases are often seen in these perylene based discotic phases due to the arrangement of the $\pi - \pi$ stacking interactions within the columns. Depending on the molecular organization and packing within these columns there are several subclasses of columnar phases such as columnar plastic, columnar rectangular, columnar oblique (Col_{ob}), columnar helical, columnar hexagonal (Col_{hex}), and columnar lamellar, Figure 1.10. Columnar hexagonal phase is the most common in disk-like molecules where several molecular columns arrange in a hexagonal fashion.[119,120] The columnar oblique phase consists of molecular columns

arranged in an oblique manner in which the columns are tilted. The occurrence of this phase is often dictated by the shape of the cores and is uncommon since it demands a strong core-core interactions within each column.[121-123]

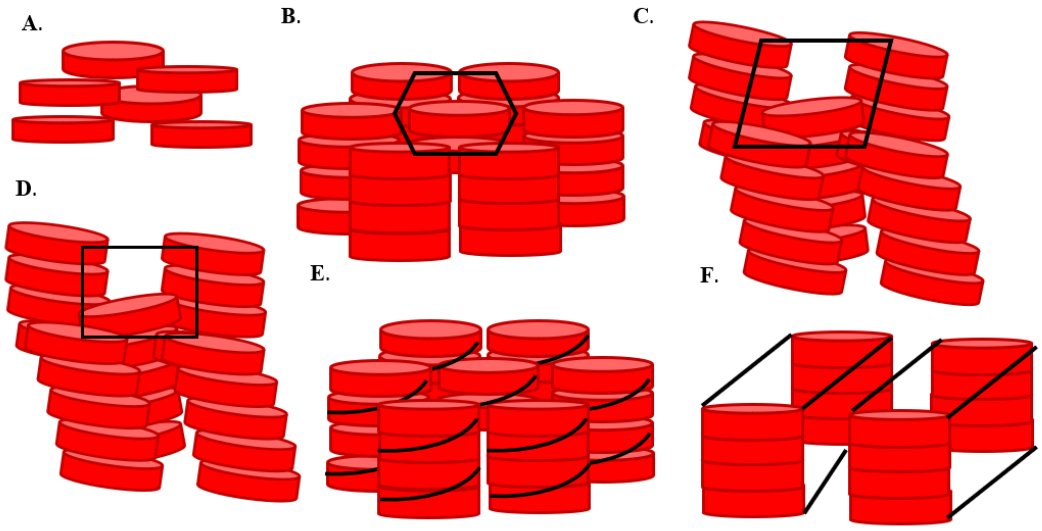

Figure 1.10 Schematic representation of different types of columnar mesophases (A) nematic discotic, (B) columnar hexagonal, (C) columnar oblique, (D) columnar rectangular, (E) columnar helical, and (E) columnar lamellar.

For the work discussed in Chapter 7 with perylene bisimide polyolefin conjugates these two phases are seen within a library of conjugates.

Within this work it is important to note that thin films are studied in which columnar hexagonal and columnar oblique phases are observed. These columnar phases can orient perpendicular (homeotropic alignment) to the chip or parallel (planar alignment) to the chip represented in Figure 1.11. Depending on the orientation of the columns depends on where the electrodes need to be in organic photovoltaics. Columnar discotic liquid crystals have significant potential for use in opto-electronic applications because of the extensive $\pi - \pi$ overlaps that aid in high charge-carrier

mobilities. Generally speaking, having columnar phases that orient homeotropically would yield most useful in such devices. One of the envisioned applications of the perylene bisimide materials is in organic photovoltaic solar cells, where liquid crystalline materials offer several benefits like spontaneous long-range ordering. The effectiveness of the conductivity along these liquid crystal columns depends on the ordering both in the column as well as laterally, and on internal reorganization energy

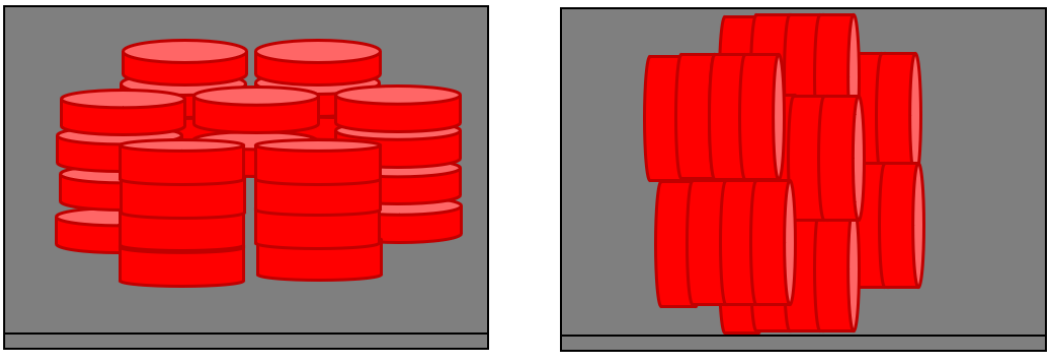

Figure 1.11 Schematic representation of a (left) homeotropic alignment and (right) planar alignment.

for electron transfer, and size of aromatic system, and the $\pi - \pi$ distance of the cores.[124-128]

1.3.5. $\pi - \pi$ Stacking

Pi-stacking ($\pi - \pi$) refers to the noncovalent interactions between pi bonds of aromatic rings. The stacking of aromatic rings is electrostatically repulsive in sandwich stacking. The commonly observed in either a staggered stacking (parallel displaced) or pi-teeing (perpendicular T-shaped) interaction are both electrostatically attractive, Figure 1.12.[129] Within perylene cores sandwich stacking is referred to as H-coupling

where there is 0 Å longitudinal slip and J-coupling is where there is greater than or equal to 7 Å longitudinal shift.[130] The self-assembly of chromophores exhibit optical properties that arise for the aggregation of either bathochromic

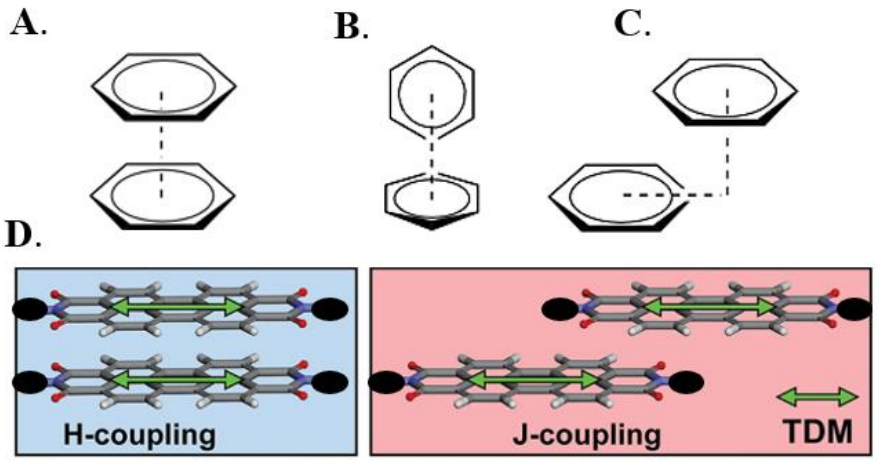

Figure 1.12 Represenative confomations of benzene pi-stacking (A) sandwich, (B) T-shaped, and (C) is parallel-displaced. (D) Black circles represent where polyolefin taiks would be attached, were H-coupling of perylene core and J-coupling are displayed with transition dipole moments (TDMs) as green arrows.

or a hypochromic shift of the absorption maximum caused by the coupling of the dyes' transition dipole moments (TDM). Depending on the direction of the shift these aggregates are either called J-aggregates or H-aggregates.[130] In order for chromophores to exhibit J-type excitation coupling they need to self-assemble into a slip-stacked arrangement. This is uncommon for perylene chromophores due to their larger π-systems and they tend to maximize dispersion interactions between the pi-scaffolds by co-facial (sandwich) stacking. It is important to note that while perylene in this pi-stacking formation contains properties such as high fluorescence, and photochemical and thermal stability the J-aggregates also possess useful properties. Such as cooperative self-assembly, usefulness in photonics and organic electronics, and exciton

migration. The self-assembly of the perylene based materials investigated within this body of work can offer insight as to how the perylene core $\pi - \pi$ stacking is oriented.

For perylene bisimide the HOMO, LUMO, and transition density distribution that the π-conjugated core possess is not electronically connected to any substituents that are attached to the imide nitrogen's on either end of the perylene core.[131] However, the substituents at core positions have a pronounced influences on the redox potentials and absorption properties within perylene dyes.[131] This can open up possibilities to tune the dye's properties while maintaining self-assembly properties within a given material.

1.3.6 Characterization

One of the most powerful methods used to confirm the presence and type of microphase separation in materials made herein is X-ray scattering. For this work, two types of X-ray sources were utilized, and three types of x-ray scattering were used. First, a Cu Kα lab scale Xenocs Seuss SAXS/WAXS/GISAXS systems. Due to the lower energy of this system, λ = 1.542 Å the exposure times on samples tend to be longer. The other x-ray source was Brookhaven National Labs (BNL) synchrotron x-rays where λ = 0.9184 Å. Due to this high-power, samples often had ten orders of magnitude greater signal to lab scale x-ray source and allows for sample to be measured for only 10 – 30 seconds exposure while the sample stage is rostered as to measure a new location of the sample in case there is sample beam damage. When the sample

contains atoms or crystals that are closely packed wide angle x-ray scattering (WAXS) is utilized. When the scattering occurs on a much larger scale, such as polymer domain structures, the detector is located farther away from the sample to collect the information known as small angle x-ray scattering (SAXS). The general layout for sample experimentation is illustrated in Figure 1.13. For SAXS experiments they are referred to as transmission because the incident beam directly passes through the sample for analysis of the bulk material. From Bragg's Law, Equation 1.6, where θ is the scattering angle, λ is the wavelength of the X-ray, and *d* is the lattice spacing. The domain periodicity can be determined by Bragg's law equation and the scattering wave vector equation, Equation 1.7, where *d* is domain spacing, and *n* is a n integer.

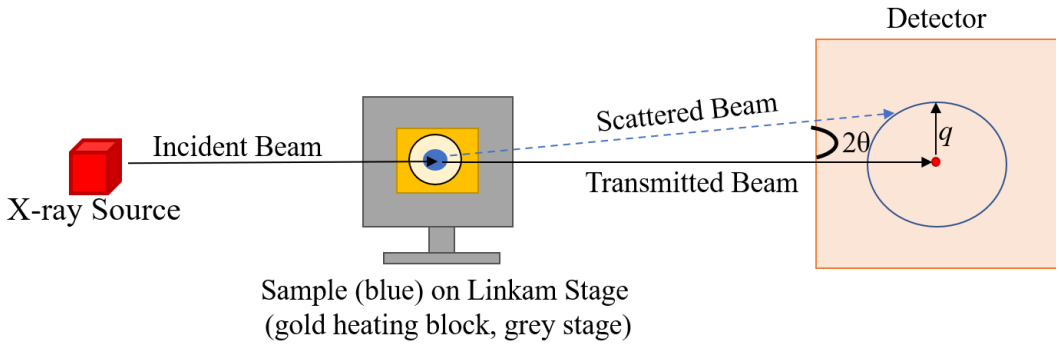

Figure 1.13 Schematic layout of SAXS where incident beam is produced from X-ray source. The beam passes through sample, illustrated here in a Kepton filmed wafer mounted to the gold heating block located on the grey Linkam stage. The beam then travels to the detector where it is blocked by the beamstop to preserve the detector and the material scatters the beam with a scattering angle, θ, which can be converetd into a scattering wavevector, *q*.

Equation 1.6 $$n\lambda = 2dsin(\theta)$$

Equation 1.7 $$\boldsymbol{d = \frac{2\pi}{q}\, n}$$

The first scattering peak observed is labeled as the principle peak q^*, and generally indicated the domain spacing within the nanostructure as well as is utilized to find analyze the phases observed. The ratio between the scattering peaks and the q^* are very indicative of the morphology of the bulk material. For example: lamellar phase (LAM) is a 1, 2, 3, 4, … q^* ratio; double gyroid (GYR) $\sqrt{3}$, $\sqrt{4}$, $\sqrt{7}$, $\sqrt{8}$, $\sqrt{10}$, … $q(\sqrt{6})/q^*$ ratio; hexagonally packed cylinders (HEX) 1, $\sqrt{3}$, $\sqrt{4}$, $\sqrt{7}$, $\sqrt{9}$, … q/q^* ratio; and body centered cubic (BCC) 1, $\sqrt{2}$, $\sqrt{3}$, $\sqrt{4}$, $\sqrt{5}$, … q/q^* *ratio.* The other type of X-ray technique is grazing incident small-angle x-ray scattering (GISAXS) where it is a reflection-based mode of SAXS best used in thin-films. For GISAXS the incident beam is directed at an angle toward the substrate with sample on it and can range from angles of 0.1 – 0.3°, within this work typically 0.15°. These X-ray scattering techniques are heavily relied upon to elucidate the self-assembly within many materials within this work including block copolymers, sugar polyolefin conjugates, and perylene bisimide polyolefin conjugates.

Atomic force microscopy (AFM) is utilized to analyze the morphologies within thin-films through tapping of a sharp tip located on a cantilever of lengths 100 – 300 μm. The detector within the AFM measures the deflection as the tip scans the samples surface thus generating an image of sample height and stiffness. AFM is useful for only surface level analysis.

1.4 Goals and Scope of this Work

Within the past several years of research the Sita Group has developed a toolbox of synthetic techniques that allow access to functionalized polyolefins, such as LCP and LCCTP. These techniques rely heavily upon the initiators chosen, percent of activation, presence of chain transfer agent, and monomer choice. This body of work can be broken down into these main goals:

1. Stereomodulate polyolefins to study the structure/ property relationship for possible new applications in thermoplastic elastomers, compatibilizers, or anti-plasticizers.
2. Utilize the functional polyolefin domains (xPAOs) with sugar head groups to expand the sugar polyolefin conjugate library and access new complex phases.
3. Create a functional polyolefin-based material with perylene to create optoelectronic relevant materials to further show xPAOs versatility.
4. Design self-assembly of conjugates employing xPAOs domains in a systematic and programable way .

Within this work the first goal is achieved by using the toolbox of living polymerization techniques to investigate neglected olefins such as 4-methyl-1pentene, 1,5-hexadiene, and 1,6-heptadiene microstructures. Through using living polymerization methods stereomodulation of poly(4-methyl-1-pentene) (PMP) has provide new fundamental forms in which thermal phase transitions, T_g and T_m can be adjusted over a wide range thus producing many polyolefin

materials from one catalytic system, Figure 1.14. In another study, 1,5-hexadiene is copolymerized with 1,6-heptadiene to break-up crystallinity while obtaining a high T_g characteristic within the material.

Furthermore, a chiral catalyst can be utilized at different ratios to achieve optically active poly(1,3-heptadiene) (PMCH) and poly(1,3-hexadiene) (PMCP).

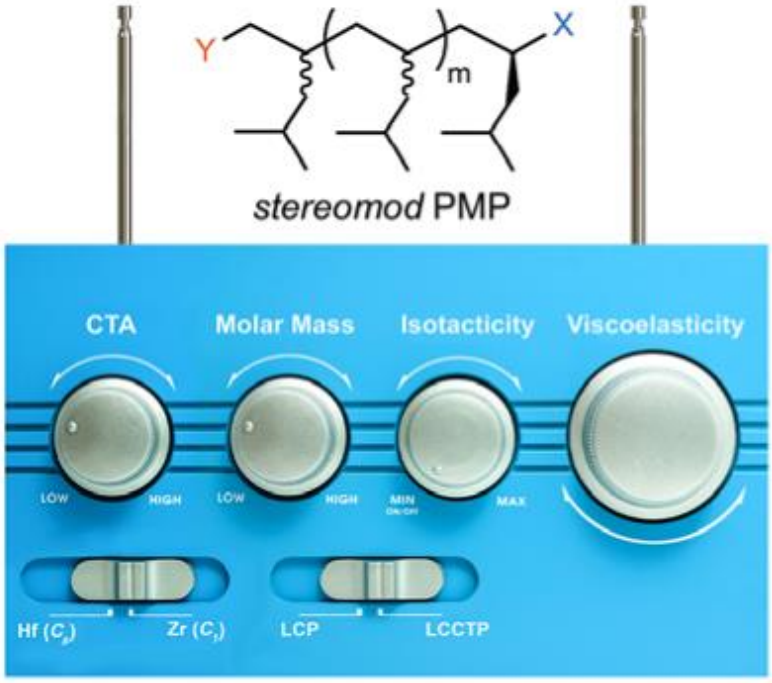

Figure 1.14 Cartooned radio to represent all the gears in the toolbox that can be adjusted to change the stereomodulated PMP materials produced.

The second goal is achieved through utilizing atactic PMP domains with sugar-head groups to access FK phases thus developing a new methodology to access these rare phases. The discoveries made within the initial serendipitous FK phase allowed for systematic design of further FK phases such as σ phase. The change in xPAO domain allows for FK phases to be observed at ambient temperatures and is the first

documented FK A15 at room temperature within soft mater materials. These studies also tackled goal number 4 since the sugar-polyolefin self-assembly was influenced by the polyolefin domain type, molecular weight, and temperature conditions.

The third goal is the first documented time that our xPAOs are utilized with a perylene based cored. In these studies, many xPAO domains are studied and prove evident that they change the properties of the perylene materials as well as the self-assembly consequently observed. Most notably, these perylene based polyolefin conjugates when combined with cobaltocene undergo a radical reduction and the radical perylene conjugate species, with optically active PMCP tails, undergoes phase separation into the rare single gyroid morphology. Overall, both the sugar polyolefin and perylene polyolefin conjugates show the versatility, scope, and effectiveness of xPAO domains to change the properties and self-assemblies of the bulk material.

One may wonder what ties all these goals, materials, and projects together and that is the design and implementation of the polymer domain within a material for a wide range of applications. The future of technological advancements relies heavily on polymer-based materials due to their adaptive nature, scalable synthesis, functionalizable, and programmability. The possibilities with xPAO domains are seemingly endless and the work herein covers part the scope at which they can be employed.

Chapter 2: Stereomodulation of Poly(4-methyl-1-pentene) [PMP]: Adoption of Neglected and Misunderstood Commercial Polyolefin†

Wentz, C. M.; Fischbach D. M.; Sita, L.R., Stereomodulation of Poly(4-methyl-1-pentene): Adoption of a Neglected and Misunderstood Commercial Polyolefin. *Angew. Chem. Int. Ed.* **2022**, e202211992.

Author Contributions:
L. R. S. Lead conceptualization, funding, and writing.
C. M. W. Supported writing, reviewing, and editing. Synthesized and characterized all materials within the study. Assisted in the synthesis and characterization of D. M. F. materials.
D. M. F. Supported writing, reviewing, and editing. Synthesized and characterized 25% and 10% activated materials with the assistance and guidance of C. M. W.

2.1 Introductions

Polyolefins continue to be one of the most widely used, sought after, and crucial materials in today's global economy, with a combined production volume of over 350 million metric tons annually.[1-3] Regrettably our dependency on commodity plastics, which arise from mainly polyolefins, has led to a plastic waste crisis.[1] In response to this predicament new strategies must be conceived and developed that not only reduce the barriers for recyclability of polymers, but also, that new polymer

† The results, figures, schemes, and tables discussed within this chapter have been reused or adapted with permission from Wentz, C. M.; Fischbach D. M.; Sita, L.R., Stereomodulation of Poly(4-methyl-1-pentene): Adoption of a Neglected and Misunderstood Commercial Polyolefin. *Angew. Chem. Int. Ed.* **2022**, e202211992.

designs can serve as commercially viable replacements for less-environmentally-benign plastics, such as polystyrene and polyvinylchloride.[4-10] The goal presented here was to address the use of a commodity monomer, 4-methyl-1-pentene (4M1P) that has been utilized in commodity thermoplastic material known as TPX found in materials such as food packaging, tuba ware, and many other commodity plastics.[11-13] Generally speaking poly(4-methyl-1-pentene) (PMP) has a lot of misconceptions and no formal stereoengineering study done on it that is found in the literature. This is quite unusual for a largely used material as other commodity plastics such as polypropylene (PP) and polyethylene (PE) have extensive studies and known standards are documented. In fact, PP and PE materials make up 50% of plastic waste globally each year.[14-16] Our goals included clearing up misconceptions made about atactic PMP (aPMP), to create a programable array of materials utilizing our synthetic toolbox and offer a possible new commodity plastic that comes from renewable sources.

To begin, it must be noted that our dependency on polyolefins for the foreseeable future is guaranteed so instead of focusing our efforts towards using less plastics there are other options. Here are a few reasons why polyolefins are guaranteed to continued being used in today's society: (1) plastics have a wide range of physical properties that can be tailored for a large variety of end-use applications so finding a replacement that is as versatile and globally available will be difficult, (2) ethene and propene are abundant and cheap feedstocks to producing material, and (3) we have already, as a civilization, invested so much infrastructure and manufacturing that goes into making and distributing these materials world-wide. When it comes to addressing waste it is important to note we have already made great strides to impact this problem

including; (1) having infrastructure in place that allows people to have access to recycling plastics with 30% of recycled plastics being high density polyethylene (HDPE) making it highly successful for a circular economy, (2) PE produced now is made through 'green' routes of bio-sourced ethene with a neutral to negative environmental carbon footprint, and (3) hydrocarbon unfunctionalized materials have many options for disposal that yield products such as fuel that we then use.[17] Altogether, it is clear that new classes of polyolefin materials with expansion of physical properties and varied options is a realistic goal. However, what new polyolefin materials do we really need?

On the one hand, the biggest challenge resides in the fact that only a small amount of industrially relevant olefin monomers exists to build new polymers from, and this list largely consists of α-olefins that can be obtained through the controlled dimerization or oligomerization of ethene and propene. Moreover, PMP can be synthesized using alkali metal catalyzed dimerization of propylene. On the other hand, Natta and coworkers[18-21] have developed the concept of polyolefin tacticity which provides a basis for creating different 'grades' of common polyolefin structures thus changing the physical properties that differ in subtle or dramatic ways. This disparities in properties comes from either a difference in linear sequence of relative configurations or adjacent stereocenters associated with pendant side groups or the overall chain length and repeat units within the given chain, *DPn*.[22,23] In the case of PP, the highly stereoregular isotactic form **I**, where R = methyl, depicted in Scheme 2.1, is a semicrystalline, thermoplastic with a high melting temperature, T_m, of 165 °C that makes it suitable for the manufacturing of sterilizable cutlery, medical devices, and

food packaging. Unfortunately, this crystalline nature requires the material to undergo high temperatures for processing, extruding, and molding thus leading to the need for more energy to be spent on making the materials. On the complete other end of the spectrum, stereorandom atactic form **II**, Scheme 2.1, is completely amorphous with a

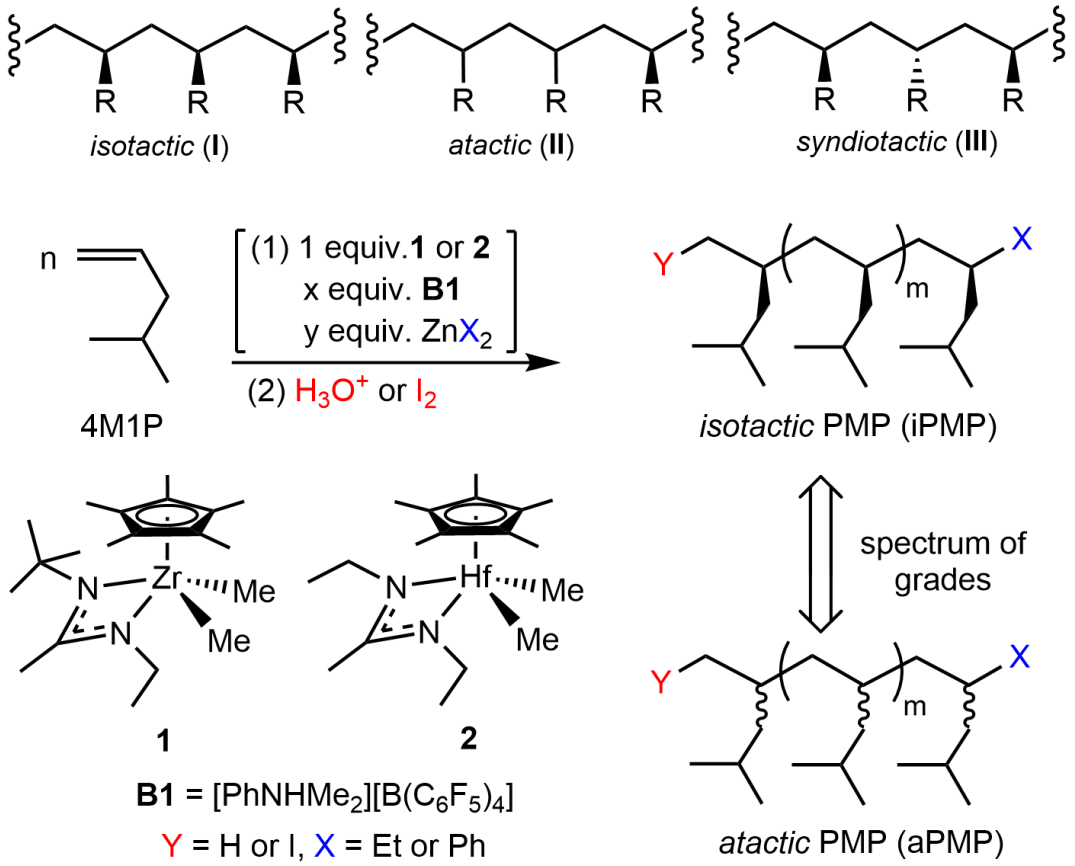

Scheme 2.1 Chemical microstructure and synthesis of poly(4-methyl-1-pentene).[†]

low glass transition temperature, T_g, of -10 °C thus having very little to no commercial value.[3] Other limiting forms of tacticity that exist for PMP materials include syndiotactic **III**. The material sold under the trade name TPX is often a blend of PMP with other comonomers or plasticizer additives in order to achieve a wider array of materials.[11]

Returning to Natta's tacticity strategy comes with the understanding that between these two limiting forms, on either side of the spectrum, means there is an infinite number of 'grades' that exist between them. This means that there is an infinite number of ways to incorporate 'stereoerrors' or change stereoregularity to consequently gain a whole new library of polyolefins with different physical properties all through the same monomer source. For the PP materials the properties of different tacticity grades include plastics that are rigid and plastics that are elastomeric as the level of stereoerrors incorporation is systematically increased.[18-21] In this work a successful endeavor has been achieved were PMP was systematically stereoengineered through the use of different strategies such as living coordination polymerization (LCP) and living coordinative chain transfer polymerization (LCCTP) to tap into the neglected potential of this commercial polyolefin, Scheme 2.1.[5] For previous stereoselective and stereomodulated LCP of α-olefins and α, ω-nonconjugated dienes that is CPAM group 4 metal complexed related to these goals presented in this work done previously see[22-30], for previously reports of two- and three-state (stereomodulated) LCCTP of ethene, α-olefins, and α, ω-nonconjugated dienes using CPAM group 4 metal complexes as related to the goals in this work see[31-44], these references are considered the 'toolbox' of techniques the Sita group has developed over the years and are relevant to mention here since the current studies relies heavily on the past successes documented.

Nearly 70 years ago Natta *et al*. reported isotactic PMP (iPMP) with a T_m value of 250 °C. The material properties made it suitable for microwave oven cookware, optical lenses, but iPMP has major drawbacks such as the physical properties of being too brittle and having overall low tensile strength.[45-47] In regards to tacticity and

property relationship for PMP, the literature is sparse, but also is riddled with errors and confusion arising from an incomplete and poorly characterized materials. Griffith and Rånby reported using dilatometric measurements to establish T_g values for a PMP series, with no documentation of molar mass or activity and simply noted varying degrees of crystallinity. A T_g value for an aPMP sample was established at 29 °C.[48] A T_g value of 18 °C was additionally discovered for an iPMP sample with a recorded 78% crystallinity within their study. Griffith and Rånby concluded that this trend of decreased *Tg* between aPMP and iPMP was most likely due to the crystalline phase being less dense than the amorphous phase.[45] It must be noted that just because a material isotactic in stereonature does not mean it is amorphous is physical properties. Very recently, Veige *et al.* have sited Griffith and Rånby's study in support of their own claim of having synthesized a cyclic atactic PMP (c-aPMP).[49] The creating of c-aPMP was done through a novel ring-expanding metathesis polymerization of 4-methyl-1-pentyne, followed by hydrogenation to create an unsaturated cyclic polymer. The noted c-aPMP within this study was documented to have a number-average molar mass index, M_n, or 99 kDa, and a molar mass distribution dispersity index, $Đ$ (= M_w/M_n) of 1.30, where M_w is the weight-average molar mass index. Both values can be found utilizing size exclusion chromatography (SEC). The investigators also made a linear atatctic PMP material (l-aPMP) with an M_n = 141 kDa and $Đ$ = 1.37. To understand the physical properties of the materials they made they used differential scanning calorimetry (DSC) was utilized, instead of dilatometric analysis reported in Griffith *et al*. study. The l-aPMP materials had a T_g value of 29 °C, while their c-aPMP material had a T_g value of 39 °C. It is known that cyclic polymers possess a higher T_g value

compared to a linear polymer. Therefore, Veige *et al.* concluded this 10 °C increase was evidence towards the presence of a cyclic structure of their material.[49] This is particularly of interest to us because in the investigation of our own PMP materials we found that with our materials, of linear structure, to have obtained T_g of the same degree. Hence, putting into question, the legitimacy of this concluded fact.

2.2 Stereomodulation of PMP through Living Coordinative Polymerization and Living Coordinative Chain Transfer Polymerization [LCP and LCCTP]

This new family of PMP of varied stereo grades along with a tacticity/ property relationship, serve to provide a foundation for the development of new PMP based products and to correct past errors and the spread of misrepresentation of the properties of regioregular atactic PMP that have been reported and discussed previously.[45]

Represented in Scheme 2.1 is a summary of the reagents and methods used in this present study, more detailed synthesis of the PMP materials can be found in the supporting experimental information (SI). Since the 2000, the Sita group has been developing a family of cyclopentadienyl, amidinate (CPAM) group 4 metal pre-initiators. These CPAM pre-initiators have the general formula of $(\eta^5\text{-}C_5R_5)[(N,N')\text{-}\kappa^2\text{-}N(R^1)C(R^2)N(R^3)]MMe_2$ (M = Zr or Hf (**1 or 2**), which upon 'activation' with a stoichiometric equivalent of the anilinium borate co-initiator, $[PhNHMe_2][B(C_6F_5)_4]$ (**B1**), provides the corresponding ion pair initiators, $\{(\eta^5\text{-}C_5R_5)[(N,N')\text{-}\kappa^2\text{-}N(R^1)C(R^2)N(R^3)]\text{-}M(Me)\{B(C_6F_5)_4\}$.[9-43] When excess equivalents of α-olefin is

present the propagation of the active species occurs, which is derived ion pair initiator form. The active species proceeds through a 1,2-migratory insertion (1,2-MI) of the monomer into a growing polymer chain. As this process is living, and known as LCP, it can be implemented as a tool to target a desired molar mass polymer with very small monodisperse molar mass distribution (MMD). Throughout this study most of the PMP materials had a dispersity, $Đ < 1.1$.[50] When it comes to the stereomodulation of PMP, in these LCP studies, it is primarily dictated by the structure of the pre-initiator **1 or 2**. For example, in the case of **1** the propagating species tacticity of the polyolefin microstructure is directly affected the bulky isopropyl group located on the amidinate ligand scaffold thus the propagating polymer units will be sterically hindered to face all the same direction . Furthermore, a fully activated C_1-symmetric Zr pre-initiator (**1**) propagation proceeds in a stereoselective fashion providing isotactic microstructure through enantiomorphic site control that is enforced by nonbonded steric interaction, as the steric size of the polymer tail increases this propagation can become 100 % stereoselective with no stereoerrors being incorporated.[22,23] With this noted, the first goal of the present study was to determine the ability of fully activated pre-initiators **1** (Zr) to provide a reference material for 1,2-regioregular iPMP which will be referred to as **ref1**. The full activation of **2** (Hf) to provide aPMP will be referred to as **ref2**, thus providing us with the end of each side of the spectrum. Both references were synthesized using LCP technique. For these reference materials an *Mn* of 50 kDA was aimed for in order to ensure that end groups do not contribute to the bulk properties, nor do they appear in ^{13}C NMR resonances. For **ref1** an *Mn* = 51.0 kDA was targeted

and analyzed by SEC with a dispersity of $Đ$ = 1.39. The difficulty with highly iPMP

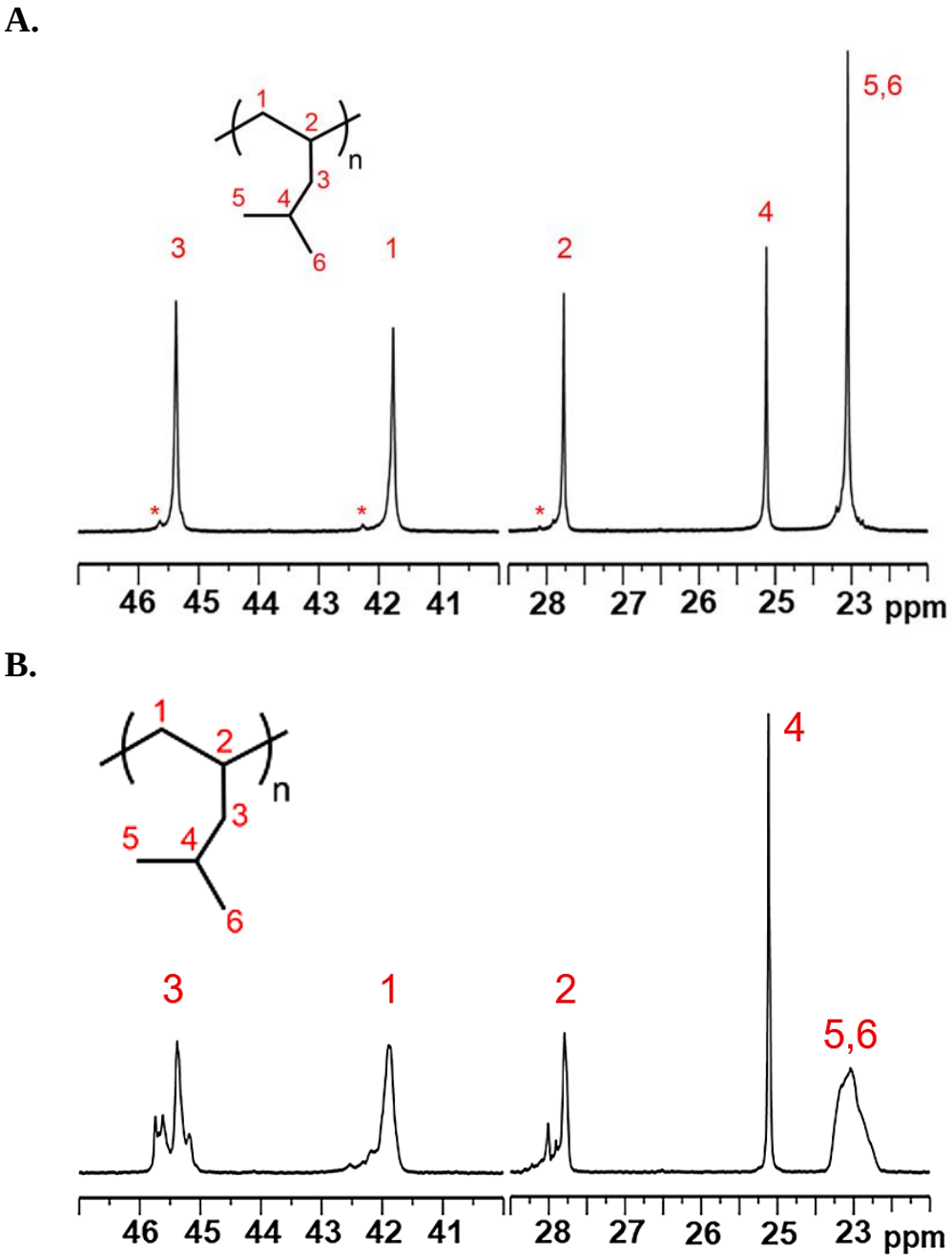

Figure 2.1 (A) ^{13}C {^{1}H} NMR (200 MHz, TCE-d2, 110 °C) spectra for *isotactic* PMP (**ref1**) M_n = 51.0 kDA, Đ = 1.39. The asterisks indicate ^{13}C resonance for a polyolefin co-product arising from an α-olefin impurity in the original 4M1P. (B) ^{13}C {^{1}H} NMR (200 MHz, TCE-d2, 110 °C) spectra for *atactic* PMP (**ref2**) M_n = 48.7 kDA, Đ = 1.19. [†]

and characterization lies in the insolubility of the material at high molar mass. This large dispersity is attributed to the inability for the material to dissolve in tetrahydrofuran (THF) and pass through the columns. Even when utilizing high temperature SEC (HT-SEC) provided at NIST the iPMP material still had large dispersity, however, that being stated the material was still monomodal.

For **ref2** an Mn = 48.7 kDa was measured via GPC with a dispersity of $Đ$ = 1.19.

The differences between the stereoregularity of the material can be seen in ^{13}C-NMR, and is easily visible in Figure 2.1. Both references were run on 200 MHz NMR at 110 °C in 1,1,2,2-tetrachloroethane-d_2 solvent. When it comes to **ref1,** Figure 6.1A, there are very sharp well-defined peaks, 5 in total, that correspond to the isotactic nature of the material. At a closer look C5 and C6 of the geminal methyl groups of the isobutyl side chains in PMP appear as magnetically equivalent due to the intrinsic C_s-symmetry of the long polymer chain.[45,51] In stark contrast, **ref2**, Figure 6.1B, shows 5 peaks each which are now broad due to the atatctic nature of the PMP material. This feature is due to the partial overlap of multiple resonances associated with different *n'ad* tacticity sequences. Even at a magnetic field strength of 200 MHz (800 MHz for ^{1}H NMR) it is not possible to resolve and unequivocally assign individual chemical shifts for the ten possible *pentad* sequences that can exist within aPMP. Based on that understanding, the use of NMR spectra is purely qualitative to relate the relative degree of stereoregularity for each member of the PMP samples by the broadness or inclusion of more minor peaks associated with stereoerrors.

Powder x-ray diffraction (XRD) analysis was performed on **ref1** and **ref2** to confirm the semicrystalline and amorphous nature of these materials. Figure 2.2

represents not only **ref1** which is 100% activated but **run 2.14** (75 %) and **run 2.16** (20%) where the decrease in crystallinity can be observed by the loss of intensity in the peaks. Common reflection planes observed in XRD are identified through an analysis software which matches the peaks with documented indexing. The form labeled within the XRD displayed from **run 2.11** (ref1), **run 2.14,** and **run 2.16** is a stable crystalline

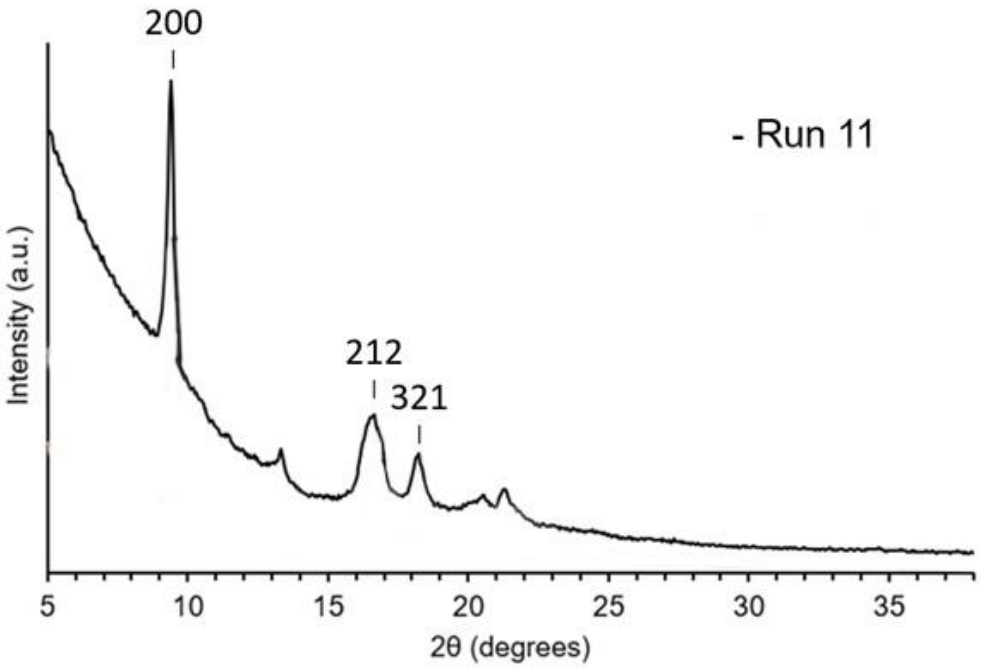

Figure 2.2 XRD profile of **run 2.11**.†

form which can occur from the melt state that then packs into a tetragonal unit cell.[5] Figure 2.3B XRD profile is of completely amorphous PMP, similar to **ref2**.

Some additional notes about physical characteristic of these reference materials includes that **ref1,** iPMP, has a flowing white powder essence, and **ref2,** aPMP, is highly soluble in a variety of organic solvents and has a hard glass appearance, Figure 2.4. Thermal analysis of these two materials by DSC revealed only a first-order T_m at

226 °C for the iPMP **ref1** material. The DSC ramp rate of 10 °C/min is utilized with a cooling rate of 5 °C/min in order to fully crystalize the material before the final heat ramp is collected and utilized to find these temperature transition numbers. The thermal analysis software is utilized to calculate percent crystallinity (*c%*), within **ref1** where *c%* = 34. In contrast, the DSC of aPMP **ref2** now displayed only a second order T_g

A.

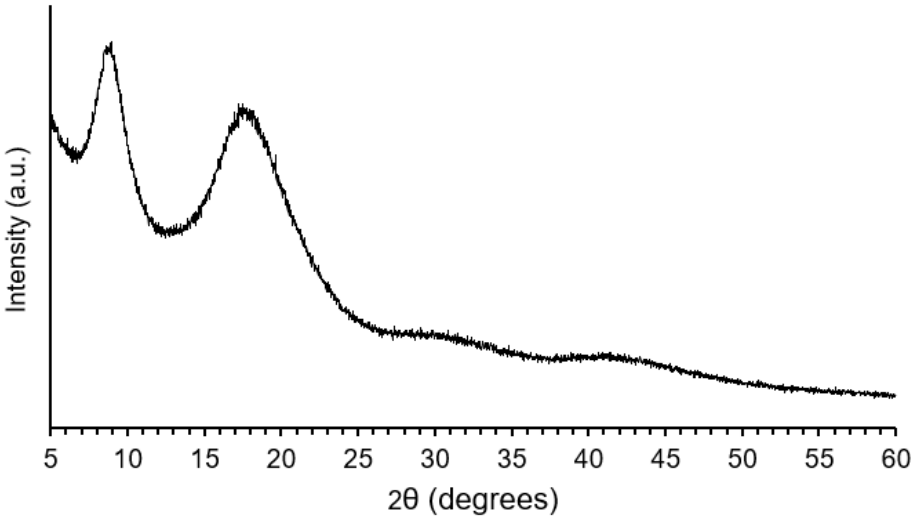

B.

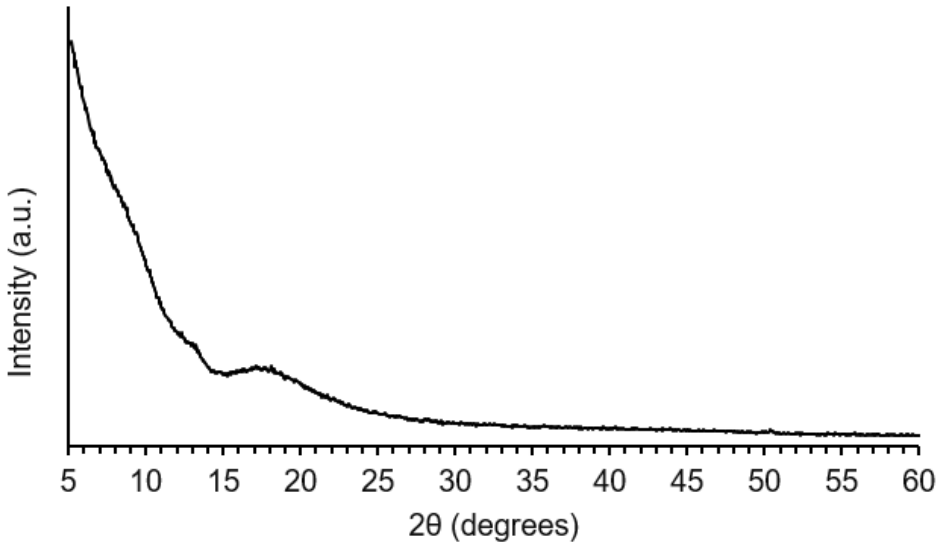

Figure 2.3 (A) XRD profile of **run 2.7** (LCP), and (B) **run 2.2** (LCCTP). The peak broadness is attributed to amorphous nature of the material. †

transition at the high value of 39.5 °C. This value of 39.5 °C is comparable to the c-aPMP in Veige *et al.* study.

2.3 Establishing *atactic* PMP

To the best of our knowledge Figure 6.1B represents the first ^{13}C NMR spectrum for authenticated regioregular aPMP to have ever been published. This is believed because the ^{13}C NMR provided in Veige *et al.*, for their l-aPMP, lacks any other characterized data that consistent with being 1,2-regioregular material. The high T_g value of the aPMP **ref2** prompted us to determine the materials ability to be manufactured as a transparent optical disk through both solvent casting (left) and

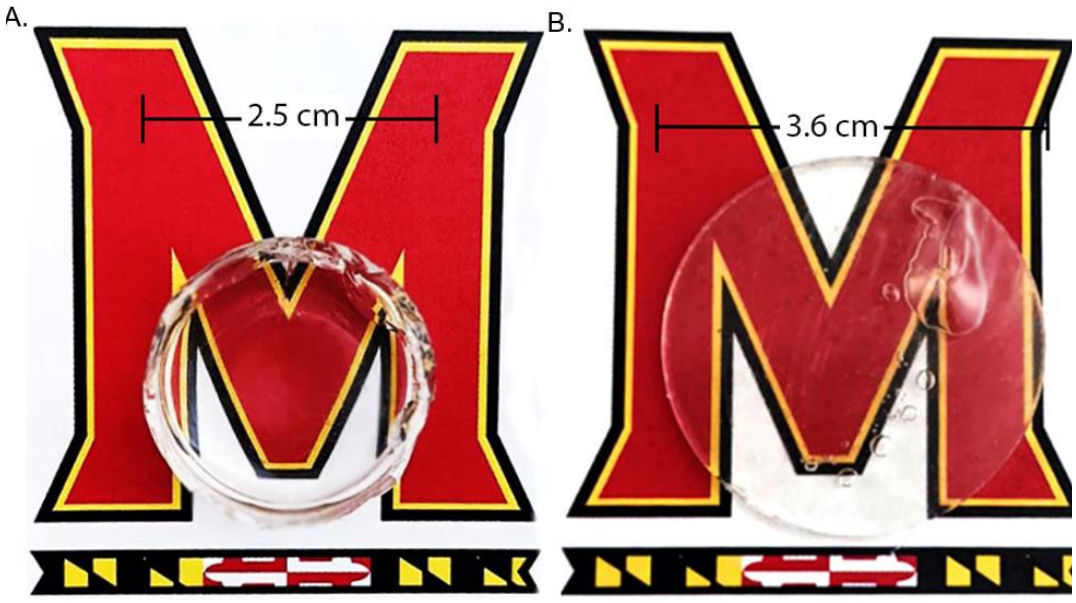

Figure 2.4 Demonstration of the manufacture of optically transparent disks from linear atactic PMP (**ref 2.2**) with T_g = 39.5 °C through (a) solvent casting from hexane (thickness = 0.5 cm) and (b) injection moulding at 150 °C (thickness = 3 mm). Diameters of each disk are indicated. †

injection molding at 150 °C (right), represented in Figure 2.4. These efforts show that this transparency for PMP is not limited to a cyclic form.

Since the surprisingly high T_g value for **ref1** was discovered it does contradict both Griffith *et al.* and Veige *et al.* reports, therefore a more thorough investigate of our aPMP materials was made. It must be noted that the increase in T_g as an increase in M_n, up to a limiting value, has already been made for a wide range of polymers.[52-54] To begin this investigation we utilized LCCTP technique which can be combined with either pre-initiator **1** (Zr) or **2** (Hf) in order to produce low molecular weight to high molecular weights polymer, while adding in the bonus of being scalable. This is done through the addition of excess equivalents of relatively inexpensive and abundant metal alkyl chain transfer agent (CTA) $ZnEt_2$. The CTA provides a much larger population of 'surrogate' chain growth centers that engage in rapid and reversible exchange of the polymeryl group.

In Table 2.1 LCP and LCCTP materials are highlighted in greater detail. LCP was implemented as a synthetic tool to see if there was much of a difference in physical properties when it came to aPMP with or without the presence of CTA. Not to surprisingly the materials of aPMP made through these two techniques were very similar with the slight difference in that LCP aPMP could achieve higher crystallinity at lower molar mass for the middle range of M_n values. Take **run 8** in comparison to **run 4** , for a Mn = 10.4 kDa a T_g is observed at 29.7 °C for the LCP **run** 8 was observed. Whereas for a Mn = 6.18 kDa a T_g = 10.3 for the LCCTP **run 4** is observed.

Table 2.1 LCCTP and LCP of 4M1P using **2**.[a]

Run	$ZnEt_2$ (eq.)	4M1P (eq.)	Yield (g)	M_n (kDa)[b]	M_w (kDa)[b]	$Đ$[b]	T_g (°C)[c]
2.1	30	713	1.45	0.835	0.967	1.15	-48.7
2.2	10	595	1.24	2.60	3.07	1.18	-6.06
2.3	5	595	1.19	3.30	3.91	1.18	3.92
2.4	5	891	1.92	6.18	7.18	1.16	10.3
2.5	2	1190	1.09	31.4	36.4	1.16	31.4
2.6	2	1220	3.56	48.7	58.2	1.19	39.5
2.7	-	12.0	0.100	3.21	3.80	1.18	7.91
2.8	-	60.0	0.500	10.4	12.2	1.17	29.7
2.9	-	595	0.990	98.7	152	1.53	39.2
2.10	-	1190	1.98	126	192	1.52	39.4

[a]For complete details of polymerization conditions for each run, see SI. [b]Determined by SEC. [c]Determined by DSC. **Runs 2.1 – 2.5** are via LCP and **runs 2.7 – 2.10** are via LCCTP. †

This difference in T_g can be related to PMP's unique ability to have chain-end control. This can be better explained when the structure of the pendant group off the backbone chain in PMP is looked at. The large isopropyl extensions of these chains influence the next chains incorporation, and PMP has the distinctive property of influencing the next unit to insert in the same direction as the previous polymer unit. Though **2** has no influence on the stereoregularity of the propagating chain the previous PMP unit does, therefore the lack of CTA present in LCP leads to less atactic nature in aPMP materials. Concluding that these middle molar mass samples can be affected by the added randomization that CTA issues when transfer chains. Finally, one can note that even with no change in amorphous nature of aPMP there is still observe difference between LCP and LCCTP produced aPMP by XRD profiles. Figure 2.3 has stacked XRD profiles in order to compare the aPMP made through LCP technique (top) verses

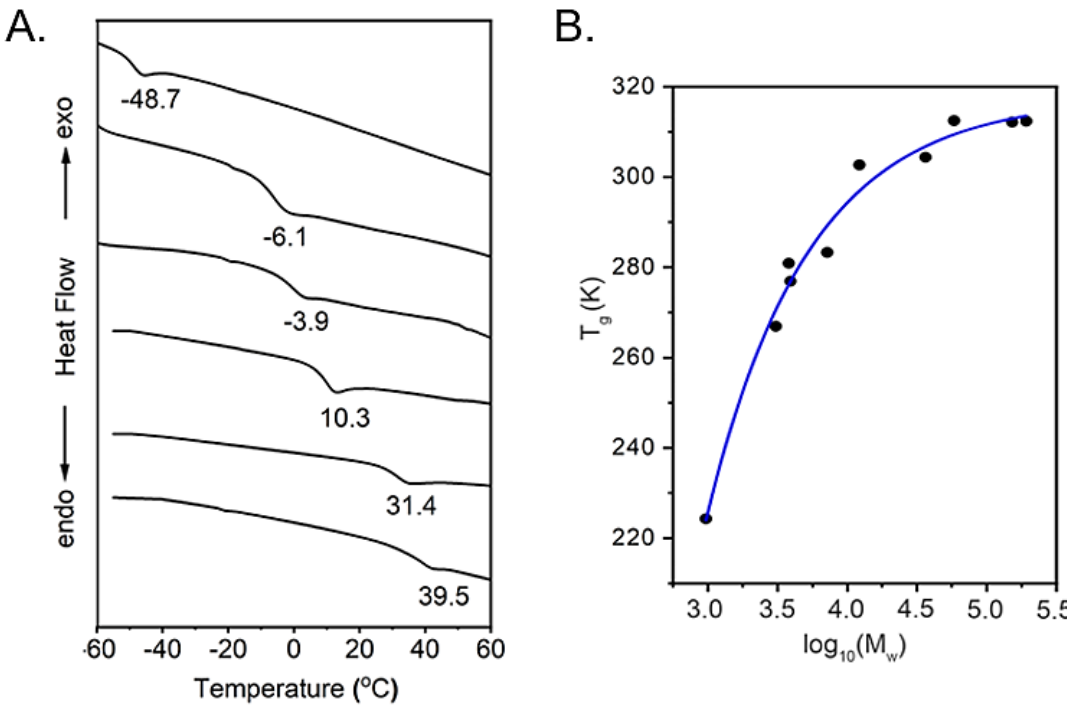

Figure 2.5 (A) Partial DSC data for aPMP obtained via LCP using 2, with Mn values (top to bottom) of 835 Da, 2.60 kDa, 3.30 kDa, 6.18 kDa, 31.4 kDa, and 48.7 kDa. (B) relationship between T_g and $\log_{10}(Mw)$ for aPMP obtained from both LCP and LCCTP, see run detail in Table 2.1. The line represents an asymptopic fit of the data ($y = a\text{-}bc^x$) with a = 317.5, b = 5676, c = 0.253, $R^2 = 0.983$.[†]

LCCTP technique (bottom). Figure 2.3A, LCP aPMP, has larger intensities than its LCCTP, Figure 2.3B, counterpart. However, both XRD profiles still contain broad signals which in known to arise from amorphous nature of these material runs.

Regardless of LCP or LCCTP differences in chain-end control, the effects of molecular weight can be clearly seen as there is an increase in T_g as a function of *DPn*. In Figure 2.5A a plot of the entire series of T_g values, based on Log_{10}(Mn), is in qualitative agreement with the Flory-Fox equation that described the dependence of T_g on molar mass.[55] In Figure 2.5B the asymptotic curve is fit to this data and shows a limiting *Tg* value of 40 °C for linear 1,2-regioregular aPMP of infinite chain length. This value is identical to **ref2** aPMP, as well as the claimed c-aPMP material of Veige

et al. Finally, given the ease with which scalable amorphous, high-T_g, regioregular aPMP it opens a new foundation to explore innovative applications of this polyolefin.[23]

2.4 Two-State Degenerative Polymerization

As noted in the introduction, there has been a remarkable lack of interest or progress made with the development of new 'grades' of iPMP. Duchateau and coworkers have provided the most detailed investigation to date.[51] Their experimentation studied the impact that stereoregularity of iPMP has on the value of T_m by synthesizing and characterizing a small series of PMP. These PMP samples were made through a library of C_2-, C_s-, and C_1-symmetric *ansa*-bridged zirconocene complexes used as a pre-catalyst with the combination of methylaluminozane as a co-catalyst.[51] Within this series of iPMP materials all T_m values were above 200 °C, which is suggestive of a high degree of regio- and stereoregularity for a predominantly isotactic microstructure. The results of Duchateau's investigation showed that the very strong stereocontrol of the growing polymer chain can exert onto the next monomer insertion during propagation, such as discussed before with the aPMP materials when differentiating between LCP and LCCTP conditions. Similar to PMP, poly(vinylcyclohexane) (PVCH) polymerization with our C_s-symmetric derivative of **1** also observe strong chain-end control effects on the materials stereoregularity. This was determined because the PVCH polymer were found to have a *mmmm > 95%*.[55] Accordingly, it is important to recognize the potential difficulties with overriding

intrinsic chain-end control in any strategy for the end goal of achieving a programmed stereomodulation of PMP tacticity as this was something taken into consideration when before attempting the currents studies endeavor.

Within the 'toolbox' of strategies our group has previously reported,[5,22-43] the first step of investigating stereomodulation of iPMP was to employ a 'two-state degenerative' LCP technique. This strategy is based on having substoichmetric activation of **1** ($x < 1.0$ in Scheme 6.1). The mechanism basis for two-state degenerative LCP stereomodulation is described in Chapter 1, but to recap the tacticity directly corresponds to the configurational stability of the population of active ion par propagators that are in equilibrium with a second population of configurationally unstable neutral and dormant species via a rapid and reversible methyl group exchange. The dormant species epimerization occurs and the stereoregularity of microstructure becomes dependent on the relative concentration of dormant states to active states. Plainly, the percent level of activation of **1** directly effects the stereoregularity within the polymer material such as 85% activation will have less stereoerrors that 50% activation which would have more. Table 2.2 summarizes the series of runs made by LCP two-state degenerative synthetic technique.

To begin, **run 2.11** is the same experimental conditions used to obtain the iPMP **ref1** material, therefore one can refer to **run 2.11** as **ref1** to avoid confusion. **Runs 2.12 – 2.17** materials track the impact that an increasing population of configurationally unstable dormant species can have on the stereoregularity or tacticity of the PMP product. Most notably for runs with activation percent's greater than or equal to 85% the T_m reported are above 200 °C, **runs 2.11 – 2.13**. However, at and below 75%

Table 2.2 Two-state Degenerative LCP of 4M1P using **1** with Varying Equivalents of **B1**.[a]

Run	[B1/2]	$ZnEt_2$ (eq.)	4M1P (eq.)	Yield (g)	M_n (kDa)[b]	M_w (kDa)[b]	Đ[b]	Tg (°C)[c]	T_m (°C)[c]	%Crystallinity[c]
2.11	1.1	-	280	0.41	51.0	70.9	1.38	-	226	33.6
2.12	0.95	-	280	0.51	48.1	66.9	1.34	-	225	31.2
2.13	0.85	-	280	0.55	61.4	81.7	1.32	-	222, 227	25.7
2.14	0.75	-	100	0.34	17.8	21.8	1.22	29.1	190, 203	8.49
2.15	0.50	-	100	0.34	16.8	19.8	1.18	27.4	145, 158	5.65
2.16	0.25	-	100	0.29	13.0	14.9	1.15	28.8	135, 151	5.26
2.17	0.10	-	100	0.22	8.80	9.94	1.13	24.9	135, 141	4.06
2.14 b[d]	0.75	-	280	0.54	91.3	104	1.14	32.6	204; 211	11.6
2.15 b[d]	0.50	-	100	0.34	17.8	21.8	1.22	29.1	190; 202	8.49
2.18[e]	1.1	5	595	0.75	6.18	22.6	3.29	-	214	23.1
2.19[e]	1.1	30	4280	3.7	7.34	14.9	2.02	28.8	223	33.3
2.20	0.95	5	595	0.96	5.01	10.2	2.04	25.3	218	26.1
2.21	0.85	5	595	0.99	3.11	5.04	1.82	22.3	217	19.1
2.22	0.75	5	595	0.75	3.95	7.65	1.94	4.56	149; 164	2.25
2.23	0.50	5	595	0.24	6.18	10.7	1.73	13.6	145; 162	3.77

[a]For details of polymerization conditions for each run, see SI. [b]Determined by SEC. [c]Determined by DSC. [d]These runs were created to show *Mn* dependency. Below dotted line LCCTP reactions. [e]These runs have same percent activation but differing molecular weighs.[†]

activation, several notable physical property changes occur, **run 2.14 – 2.17**. First, the T_m of the materials falls below the 200 °C for the first documented time in literature and continues to systematically decrease along with percent crystallinity as a function of a decreasing activation with a drop of 50 – 30 °C noted. Additionally, at and thereafter 75% activation a T_g transition now occurs, indicating the presence of a rubbery component. Lastly, the presence of double or multiple melting transition temperatures now appears. This is not unusual or unprecedented for semicrystalline polymers as this feature suggests that crystallites of varying sizes are now present, these physical properties discussed can be seen in Figure 2.6B. Figure 2.6A shows a selection of runs were partial ^{13}C NMR spectra are stacked. Once again this NMR cannot be used to quantify stereochemical microstructures but does offer a qualitative view of the trend

that exists within the material as percent activation is decreased. It is also important to note that the decrease in molar mass that is observed, as a function of percent

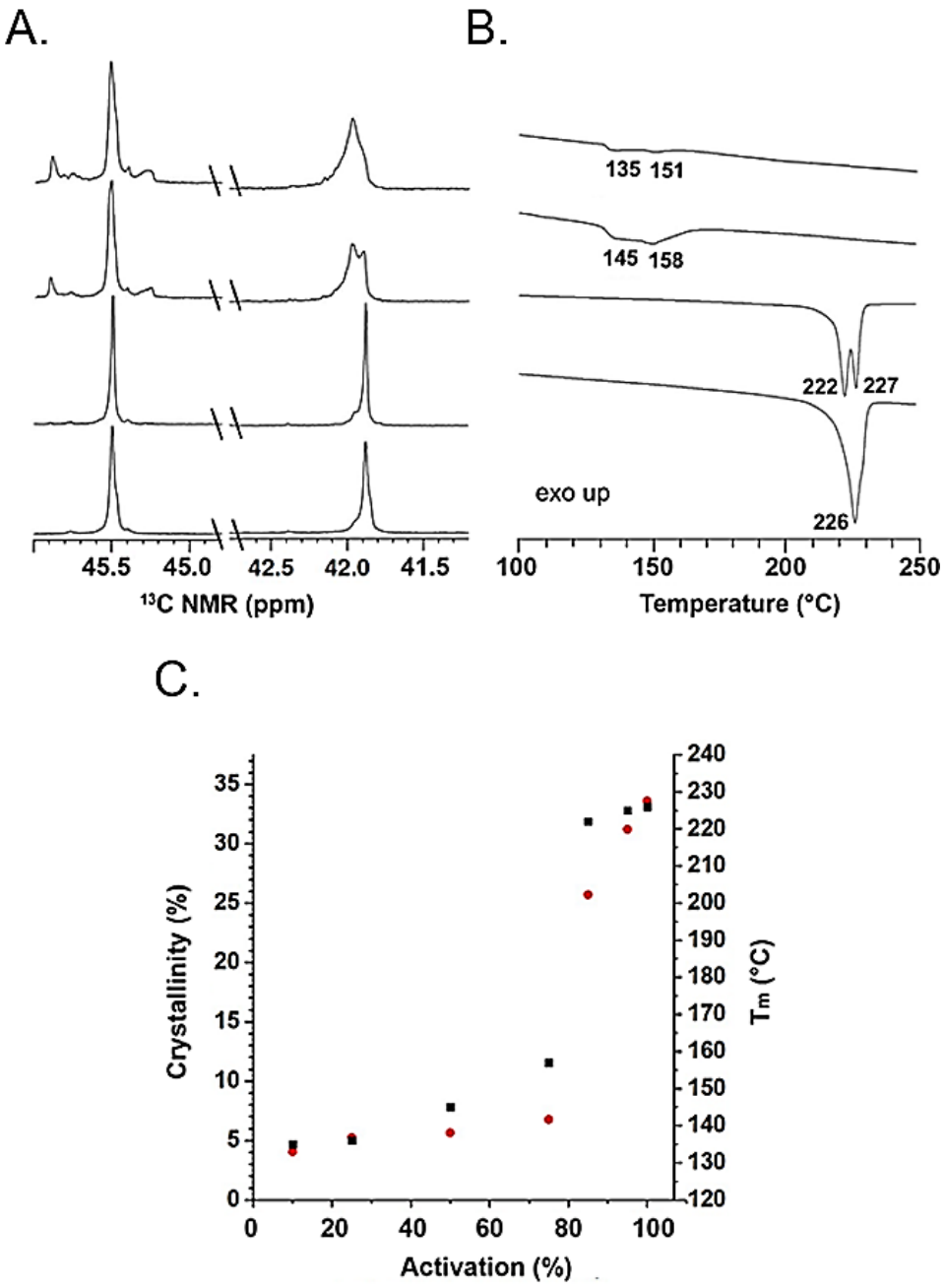

Figure 2.6 (A) Partial ^{13}C {^{1}H} NMR (200 MHz, TCE-d2, 110 °C) spectra according from bottom to top **runs 12.11, 2.13, 2.14,** and 2.**15**. (B) Partial DSC data for the same PMP samples and in the same order as in (A). (C) Plot of *Tm (red dots)* and percent crystallinity *(black squares)* as a function of percent activation of **1** by **B1** for **runs 2.11** – **2.17** of Table 2.2.†

activation, for the same equivalence of 4M1P can be explained by the decreasing number of active sites that are propagating over a period of time. Regardless of the percent activation each LCP reaction was run for a set time of 6 hours thus for these specified runs that time frame would need to be doubled or quadrupled to reach similar polymer chain lengths. Figure 2.6C shows a graphical comparison between percent activation (x-axis) and *c%* or the change in T_m (y-axis). Contrasting aPMP's linear trend between M_n and T_g, within the iPMP materials the relationship can be described as exponential.

2.5 Molecular Weight Dependency Effects on iPMP Microstructure and Physical Properties

Molecular weight dependency for tracking the stereomodulation, crystallinity, and melting points within these materials has been investigated as well. Gratefully, when away on medical leave due to brain surgery co-worker Danyon M. Fischbach worked on making samples in this study to investigate 25% and 10% activation. Accidently but fortunately these materials were of different molecular weight than the original study and samples made. This led to a series of materials of differing molecular weights to be examined to understand and investigate the correlation between properties/ structure/ and molecular weight. In Table 2.2 **run 2.14b**'s and **run 2.15b**'s molecular weights are magnitudes higher than their counterparts **run 2.14** and **run 2.15**. Regardless of this change these runs still fit within the trend and do not surpass

the higher percent activated species above it. Take **run 2.14b**, for example, which has a M_n of 104.1 kDa in comparison to **run 2.14** with an M_n of 21.8 kDa. The partial ^{13}C NMR shown in Figure 2.7 allows an understanding of that the microstructure difference and does appear different between the two differing molecular weights with the same percent activation, but these microstructures are not greater than or less than the runs of higher or lower percent activation i.e., **runs 2.13** or **2.17**). In other words, increasing or lowering the molecular weight does change the NMR profile observed but that profile still fits within the trend. To make it easier to visualize the details and labels of the runs are included in Figure 2.7 with comparative runs being color coordinated, such as **run 2.14** and 2.**14b** labeled in red and **run 2.15** and **2.15b** labeled in blue on the NMR spectra.

When it comes to the thermal analysis of these additional runs, the comparative DSC Figures 2.8 provides further insight into how molecular weight effects T_m and *c%*. When increasing molecular weight one can increase the Tm and percent crystallinity within the material but once again using example **run 2.14** verses **run 2.14b** the material still falls within the trend not going over the run 13 or under run 17 T_m or *c%*. In other words, increasing the molecular weight of a given stereomodulated PMP may prove to have a different T_m and percent crystallinity but still fall within the trend of the other materials. Our conclusion is that the T_m, crystallinity, and stereoregularity is dependent on the molecular weight of the material. More importantly, the stereomodulation has a greater effect on these physical properties therefore both must be taken into consideration when evaluating a PMP based sample.

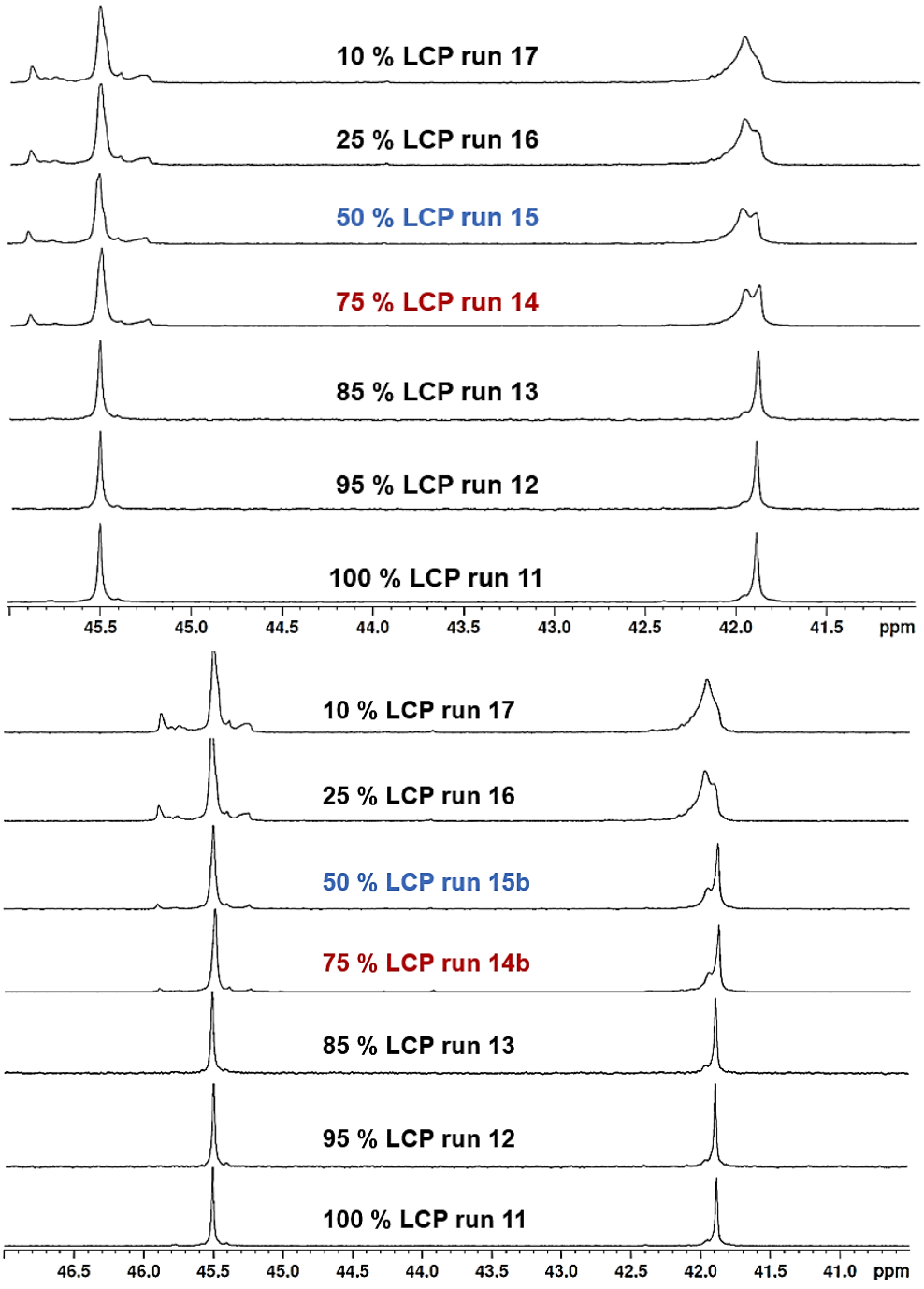

Figure 2.7 Partial vertically stacked ^{13}C {^{1}H} NMR (200 MHz, TCE-d2, 110 °C) spectra for specified runs including Table 2.2. Differences between top and bottom arranged NMR spectra is the change in molecular weight for spectra that is consequently color coordinated (red = **run 2.14** vs. **run 2.14b**; blue = **run 2.15** vs. **run 2.15b**).

The two-state degenerative technique is further implemented with CTA agent presence thus making it a two-state degenerative chain transfer system. These samples include runs **2.18** – **2.23** with more details found in Table 2.2. Overall, iPMP when made through LCCTP lead to all the same conclusions. Overall, the *c%* was lower which is attributed to the added randomness that CTA adds to the polymerization. It is important to note that regardless of CTA equivalents the material stays isotactic and crystalline in nature, take **run 2.18** verses **run 2.19** for example. Where **run 2.18** only uses 5 equivalences of $ZnEt_2$ and **run 2.19** uses 30 equivalents of $ZnEt_2$ they both still have high *Tm* and high *c%* properties. Concluding that the amounts of CTA precent during polymerization is not a limiting factor in the ability to make iPMP polymers.

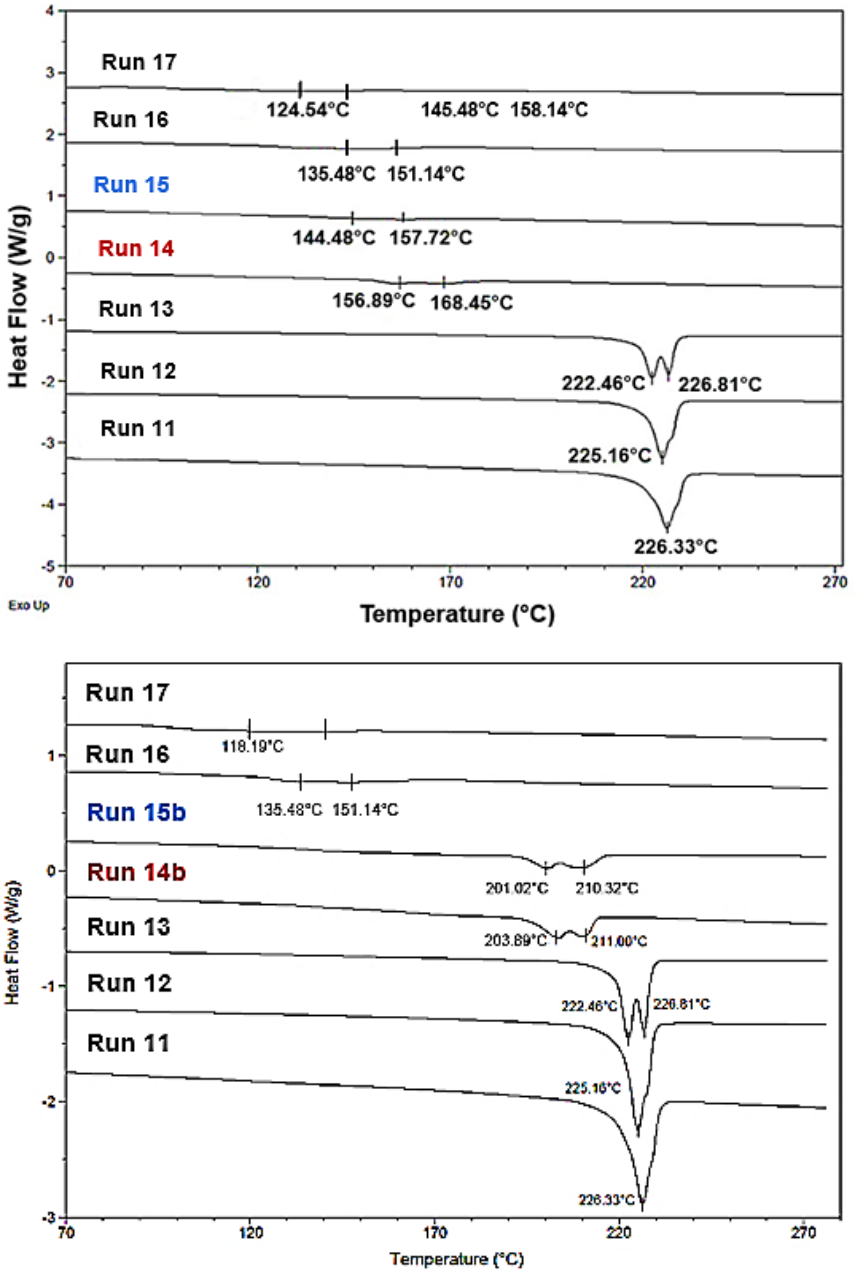

Figure 2.8 Stacked DSC traces for specified runs including Table 2.2. of only cycle 3 of a heat/cool/heat cycle with a ramp rate of 10 °C/min from 30 – 280 °C.. Differences between top and bottom arranged DSC spectra is the change in molecular weight for spectra color coordinated (red = **run 2.14** vs. **run 2.14b**; blue = **run 2.15** vs. **run 2.15b**).

2.6 Conclusions

In summary, the results presented within this study demonstrate the ability to further stereoengineer the tacticity and physical properties of a polyolefin that has only ever been commercialized as a highly isotactic form by Mitsui under the name TPX. The challenge of overriding a strong degree of chain-end control exerted by the growing PMP chain can be met by employing the toolbox of LCP and LCCTP techniques in a designable fashion. The saying ‘one-catalyst, many materials’ our group has made in the past rings strong as this study provides clear evidence of such. Through the creation of a large family of stereomodulated polymers only through small changes in the system while employing one catalysis motif. Lastly, the documentation of all these 1,2-regioregular atactic PMP materials helps clear up past misunderstandings and misinformation regarding the properties of similar material. The results of this study have only further assisted in more novel PMP-based materials to be made. These efforts immediately pay off and can be seen in the next chapter.

2.7 Supporting Experimental Information†

2.7.1 Synthetic Procedures

All manipulations of air and moisture sensitive compounds were carried out under N_2 atmospheres with standard Schlenk line or glovebox techniques. Toluene (ReagentPlus, 99%) was dried and deoxygenated by passage over activated alumina and GetterMax® 135 catalyst (purchased from Research Catalysts, Inc.) and collected prior to use. Chlorobenzene (Acros Organic, 99%) was dried over calcium hydride by refluxing at 130 ^oC for three days and distilled under N_2 prior to use. 1, 1, 2, 2-Tetrachloroethane(C_2Cl_4)-*d2* was purchased from Cambridge Isotopes and used as received. Chloroform-d_1 was purchased from Cambridge Isotopes and used as received. 4-methyl-1-pentene (>97%) were purchased from TCI Chemicals, dried over Na/K alloy and isolated by vacuum-transfer prior to use. Diethylzinc (>52wt.% Zn) was purchased from Sigma-Aldrich and used as received. All other solvents and reagents were used as received unless otherwise stated.

General procedure for living coordinative chain transfer polymerization (LCCTP) of atactic poly(4-methyl-1-pentene) (aPMP) via Hafnium Diethyl Catalyst (2 in pp 1b in SI).

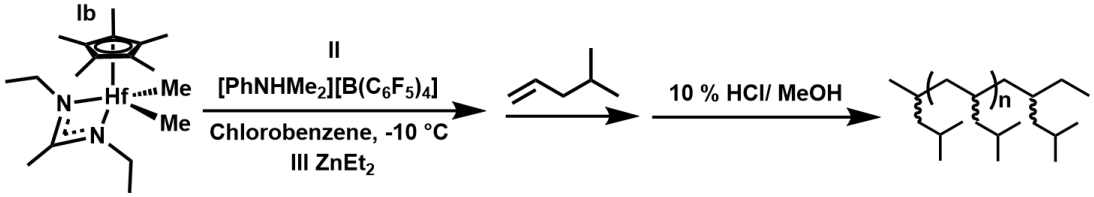

In a round bottom flask, 40 mL of toluene was cooled to -5 °C. The 4M1P monomer of targeted equivalents was added to the flask. Then chain transfer agent **III**, was added

to the flask. Then a solution of **Ib** (0.04 mmol, 18.3 mg), in -5 °C 1.0 mL PhCl was added to **II** (0.044 mmol, 35.3 mg) which was vigorously agitated until dissolved and activated, whereupon it was added to the flask. The flask was stirred for typically 18 hours at -5 °C and quenched with 10% HCl/ methanol. The material was then run through a silica column using hexane, collected into a pre-weighed vial, and dried under vacuum. Details on the amount of the reagents and polymer's characterization are provided in **Table S2.1, runs 2.1 – 2.6**.

General Procedure for Living Coordinate Polymerization (LCP) of poly(4-methyl-1-pentene) (PMP) via Hafnium Diethyl Catalyst. (2 in pp 1b in SI).

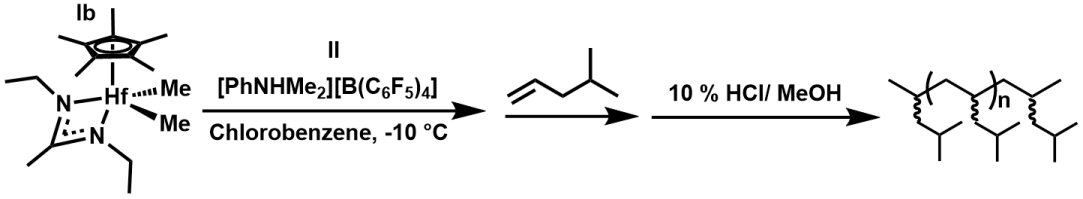

In a round bottom flask, 50 mL of toluene was cooled to -5 °C. The 4M1P monomer of targeted equivalents was added to the flask. Then a solution of **Ib** (0.05 mmol, 22.9 mg), in -5 °C 1.0 mL PhCl was added to **II** (0.055 mmol, 44.1 mg) which was vigorously agitated until dissolved and activated, whereupon it was added to the flask. The flask was stirred for typically 4 hours at -5 °C and quenched with 10% HCl/ methanol. The material was then run through a silica column using hexane, collected into a pre-weighed vial, and dried under vacuum. Details on the amount of the reagents and polymer's characterization are provided in Table S2.1, **runs 2.7 – 2.10**.

General Procedure for Living Coordinate Polymerization (LCP) of poly(4-methyl-1-pentene) (PMP) with varied activation via Zirconium Catalyst (1 in pp and 1a in SI)..

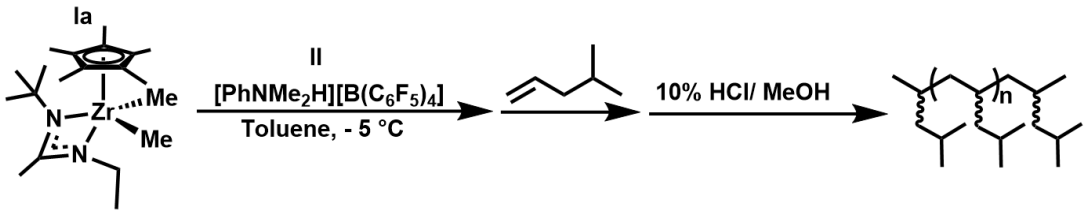

In a round bottom flask, 50 ml of chlorobenzene (PhCl) was cooled to -10 °C. 4-methly-1-pentene (4M1P) monomer of targeted equivalents was added to the flask. Preweighed **Ia** (0.05 mmol, 19.9 mg) is mixed with **II**, with 1.0 ml of cold PhCl and added to the reaction mixture resulting in a bright yellow color. The reaction mixture stirred typically for 4 hr. The reaction was removed from the glovebox and quenched/precipitated in 500 mL of acidic methanol (10% HCl) overnight. The polymer was vacuum filtered and washed with methanol (x3) then collected in a pre-weighed vial and dried under vacuum. Samples polymerized via LCP conditions using substoichiometric amounts of **II** (i.e. [**II**]/[**I**] < 1.0), activation of precatalyst still resulted in the bright yellow color and followed the same procedure as before. Details on the amount of the reagents and polymer's characterization are provided in Table S2.2, **runs 2.11 – 2.17**.

General procedure for living coordinative chain transfer polymerization (LCCTP) of atactic poly(4-methyl-1-pentene) (aPMP) via Zirconium Catalyst (1 in pp and 1a in SI).

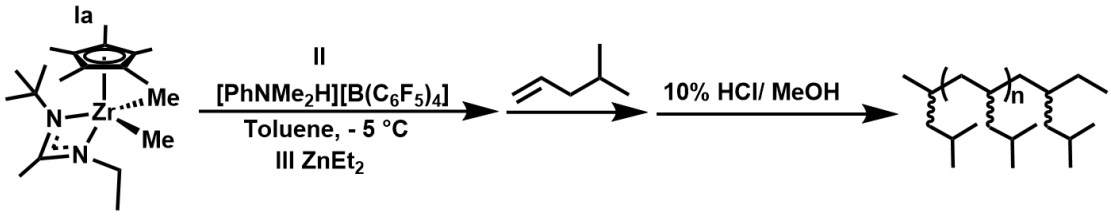

In a round bottom flask, 20 mL of toluene was cooled to 0 °C. The 4M1P monomer (11.9 mmol, 1.0 g) was added to the flask. Then chain transfer agent **III** (0.1 mmol, 12.4 mg), was added to the flask. Then a solution of **Ia** (0.02 mmol, 7.95 mg), with 0 °C 1.0 mL PhCl was added to **II** which was vigorously agitated until dissolved and activated, whereupon it was added to the flask. The reaction was removed from the glovebox, after typically 18 hr, and quenched/precipitated in 500 mL of acidic methanol (10% HCl) for at least 1 hr. The polymer was vacuum filtered and washed with methanol (x3) then collected in a pre-weighed vial and dried under vacuum. Samples polymerized via LCCTP conditions using substoichiometric amounts of **II** (i.e. [**II**]/[**I**] < 1.0), activation of precatalyst still resulted in the bright yellow color and followed the same procedure as before. Details on the amount of the reagents and polymer's characterization are provided in Table S2.2, **runs 2.18 – 2.23**.

Table S2.1. LCCTP and LCP of aPMP.

Run	$ZnEt_2$ (equiv.)	4M1P (equiv.)	Yield (g)	M_n (kDa)[b]	M_w (kDa)[b]	Đ[b]	Tg (°C)[c]
2.1	30	713	1.45	0.835	0.967	1.15	-48.7
2.2	10	595	1.24	2.60	3.07	1.18	-6.06
2.3	5	595	1.19	3.30	3.91	1.18	3.92
2.4	5	891	1.92	6.18	7.18	1.16	10.32
2.5	2	1190	1.09	31.4	36.4	1.16	31.4
2.6	2	1220	3.56	48.7	58.2	1.19	39.5
2.7	-	12.0	0.100	3.21	3.80	1.18	7.91
2.8	-	60.0	0.500	10.4	12.2	1.17	29.7
2.9	-	595	0.990	98.7	152	1.53	39.2
2.10	-	1190	1.98	126	192	1.52	39.4

[a]For complete details of polymerization conditions for each run, see SI. [b]Determined by SEC. [c]Determined by DSC. **Runs 2.1 – 2.6** are via LCP and **Runs 2.7 – 2.10** are via LCCTP.

Table S2.2. LCP (top half) and LCCTP (bottom half) of 4M1P using 2 and varying equivalents of B1 and CTA

Run	[II/I]	$ZnEt_2$ (eq)	4M1P (eq)	Yield (g)	M_n (kDa)[a]	M_w (kDa)[a]	Đ[a]	Tg (°C)[b]	Tm (°C)[b]	%Crystallinity
2.11	1.1	-	280	0.409	51.0	70.9	1.38	-	226	33.6
2.12	0.95	-	280	0.512	48.1	66.9	1.34	-	225	31.2
2.13	0.85	-	280	0.548	61.4	81.7	1.32	-	222; 227	25.7
2.14[c]	0.75	-	100	0.336	16.8	19.8	1.43	29.4	157; 168	6.78
2.15[c]	0.50	-	100	0.335	16.8	19.8	1.18	27.4	145; 158	5.65
2.16	0.25	-	100	0.289	13.0	14.9	1.15	28.8	136; 151	5.26
2.17	0.10	-	100	0.220	8.80	9.94	1.13	24.9	135; 151	4.06
2.14b[c]	0.75	-	280	0.538	91.3	104.1	1.14	32.6	204; 211	11.6
2.15b[c]	0.50	-	100	0.336	17.8	21.8	1.22	29.1	190; 202	8.49
2.18[e]	1.1	5	595	0.745	6.18	22.6	3.29	-	214	23.1
2.19[e]	1.1	30	4280	3.67	7.34	14.95	2.02	28.8	223	33.3
2.20	0.95	5	595	0.955	5.01	10.2	2.04	25.3	218	26.1
2.21	0.85	5	595	0.999	3.11	5.04	1.82	22.3	217	19.1
2.22	0.75	5	595	0.748	3.95	7.65	1.94	4.56	149; 164	2.25
2.23	0.50	5	595	0.240	6.18	10.7	1.73	13.6	145; 162	3.77

[a]For details of polymerization conditions for each run, see SI. [b]Determined by SEC. [c]Determined by DSC. [d]These runs were created to show *Mn* dependency. Below dotted line LCCTP reactions. [e]These runs have same percent activation but differing molecular weighs.

2.7.2 Characterization Parameters

Nuclear Magnetic Resonance (NMR) Spectroscopy of ^{1}H and $^{13}C\{1H\}$ nuclei was carried out with a Bruker DRX 600 with BBFO probe or Bruker AVIII-HD 800 spectrometer fitted with a cryo-QCI probe. Chloroform-*d1* was used as the solvent for polymer samples using LCCTP synthesis. 1,1,2,2-C_2Cl_4-*d2* was used as the solvent for polymer samples using LCP synthesis and heated to 110 °C. All spectra were referenced to tetramethyl silane using residual ^{1}H and $^{13}C\{^{1}H\}$ chemical shifts of the deuterated solvents.

Gel Permeation Chromatography (GPC) was used to obtain molecular weight (Mn and Mw) and polydispersity index (PDI) of polymers using Viscotek GPCMax equipped with three columns (Styragel HR 4, HR 3, and HR 1) in a column oven and differential refractometer (Viscotek TDA 302) maintained at 40 °C. Tetrahydrofuran (HPLC Grade) was used as the eluent with a flow rate of 1 mL/min. Polystyrene standards (from Agilent Technologies, 370 Da – 128.7 kDa) were used for calibration. For GPC sample preparation, 2 mg of dry polymer sample was dissolved in 1 mL of THF (HPLC Grade).

Size Exclusion Chromatography (SEC). High temperature size exclusion chromatography was performed using a Tosoh HT-Eco SEC instrument with differential refractive index detection. Narrow dispersity polystyrene standards were used for calibration. Measurements were performed at 135 °C using 1,2,4-

trichlorobenzene as the mobile phase (300 mg/kg Irganox 1010 was added as antioxidant to the solvent). The stationary phase was a set of 3 Tosoh HTs columns (2 Tosoh TSKgel GMHhrH (S) HT2, 13 μm mixed bed, 7.8 mm ID × 30 cm columns and 1 Tosoh TSKgel GMHHR-H (20) HT2, 20 μm, 7.8 mm ID × 30 cm column with an exclusion limit ~4 × 108 g/mol).

Differential scanning calorimetry (DSC) was used to obtain thermal transition (Tg and Tm) values using TA instruments DSC Q1000 system. Samples were run in sealed hermetical aluminum pans with an empty pan as reference. A heat/cool/heat temperature program was used at a ramp rate of 10 or 20 °C/min with varied temperature ranges. The initial mass of the sample was between 4.5 -10 mg.

Powder X-ray Diffraction (XRD) Samples were carried out with a D8 Advanced Diffractometer equipped with a LynxEye detector under ambient conditions. On a scatter less sample holder the sample was compacted in a circle with a diameter of 2mm for measurement. X-rays from Cu Kα radiation source with a wavelength of 1.5418 Å was used, and the θ-angle starting at 5° ending at 60° with a 0.05° step. The data profiles were processed using Advanced TOPAS.

2.7.3 Supporting Results

A.

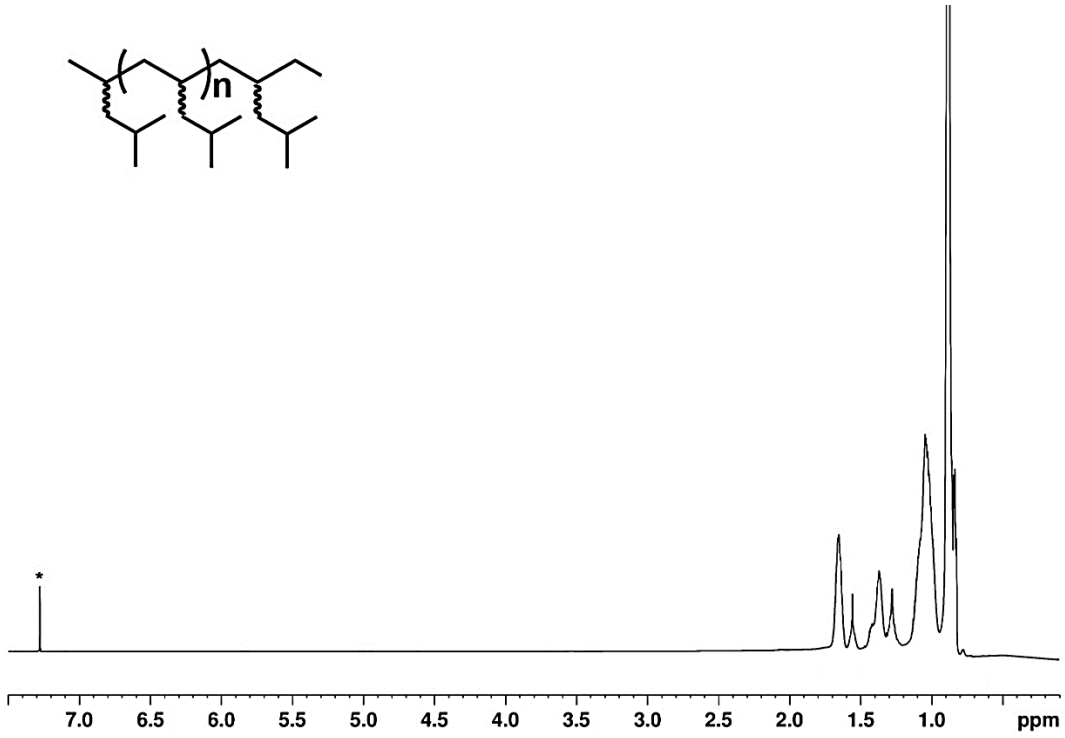

B.

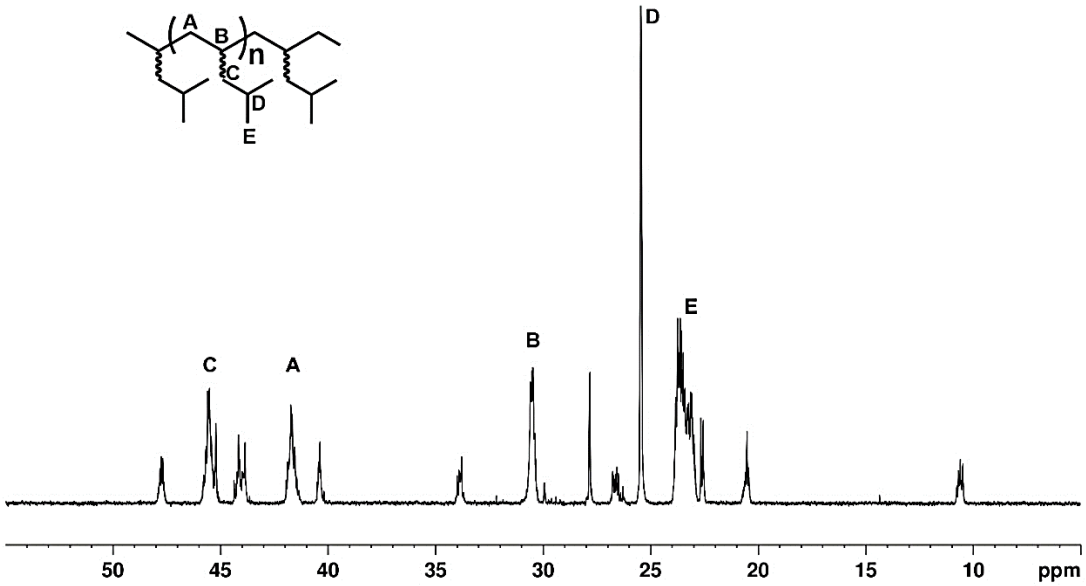

Figure S2.1. (A) ^{1}H NMR (600 MHz, *Chloroform-d1) of **run 2.1.** (B) partial ^{13}C-NMR (150 MHz, *Chloroform-d1) of **run 2.1.**

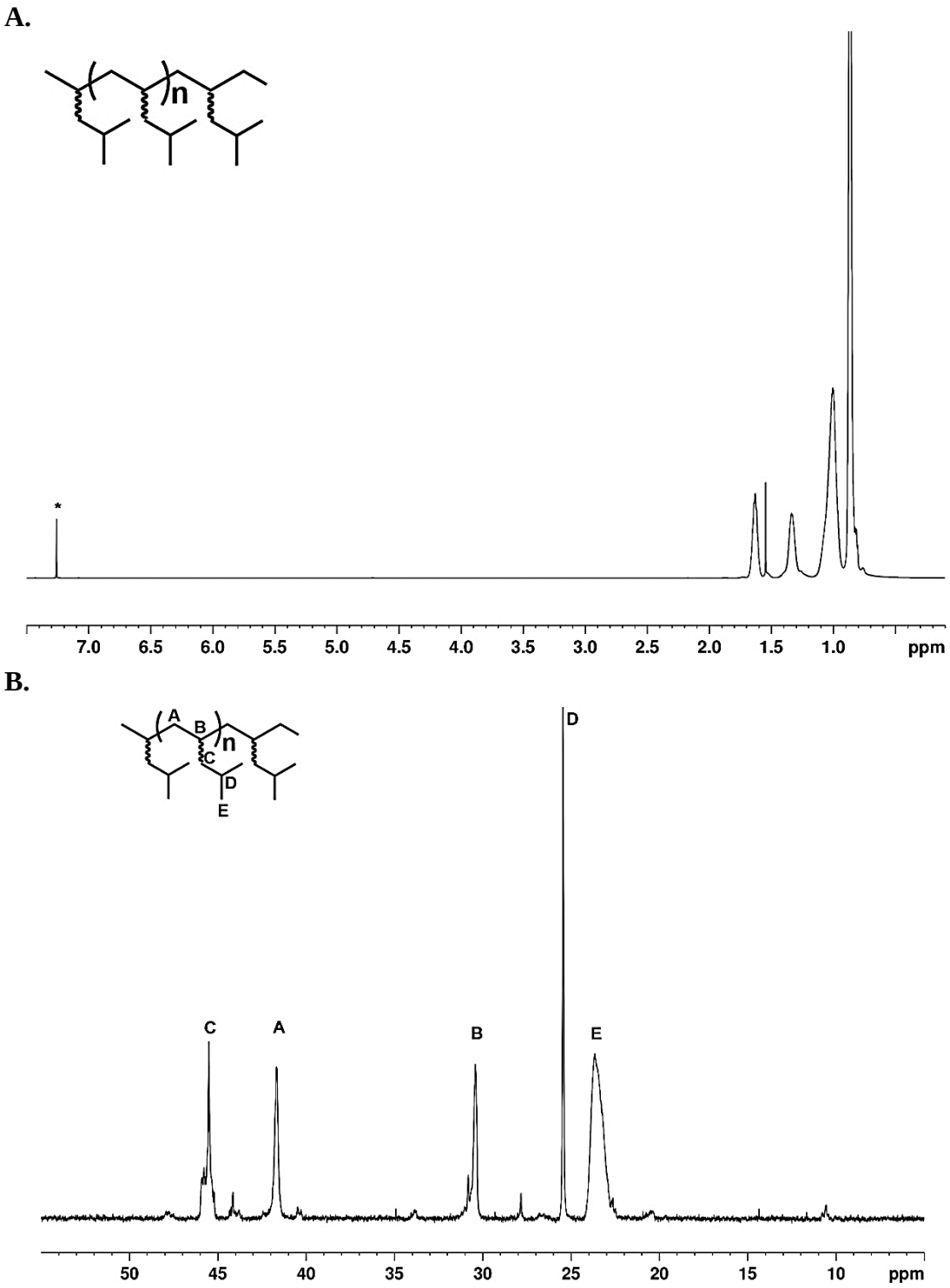

Figure S2.2. (A) ^{1}H NMR (600 MHz, *Chloroform-d1) of **run 2.2**. (B) partial ^{13}C-NMR (150 MHz, *Chloroform-d1) of **run 2.2**.

A.

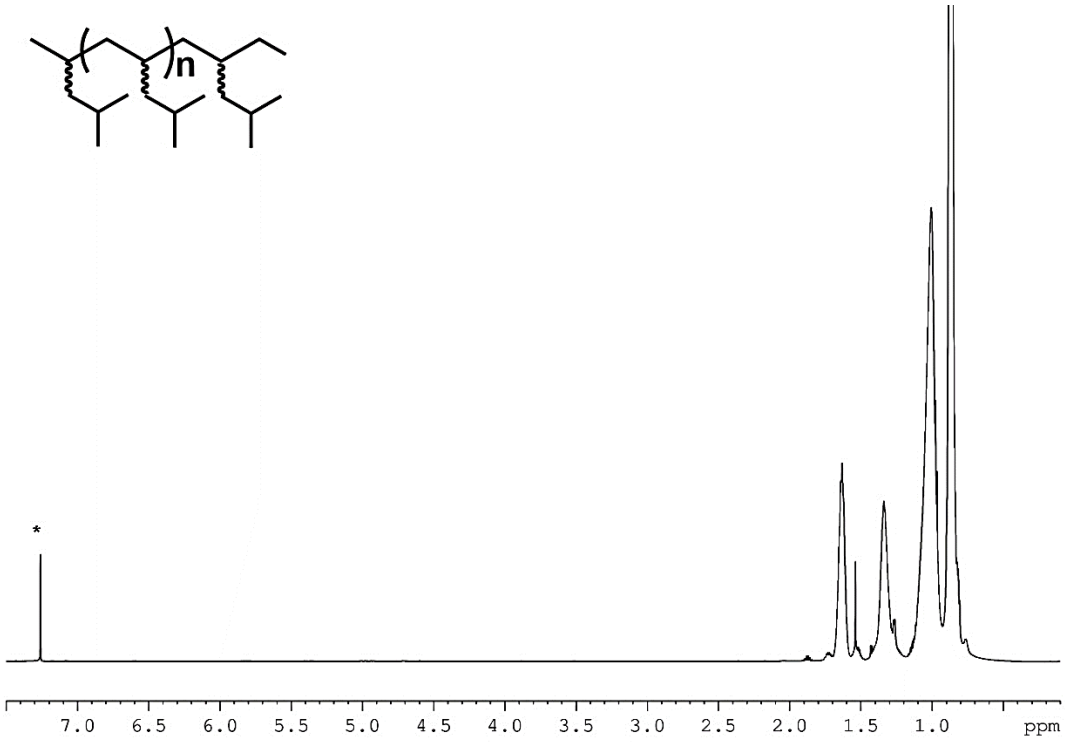

B.

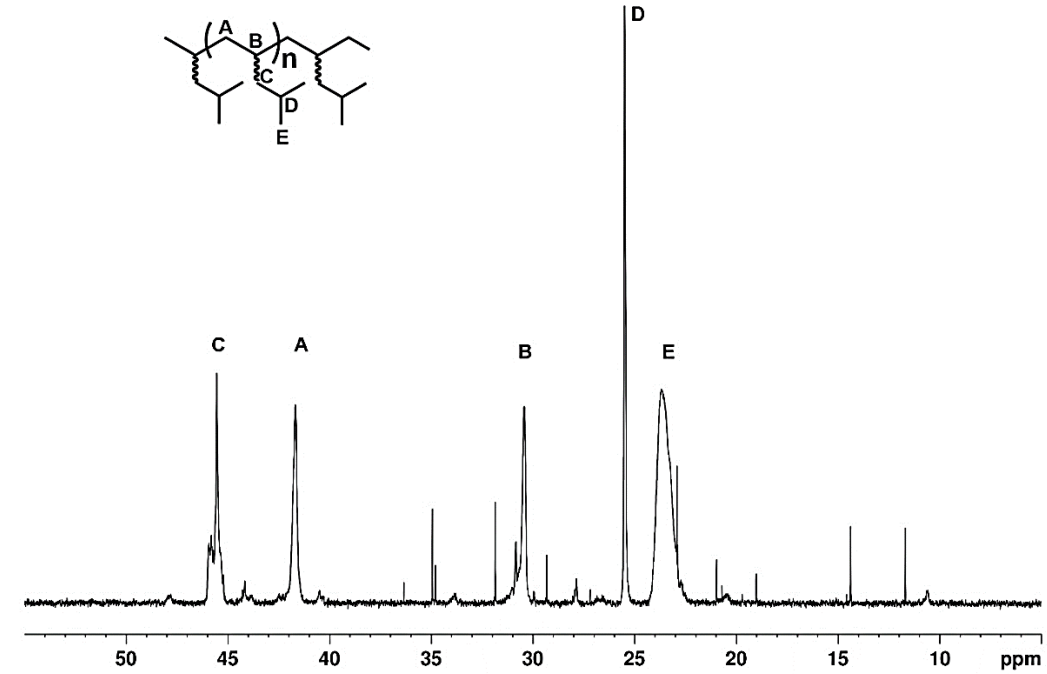

Figure S2.3. (A) ^{1}H NMR (600 MHz, *Chloroform-d1) of **run 2.3**. (B) partial ^{13}C-NMR (150 MHz, *Chloroform-d1) of **run 2.3**.

A.

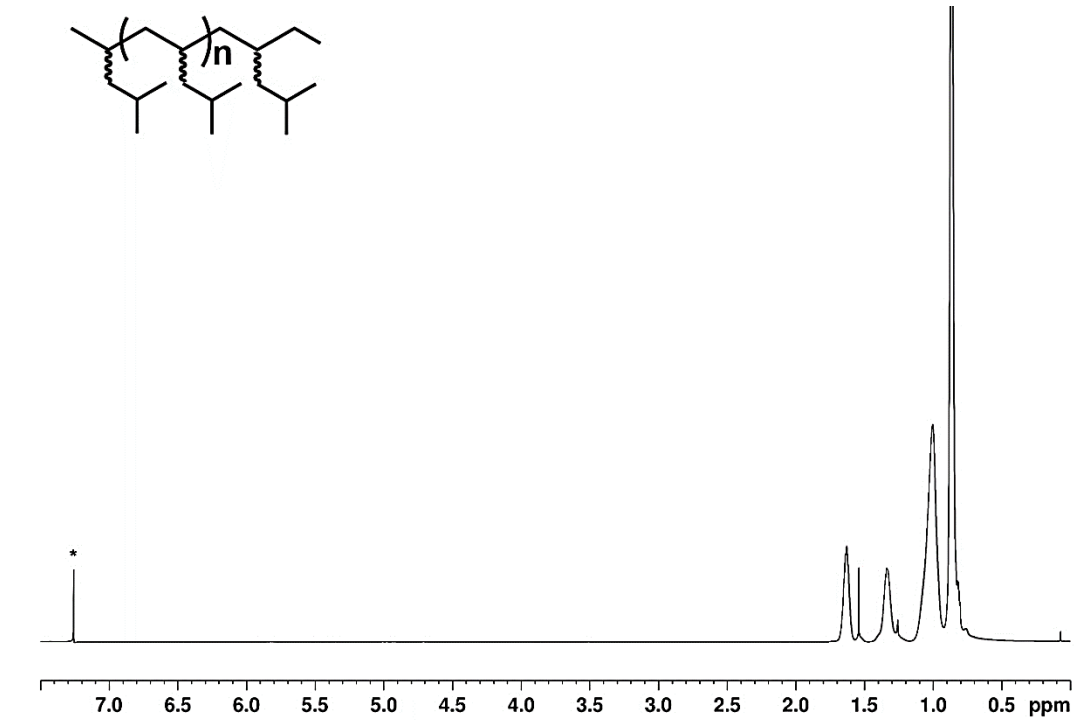

B.

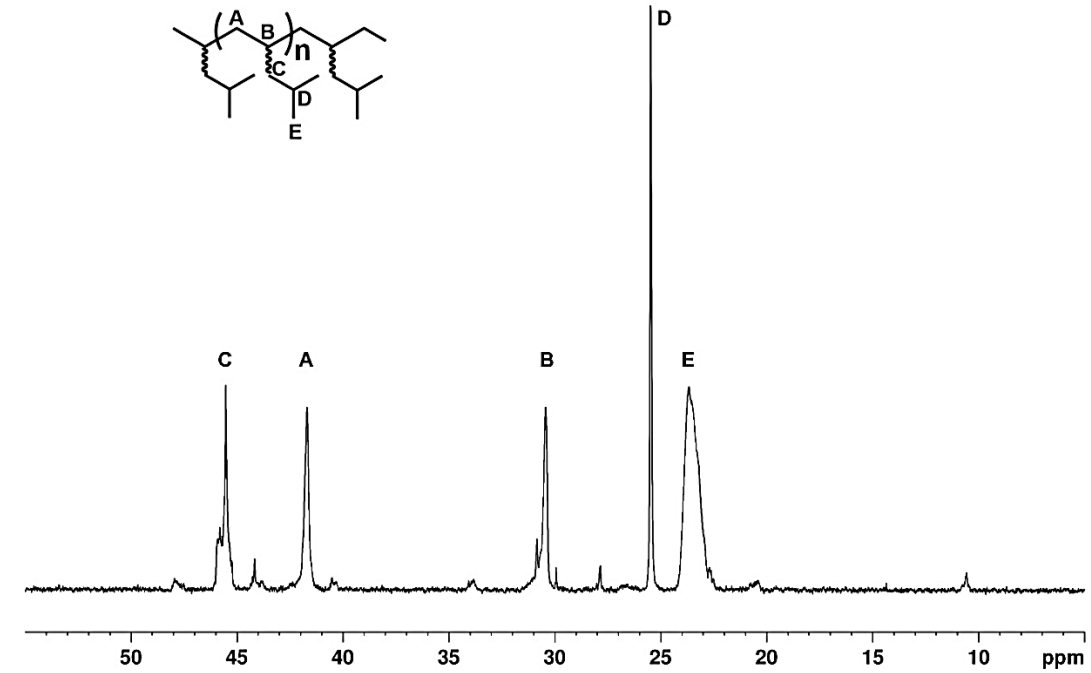

Figure S2.4. (A) ^{1}H NMR (600 MHz, *Chloroform-d1,) of **run 2.4**. (B) partial ^{13}C-NMR (150 MHz, *Chloroform-d1) of **run 2.4** (6.18 kDa Hf LCCTP).

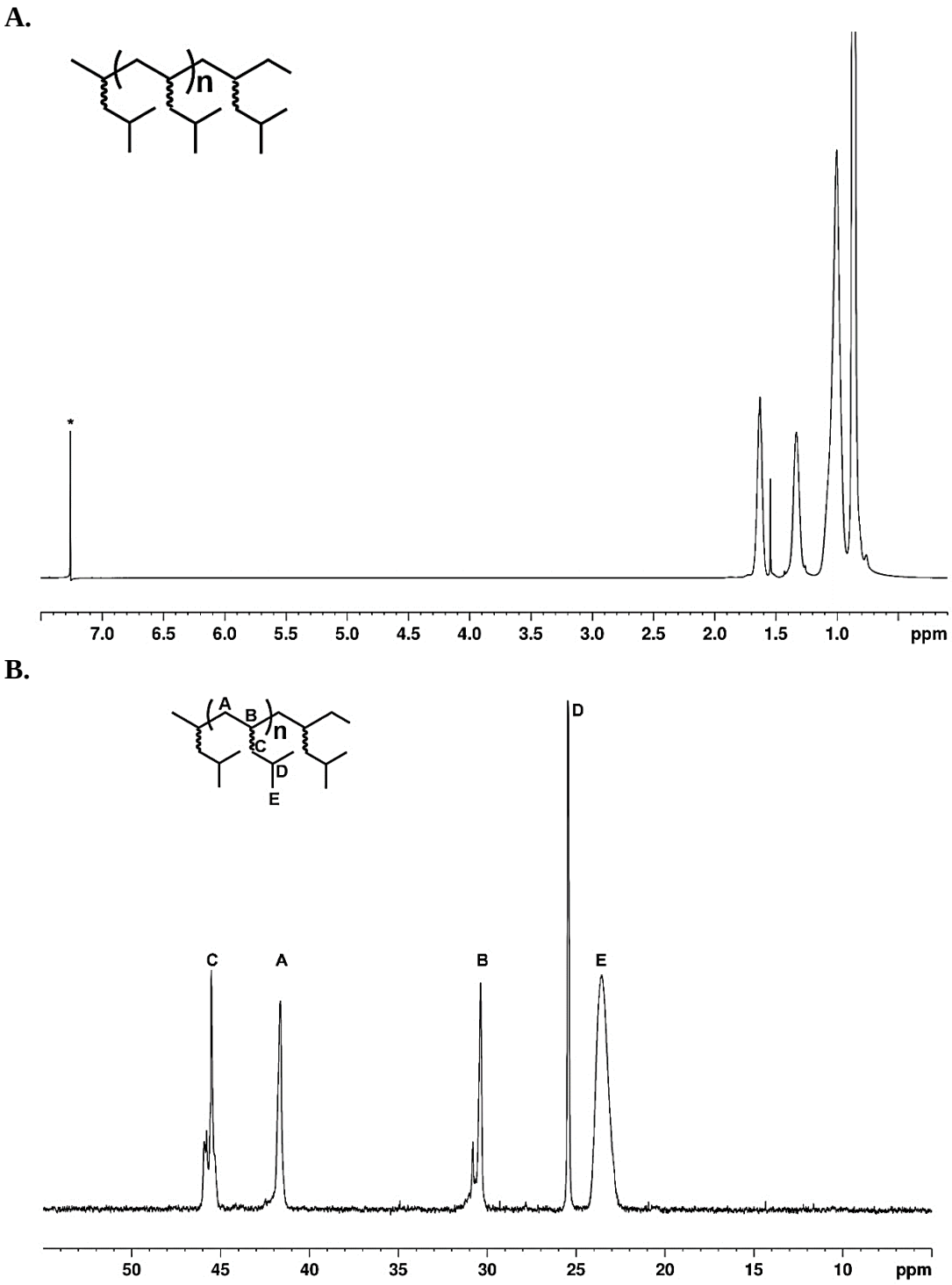

Figure S2.5. (A) ^{1}H NMR (600 MHz. *Chloroform-d1) of **run 2.5**. (B) partial ^{13}C-NMR (150 MHz, *Chloroform-d1) of **run 2.5**.

A.

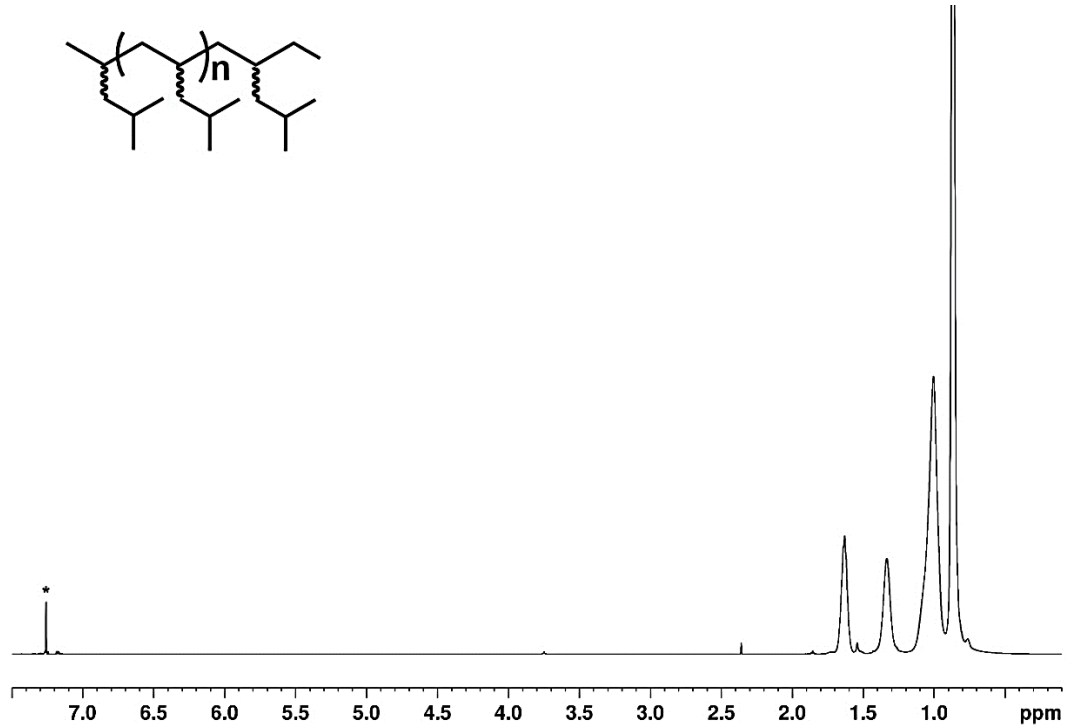

B.

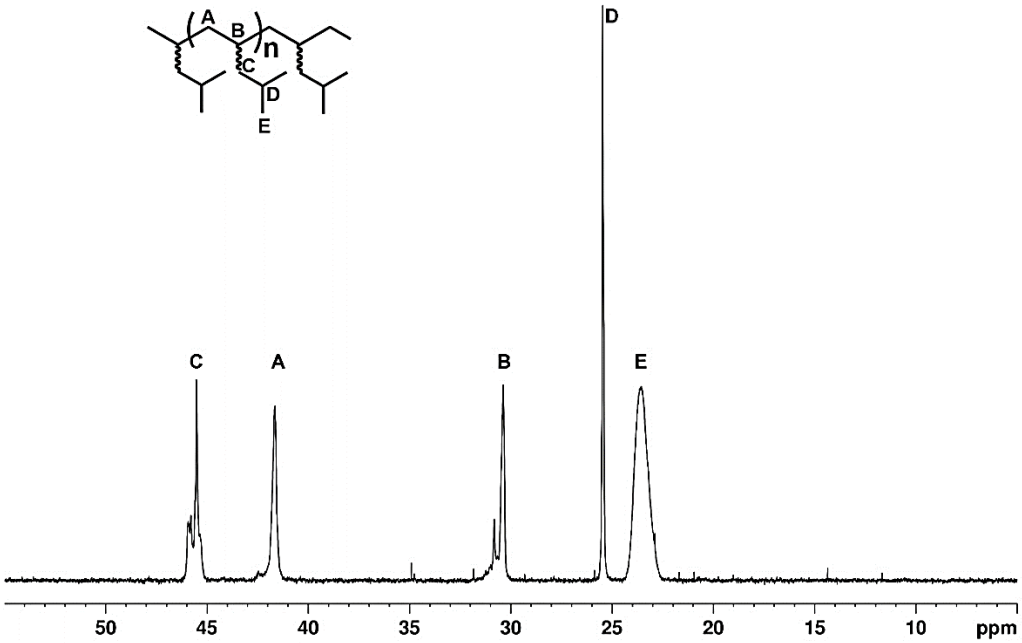

Figure S2.6. (A) ^{1}H NMR (600 MHz. *Chloroform-d1) of **run 2.6**. (B) partial ^{13}C-NMR (150 MHz, *Chloroform-d1) of **run 2.6**.

A.

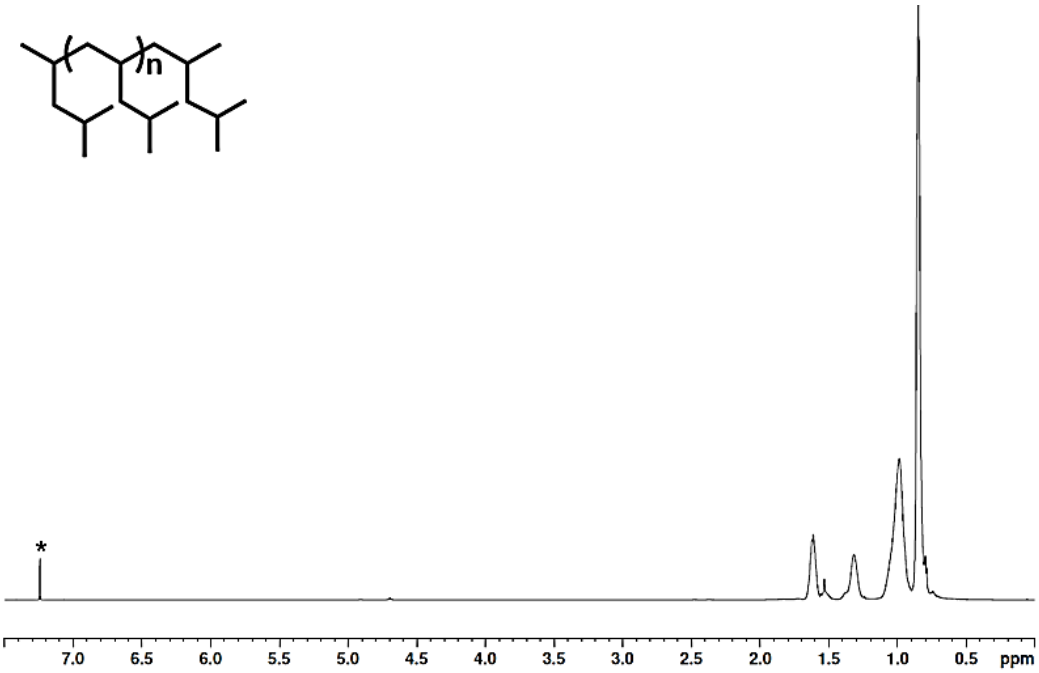

B.

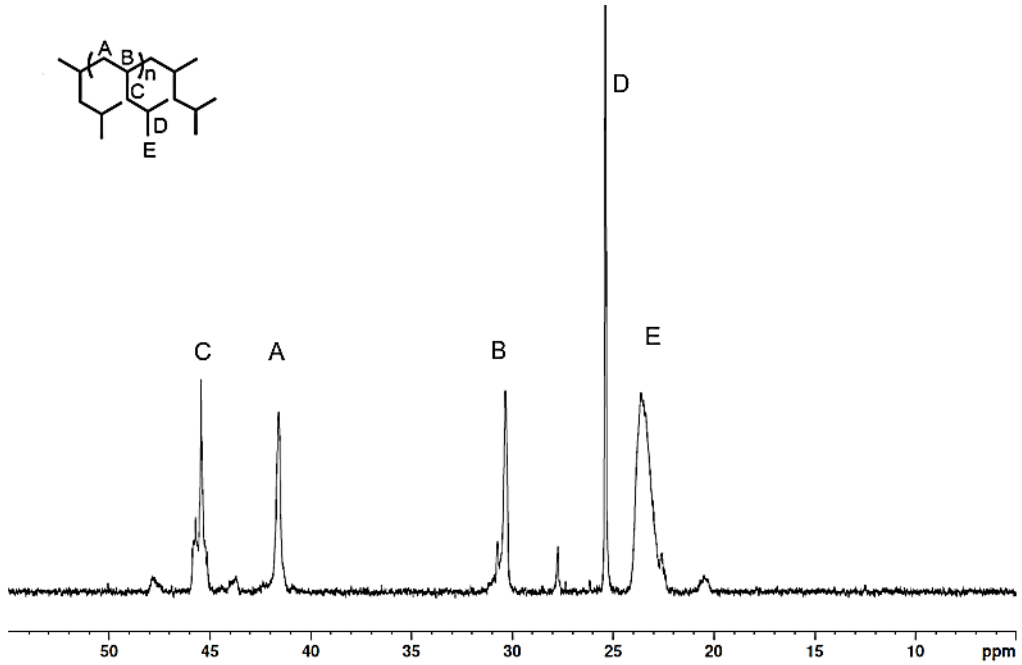

Figure S2.7. (A) ^{1}H NMR (600 MHz. *Chloroform-d1) of **run 2.7**. (B) partial ^{13}C-NMR (150 MHz, *Chloroform-d1) of **run 2.7**.

A.

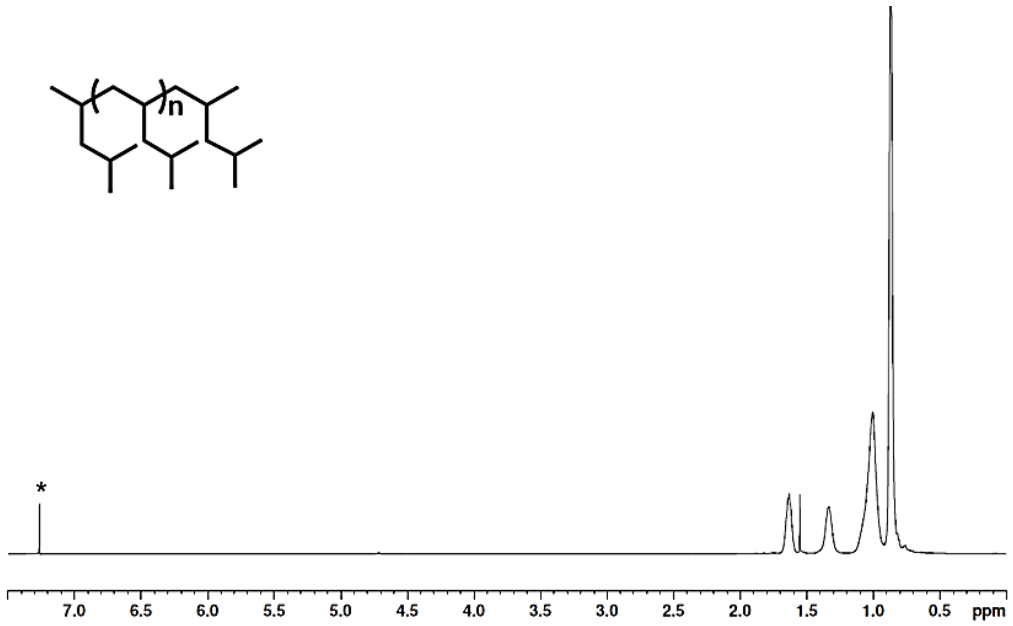

B.

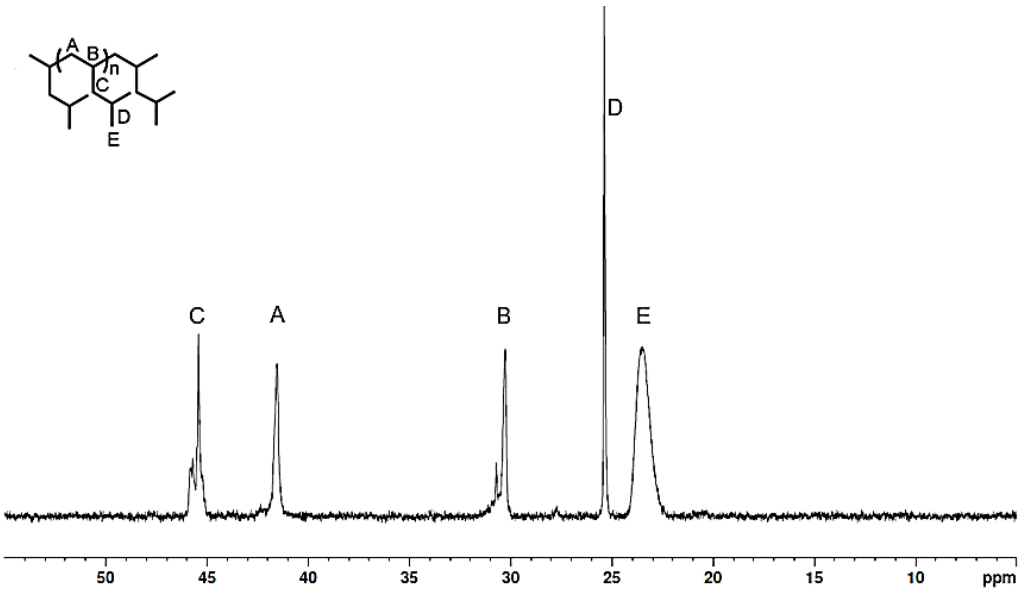

Figure S2.8. (A) ^{1}H NMR (600 MHz. *Chloroform-d1) of **run 2.8**. (B) partial ^{13}C-NMR (150 MHz, *Chloroform-d1) of **run 2.8**.

A.

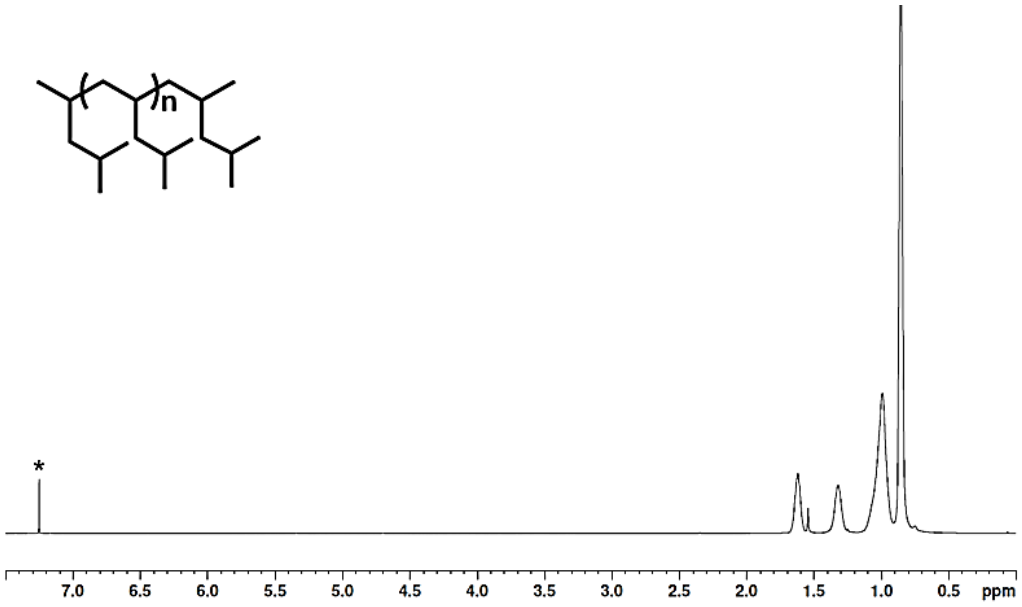

B.

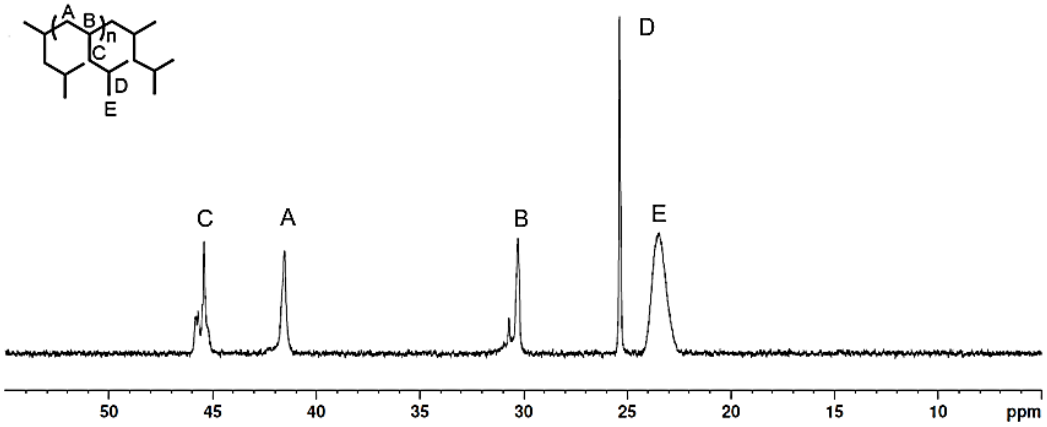

Figure S2.9. (A) ^{1}H NMR (600 MHz. *Chloroform-d1) of **run 2.9.** (B) partial ^{13}C-NMR (150 MHz, *Chloroform-d1) of **run 2.9.**

A.

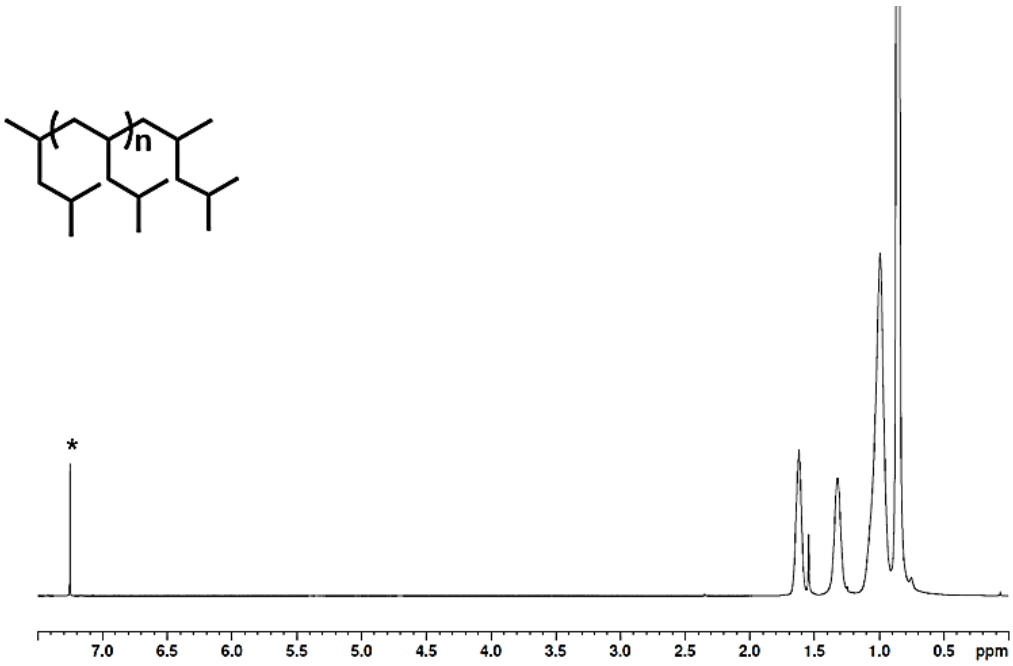

B.

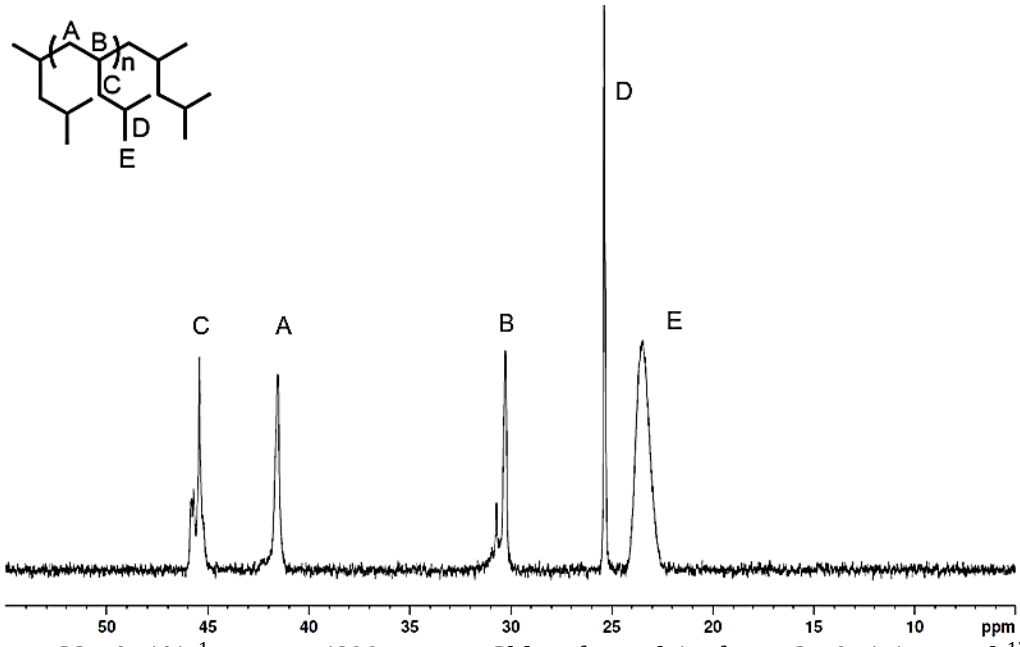

Figure S2.10. (A) ^{1}H NMR (600 MHz. *Chloroform-d1) of **run 2.10.** (B) partial ^{13}C-NMR (150 MHz, *Chloroform-d1) of **run 2.10.**

A.

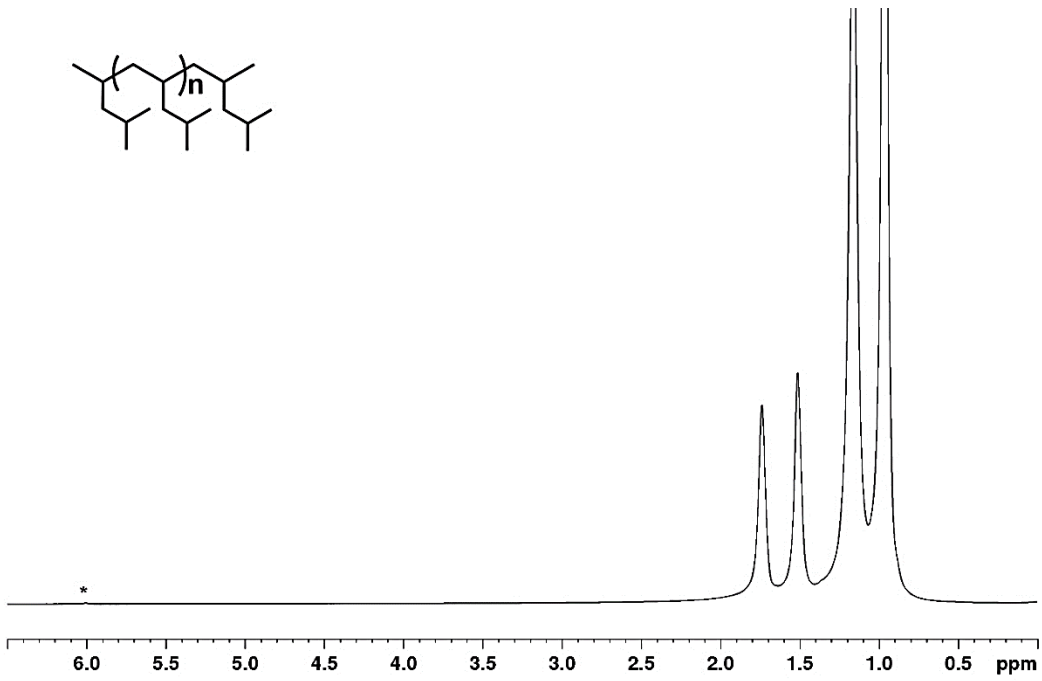

B.

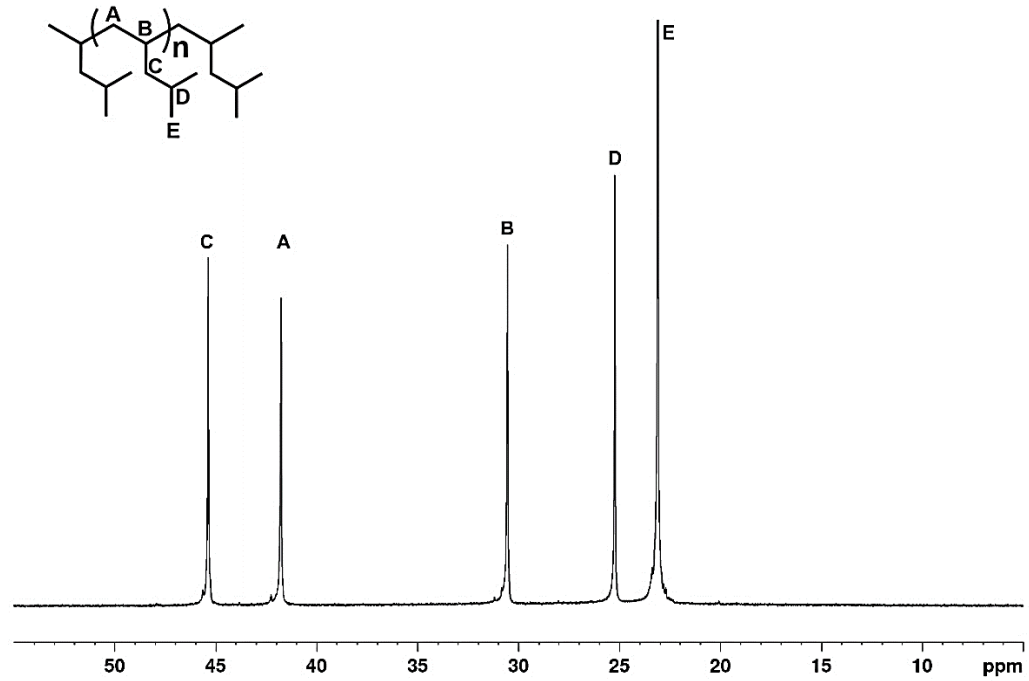

Figure S2.11: (A) ^{1}H-NMR (600 MHz, *1,1,2,2-C_2Cl_4-*d2*, 110 °C after 1 h of temperature equilibration) of **run 2.11**. (B) partial ^{13}C NMR (150 MHz, *1,1,2,2-C_2Cl_4-*d2*, 110 °C after 1 h of temperature equilibration) of **run 2.11**.

A.

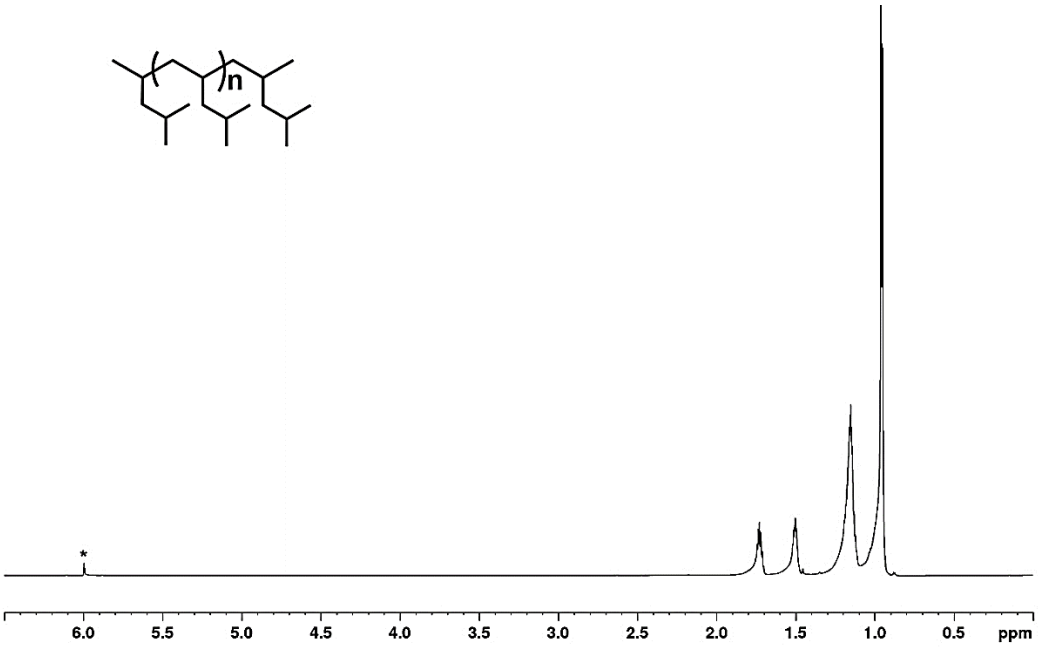

B.

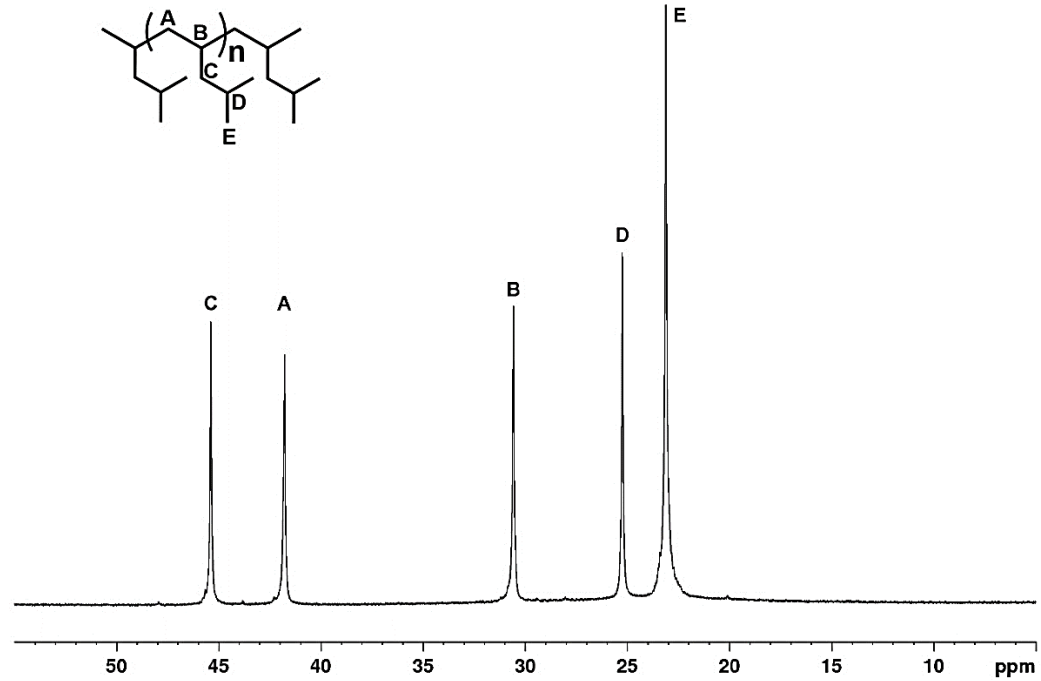

Figure S2.12: (A) ^{1}H-NMR (800 MHz, *1,1,2,2-C_2Cl_4-*d2*, 110 °C 1 h of temperature equilibration) of **run 2.12**. (B) partial ^{13}C NMR (200 MHz, *1,1,2,2-C_2Cl_4-*d2*, 110 °C after 1 h of temperature equilibration) of **run 2.12**.

A.

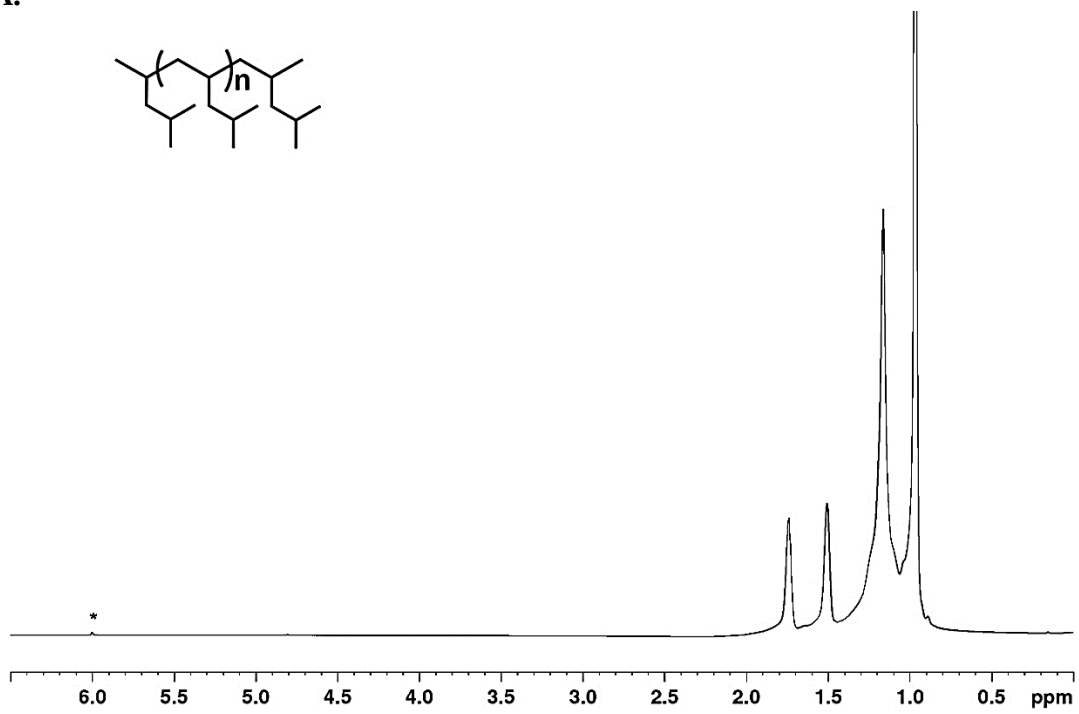

B.

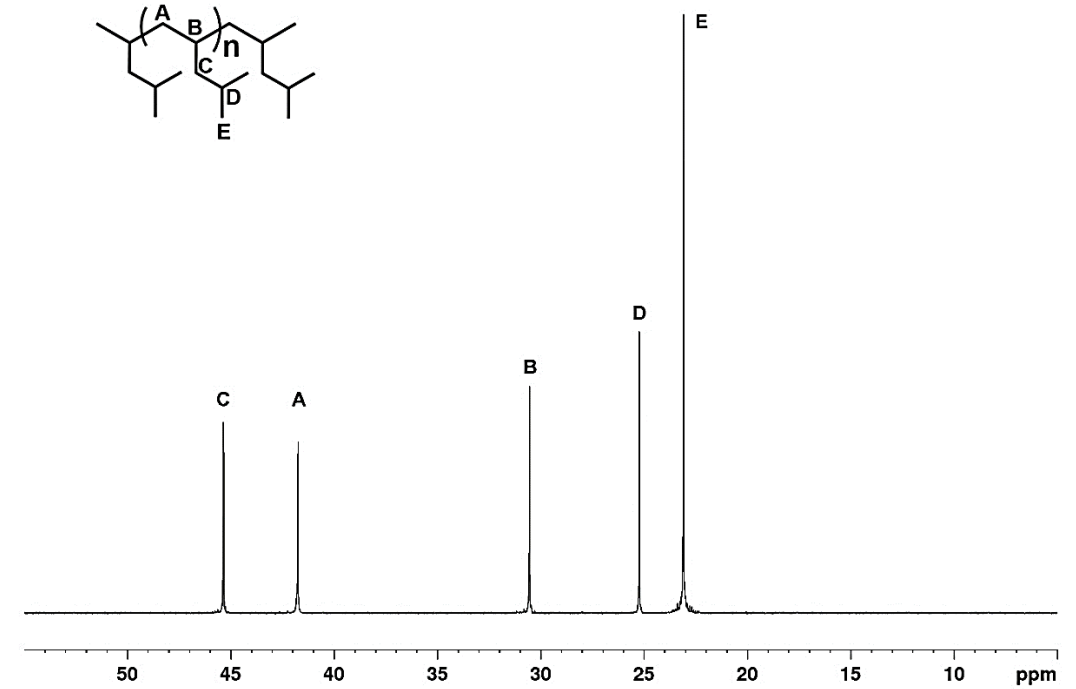

Figure S2.13: (A) ^{1}H-NMR (800 MHz, *1,1,2,2-C_2Cl_4-*d2*, 110 °C after 1 h of temperature equilibration) of **run 2.13**. (B) partial ^{13}C NMR (200 MHz, *1,1,2,2-C_2Cl_4-*d2*, 110 °C after 1 h of temperature equilibration) of **run 2.13**.

A.

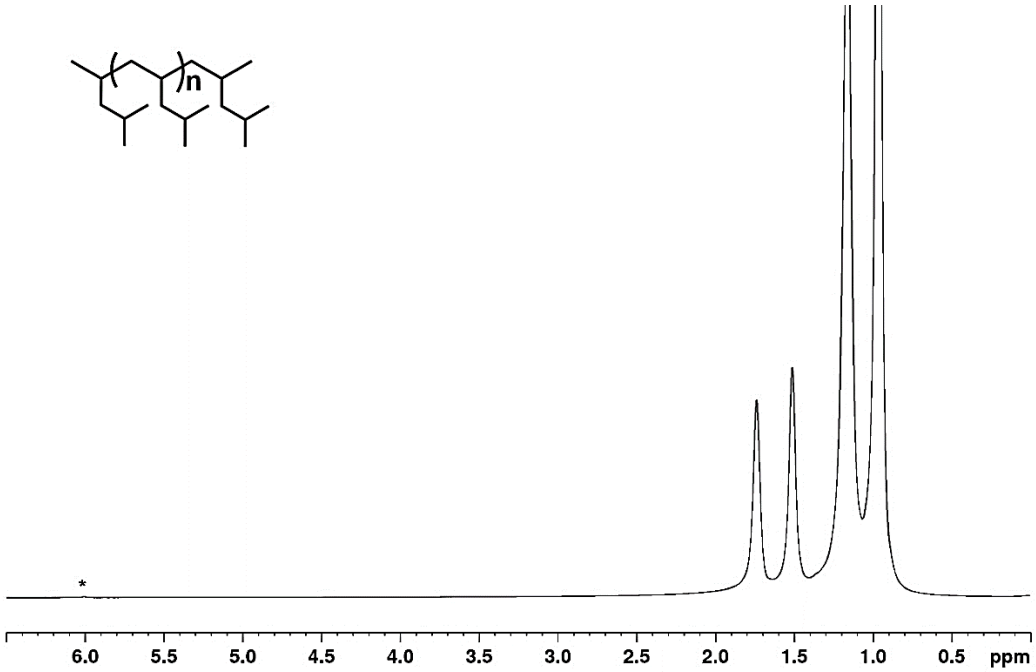
n
*
6.0
5.5
5.0
4.5
4.0
3.5
3.0
2.5
2.0
1.5
1.0
0.5
ppm

B.

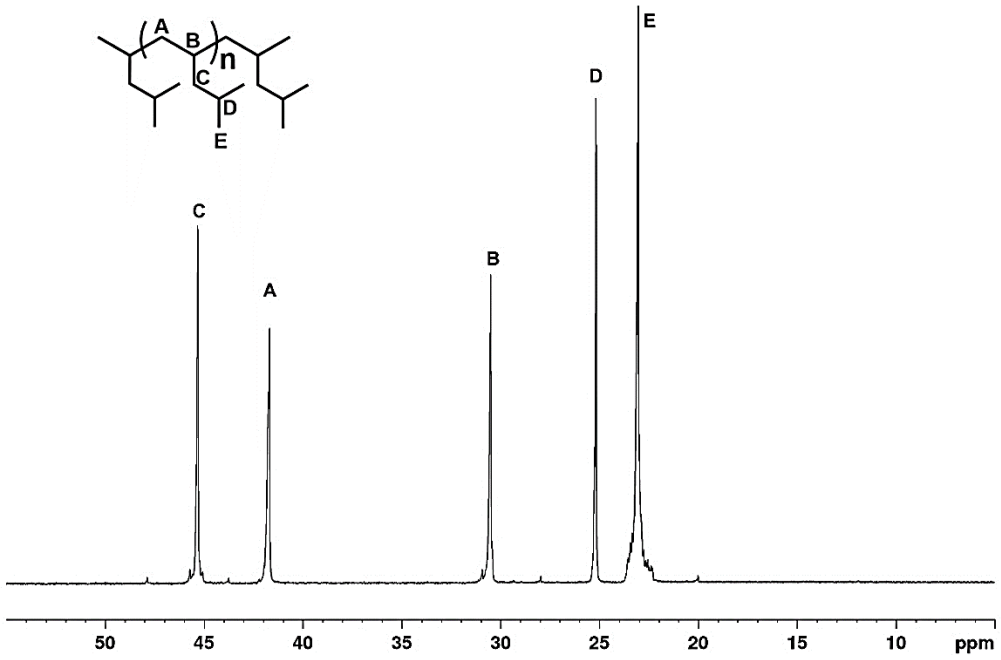
A
B
n
C
D
E
C
A
B
D
E
50
45
40
35
30
25
20
15
10
ppm

C.

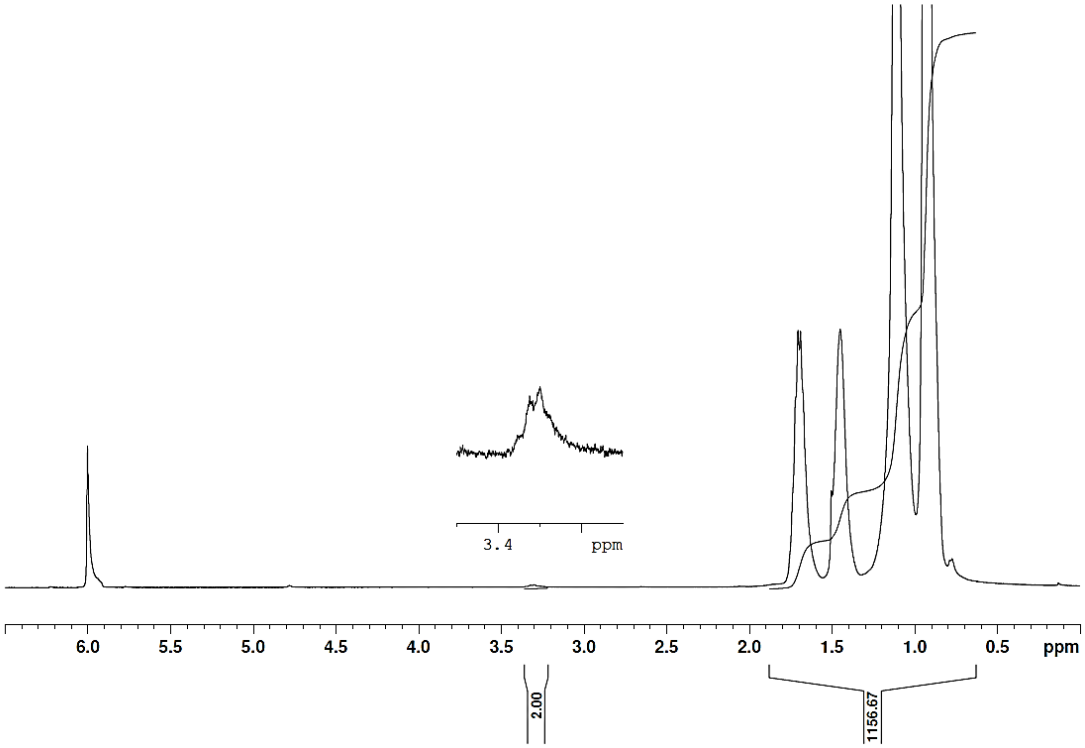

Figure S2.14: (A) ^{1}H-NMR (600 MHz, *1,1,2,2-C_2Cl_4-*d2*, 110 °C after 20 minutes of temperature equilibration) of **run 2.14**. (B) partial ^{13}C NMR (150 MHz, *1,1,2,2-C_2Cl_4-*d2*, 110 °C after 20 minutes of temperature equilibration) of **run 2.14**. (C) ^{1}H-NMR (600 MHz, *1,1,2,2-C_2Cl_4-*d2*, 110 °C after 20 minutes of temperature equilibration) of I_2 quenched **run 2.14** with a molecular weight calculated to be 8.1 kDa through integration of a 90° pulse program.

A.

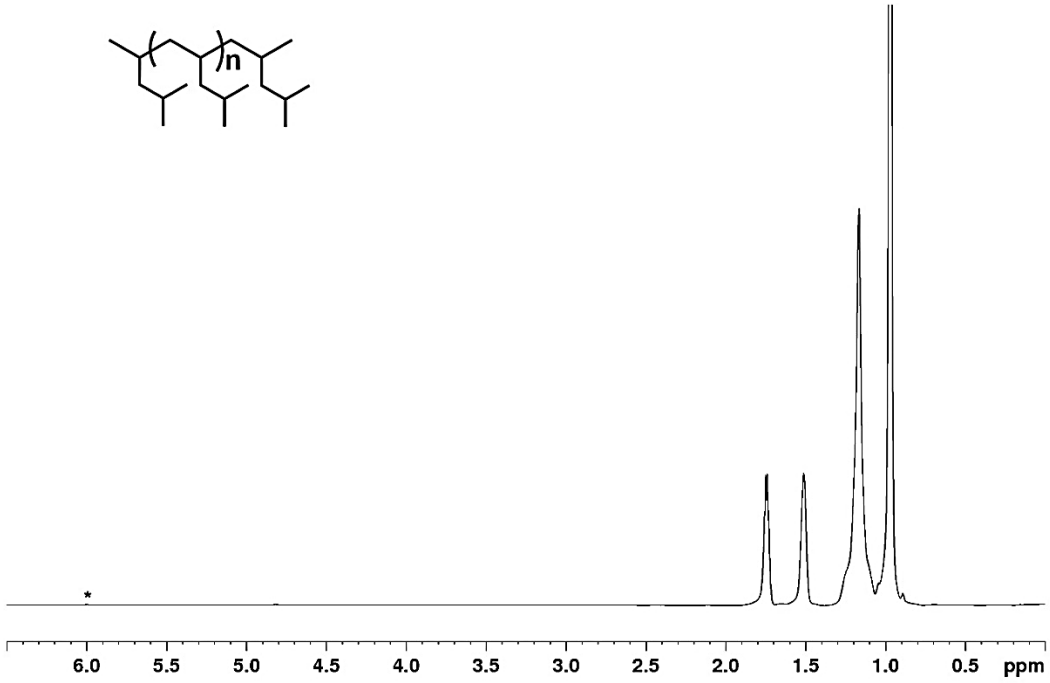

B.

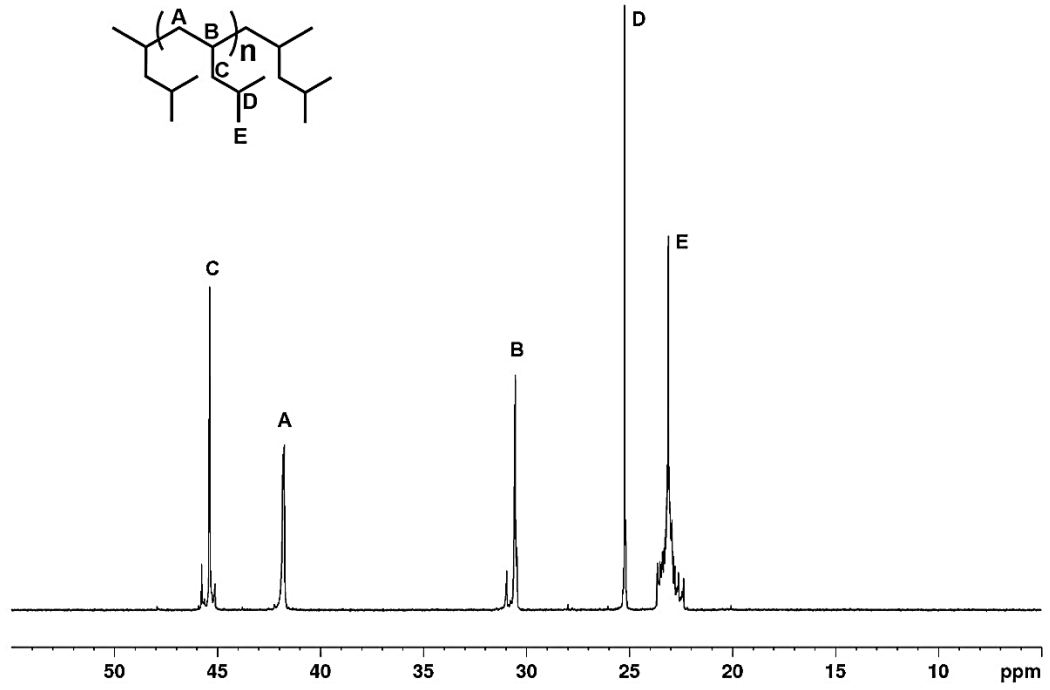

Figure S2.15: (A) ^{1}H-NMR (600 MHz, *1,1,2,2-C_2Cl_4-*d2*, 110 °C after 1 h of temperature equilibration) of **run 2.15**. (B) partial ^{13}C NMR (150 MHz, *1,1,2,2-C_2Cl_4-*d2*, 110 °C after 1 h of temperature equilibration) of **run 2.15.**

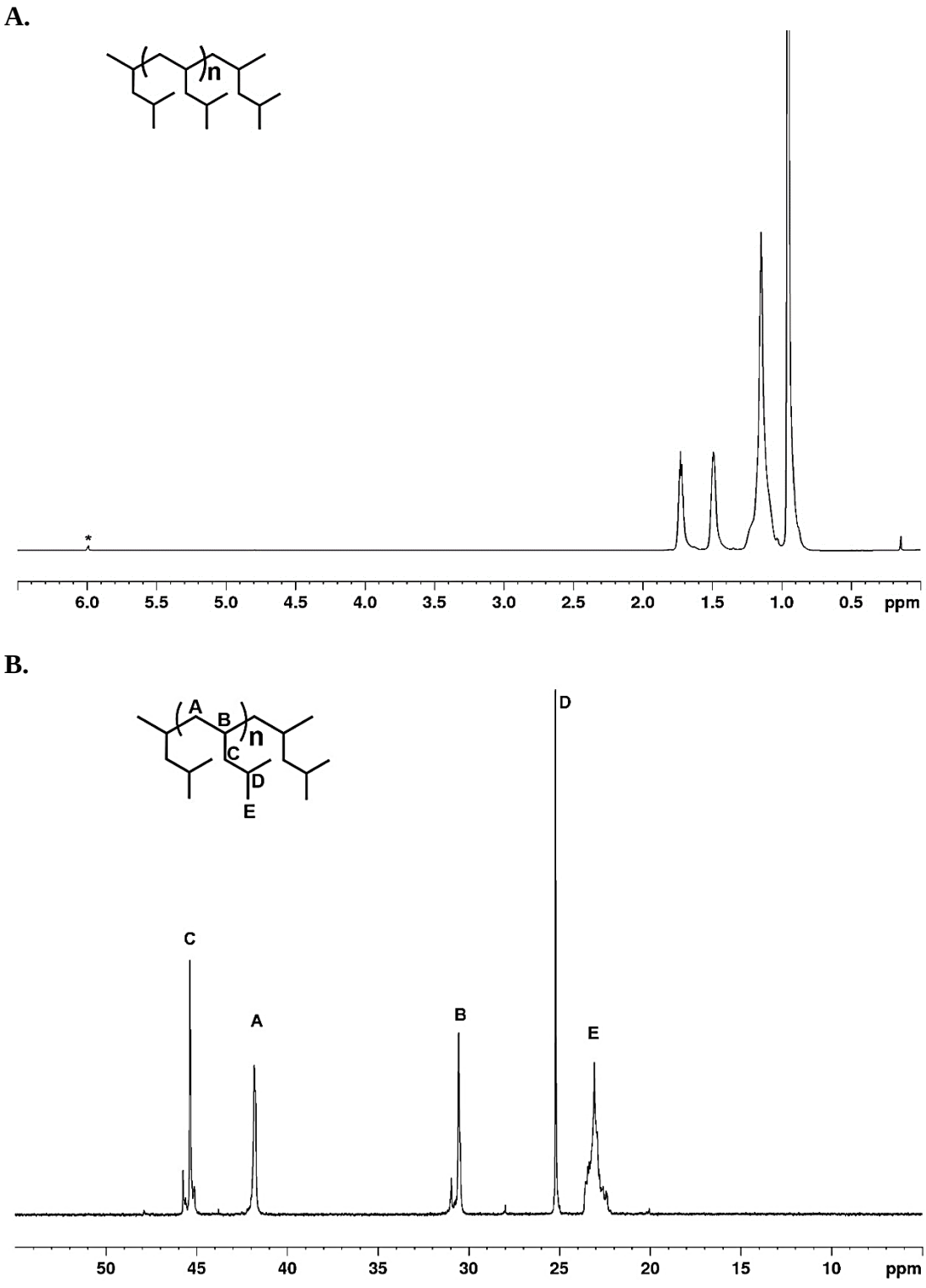

Figure S2.16. (A) ^{1}H NMR (800 MHz, *1,1,2,2-C_2Cl_4-*d2*, 110 °C after 1 hr of temperature equilibration) of **run 2.16**. (B) partial ^{13}C-NMR (200 MHz, *1,1,2,2-C_2Cl_4-*d2*) of **run 2.16.**

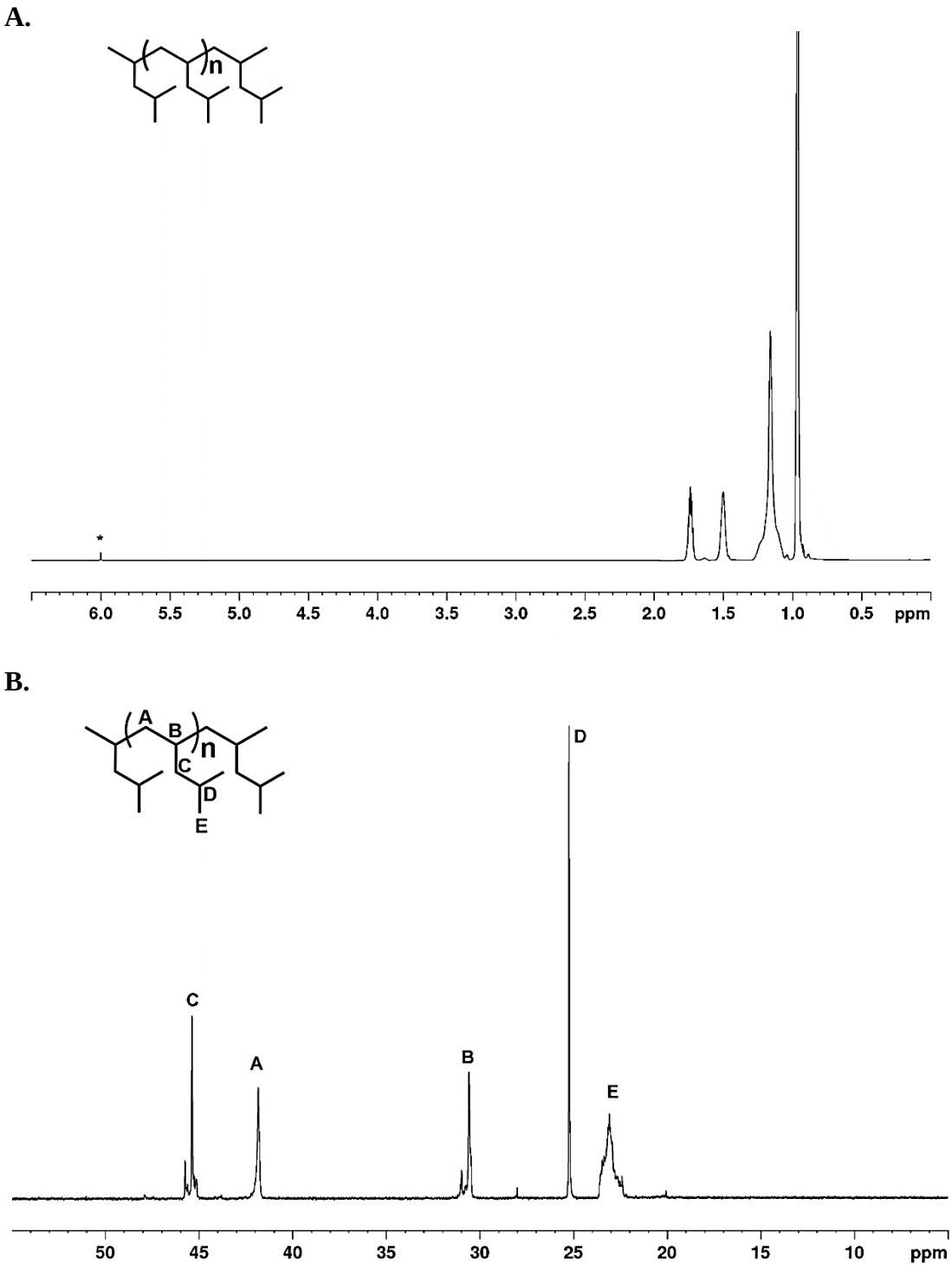

Figure S2.17. (A) ^{1}H NMR (800 MHz, *1,1,2,2-C_2Cl_4-*d2*, 110 °C after 1 hr of temperature equilibration) of **run 2.17**. (B) partial ^{13}C-NMR (200 MHz, *1,1,2,2-C_2Cl_4-*d2*) of **run 2.17.**

A.

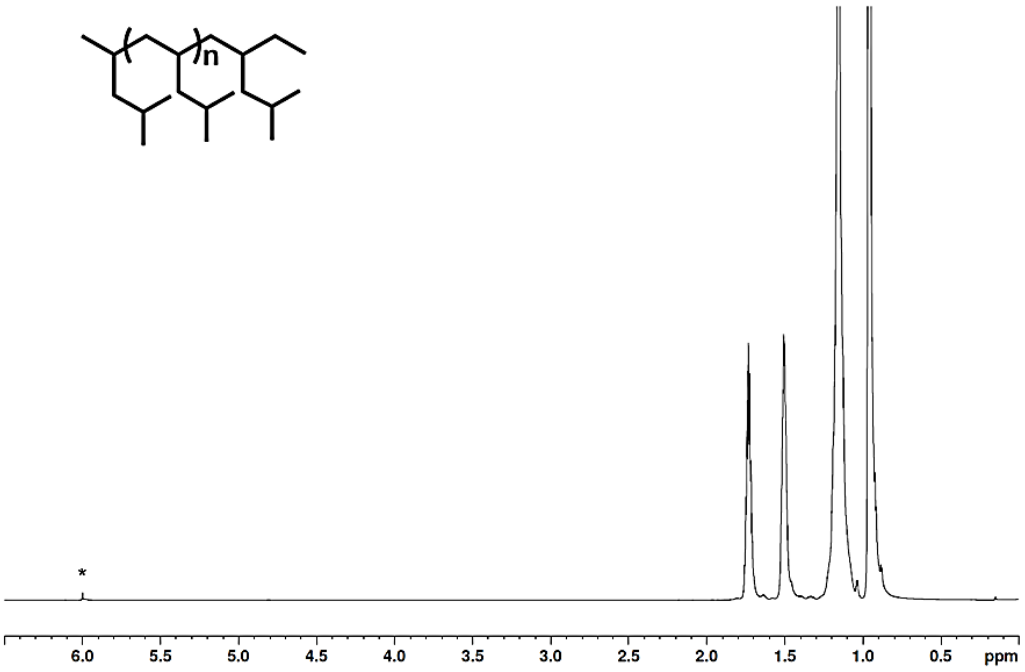

B.

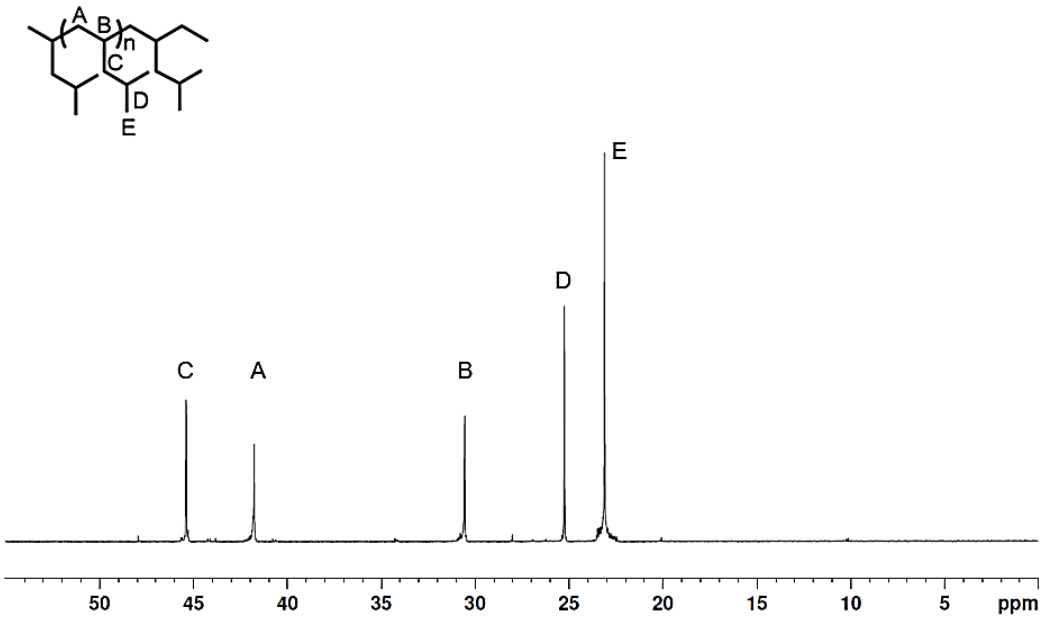

Figure S2.18. (A) ^{1}H NMR (800 MHz, *1,1,2,2-C_2Cl_4-*d2*, 110 °C after 1 hr of temperature equilibration) of **run 2.18**. (B) partial ^{13}C-NMR (200 MHz, *1,1,2,2-C_2Cl_4-*d2*) of **run 2.18.**

A.

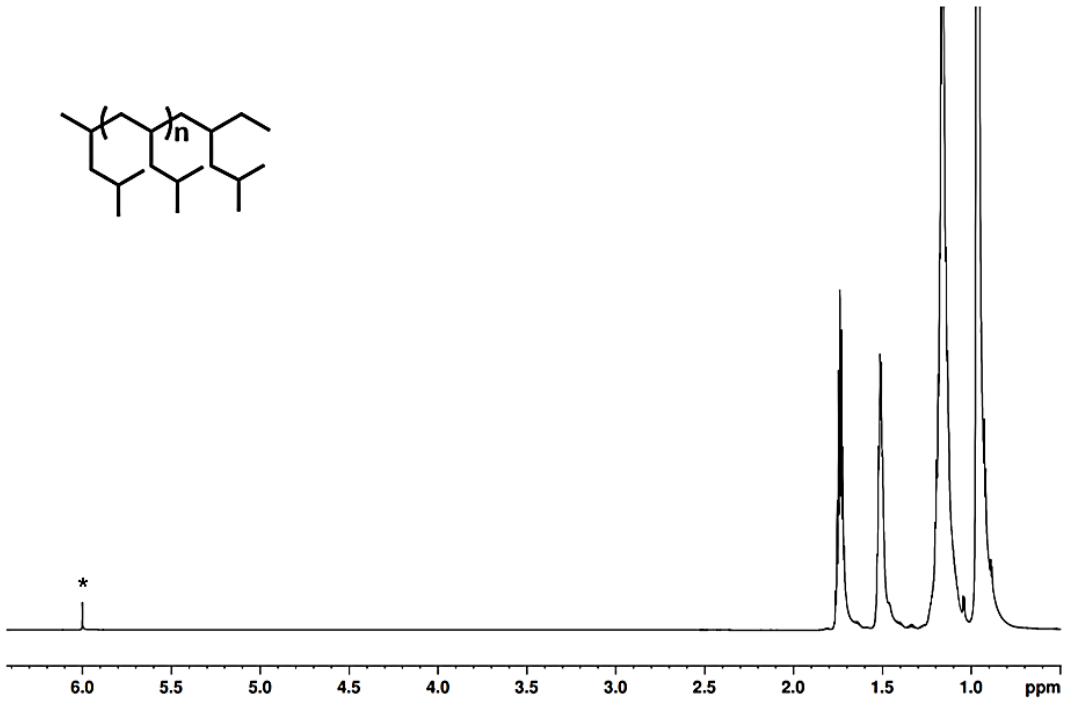
n
*
6.0
5.5
5.0
4.5
4.0
3.5
3.0
2.5
2.0
1.5
1.0
ppm

B.

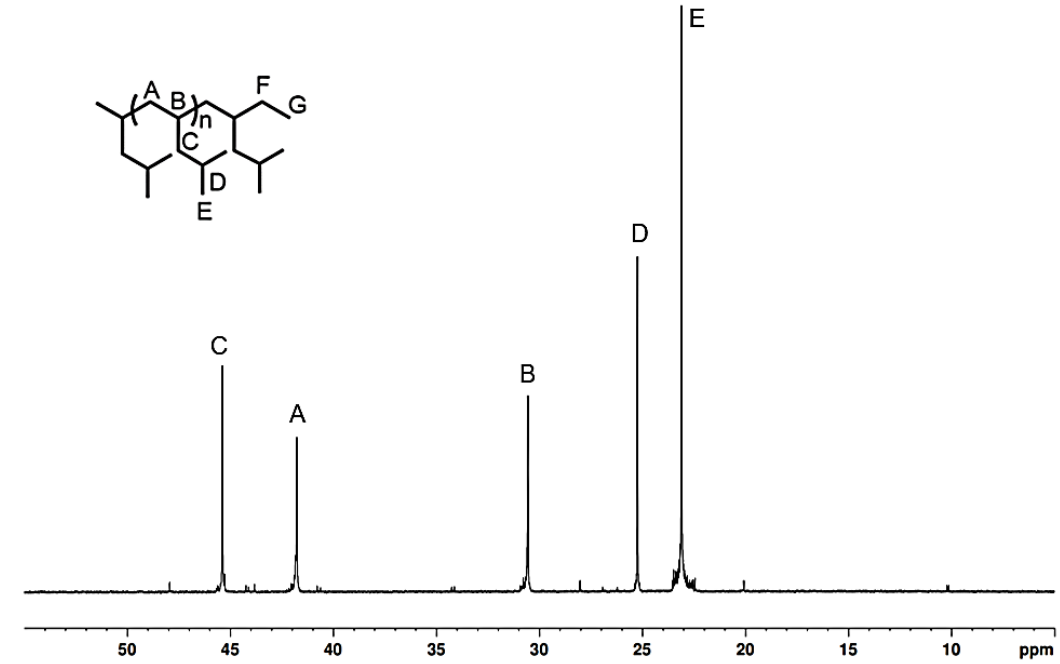
A
B
n
C
D
E
F
G
C
A
B
D
E
50
45
40
35
30
25
20
15
10
ppm

C.

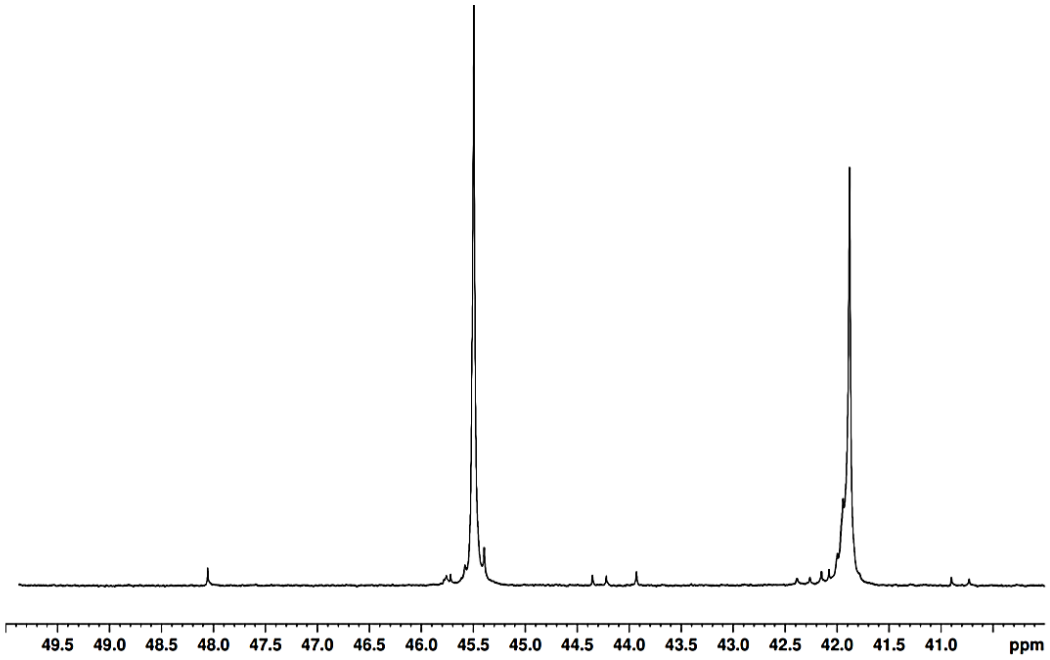

D.

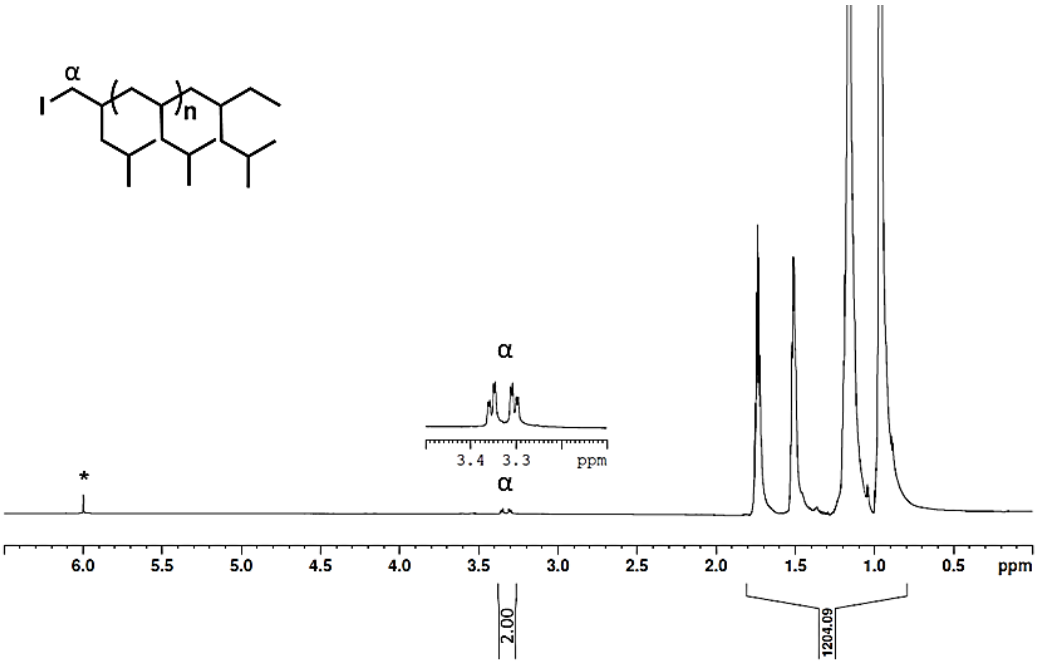

Figure S2.19. (A) ^{1}H NMR (800 MHz, *1,1,2,2-C_2Cl_4-*d2*, 110 °C after 1 hr of temperature equilibration) of **run 2.19**. (B) partial ^{13}C-NMR (200 MHz, *1,1,2,2-C_2Cl_4-*d2*) of **run 2.19**. (C) partial ^{13}C-NMR (200 MHz, *1,1,2,2-C_2Cl_4-*d2*) of **run 2.19.** (D) I2 aliquot with integration for molecular weight (8.4 kDa by integration) of **run 2.19**.

A.

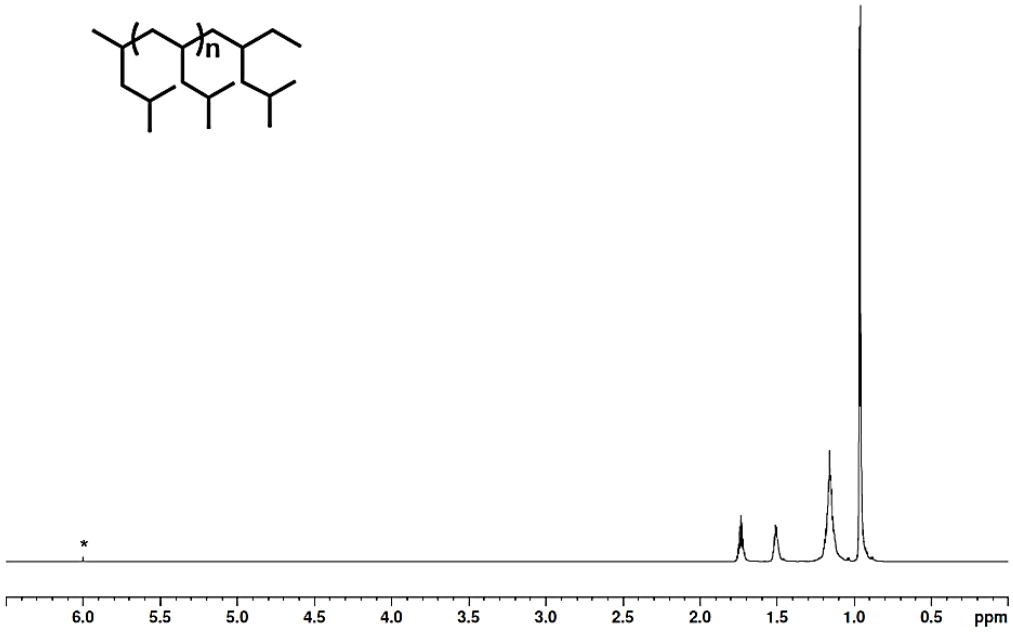

B.

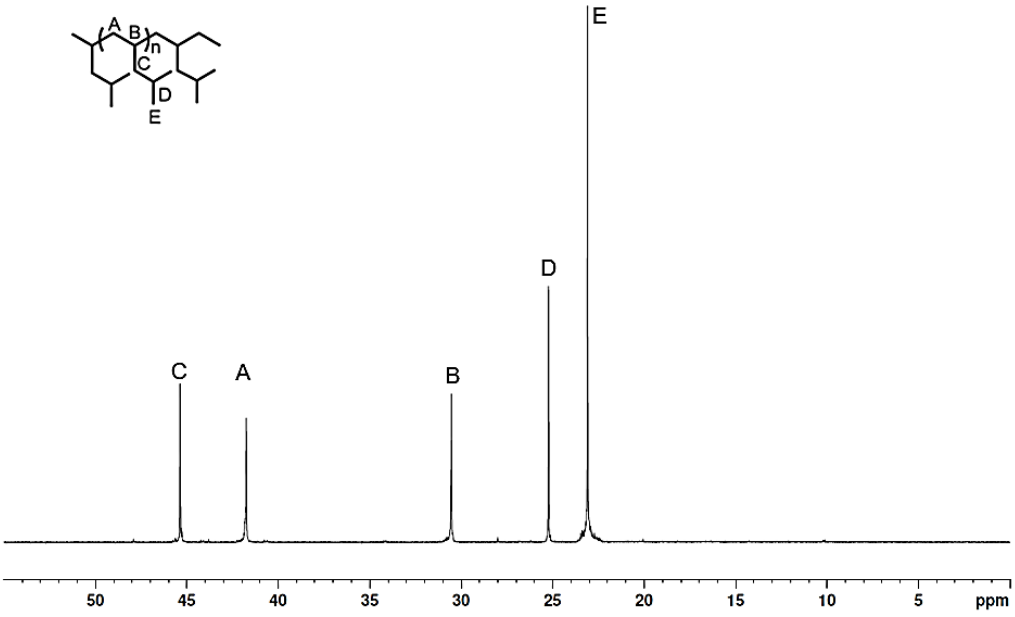

Figure S2.20. (A) ^{1}H NMR (800 MHz, *1,1,2,2-C_2Cl_4-*d2*, 110 °C after 1 hr of temperature equilibration) of **run 2.20**, (B) partial ^{13}C-NMR (200 MHz, *1,1,2,2-C_2Cl_4-*d2*) of **run 2.20.**

A.

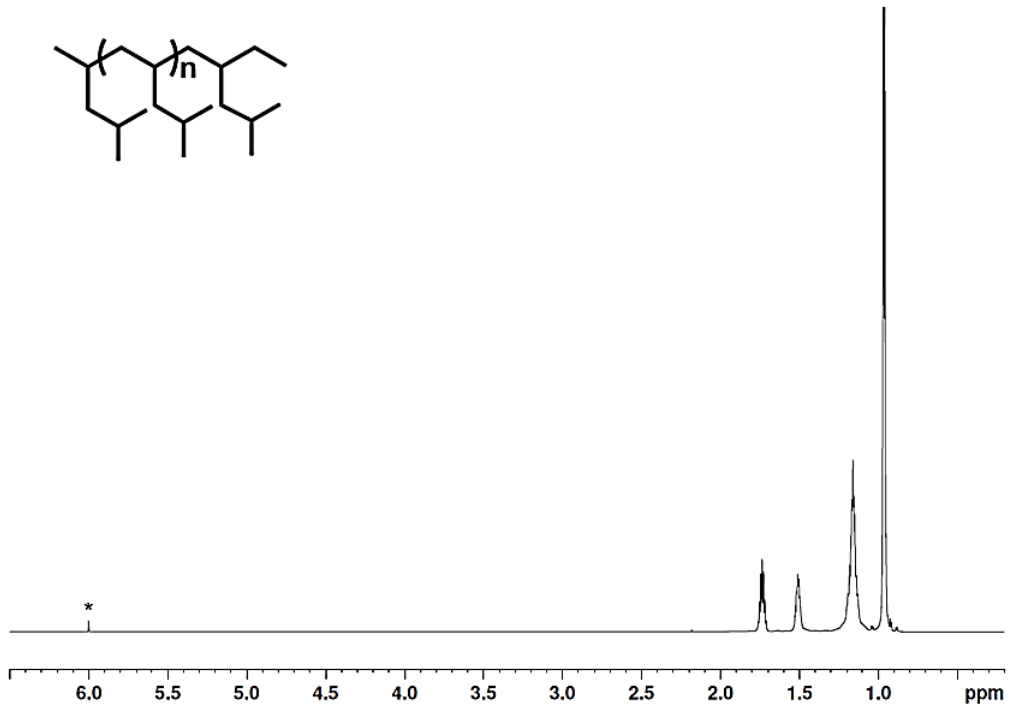

B.

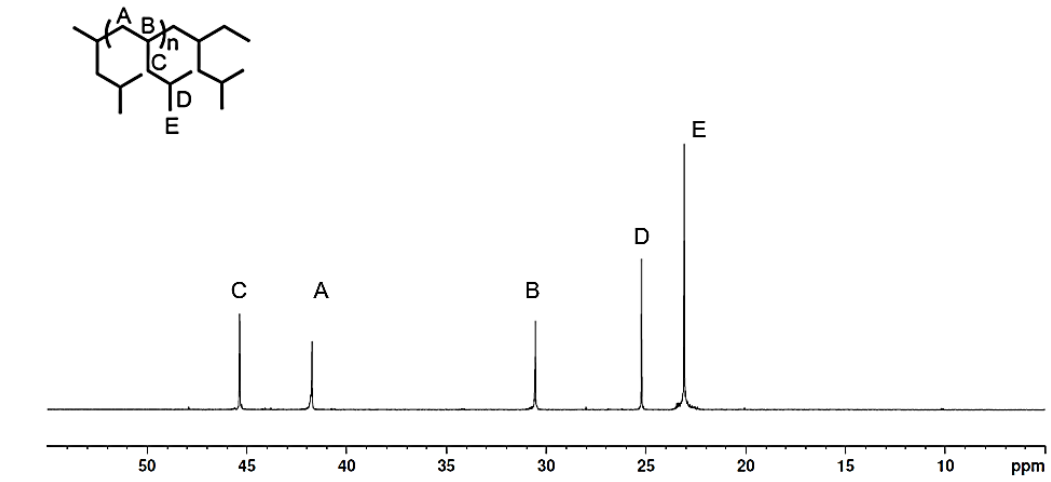

Figure S2.21. (A) ^{1}H NMR (800 MHz, *1,1,2,2-C_2Cl_4-*d2*, 110 °C after 1 hr of temperature equilibration) of **run 2.21**. (B) partial ^{13}C-NMR (200 MHz, *1,1,2,2-C_2Cl_4-*d2*) of **run 2.21.**

A.

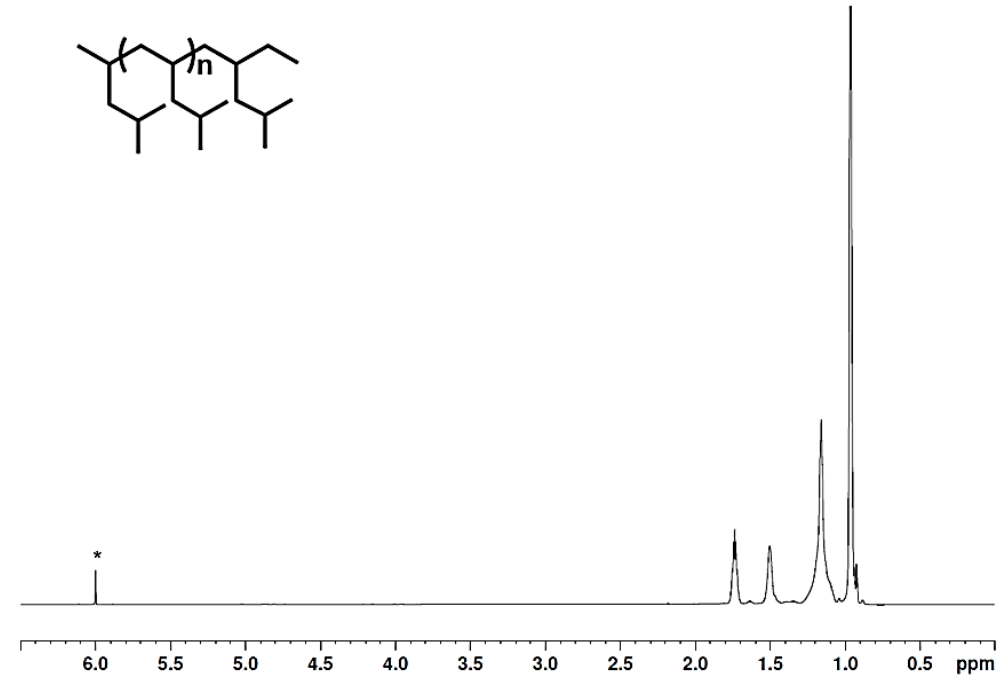

B.

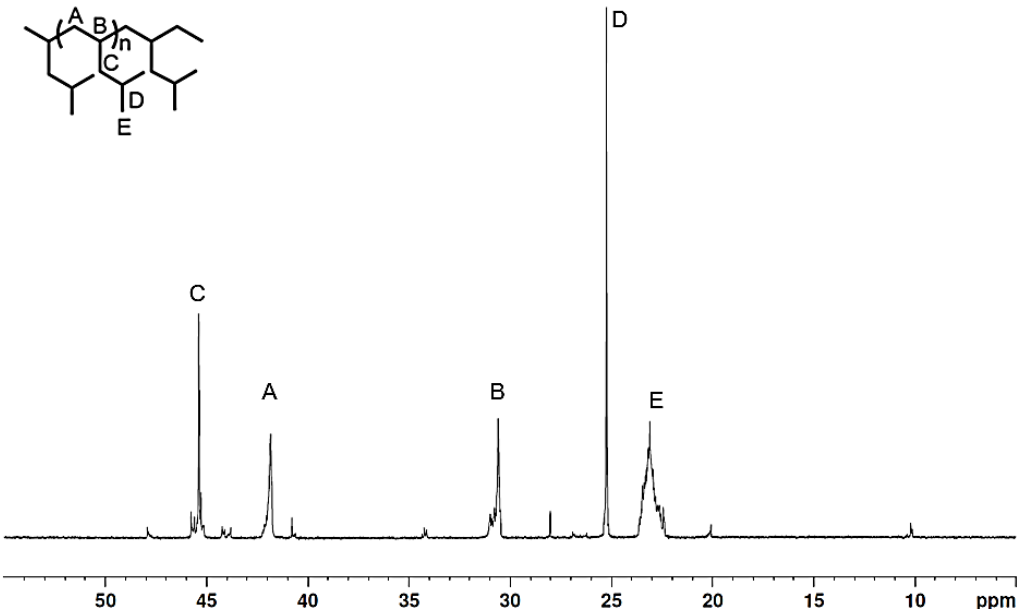

Figure S2.22. (A) ^{1}H NMR (800 MHz, *1,1,2,2-C_2Cl_4-*d2*, 110 °C after 1 hr of temperature equilibration) of **run 2.22.** (B) partial ^{13}C-NMR (200 MHz, *1,1,2,2-C_2Cl_4-*d2*) of **run 2.22.**

A.

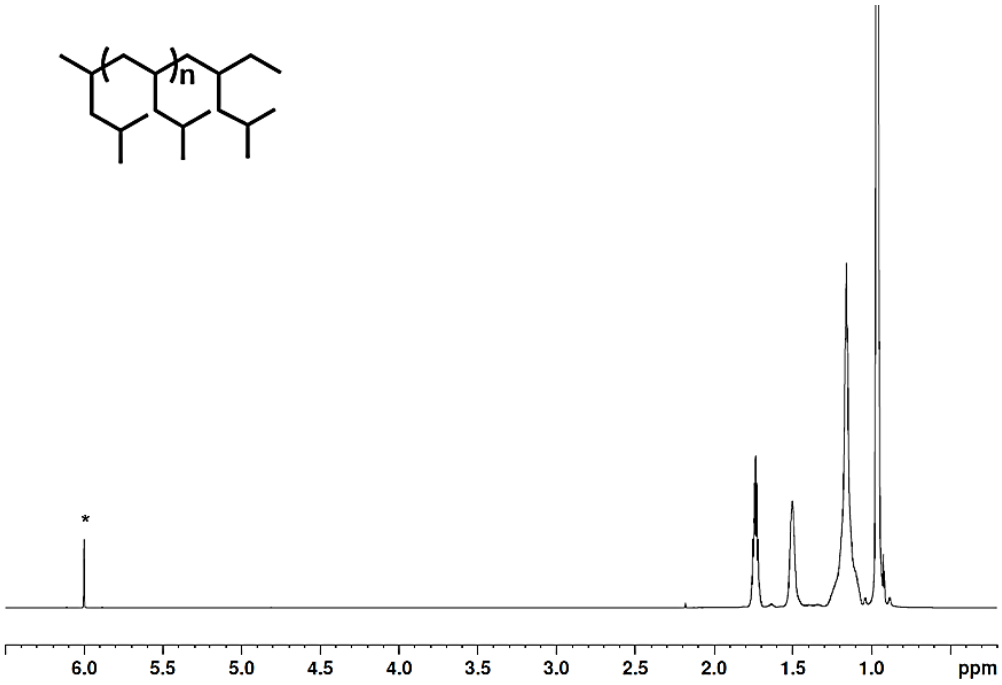

B.

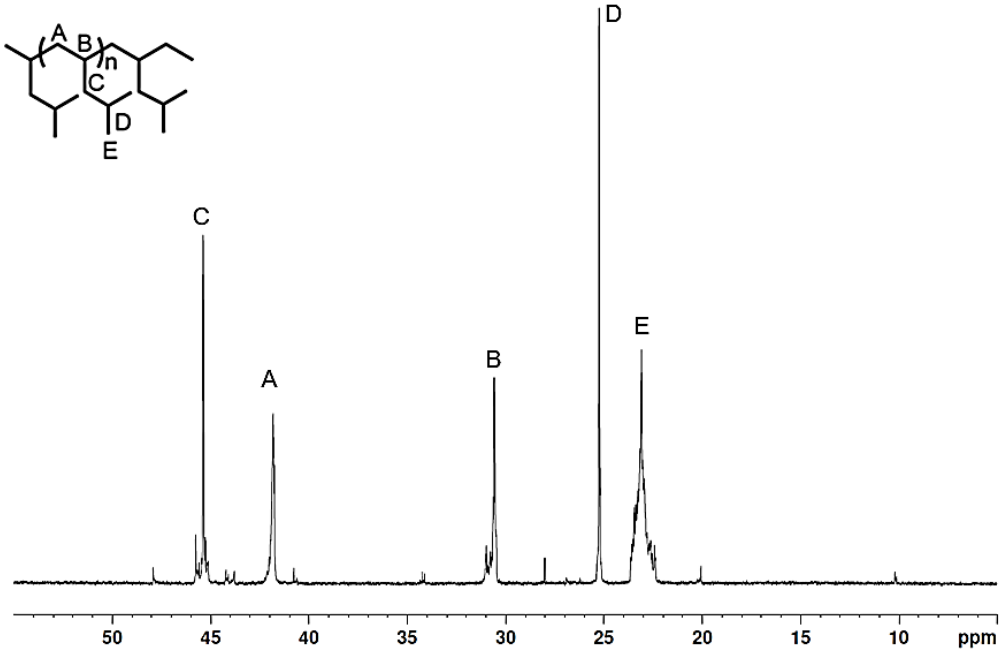

Figure S2.23. (A) ^{1}H NMR (800 MHz, *1,1,2,2-C_2Cl_4-*d2*, 110 °C after 1 hr of temperature equilibration) of **run 2.23**. (B) partial ^{13}C-NMR (200 MHz, *1,1,2,2-C_2Cl_4-*d2*) of **run 2.23.**

A.

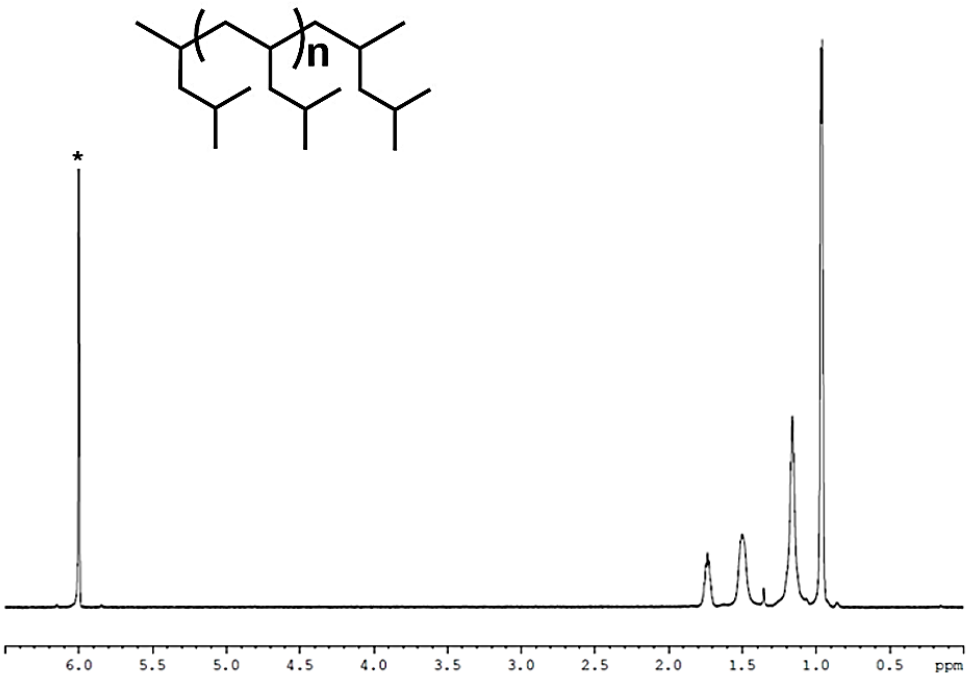

B.

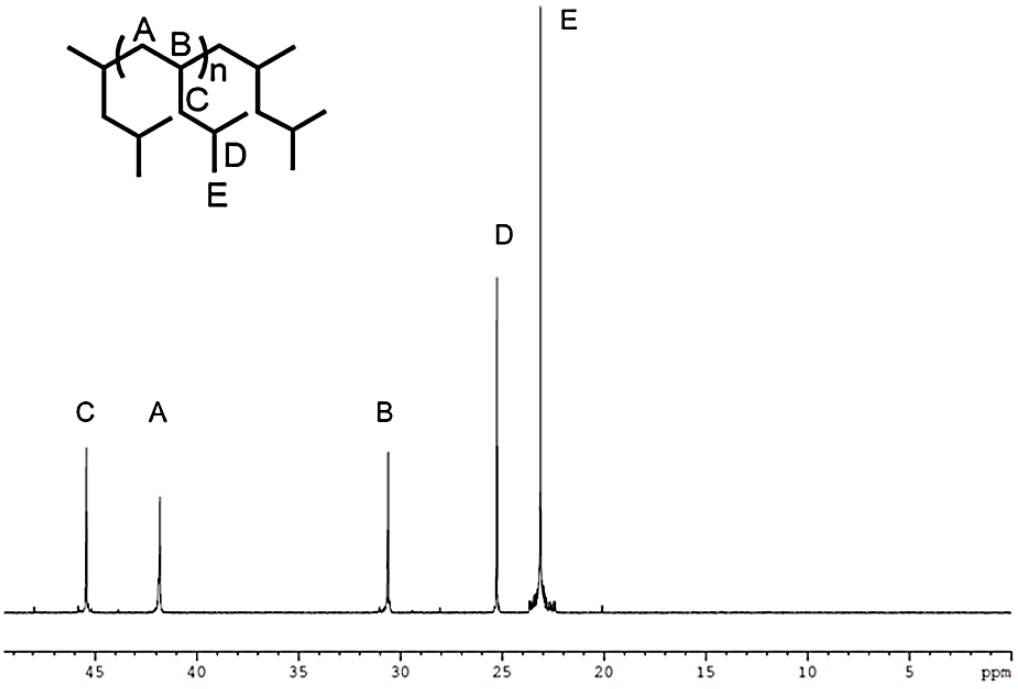

Figure S2.24: (a) ^{1}H-NMR (600 MHz, *1,1,2,2-C_2Cl_4-*d2*, 110 °C after 20 minutes of temperature equilibration) of **run 2.14b**. (b) partial ^{13}C NMR (150 MHz, *1,1,2,2-C_2Cl_4-*d2*, 110 °C after 20 minutes of temperature equilibration) of **run 2.14b**.

A.

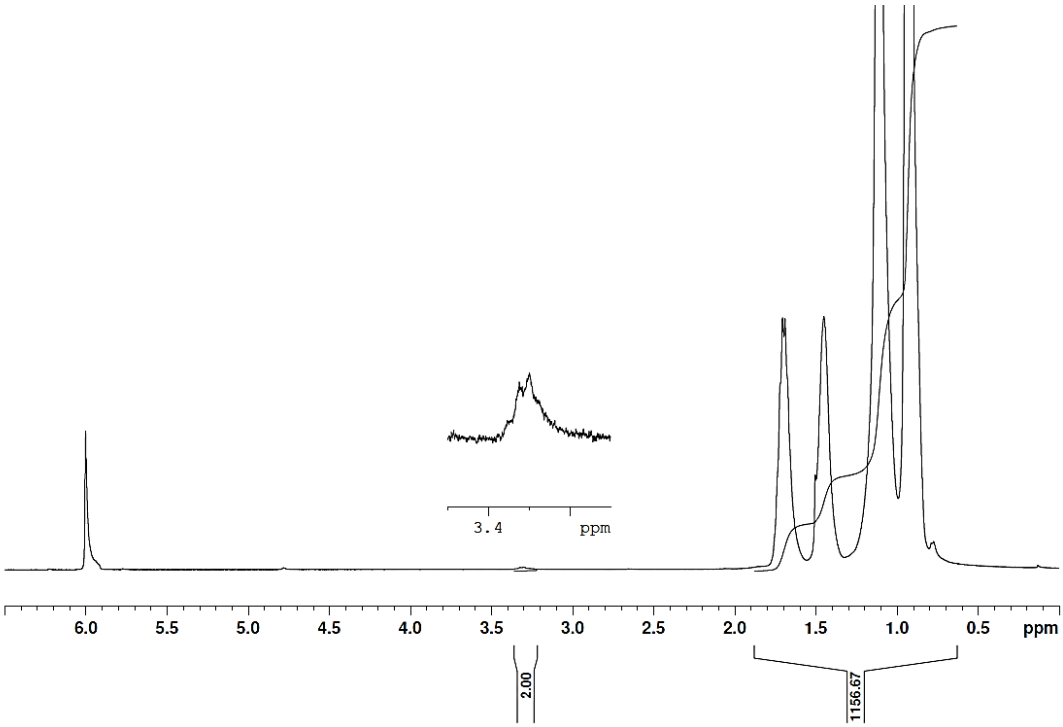
3.4
ppm
6.0
5.5
5.0
4.5
4.0
3.5
3.0
2.5
2.0
1.5
1.0
0.5
ppm
2.00
1156.67

B.

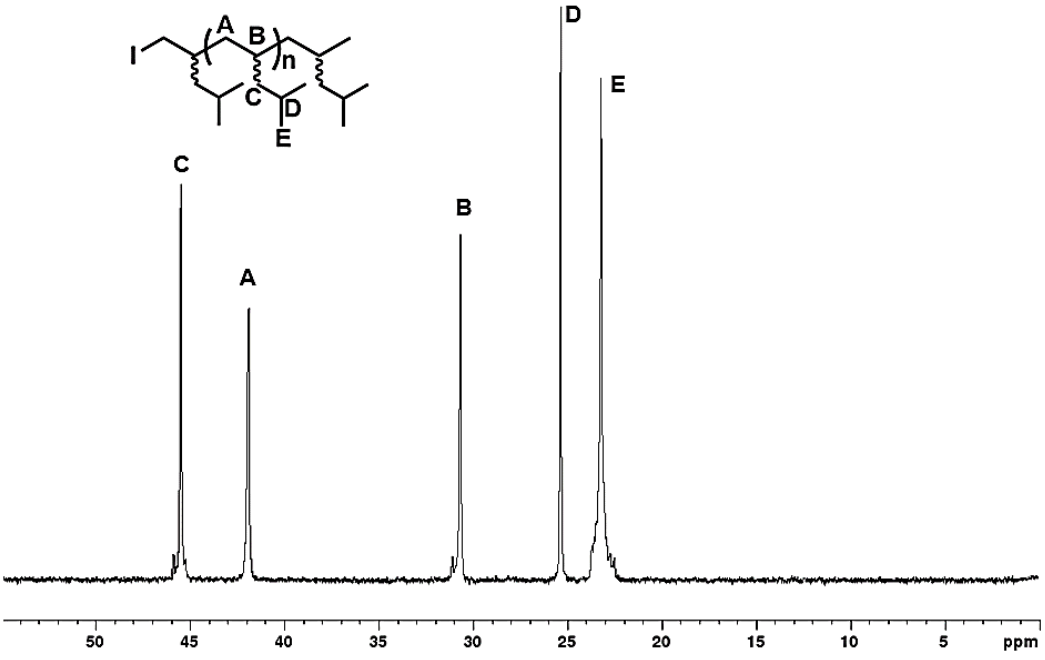
I
A
B
n
C
D
E
C
A
B
D
E
50
45
40
35
30
25
20
15
10
5
ppm

C.

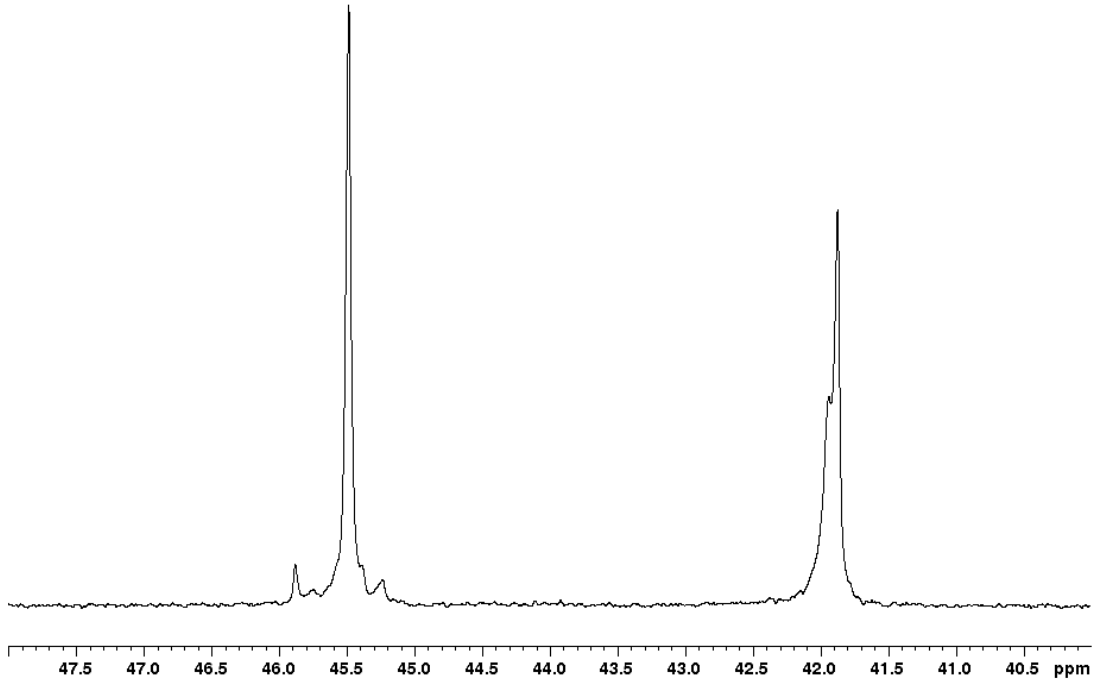

Figure S2.25: (A) ^{1}H-NMR (600 MHz, *1,1,2,2-C_2Cl_4-*d2*, 110 °C after 20 minutes of temperature equilibration) of I_2 quenched **run 2.15b** with a molecular weight calculated to be 8.1 kDa through integration of a 90° pulse program. (B) partial ^{13}C NMR (150 MHz, *1,1,2,2-C_2Cl_4-*d2*, 110 °C after 20 minutes of temperature equilibration) of **run 2.15b**. (C) partial ^{13}C-NMR (200 MHz, *1,1,2,2-C_2Cl_4-*d2*) of **run 2.15b.**

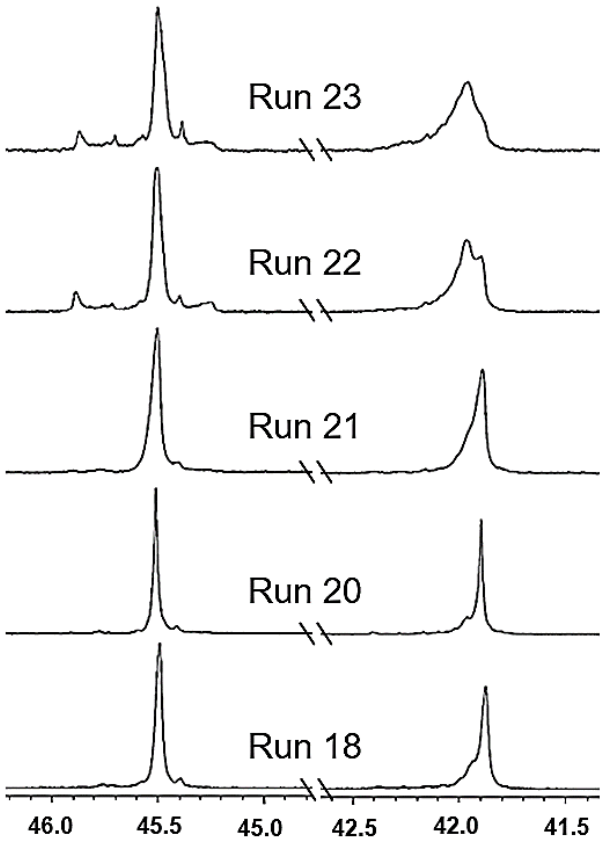

Figure S2.26. Partial ^{13}C-NMR (200 MHz, *1,1,2,2-C2Cl4-d2) of **run 2.18, 2.20 – 2.23** LCCTP iPMP.

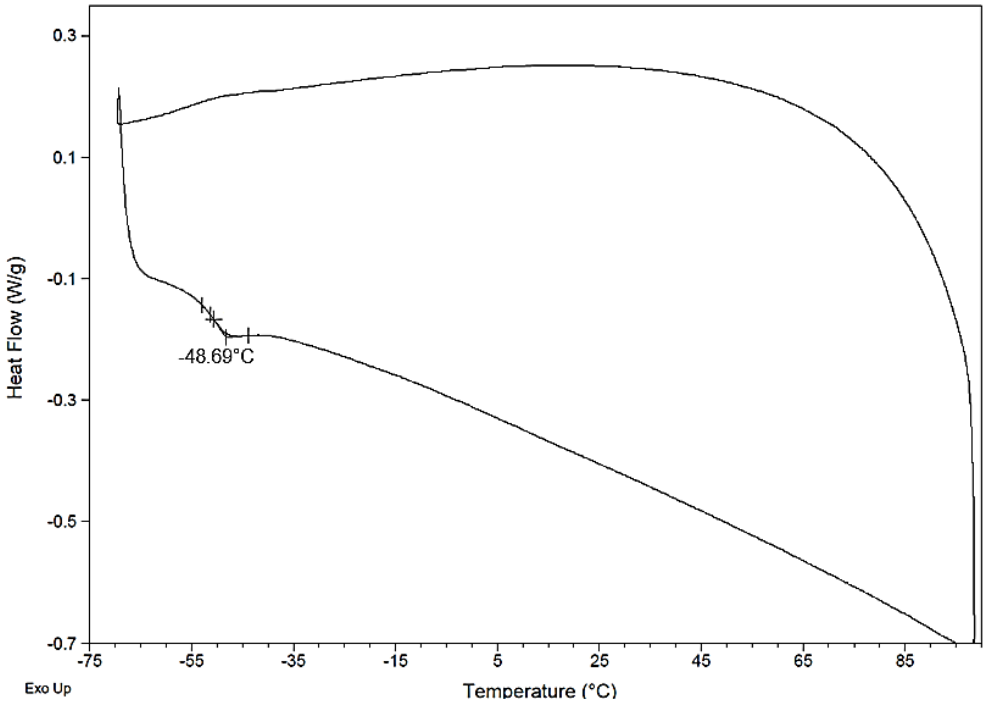

Figure S2.27. DSC full trace of a heat/cool/heat cycle, cycle 1 removed, with a ramp rate of 20 °C/min from -70 – 200 °C of **run 2.1**.

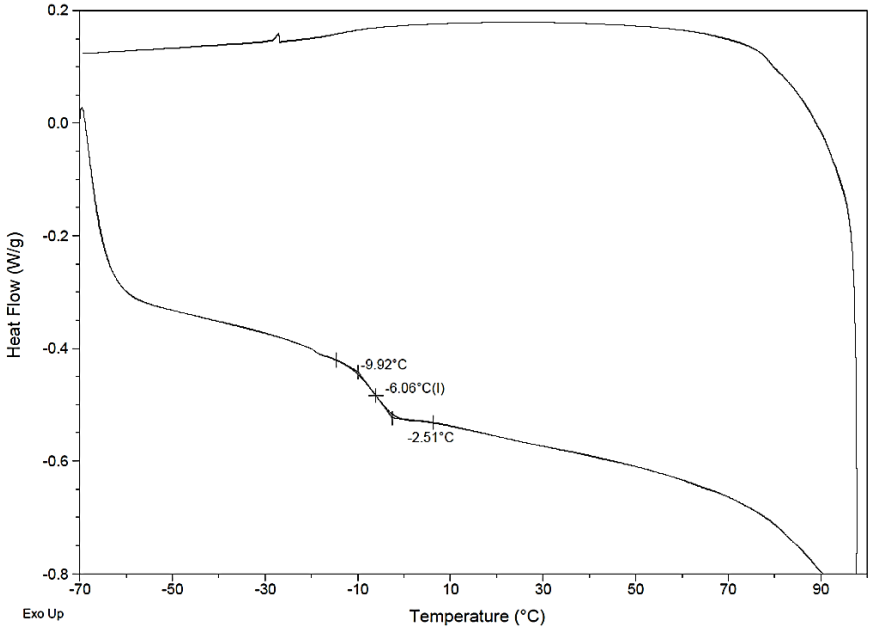

Figure S2.28. DSC full trace of a heat/cool/heat cycle, cycle 1 removed, with a ramp rate of 20 °C/min from -70 – 200 °C of **run 2.2**.

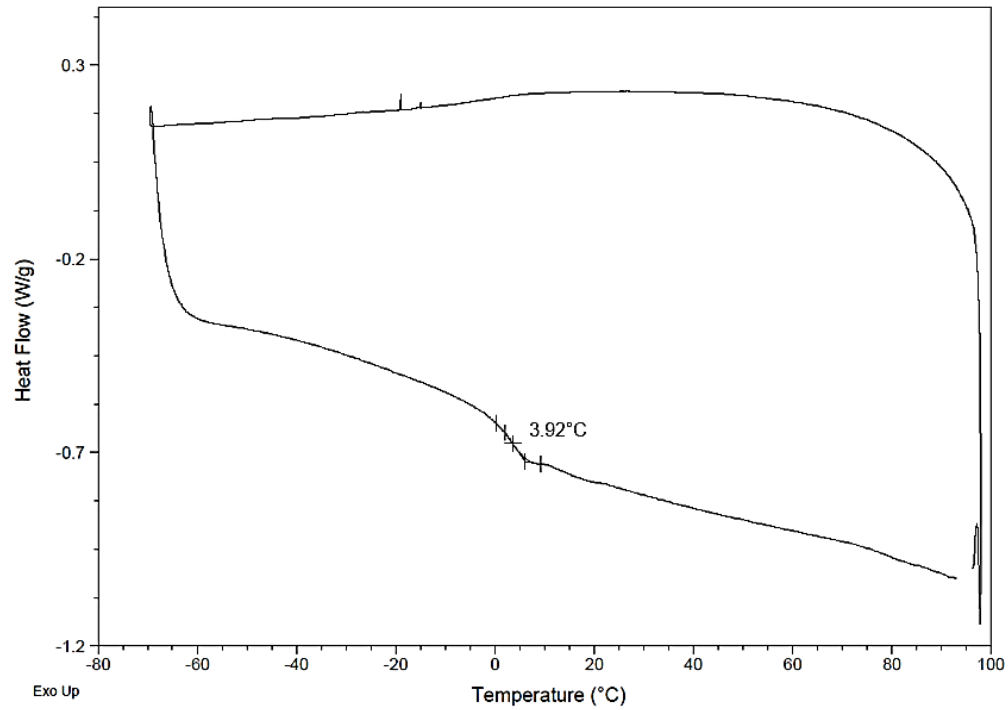

Figure S2.29. DSC full trace of a heat/cool/heat cycle, cycle 1 removed, with a ramp rate of 20 °C/min from -70 – 200 °C of **run 2.3**.

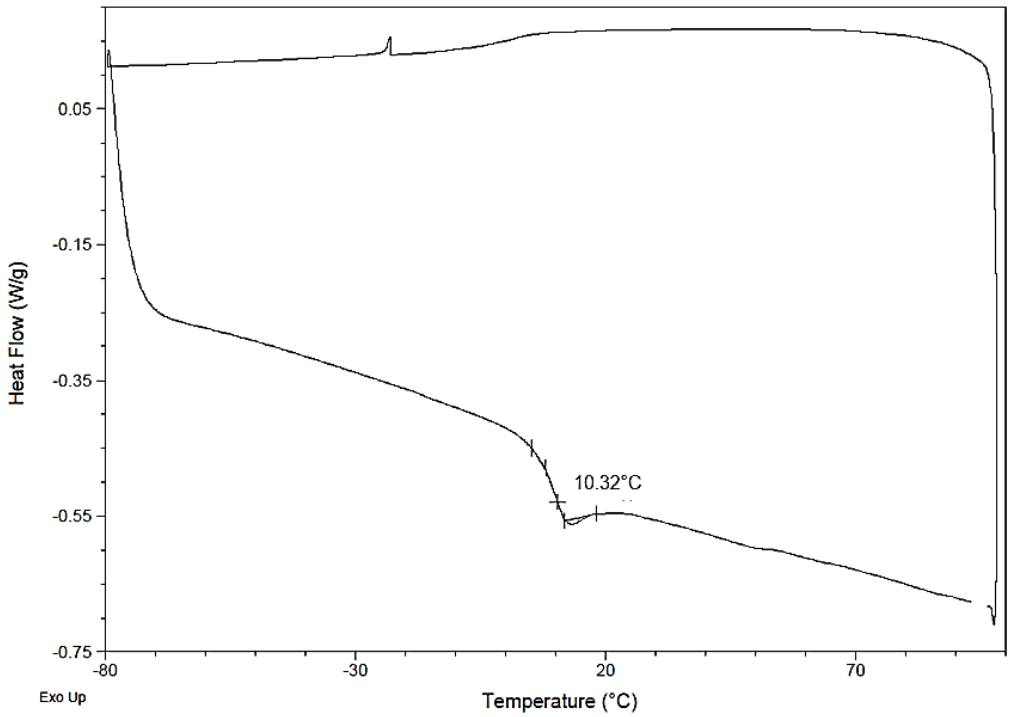

Figure S2.30. DSC full trace of a heat/cool/heat cycle, cycle 1 removed, with a ramp rate of 20 °C/min from -70 – 200 °C of **run 2.4**.

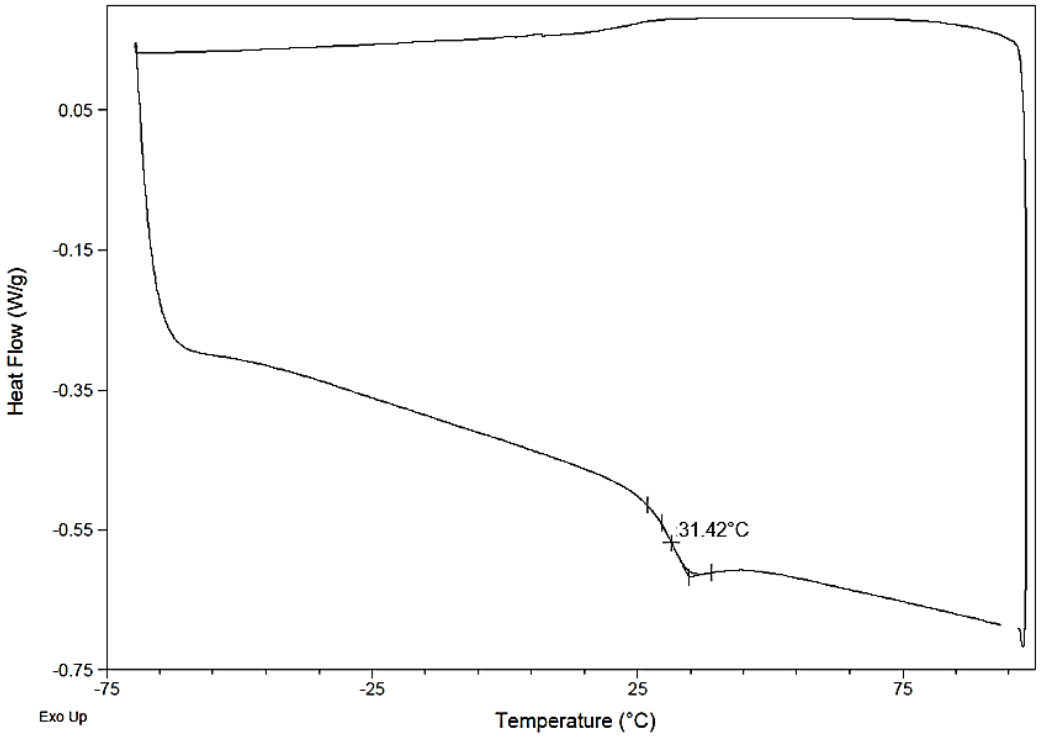

Figure S2.31. DSC full trace of a heat/cool/heat cycle, cycle 1 removed, with a ramp rate of 20 °C/min from -70 – 200 °C of **run 2.5**.

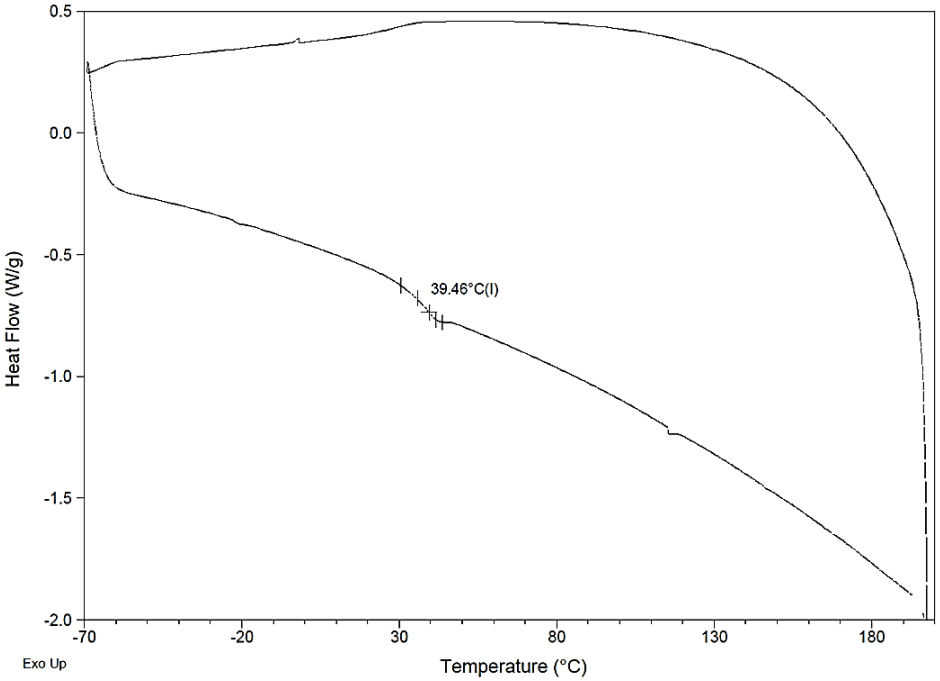

Figure S2.32. DSC full trace of a heat/cool/heat cycle, cycle 1 removed, with a ramp rate of 20 °C/min from -70 – 200 °C of **run 2.6**.

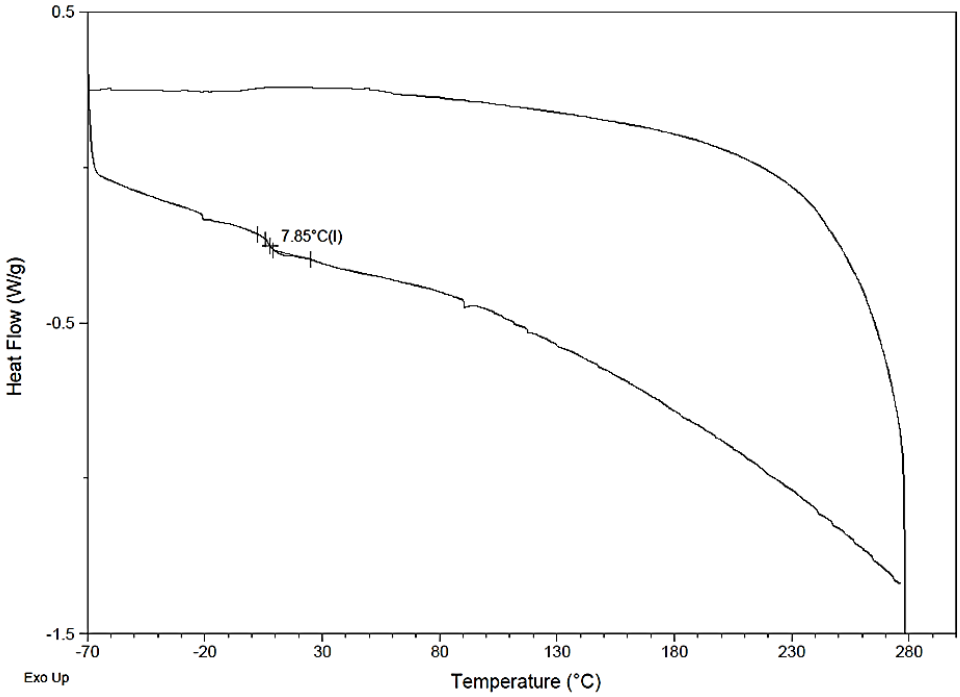

Figure S2.33. DSC trace of a heat/cool/heat cycle, cycle 1 removed, with a ramp rate of 20 °C/min from -70 – 300 °C of **run 2.7**.

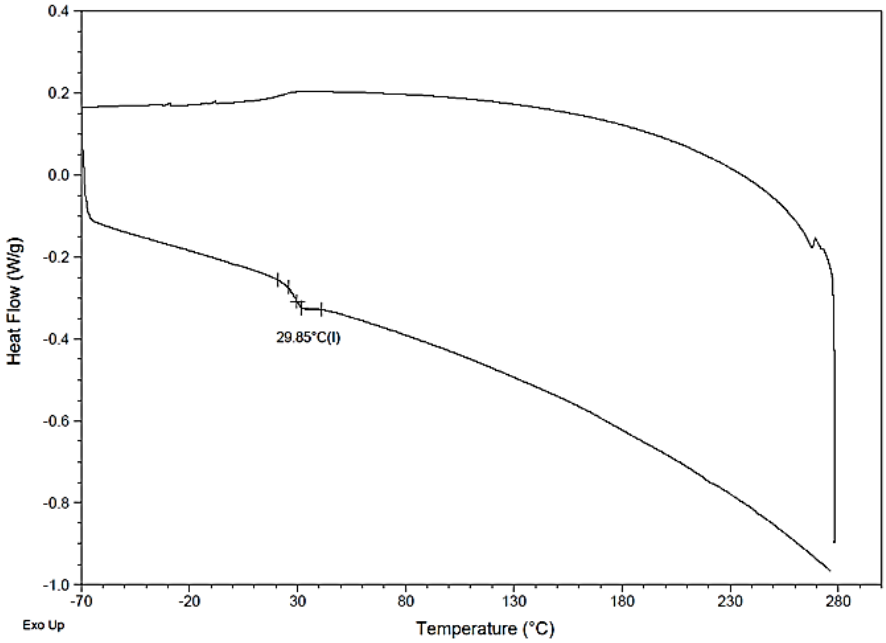

Figure S2.34. DSC trace of a heat/cool/heat cycle, cycle 1 removed, with a ramp rate of 20 °C/min from -70 – 300 °C of **run 2.8**.

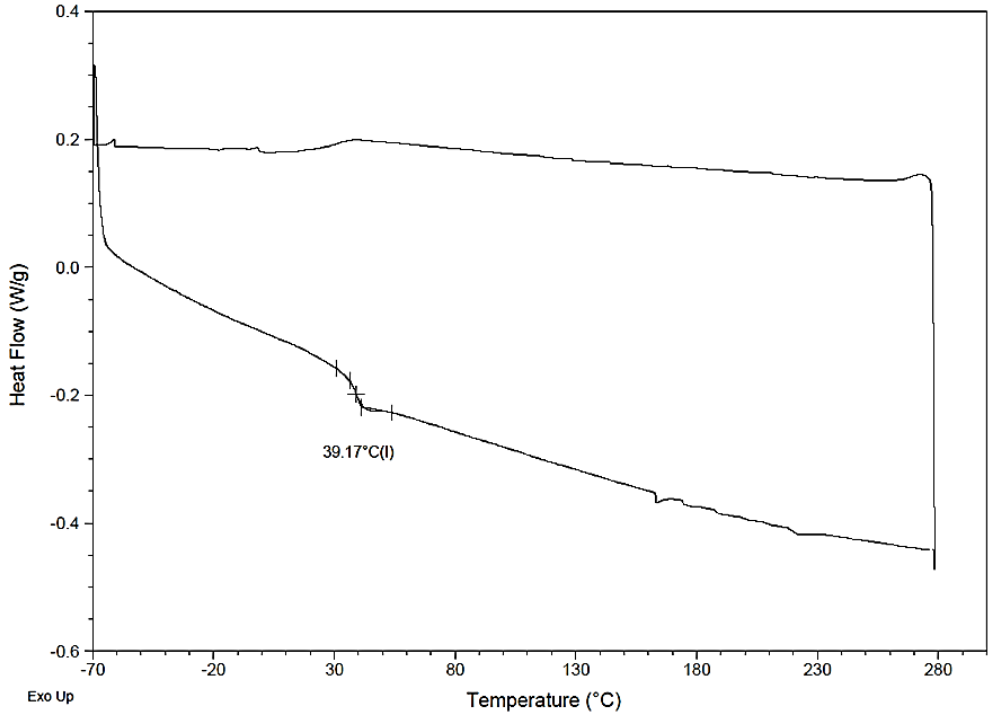

Figure S2.35. DSC trace of a heat/cool/heat cycle, cycle 1 removed, with a ramp rate of 20 °C/min from -70 – 300 °C of **run 2.9**.

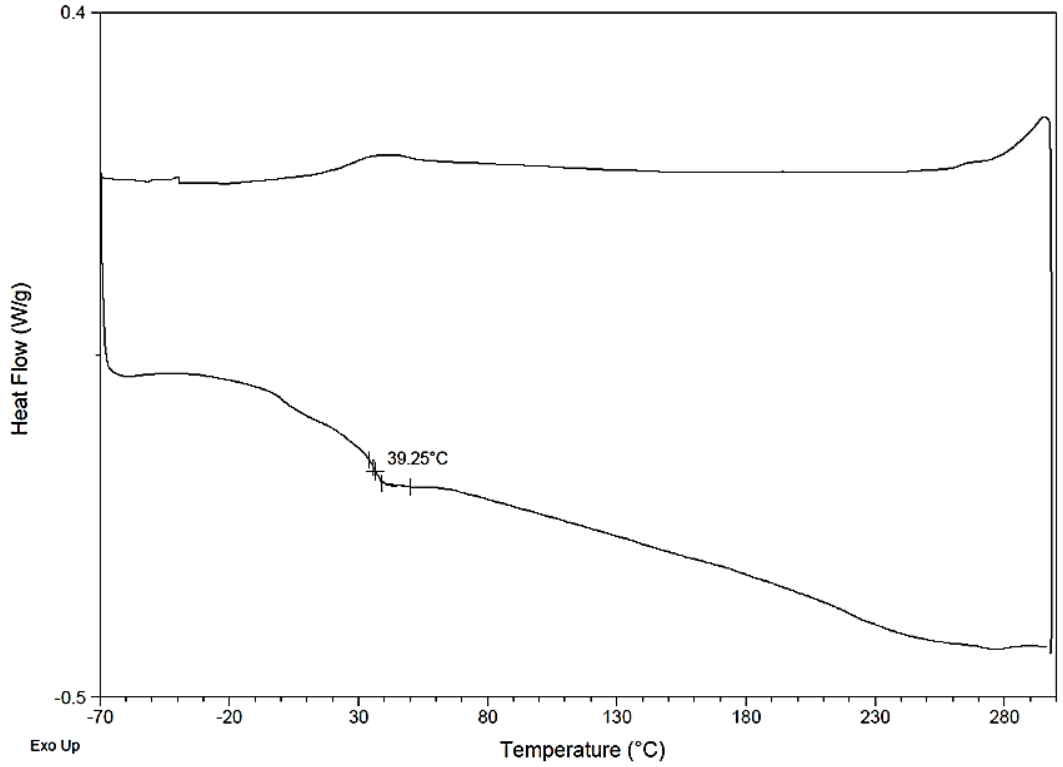

Figure S2.36. DSC trace of a heat/cool/heat cycle, cycle 1 removed, with a ramp rate of 20 °C/min from -70 – 300 °C of **run 2.10**.

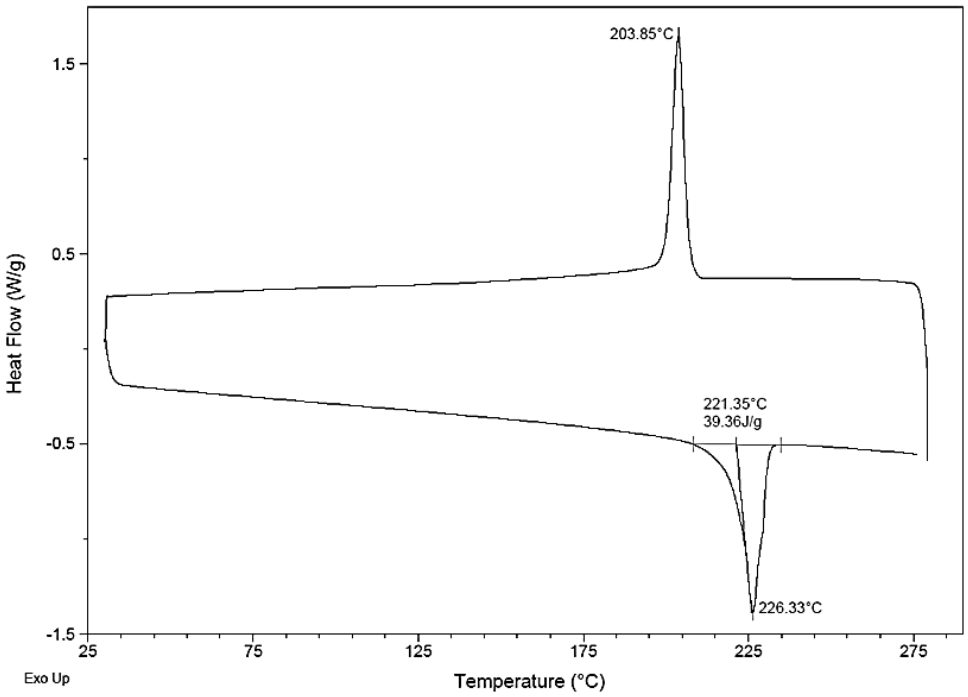

Figure S2.37. DSC full trace of a heat/cool/heat cycle, cycle 1 removed, with a ramp rate of 10 °C/min from 30 – 280 °C of **run 2.11**.

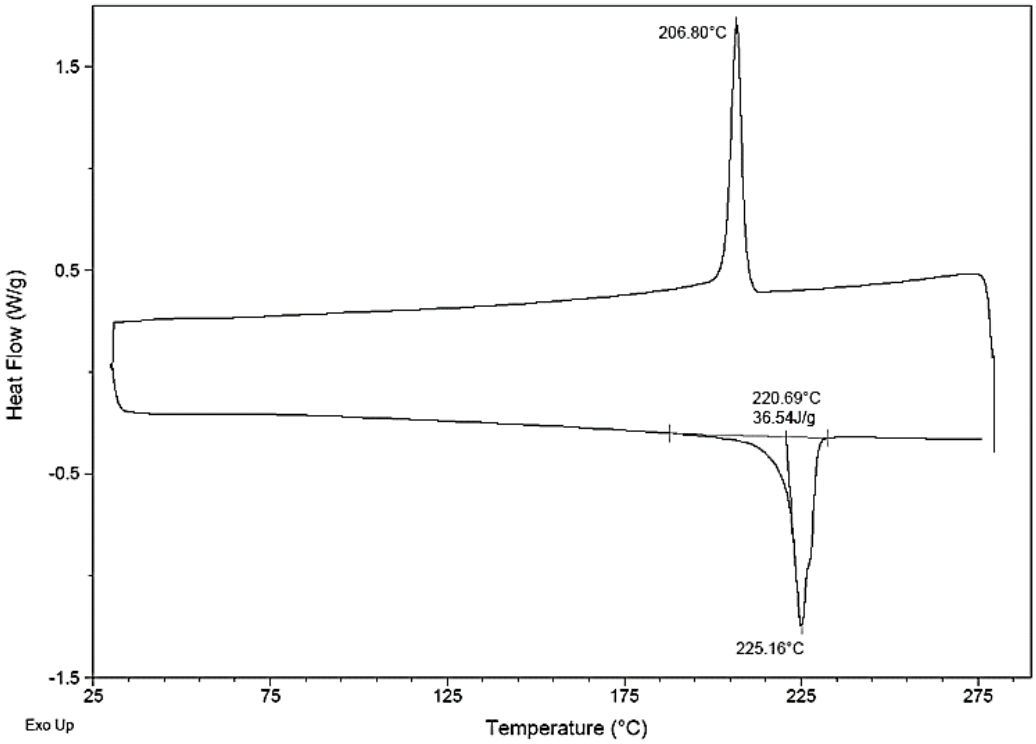

Figure S2.38. DSC full trace of a heat/cool/heat cycle, cycle 1 removed, with a ramp rate of 10 °C/min from 30 – 280 °C of **run 2.12.**

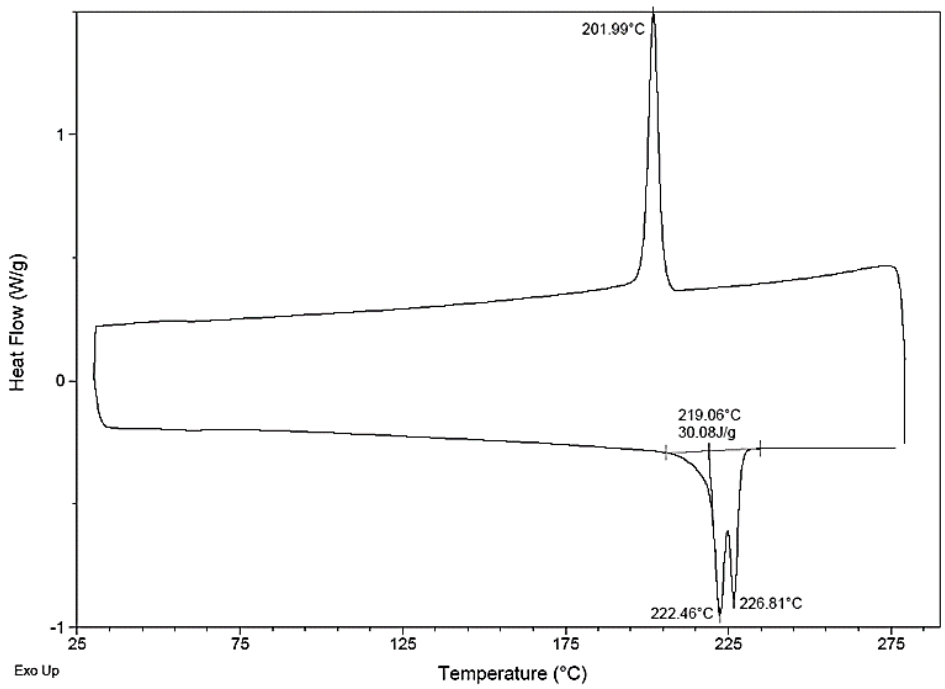

Figure S2.39. DSC full trace of a heat/cool/heat cycle, cycle 1 removed, with a ramp rate of 10 °C/min from 30 – 280 °C of **run 2.13**.

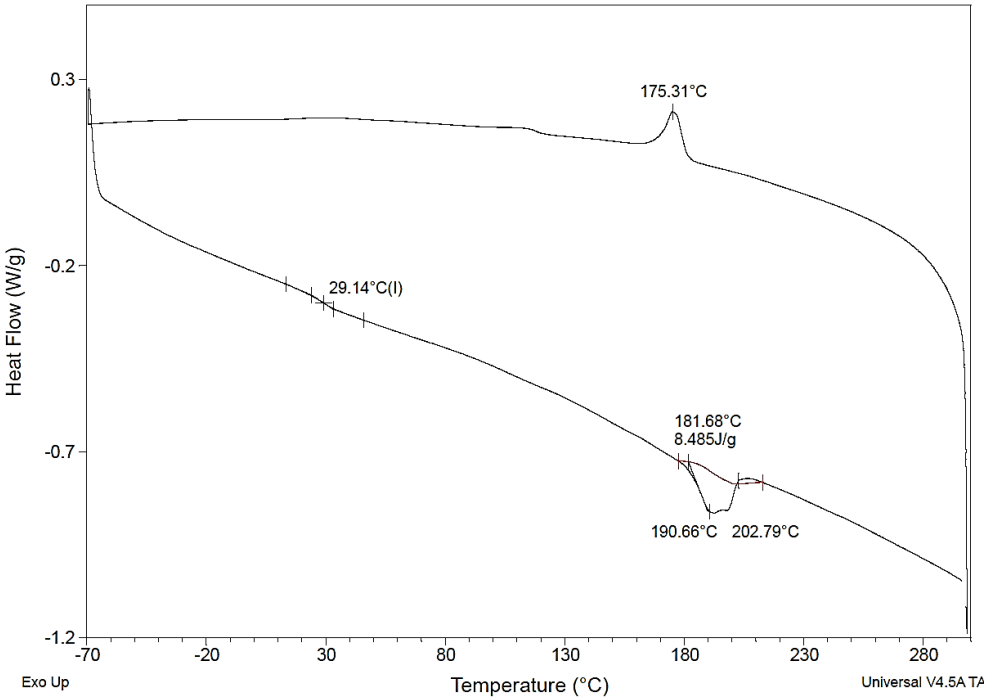

Figure S2.40. DSC full trace of heat/cool/heat cycle, cycle 1 removed, with a ramp of 10 °C/min from -70 – 300 °C of **run 2.14**.

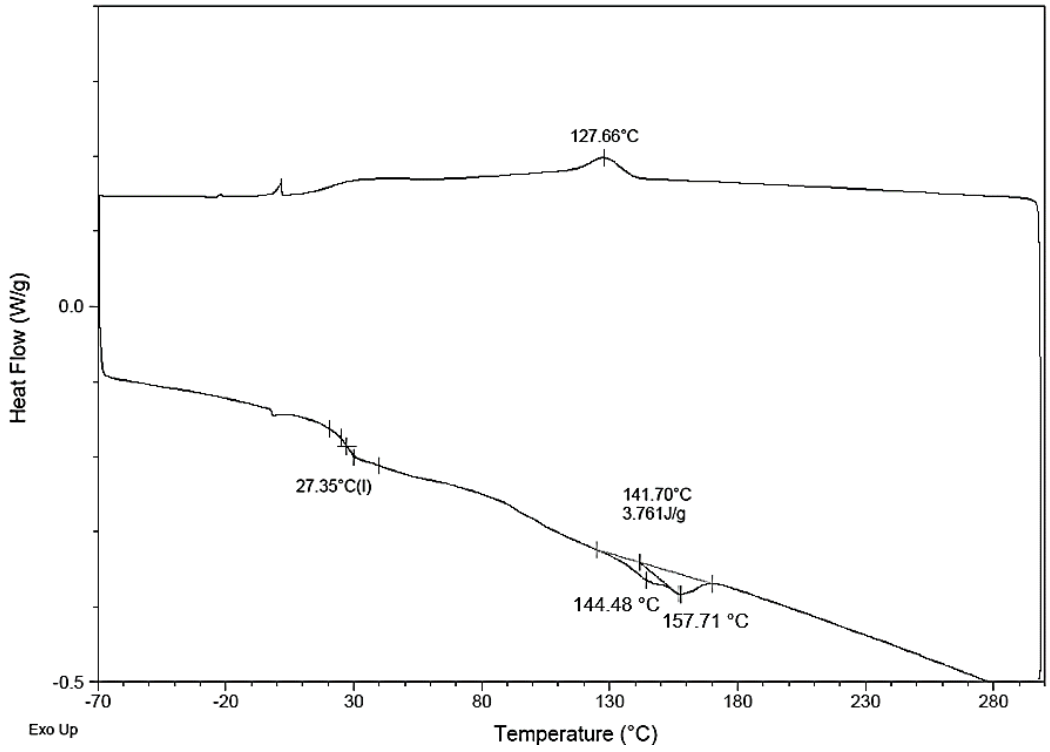

Figure S2.41. DSC full trace of heat/cool/heat cycle, cycle 1 removed, with a ramp of 10 °C/min from -70 – 300 °C of **run 2.15**.

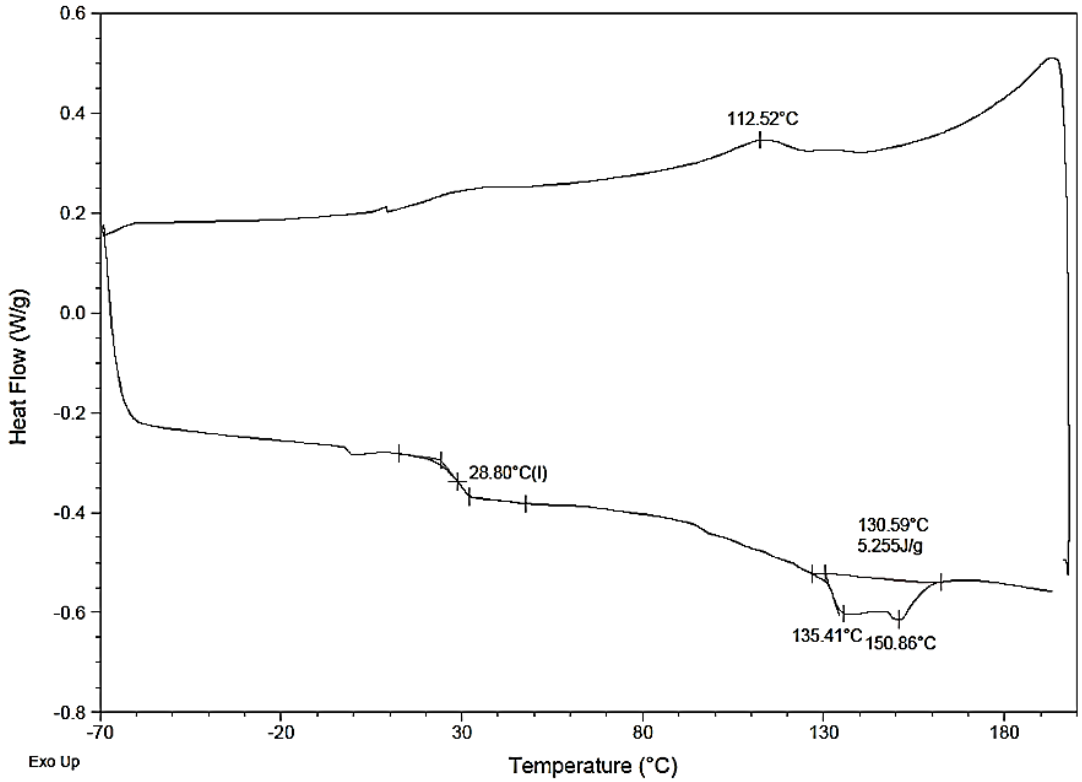

Figure S2.42. (a) DSC full trace of a heat/cool/heat cycle, cycle 1 removed, with a ramp rate of 20 °C/min from 30 – 280 °C of **run 2.16**.

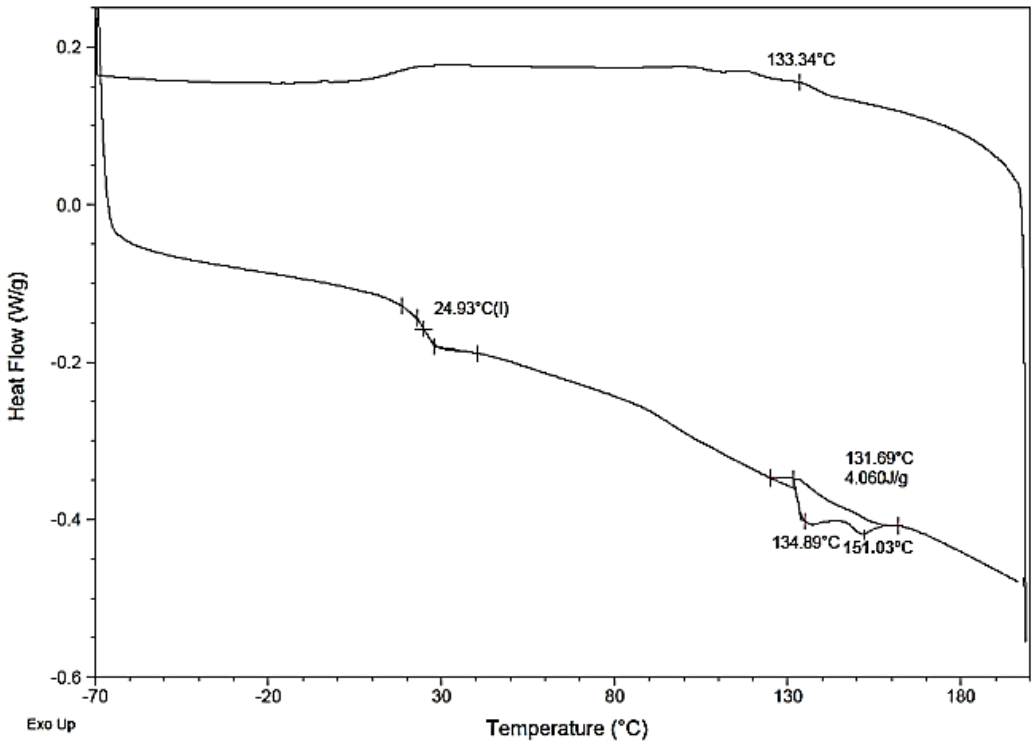

Figure S2.43. (a) DSC full trace of a heat/cool/heat cycle, cycle 1 removed, with a ramp rate of 20 °C/min from 30 – 280 °C of **run 2.17**.

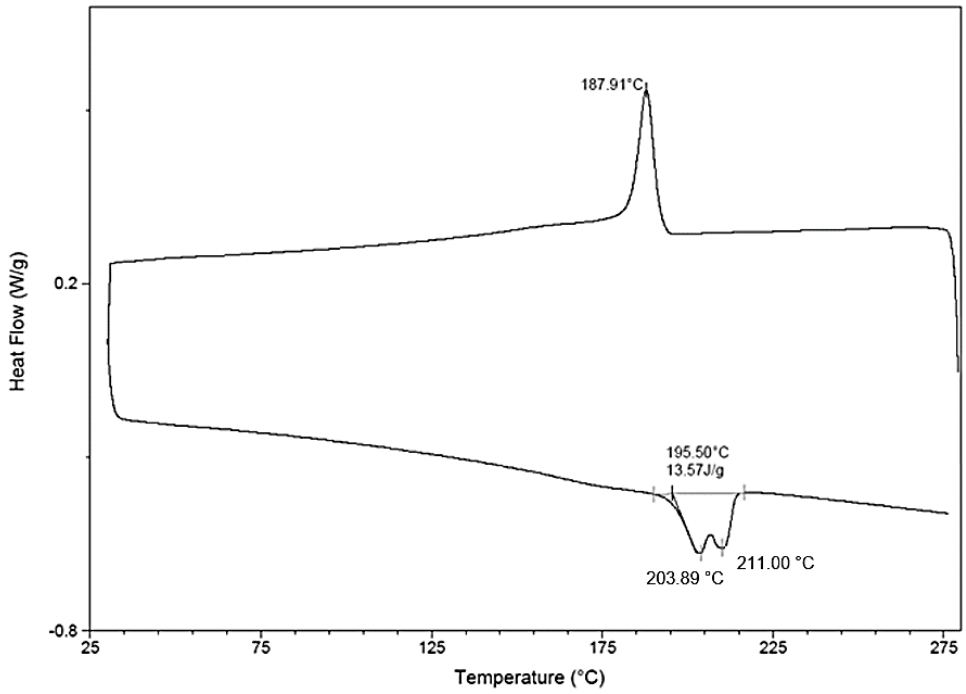

Figure S2.44. (a) DSC full trace of a heat/cool/heat cycle, cycle 1 removed, with a ramp rate of 10 °C/min from -70 – 300 °C of **run 2.14b**.

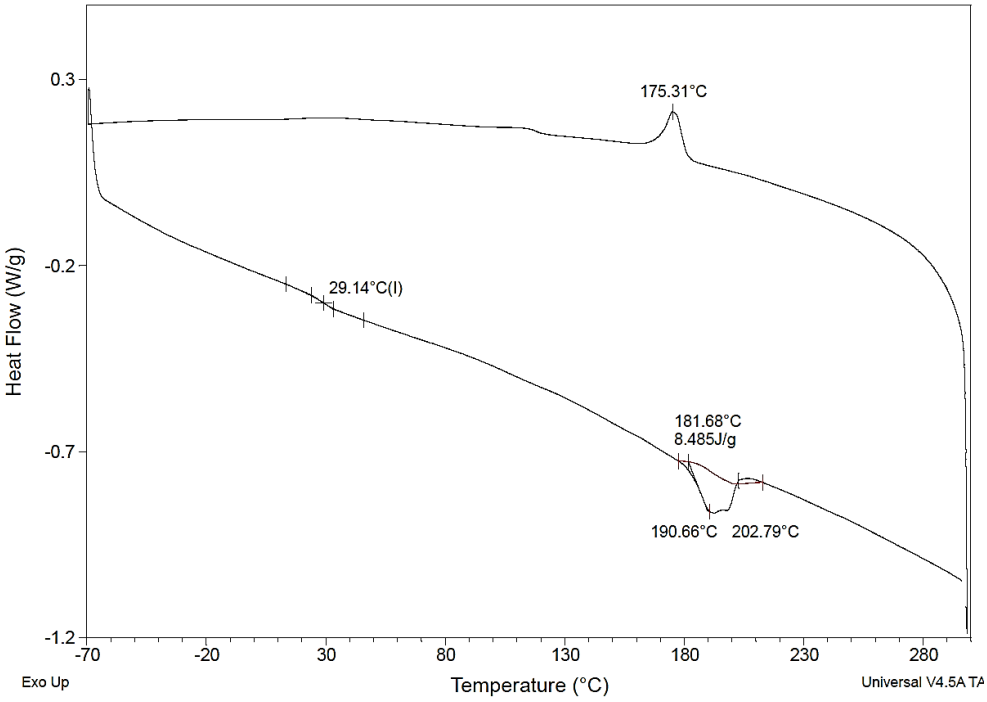

Figure S2.45. DSC full trace of a heat/cool/heat cycle, cycle 1 removed, with a ramp rate of 10 °C/min from 30 – 280 °C of **run 2.15b** .

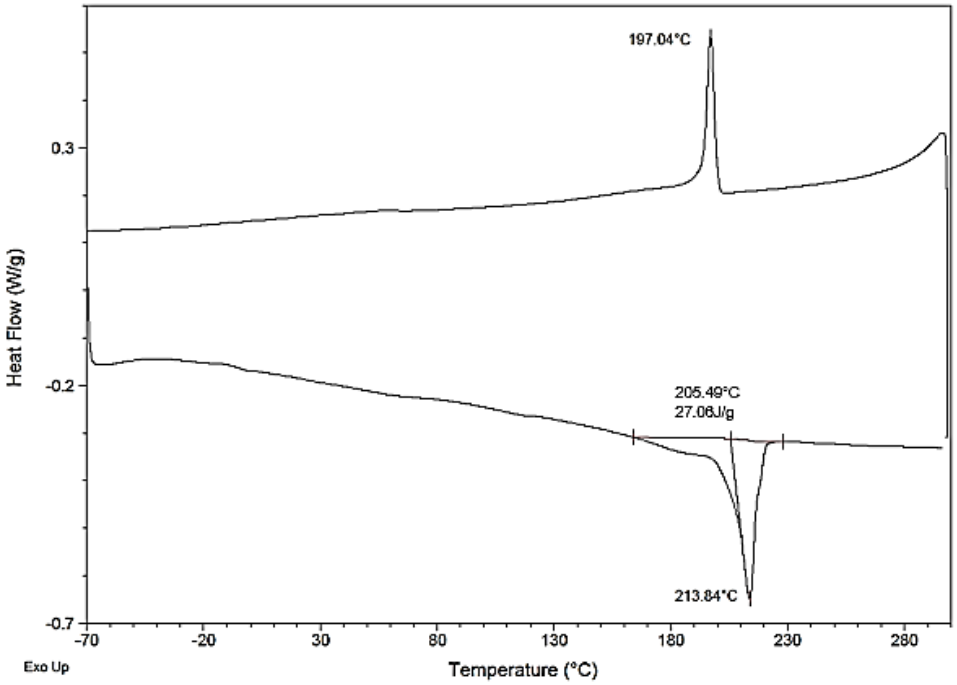

Figure S2.46. DSC trace of a heat/cool/heat cycle, cycle 1 removed, with a ramp rate of 10 °C/min from -70 – 300 °C of **run 2.18**.

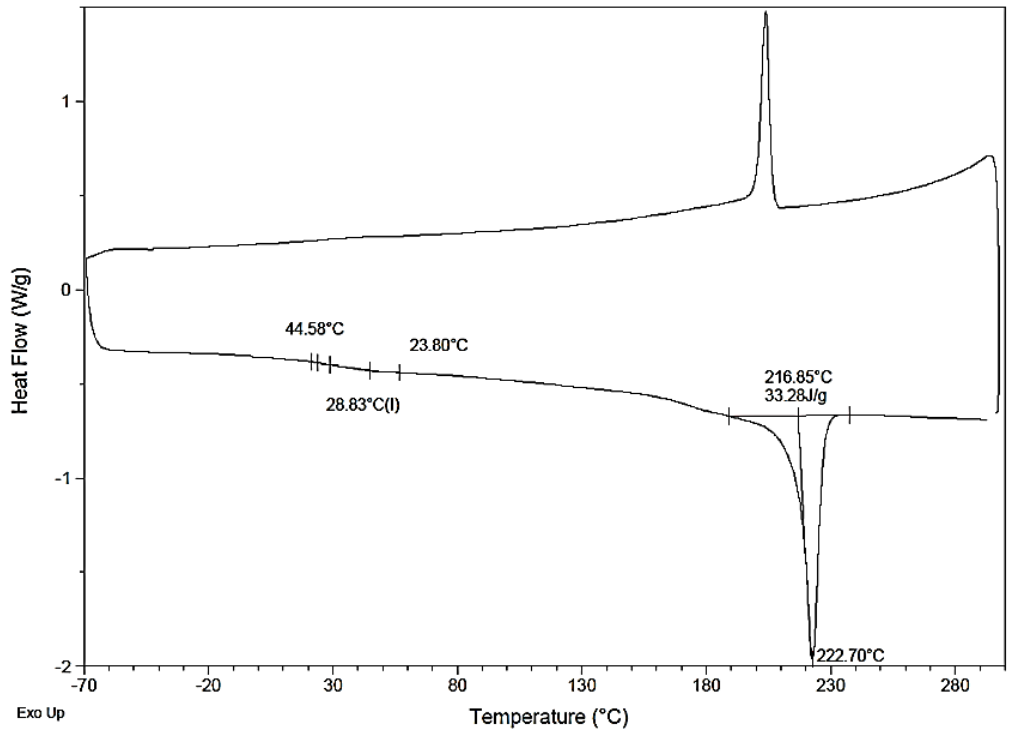

Figure S2.47. DSC trace of a heat/cool/heat cycle, cycle 1 removed, with a ramp rate of 10 °C/min from -70 – 300 °C of **run 2.19**.

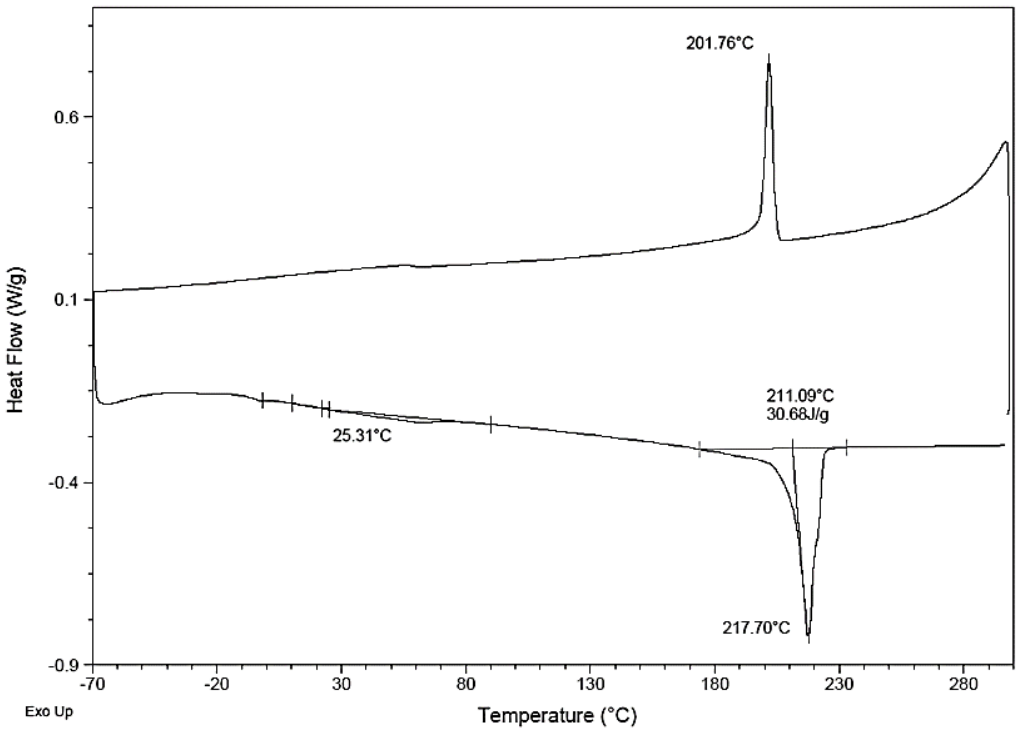

Figure S2.48. DSC trace of a heat/cool/heat cycle, cycle 1 removed, with a ramp rate of 10 °C/min from -70 – 300 °C of **run 2.20**.

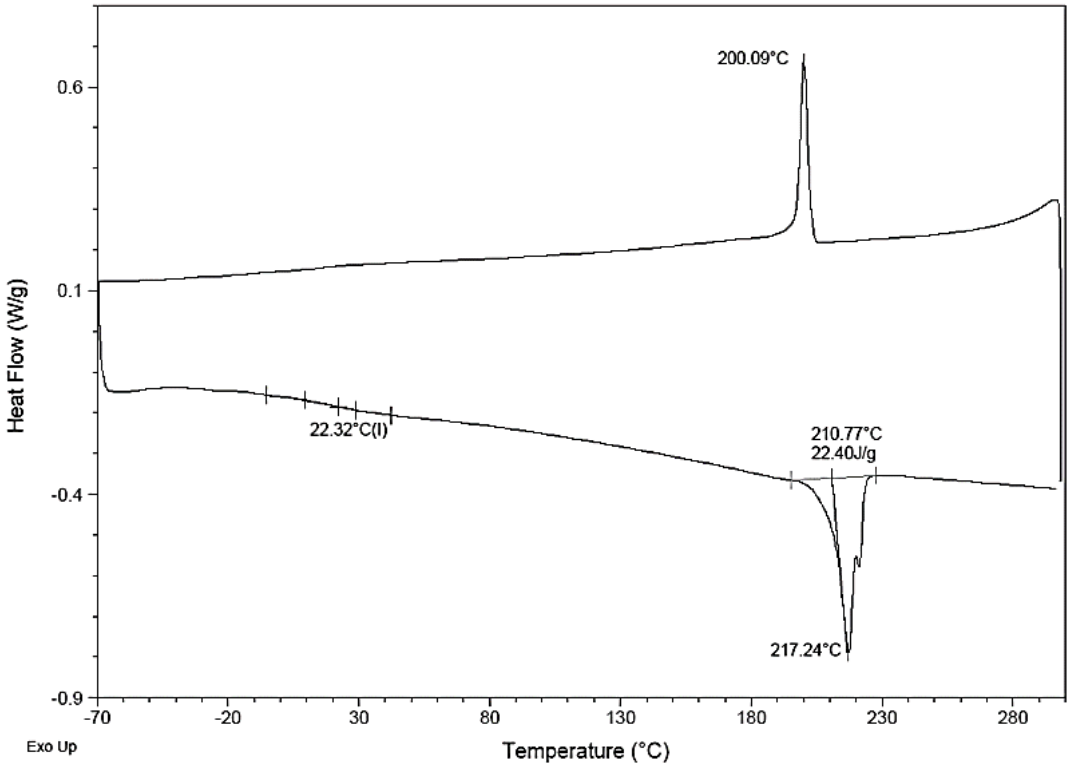

Figure S2.49. DSC trace of a heat/cool/heat cycle, cycle 1 removed, with a ramp rate of 10 °C/min from -70 – 300 °C of **run 2.21**.

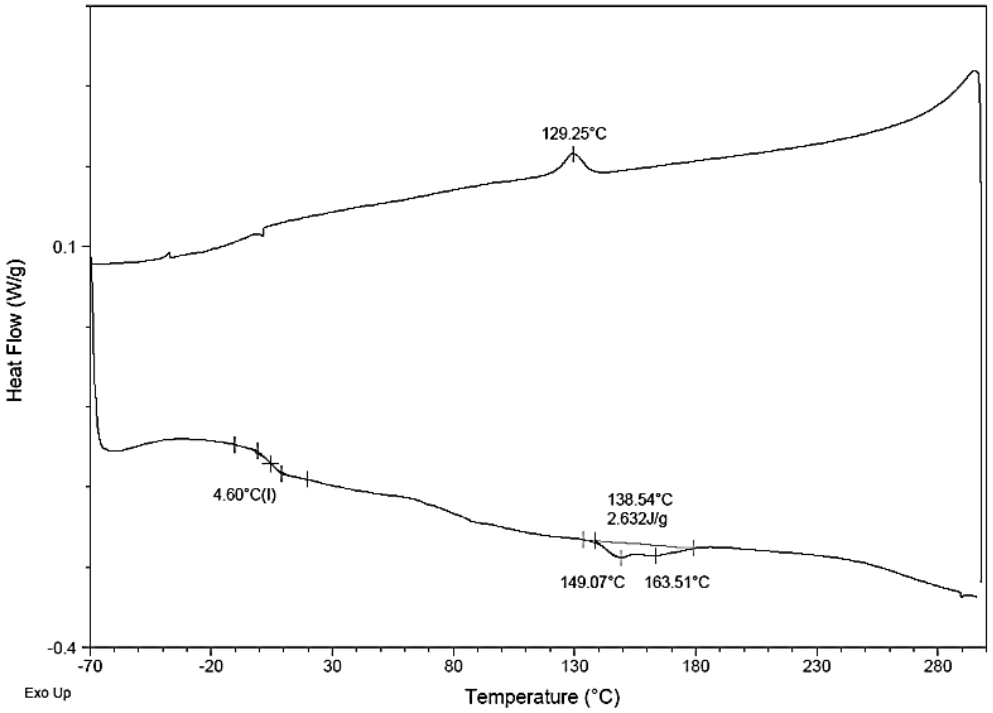

Figure S2.50. DSC trace of a heat/cool/heat cycle, cycle 1 removed, with a ramp rate of 10 °C/min from -70 – 300 °C of **run 2.22**.

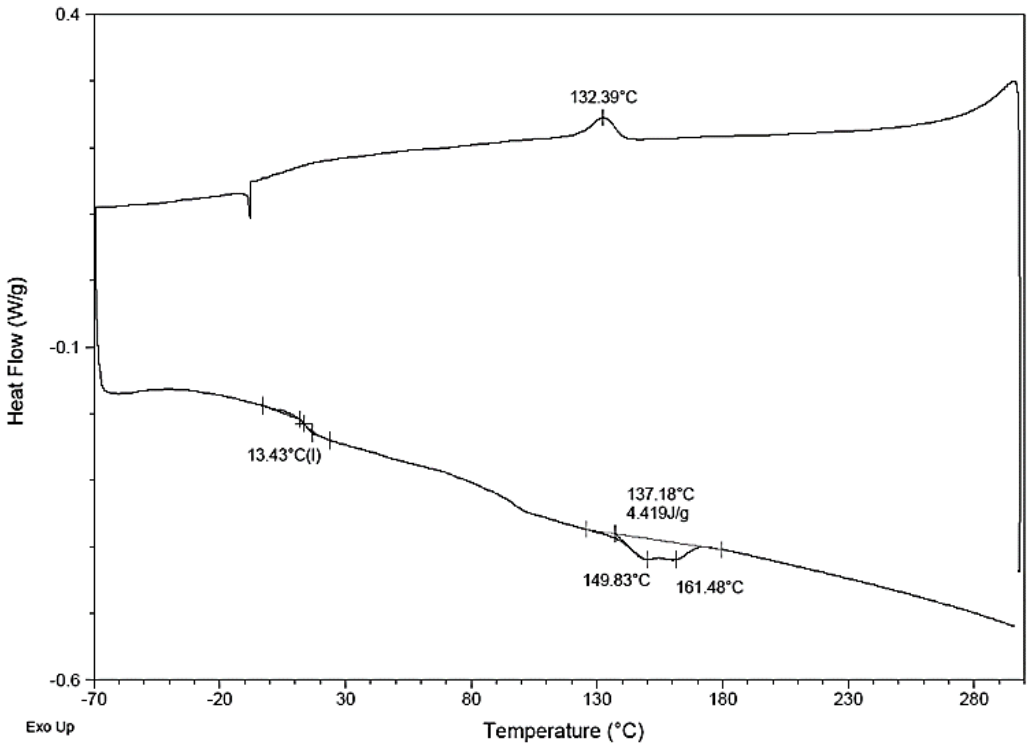

Figure S2.51. DSC trace of a heat/cool/heat cycle, cycle 1 removed, with a ramp rate of 10 °C/min from -70 – 300 °C of **run 2.23.**

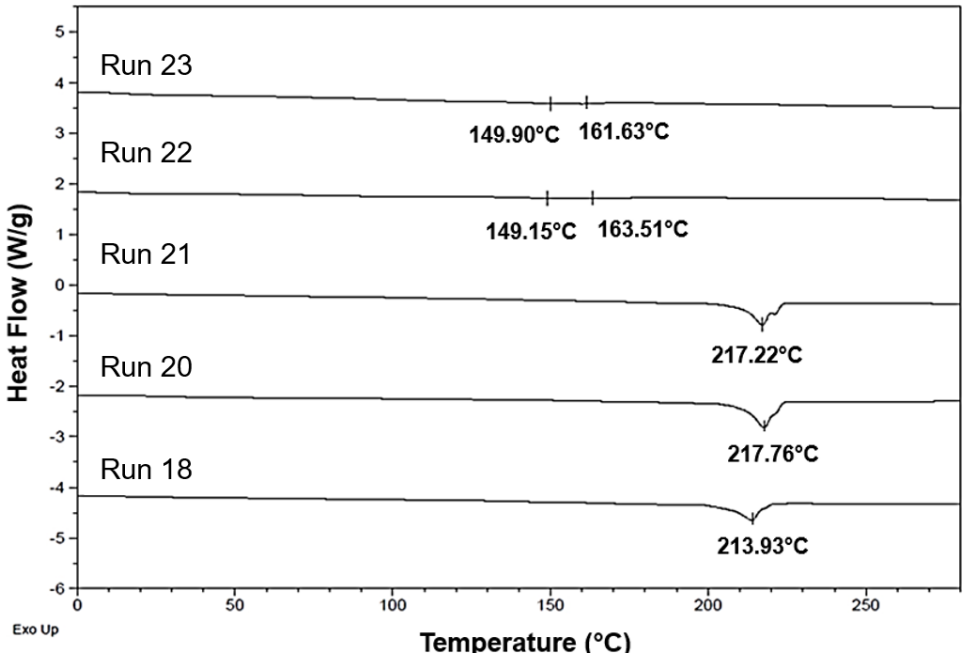

Figure S2.52. Stacked DSC trace of a heat/cool/heat cycle, cycle 1 removed, with a ramp rate of 10 °C/min from -70 – 300 °C of **run 18, 20-23.**

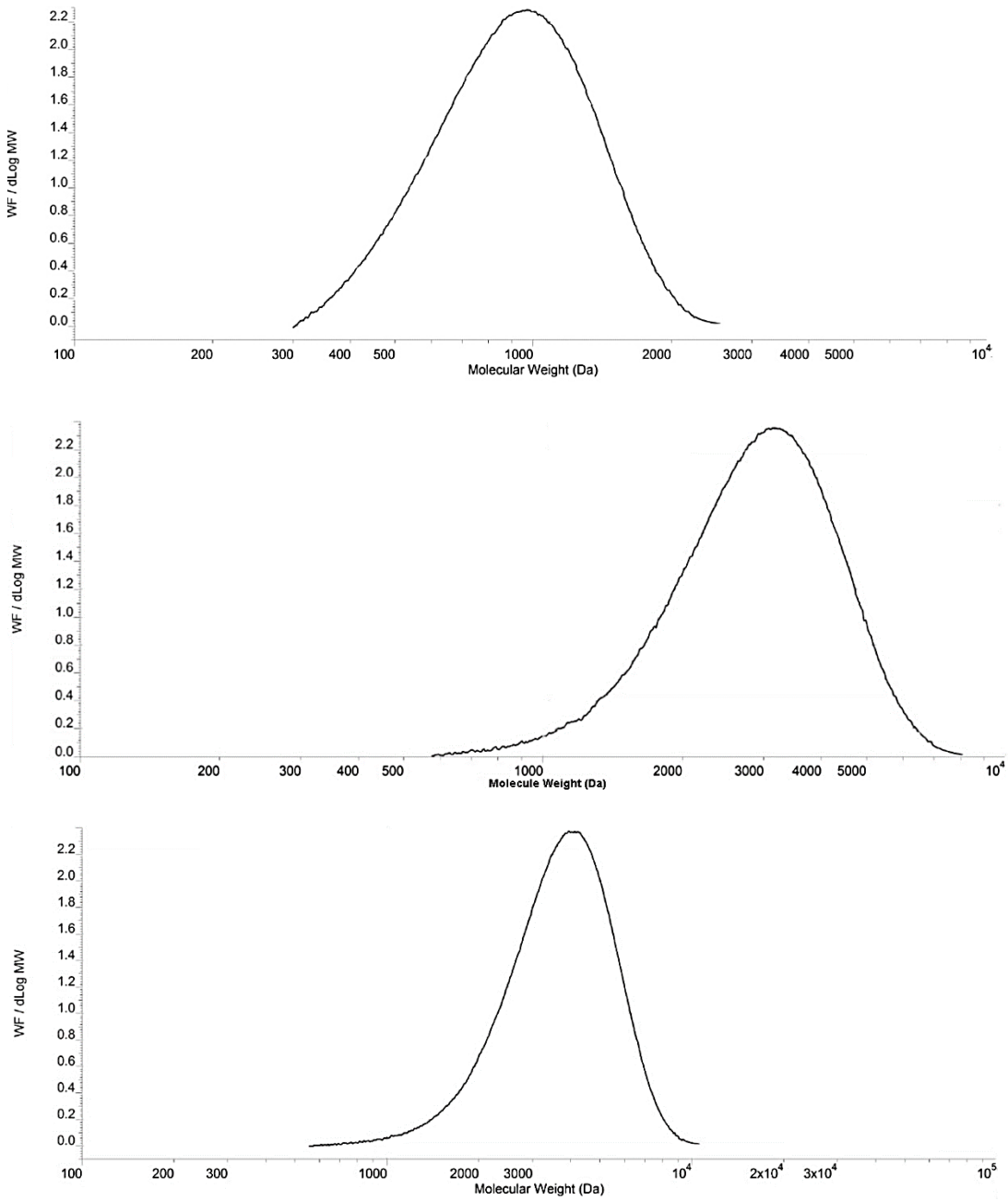

Figure S2.53. GPC trace of aPMP from **run 2.1** (top). GPC trace of aPMP from **run 2.2** (middle). GPC trace of aPMP from **run 2.3** (bottom).

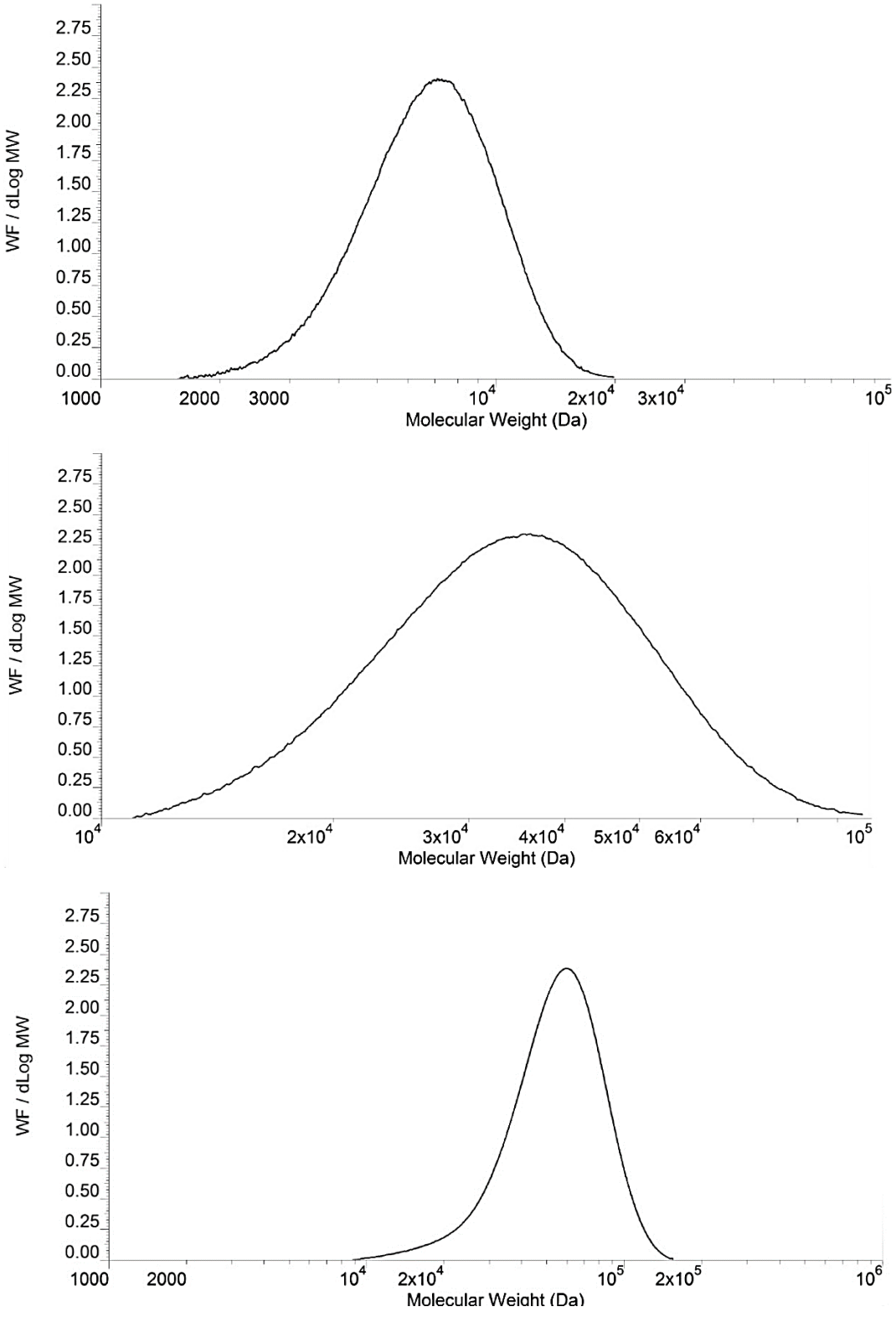

Figure S2.54. GPC trace of aPMP from **run 2.4** (top). GPC trace of aPMP from **run 2.5** (middle). GPC trace of aPMP from **run 2.6** (bottom).

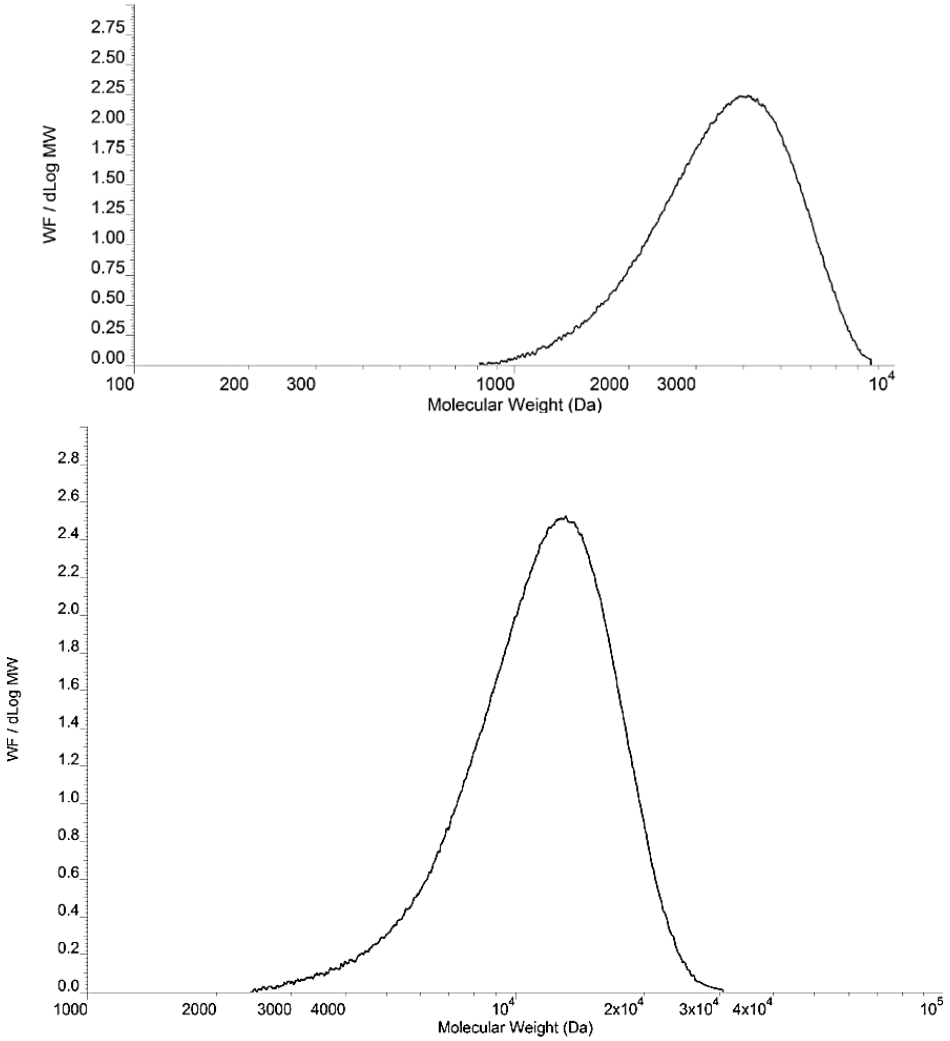

Figure S2.55. GPC trace of PMP from **run 2.7** (top). GPC trace of PMP from **run 2.8** (bottom)**.**

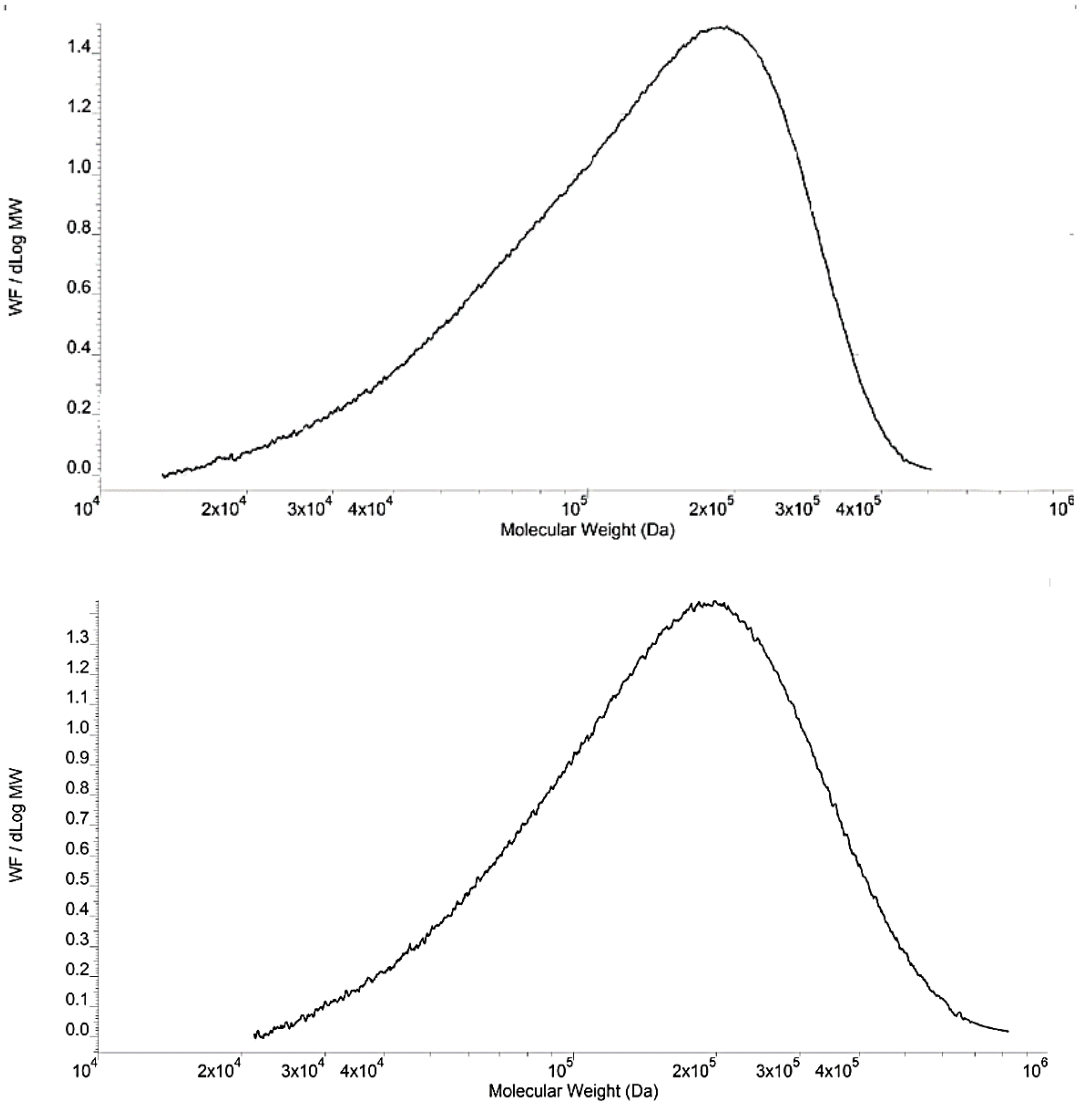

Figure S2.56. GPC trace of PMP from **run 2.9** (top)**.** GPC trace of PMP from **run 2.10** (bottom)**.**

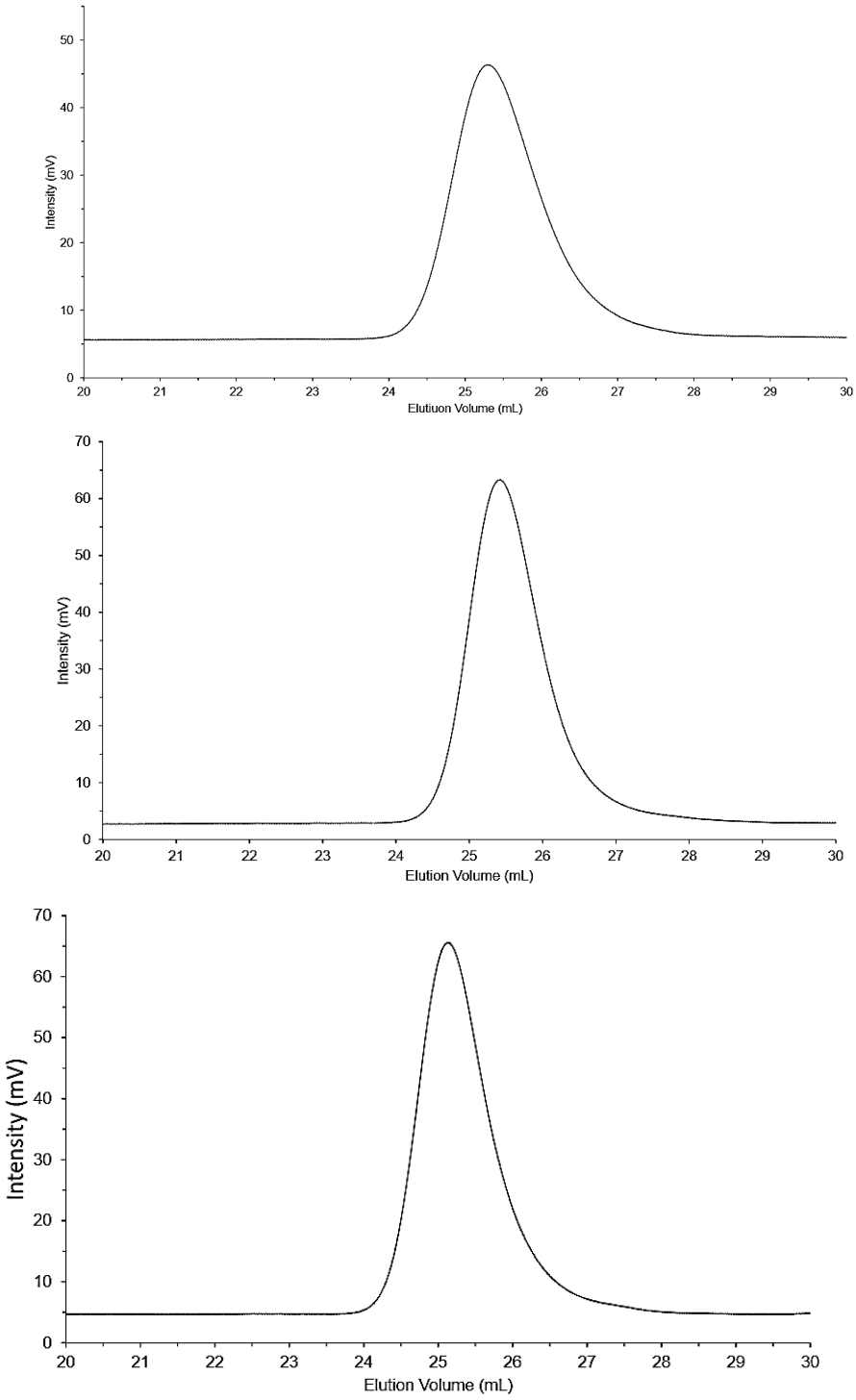

Figure S2.57. High temperature (HT-) GPC trace of PMP from **run 2.11** (top). HT-GPC trace of PMP from **run 2.12** (middle). HT-GPC trace of PMP from **run 2.13** (bottom). HT-GPC was taken at NIST, in trichlorobenzene (TCB) at 135 °C, calibrated with styrene standards.

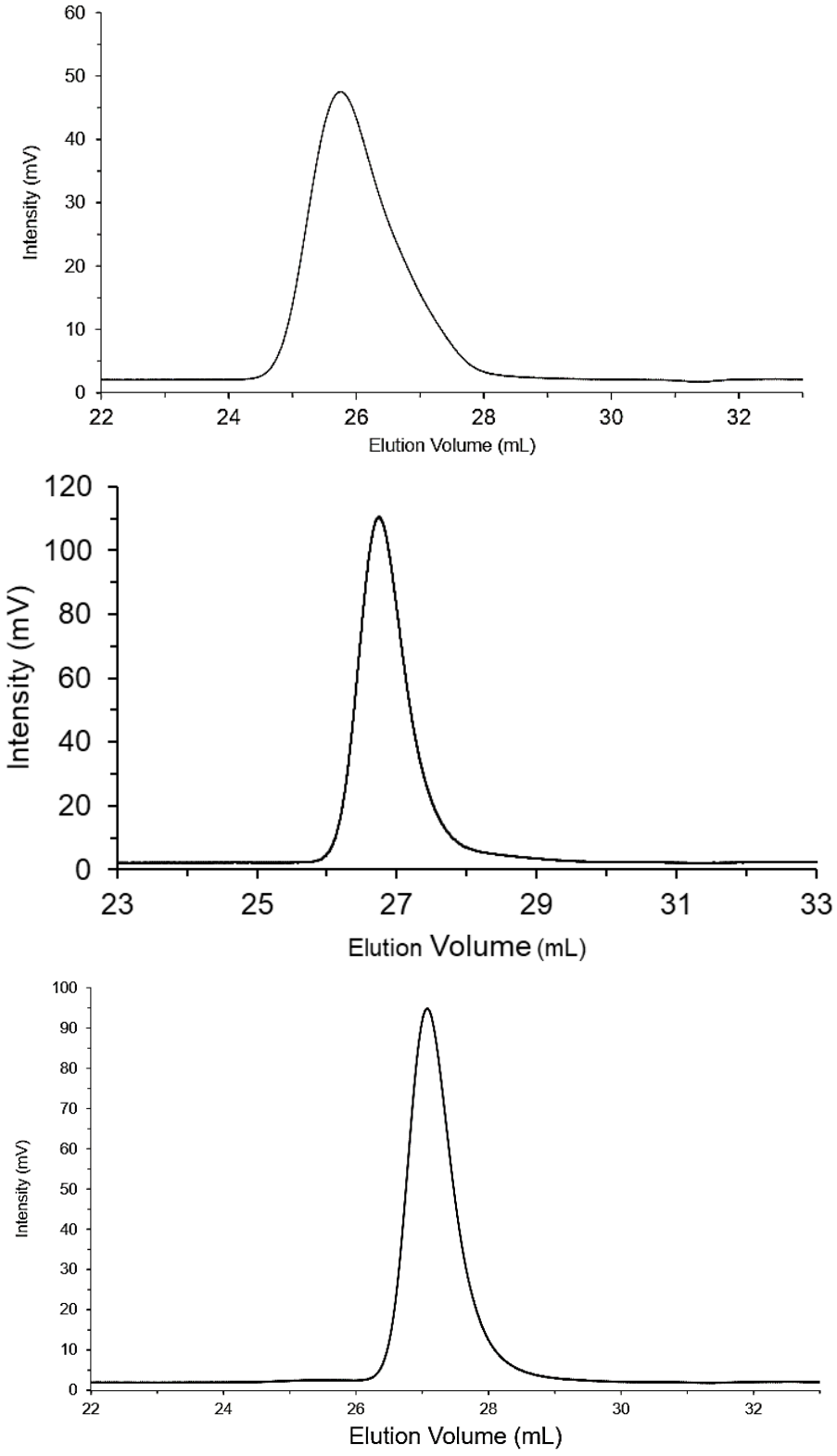

Figure S2.58. HT-GPC trace of PMP from **run 2.14** (top). HT-GPC trace of PMP from **run 2.15** (middle). HT-GPC trace of PMP from **run 2.16** (bottom). HT-GPC was taken at NIST, in TCB at 135 °C, calibrated with styrene standards.

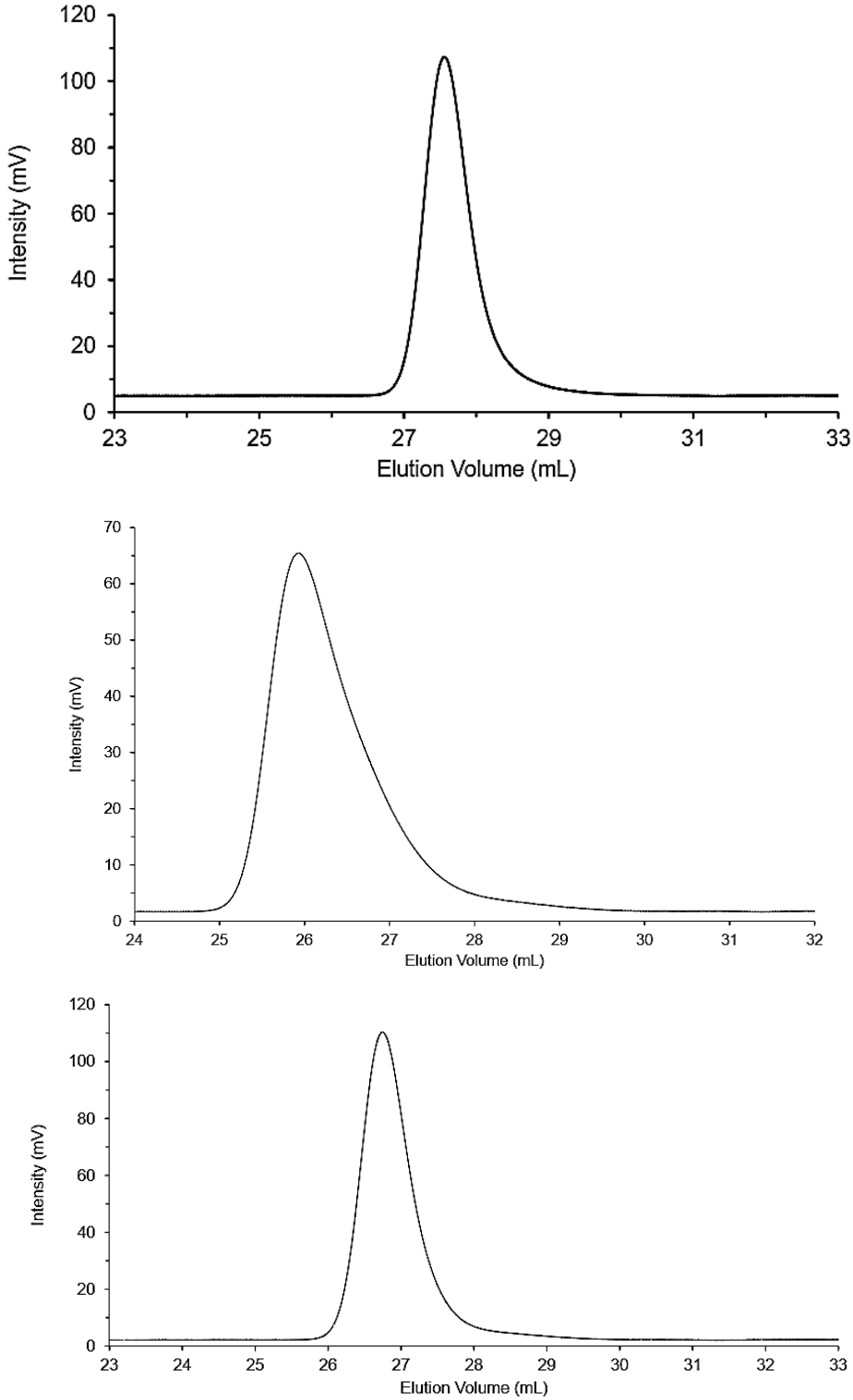

Figure S2.59. HT-GPC trace of PMP from **run 2.17** (top). HT-GPC trace of PMP from **run 2.18** (middle). HT-GPC trace of PMP from **run 2.19** (bottom). HT-GPC was taken at NIST, in TCB at 135 °C, calibrated with styrene standards.

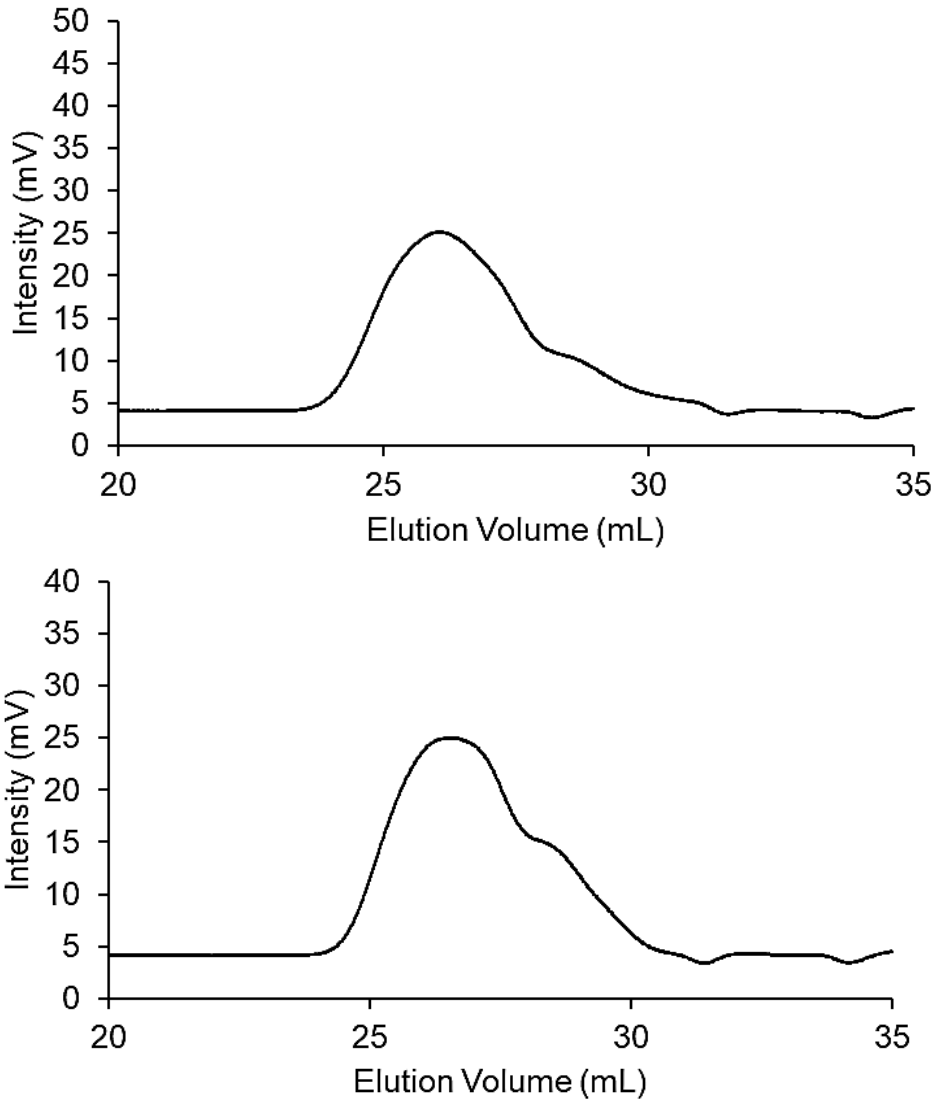

Figure S2.60. HT-GPC trace of **run 2.20** (top). HT-GPC trace of **run 2.21** (bottom)**.**

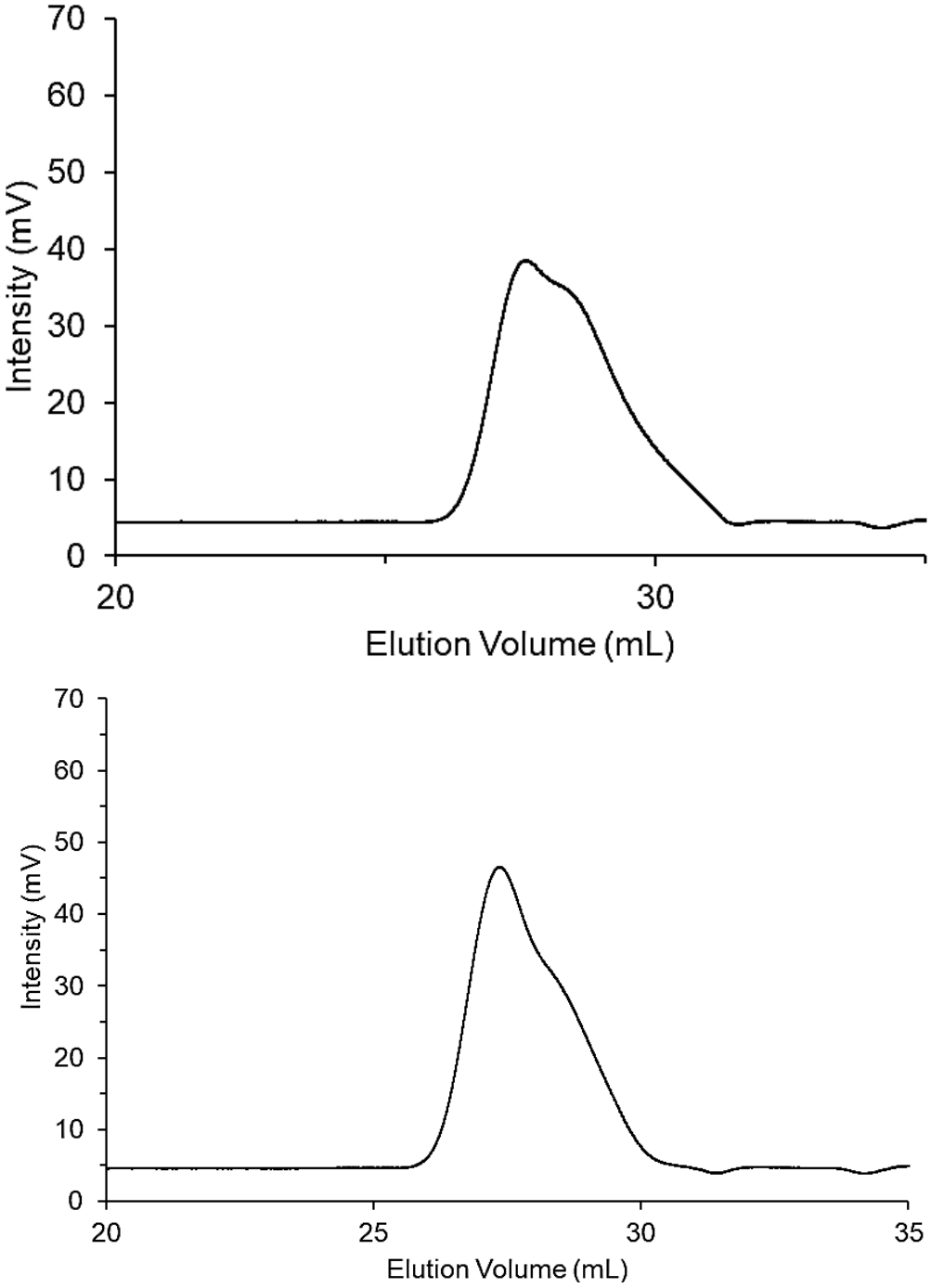

Figure S2.61. HT-GPC trace of **run 2.22** (top). HT-GPC trace of **run 2.23** (bottom)**.**

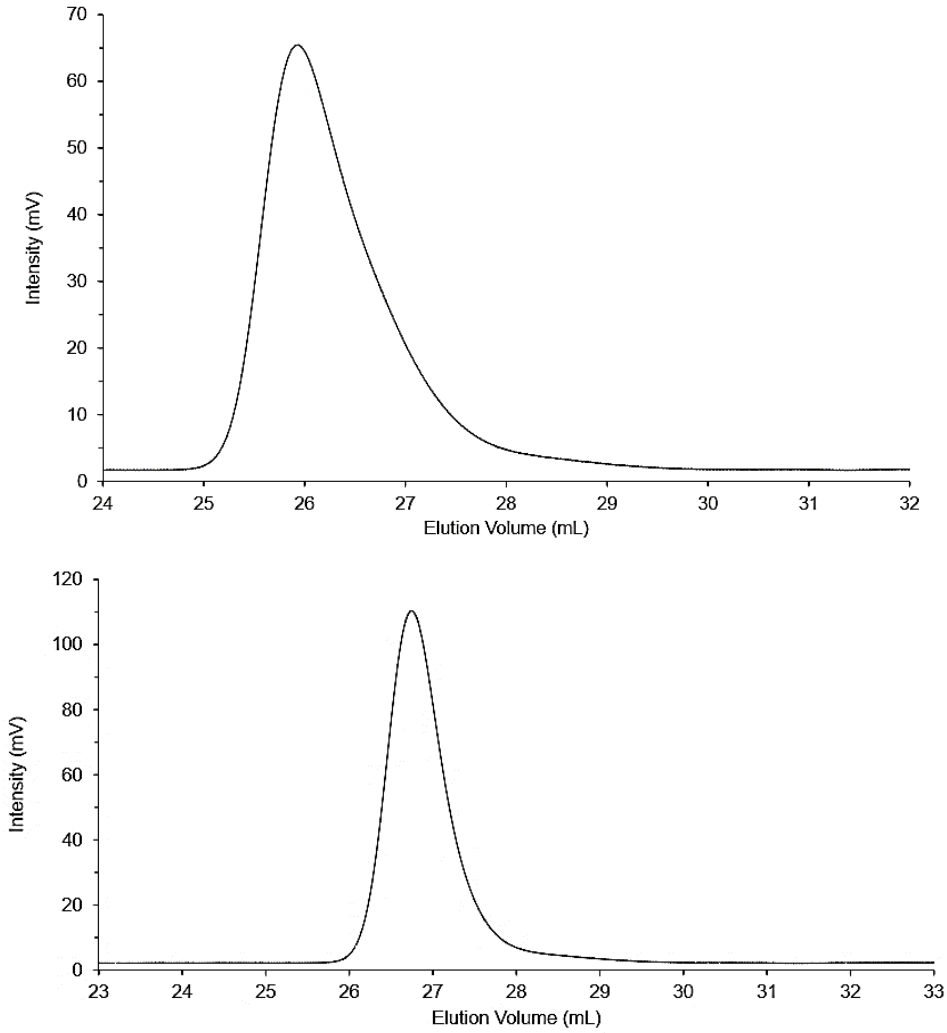

Figure S2.62. HT-GPC trace of PMP from **run 2.14b** (top). HT-GPC trace of PMP from **run 2.15b** (bottom).

Chapter 3: Investigation into Synthesizing a Stereoblocky PMP Material

3.1 Brief Introduction of 'Stereoblocky' Materials

Obtaining polyolefins with unique architectural design that consequently effects the overall property of the material has been investigated in many cases in order to develop new polymer technologies and applications. For several cases this was pursued with the goal that these polyolefin materials are useful as thermoplastic elastomers or heterophase compatiblizers.[1-3] Thermoplastic elastomers (TPE) are materials described to combine the thermoplastics and rubber properties into one material through both rigidity and flexibility contained within the structure of the polymer.[4] Generally this is achieved within TPE because the polymer contains hard segments (high T_g or semicrystalline) and soft segments (low T_g or amorphous). Some examples of well know TPE include commercialized polyurethanes and styrene-based materials, and something we've all come into contact with flexible phone cases, is an example of an everyday thermoplastic elastomer due to its strength in protecting a phone but also in the materials flexibility to wrap around the device.[5]

Discussed thoroughly in the last chapter, Natta first discovered that physical properties of polypropylenes (PP) can be controlled through changing the chain microstructure.[2] In line with stereoblocky materials this means that the mechanical properties and elastomeric properties must be controlled within the PP by crystalline-amorphous block structures coexisting either randomly or in a multiblock pattern.[6-17]

Achieving a polyolefin of ‘unattainable’ architecture were the adjoining chain segments are distinctly different stereoregularities which produce stereoblocky polymers has been of great interest in the polymer community ever since Natta’s first discovery with PP because of the materials outstandingly wide application reach.

A more recent study involving synthesis of stereoblocky materials includes Lieber and coworkers, which are the closest resembling system to what is discussed within the current work herein. In this investigation they tried to achieve stereoblocky polymers using a combination of chain transfer alkylaluminium cocatalyst alongside different *ansa*-Zirconocenes in one-pot reaction with propene.[2] They proposed that the chain transfer agents (CTA) alkyl bridging allowed for the polymer chains to pass between the two differing catalyst present within the one synthesis. They concluded that each of the combined catalysts had a different effect on the orientation and stereodirection of the growing PP chain therefore as the growing chain passed between the two catalysts the PP would change in direction (*mm*-*nn*) depending on which active species it was on for a short extended *DPn*. In this study they successfully made a small library of PP materials that utilized these two catalysts with CTA as a three-component system.

Within the Sita group we have also experimented with polyolefin stereocontrol and effecting the microstructure and therefore properties of materials in the past. In the previous chapter an extensive list was provided of such studies. However, this concept has been explored extensively with propene but has yet to be documented in the literature with 4-methyl-1-pentene (4M1P). Toward the continued advancement of LCCTP, and the goal of discovering new PMP materials, this work will present a new

method that expands the scope of this system and produces not stereoblock PMP materials but instead a blend of the homopolymers. These blended PMP materials can offer a solution to the downfalls of fully isotactic brittle PMP or amorphous atactic PMP by having new novel physical properties that can be useful as a compatibilizer or a thermoplastic elastomer.

3.2 Three-Component LCCTP System

Using a combination of both Zr (**1**) or Hf (**2**) CPAM pre-initiators which upon 'activation' with stoichiometric equivalents of borate co-initiator (**B1**) ,in the presence of chain transfer agent $ZnEt_2$ and excess 4M1P monomer, a targeted molar mass with a specific number-average degree of polymerization (DP_n) of PMP is achieved. A general outline of the synthesis described and employed within this study is displayed in Scheme 3.1. The symmetry characteristics of the pre-initiators correlate to the tacticity that is observed within the microstructure of the polymer. More specifically when LCP of **1** in used isotactic PMP is yielded while on the other hand through LCP full activation of **2** the resulting PMP with be atactic. When the addition of $ZnEt_2$ is added to the already existing system which contains a combination of both **1** and **2** the system becomes an LCCTP process. We propose that during polymerization the growing chain on **1** or **2** gets passed to the $ZnEt_2$ CTA and back to either pre-initiator at random. Thus, as the polymer grows on **1** it creates stereoregular units (blocks of unknown length) which can then be passed off to **2** which propagates atactic units (blocks of unknown length) overall hopefully creating a stereorandom

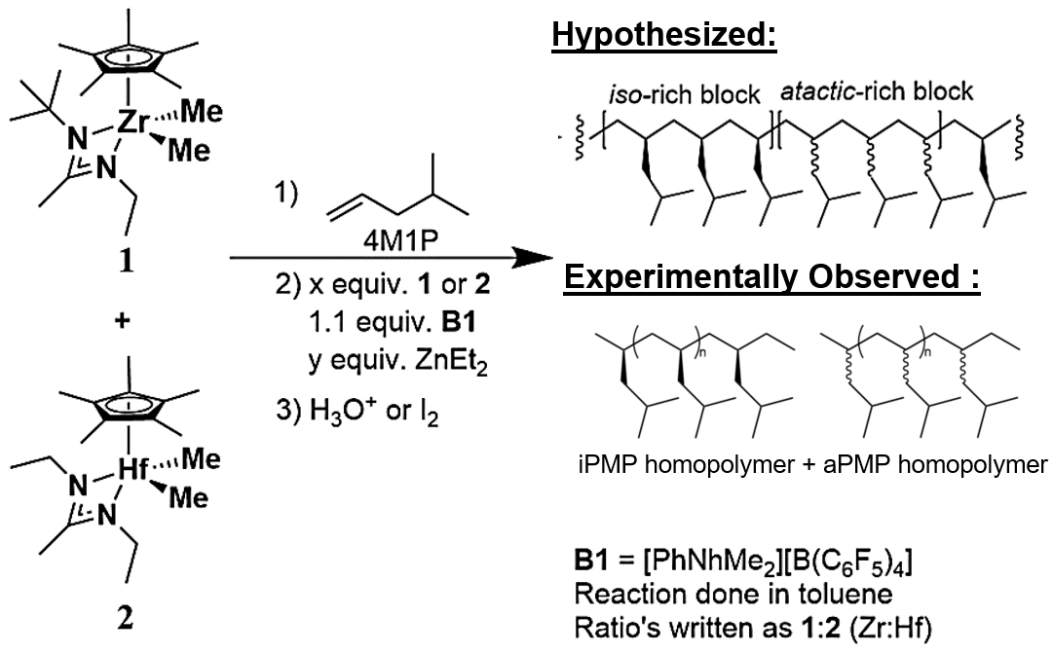

Scheme 3.1 Summary of the reagents and methods that were employed in the one-pot LCCTP of 4M1P using a dual pre-initiator system.

blocky PMP material.

Knowing this, the first goal of the present study was to determine the stereochemical microstructure of PMP in the presence of both **1** and **2**, under chain transfer conditions. Potential products include (1) a stereoblock-like PMP copolymer with a mixture of tacticity's (2) two separate PMP homopolymers with dissimilar tacticity's, or (3) the dimerization of activated **1** and **2** to cause no product to form. Though the main investigation was to create a stereoblocky PMP material interestingly through purification techniques it was determined that this process results in (2), two separate homopolymers made through LCCTP that resulted in a blended material of PMP polymers with a mixture of tacticity's that vary as the ratio of **1** to **2** is changed. As a standard for comparison, we synthesized two versions of PMP from either full activation of **1** or **2** to create completely iPMP (Mn = 51.0 kDa, Đ = 1.39) and aPMP

(Mn = 48.7 kDa, Đ = 1.19), respectively. These two materials are **ref1** and **ref2** from chapter 2 study. For the purpose of this study, it is helpful once again to look at the ends of the spectrum of the 'grades' of PMP materials that can be made with our LCCTP system. Figure 3.1 presents the corresponding $^{13}C\{^{1}H\}$ NMR (200 MHz) spectra for these materials in 1,1,2,2-tetrachloroethane-d2 (TCE-d_2) at 110 °C. To repeat, the spectrum of **iPMP** (Figure 3.1A) shows the appearance of five sharp 13C resonances that are consistent with $^{13}C\{^{1}H\}$ NMR spectra reported for other highly regioregular and stereoregular iPMP materials in which C5 and C6 of the geminal methyl groups of the isobutyl side chains appear as being magnetically equivalent due to the intrinsic C_s-symmetry of a sufficiently long isotactic chain.[3,7cw] In contrast, the $^{13}C\{^{1}H\}$ spectrum of **aPMP** (Figure 3.1B), shows that each of the corresponding 13C resonances are now broad. This feature is due to the partial overlap of multiple resonances associated with different tacticity sequences. Accordingly, once again in the present study, we cannot perform the type of extensive quantitative ^{13}C NMR investigations of stereochemical microstructure that have been reported for PP, and instead, only qualitative assessments and comparisons of the relative degree of stereoregularity for each member of a collection of PMP samples can be made. Towards the goal of this current study, a mixture of **1** and **2** at a 50:50 ratio (Zr:Hf) were used to polymerize 4M1P in the presence of $ZnEt_2$, **run 3.5** in Table 3.1. The corresponding $^{13}C\{^{1}H\}$ NMR spectrum , in Figure 3.1C, shows a mixture of atactic and isotactic like character. The profile of the peak at 23 ppm in Figure 3.1C, for **run 3.5**, shows both the broadness of aPMP in Figure 3.1B, and the sharpness of iPMP in Figure 3.1A.

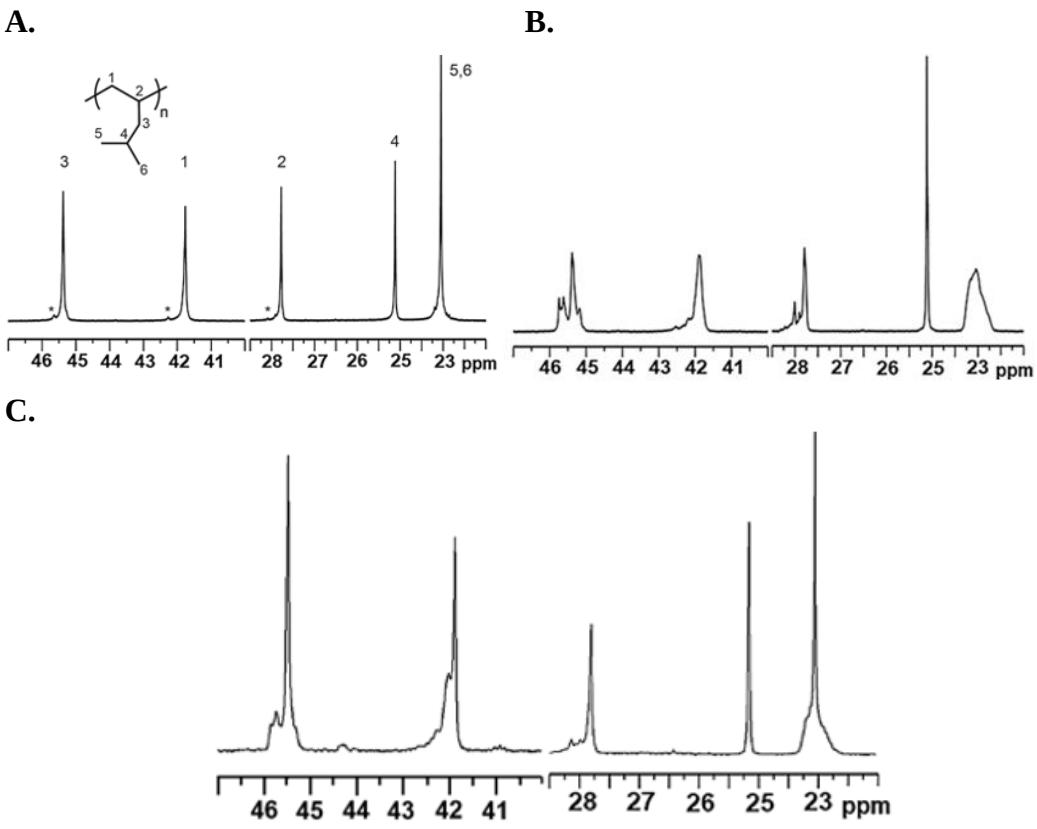

Figure 3.1 $^{13}C\{^{1}H\}$ NMR spectra (200 MHz, TCE-d_2, 110 °C) for (A) **iPMP** (100:0) (Mn = 51.0 kDa, Đ = 1.39), (B) **aPMP** (0:100) (Mn = 48.7 kDa, Đ = 1.19), and (C) homopolymer PMP blend **run 3.5** (50:50) (Mn=5.05 kDa, Đ = 1.16). The asterisks in (A) indicate 13C resonances for a polyolefin co-product arising from an α-olefin impurity in the original 4M1P.

3.3 Results of LCCTP with Two Stereo-influencing Catalysts in a One-Pot Polymerization

Next, a series of stereoengineered PMP was developed using a mixture of **1** and **2** ranging from 90:10 to 10:90 (**1**:**2**, Zr:Hf) with uniquely distinct properties for each 'grade' of polyolefin observed, Table 3.1. First, it is important to note that

polymerizations were run under 100% activation of both catalysts. We originally

Table 3.1. LCCTP conditions and PMP results using both **1** and **2** simultaneously.

Run	1:2	$ZnEt_2$ (eq.)	4M1P (eq.)	Yield (g)	M_n (kDa)[b]	M_w (kDa)[b]	Đ[b]	T_g (°C)[c]	T_m (°C)[c]	%Crystal-linity[c]
3.1	90:10	5	595	1.73	4.29	8.40	1.96	-	221.5	25.7
3.2	80:20	5	595	1.89	1.55	2.13	1.37	-	219.5	23.3
3.3	70:30	5	595	1.99	2.33	2.81	1.21	-	217.3	18.1
3.4	60:40	5	595	1.86	2.92	3.39	1.16	12.58	214.5; 220.4	13.0
3.5	50:50	5	595	1.89	4.55	5.27	1.16	19.1	216.2; 221.6	10.9
3.6	40:60	5	595	1.67	5.05	5.85	1.16	18.2	215.2; 221.2	5.12
3.7	30:70	5	595	1.88	5.38	6.38	1.19	20.1	209.0; 217.0	4.70
3.8	20:80	5	595	1.78	4.86	5.58	1.15	6.68	203.7; 212.3	1.92
3.9	10:90	5	595	1.97	4.62	5.45	1.18	12.8	196.3; 208.0	0.92

[a]For complete details of polymerization conditions for each run, see SI. [b]Determined by SEC. [c]Determined by DSC.

proposed, just like Libeler and coworkers, that the CTA is present to help shuttle the growing polymer chains between the different catalysts. However, this ended up not being the case for our polymerization system. The stereoregularity of microstructure of each homopolymer within the blend becomes dependent on the relative ratio between **1** and **2,** or put more simply, which species is most present in the polymerization. This stereochemical dependence is visible in $^{13}C\{^1H\}$ NMR and differential scanning calorimetry (DSC). As the presence of C_s-symmetric **2** is increased, $^{13}C\{^1H\}$ NMR spectra show an increase in atactic resonances, specifically at carbons C1 and C3 in Figure 3.2A, see SI for full stacked spectra of all sample runs. Additionally, as **2** is increased, DSC measurements show a decrease in melting point (T_m) and the distinct

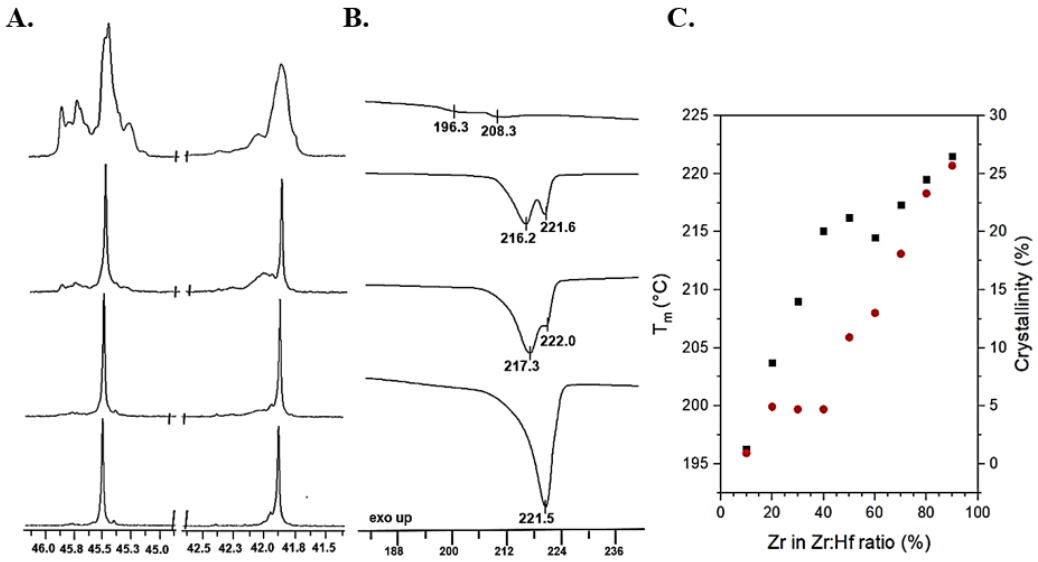

Figure 3.2 (A) Partial $^{13}C\{^{1}H\}$ NMR spectra (200 MHz, TCE-d_2, 110 °C) for homopolymer blended PMP bulk materials obtained from runs **3.1**, **3.3**, **3.5,** and **3.9** (from bottom to top). (B) Partial DSC traces for the same PMP samples, runs **3.1**, **3.3**, **3.5**, and **3.9** (from bottom to top). (C) Plots of T_m and percent crystallinity as a function of percent **1** in the ratio of **1**:**2** for runs **3.1**-**3.9** in Table 3.1.

appearance and a glass transition temperature (T_g) (Figure 3.2B). For **runs 3.1 – 3.3**, no T_g was detected due to the high crystallinity of the material blend. **Runs 3.4 – 3.9** show two melting point peaks, indicating the presence of crystallites of various size. The integral of the T_m peak, the enthalpy of fusion (ΔH_f), can be used to determine the percent crystallinity of each sample. As the enthalpy of fusion of a perfect isotactic PMP sample (ΔH_f^*) was reported as 117.2 J g^{-1}, the ratio of enthalpies is indicative of crystallinity. As the amount of **1** is increased, both the melting point and crystallinity increases within the polymer, suggesting the presence of more isotactic regions, therefore more crystalline domains within the polymer (Figure 3.2C). The synthesis of these materials guided us to the assumption that the chain transfer agent is in fact still acting as a surrogate for chain growth, however instead of passing the chains between catalysts **1** and **2** it stays in proximity to the same catalysis only allowing for chain

transfer to occur on the same matched catalysis, resulting in materials that are comprised of two homopolymers blended together at varied ratios based on the ration of **1** or **2** during the synthesis.

The discovery that the bulk material was comprised of two homopolymers was determined by Danyon M. Fischbach when the bulk resulting material was loaded into an extraction thimble. This thimble was placed inside the Soxhlet, and round bottom was loaded with 200 mL of hexane. The hexane refluxed at 80 °C for 16 hours. The extracted polymer in the RBF was dried and massed. The thimble was dried, and the polymer left inside was dried and massed as well. In Figure 3.3 is an image of the two separated homopolymers that came from the original **run 3.5** bulk material which can be seen in Figure 3.4.

Thermal properties are not the only physical property to vary over the range of these PMP samples. Even though they are at their core blends of homopolymers samples look and feel different from each other as well as different from the 100% aPMP and 100% iPMP references, Figure 3.4. Low *Mn* aPMP is liquid-like and tacky

Figure 3.3 Image of separated homopolymers from bulk material, run **3.5,** left image is of the isotactic homopolymer and left image is of the atactic homopolymer.

while the iPMP is a flowing, fine white powder. In complete contrast, the blended PMP materials made through the one-pot synthesis with both pre-initiators have properties such as paper (10:90 sample in Figure 3.3), moldable wax, fake snow, and fluffy powder (50:50 sample in Figure 3.4).

Utilizing the instrumentation dynamic mechanical analysis (DMA) the PMP materials varied physical properties can be quantitatively determined. Shown in Table 3.2 and Figure 3.4 are DMA results of selected materials. The PMP homopolymer blends made with majority **1** were too brittle to measure, as mentioned is a drawback to highly crystalline iPMP. Notably, there is a drastic difference between aPMP and **run 3.9** in comparison to all other PMP materials. **Run 3.9** only has a small

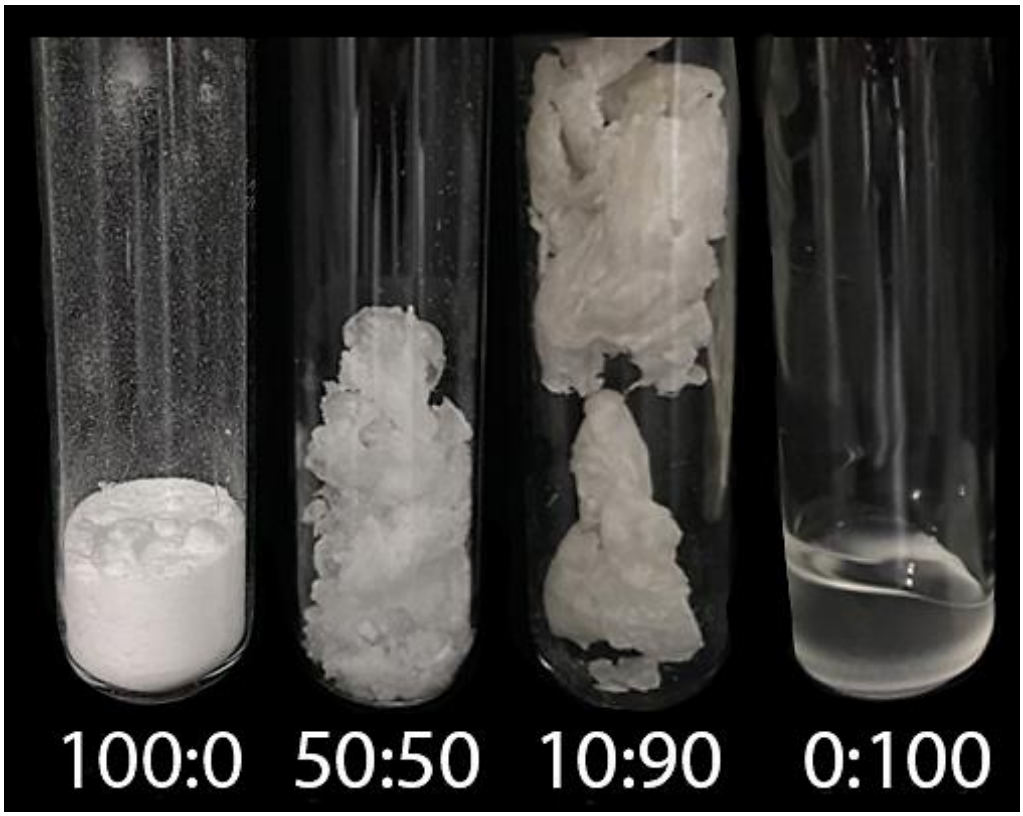

Figure 3.4 Image of iPMP (left), bulk PMP blends runs **3.5** and **3.9** (middle) and aPMP (right). The iPMP and aPMP represented in this image come from experiments made in the previous chapter, Chapter 2.

incorporation of **1** (10:90) and yet in a dramatic fashion differs from neat aPMP polymers. Specifically, the aPMP sample is a brittle plastic and was found to have the lowest elongation at break of 0.495% but the highest Young's modulus of 122 MPa. The profile shape of aPMP in Figure 3.4 indicated that the material undergoes only a small amount of elastic deformation before its breaking point. Alternatively, **run 3.9** is an elastomer as it has the largest capacity for flexible deformation with a Young's modulus of 0.704 MPa. Additionally, **run 3.9** has a maximum elongation of 346%,

Table 3.2. Dynamic mechanical analysis (DMA) results of selected PMP samples.

Run	Young's Modulus (MPa)[a]	Elongation at Break (%)[a]
aPMP	122	0.495
3.5	24.7	19.4
3.6	0.938	225
3.8	0.805	346[b]
3.9	0.704	346[b]

[a]TA analysis calculations. [b]Samples reached instrument limits. Run at 0.1N to 18N ramp at room temperature.

prior to breaking. As the incorporation of **1** is increased, the tensile strength decreases and the elongation at break decreases, except for **run 3.8**, where the maximum elongation before break of 346% was also reached. Also found was that the lowest elongation at break of 19.4% of these blends measured within **run 3.8**. The properties of **run 3.5** are the closest to that of pure aPMP. In Figure 3.5, it's not obvious just how brittle **run 3.5** is compared to **run 3.9** visually. However, DMA results quantitatively shows how drastically different the materials' physical properties change by simple incorporation of **1** into the polymerization. In Figure 3.6 images of sample **run 3.9** are taken to show the materials properties during the DMA instrumental

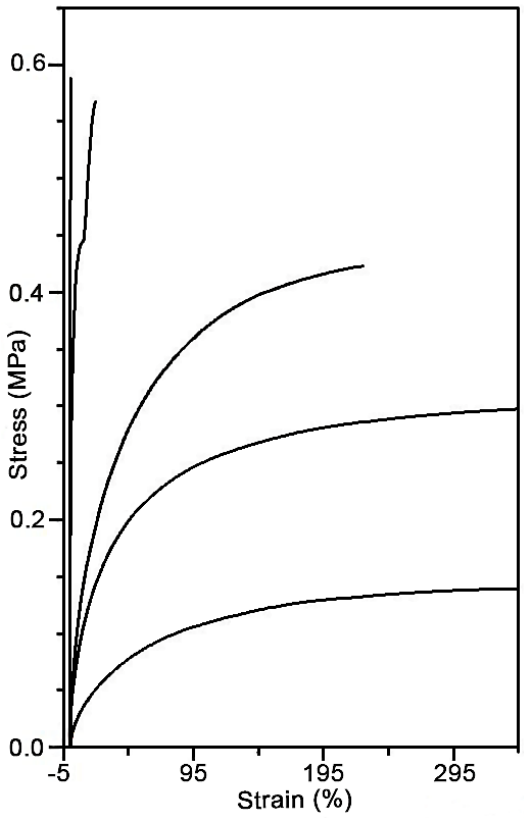

Figure 3.5 Stress-strain curves for aPMP (0:100), **3.5** (50:50), **3.6** (40:60), **3.8** (20:80), and runs **3.9** (10:90), (in order from top to bottom).

analysis testing. The leftmost image is the sample before the DMA experiment begins, the middle image is during the DMA run, and the rightmost image is near the end of the DMA testing. These images help comprehend how elastic a 10:90 blend of homopolymer PMP materials, made in the one-pot synthesis bulk material, even at very small dimensions of 1.3 mm thick, 8.18 mm long (within the grasp of the clamps of the DMA), and 5.32 mm wide.

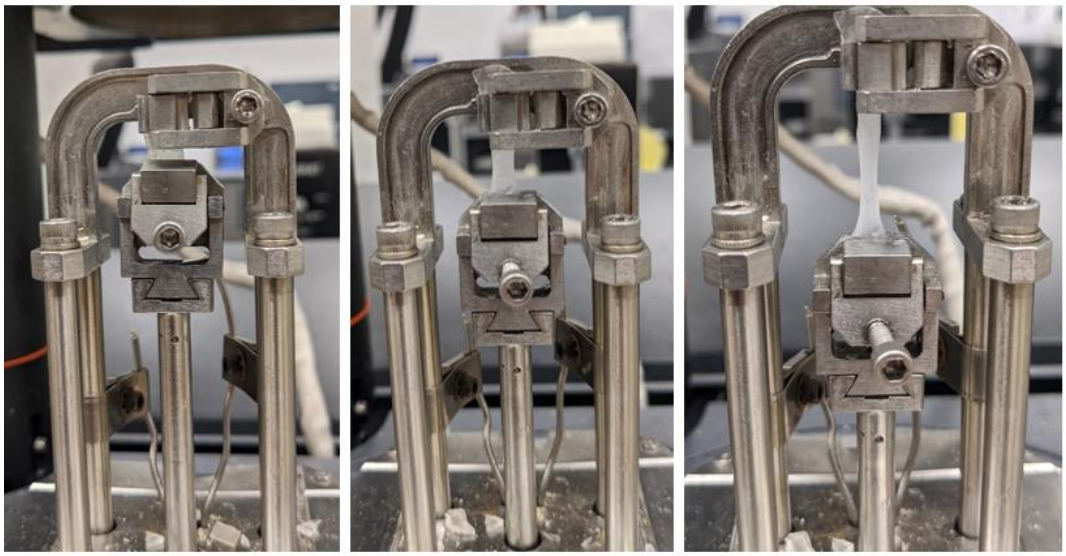

Figure 3.6 Images of DMA experiments with sample **run 3.9**. From left to right the *N* force applied increases and the elastic nature of the PMP homopolymer blended material is observed.

The original investigation was to synthesize and control stereoblocky PMP materials and originally this was believed to be the results. However, due to the concern that these materials could be blends of two homopolymer species, and the CTA did not in fact swap chains between pre-initiators of **1** and **2,** a control $^{13}C\{^{1}H\}$ NMR spectrum was gathered of a 50:50 mixture by mass of **aPMP** and **iPMP** homopolymers, Figure 3.7. This NMR did not clear up any confusion however, as its profile had extremely similar peak shapes to **run 3.6**. Regardless of this similarity, it is still evident that the presence of distinct regions of atactic and isotactic PMP occur in this NMR. This is what led to the investigation in separating out possible homopolymers within the bulk materials collected at the end of the synthesis. There were many characterization factors that continues to unknowingly indicate that these were stereoblocky materials not just blends of two separate homopolymers. First, the GPC trace of **run 3.5** maintains a monomial distribution with low dispersity. It was hypothesized that if the

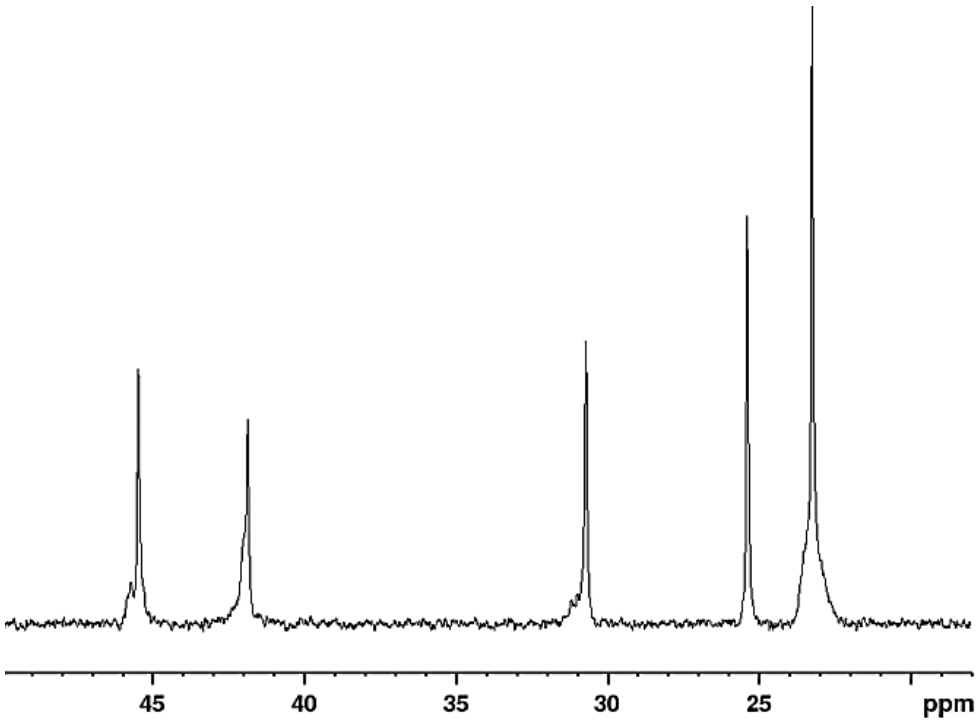

Figure 3.7 $^{13}C\{^{1}H\}$ NMR spectra (200 MHz, TCE-d_2, 110 °C) for a 1:1 by weight blend of iPMP and aPMP.

rate of propagation from **1** and **2** are different, the atactic and isotactic homopolymers would have different molar masses, leading to a bimodal GPC trace with a larger dispersity. Second, iPMP polymer blended with aPMP polymer would not create the same bulk material properties seen in Figure 3.4. This is mainly due to the insolubility of iPMP and this blended material made through synthetic means may be the only way to homogeneously blend the two distinctly separate end's of the spectrum, aPMP and iPMP. Third, one would have to assume that the CTA is either inactive in this system or each time it chain-transfers it must transfer back to the same exact pre-initiator thus keeping a homopolymer of the same microstructure throughout. The probability of this phenomenon occurring is seemed originally low. All three off these arguments and experimental evidence supports the synthesis of blocky-like polymers of the PMP with both isotactic and atactic microstructure incorporated throughout the bulk polymer

rather than a blend of two distinctly different homopolymers. However, what was observed and discovered was that in fact two distinct homopolymers were being synthesized together in the one-pot system and the bulk materials of such blends had distinct properties never before seen or understood within PMP materials. Mechanism, kinetics, and investigations into why the CTA stays matched to the same pre-intiator throguhout the polymerization is currently underway.

3.4 Conclusions

Overall, PMP copolymers with distinct regions of atactic and isotactic microstructures were not synthesized by using a two-catalyst system in the presence of a chain transfer agent but instead blends of homopolymers were made. These two pre-initiators, **1** and **2**, impose different degrees of stereocontrol on the inserting 4M1P monomer unit, leading to segments homopolymers of either atactic or isotactic nature. The amount of each homopolymer present in the bulk material can be easily controlled through the ratio of catalysts during polymerization. The ratio of such homopolymer content has a drastic impact on the physical properties of the material, leading to elastomers, even when brittle iPMP and aPMP units exist within the same blended material. This study has successfully applied the 'toolbox' of techniques and knowledge gained from the previous study, chapter 2, to discover a new way of making PMP materials through blends. For the future, it is of interest to create stereoblocky PMP materials and better understand the mechanism at which the current synthesis is undergoing.

3.5 Supporting Experimental Information

3.5.1 Synthetic Procedures

All manipulations of air and moisture sensitive compounds were carried out under N_2 atmospheres with standard Schlenk line or glovebox techniques. Toluene (ReagentPlus, 99%) was dried and deoxygenated by passage over activated alumina and GetterMax® 135 catalyst (purchased from Research Catalysts, Inc.) and collected prior to use. Chlorobenzene (Acros Organic, 99%) was dried over calcium hydride by refluxing at 130 ^oC for three days and distilled under N_2 prior to use. 1, 1, 2, 2-Tetrachloroethane(C_2Cl_4)-*d2* was purchased from Cambridge Isotopes and used as received. Chloroform-d_1 was purchased from Cambridge Isotopes and used as received. 4-methyl-1-pentene (>97%) were purchased from TCI Chemicals, dried over Na/K alloy and isolated by vacuum-transfer prior to use. Diethylzinc (>52wt.% Zn) was purchased from Sigma-Aldrich and used as received. All other solvents and reagents were used as received unless otherwise.

General procedure for living coordinative chain transfer polymerization (LCCTP) of atactic poly(4-methyl-1-pentene) (aPMP) via Zirconium (Ia in SI and 1 in text) and Hafnium Catalyst (Ib in SI and 2 in text) with changing ratios.

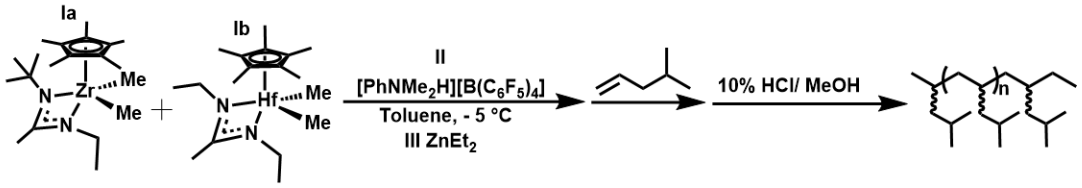

In a round bottom flask, 15 mL of toluene was cooled to 0 °C. The 4M1P monomer (23.8 mmol, 2.0 g) was added to the flask. Then chain transfer agent **III** (0.2 mmol, 24.7 mg), was added to the flask. Then a solution of **Ia** and **1b** , with 0 °C 1.0 mL PhCl

was vigorously activated with **II** (0.044 mmol, 35.2 mg) and added to the flask. The flask was stirred for typically 24 hr at 0 °C and quenched with 10 % HCl/ methanol. An aliquot of the material was also quenched with I2 for NMR quantitation of molecular weight. The material was then precipitated in MeOH for a minimum of 1 hr, then vacuum filtered and washed with MeOH before being collected in a pre-weighed vial and dried under vacuum. Details on the ratios of Zr to Hf catalyst and other details of the polymer's characterization are provided in Table 3.1.

3.5.2 Characterization Parameters

Nuclear Magnetic Resonance (NMR) Spectroscopy of ^{1}H and $^{13}C\{1H\}$ nuclei was carried out with a Bruker DRX 600 with BBFO probe or Bruker AVIII-HD 800 spectrometer fitted with a cryo-QCI probe. Chloroform-*d1* was used as the solvent for polymer samples using LCCTP synthesis. 1,1,2,2-C_2Cl_4-*d2* was used as the solvent for polymer samples using LCP synthesis and heated to 110 °C. All spectra were referenced to tetramethyl silane using residual ^{1}H and $^{13}C\{^{1}H\}$ chemical shifts of the deuterated solvents.

Gel Permeation Chromatography (GPC) was used to obtain molecular weight (Mn and Mw) and polydispersity index (PDI) of polymers using Viscotek GPCMax equipped with three columns (Styragel HR 4, HR 3, and HR 1) in a column oven and differential refractometer (Viscotek TDA 302) maintained at 40 °C. Tetrahydrofuran (HPLC Grade) was used as the eluent with a flow rate of 1 mL/min. Polystyrene standards (from Agilent Technologies, 370 Da – 128.7 kDa) were used for calibration. For GPC sample preparation, 2 mg of dry polymer sample was dissolved in 1 mL of THF (HPLC Grade).

3.5.3 Supporting Results

A.

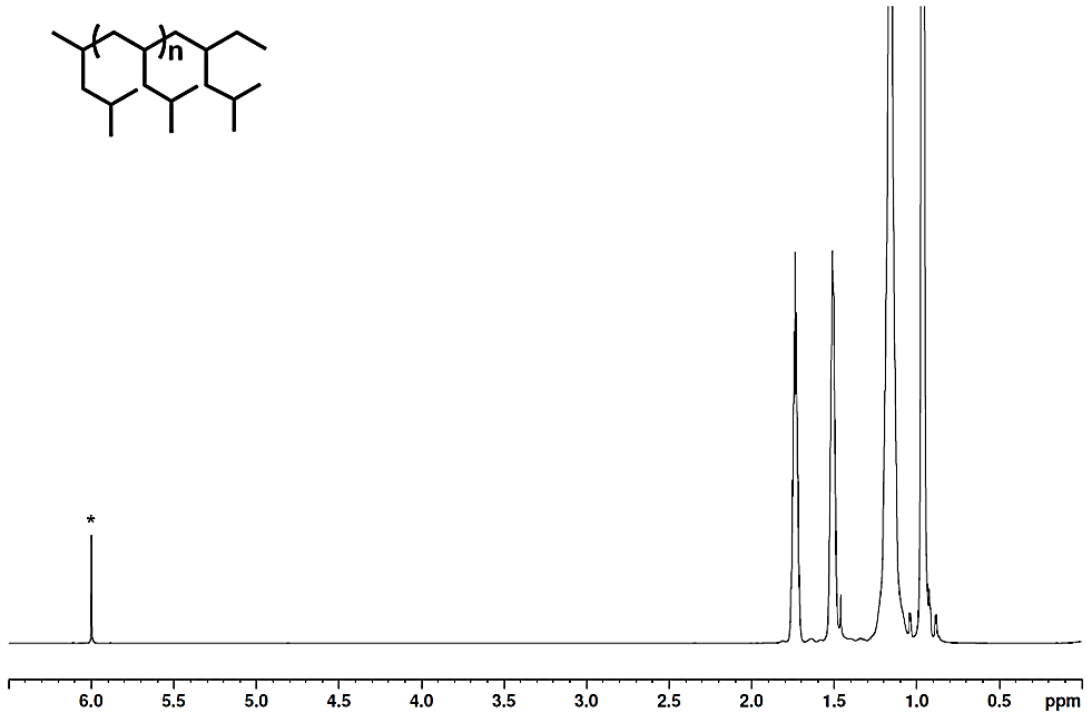

B.

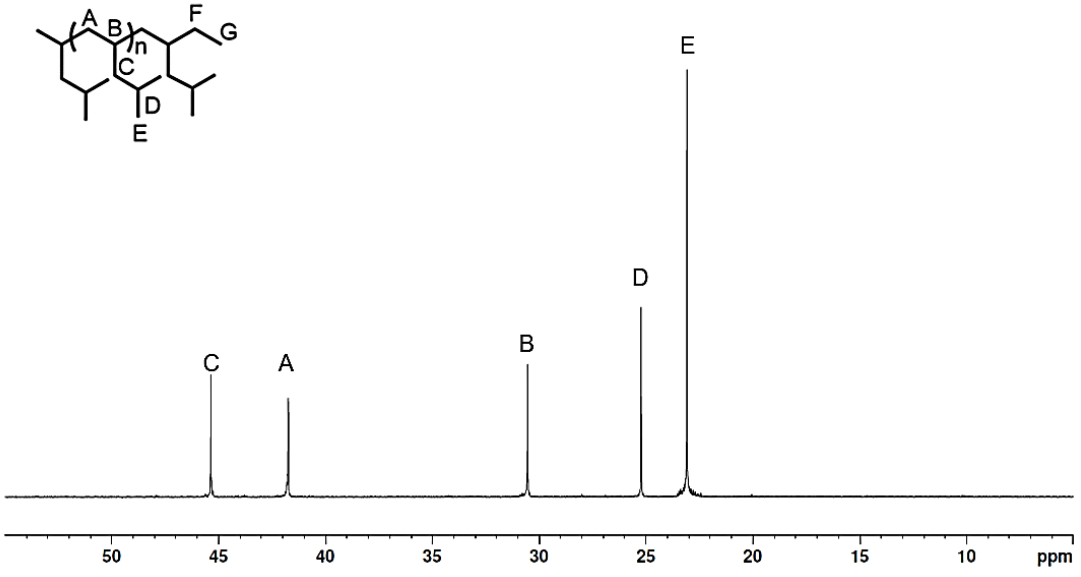

Figure S3.1. (A) ^{1}H NMR (800 MHz, *1,1,2,2-C_2Cl_4-*d2,* 110 °C after 1 hr of temperature equilibration) of **run 3.1**, (B) partial ^{13}C-NMR (200 MHz, *1,1,2,2-C_2Cl_4-*d2*) of **run 3.1** (90:10).

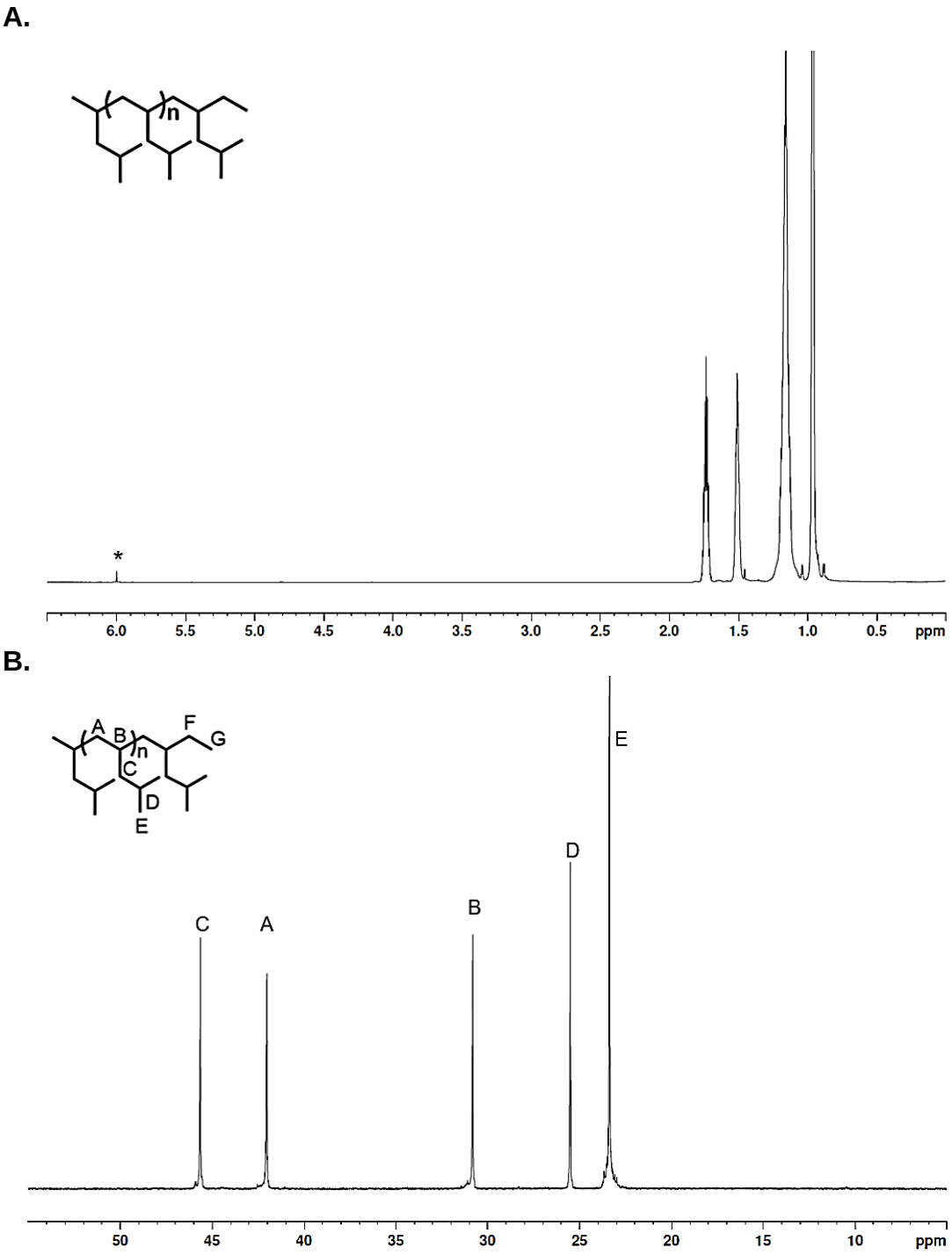

Figure S3.2. (A) ^{1}H NMR (800 MHz, *1,1,2,2-C_2Cl_4-*d2,* 110 °C after 1 hr of temperature equilibration) of **run 3.2**, (B) partial ^{13}C-NMR (200 MHz, *1,1,2,2-C_2Cl_4-*d2*) of **run 3.2** (80:20).

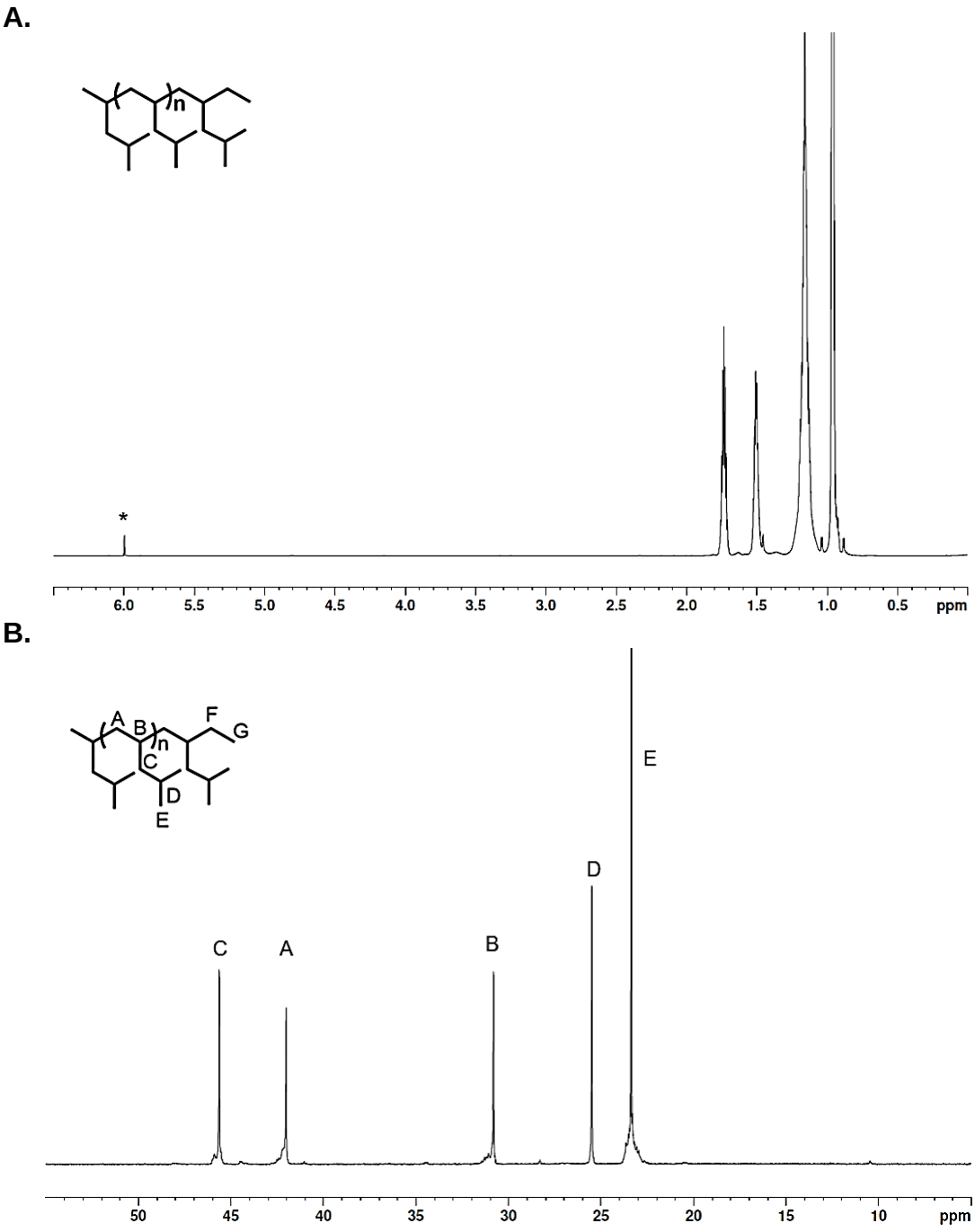

Figure S3.3. (A) ^{1}H NMR (800 MHz, *1,1,2,2-C_2Cl_4-*d2,* 110 °C after 1 hr of temperature equilibration) of **run 3.3**, (B) partial ^{13}C-NMR (200 MHz, *1,1,2,2-C_2Cl_4-*d2*) of **run 3.3** (70:30).

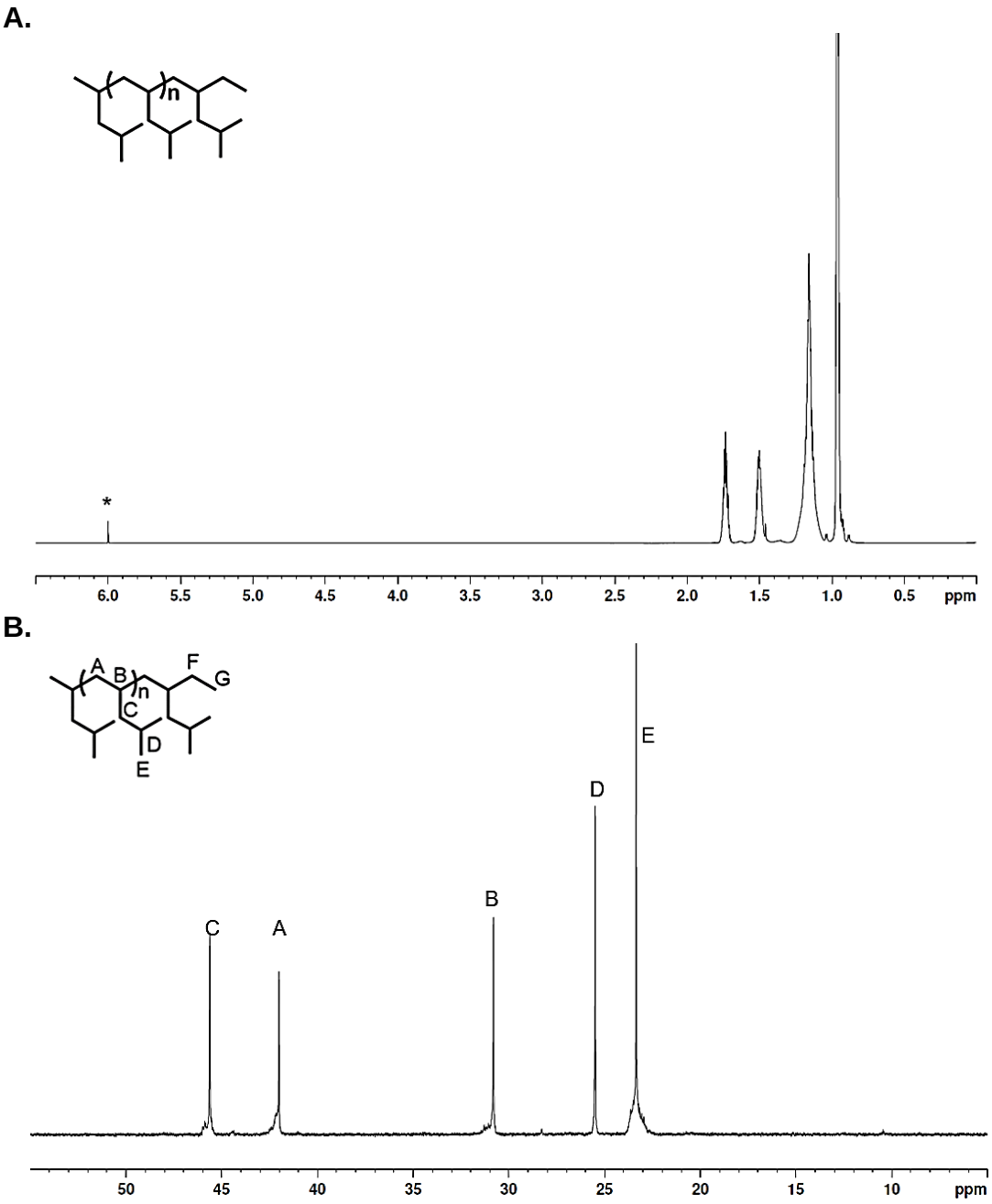

Figure S3.4. (A) ^{1}H NMR (800 MHz, *1,1,2,2-C_2Cl_4-*d2,* 110 °C after 1 hr of temperature equilibration) of **run 3.4**, (B) partial ^{13}C-NMR (200 MHz, *1,1,2,2-C_2Cl_4-*d2*) of **run 3.4** (60:40)**.**

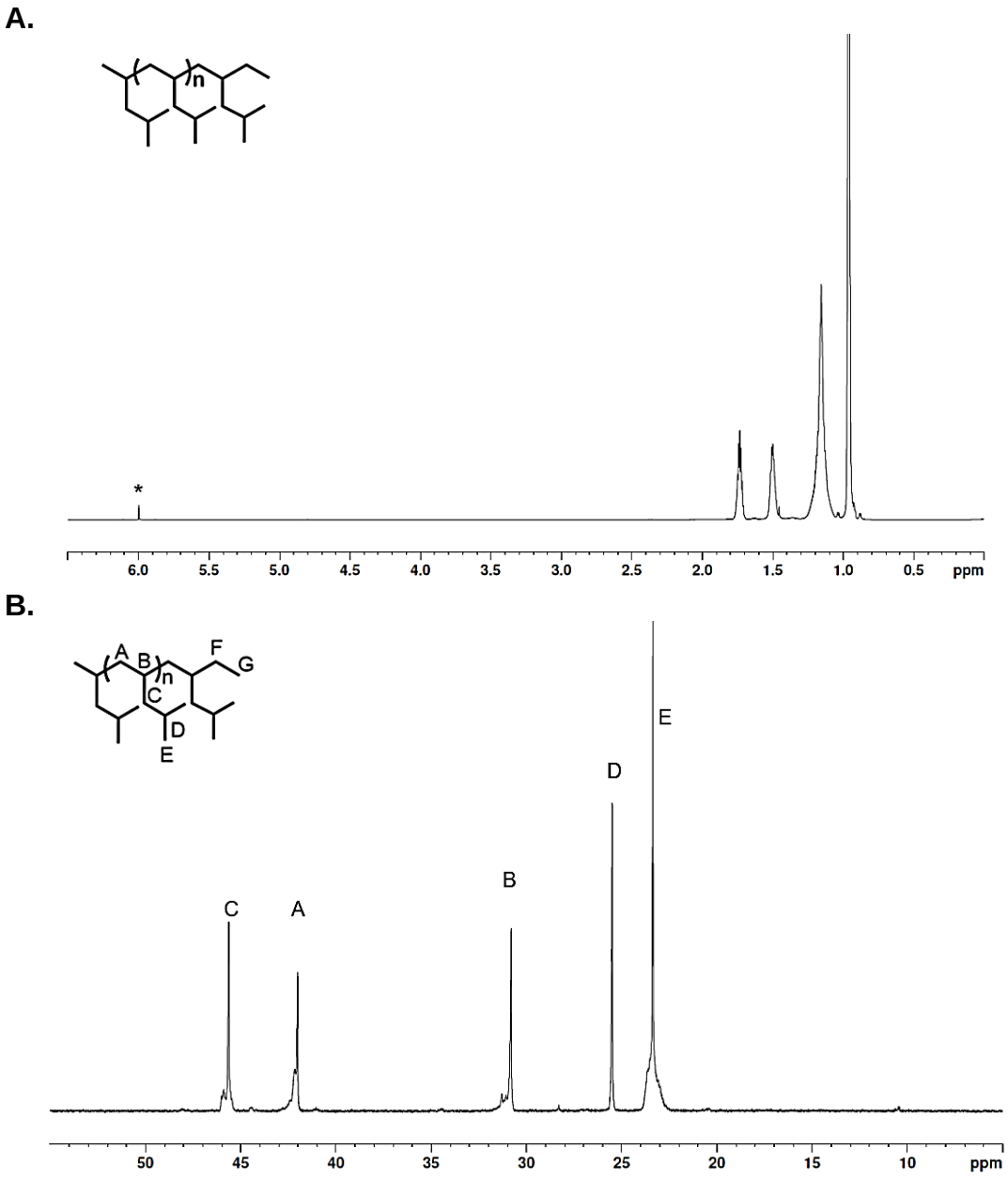

Figure S3.5. (A) ^{1}H NMR (800 MHz, *1,1,2,2-C_2Cl_4-*d2,* 110 °C after 1 hr of temperature equilibration) of **run 3.5**, (B) partial ^{13}C-NMR (200 MHz, *1,1,2,2-C_2Cl_4-*d2*) of **run 3.5** (50:50)**.**

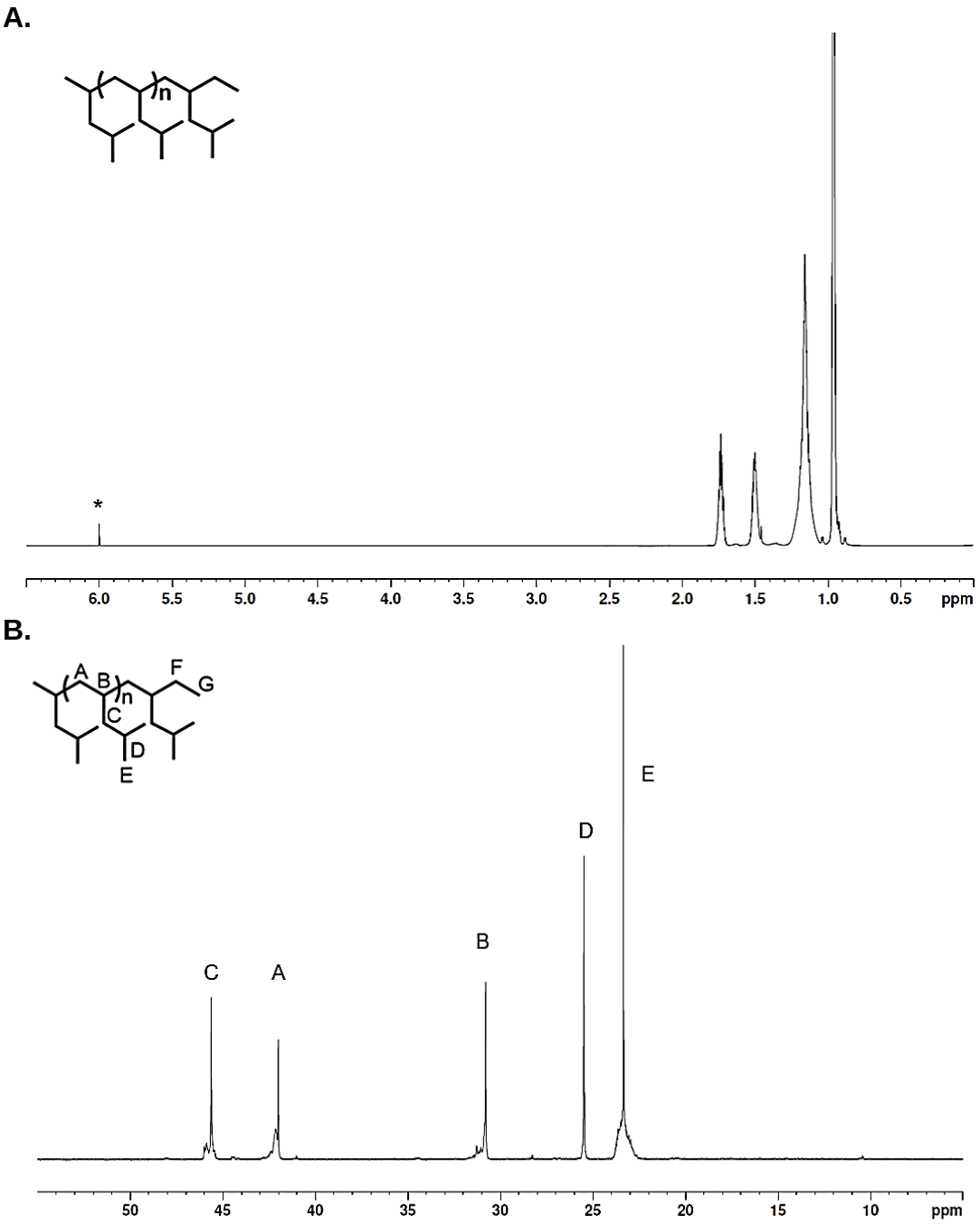

Figure S3.6. (A) ^{1}H NMR (800 MHz, *1,1,2,2-C_2Cl_4-*d2,* 110 °C after 1 hr of temperature equilibration) of **run 3.6**, (B) partial ^{13}C-NMR (200 MHz, *1,1,2,2-C_2Cl_4-*d2*) of **run 3.6** (40:60)**.**

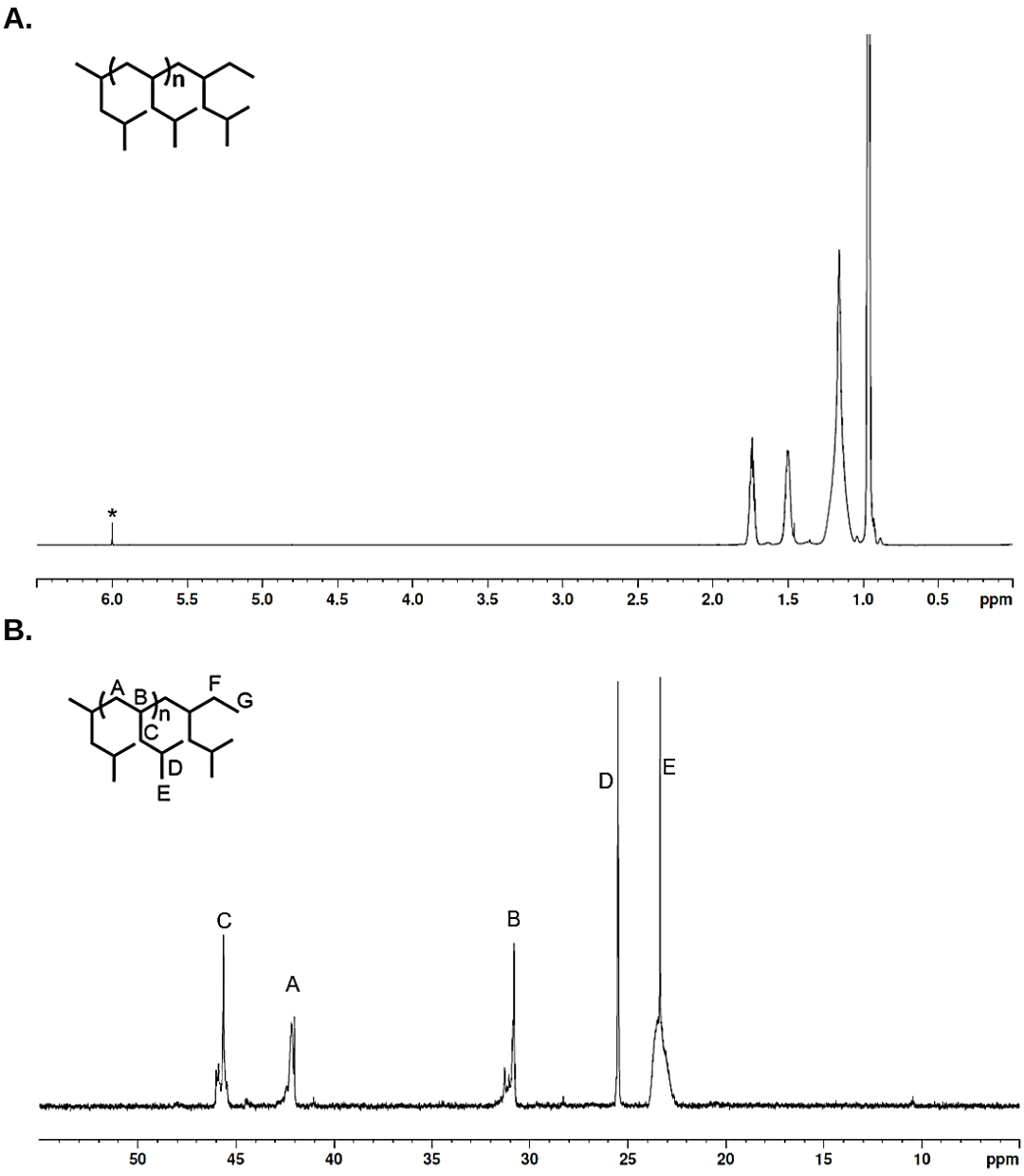

Figure S3.7. (A) ^{1}H NMR (800 MHz, *1,1,2,2-C_2Cl_4-*d2,* 110 °C after 1 hr of temperature equilibration) of **run 3.7** (B) partial ^{13}C-NMR (200 MHz, *1,1,2,2-C_2Cl_4-*d2*) of **run 3.7** (30:70)**.**

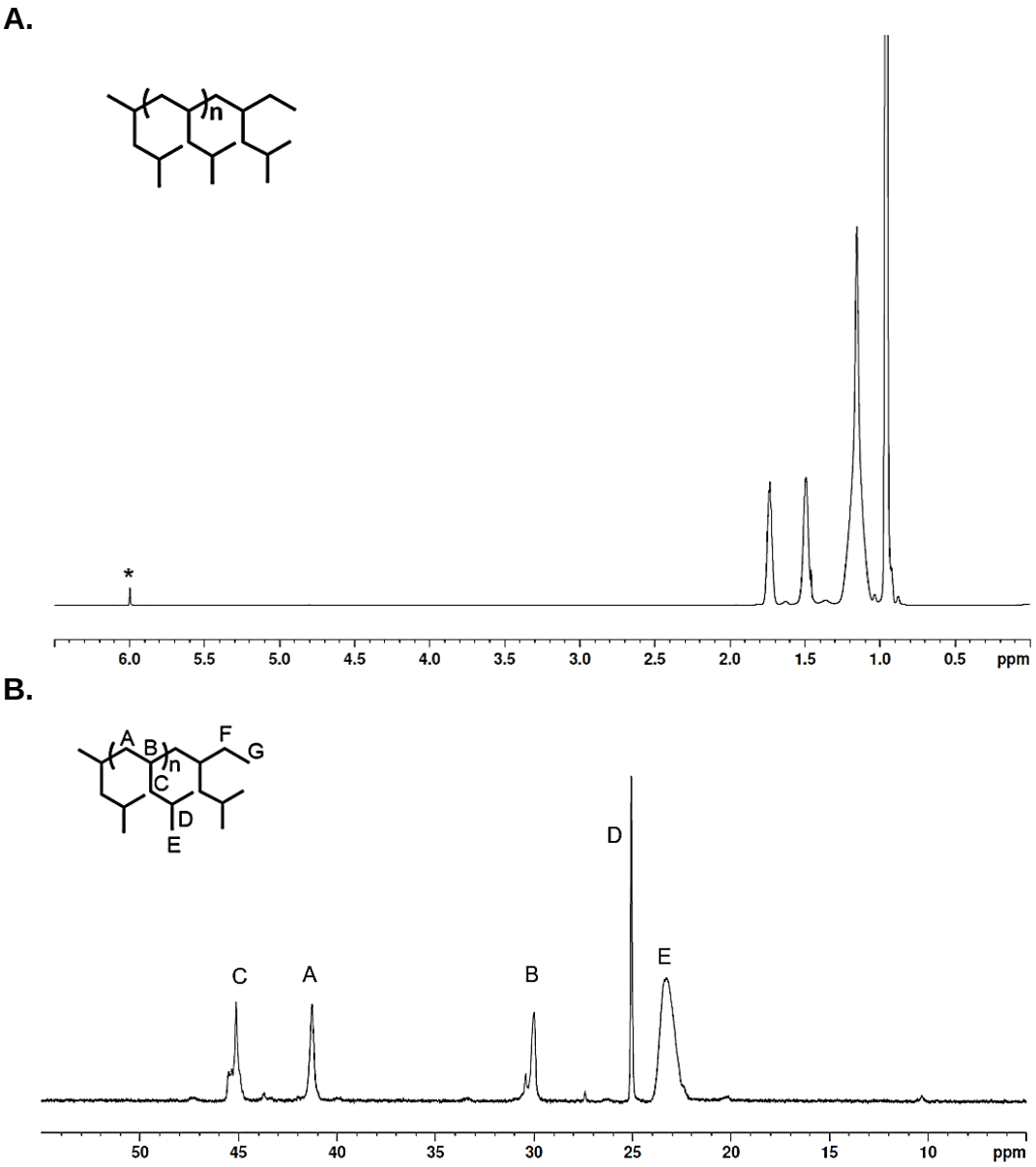

Figure S3.8. (A) ^{1}H NMR (800 MHz, *1,1,2,2-C_2Cl_4-*d2,* 110 °C after 1 hr of temperature equilibration) of **run 3.8**, (B) partial ^{13}C-NMR (200 MHz, *1,1,2,2-C_2Cl_4-*d2*) of **run 3.8** (20:80)**.**

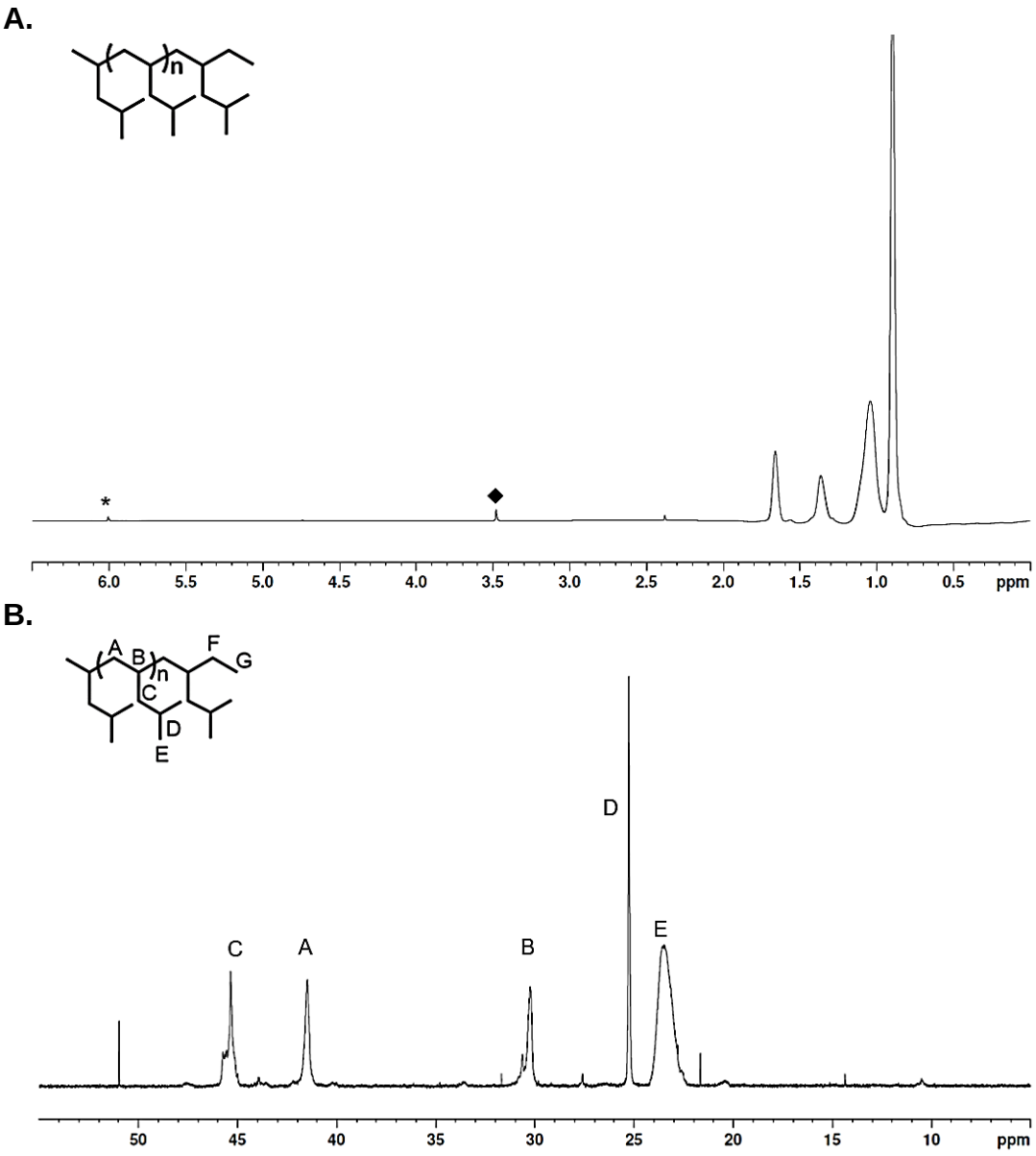

Figure S3.9. (A) ^{1}H NMR (800 MHz, ◆ methanol, *1,1,2,2-C_2Cl_4-*d2,* 110 °C after 1 hr of temperature equilibration) of **run 3.9**, (B) partial ^{13}C-NMR (200 MHz, *1,1,2,2-C_2Cl_4-*d2*) of **run 3.9** (10:90)**.**

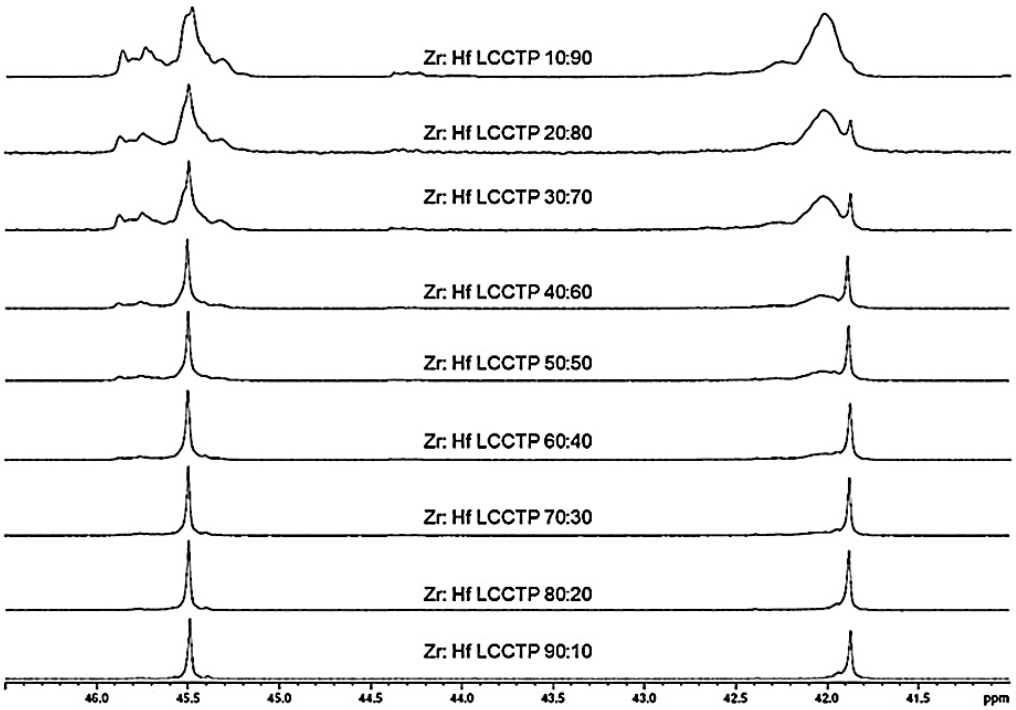

Figure S3.10. Partial ^{13}C-NMR (200 MHz, *1,1,2,2-C_2Cl_4-*d2*) of **run 3.1 - 3.9.**

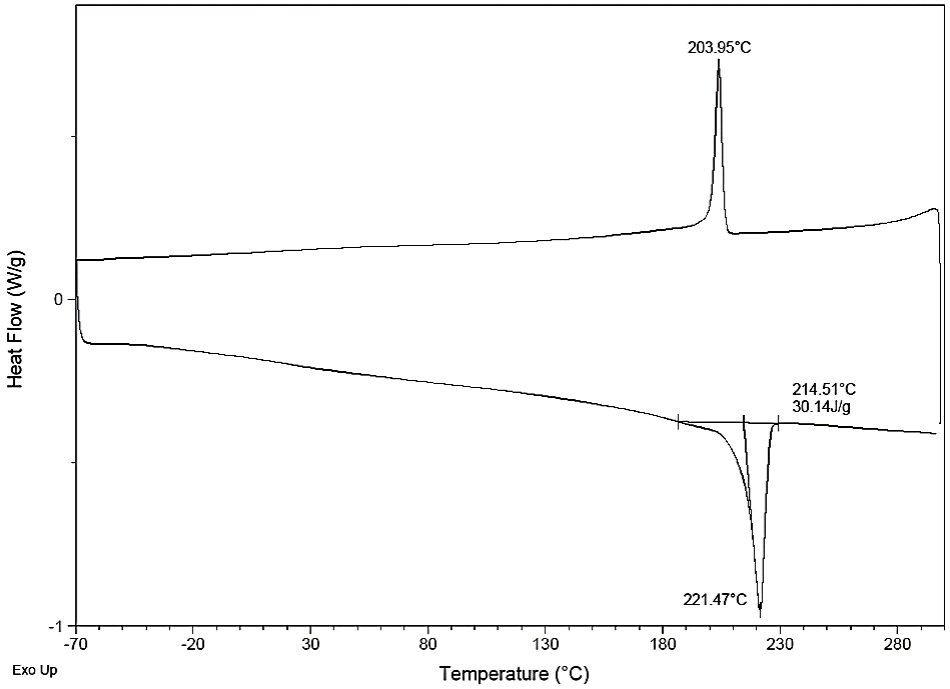

Figure S3.11. DSC trace of a heat/cool/heat cycle, cycle 1 removed, with a ramp rate of 10 °C/min from -70 – 300 °C of **run 3.1** (90:10).

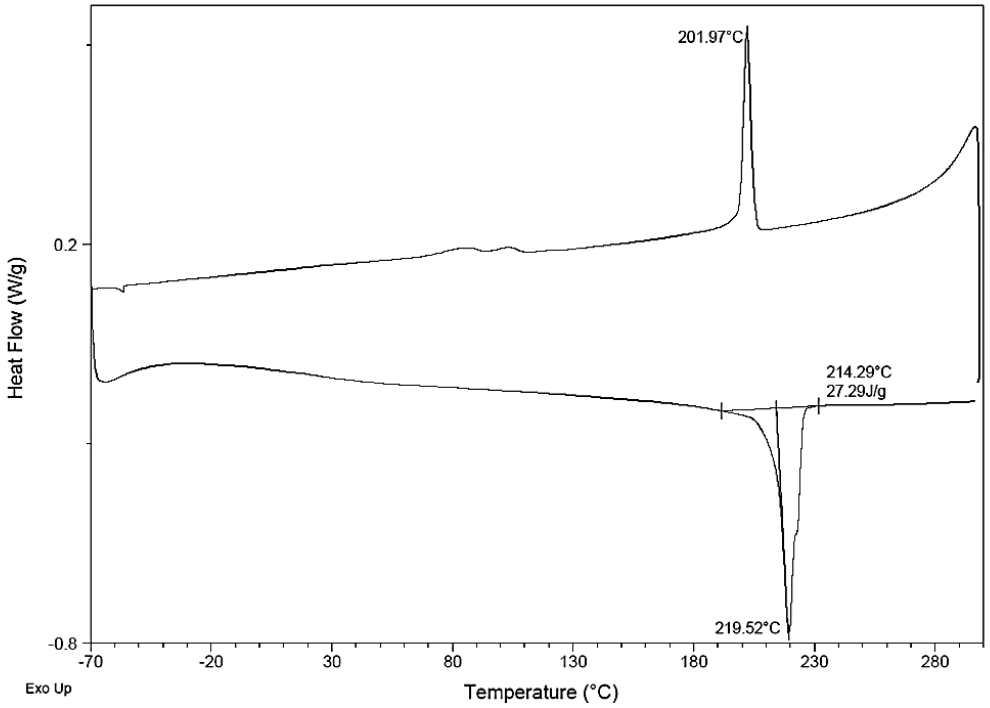

Figure S3.12. DSC trace of a heat/cool/heat cycle, cycle 1 removed, with a ramp rate of 10 °C/min from -70 – 300 °C of **run 3.2** (80:20).

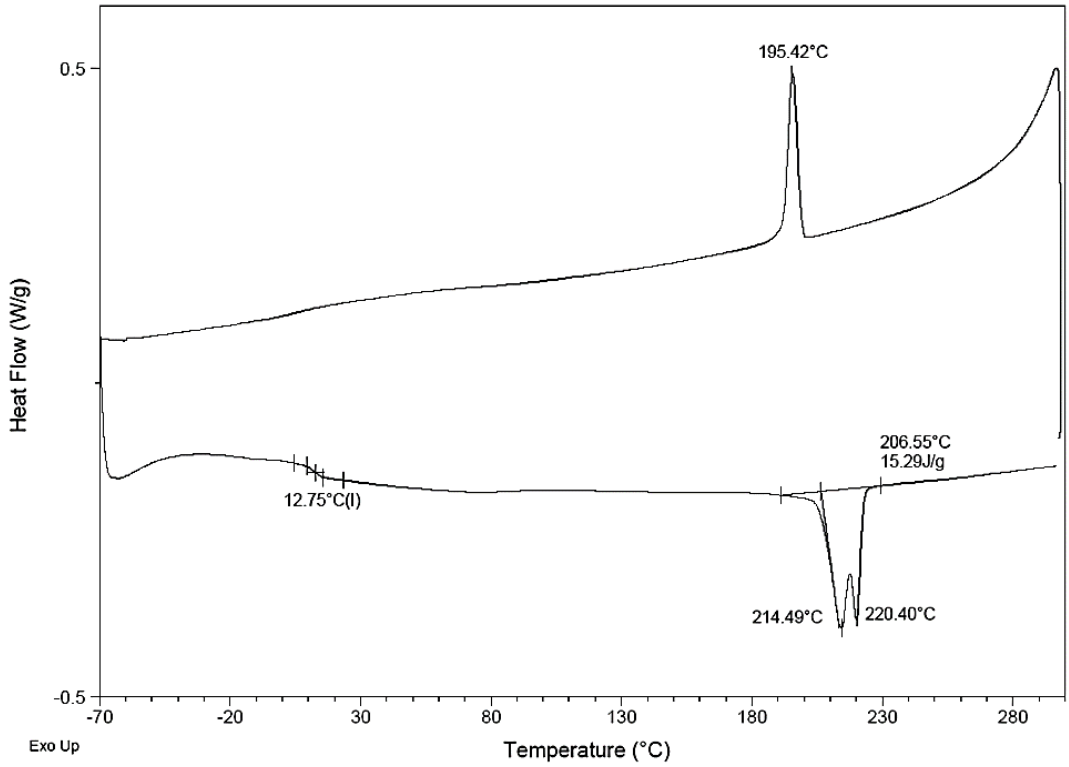

Figure S3.13. DSC trace of a heat/cool/heat cycle, cycle 1 removed, with a ramp rate of 10 °C/min from -70 – 300 °C of **run 3.4** (60:40).

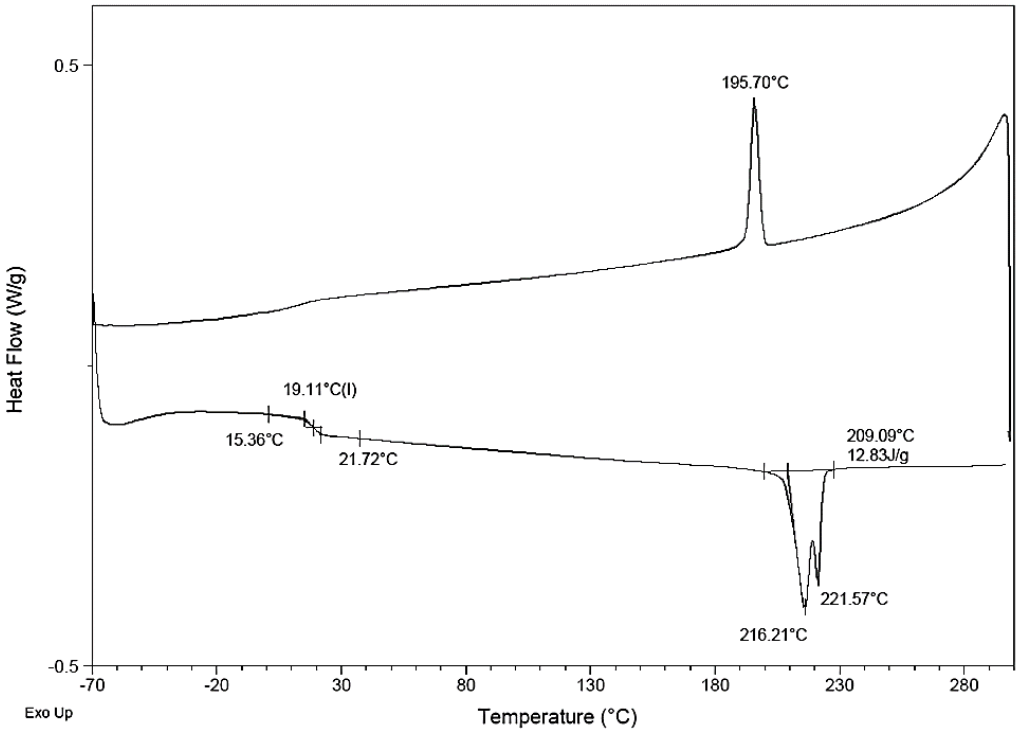

Figure S3.14. DSC trace of a heat/cool/heat cycle, cycle 1 removed, with a ramp rate of 10 °C/min from -70 – 300 °C of **run 3.5** (50:50).

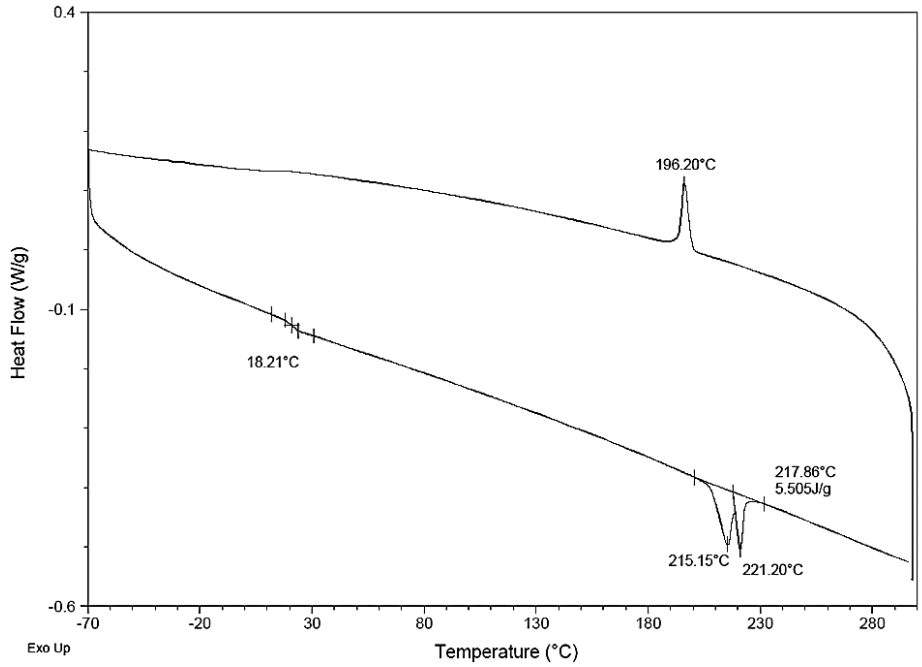

Figure S3.15. DSC trace of a heat/cool/heat cycle, cycle 1 removed, with a ramp rate of 10 °C/min from -70 – 300 °C of **run 3.6** (40:60).

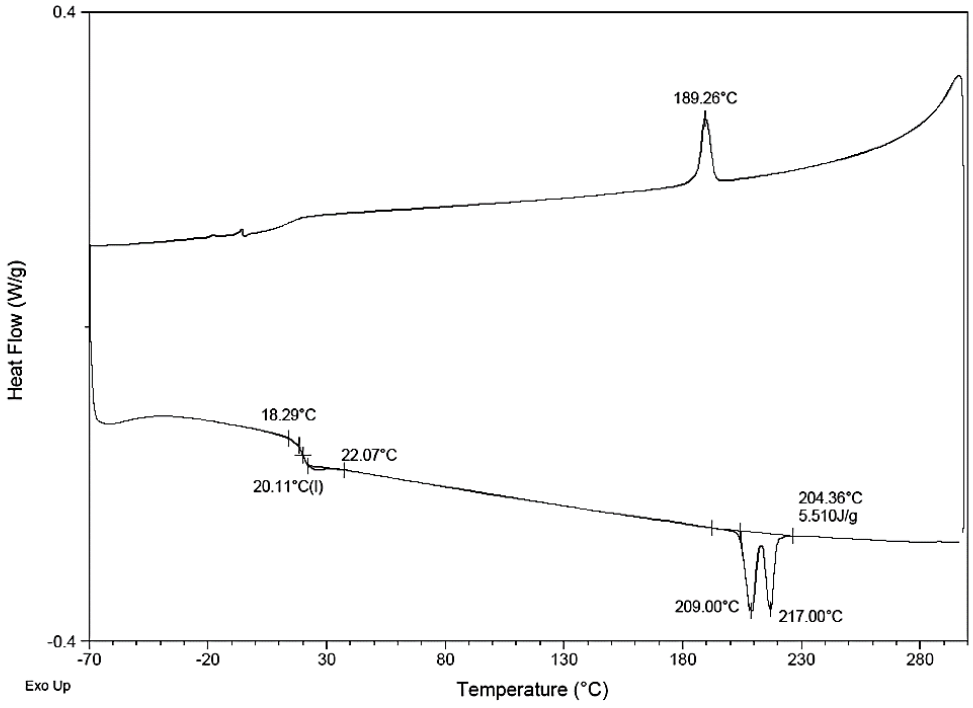

Figure S3.16. DSC trace of a heat/cool/heat cycle, cycle 1 removed, with a ramp rate of 10 °C/min from -70 – 300 °C of **run 3.7** (30:70).

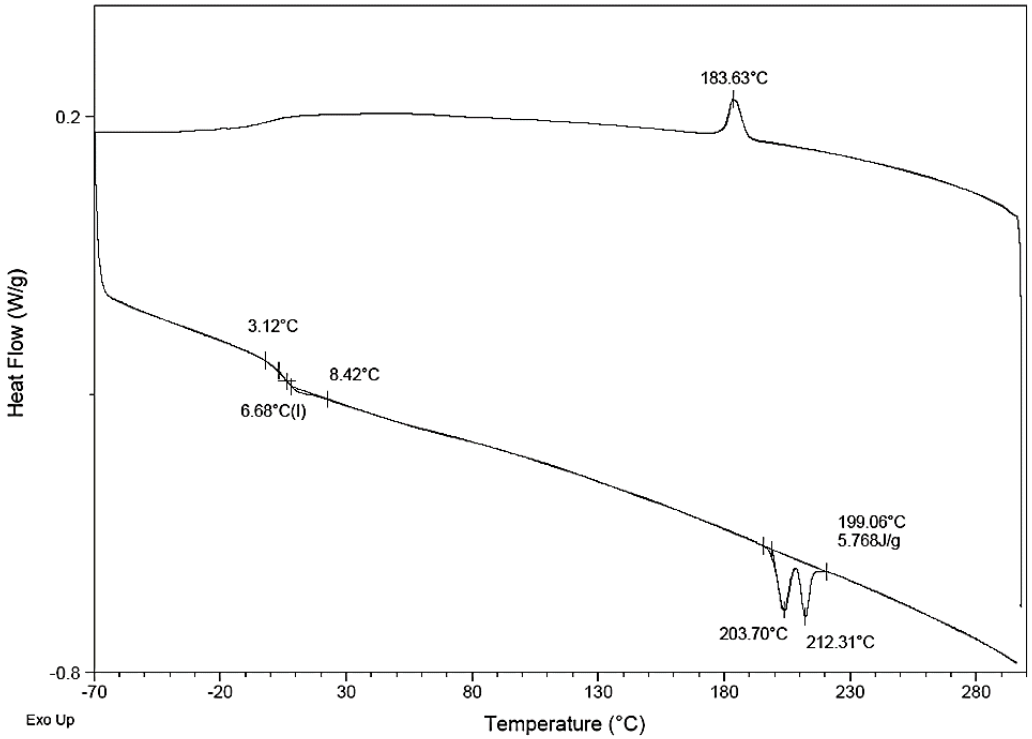

Figure S3.17. DSC trace of a heat/cool/heat cycle, cycle 1 removed, with a ramp rate of 10 °C/min from -70 – 300 °C of **run 3.8** (20:80).

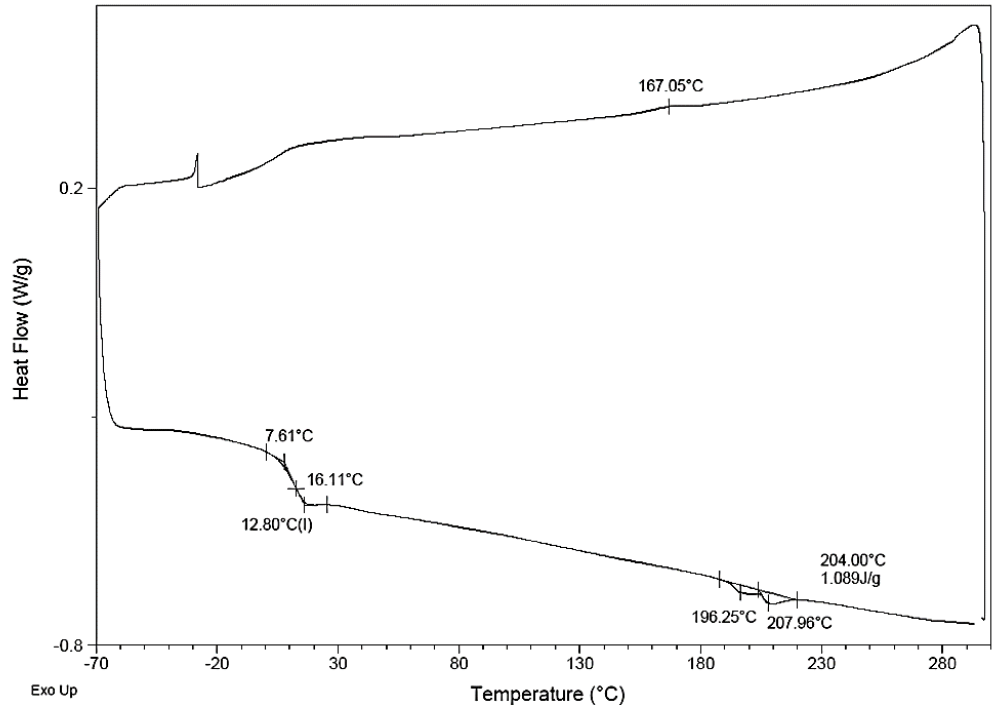

Figure S3.18. DSC trace of a heat/cool/heat cycle, cycle 1 removed, with a ramp rate of 10 °C/min from -70 – 300 °C of **run 3.9** (10:90).

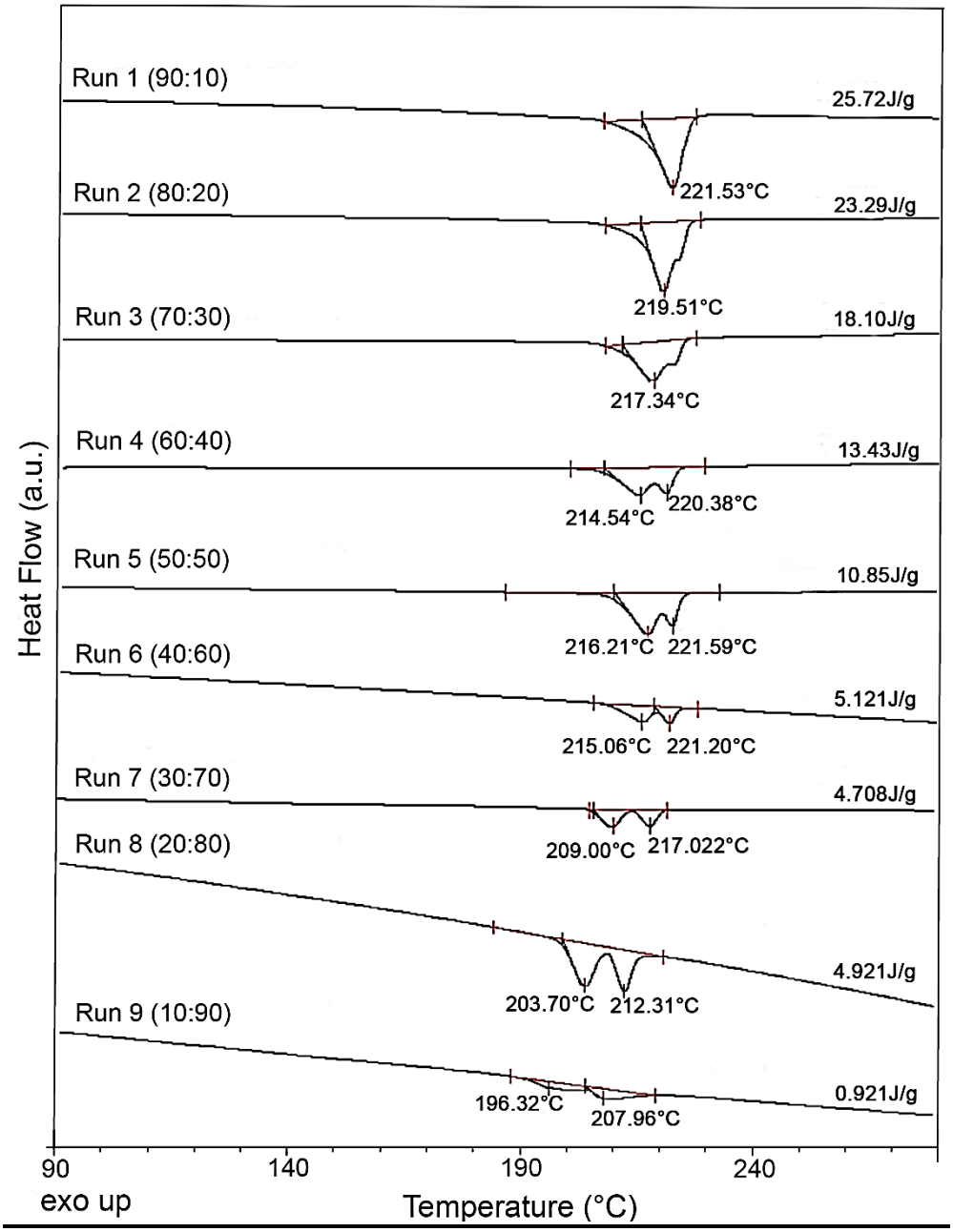

Figure S3.19. Partial DSC trace of a heat/cool/heat cycle, cycle 1 and 2 removed, with a ramp rate of 10 °C/min from -70 – 300 °C of **runs 3.1 – 3.9**.

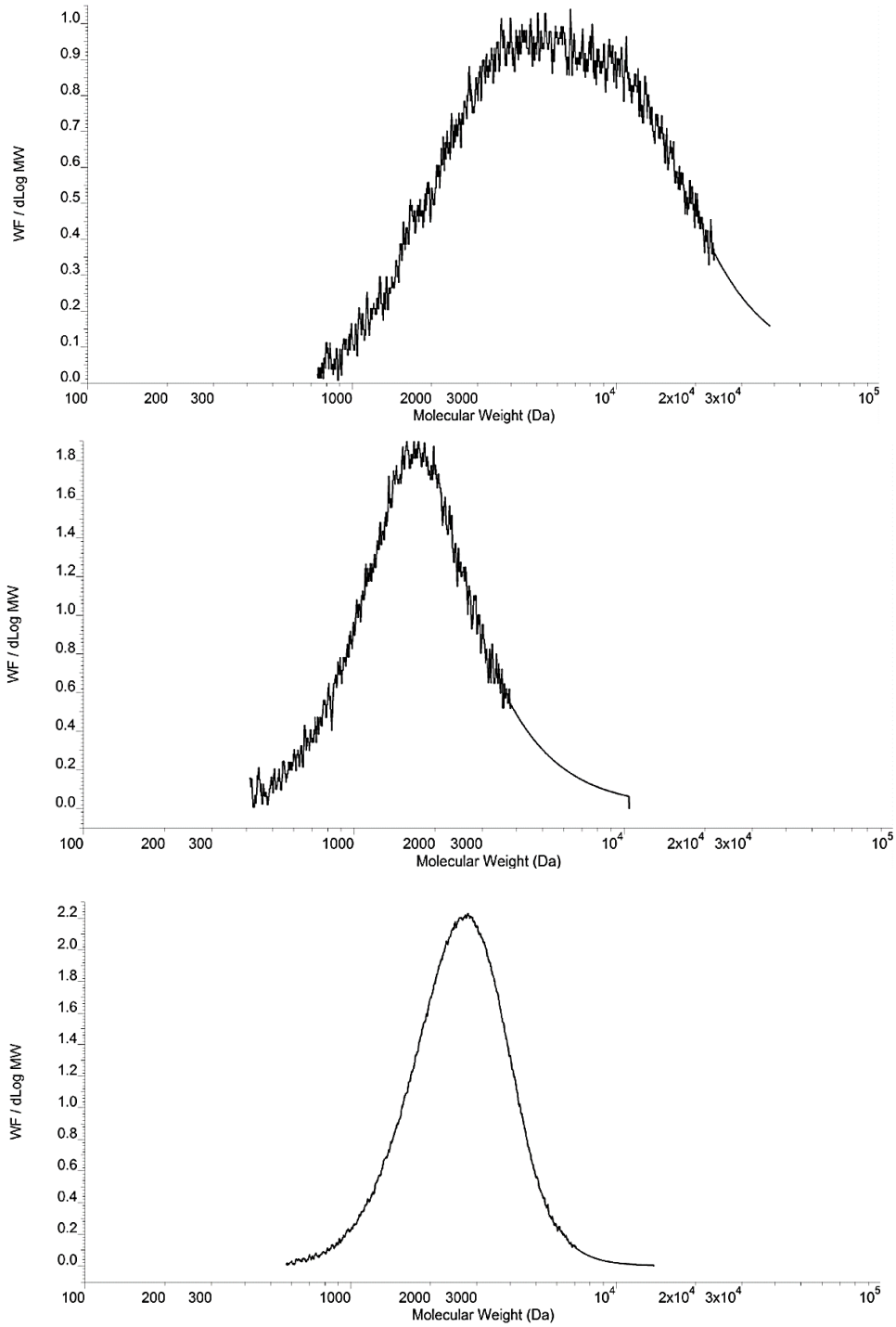

Figure S3.20. GPC trace of **run 3.1**, (due to high crystallinity and insolubility the peak is noisy (top). GPC trace of **run 3.2**, due to high crystallinity and insolubility peak is noisy (middle). GPC trace of **run 3.3** (bottom)**.**

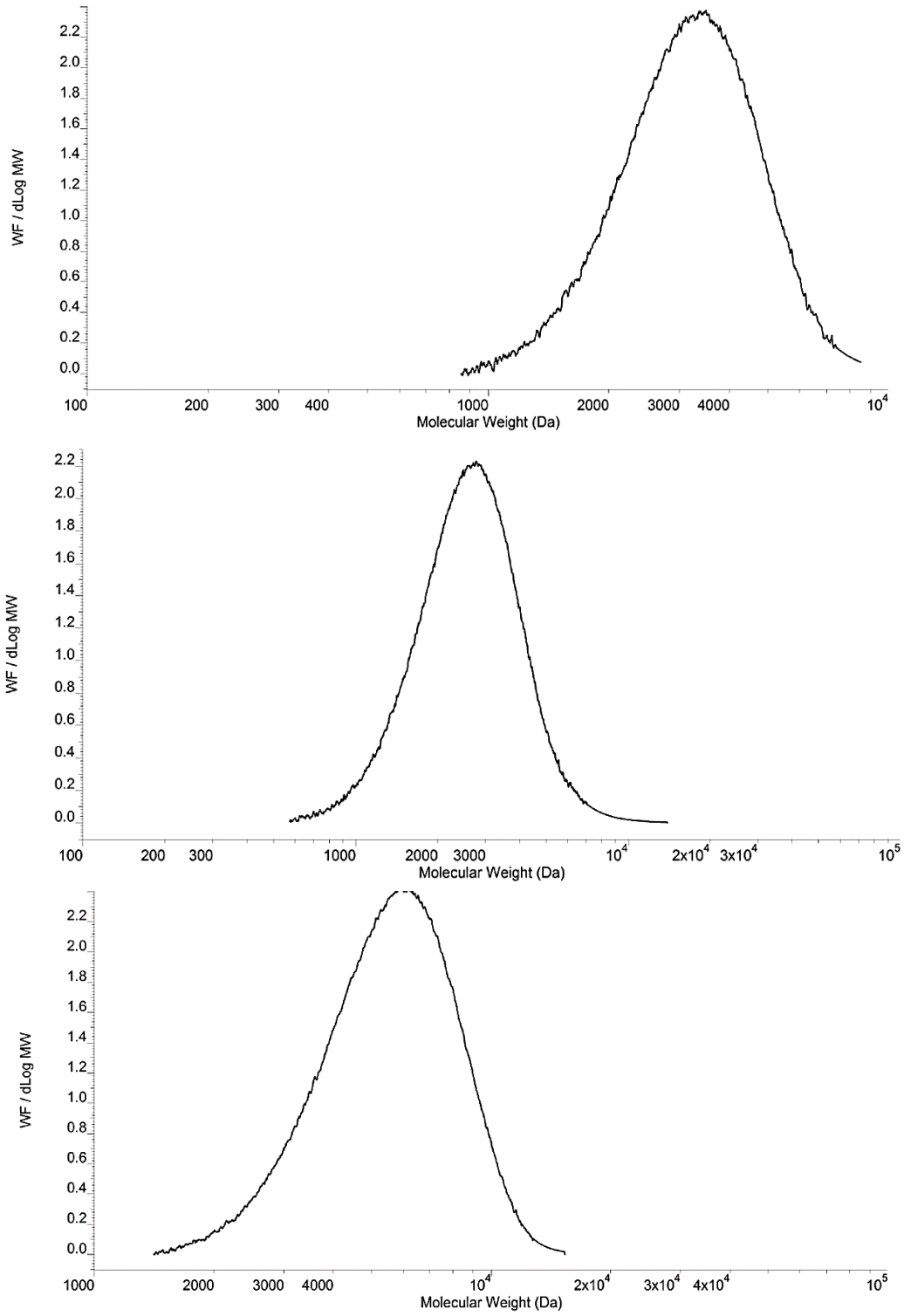

Figure S3.21. GPC trace of **run 3.4** (top). GPC trace of **run 3.5** (middle). GPC trace of **run 3.6** (bottom)**.**

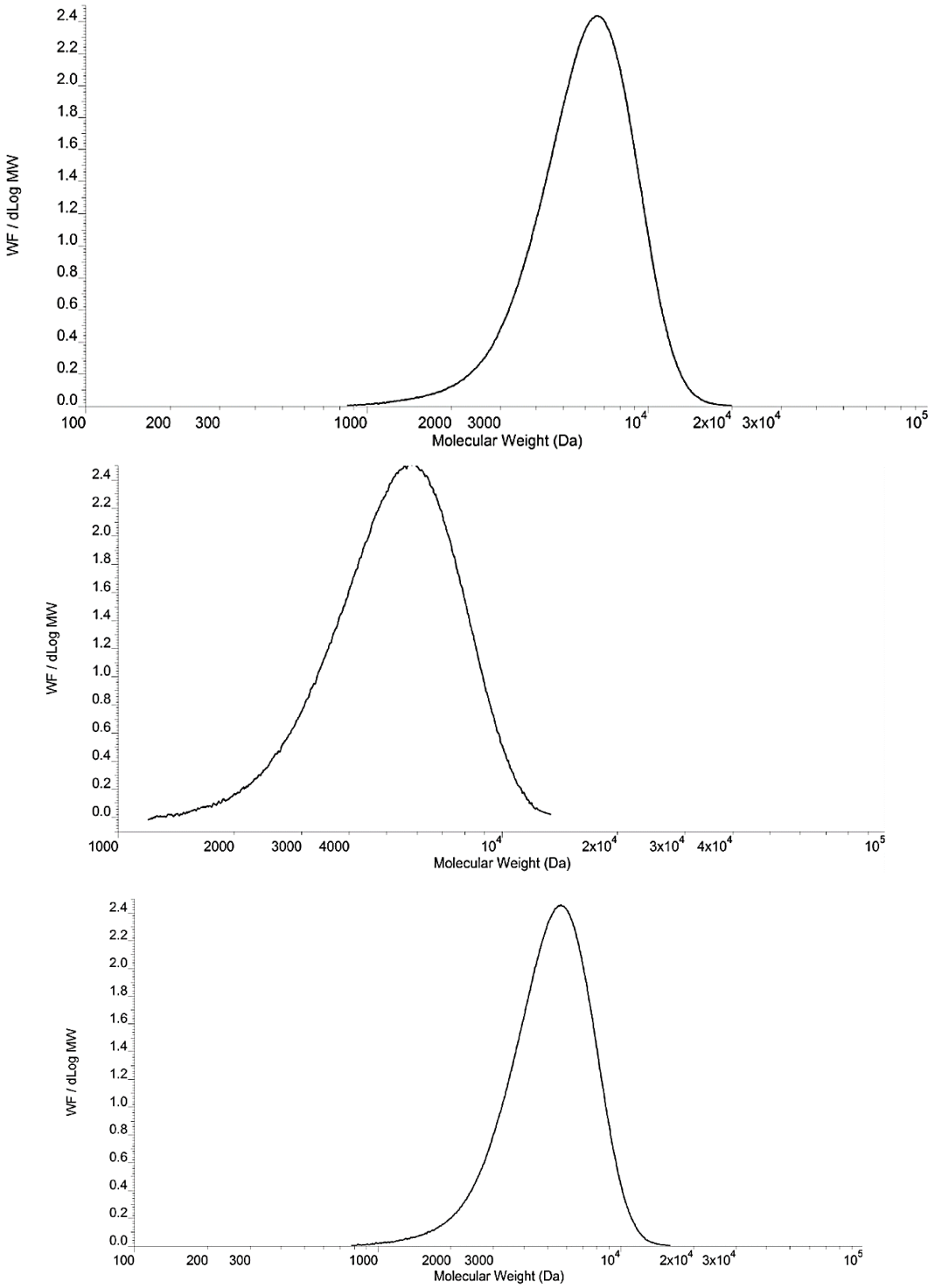

Figure S3.22. GPC trace of **run 3.7**(top). GPC trace of **run 3.8** (middle). GPC trace of **run 3.9** (bottom)**.**

Chapter 4: Design of Stereo- and Enantioselectivity in α,ω-Nonconjugated Dienes for New Building Blocks or Properties†

Wallace, M. A.; Wentz, C. M.; Sita, L. R. Optical Purity as a Programmable Variable for Controlling Polyolefin Tacticity in Living Coordinative Chain Transfer Polymerization: Application to the Stereomodulated LCCTP of α,ω-Nonconjugated Dienes. *ACS Catal*. **2020**, *11*, 4583-4592.

Author Contributions:
L. R. S. Lead conceptualization, funding, and writing.
M. A. W. Supported writing, reviewing, and editing. Synthesized and characterized all materials.
C. M. W. Supported writing, reviewing, and editing. Supported synthesis and characterization of polyolefin materials.

4.1 Background

As previously mentioned most commercially viable polymer materials used today come from α-olefins. There is a lot of room for discovery when it comes to usefulness and understanding behind stereoengineering α,ω-nonconjugated olefins. The design and implementation of new polymerization processes that can make polyolefins with unprecedented structures and properties from the limited pool of commercially available and viable olefin monomers is of substantial academic and

† The results, tables, figures, and schemes presented and discussed in this chapter have been used or adapted with permission from Wallace, M. A.; Wentz, C. M.; Sita, L. R. Optical Purity as a Programmable Variable for Controlling Polyolefin Tacticity in Living Coordinative Chain Transfer Polymerization: Application to the Stereomodulated LCCTP of α,ω-Nonconjugated Dienes. *ACS Catal*. **2020**, *11*, 4583-4592. Copyright © 2020, American Chemical Society.

industrial interest.[1-3] The main two monomer sources investigated within this chapter include 1,5-heptadiene which once polymerized creates poly(methylene-1,3-cyclopentane) PMCP, and 1,6-heptadiene which once polymerized produces poly(methylene-1,3-cyclohexane) PMCH. The processes utilized to yield these polymers are LCP and LCCTP with the change of an enantiopure catalyst to access new properties never explored with these systems.

When it comes to PMCP there has been extensive investigations into steric environments control on the stereoregularity of the polymer. Coates and Waymouth,[4,5] pioneered work involving optically active PMCP but this was done through a non-living polymerization that yielded PMCP materials of substantially large molecular weights and large dispersity's. Within the Sita group there has been previous investigation using LCCTP technique with 1,5-hexadiene by the C_2-symmetric Hf initiator to make a library of PMCP or PMCH materials with varied physical properties for the possibility of utilizing these polymers as building blocks or new polyolefin applications, but these materials were not probed for optical activity.[233] More recently, Mark A. Wallace synthesized a new Hf pre-initiator with the goal of enforcing optical activity onto the polymer chains through enantioselective control. Seen in Scheme 4.1, (S_c, S_{Hf})-**1** and (R_c, R_{Hf})-**1** were applied with $ZnEt_2$ to produce scalable cis/trans, isotactic PMCP materials comprised of optical active handiness.[6,7] These studies done allow for new building block materials to be utilized after I_2 quenching that can consequently open new applications and properties utilizing α,ω-nonconjugated dienes.

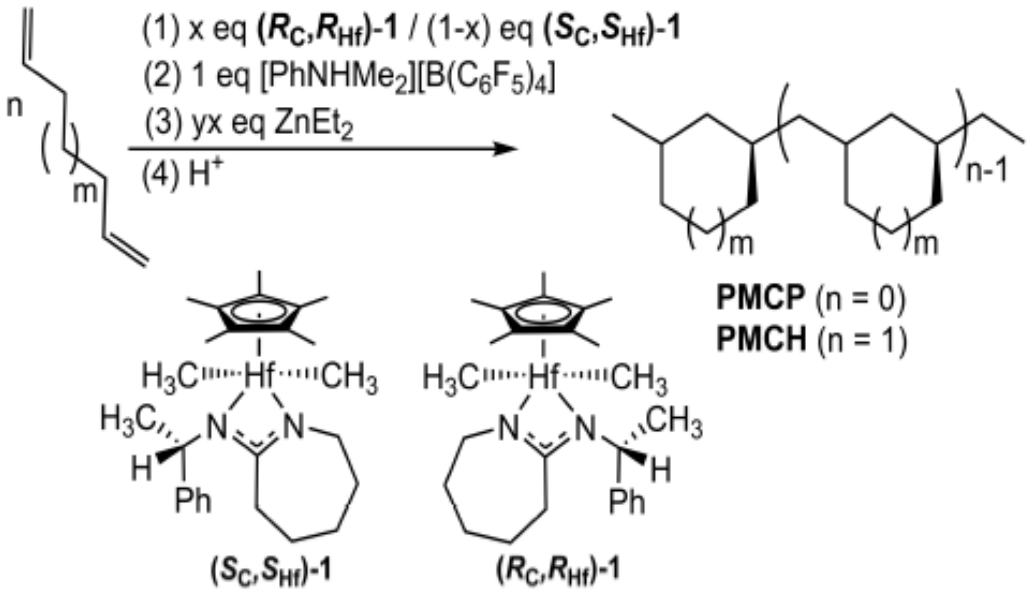

Scheme 4.1 Stereomodulated living coordinative chain transfer cyclopolymerization of 1,5-hexadiene and 1,6-heptadiene.†

In contrast to the expansive literature on PMCP samples there are few examples that explore coordinative cyclopolymerization of 1,6-heptadiene. However, the few reports found present results that show a high degree of its selectivity for the insertion of cis-diastereoselective cyclization, yielding highly crystalline values for PMCH.[8,9] Within Scheme 4.2 one can observe the nomenclature used for cataloging the stereochemical microstructures that can exist within these materials. The relationship between adjacent stereocenters on two different cycloalkane rings are describes as either meso (*m*) or racemic (*r*), while the M and R describe the stereochemical, cis or trans relationship between adjacent stereochemical tetrads. There are four total varied structures that can exist within PMCP or PMCH.

The goals of the current work include three main objectives: (1) creating a variety of PMCH and PMCP building blocks that can add in additional functionality

of optically active polyolefin domains to later be used in conjugates, (2) investigate the less well-known PMCH material to see if the newly developed enantioselective catalyst has control over the microstructure of the material, and (3) utilize PMCH (non-optically active) as an anti-plasticizer to modulate the physical properties within PMCP through copolymerization of the two monomer sources under LCCTP methodology.

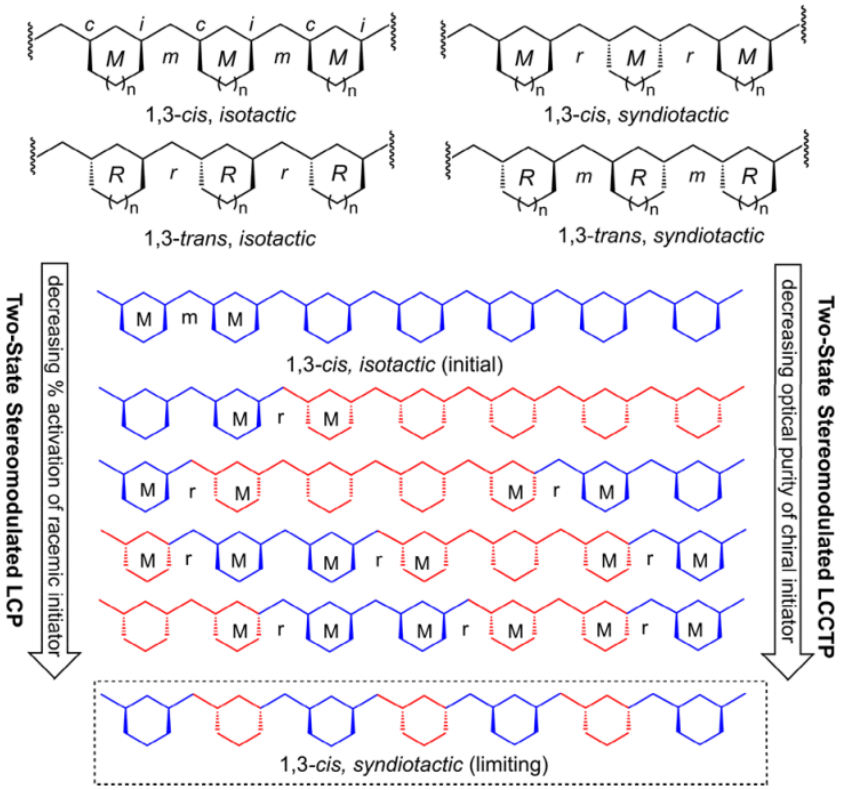

Scheme 4.2 Stereoengineering of PMCH microstructure.†

These objectives steam from the goal to discovery new polymerization technologies that can be utilized and novel polyolefin building blocks that can be useful in other material complexes for self-assembly.

4.2 Application of Optical Purity as a Programmable Variable for Stereomodulated LCCTP of 1,6-heptadiene and 1,5-hexadiene.

Two bring to fruition the first two objectives of this study, enantiopure samples of (S_c, S_{Hf})-**1** and (R_c, R_{Hf})-**1** were prepared by Mark A. Wallace according to published procedures.[6,7,10] Through the polymerization of varied enantiopurity we can design the optical purity (*ee*) within the polymers. From this study a library of LCP or LCCTP PMCH materials seen in Table 4.1 was synthesized and characterized to observe microstructures, physical properties, and any detectable trend within the polymer material. First, the LCP of 1,6-heptadiene using enantiopure (R_c, R_{Hf})-**1** pre-initiator, **run 4.1**, and produces highly crystalline PMCH polymer that exhibit low solubility in many organic solvents so in order to study the characterization of the material by NMR it was important to heat up the sample, ^{13}C {^1H} NMR analysis (200 MHz, 1,1,2,2-tetrachloroethane-*d2*, at 100 °C) revealed that the stereochemical microstructure analysis of PMCH was highly 1,3-cis, isostatic observed in Figure 4.1A. Wide-angle x-ray powder diffraction revealed that the presence of 1,3-trans cyclohexane rings decreases the crystallinity of the PMCH material, see SI. This is believed to occur because the insertion of these 1,3-trans cyclohexane rings breaks up the microstructure and prevent even crystallization of the bulk material. Unfortunately, unlike optically active PMCP materials previously reported, the PMCH product from this **run 4.1** displayed no optical activity when in solution polarimetry. This phenomenon is believed to occur because of the stereoregular 1,3-cis, isotactic microstructures do not present optical activity. Lastly, the **run 4.1** is established as a reference/ baseline for all

other materials made within this study because it was run under LCP conditions with only enantiopure pre-initiator. Other runs comparatively use enantiopure (R_c, R_{Hf})-**1** and 10 equivalents of $ZnEt_2$ thus making it LCCTP or use a mixture of enantioselective catalyst thus making it enatiorandom.

Table 4.1 LCP[a] and LCCTP[b] of 1,5-hexadiene (HXD and 1,6-heptadiene (HPD) with Different Enantiomeric Excess (*ee*) values for (R_c, R_{Hf})-1 or (S_c, S_{Hf})-1.

Run	(R_c,R_{Hf})- / (S_c,S_{Hf})-**1**	*ee*	Diene (eq.)	$ZnEt_2$ (eq.)	M_n (kDa)[c]	M_w (kDa)[c]	$Đ$[c]	T_g (°C)[d]	T_m (°C)[d]
4.1	0:100	100	HXD (100)	0	16	17.6	1.09	-5.52	97.5
4.2	0:100	100	HXD (100)	10	3.8	4.3	1.12	-48.0	64.1
4.3	50:50	0	HXD (912)	10	7.5	9.2	1.22	-24.8	84.8
4.4	100:0	100	HPD (83)	0	8.6	11	1.29	96.2	166.3
4.5	100:0	100	HPD (416)	10	2.1	2.5	1.19	60.0	-
4.6	90:10	80	HPD (236)	5	2.0	2.4	1.20	68.9	-
4.7	80:20	60	HPD (236)	5	2.2	2.7	1.22	63.2	-
4.8	70:30	40	HPD (236)	5	2.0	2.4	1.21	64.0	-
4.9	50:50	0	HPD (236)	5	2.1	2.4	1.22	59.1	-

[a]LCP performed using 44 μmol of **1** in 7 mL of chlorobenzene (PhCl) at -5 °C. [b]LCCTP performed using 44 μmol of **1** in 7 mL of toluene at -5 °C. [c]Determined by

Using LCCTP with (R_c, R_{Hf})-**1** resulted in PMCH materials that displayed a distinctive physical property change that greatly differed from reference **run 4.1**. Before comparing the LCP and LCCTP PMCH material it is important to note that the decrease in molecular weight is due to the reversible chain transfer process that is observed within LCCTP and observed through GPC instrumentation analysis. Material

run 4.2, LCCTP enantiopure synthesis, was analyzed to have a reduction of the crystallinity in comparison to reference **run 4.1,** LCP enantiopure synthesis, and overall slow crystallization kinetics which can be observed through the absence of an observable T_m.[9] Other trends observed within this study provided evidence that the T_g of these PMCH materials could be decreased systematically with the decrease in molecular weight of the PMCH polymer material thus establishing a trackable and programmable design based on molecular mass. Comparison of ^{13}C and ^{1}H NMR between PMCH materials from **run 4.1** and **4.2** demonstrate two key features when employing LCP verses LCCTP, Figure 4.1. First, there is no dramatic decrease in the degree of diastereoselectivity of cyclization under the LCCTP process. Second, the appearance of new resonances can be assigned to MrM (1,3-cis, syndiotactic) tetrads that indicated a slight loss of stereoselectivity when inserting the next monomer unit is detected. The overlapping of resonances within a very small chemical shift window does not allow for quantitative assessment of the α or σ values within the material. None-the-less, it is clear that LCCTP of 1,6-heptadiene is less stereoselective than that LCP.

While still trying to reach objective (2), investigate the less well-known PMCH material to see if the newly developed enantioselective catalyst has control over the microstructure of the material, the results of **run 4.2** did not immediately lead us to believe it was unattainable. The combination of both (S_c, S_{Hf})-**1** and (R_c, R_{Hf})-**1** at varied amounts to produce (+ or -)-PMCH characteristics resulting in material **run 4.3-4.9** provided hopeful results that contradicted what was observed in **run 4.2**. The

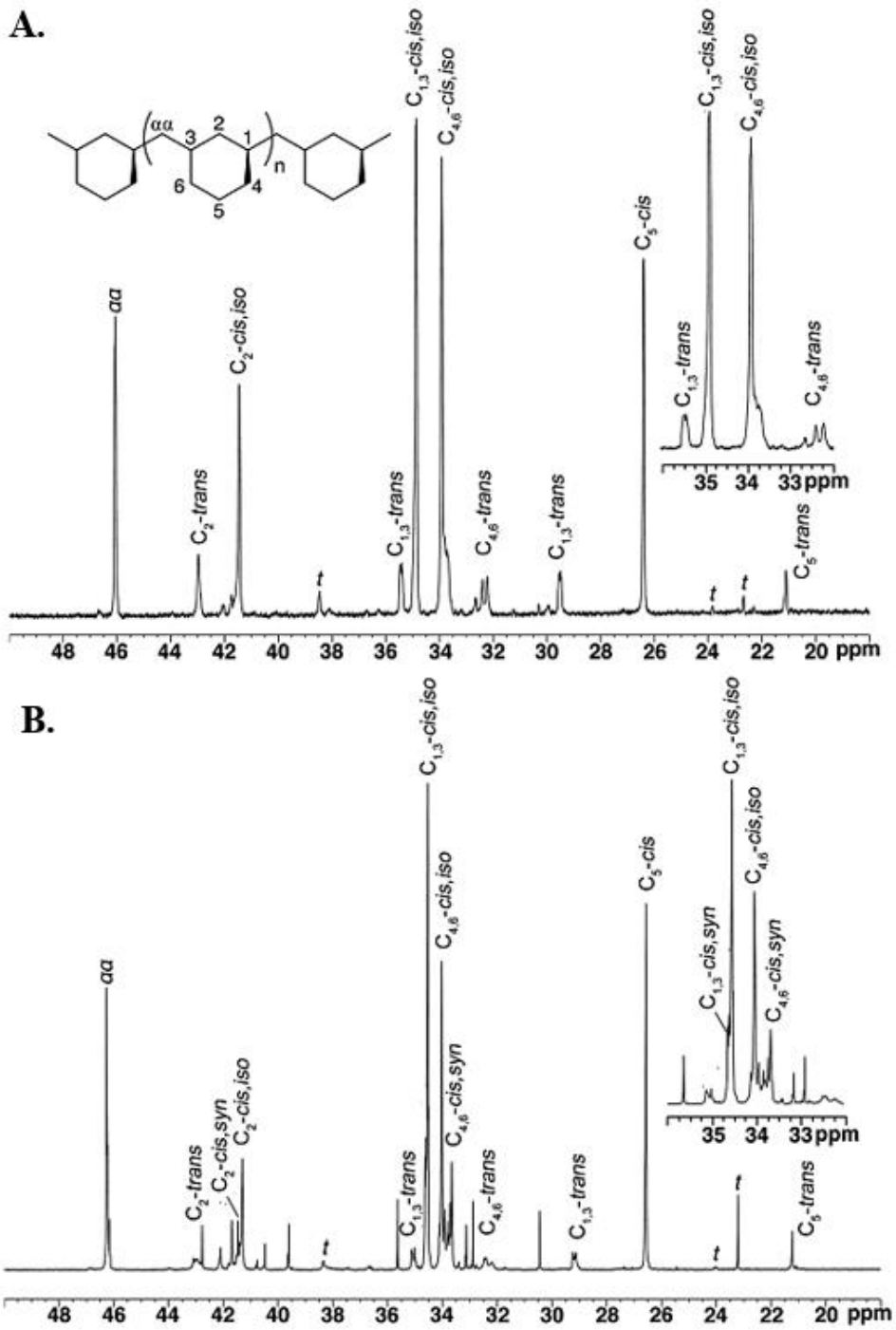

Figure 4.1 ^{13}C {^{1}H} NMR (200 MHz, 1,1,2,2-tetrachloroethane-*d2*, 100 °C) spectra of PMCH from run 4.1 (A) and run 4.2 (B) in Table 4.1. Resonance assignments are based on those previously reported for highly stereoregular 1,3-cis, isotactic PMCH and for a series of PMCH materials prepared through two-state stereomodulated LCP.[†]

combination of both enantioselective catalysts was employed in order to adjust the optical purity of the resulting polymer. As presented in Table 4.1, the materials produced did not show any significant variation form the reference baseline material PMCH in **run 4.2** in terms of M_n, M_w, and $Đ$ values. Furthermore, all PMCH products

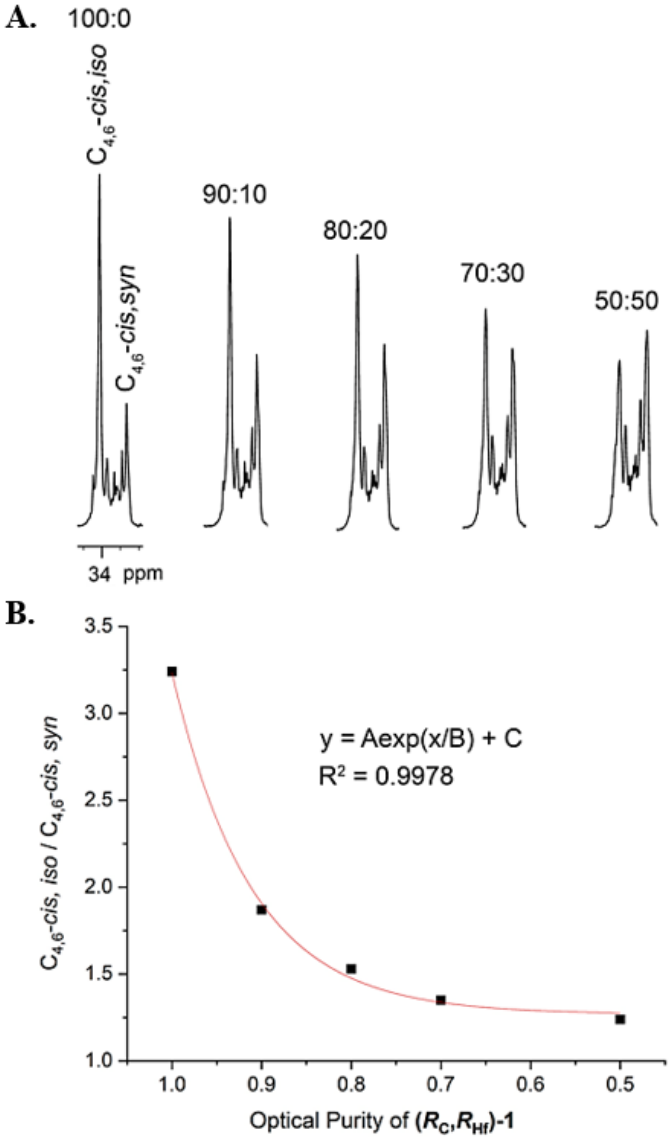

Figure 4.2 (A) Partial ^{13}C {^{1}H} NMR (200 MHz, 1,1,2,2-tetrachloroethane-*d2*, 100 °C) spectra for the $C_{4,5}$ resonances of the series of PMCH products of Table 4.1 for runs left to right 4.60-4.9. (B) Quantitative analysis of the ratio of the MmM/ MrM tetrads for $C_{4,6}$ resonances of (A) as a function of optical purity of (R_c, R_{Hf})-**1.** The red line is an exponential fit of the data with the coefficient of determination (R^2) shown. Seen SI for variable numerical values.[†]

were seen to have less crystallinity despite the largely unchanged T_g values measured by DSC, seen in wide-angle x-ray powder diffraction, see SI. To examine the microstructure of these materials made through LCCTP of both enantioselective catalysts ^{13}C NMR is employed and in Figure 4.2A a comparison of the partial ^{13}C NMR spectra for the series of PMCH materials zoomed in on the $C_{4,6}$-syndio resonances. This spectra profile provided a trend that there is an increase in the MrM tetrads as a function of decreasing optical purity. Dr. Lawrence R. Sita ran a quantitative fit of the change of the ratio of $C_{4,6}$-tans. $C_{4,6}$-syndio resonances as a function of optical purity to an exponential decay, represented in Figure 4.2B. These calculations are in keeping with results seen in previous studies of two-state stereomodulated LCP of propene and 1,6-heptadiene. [9,11]

In summary, objectives (1) and (2) were achieved through utilizing (R_c, R_{Hf})-**1** and (S_c, S_{Hf})-**1** together in LCCTP synthesis, thus creating a series of differing grades of polyolefins through implementation of LCCTP and optically pure catalysts. Importantly with the last objective in mind this study has helped advanced access to unique polyolefin products and a develop a better understanding of PMCH behavior and properties which is immediately used in the next study.

4.3 Effects of Crystallinity Within PMCP-*co*-PMCH Materials

.

Wentz, C. M.; Burgenson, W. R.; Sita, L. R., Controlling Crystallinity Through Copolymerization of 1,5-Hexadiene and 1,6-Heptadiene, (*manuscript in preparation*).

Author Contributions:
L. R. S. Lead conceptualization, funding, and writing.
C. M. W. Supported synthesis and characterization of all polyolefin materials. Synthesized and characterized half of all materials.
W. R. B. Synthesized half of all materials with the assistance of C. M. W. Conducted calculations with materials to correlate properties to ratio of PMCP to PMCH domains.

Stereochemistry within a material has a direct importance to the function, and this is general well understood, however, to date control over the crystallinity, stereostructure, and adaptation of poly(1,3-methylenecyclopentane) (PMCP) has yet to be fully realized. Notably, PMCP is a unique polymer but is the subject of limited use. Most unique about it is even the atactic polymer (aPMCP) is crystalline, a property typically only reserved for isotactic polymers. This crystallinity is cause by the hexagonal packing of chain axes of the polymer.[12] Many have explored PMCP properties when pair with other monomers including ethylene,[13,14] styrene,[14,15] and others,[16-18] or with different catalytic systems in order to control the materials stereostructure.[19] The scope and design of this polymer with respect to stereochemistry has already provided many 'materials' advanced. However, with further synthetic advance there remains significant opportunities for stereochemical control of the materials properties to impact a wide range of application.[20] In this study we combine 1,5-hexadiene with 1,6-heptadiene (poly (1,3-methylenecyclohexane) (PMCH)), to create a copolymer of PMCP-co-PMCH, which to the best of our knowledge has never

been achieved before. Ultimately, in our system we can break the PMCP crystallinity, even at low loading of 1,6-heptadiene monomer (<10%) and control the glass transition temperature (T_g) that exists within the bulk material. This study address's objective (3), utilize PMCH (non-optically active) as an anti-plasticizer to modulate the physical properties within PMCP through copolymerization's.

As of 2017, polyethylene is the most widely produced plastic, comprising 34% of plastic produced by the polymer industry.[21] While PE is recyclable, the polymer degrades with each recycling process, and the viability of using this polymer decreases as well. However, instead of recycling the polymer, more efforts should be made to upcycle the polymer into different commodities. Recent efforts into the upcycling of polyolefins have yielded an economically viable process that creates α,ω-dienes via desaturation/ethenolysis of polyethylene.[22] While these processes have only produced higher molecular-weight dienes (671 Da), there is no doubt that the process can still yield lower molecular-weight dienes given the effort to make them. Conveniently, the monomers used in this study are both α,ω-dienes that can theoretically be produced via upcycling of polyethylene. Should this process be used by the polymer industry, it could be a viable alternative to traditional polyethylene recycling, while still producing a high-value polymer product.

For reference, Figure 4.3, consists of 100% PMCP (top) **run 4.10**, and 100 % PMCH (bottom) partial ^{13}C NMRs **run 4.18** with all the stereo-orientations displayed for each homopolymer above each NMR. PMCP is a semi-crystalline, low T_g polyolefin with a rigid five-membered ring structure formed through the polymerization of 1,5-hexadiene. While, on the other hand, PMCH is an amorphous,

high T_g polyolefin with a more flexible six membered ring structure. Both of these molecules individually are not used in any of today's commodity plastics due to PMCP highly crystalline and brittle behavior and PMCH high T_g but expensive monomer feedstock. That being said, the necessity for a commodity plastic to be durable yet easily processable requires a material that contains a high Tg but be more structurally durable than just these homopolymers alone. Therefore, creating a copolymer of both can ultimately unveil a new useful material.

Before beginning, it is important to note that 1,6-heptadiene has been incorporated with 1-hexene to generate a spectrum of different physical forms of poly(1,3-methylenecyclohexane) (PMCH) in which stereochemical microstructure was systematically controlled. These ma-erials had possessed a high T_g and microphase separation that was thermal stimuli responsive.[10cw] These materials nevertheless still contained a T_m and highly crystal-line nature. The current study looks to have a high T_g material with no crystalline nature.

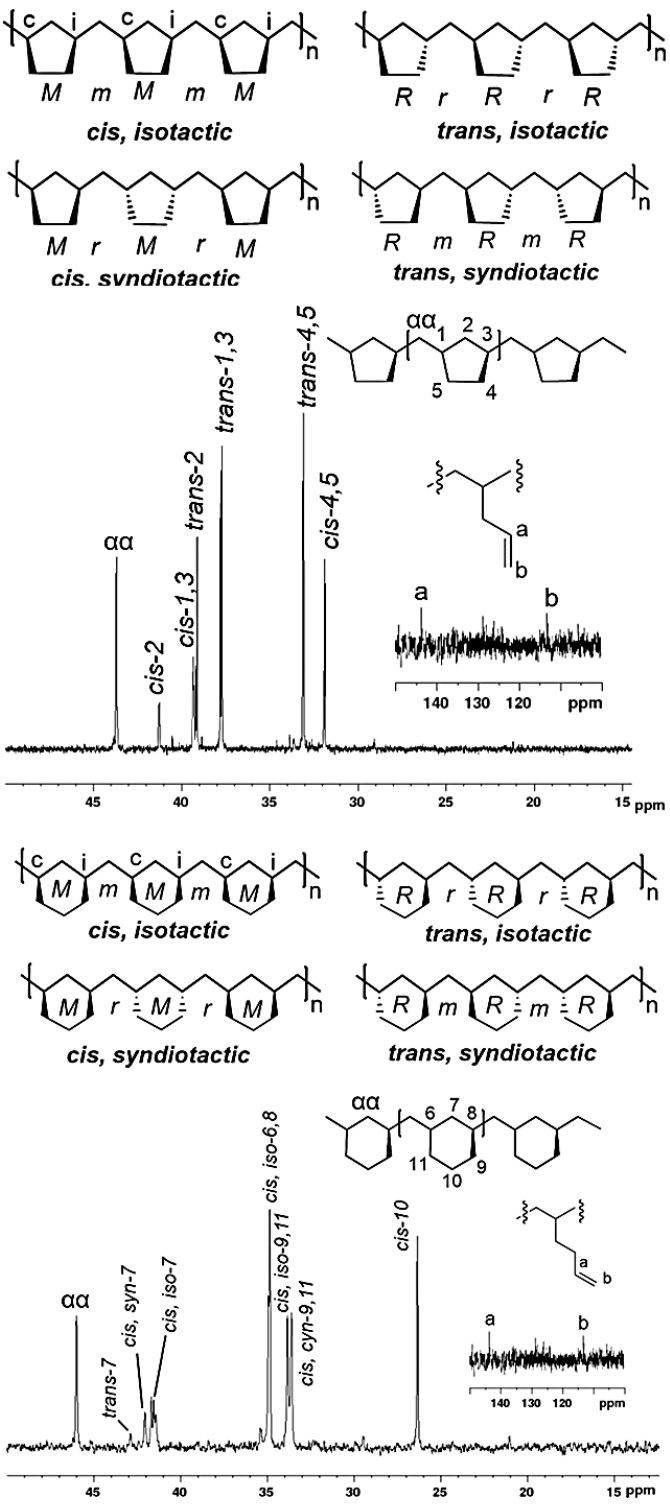

Figure 4.3 (A) Partial ^{13}C {^{1}H} NMR (200 MHz, 1,1,2,2-tetrachloroethane-*d2*, 110 °C) spectra for top PMCP and bottom PMCH.

Table 4.2 LCCTP of Copolymer Materials (PMCP-*co*-PMCH).[a]

Run	PMCP: PMCH Target	PMCP: PMCH Ratio NMR Integrated	HXD (eq.)	HPD (eq.)	Yield (g)	M_n (kDa)[b]	M_w (kDa)[b]	$Đ$[b]	T_g (°C)[c]	(
4.10	100:0	100:0	1188	0.000	1.68	10.1	12.2	1.20	-	9
4.11	90:10	91.7:8.33	1077	120.0	1.64	13.7	16.1	1.18	-3.97	
4.12	80:20	81.9:18.1	942.0	235.0	1.76	9.32	10.4	1.12	10.9	
4.13	70:30	69.5:30.5	811.0	347.0	1.66	13.1	15.4	1.18	37.1	
4.14	60:40	62.0:38.0	684.0	456.0	1.58	13.7	16.1	1.18	45.2	
4.15	53:47	57.9:42.1	609.0	520.0	1.68	13.3	15.7	1.18	50.5	
4.16	40:60	41.5:58.5	441.0	663.0	1.48	17.9	20.6	1.14	68.6	
4.17	20:80	18.8:81.2	855.0	214.0	1.78	11.4	12.9	1.12	76.8	
4.18	0:100	0:100	0.000	2852	2.24	12.1	13.4	1.10	98.6	

[a]All polymerizations were done under 5 eq, except **run 4.18**, which was done under 20 eq. [b]Determinedby GPC. [c]Determined by DSC.

This is a goal reached in the current study and has great impact on the development of polyolefin-based structural materials. The copolymers studied within were synthesized via living coordinative chain transfer cyclo-polymerization (LCCTP) of 1,5-hexadiene and 1,6-heptadiene, Scheme 4.3, where pre-initiator **I** was activated by **II**, with the inclusion of chain transfer agent $ZnEt_2$, **III**, in one-pot synthesis at varied equivalence if monomers, see Table 4.2 for details. William Burgenson, undergraduate researcher, under guidance and mentorship, helped synthesize and characterize some of the materials within this study. To represent the frequency of the adjacent 5 membered rings, 6 membered rings, and 5 to 6 membered rings, dyads were used to determine not only the composition of the polymer, but also the block-forming tendency of the copolymerization indicated in Scheme 4.3. Were the symbol (▼) represents a 6-mebered ring followed by another, the symbol (●) represents a five-

membered ring followed by another, and the symbol (■) represents a 5-memebered ring followed by a 6-memebered ring or visa-versa. In Figure 4.4, as the incorpo-ration of PMCH is increased we can see a decrease in ■ due to the decrease in PMCP repeat units being present, consequently there is a drastic increase in ▼ due to the increased presence of PMCH throughout the copolymer. Throughout, the series of materials these dyads are easily tracked to help predict the 'actual' ratio of one unit to another. The percent incorporation of PMCH was deter-mined using integration obtained from ^{13}C-NMR with inverse-gated proton decoupling, see SI.

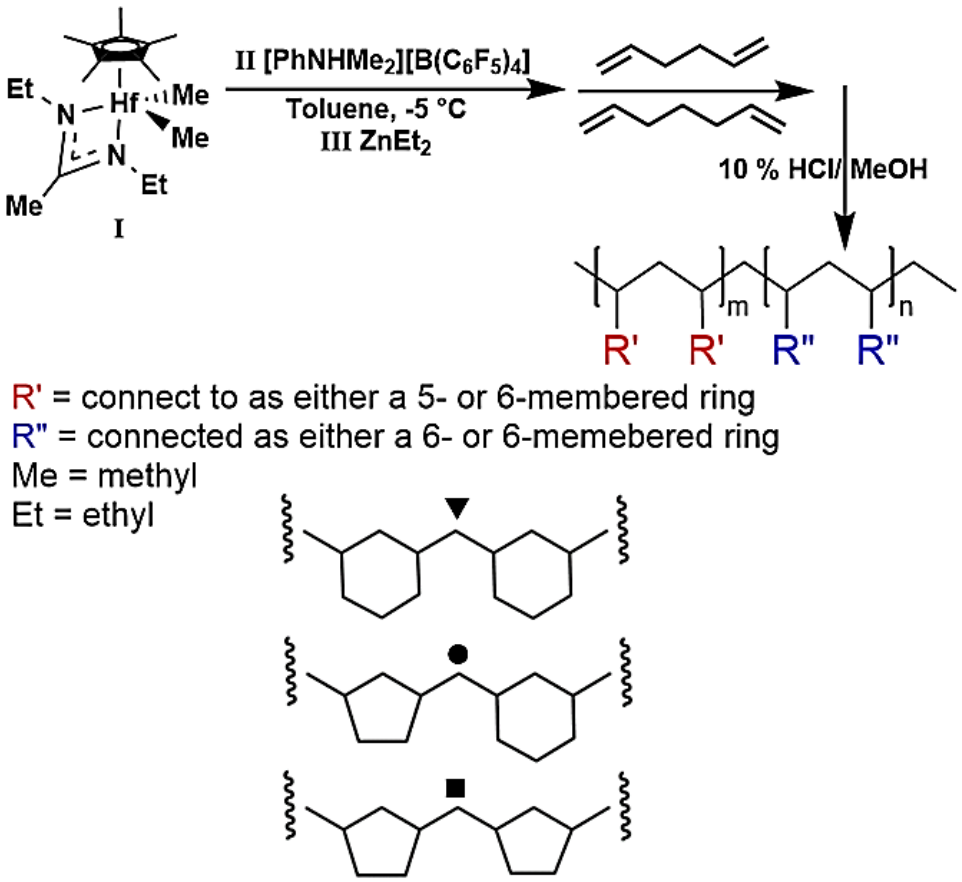

Scheme 4.3 LCCTP of Copolymer Materials (PMCP-*co*-PMCH).

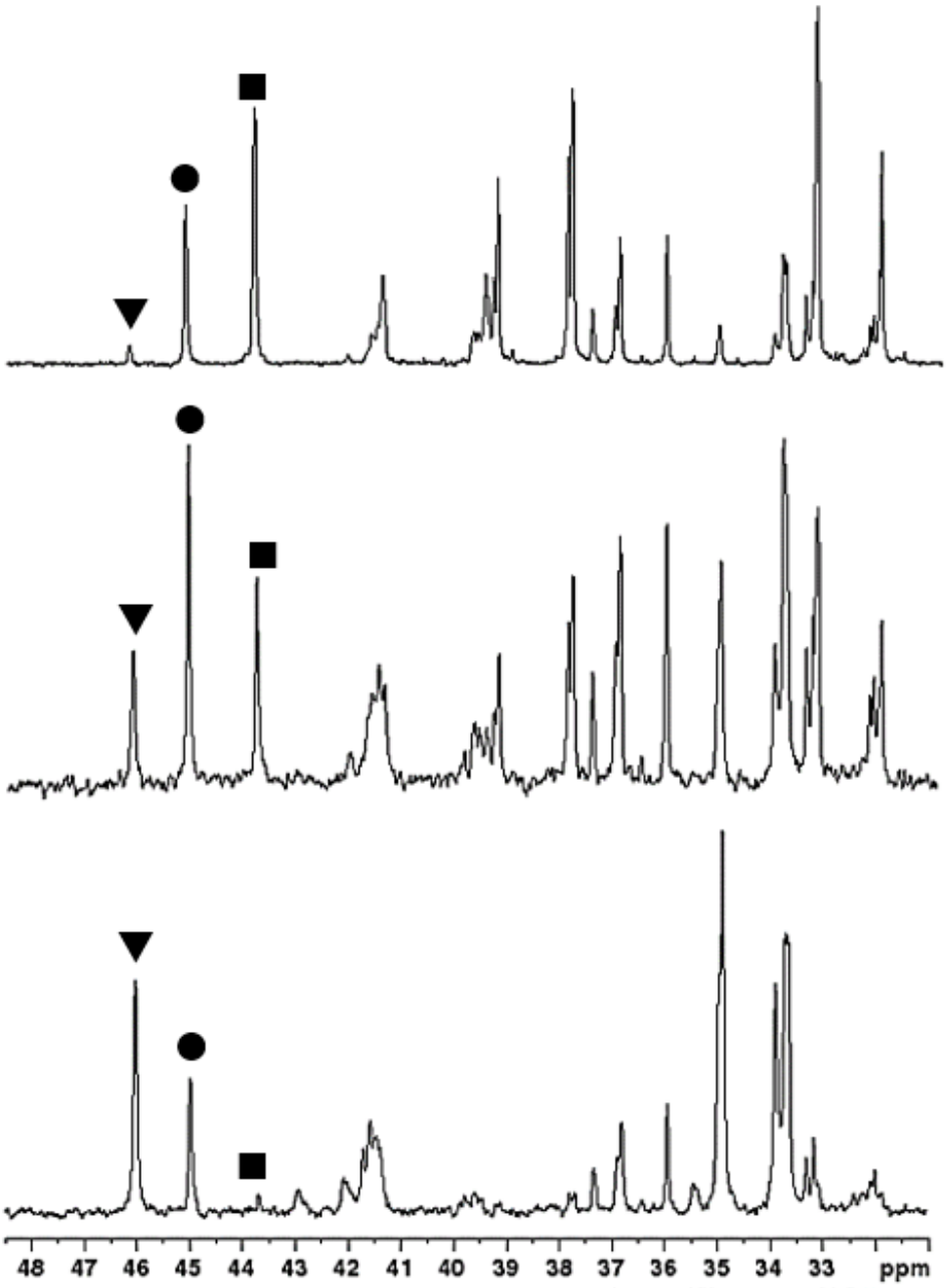

Figure 4.4 Partial ^{13}C {^{1}H} NMR (200 MHz, 1,1,2,2-tetrachloroethane-*d2*, 110 °C) spectra for copolymers PMCP-*co*-PMCH from top to bottom **runs 4.13, 4.15, and 4.18**.

The lowest observed incorporation of 1,6-heptadiene, **run 4.11**, had an incorporation of 7.66 mol%. To determine the average length of the repeating PMCP blocks, a first-order Markov model was used to deter-mine the probabilities of each

comonomer adding to the growing copolymer. (1,3-methylene) cyclopentane block length of 12.05 units. Additionally, the DSC trace of this polymer shows a complete absence of any melting point. Indeed, even a small disruption in the structure of the PMCP crystal structure is enough to totally disrupt crystallinity of the copolymer. The materials in this study are all monomodal by GPC with low polydispersity's, confirming that this is a random copolymer produced from a living-controlled system. This material represents the lowest loading of PMCH into the copolymer which breaks up crystallinity but still leaves the material with a low T_g of -3.97 °C. It is not until 80

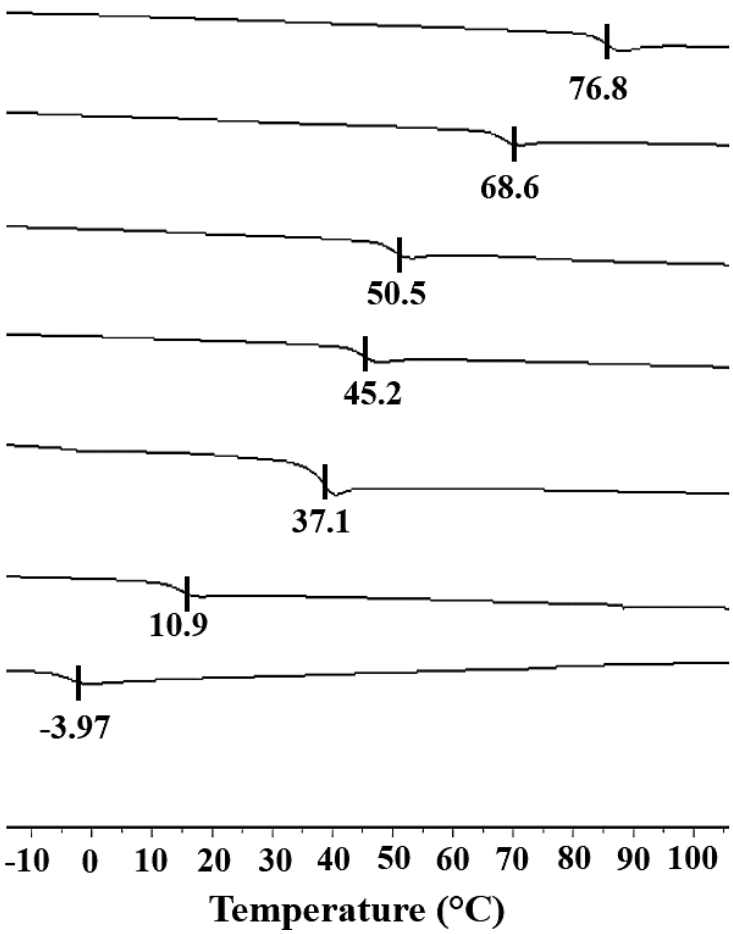

Figure 4.5 Partial DSC traces of **run 4.11-4.17** where the last heat cycle is shown for a 10 °C/min ramp from -70 to 220 °C.

% loading of PMCH into the copolymer leads to what we would call a significantly high Tg of 76.8 °C. The PMCP-co-PMCH copolymer never reaches the same T_g as a 100 % PMCH material but it must be noted that these materials are all run around 9-18 kDa range and higher T_g can be predicted for larger copolymer.

Most surprising, was not our ability to break up crystallinity with such a small incorporation of 1,6-heptadiene, but to access complete control over its physical properties. This array of stereocontrolled materials has glass transition temperatures that follow a clean, lin-ear trend with respect to mol% PMCH incorporation. Therefore, the ability of the PMCH monomer unit to dis-rupt crystallinity of a polymer and simultaneously control glass-transition temperature to a fine degree is con-firmed, Figure 4.5. To control a material T_g is no small task and asides from our previous study, with atactic poly(4-methyl-1-pentene) (PMP)[23] in which we controlled the T_g of the material through increased molecular weights, to the best of the authors knowledge this have never been done with either PMCP or PMCH.

A graphical representation of the *Tg* results verses the percent incorporation of PMCH is shown in Figure 4.6. William Burgenson utilized this mathimatical equations discussed to graphically A naive, but relatively straightforward method to predict the Tg of a copolymer is to use the percent composition of the homopolymers to derive the model, Equation 4.1. where Tg represents the glass transition temperatures of the respective polymers, and represents the weight percentage of the homopolymer in the copolymer. The graph of this relationship is linear. Some copolymers follow this

Equation 4.1 $$\boldsymbol{T_g = T_{g1} * w1 + T_{g2} * w2}$$

relationship, but most don't. The Tg vs. monomer incorporation for most copolymers has a nonlinear shape, usually concave up. More recent models use the parameter R, which represents the ratios of an unknown parameter in the individual monomer units that affects the glass transition temperature. Using this parameter changes the linear equation to, Equation 4.2.

Equation 4.2 $$\frac{\mathbf{1}}{\boldsymbol{T_g}} = \left[\frac{\mathbf{1}}{\boldsymbol{w1+R*+w2}}\right]\left[\frac{w1}{T_{g1}} + \frac{Rw2}{T_{g2}}\right] where\ R = \frac{T_{g2}\,A2}{T_{g1}A1}\ wheere\ A\ is\ an\ unknown\ parameter$$

This model was first proposed by Wood in 1958. The best explanation for this value R is the ratio of free-space associated with each monomer in the polymer chain. With a series of copolymers, it is possible to fit a value for R. This fitting was done with a least-squares regression, changing R to find the best fit of the Wood equation to the plot of Tg vs monomer incorporation. Typically, the value of A2/A1 is near 1, which creates a non-linear, concave up graph. Interestingly, for the PMCP-PMCH copolymer, the value of A2/A1 is less than the value of T_{g1}/T_{g2}, which makes the T_g spectrum concave down. To our knowledge, this copolymer is the first to have a value of R to make the graph of Tg concave down.. The linear progression of T_g as a function of PMCH incorrporation is observed and can be utilized to make

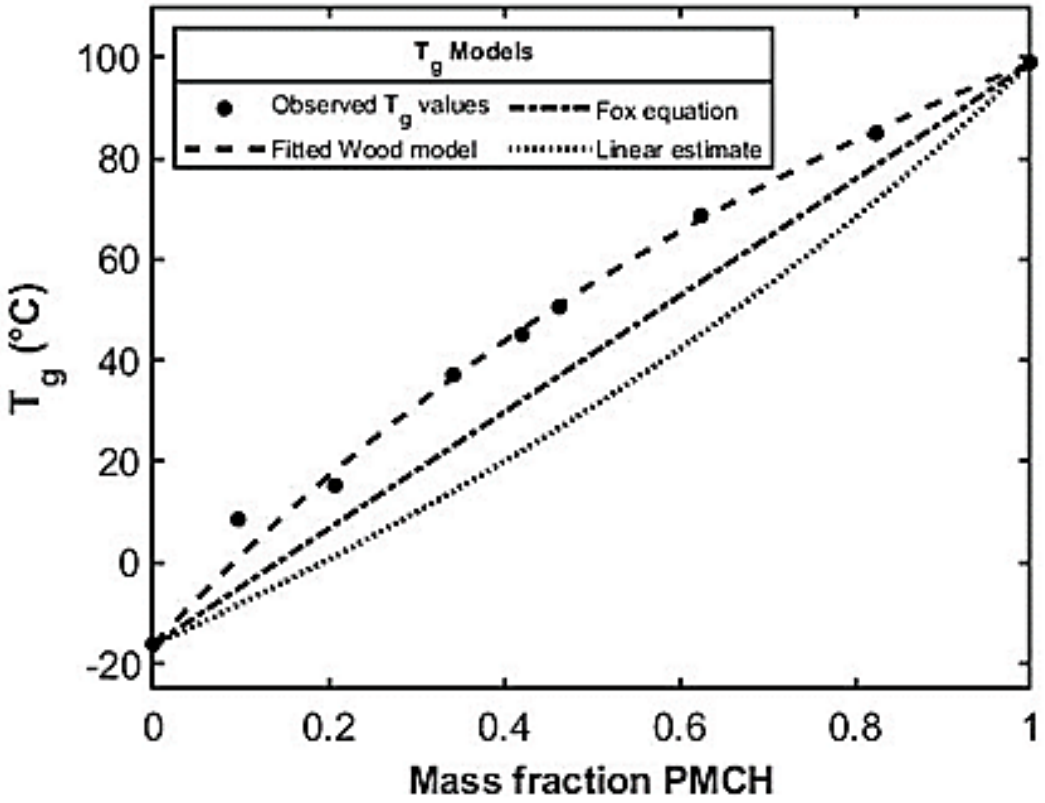

Figure 4.6 The whole series of PMCP to PMCP-*co*-PMCH to PMCH materials in run's **4.10 – 4.18** displayed as observed, by the Fox equation, Linear equation, and Wood equation.

copolymers by design and target specific physical properties. The values of the equations utilized help create and idea of how experimental results compare to theoretical hypothesis.

In summary, a series of random copolymers of PMCP and PMCH were synthesized via copolymerization of 1,5-hexadiene and 1,6-heptadiene. With 1,5-hexadiene and 1,6-heptadiene being potential products from upcycling polyethylene, we demonstrate a high-value polymer can be produced from otherwise discarded material. At in-corporation levels as low as 7.66%, and average PMCP block length of

12 units, the crystallinity from the PMCP polymer was completely absent. Beyond breaking up crystallinity, the degree of incorporation of 1,6-heptadiene into the copolymer allows for fine tuning of the glass transition temperature of the polymer. Additionally, using 1,6-heptadiene in the copolymer allows for tuning of the glass-transition temperature to temperatures well over 100 °C. There is a clear industrial demand for control of crystallinity and glass-transition temperatures of polymers, and the ability for a single system to be able to control both of these properties is highly desired. With this study, the Hf-based catalyst system is demonstrated to be able to control both properties with incorporation of 1,6-heptadiene.

4.4 Conclusions

Overall, a series of new optically active and non-optically active PMCP, PMCH, and PMCP-*co*-PMCH polyolefin materials were synthesized and characterized. Many of these materials have never been documented in the literature and contain varied physical properties and microstructures which open many doors of possibilities. These materials can stand alone as unique, potentially commercially viable materials, or as building blocks when end-group functionalized can be used in conjugates to access new phase separation behavior or bulk properties.

With the development of enantio- and stereoselective synthesis utilizing (R_c, R_{Hf})-**1** and (S_c, S_{Hf})-**1** the future investigation relies on new ligand scaffolds to be created because the major drawback to the current system is it only works with α,ω-nonconjugated dienes. To develop a pre-initiator that allows for living polymerization

of optically active polyolefins would expand the capabilities to access new grades and properties within polymer materials. The discoveries made within these studies will allow for that target to come to realization as well as establish PMCH as a relevant polyolefin to utilize commercially.

4.5 Supporting Experimental Information

4.5.1 Synthetic Procedures

All manipulations with air and moisture sensitive materials were carried out under N_2 using standard Schlenk or glovebox techniques. Toluene (ReagentPlus, 99%) was dried and deoxygenated by passage over activated alumina and activated copper catalyst (GetterMax 135) and collected under N_2 prior to use. Chlorobenzene (ReagentPlus, 99%) was dried over calcium hydride by refluxing at 130 ^oC for three days and distilled under N_2 prior to use. Chloroform-d_1 and tetrachloroethane-d_2 were purchased from Cambridge Isotopes and used as received. 1,6-heptadiene was purchased from TCI Chemicals, dried over Na/K alloy and isolated by vacuum-transfer prior to use. $[PhNMe_2H][B(C_6F_5)_4]$ was purchased from Boulder Scientific and used as received. Catalyst **(*R*$_C$, *R*$_{Hf}$)-1** and **(*S*$_C$, *S*$_{Hf}$)-1** were synthesized according to published procedures by our group.

LCP of 1,6-heptadiene.

To a 25 mL round bottom with a 7 mL chlorobenzene solution of 38.0 mg (0.048 mmols) of $[PhNMe_2H][B(C_6F_5)_4]$ chilled to -5 ^oC was added 24.6 mg (0.044 mmols) of **(*R*$_C$, *R*$_{Hf}$)-1** in 1 mL of chlorobenzene prechilled to -5 ^oC. The solution was stirred and allowed to equilibrate for 10 minutes, turning a pale-yellow color. To the pale-yellow solution, 0.352 g (3.66 mmols) of 1,6-heptadiene prechilled to -5 ^oC was added all at once. The reaction mixture was stirred for 20 hours at -5 ^oC before precipitating from 500 mL acidic methanol (10% concentrated HCL). The polymer material was

collected via filtration and washed 2x with methanol. The polymer was dried overnight before characterization.

General Procedure for the LCCTP of 1,6-heptadiene.

To a 25 mL round bottom with a 7 mL toluene solution of 38.0 mg (0.048 mmols) of $[PhNMe_2H][B(C_6F_5)_4]$ chilled to -5 ^oC was added 24.6 mg (0.044 mmols) of **(*R*$_C$, *R*$_{Hf}$)-1** in 1 mL of chlorobenzene prechilled to -5 ^oC. The solution was stirred and allowed to equilibrate for 10 minutes, turning a pale-yellow color. 55.0 mg (0.440 mmol) of $ZnEt_2$ prechilled to -5 ^oC was added to the solution followed by 1.76 g (18.3 mmols) of 1,6-heptadiene, prechilled to -5 ^oC, added all at once. The reaction mixture was stirred for 24 hours at -5 ^oC before quenching with 2.0 mL of acidic methanol (10% concentrated HCl). Solvent was removed *in vacuo* and residue was collected in hexanes and passed through a silica plug. Solvent was removed *in vacuo* and the isolated polymer was dried overnight before GPC and NMR analysis. Details on the amount of the reagents, polymerization time, and polymer characterization are provided in **Table S4.1**.

General procedure for living coordinative chain transfer polymerization (LCCTP) of poly(1,5-heptadiene)-*c*-(1,6-hexadiene) (PMCP-*c*-PMCH), run 4.11-4.17.

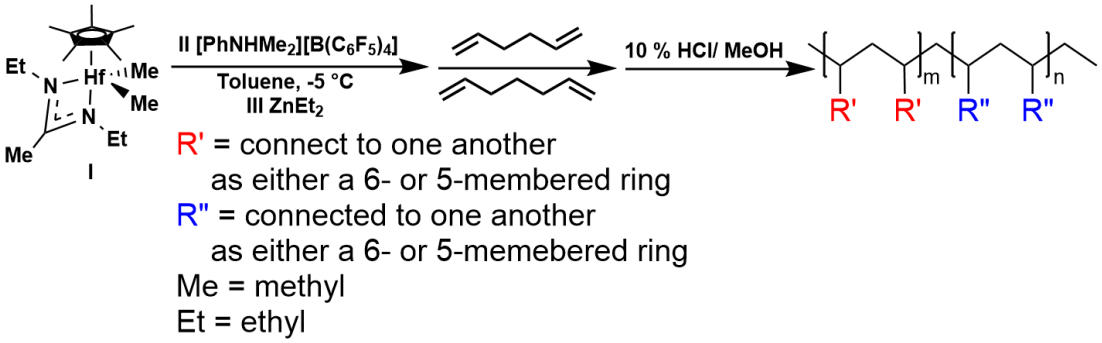

In a round bottom flask, 20 mL of toluene was cooled to -5 °C. The 1,5-heptadiene and 1,6-hexadiene monomers of targeted equivalents were added to the flask. Then chain transfer agent **III**, was added to the flask. Then a solution of **I** (0.02 mmol, 9.14 mg), in -5 °C 1.0 mL PhCl was added to **II** (0.022 mmol, 18.5 mg) which was vigorously agitated until dissolved and activated, whereupon it was added to the flask. The flask was stirred for typically 18 hours at -5 °C and quenched with 10% HCl/ methanol. The material was then run through a silica column using hexane, collected into a pre-weighed vial, and dried under vacuum. Details on polymer's characterization are provided in **Table 4.2,** runs 4.11- 4.17.

Table S4.1 LCP and LCCTP of 1,5-Hexadiene (HXD) and 1,6-Heptadiene (HPD) with Different Enatiometric Excess (*ee*) Values for ***(R*c*, R*Hf*)*-1.

run	(R_C,R_{Hf})-/(S_C,S_{Hf})-1	ee	diene (equiv)	$ZnEt_2$ (equiv)	t_p (h)	yield (g)	T_g (°C)[c]	T_m (°C)[c]	M_n (kDa)[d]	M_w (kDa)[d]	$Đ$[d]
4.1	0:100	100	HXD (100)	0	21	1.04	−5.52	97.5	16	17.6	1.09
4.2	0:100	100	HXD (486)	10	25	1.35	−48.0	64.1	3.8	4.3	1.12
4.3	50:50	0	HXD (912)	10	24	1.98	−24.8	84.8	7.5	9.2	1.22
4.4	100:0	100	HPD (83)	0	20	0.30	96.1	166.3	8.6	11	1.29
4.5	100:0	100	HPD (416)	10	24	1.20	62.3		2.1	2.5	1.19
4.6	90:10	80	HPD (236)	5	24	0.69	64.4		2.0	2.4	1.20
4.7	80:20	60	HPD (236)	5	24	0.80	70.3		2.2	2.7	1.22
4.8	70:30	40	HPD (236)	5	24	0.79	66.1		2.0	2.4	1.21
4.9	50:50	0	HPD (236)	5	24	0.81	61.3		2.1	2.4	1.22

[a] LCP performed using 44 μmol of 1 in 7 mL of PhCl at −5 °C. [b] LCCTP performed using 44 μmol of 1 in 7 mL of toluene at −5 °C. [c] Determined by DSC. [d] Determined by GPC.

4.5.2 Characterization Parameters

Gel permeation chromatography (GPC) was performed using a Viscotek GPCMax equipped with an autosampler and integrated oven maintained at 40 °C and housing a differential refractometer (RI) detector and four columns (Styragel HR-4, HR-3 and HR-1) connected in series. Tetrahydrofuran (non-stabilized HPLC Grade) was used as the eluent at a flow rate of 1 mL/min and molecular weight indices (M_n, M_w *and* $Đ$) were obtained using a conventional calibration curve established by a set of 11 polystyrene narrow standards ranging from 580 Da to 3,039 kDa and the OmniSec software package.

Nuclear Magnetic Resonance (NMR) Spectroscopy for ^{1}H and $^{13}C\{^{1}H\}$ nuclei was carried out on Brucker AVIII-HD 800 spectrometer fitted with a Cryo-QCl probe. Chloroform-d_1 was used as the solvent for low MW polymer samples. Tetrachloroethane-d_2 was used for high MW polymer samples with spectra collected at 110 ^{o}C after equilibrating the sample for ten minutes. Spectra were referenced to tetramethylsilane using residual ^{1}H and $^{13}C\{^{1}H\}$ chemical shifts of the deuterated solvents. $^{13}C\{^{1}H\}$ NMR assignments for the four limiting microstructures of poly(methylene-1,3-cyclohexane) (**Figure S4.2**) were made according to previously reported assignments.[2]

Powder X-ray Diffraction (XRD) of samples was carried out with a D8 Advanced diffractometer equipped with a LynxEye detector under ambient conditions. On a scatter less sample holder the sample was compacted in a circle with a diameter of 2mm for measurement. X-rays from a Cu Kα radiation source with a wavelength of 1.5418 Å was used, and the θ-angle starting at 5° ending at 60° with a 0.05° step. The data profiles were processed using Advanced TOPAS.

Differential scanning calorimetry (DSC) was performed using a temperature-calibrated (In metal) TA Instruments Q1000 instrument and samples that were crimped sealed in aluminum pans and subjected to a heat-cool-heat cycle between -5 °C and 220 °C using a ramp profile of 20 °C /min for heating and a ramp rate of 5 ^{o}C/ min for cooling under an inert atmosphere of N_2. Phase transition temperatures (T_g and T_m) were determined from the second heat ramp and the TA Universal software package

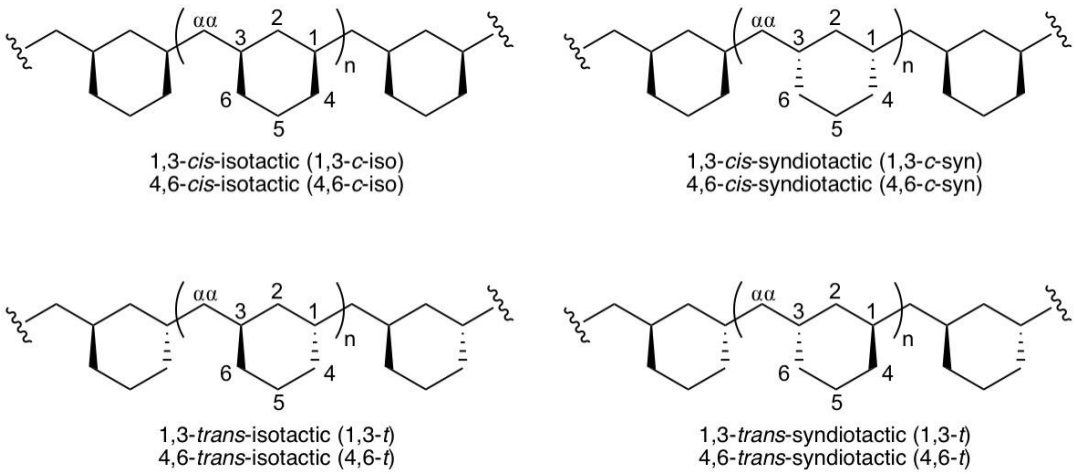

Figure S4.1 Limiting stereochemical microstructures of PMCH.

4.5.3 Supporting Results

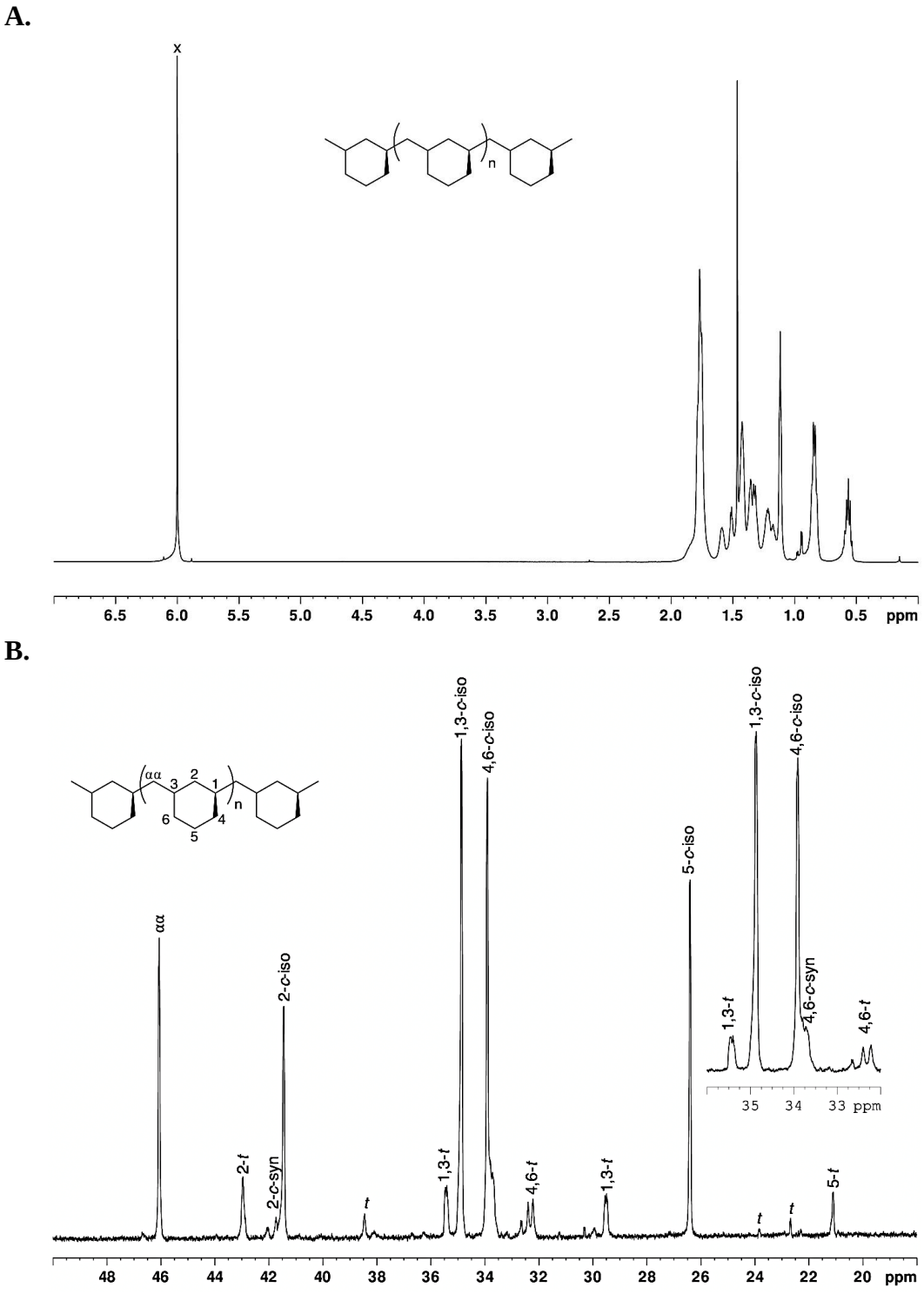

Figure S4.2. (A) ^{1}H NMR (800 MHz, TClE-d_2, 110 ^{o}C) of run 1. (B) Partial ^{13}C{^{1}H} NMR (200 MHz, TClE-d_2, 110 ^{o}C) of **run 4.1**; X denotes solvent peak.†

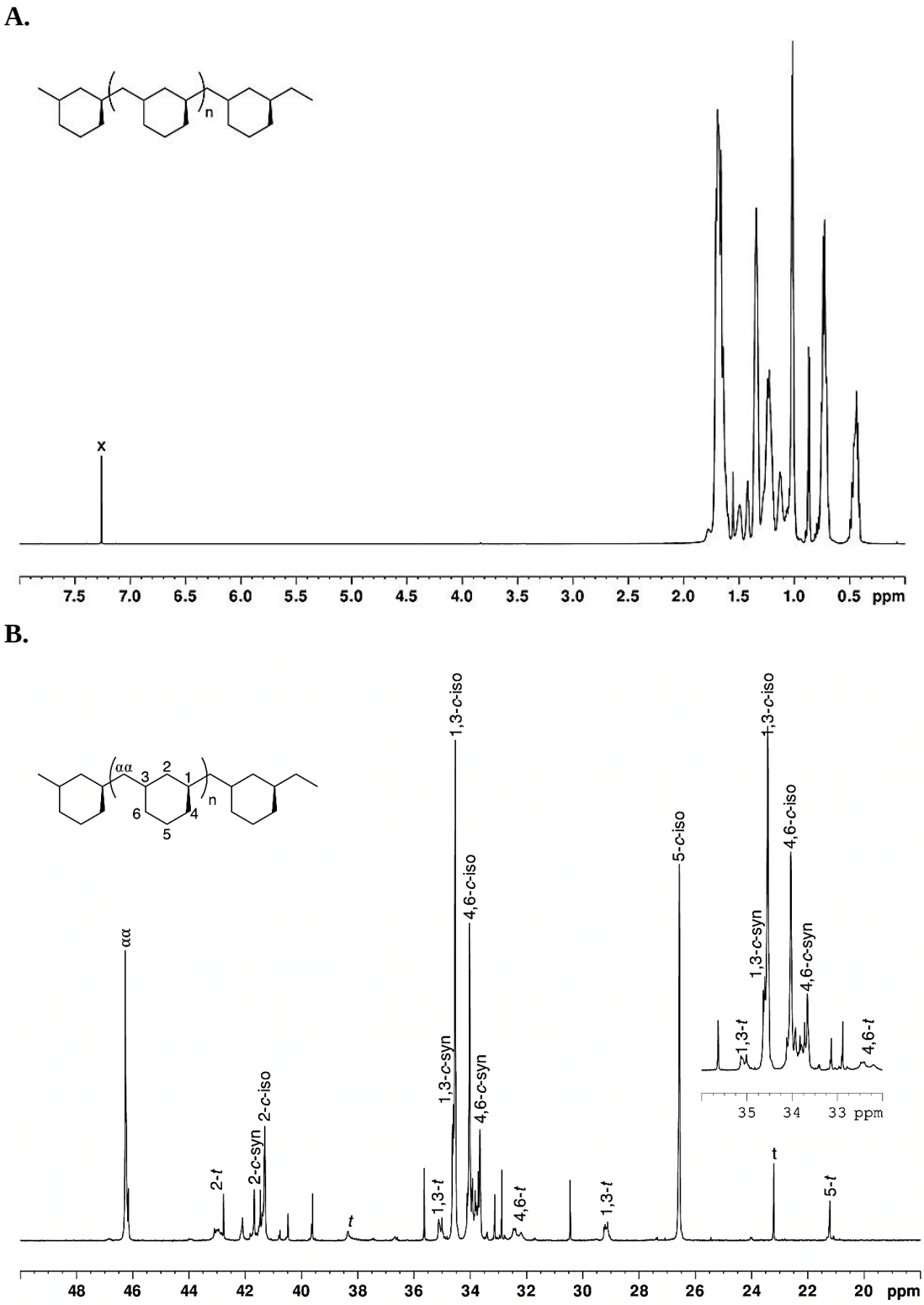

Figure S4.3. (A) ^{1}H NMR (800 MHz, C*D*Cl$_3$, 25 ^{o}C) of **run 4.2**. (B) Partial ^{13}C{^{1}H} NMR (200 MHz, C*D*Cl$_3$, 25 ^{o}C) of **run 4.2;** X denotes solvent peak.†

A.

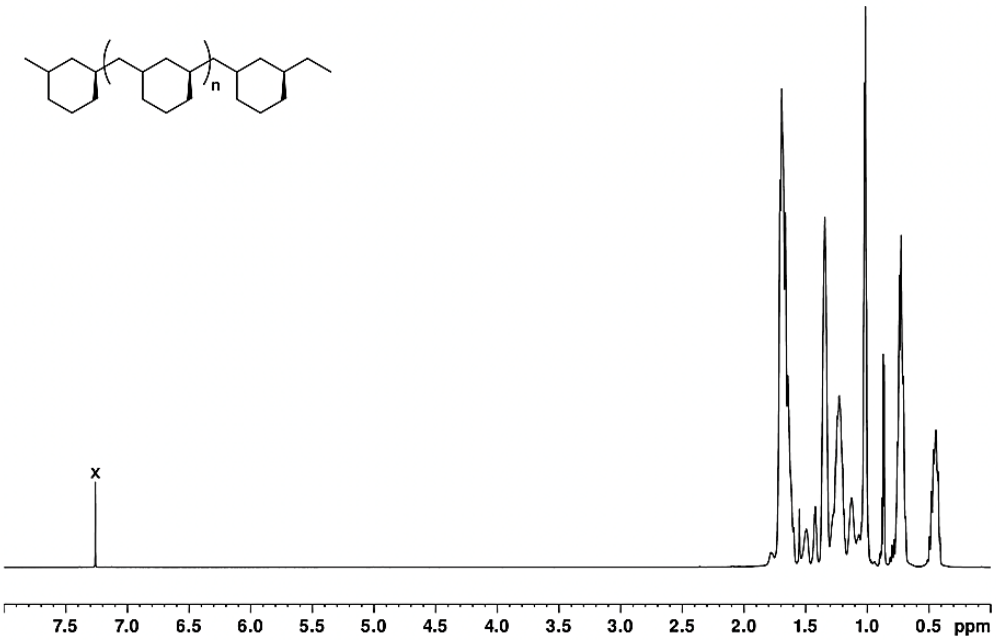

B.

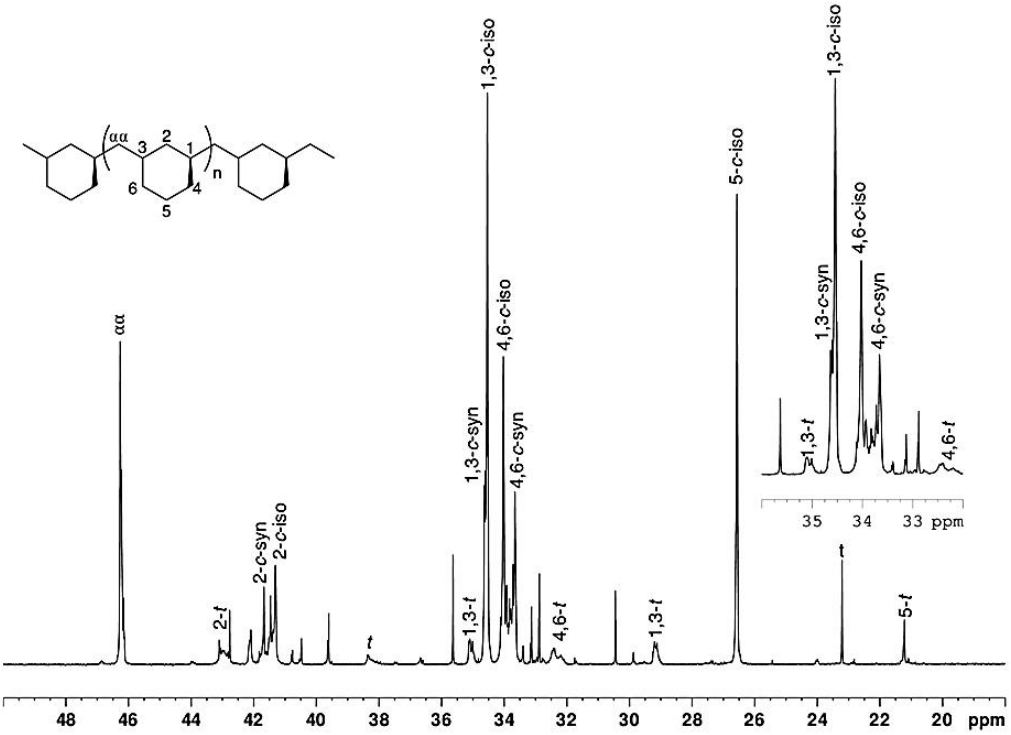

Figure S4.4. A) ^{1}H NMR (800 MHz, C*D*Cl$_3$, 25 ^{o}C) of **run 4.3**. B) Partial ^{13}C{^{1}H} NMR (200 MHz, C*D*Cl$_3$, 25 ^{o}C) of **run 4.3**; X denotes solvent peak. †

A.

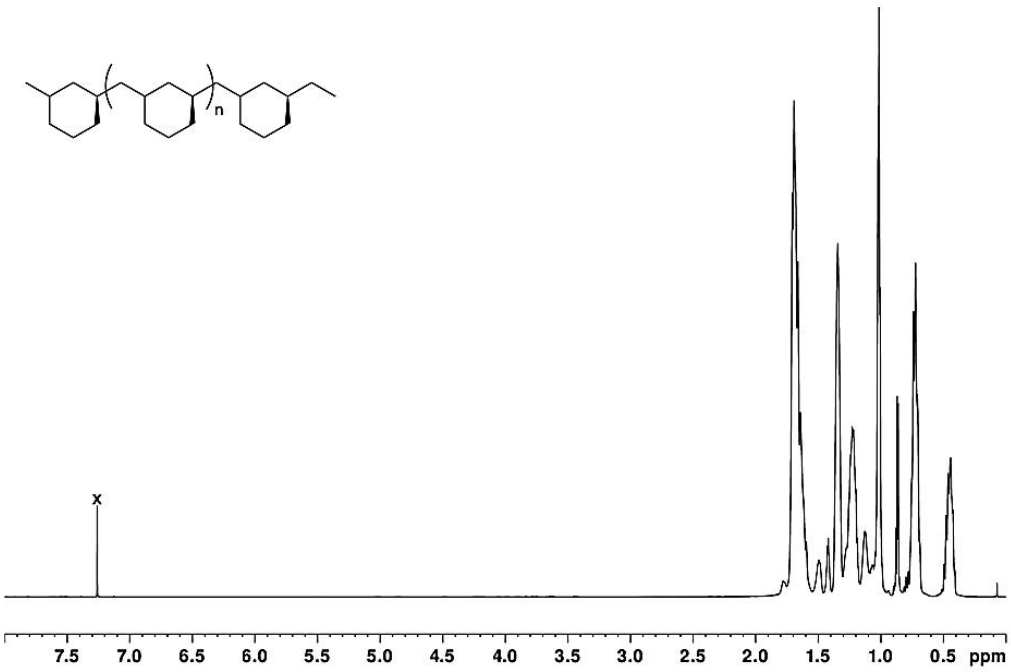

B.

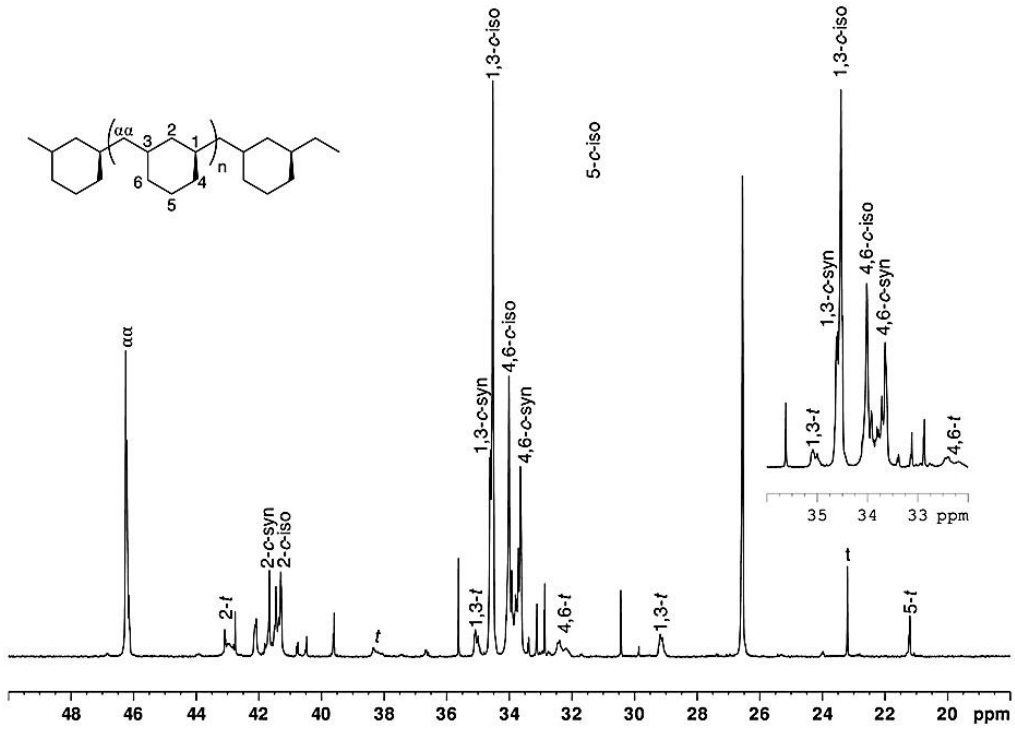

Figure S4.5. (A) ^{1}H NMR (800 MHz, C*D*Cl$_3$, 25 ^{o}C) of **run 4.4**. (B) Partial ^{13}C{^{1}H} NMR (200 MHz, C*D*Cl$_3$, 25 ^{o}C) of **run 4.4**; X denotes solvent peak.†

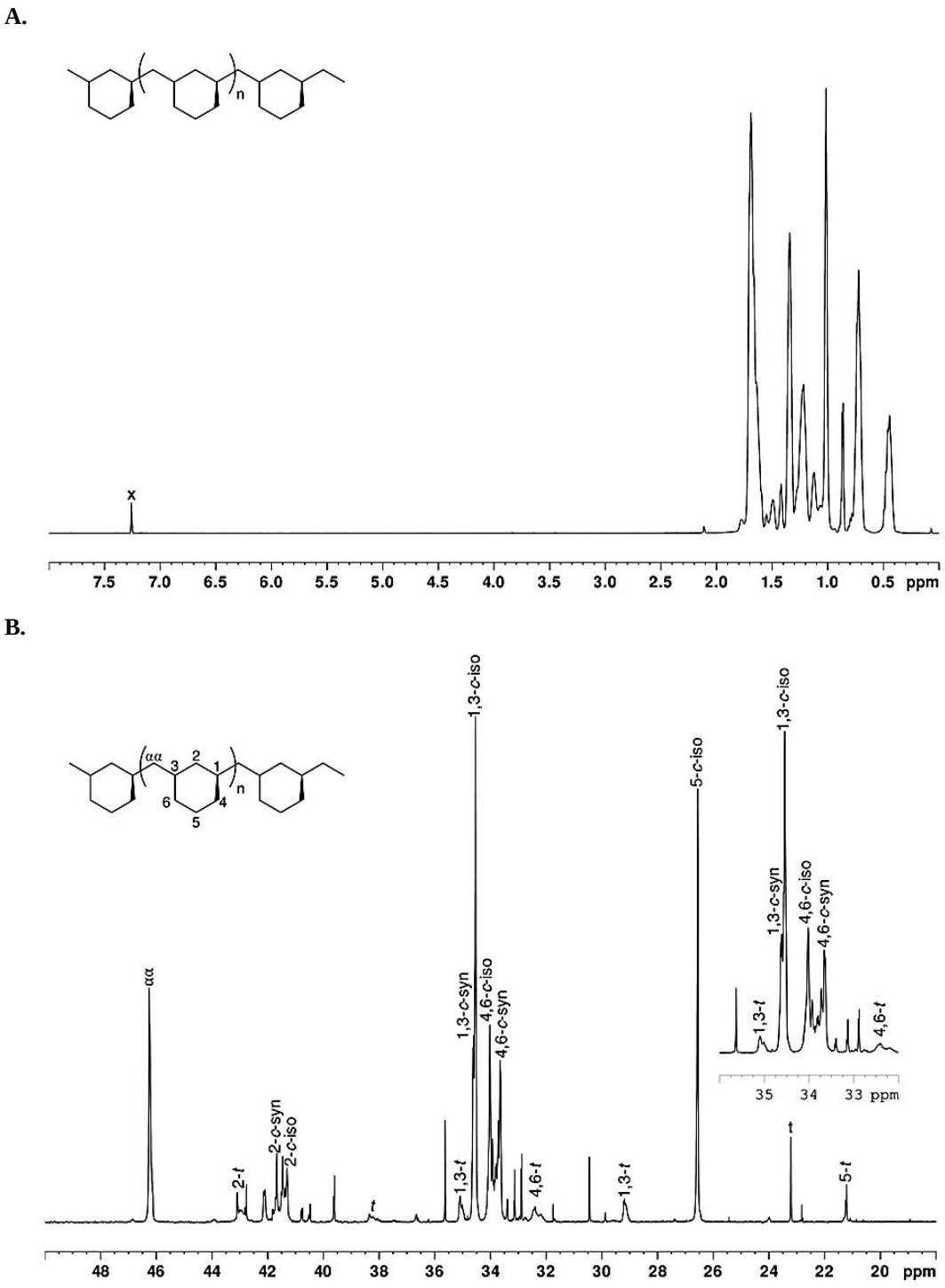

Figure S4.6. A) ^{1}H NMR (800 MHz, C*D*Cl$_3$, 25 ^{o}C) of **run 4.5**. B) Partial ^{13}C{^{1}H} NMR (200 MHz, C*D*Cl$_3$, 25 ^{o}C) of **run 4.5**; X denotes solvent peak. †

A.

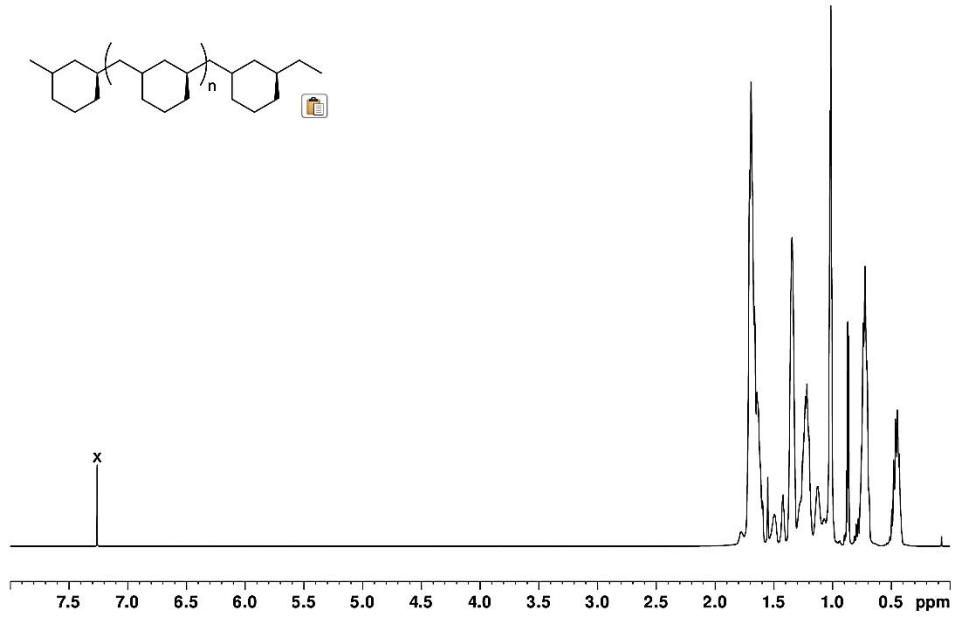

B.

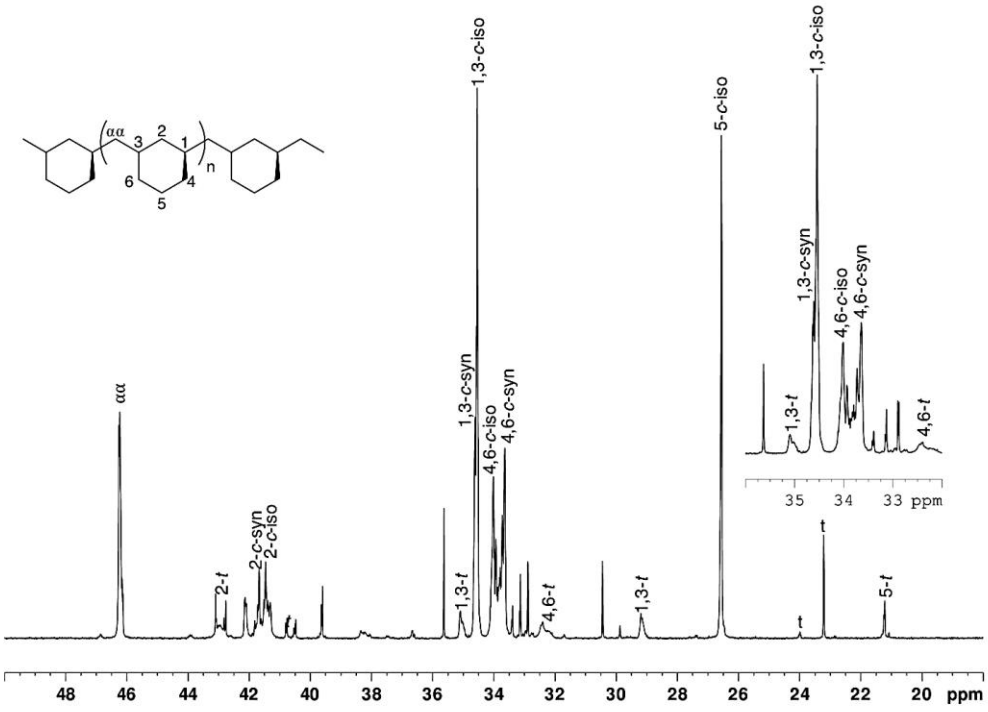

Figure S4.7. (A) ^{1}H NMR (800 MHz, C*D*Cl$_3$, 25 ^{o}C) of **run 4.6**. (B) Partial ^{13}C{^{1}H} NMR (200 MHz, C*D*Cl$_3$, 25 ^{o}C) of **run 4.6**; X denotes solvent peak.[†]

A.

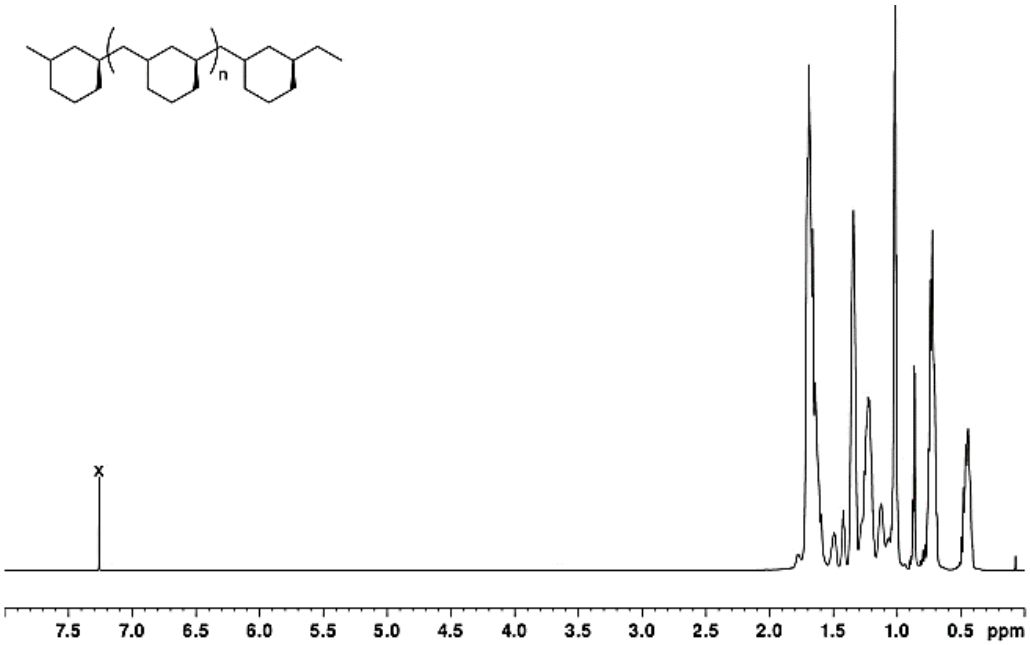

B.

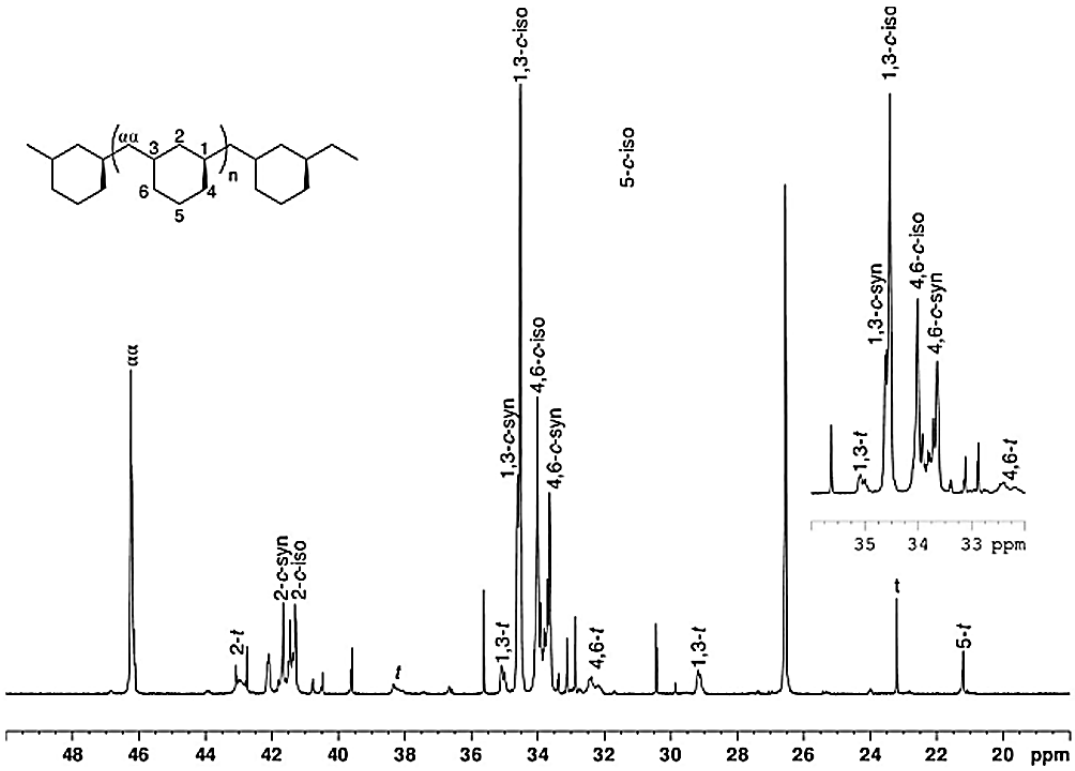

Figure S.4.8. (A) ^{1}H NMR (800 MHz, C*D*Cl$_3$, 25 ^{o}C) of **run 4.7**. (B) Partial ^{13}C{^{1}H} NMR (200 MHz, C*D*Cl$_3$, 25 ^{o}C) of **run 4.7**; X denotes solvent peak.†

A.

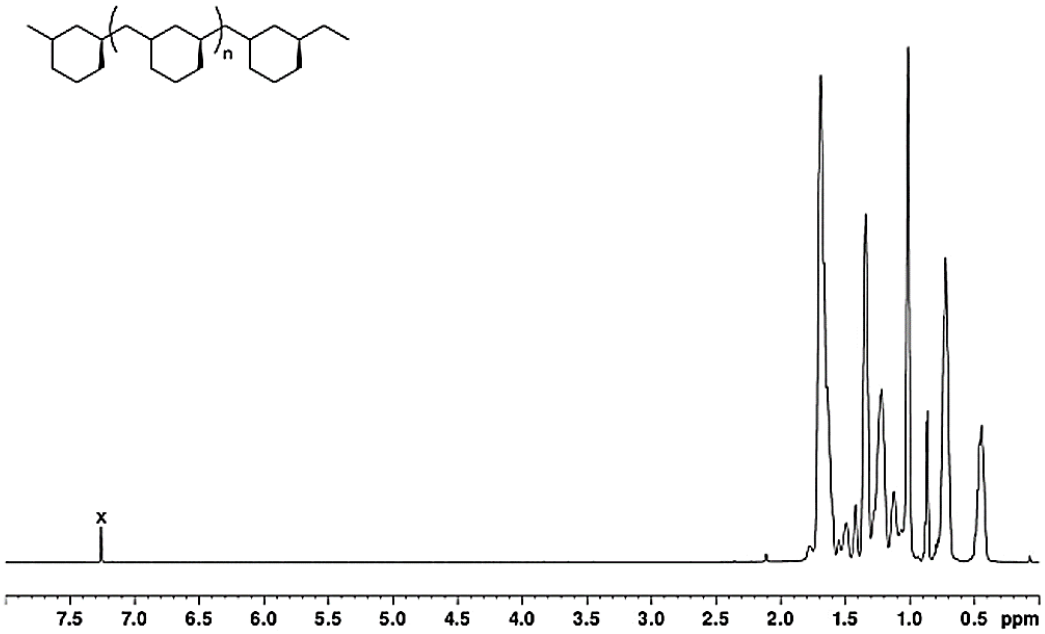

B.

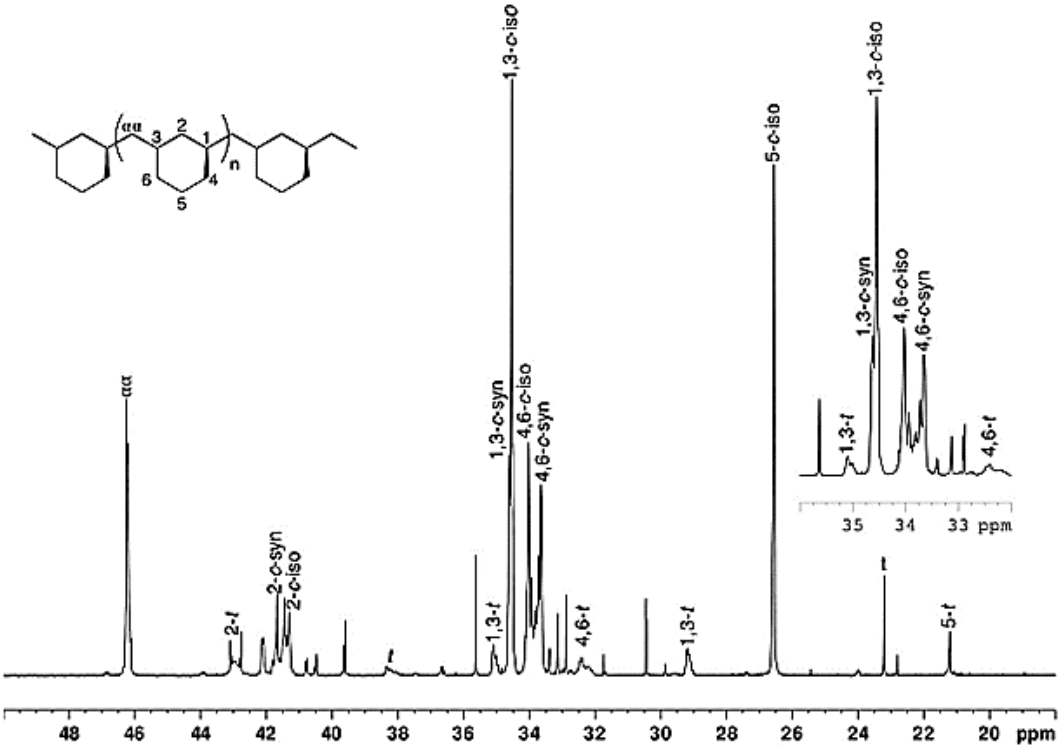

Figure S4.9. (A) ^{1}H NMR (800 MHz, C*D*Cl$_3$, 25 ^{o}C) of **run 4.8**. (B) Partial ^{13}C{^{1}H} NMR (200 MHz, C*D*Cl$_3$, 25 ^{o}C) of **run 4.8**; X denotes solvent peak.†

A.

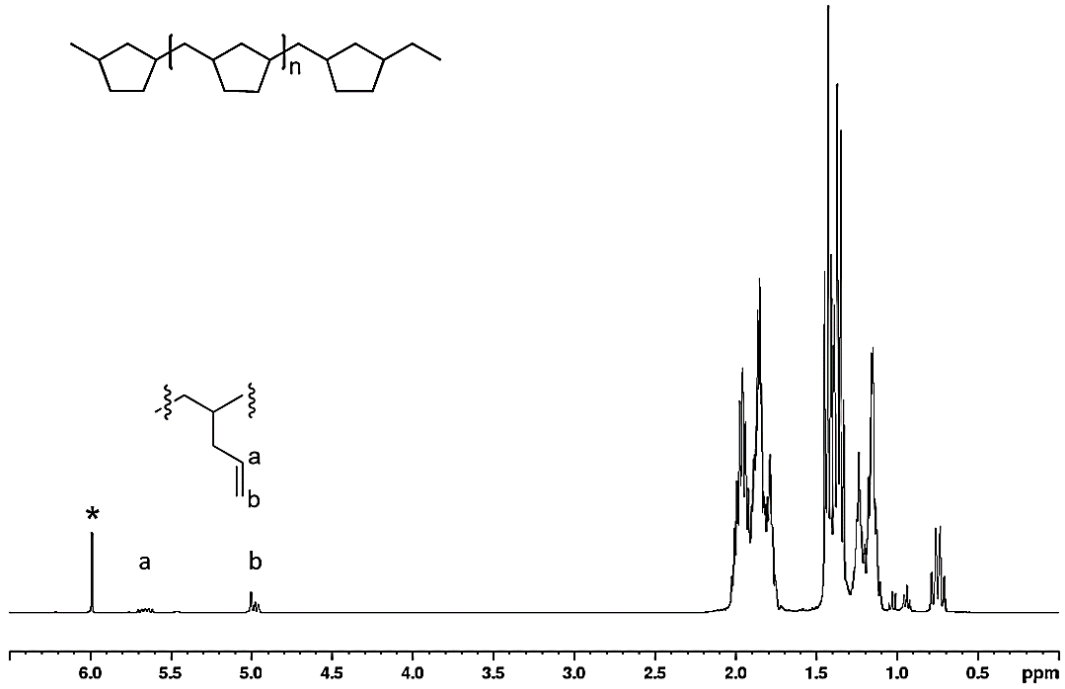

B.

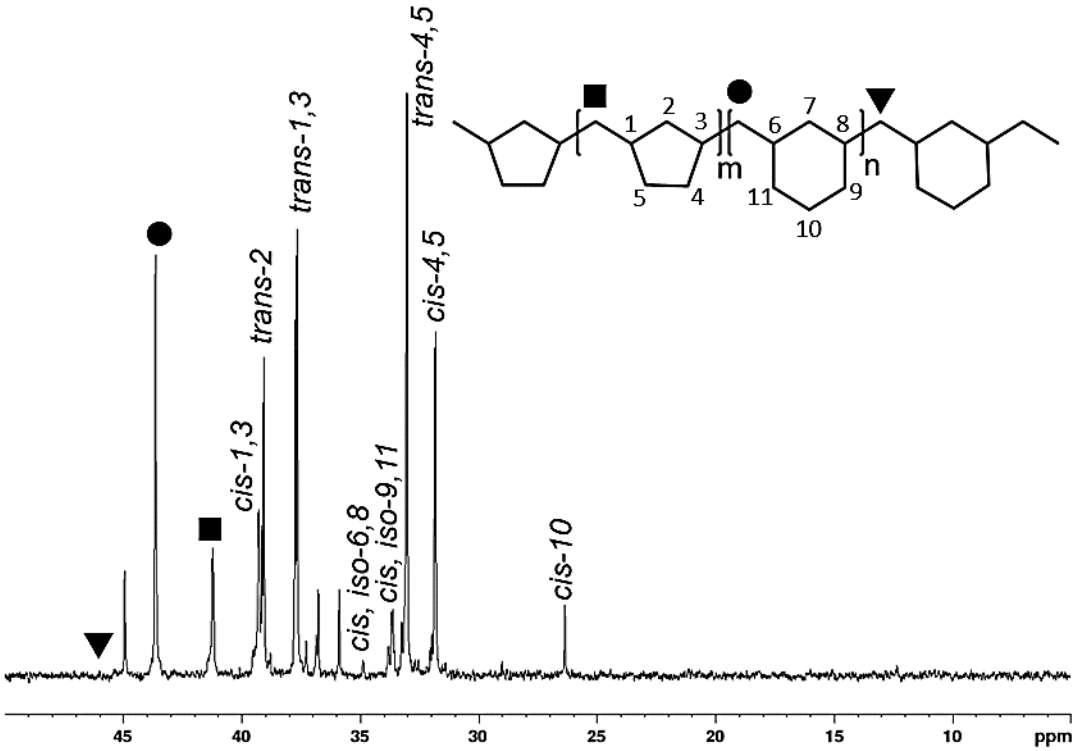

Figure S4.10. (A) ^{1}H NMR (400 MHz, *1,1,2,2,C_2Cl_4-d2) of **4.10.** (B) partial ^{13}C-NMR (100 MHz, ,1,2,2,C_2Cl_4-d2) of **run 4.10** (100:0, PMCP:PMCH), notice the presence on vinyl peaks, this is present in all runs **4.10-4.18**.

A.

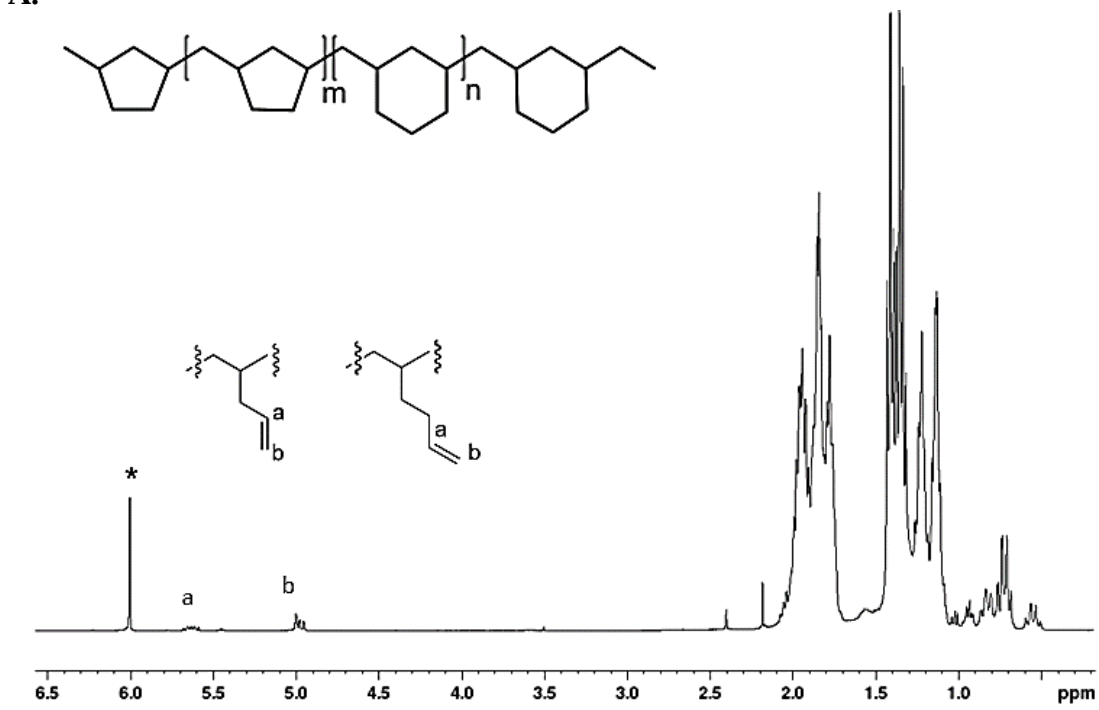
m
n
a
b
a
b
*
a
b
6.5
6.0
5.5
5.0
4.5
4.0
3.5
3.0
2.5
2.0
1.5
1.0
ppm

B.

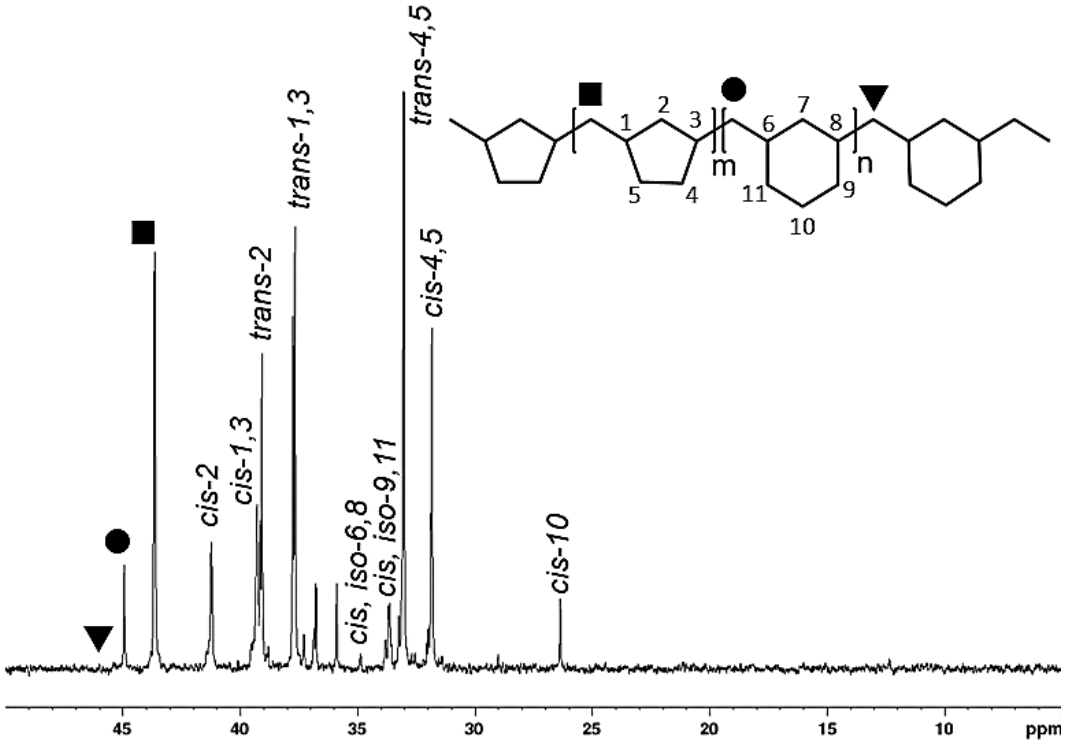
trans-4,5
trans-1,3
trans-2
cis-4,5
cis-2
cis-1,3
cis, iso-6,8
cis, iso-9,11
cis-10
1
2
3
4
5
6
7
8
9
10
11
m
n
45
40
35
30
25
20
15
10
ppm

C.

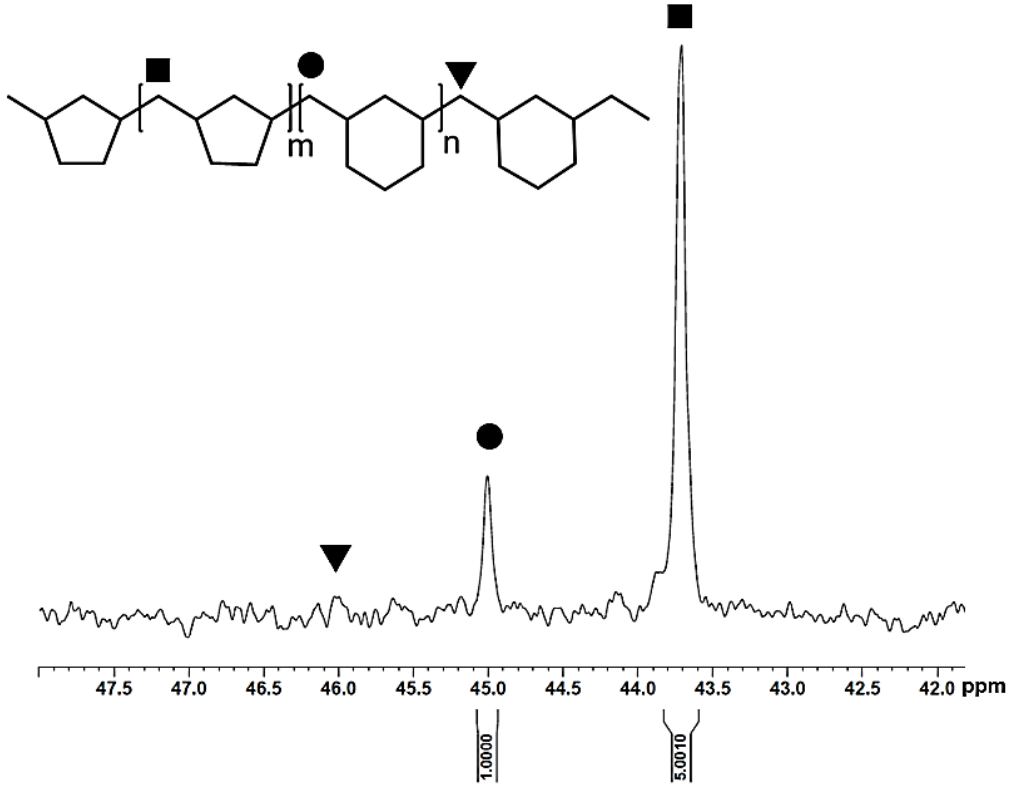

Figure S4.11. (A) ^{1}H NMR (400 MHz, *1,1,2,2,C_2Cl_4-d2) of **2.** (B) partial ^{13}C-NMR (100 MHz, ,1,2,2,C_2Cl_4-d2) of **run 4.11** (90:10, PMCP:PMCH). (C) partial inverse gated ^{13}C-NMR (100 MHz, ,1,2,2,C_2Cl_4-d2) of **run 4.11,** used for integration.

A.

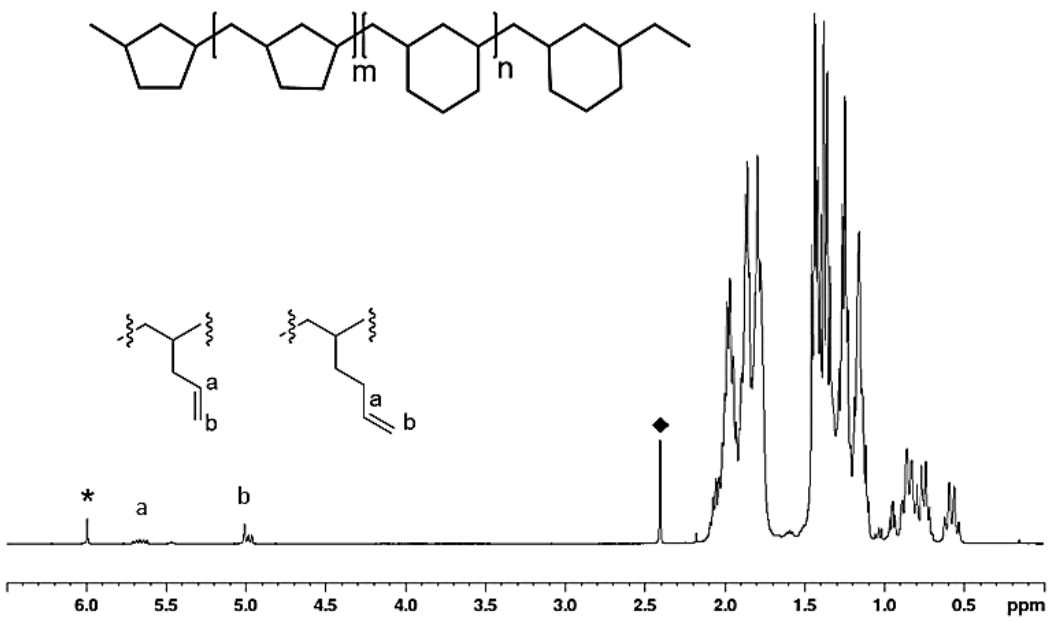
m
n
a
b
a
b
*
a
b
6.0
5.5
5.0
4.5
4.0
3.5
3.0
2.5
2.0
1.5
1.0
0.5
ppm

B.

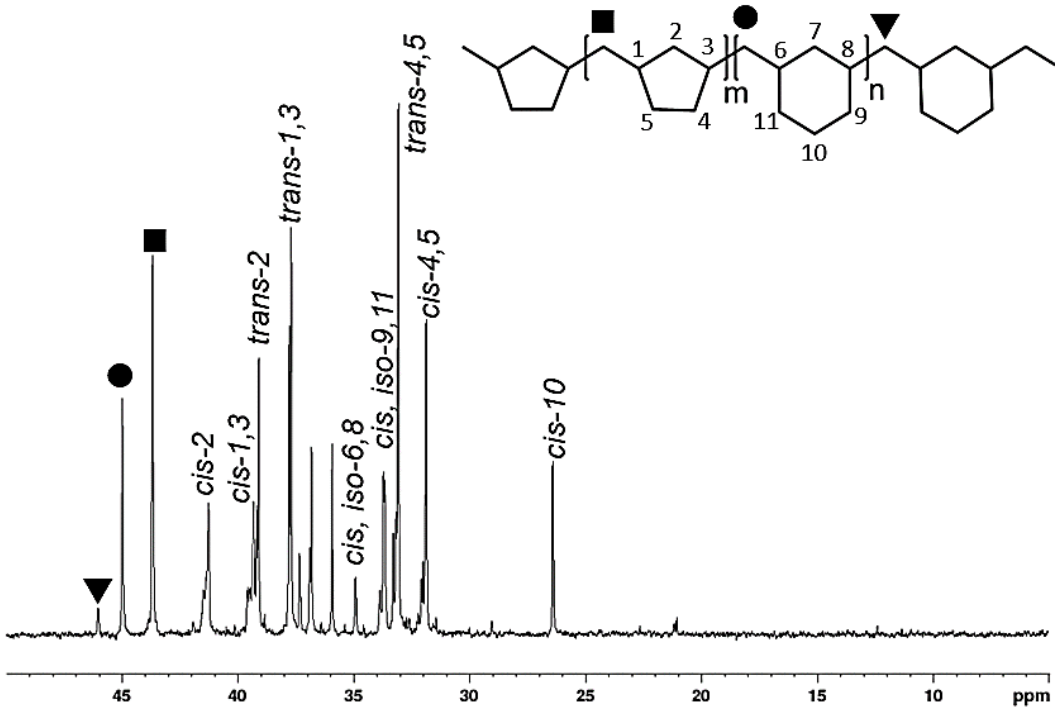
1
2
3
6
7
8
m
n
5
4
11
9
10
cis-2
cis-1,3
trans-2
trans-1,3
cis, iso-6,8
cis, iso-9,11
trans-4,5
cis-4,5
cis-10
45
40
35
30
25
20
15
10
ppm

C.

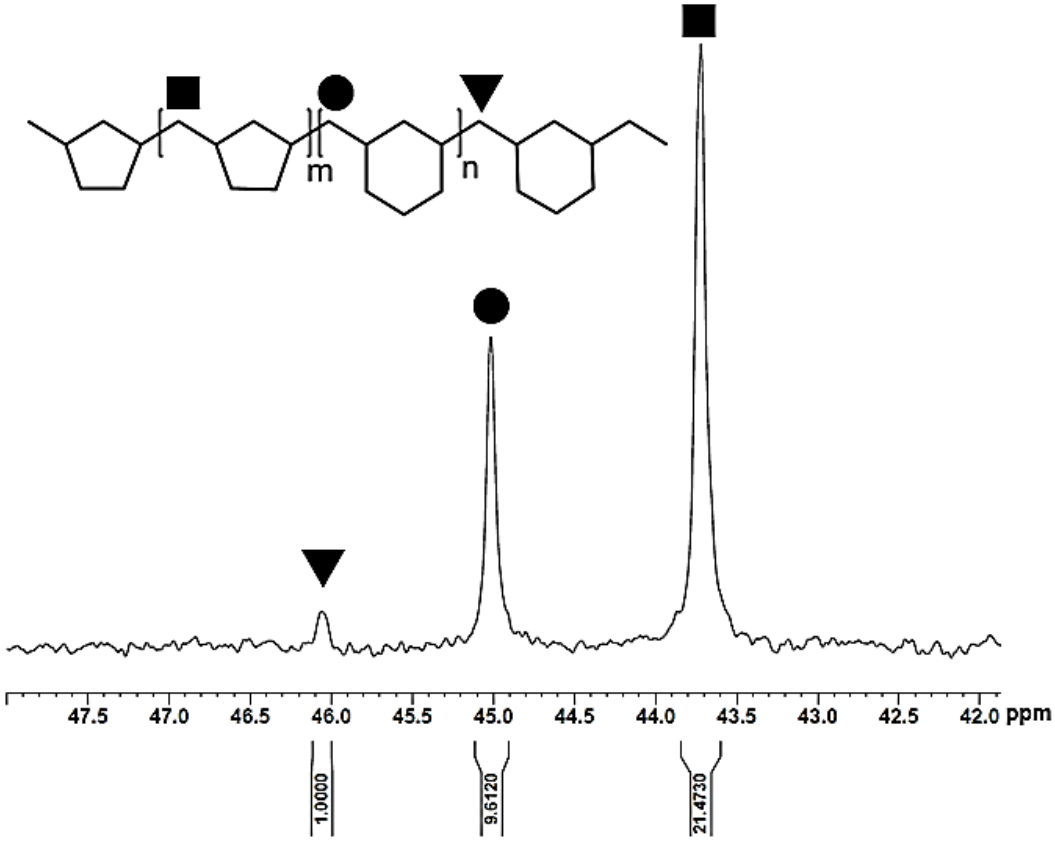

Figure S4.12. (A) ^{1}H NMR (400 MHz, *1,1,2,2,C_2Cl_4-d2, ◆-toluene) of **run 4.12 .** (B) partial ^{13}C-NMR (100 MHz, ,1,2,2,C_2Cl_4-d2) of **run 4.12** (80:20, PMCP:PMCH). (C) partial inverse gated ^{13}C-NMR (100 MHz, ,1,2,2,C_2Cl_4-d2) of **run 4.12,** used for integration.

A.

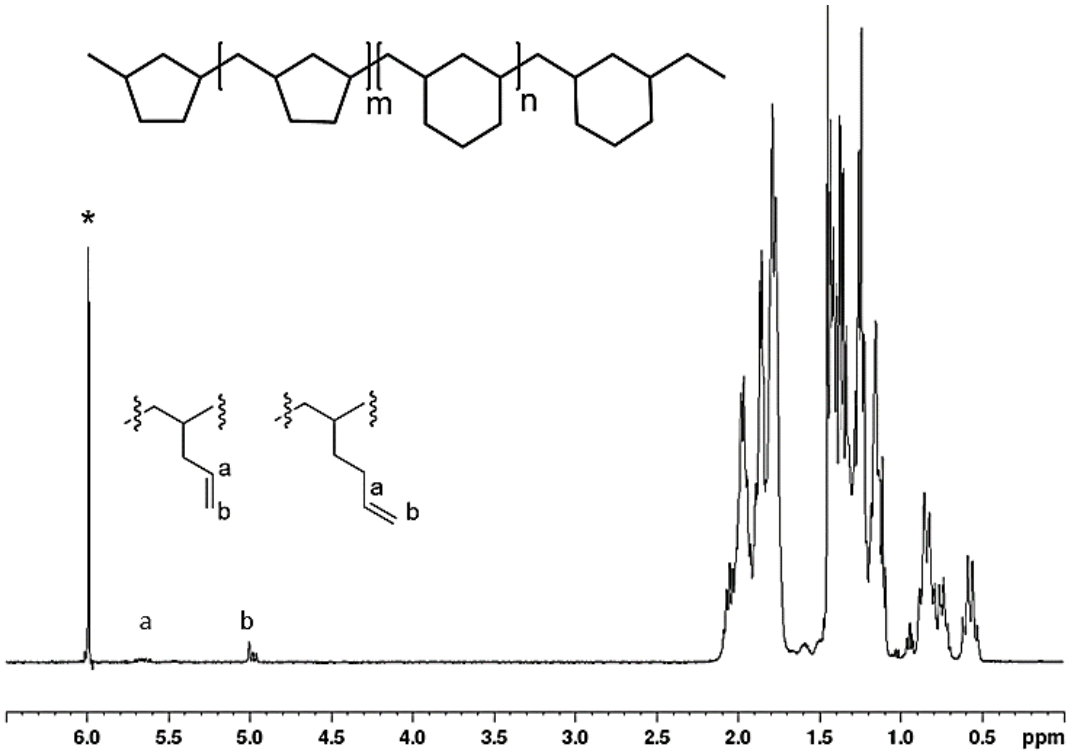
m
n
*
a
b
a
b
a
b
6.0
5.5
5.0
4.5
4.0
3.5
3.0
2.5
2.0
1.5
1.0
0.5
ppm

B.

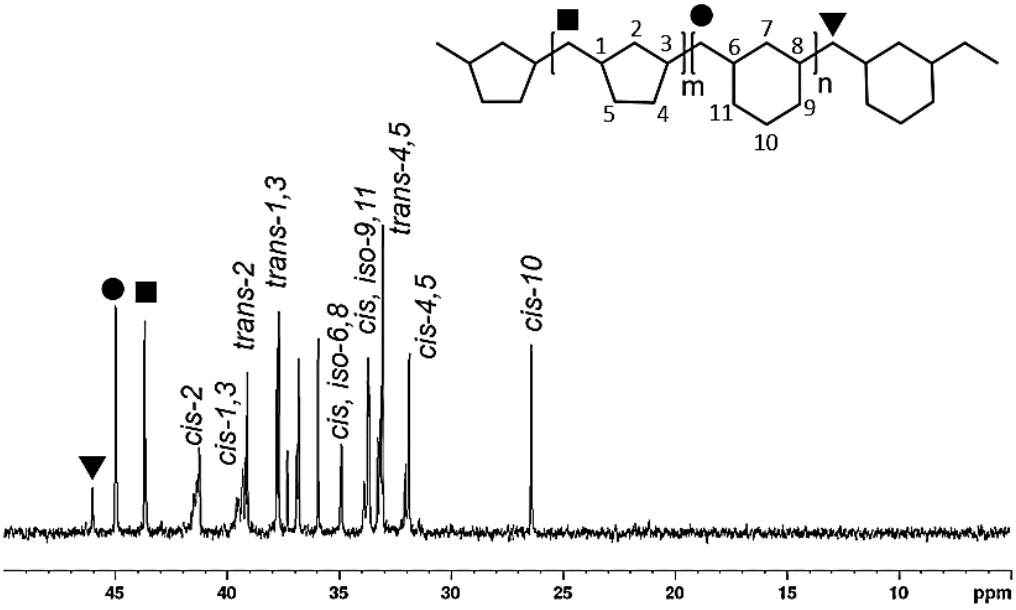
1
2
3
4
5
6
7
8
9
10
11
m
n
cis-2
cis-1,3
trans-2
trans-1,3
cis, iso-6,8
cis, iso-9,11
trans-4,5
cis-4,5
cis-10
45
40
35
30
25
20
15
10
ppm

C.

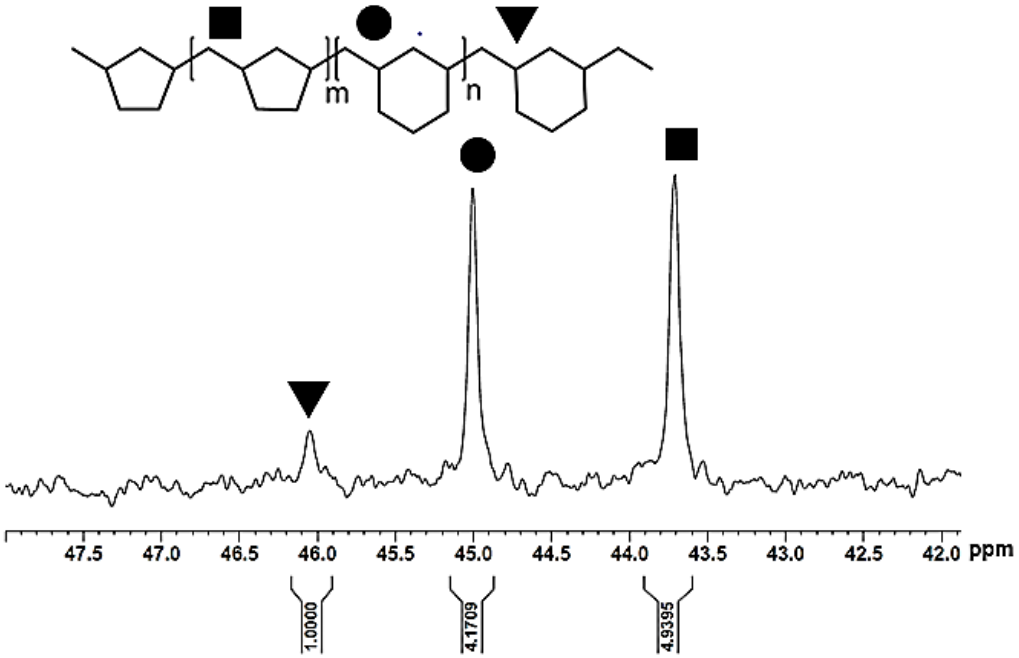

Figure S4.13. (A) ^{1}H NMR (400 MHz, *1,1,2,2,C_2Cl_4-d2) of **4.** (B) partial ^{13}C-NMR (100 MHz, ,1,2,2,C_2Cl_4-d2) of **run 4.13** (70:30, PMCP:PMCH). (C) partial inverse gated ^{13}C-NMR (100 MHz, ,1,2,2,C_2Cl_4-d2) of **run 4.13,** used for integration.

A.

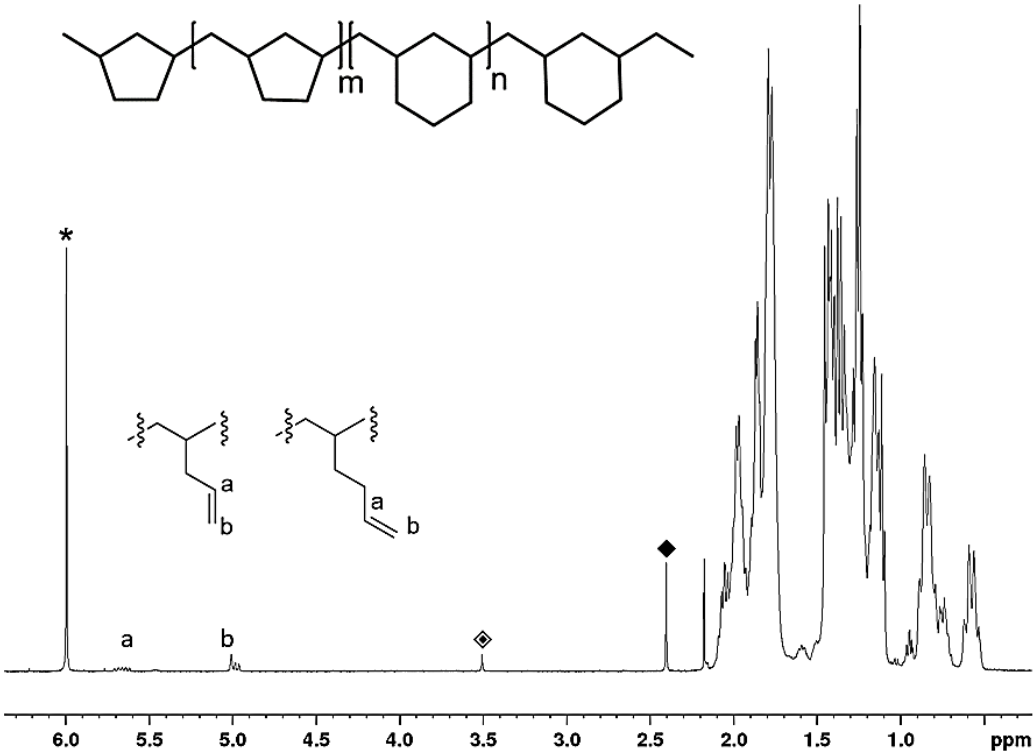
m
n
*
a
b
a
b
a
b
a
b
6.0
5.5
5.0
4.5
4.0
3.5
3.0
2.5
2.0
1.5
1.0
ppm

B.

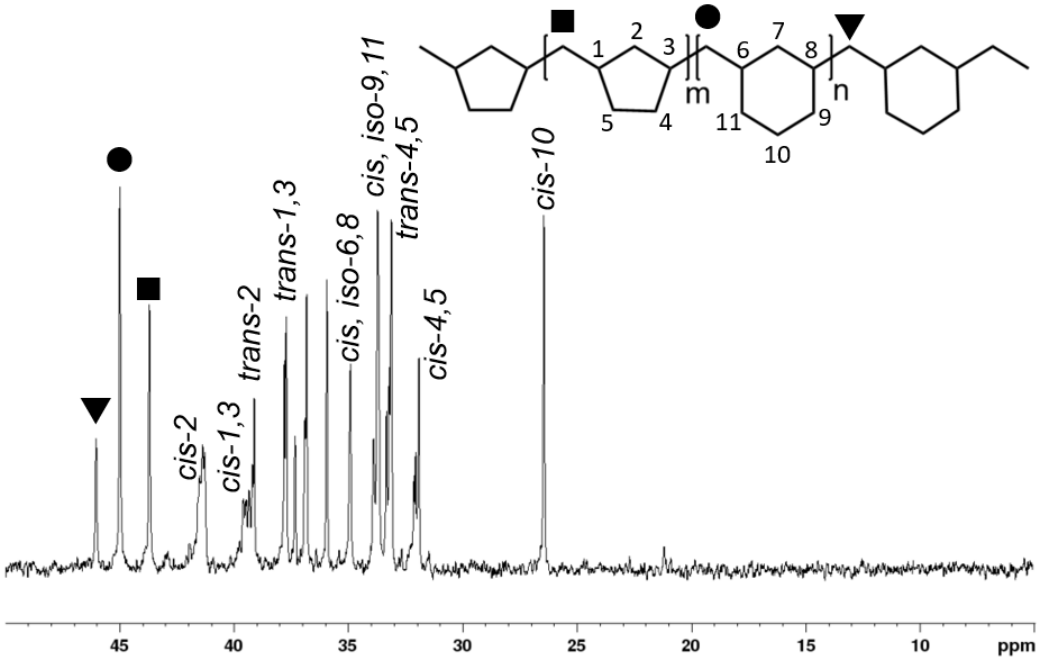
1
2
3
4
5
6
7
8
9
10
11
m
n
cis-10
cis-4,5
cis, iso-6,8
trans-1,3
trans-2
cis-1,3
cis-2
trans-4,5
cis, iso-9,11
45
40
35
30
25
20
15
10
ppm

C.

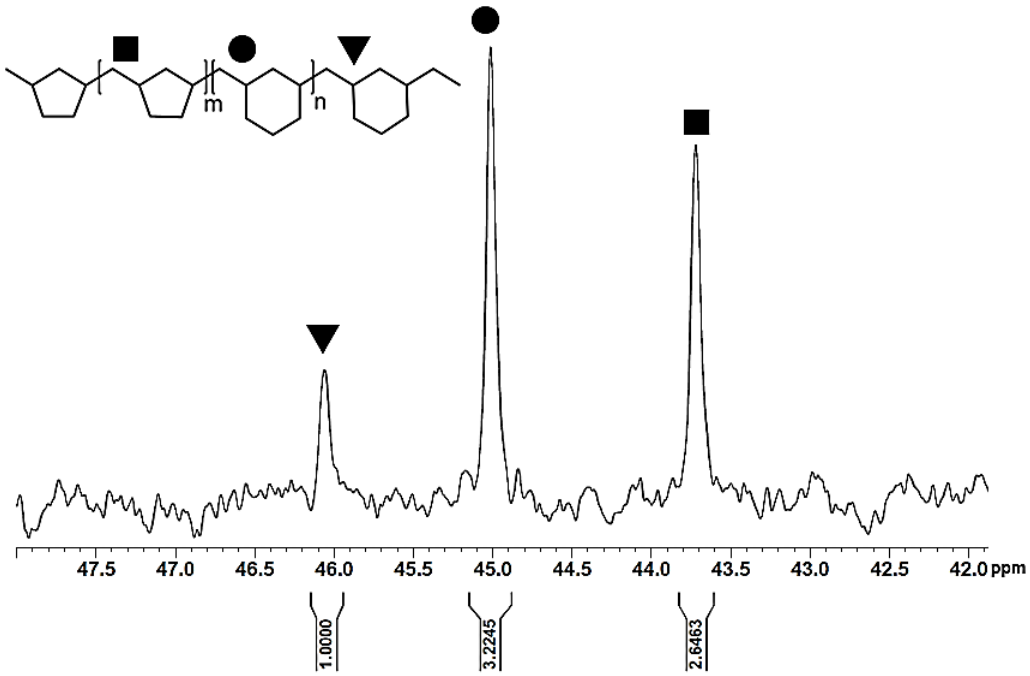

Figure S4.14. (A) ^{1}H NMR (400 MHz, *1,1,2,2,C_2Cl_4-d2, ◈-methanol, ◆-toluene) of **run 4.14.** (B) partial ^{13}C-NMR (100 MHz, ,1,2,2,C_2Cl_4-d2) of **run 4.14** (60:40, PMCP:PMCH). (C) partial inverse gated ^{13}C-NMR (100 MHz, ,1,2,2,C_2Cl_4-d2) of **run 4.14,** used for integration.

A.

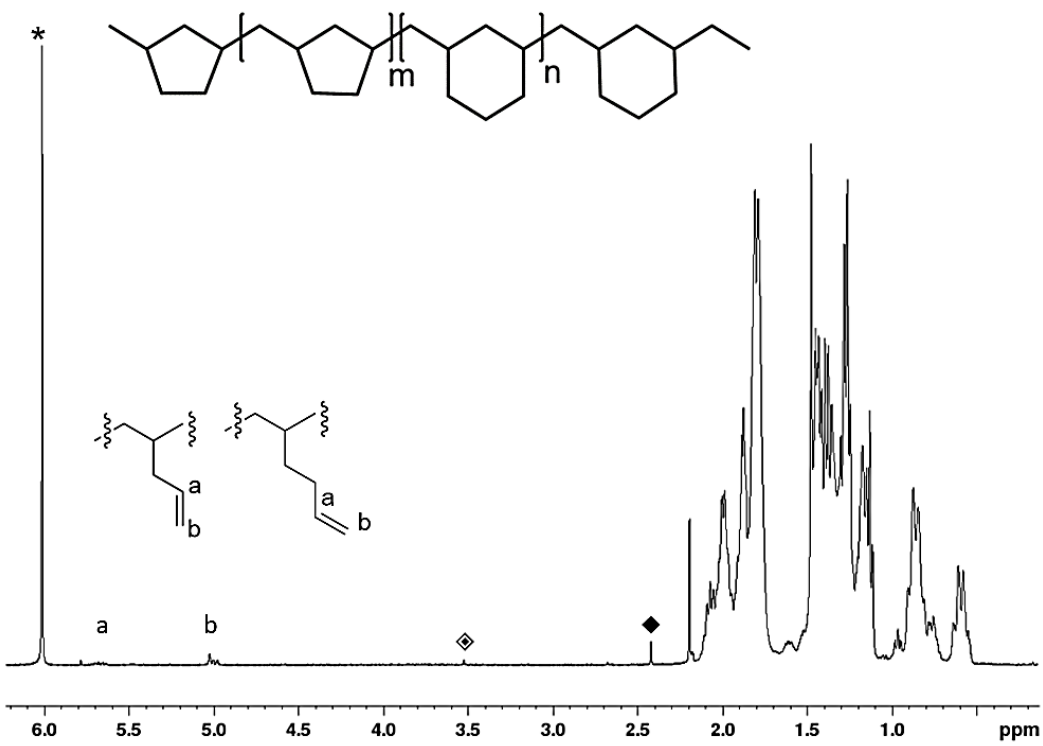
*
m
n
a
b
a
b
a
b
6.0
5.5
5.0
4.5
4.0
3.5
3.0
2.5
2.0
1.5
1.0
ppm

B.

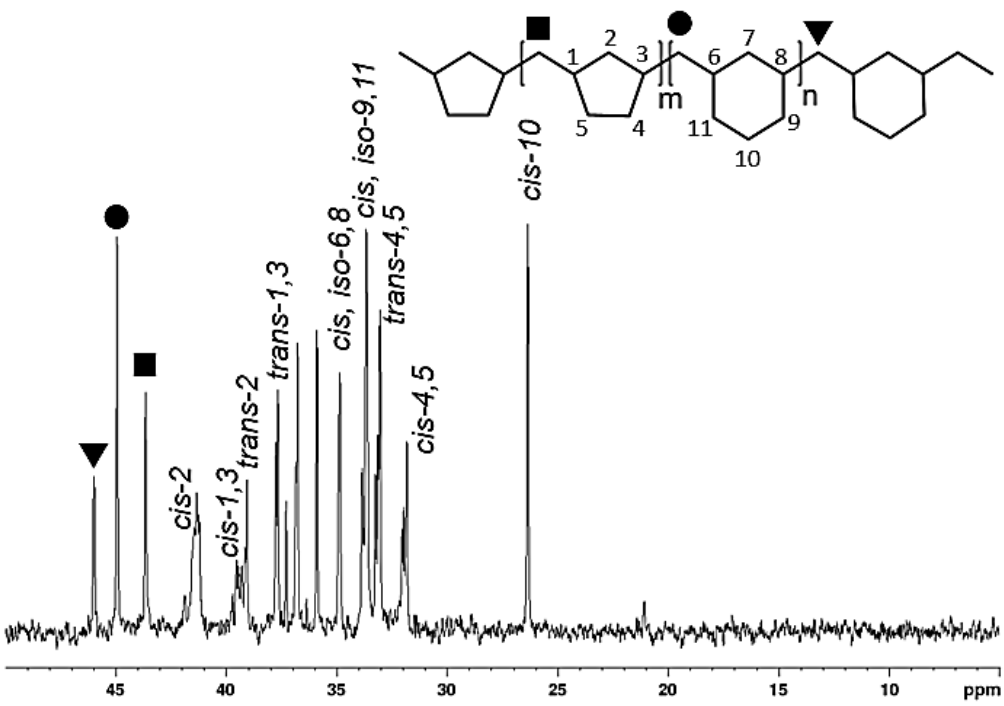
1
2
3
m
6
7
8
n
5
4
11
9
10
cis-10
cis, iso-9,11
cis, iso-6,8
trans-4,5
trans-1,3
trans-2
cis-4,5
cis-2
cis-1,3
45
40
35
30
25
20
15
10
ppm

C.

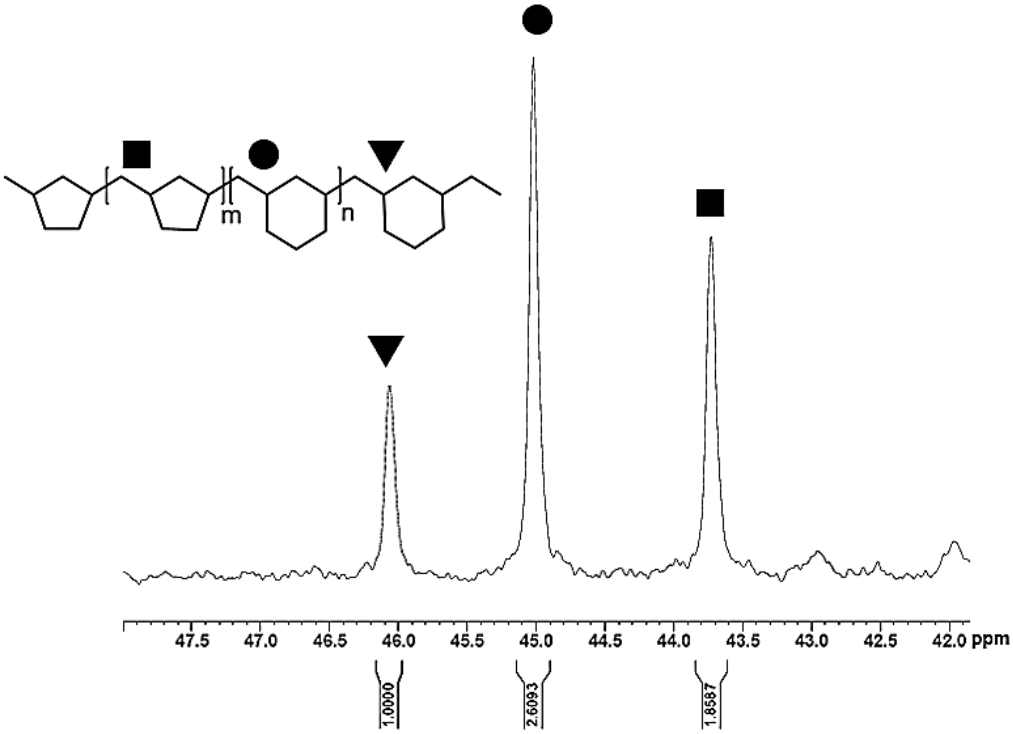

Figure S4.15. (A) ^{1}H NMR (400 MHz, *1,1,2,2,C_2Cl_4-d2, ◈-methanol, ◆-toluene) of **run 4.15.** (B) partial ^{13}C-NMR (100 MHz, ,1,2,2,C_2Cl_4-d2) of **run 4.15** (50:50, PMCP:PMCH). (C) partial inverse gated ^{13}C-NMR (100 MHz, ,1,2,2,C_2Cl_4-d2) of **run 4.15,** used for integration.

A.

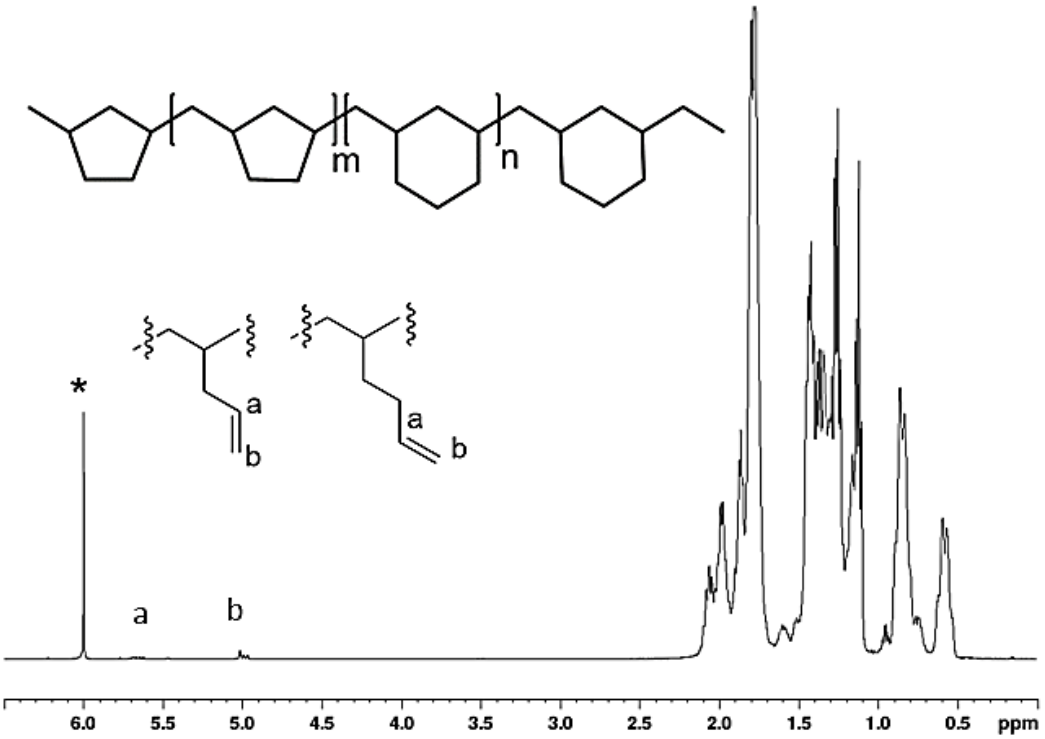
m
n
*
a
b
a
b
a
b
6.0
5.5
5.0
4.5
4.0
3.5
3.0
2.5
2.0
1.5
1.0
0.5
ppm

B.

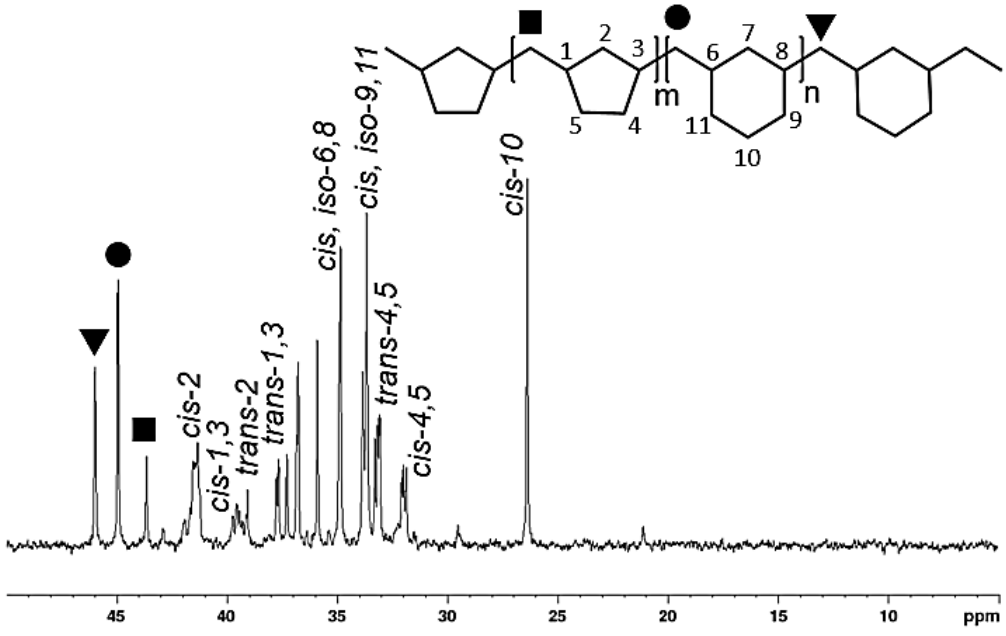
1
2
3
4
5
6
7
8
9
10
11
m
n
cis-10
cis, iso-6,8
cis, iso-9,11
trans-4,5
cis-4,5
cis-2
cis-1,3
trans-2
trans-1,3
45
40
35
30
25
20
15
10
ppm

C.

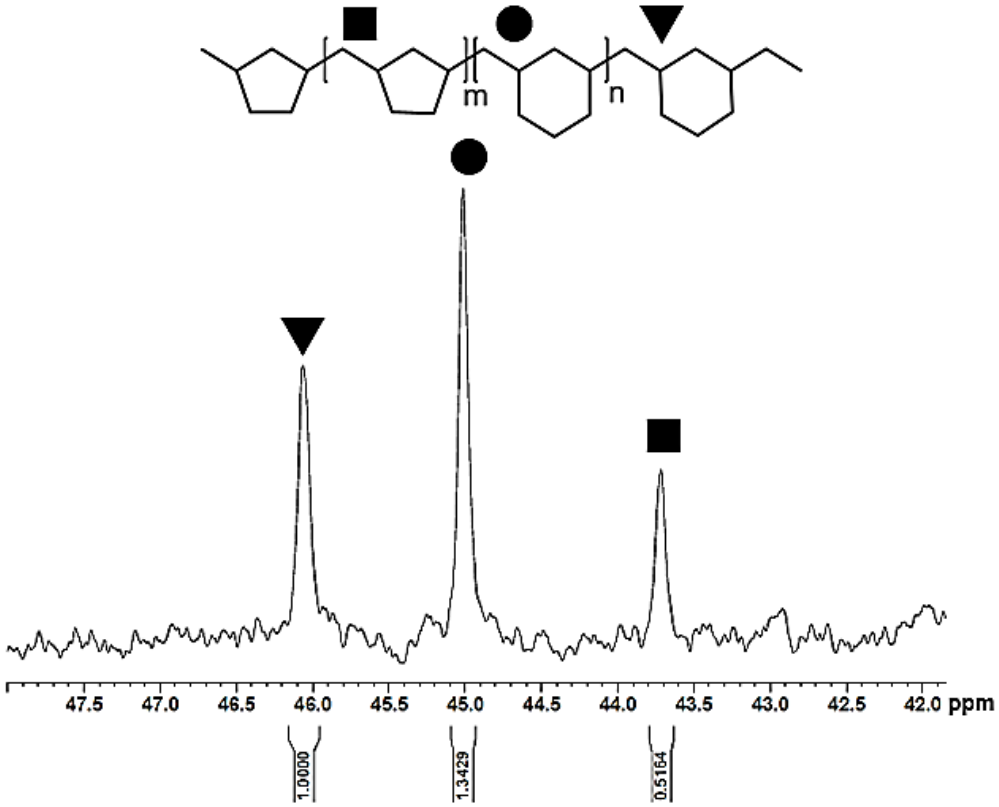

Figure S4.16. (A) ^{1}H NMR (400 MHz, *1,1,2,2,C_2Cl_4-d2) of **run 4.16.** (B) partial ^{13}C-NMR (100 MHz, ,1,2,2,C_2Cl_4-d2) of **run 4.16** (40:60, PMCP:PMCH). (C) partial inverse gated ^{13}C-NMR (100 MHz, ,1,2,2,C_2Cl_4-d2) of **run 4.16,** used for integration.

A.

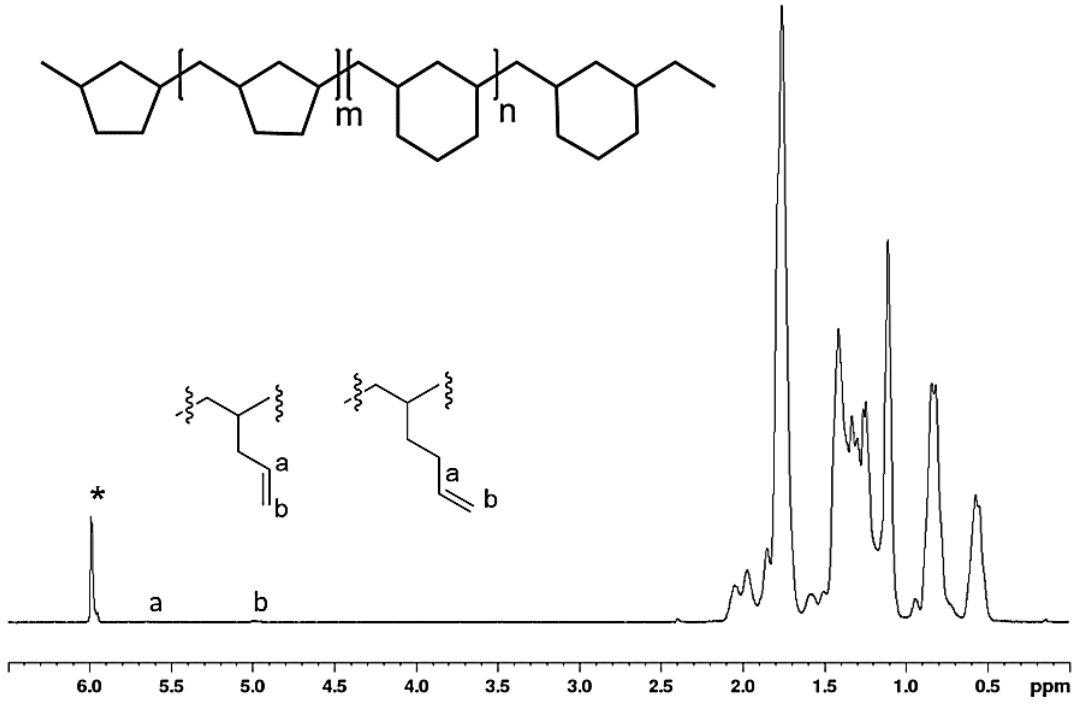

B.

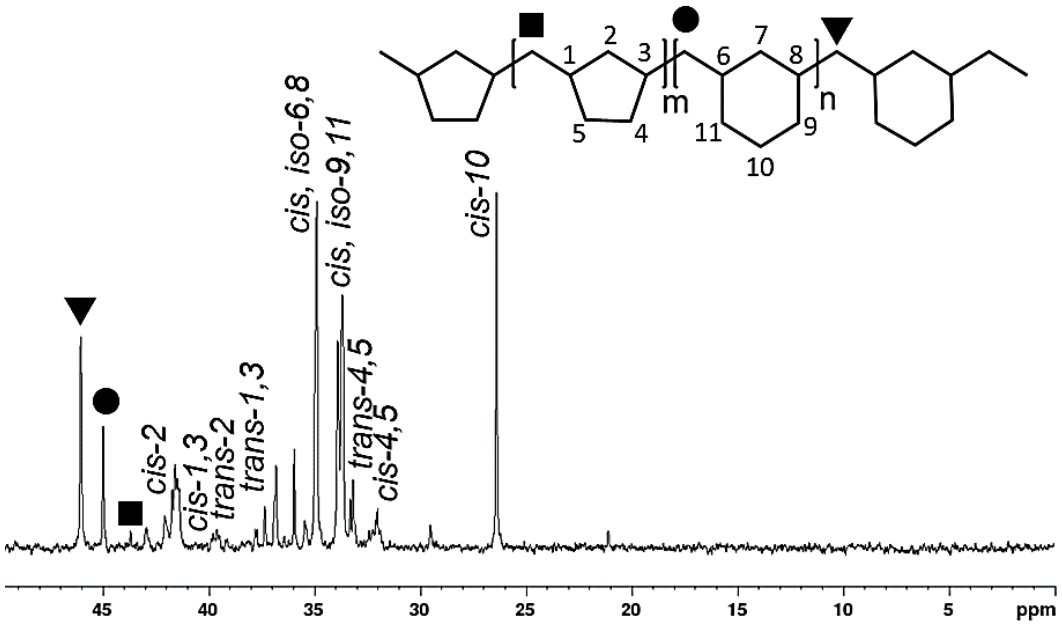

Figure S4.17. (A) ^{1}H NMR (400 MHz, *1,1,2,2,C_2Cl_4-d2) of **run 4.17.** (B) partial ^{13}C-NMR (100 MHz, ,1,2,2,C_2Cl_4-d2) of **run 4.17** (20:80, PMCP:PMCH).

A.

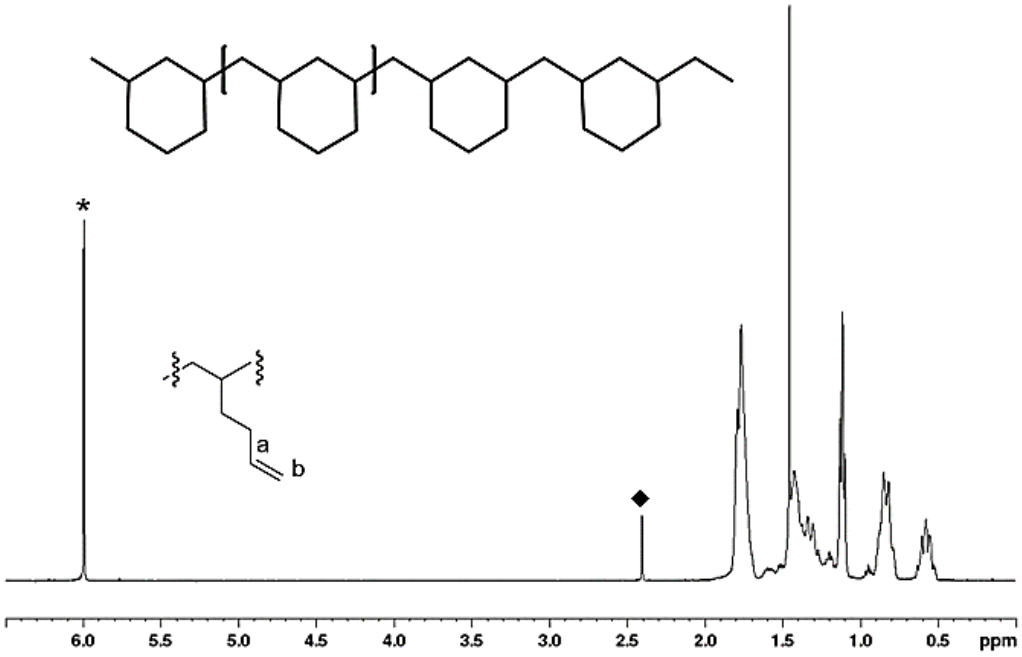

B.

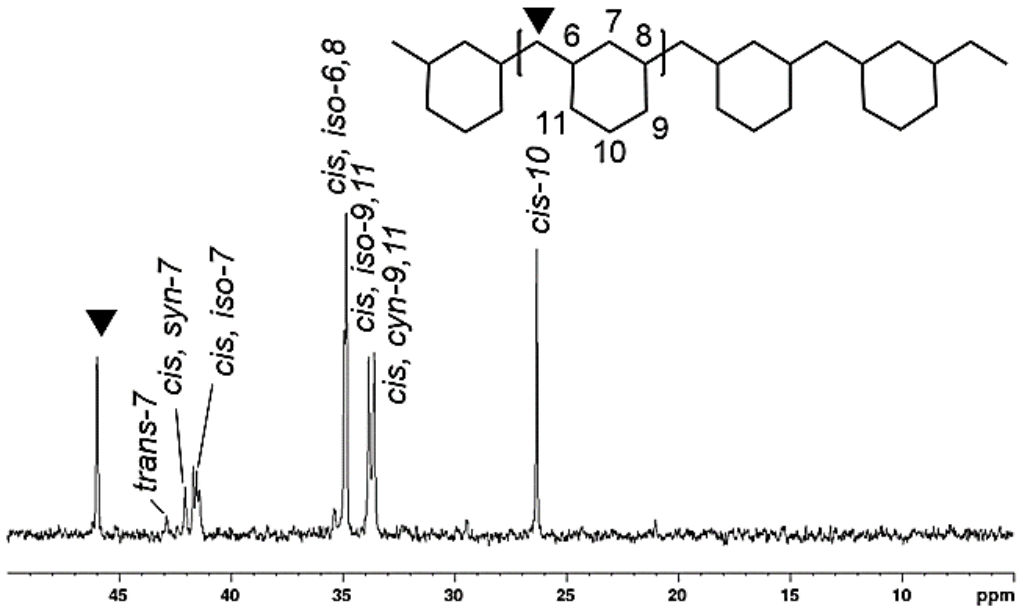

Figure S4.18. (A) ^{1}H NMR (400 MHz, *1,1,2,2,C_2Cl_4-d2) of **run 4.18.** (B) partial ^{13}C-NMR (100 MHz, ,1,2,2,C_2Cl_4-d2) of **run 4.18** (0:100, PMCP:PMCH).

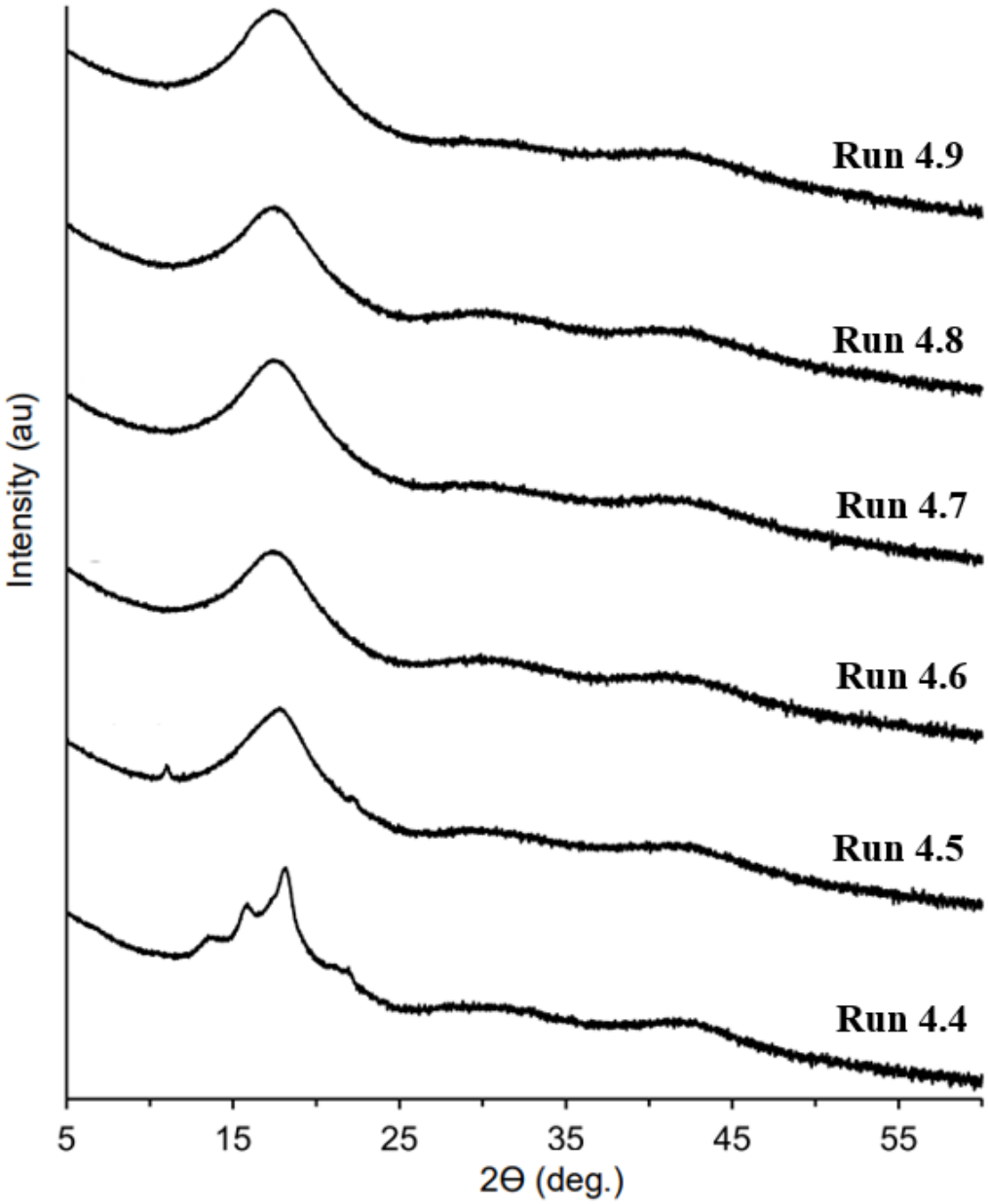

Figure S4.19. Stacked Wide-angle powder x-ray scattering traces of the crystalline and amorphous phases of PMCH from **runs 4.4 – 4.9**.

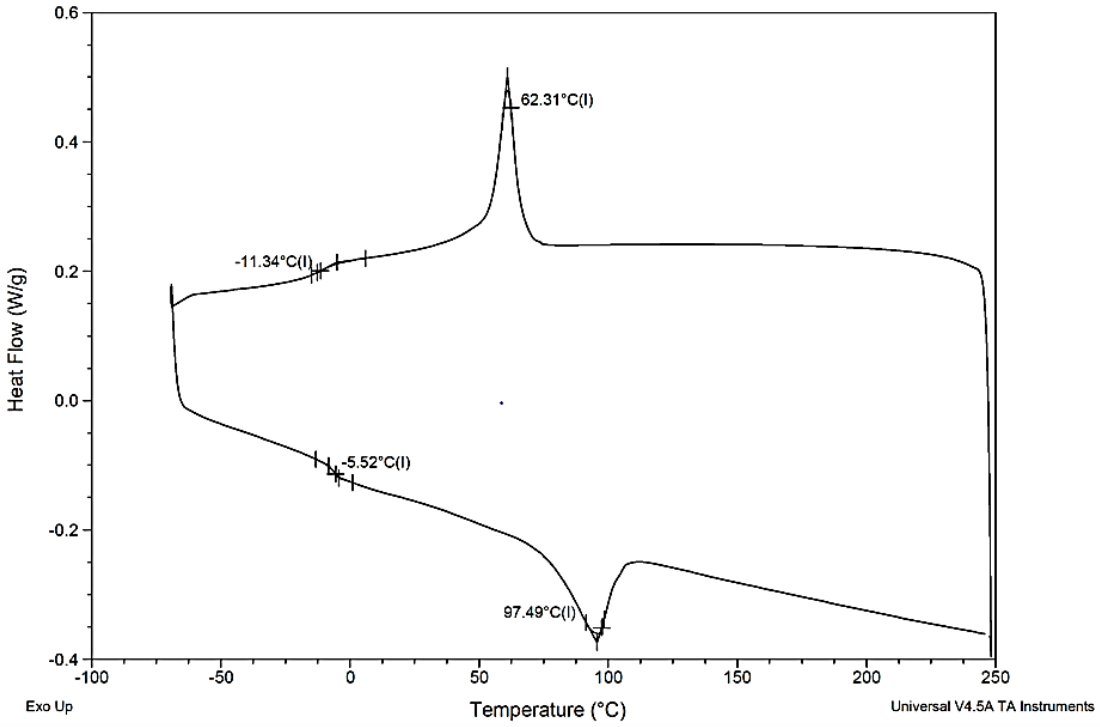

Figure S4.20. DSC trace of the second heating cycle and cooling cycle of PMCP from **run 4.1**.

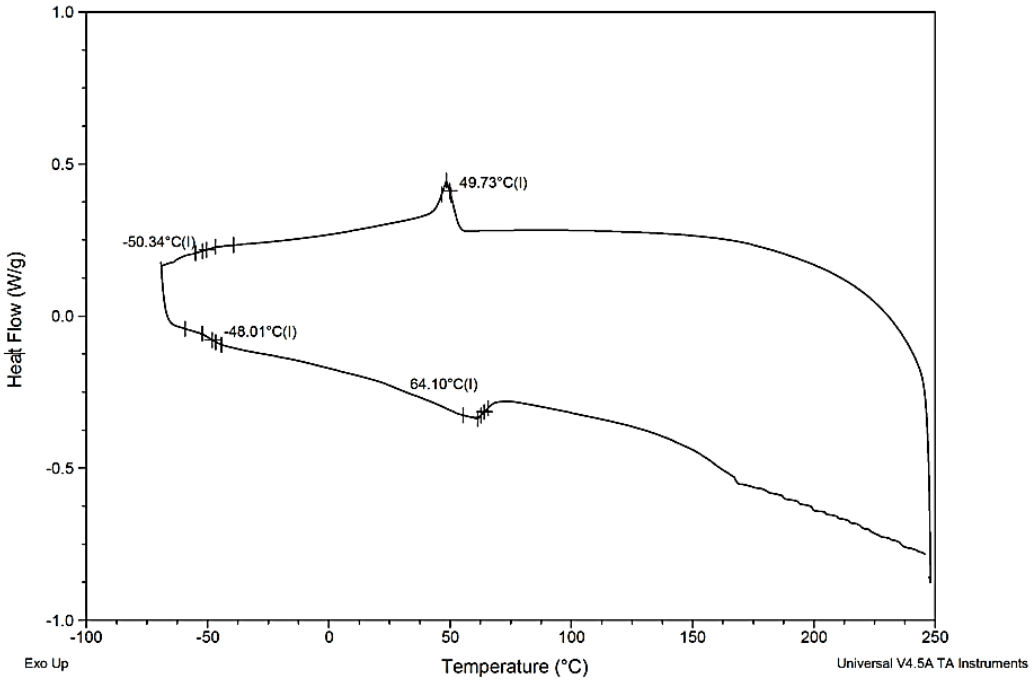

Figure S4.21. DSC trace of the second heating cycle and cooling cycle of PMCP from **run 4.2**.

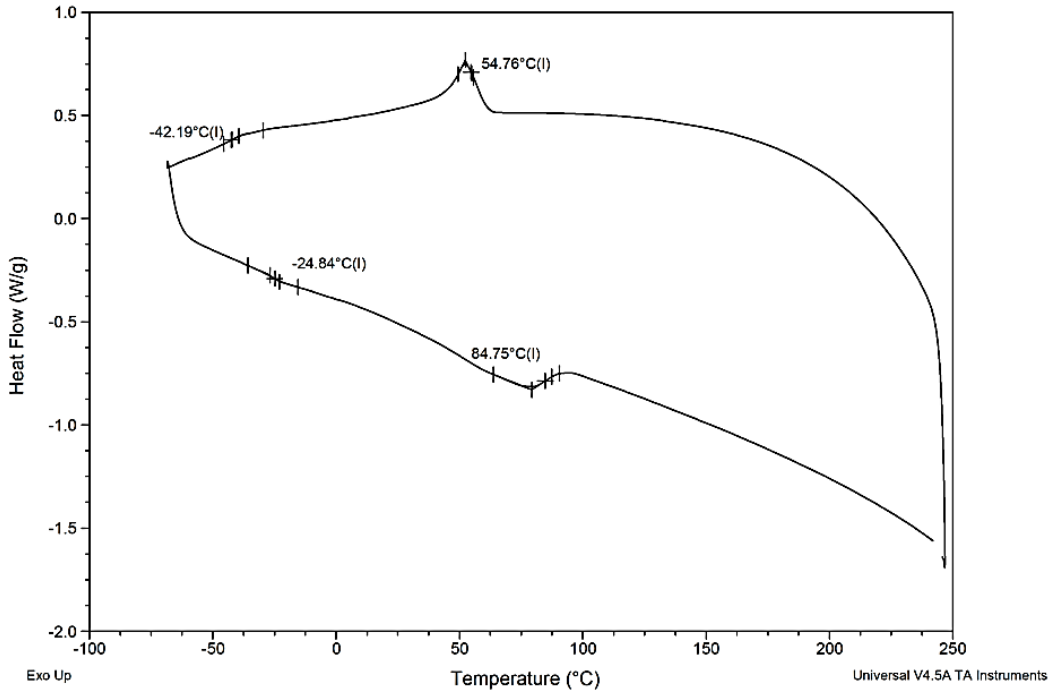

Figure S4.22. DSC trace of the second heating cycle and cooling cycle of PMCP from **run 4.3**.

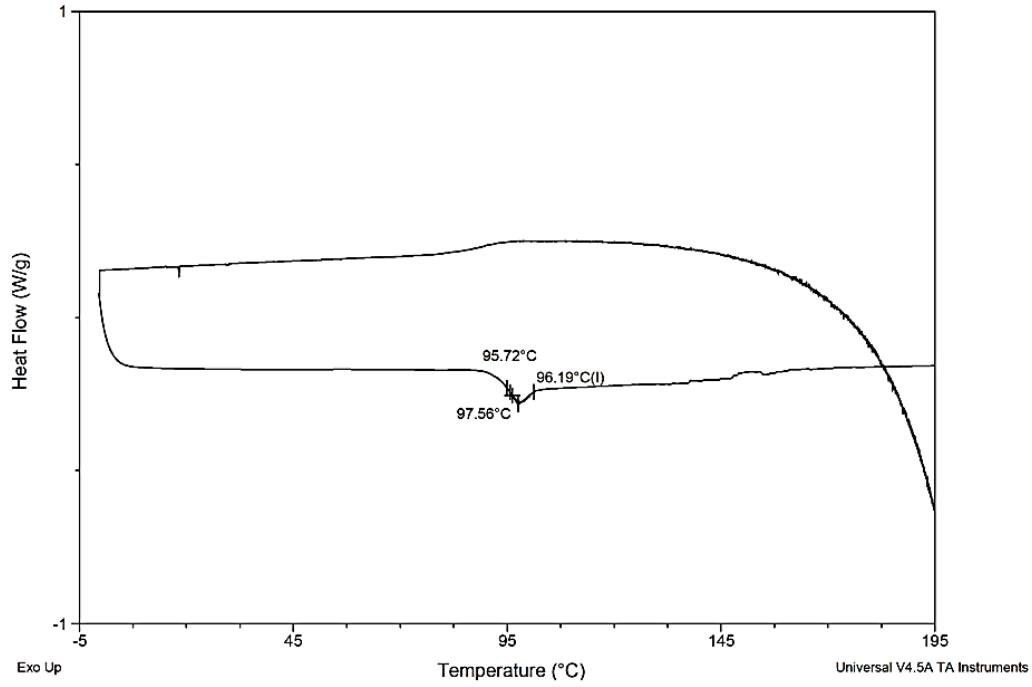

Figure S4.23. DSC trace of the second heating cycle and cooling cycle of PMCP from **run 4.4**.

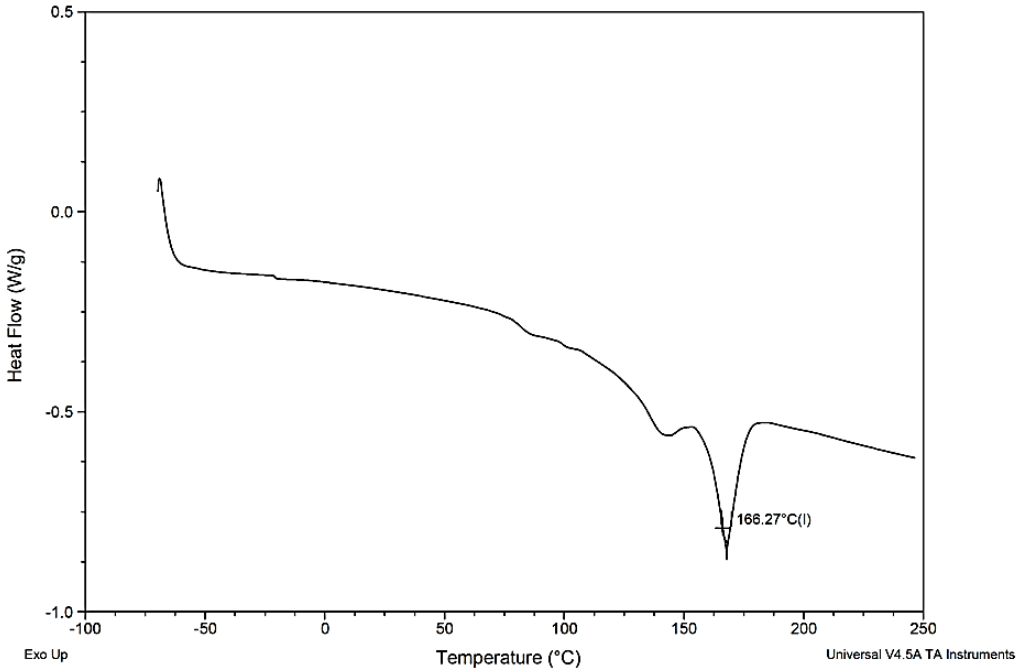

Figure S4.24. DSC trace of the second heating cycle and cooling cycle of PMCP from **run 4.4**.

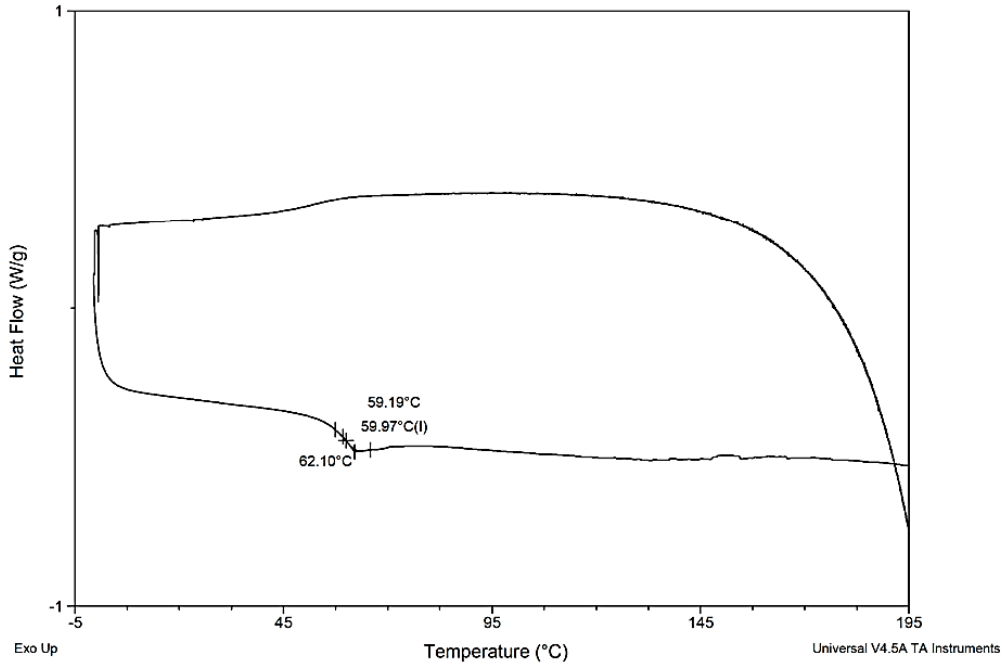

Figure S4.25. DSC trace of the second heating cycle and cooling cycle of PMCP from **run 4.5.**

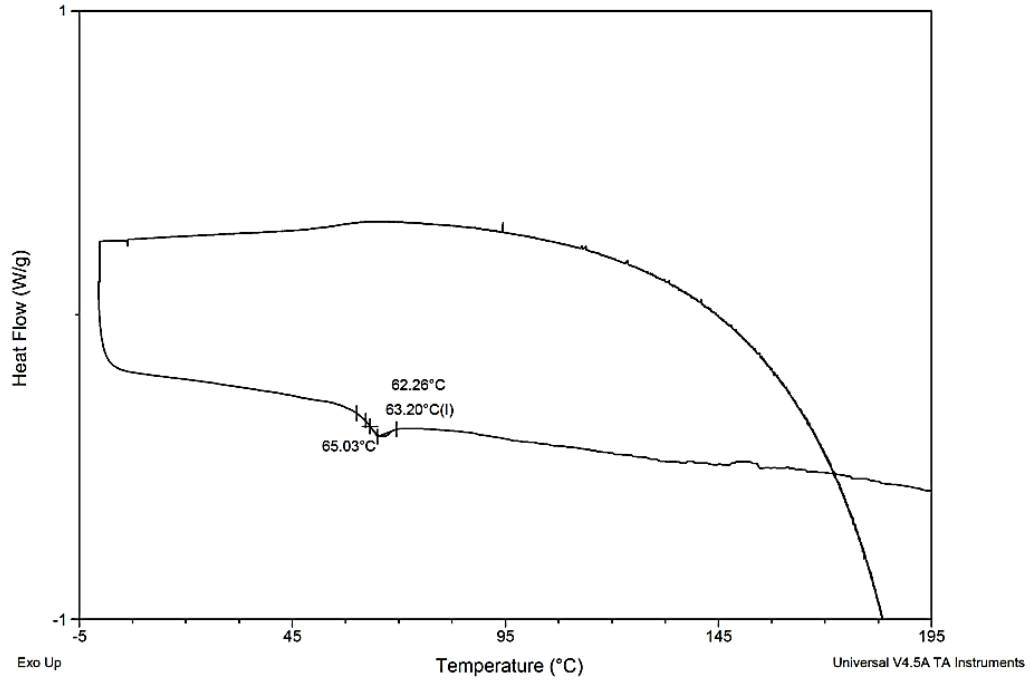

Figure S4.26. DSC trace of the second heating cycle and cooling cycle of PMCP from **run 4.6.**

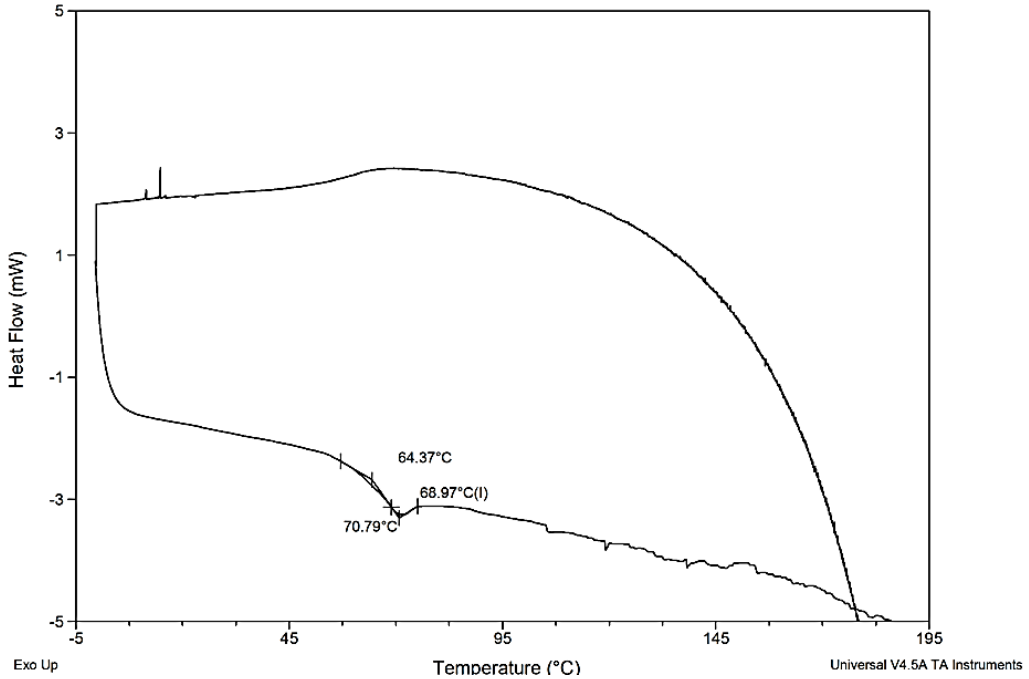

Figure S4.27. DSC trace of the second heating cycle and cooling cycle of PMCP from **run 4.7.**

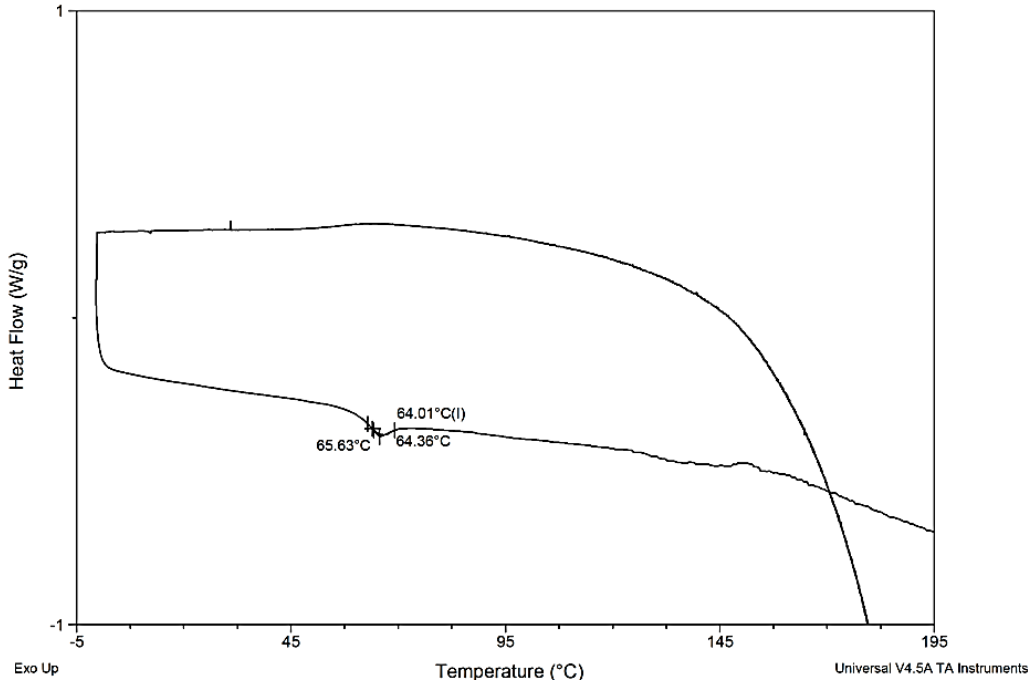

Figure S4.28. DSC trace of the second heating cycle and cooling cycle of PMCP from **run 4.8.**

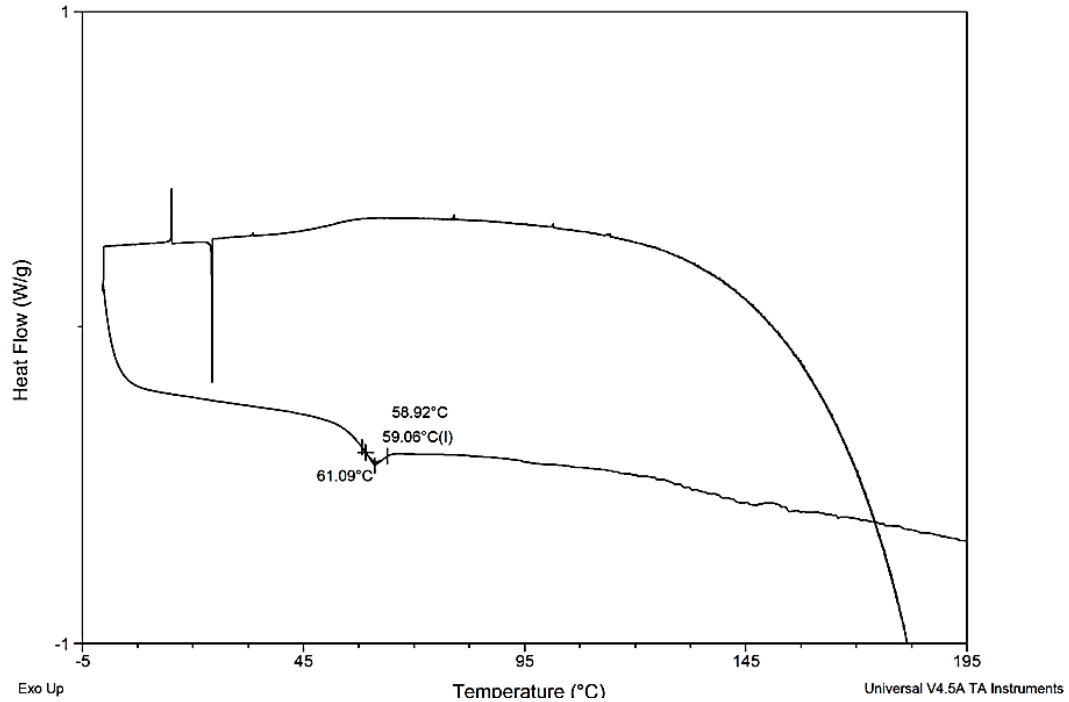

Figure S4.29. DSC trace of the second heating cycle and cooling cycle of PMCP from **run 4.9.**

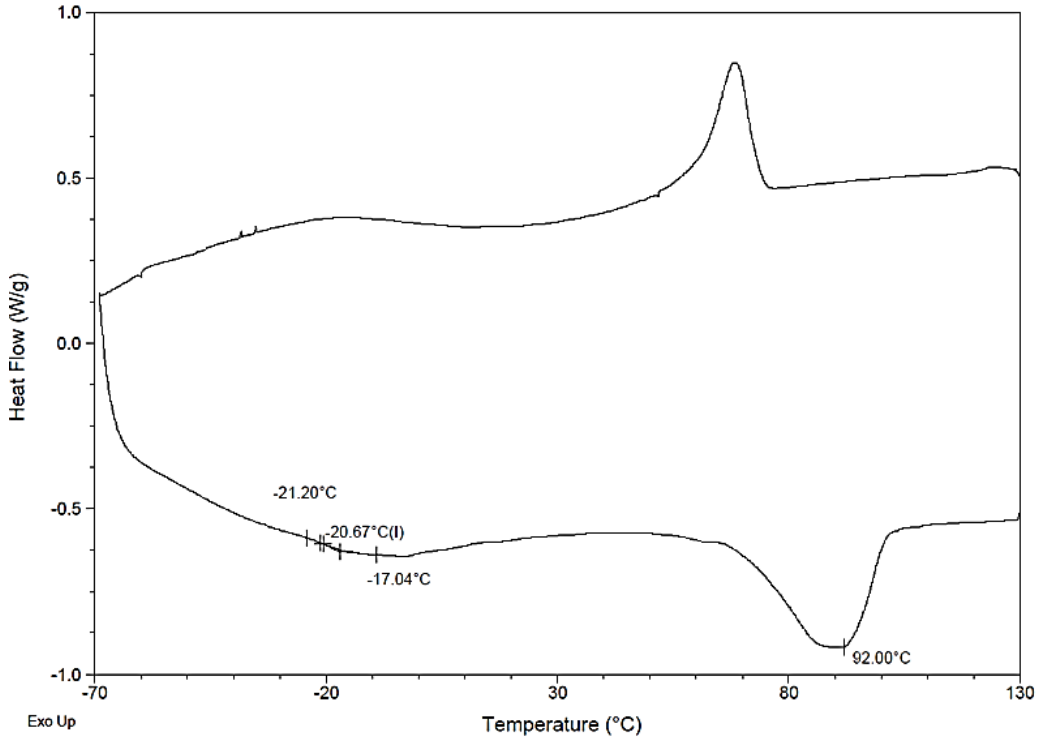

Figure S4.30. DSC trace of the second heating cycle and cooling cycle of PMCP from **run 4.10** (100:0).

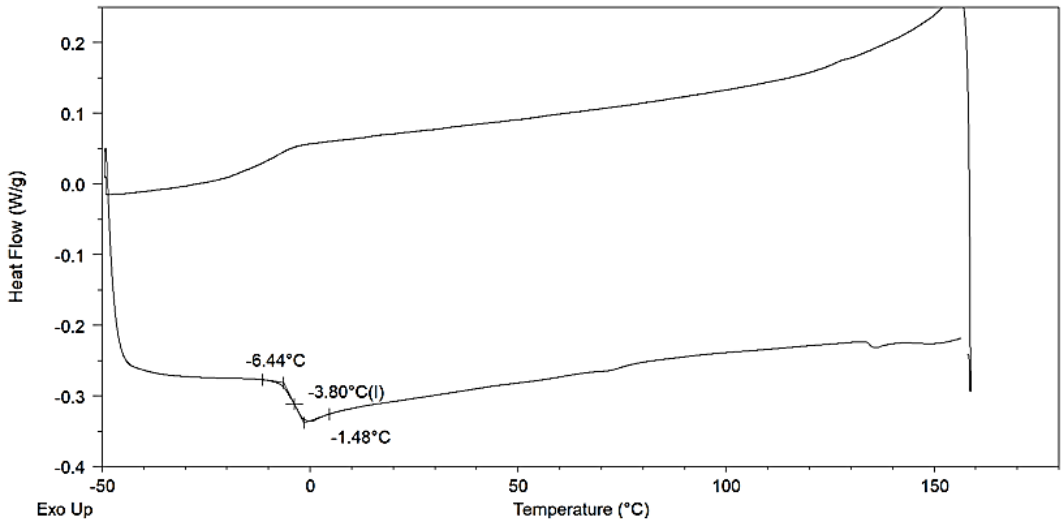

Figure S4.31. DSC trace of a heat/cool/heat cycle, cycle 1 removed, with a ramp rate of 10 °C/min from -70 – 300 °C of **run 4.11** (90:10).

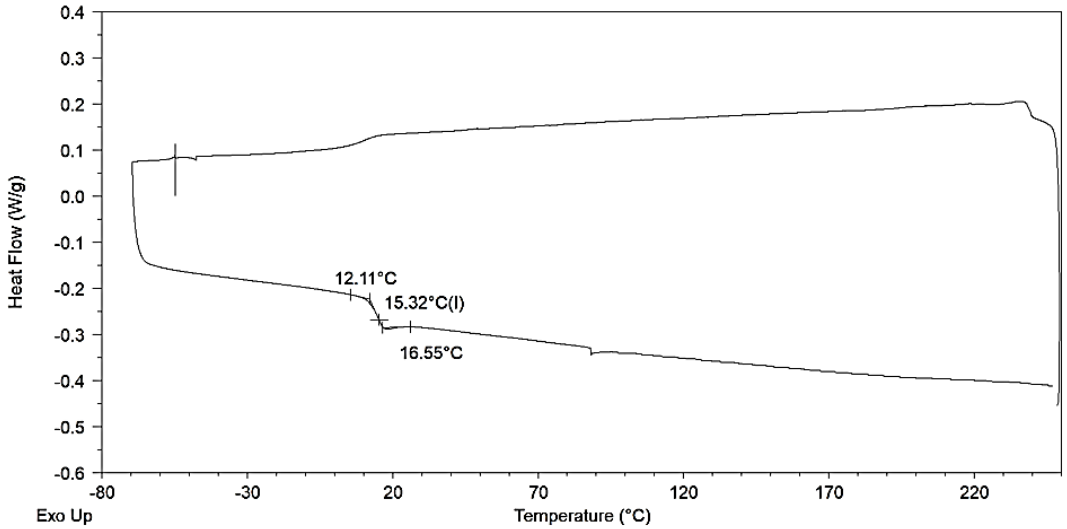

Figure S4.32. DSC trace of a heat/cool/heat cycle, cycle 1 removed, with a ramp rate of 10 °C/min from -70 – 300 °C of **run 4.12** (80:20).

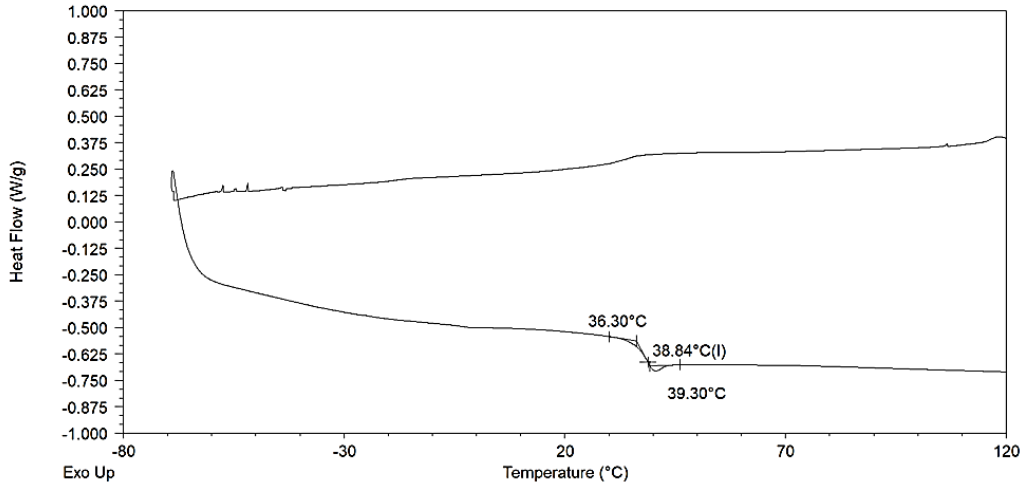

Figure S4.33. DSC trace of a heat/cool/heat cycle, cycle 1 removed, with a ramp rate of 10 °C/min from -70 – 300 °C of **run 4.13** (70:30).

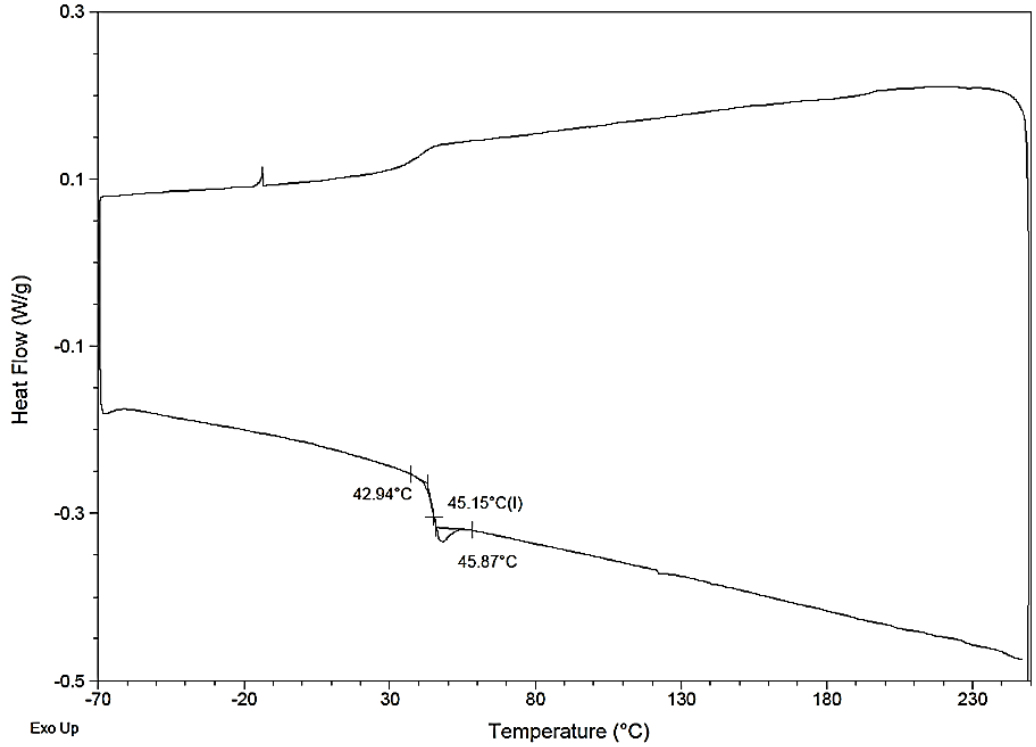

Figure S4.34. DSC trace of a heat/cool/heat cycle, cycle 1 removed, with a ramp rate of 10 °C/min from -70 – 300 °C of **run 4.14** (60:40).

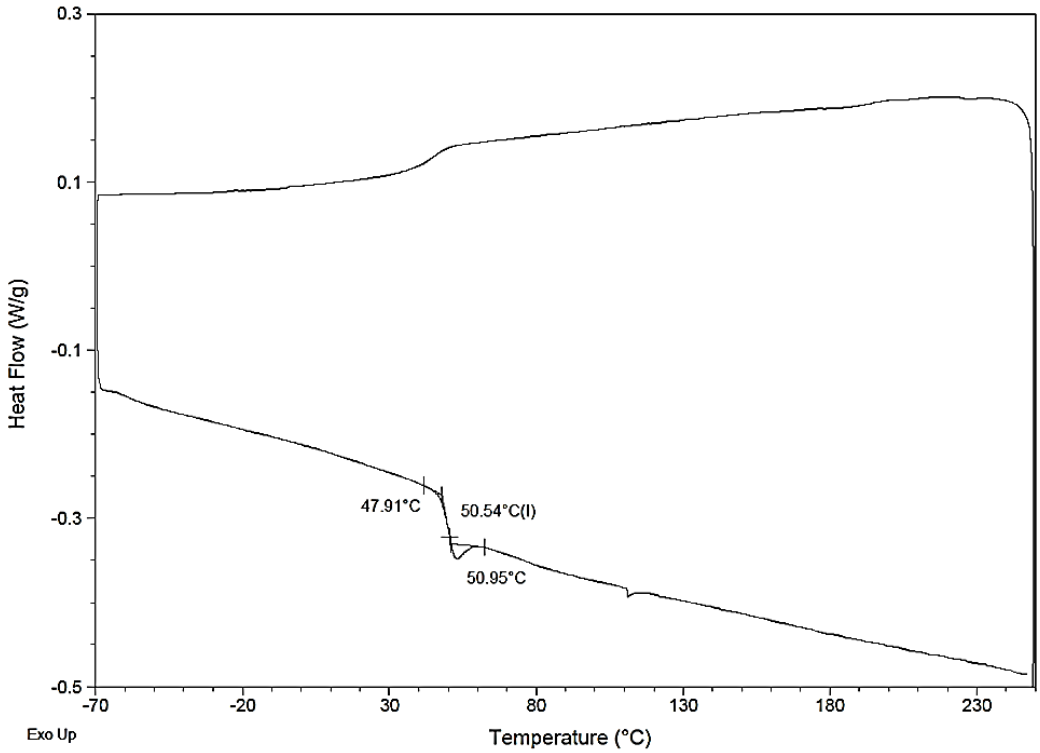

Figure S4.35. DSC trace of a heat/cool/heat cycle, cycle 1 removed, with a ramp rate of 10 °C/min from -70 – 300 °C of **run 4.15** (50:50).

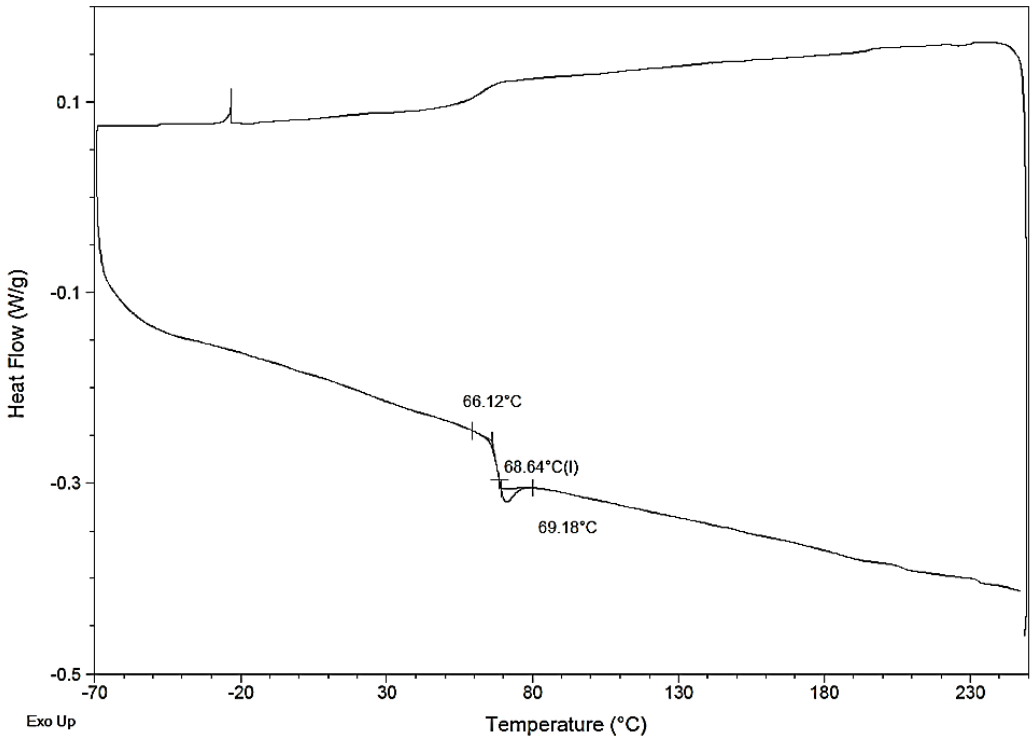

Figure S4.36. DSC trace of a heat/cool/heat cycle, cycle 1 removed, with a ramp rate of 10 °C/min from -70 – 300 °C of **run 4.16** (40:60).

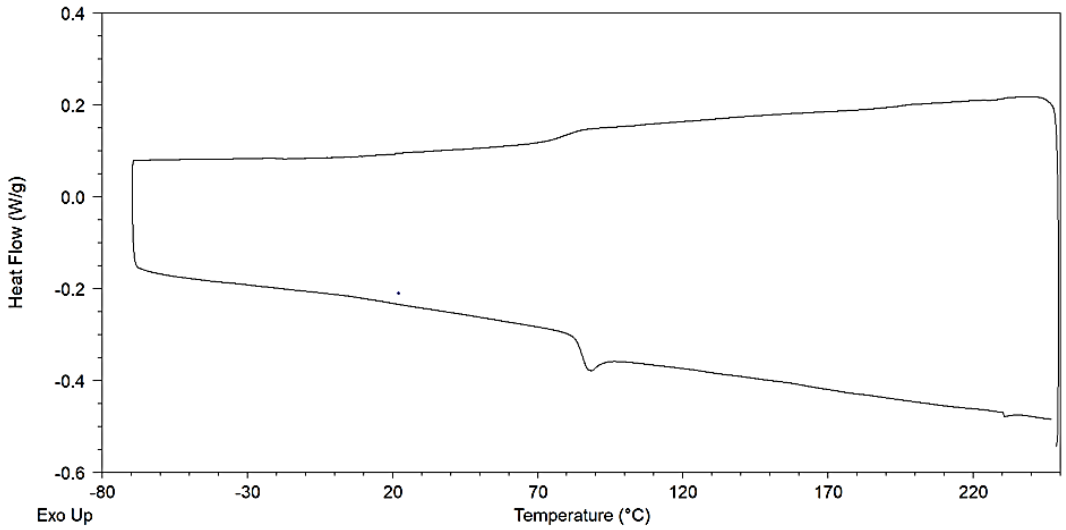

Figure S4.37. DSC trace of a heat/cool/heat cycle, cycle 1 removed, with a ramp rate of 10 °C/min from -70 – 300 °C of **run 4.17** (20:80).

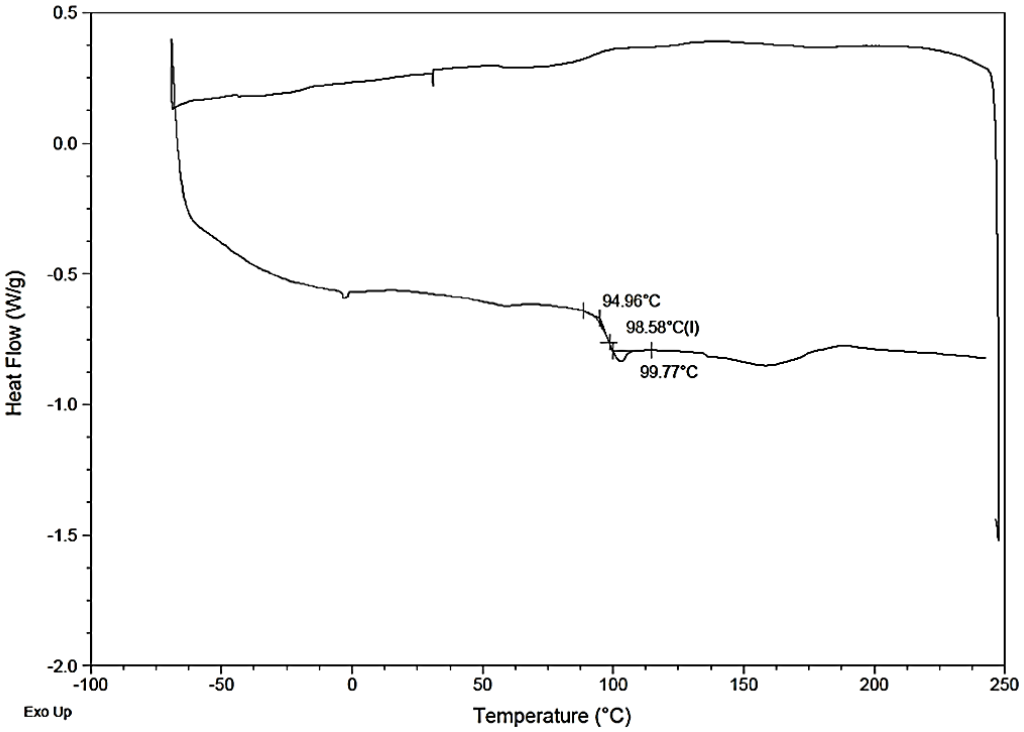

Figure S4.38. DSC trace of a heat/cool/heat cycle, cycle 1 removed, with a ramp rate of 10 °C/min from -70 – 300 °C of **run 4.18** (0:100).

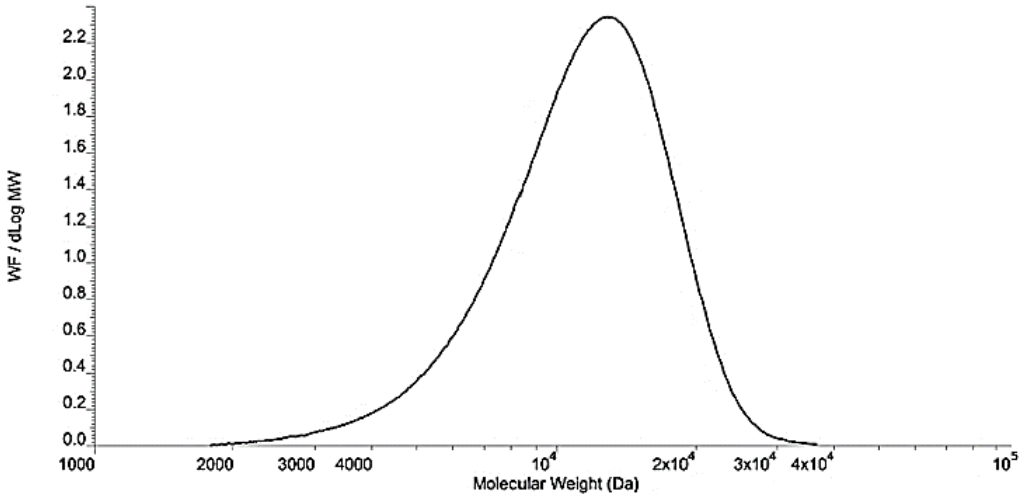

Figure S4.39. GPC trace of aPMP from **run 4.10** (100:0) Mn: 10,130 Da; Mw: 12,193 Da; PDI: 1.20.

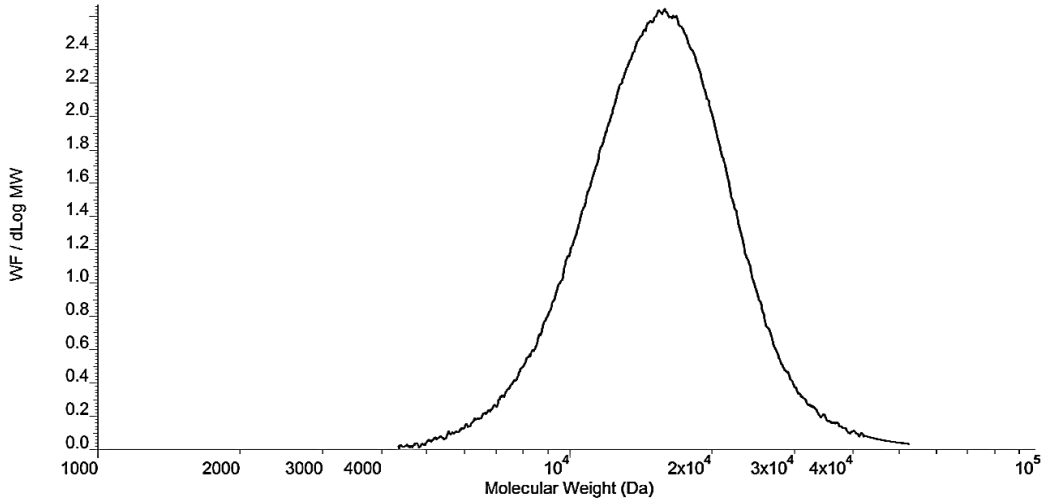

Figure S4.40. GPC trace of aPMP from **run 4.11** (90:10) Mn: 14,314 DA; Mw: 16,410 Da; PDI:
1.15.

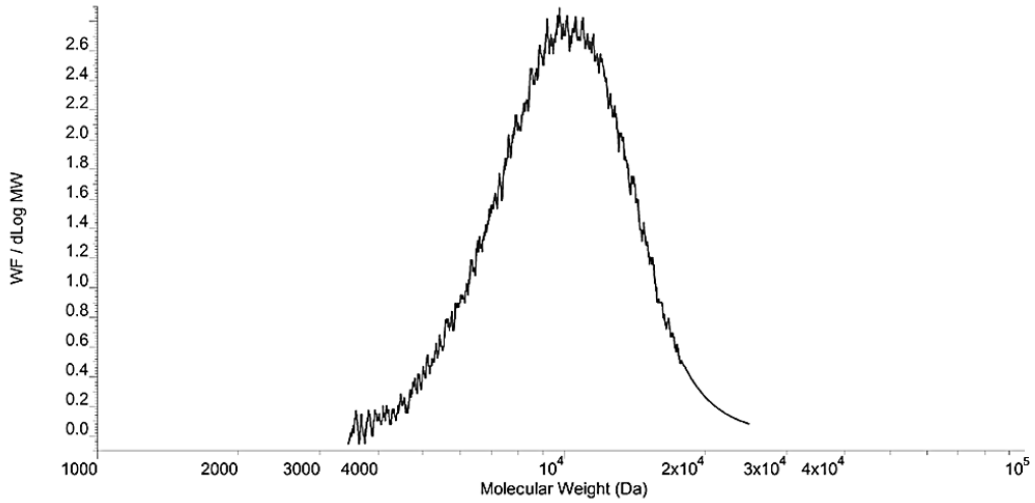

Figure S4.41. GPC trace of aPMP from **run 4.12** (80:20) Mn: 9,321 Da; Mw: 10,413 Da; PDI: 1.12 (highly crystalline causes decreases solubility and increased noise).

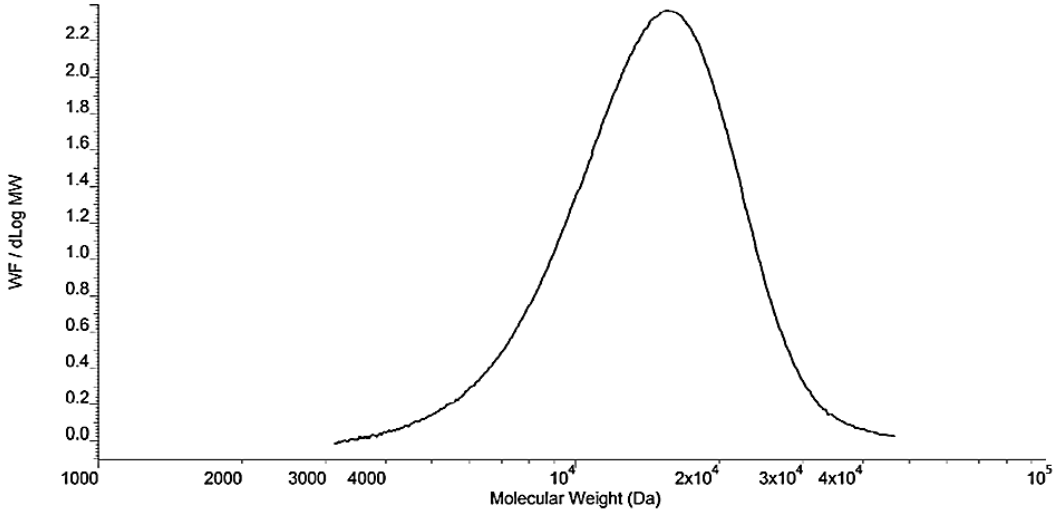

Figure S4.42. GPC trace of aPMP from **run 4.13** (70:30) Mn: 13,057 Da; Mw: 15,370 Da; PDI: 1.18.

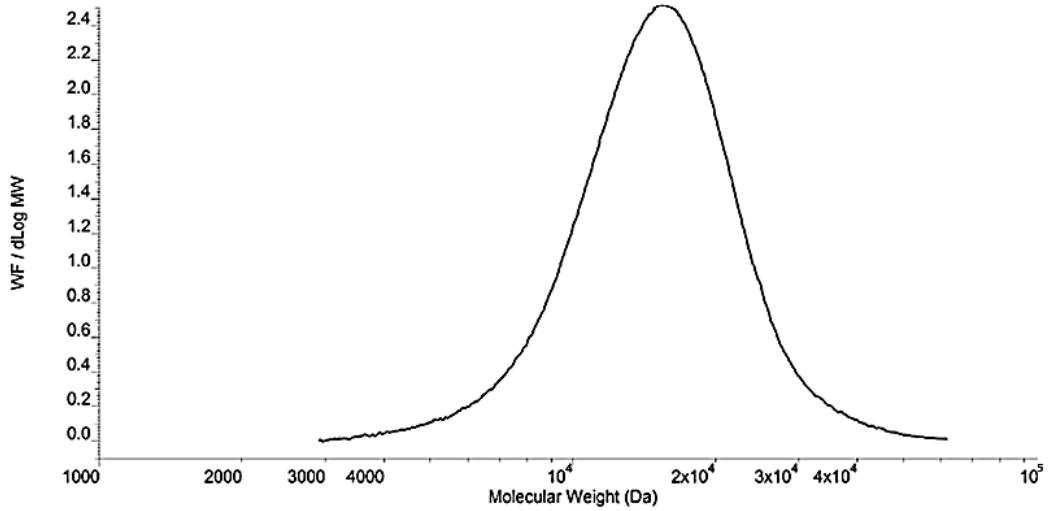

Figure S4.43. GPC trace of aPMP from **run 4.14** (60:40) Mn: 13,680 Da; Mw: 16,110 Da; PDI: 1.18.

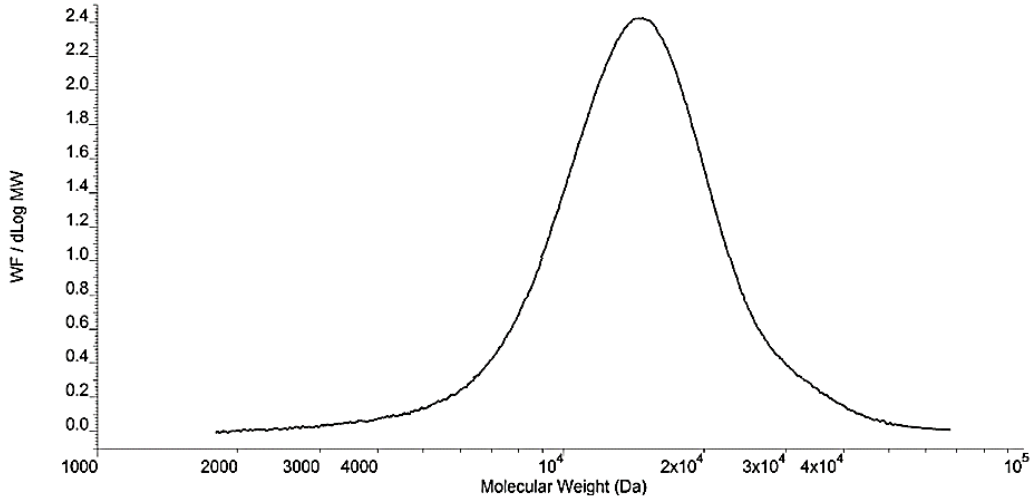

Figure S4.44. GPC trace of aPMP from **run 4.15** (50:50) Mn: 12,858 Da; Mw: 15,656; PDI: 1.22.

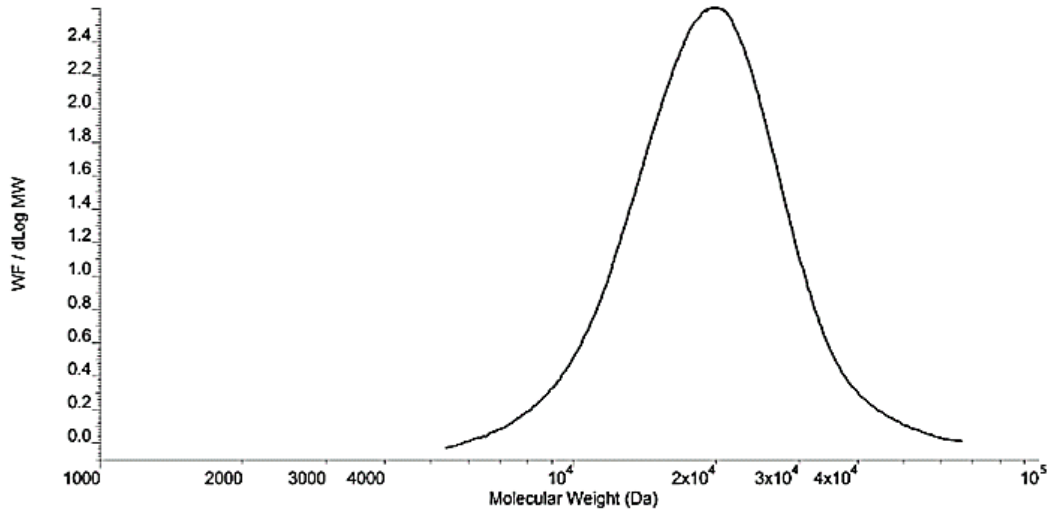

Figure S4.45 GPC trace of aPMP from **run 4.16** (40:60) Mn: 17,990 Da; Mw: 20,560 Da; PDI: 1.14.

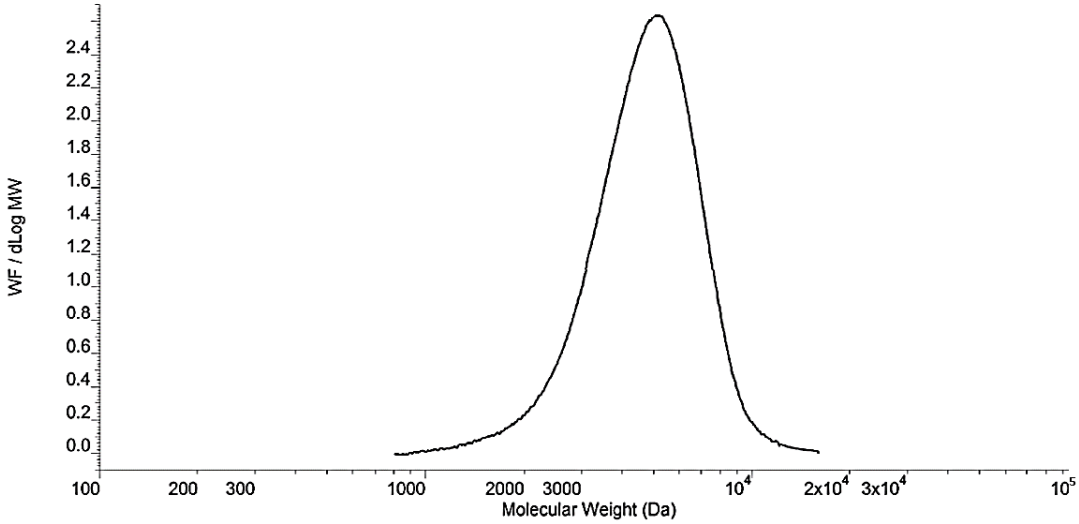

Figure S4.46. GPC trace of aPMP from **run 4.17** (20:80) Mn: 4,339 Da; Mw: 5,006 Da; PDI: 1.15.

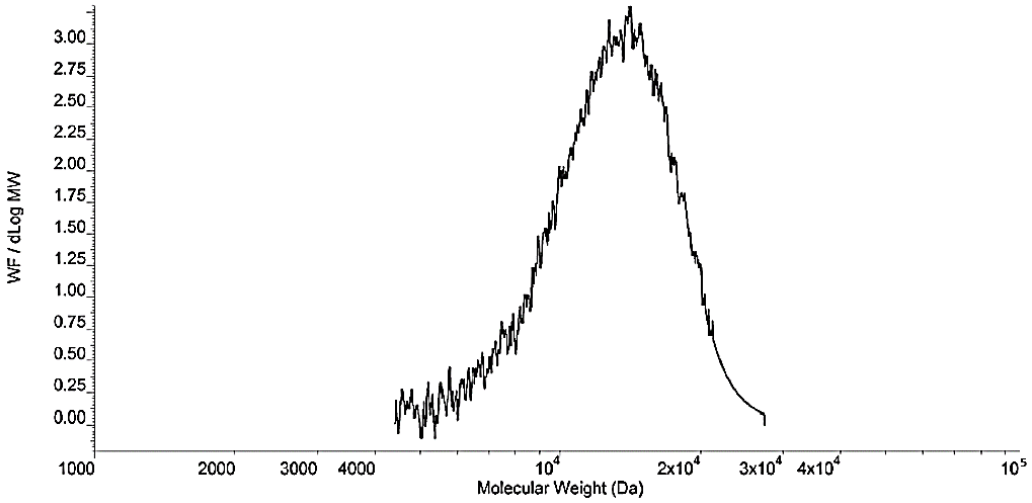

Figure S4.47. GPC trace of aPMP from **run 4.18** (0:100) Mn: 12,142 Da; Mw: 13,372 Da; PDI: 1.01 (highly crystalline causes decreases solubility and increased noise).

Chapter 5: Block Copolymers (BCP)

5.1 Background

Up until this point the polyolefin domains have been stereomodulated and explored for the purpose of creating a library of ‘grades’ of polymer materials with a wide range of physical properties while utilizing ‘simple’ synthetic techniques to create multiple polyolefin materials from a one catalyst system. These previous polyolefin materials have been homopolymers, comprised of one monomer type. These past studies allowed for a better understanding and discovery of polyolefin units to be treated as designable building blocks that can be utilized in a multitude of applications. Toward the goal of utilizing LCP and LCCTP systems it was paramount to show the utility of the designed polyolefin domains in a way to promote self-assembly. To showcase this design element hard-soft block copolymers (BCP) were synthesized utilizing LCP techniques. Block copolymers are comprised of two or more distinctly different monomer units. For example, diblock copolymers have individual unit A and individual unit B chemically linked and in the case of hard-soft block copolymers it means that one unit ‘A’ is comprised of a polymer that has crystalline characteristics, and the other unit ‘B; is comprised of a polymer that has amorphous characteristics. These materials are often shorthanded as A-*block*-B, A-*b*-B , or A-B to make clear that these units are separate. In contrast, the previous case of copolymers of random organization the shorthand is A-*co*-B. Hard-soft BCP were chosen as a material because of the Sita Group’s ability to design the stereochemistry and properties within

each block precisely. Additionally, hard-soft BCP have been observed to have thermoplastic elastomeric properties with a few documentations of the unique behavior of these materials so there is great academic interest and industrial relevance to study hard-soft BCPS.[5,6] The characteristic lengths of the microphase structures that can occur depend on their molecular weights and generally range from 10 – 100 nm. Highly ordered nanostructures can be prepared by simple methods such as spin coating and thus microphase-separated structures have been investigated for diverse nanotechnology applications, for example, etching masks in lithography,[52] photonic crystals,[53] laser devices,[54] filtration,[55] and photovoltaic devices.[56,50,51]

The morphology of crystalline(hard)-amorphous(soft) block copolymer has been investigated for years due to the interactions that arise between the two distinctly different units that microphase separate into unique morphologies due to this difference. Aside from the 'classical' morphologies generated through BCPs of spheres, cylinders, double gyroid, and lamellae, in hard-soft BCPs the crystallizable block can generate semicrystalline lamellae,[1,2] zig-zag morphologies,[3] and frustrated crystallization[4] structures. It is generally accepted that the solid-state morphologies in crystalline-amorphous BCP systems is controlled by three key temperatures within the bulk material: (1) the glass transition temperature of the amorphous block, T_g, (2) the crystallization temperature of the crystalline block, T_c, and (3) the order-disorder transition temperature of the BCP, T_{OD}.[6-8] Microphase separated structures in confined geometries have received much attention, because BCP morphologies differ greatly from those in the bulk verses in films due to spatial constraints. Dimensionality is a crucial factor for categorizing confinement systems for microphase separated structures

such as a thin film is a one-dimensional confinement system in which it is limited by the thickness of the film. It has been documented that a strong confinement effect occurs when $T_{OD} > T_g > T_c$, which result in the crystalline block being confined within the BCP microdomains.[10-16] When it comes to weak confinement, $T_{OD} > T_C > T_g$, crystallization occurs when the amorphous block is still above T_g and a large crystalline structure tends to be observed therefore overriding and BCP microphase separation.[49] It is of great interest to not only study the bulk properties of BCP make through our LCP synthesis but also the properties of the material once put under confinement.

Theoretical models for hard-soft BCP were first introduced in the early 1980's but any experimental proof did not appear in the literature until the mid-1990's. Di Marzio *et al.*, Whitmore and Noolandi, and Vilgis and Halperin investigated the correlation between phase separation and crystallization in hard-soft BCP systems.[17-19] Based on these theoretical models, morphologies of the materials were able to be predicted. The domain periodicity D can be estimated using the total degree of polymerization of BCP, N_t, and degree of polymerization of the amorphous block, N_a, with an overall prediction that $D \sim N_t N_a^{1/3}$ for symmetric BCP systems. Recently, new models and calculations have been implemented in order to relate the mechanical responses of hard-soft copolymer systems with their microstructures utilizing a coarse-grain molecular dynamics approach.[6]

Within strong confinement hard-soft BCP materials Cohen *et al.* first showed the phase behavior for crystalline-amorphous BCP with a series of polystyrene-*b*-hydrogenated (*b* = block separation) polybutadiene polymers.[9] Through different thermal stimuli temperatures they were able to show that depending on crystallization

pathways there was varied morphologies. Within weak confinement crystalline-amorphous BCP materials Nojima *et al.* reported an investigation of crystallinity, crystallization kinetics, and crystalline orientation.[20-22] These studies elucidated that a crosslink of rubbery amorphous domains can create a matric that restricts the crystalline blocks from forming therefore exhibiting lower crystallinity and lower melting points within that domain. More recently, Bates *et al.* and Register *et al.* synthesized a series of hard-soft BCP comprised of polyethylene-*b*-poly(ethylene-*co*-propylene) (PE-PEP), polyethylene-*b*-poly(ethyl ethylene) (PE-PEE), and polyethylene-*b*-poly(3-methyl-1-butene) (PE-PMB).[23-27] These studies lead to investigations geared around the viscoelastic behavior of molten BCP and how each domain governs the resulting microdomain structures. Amongst others crystalline-amorphous BCP systems with weak segregation,[23,28-30] and strong segregation[16,22,27,31,32] it has been determined that the crystallin block form into weak segregation systems are likely to form lamellae structures while in strong segregation systems other morphologies arise.

When it comes to low molecular weight BCP microphase separation studies there has been little work done as many understand BCP microphase separation does rely on the chain entanglement limit as well as the units within the BCP having a high enough dissimilarity to microphase separate. In this chapter, the polyolefin building blocks are designed and utilized to study hard-soft BCP microphase separation at lower molecular weights to show the versatility and application of the Sita Group LCP and LCCTP systems.

5.2 Crystalline-Amorphous Block Copolymers (BCP)

Through judicious selection polyolefin domains were designed, synthesized, and characterized to create several new classes of amorphous (coil) linked to crystalline (rod) like BCPs that undergo microphase separation in the solid state by virtue of strong conformational asymmetry that exists between the rod-coil block domains. Generally speaking, supramolecular assembly of rod-coil BCPs provide entry into fascinating and diverse array of nanostructured materials.[33, 34-37] The principle driving force for such assembly is the microphase separation of structurally dissimilar (rod / coil) segments that is coupled with the anisotropic ordering associated with the aggregation, and often times crystallization, of conformationally rigid rod domains.[29,37,38] Importantly, within materials derived from rod-coil architecture, supramolecular assembly can contain much smaller feature sizes than those typically obtained within equilibrium microphase separated morphologies of coil-coil block copolymers < 10 nm[39]. Further, there is a noticeable absence of known polymer types that undergo supramolecular assembly in simple low molecular weight saturated hydrocarbon-based polyolefins leaving room for much to be discovered and understood.

To begin, pre-initiator (η_5-C_5Me_5)$ZrMe_2$ [N(Et)C(Me)N(t-Bu)] was used with co-initiator [$PhNHMe_2$][$B(C_6F_5)_4$] in chlorobenzene at -10 °C. Once fully activated 1-hexene monomer is added to the reaction flask for 1.5 - 2hrs before the next block is added in, which was 4-methyl-1-pentene monomer. Depending on the goal of a diblock or triblock would change whether a final additional of 1-hexene was added before

quenching with 10 % HCl/MeOH at RT. General summary of synthesis can be seen in Scheme 5.1. The BCP materials yielded was thus poly(1-hexene)-*b*-poly(4-methyl-1-

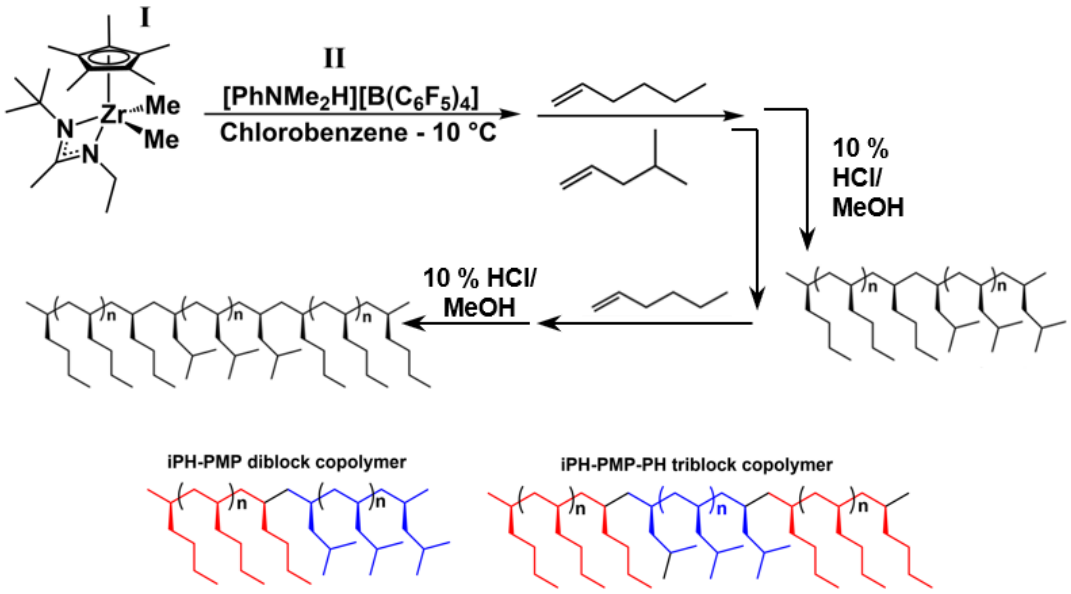

Scheme 5.1 Summary of synthesis of di- and triblock polymers made through LCP techniques (top) and structure of block copolymer color coordinated by block units of PH (red) and PMP (blue).

pentene) (iPH-PMP) AB di- and iPH-PMP-PH ABA tri-block copolymers, sample details can be found in Table 5.1. These components of the BCPS were specifically chosen because iPMP is highly crystalline, with literature reporting melting temperatures as high as 245 °C. Furthermore, it is known that the commercially relevant PMP is known to adopt a 7_2 helical structure in the solid state resulting in strong nonbonded steric interactions between the isobutyl side chains which serve to retain this structure in the melt.[40,41]

Given these properties iPMP is expected to act in a rod shape as the hard domain. For the coil component, iPH was utilized since it is known to have a sub-ambient glass transition temperature of –55 °C.[42]

Table 5.1 Di- and Triblock copolymers (PH-PMP-PH or PH-PMP).

BCP	M_n *PH* (kDa)[a]	M_n *PH* (kDa)[a]	M_n *PMP* (kDa)[a]	M_n *Total* (kDa)[a]	$Đ^a$	f_{PMP}	ϕ_{PMP}	T_g (°C)[b]	T_m (°C)[b]
5.1	10.6	11.6	10.2	32.4	1.4	0.34	0.36	-40.6	130; 139
5.2	10.2	8.8	9.4	28.5	1.2	0.31	0.34	-39.5	93.8; 133
5.3	10.8	13.4	-	24.2	1.1	0.55	0.55	-35.2	154; 165

[a]Determined by GPC. [b]Determined by DSC.

Within these hard-soft BCP structures there was observation of segregate into rigid lamellae crystalline domains. Using ps-tm atomic force microscopy (AFM) phase mapping was able to capture the formation of long rigid rods, in both iPH-PMP and iPH-PMP-PH samples, that created unique patterns across carbon coated silica chips, Figure 5.1. It is important to note that these materials were spun cast at 0.15 wt% to 1 wt% with the aim of creating a confined 1D system. The film thickness of these materials ranged from 5 – 20 nm thick. Within the as-cast the PH-PMP-PH BCP **5.1** there was observed to be the predicted behavior for weak segregation regimes as crystalline lamellae persisted as the only observed phase both in AFM and in SAXS, see SI. This matches literature predictions and hypotheses that the amorphous PH domain that cap either side of the crystallin PMP domain can be disrupting the crystallization of PMP.

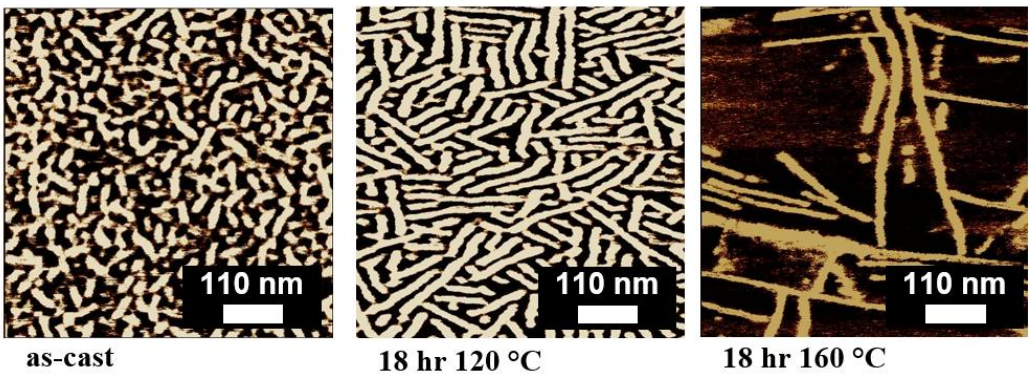

Figure 5.1 Block copolymer PH-PMP-PH **5.1** spun-cast at 1 wt% in toluene measure by ps-tm AFM phase map on carbon-coated SI (c-Si) substrate before and after annealing the sample in a vacuum oven at varied temperatures.

The BCP were thermally annealed to study the crystallization of the hard domains. For sample **5.2** and as temperatures rose the rod shapes began to orient in groups with perpendicular intercrossing's into shapes such as triangles, arrows, or T-shapes, in Figure 5.2. The only difference between BCP **5.1** and **5.2** is the decrease in molecular weight of the PH amorphous domains. This unique results of seeing an array of microstructures makes sense for strong segregation regime and could now be accessed due to the decrease in the amorphous domain. There was no pattern as to whether a square, triangle, herring bow, or long rod was observed at any given point on the thin-film carbon coated chip. It is hypothesized though that imperfections in the chip or carbon coating on the chip could lead to accumulations of the shapes. For example, if the chip has an even distribution of carbon-coating and no imperfections one can assume the crystalline domain in the block copolymer will continue in a linear fashion, but if and imperfection were to occur or uneven coating it may change the orientation of the crystalline grown of these domains. Given this discovery it was of interest to decrease the overall molecular weight of the BCP

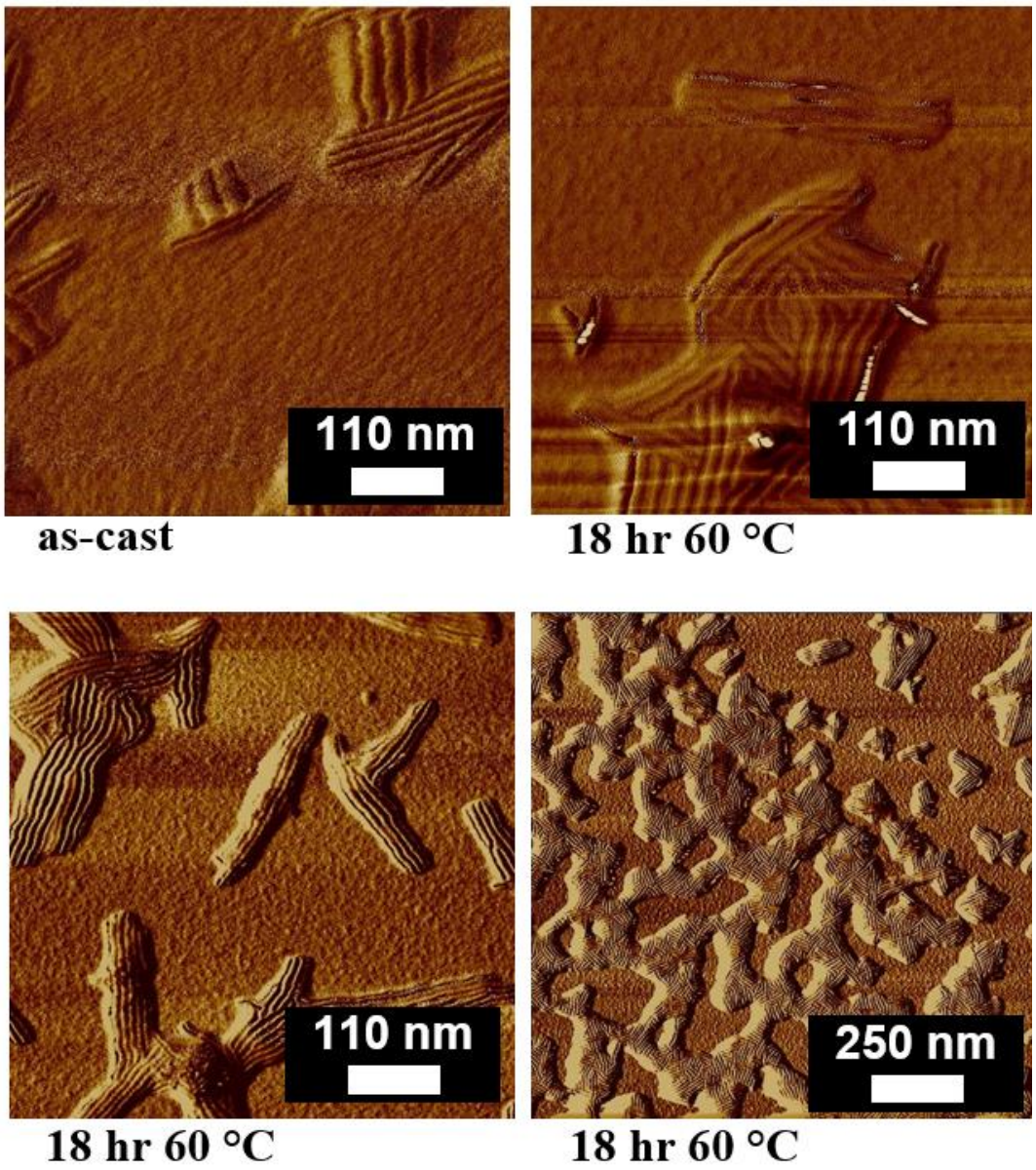

Figure 5.2 Block copolymer PH-PMP-PH **5.2** spun-cast at 0.15 wt% in toluene measure by ps-tm AFM phase map on carbon-coated SI (c-Si) before and after annealing the sample in a vacuum oven at varied temperatures.

materials by completely excluding the last domain thus making a diblock rather than triblock.

In iPH-PMP BCP **5.3**, the crystalline rod domains look like rice and when annealed to higher temperature the crystalline rod domains began to grow into long fibers

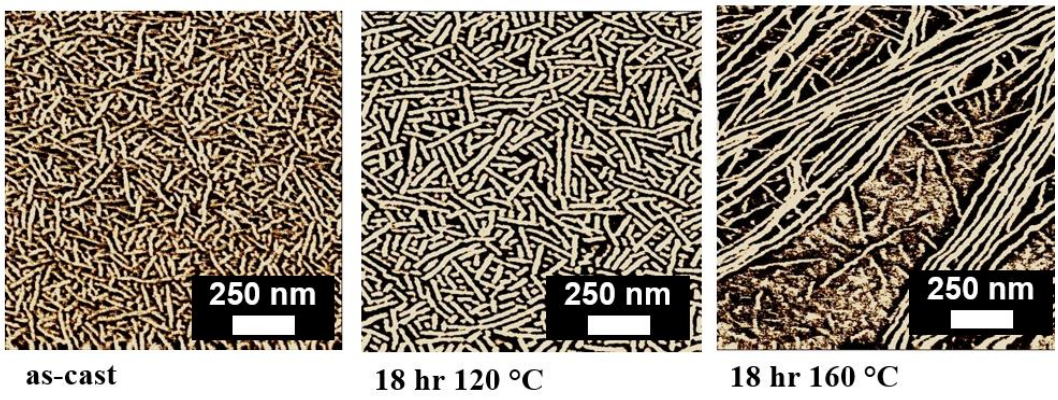

Figure 5.3 Block copolymer PH-PMP **5.3** spun-cast at 3 wt% in toluene measure by ps-tm AFM phase map on carbon-coated SI (c-Si) before and after annealing the sample in a vacuum oven at varied temperatures.

crisscrossing along the thin film randomly, Figure 5.3. These results are very similar to the iPH-PMP-PH BCP **5.1** self-assembling behavior. Unfortunately, reducing the overall molecular weight of the BCP through decreasing the number of blocks did not yield new or interesting results from the triblock previously made. However, the AFM images illuded that the iPH-PMP BCP **5.3** was able to accommodate more rod structures in a smaller space and yielded even longer fibral domains that the triblock did. All samples were measure on SAXS using the on-site x-ray, but the resulting diffraction only elucidated weak lamellae morphology for all samples. To try and discover different and better periodicity microstructures the hard-soft domains were swapped out for new monomer sources.

Utilizing the same LCP technique for the previous BCP materials the synthesis of *isotactic* poly(1-decene)-*b*-poly(methyl-1,3-cyclopentance) (iPD-PMCP) block copolymers was explored. PMCP has a different overall structure and behavior for crystallization than PMP, and PD has a longer pendant chain that has more amorphous behavior than PH thus hopefully influencing new microdomains and microphase

separation to occur. Table 5.2 lists sample characteristics for the iPD-PMCP BCPs made herein.

Table 5.2 Diblock copolymers (PD-PMCP)

BCP	M_n *PD* (kDa)[a]	M_n *PMCP* (kDa)[a]	M_n *Total* (kDa)[a]	$Đ^a$	f_{PMCP}	ϕ_{PMCP}	T_g (°C)[b]	T_m (°C)[b]
5.4	16.7	13.1	29.8	1.3	0.44	0.43	-10.4	91.9
5.5	10.8	13.2	24.0	1.1	0.23	0.18	-	-

[a]Determined by GPC. [b]Determined by DSC.

The molecular weight of the iPD-PMCP BCPs were kept to similar molecular weight as the iPH-PMP BCPs. The length of each block however was changed and both 50:50 domain units and 80:20 domain units were explored. Within BCP material **5.4**, PD and PMCP domains were nearly 50:50, hexagonally pack cylinders (*C*) morphology was observed in the bulk. SAXS data in Figure 5.4 was able to capture this microphase separation as early as room temperature with better resolution at elevated temperature of 100 °C. No order-disorder phase transition was ever observed. Unfortunately, in the BCP **5.5** where PD was about 80% of the total molecular weight no phase behavior was detected. This is hypothesized to have occurred because there is a limit to how much amorphous domain exists within a hard-soft BCP for it to crystallize and therefore microphase separate. For these materials AFM was not utilized as future studies of how confinement can play a role in phase behavior is yet to be conducted.

Overall BCP samples **5.1 – 5.5** are polymer materials that show the utility of LCP technique to synthesize polyolefins with distinct microstructures. These materials are just the beginning to what designed domains can do and how they influence self-assembling within BCP materials. There is still much room for exploration with these

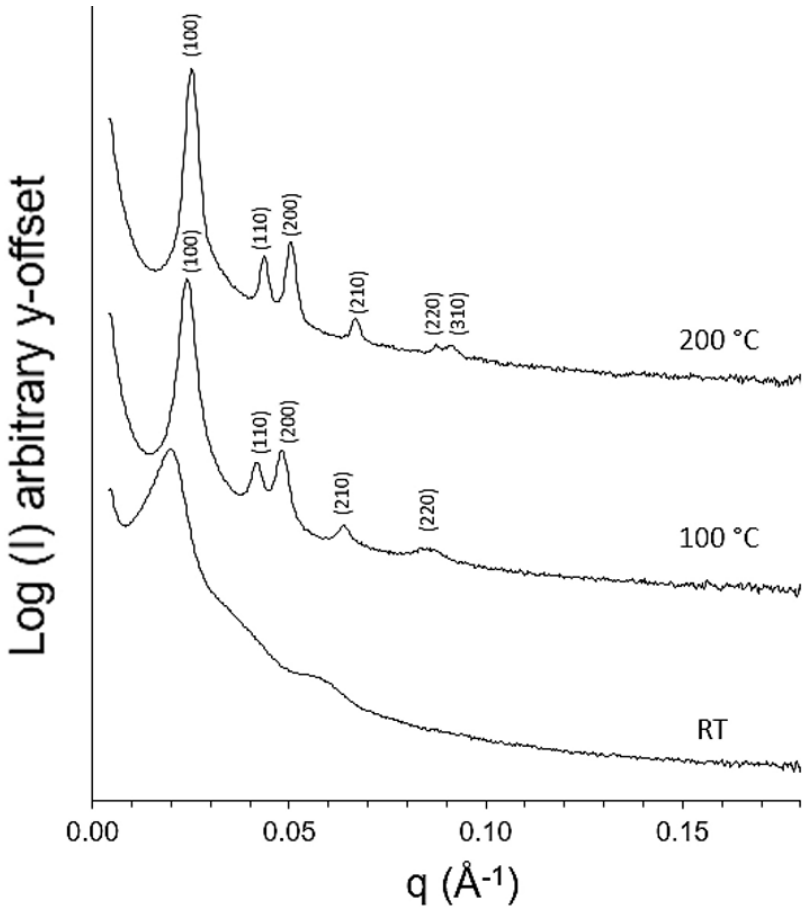

Figure 5.4 SAXS on-site thermal annealing study of PD-PMCP 5.4, with hexagonal cylinders (*C*) indexed *hkl* Miller indices, d_c = 26.11 nm.

materials, but these begin to scratch the surface of hard-soft BCPs. Future work with BCPs is endless but some examples of future studies can include exploring aPMP domains as an amorphous/soft region in BCPs as we can now programmable alter the T_g of aPMP. This would allow for a systematic study of the effects of T_g on the microphase separations of hard-soft BCP using LCP or LCCTP system. Additionally, optically active PMCP domains can be implemented as crystalline/hard domain within hard-soft BCPs to study the effects of optical activity on bulk microphase separation behavior.

5.3 End-Group Functionalized Building Block Polymers†

Burkey A. A.; Fischbach D. M.; Wentz, C. M.; Beers, K. L.; Sita, L.R., Highly Versatile Strategy for the Production of Telechelic Polyolefins *ACS Macro Lett.* **2022**, *11*, 402-409.

Author Contributions:
L. R. S. Lead conceptualization, funding, and writing.
A. A. B. Supported writing, reviewing, and editing. Synthesized and characterized ethylene-based materials.
D. M. F. Supported writing, reviewing, and editing. Synthesized and characterized all other polyolefin materials.
C. M. W. Supported writing, reviewing, and editing. Assisted in the characterization of block copolymer materials via atomic force microscopy. Analyzed block copolymer materials by small angle x-ray scattering.

Block copolymers are routinely synthesized through living polymerization systems where new monomer species is introduced at an increment of time to create distinct polymer blocks of differing architecture within on material. Toward the goal of creating recyclable polyolefin materials, it is of interest to make BCP that can be broken back down into reusable polyolefin domains rather than back to the monomer feedstock thus avoiding the need to repolymerize the material. To reach this goal of a recyclable BCP it was hypothesized that each polyolefin domain can be synthesized with functionalized end-groups on both sides of the polymer and then synthetically linked. These linkages can contain differing characteristics to one another in order to achieve BCP of AB or ABA or ABBA or ABAB architecture to hopefully inducing

† The results, tables, figures, and schemes presented and discussed in this chapter have been used or adapted with permission from Burkey A. A.; Fischbach D. M.; Wentz, C. M.; Beers, K. L.; Sita, L.R., Highly Versatile Strategy for the Production of Telechelic Polyolefins *ACS Macro Lett.* **2022**, *11*, 402-409. Copyright © 2022, American Chemical Society.

microphase separation. The work presented herein was produced with Danyon M. Fischbach and Aaron A. Burkey, were they synthesized and characterized the materials. While any characterization of phase behavior of BCP materials were conducted through Charlotte M. Wentz's assistance and efforts.

Materials made within this study utilize LCCTP techniques illustrated in Scheme 5.2 were either Hf or Zr pre-initiator is utilized with CTA $ZnPh_2$ so as to synthesis atactic or isotactic homopolymers with phenyl termination. They are then I_2 quenched to get iodo termination on the other end of the polymer chain. Thus, making these materials telechelic with end-group functionality on both ends of the polymer

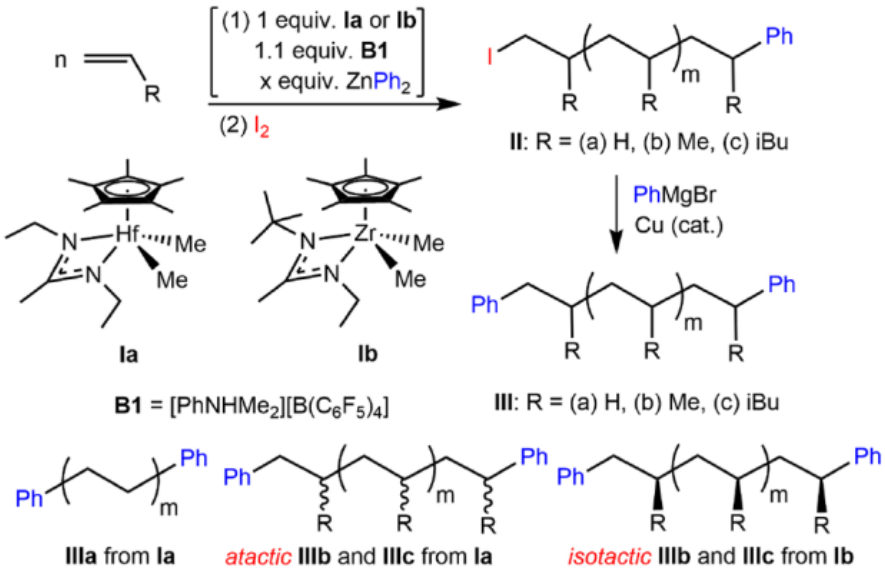

Scheme 5.2 Production of Hetereotelechelic α-Iodo, ω-Phenyl-Terminated (**II**) and Homotelechelic α,ω-Bis(phenyl)-Terminated (**III**) Polyolefins.[†]

material. However, it was of importance to chemical change the iodo functionality also into a phenyl as it is well known that phenyl functionality can lead to more synthetic modifications to be easily made. The modification made thereafter involved Friedel-Crafts acylation using acetyl chloride in combination with aluminum trichloride as a

Lewis acid to add a *para*-acetophenone group on the phenyls capping either end of the polymer chain. These ketone functionalities were synthetically modified to alcohols through reduction using lithium aluminum hydride. This was done with the intention of creating an alcohol functionality that can consequently ring open caprolactone in order to create BCP materials of amphiphilic nature for possible self-assembly. Poly(ε-caprolactone) is also BioSource from crude oil and is biodegradable. Additionally, ester linkages that are created in this BCP are known to be reversible allowing for all polymer domains to be broken apart and recycled.

The library of materials made utilizing this telechelic building block technique is expansive are represent only the tip of the iceberg of possibilities and innovation to new polyolefin materials, see Table 5.3 for sample information and SI for structural, physical property, and behavior analysis. Within this study the end group functionalized polyolefins (x-PAOs) are used as swappable building blocks that can be post polymerization modified to be used in combination with caprolactone to make PAO-PCL BCPs. These materials include polyethylene-*b*-poly(ε-caprolactone) (PE-PCL), atactic poly(4-methyl-1-pentene)-*b*-poly(ε-caprolactone) (aPMP-PCL) (**VIII**), and poly(ε-caprolactone)-*b*-atactic polypropylene-*b*-poly(ε-caprolactone) (PCL-aPP-PCL) (**IX**) BCP materials. Importantly, as presented in Figure 5.5, the nature of the x-PAO and PCL block domains create strong microphase-segregated morphologies in the solid-state with the nanostructures influenced by the mole fraction of the PCL domain (f_{PCL}).[29] For sample **VIII** aPMP-PCL BCP a body centered cubic (BCC) spherical mesophase is observed in sub-100 nm-thick ultrathin films by phase tapping mode (ps-tm) AFM. Within the bulk materials, observed through small-angle-x-ray-

Table 5.3 Telechelic polyolefins, **III** – **V**, and heterotelechelic polyolefins, **VI** and **VII**, via post polymerization reactions.[a]

initial[b]	reagents	final[b]	% yield	M_n[c] (kDa)	$Đ$[c]	T_g[d] (°C)	T_m[d] (°C)
I-PE-Ph (**IIa**)	PhMgCl	Ph-PE-Ph (**IIIa**)	>99	1.0	1.18	nd	104
Ph-PE-Ph (**IIIa**)	$AcCl/AlCl_3$	AcPh-PE-PhAc (**IVa**)	99	0.8	1.30	nd	107
AcPh-PE-PhAc (**IVa**)	$LiAlH_4$	HOBn-PE-BnOH (**Va**)	>99	0.8	1.27	nd	110
I-aPP-Ph (***a*-IIb**)	PhMgBr	Ph-aPP-Ph (***a*-IIIb**)	88	14.0	1.08	−6	
Ph-aPP-Ph (***a*-IIIb**)	$AcCl/AlCl_3$	AcPh-aPP-PhAc (***a*-IVb**)	95	13.6	1.11	−9	
AcPh-aPP-PhAc (***a*-IVb**)	$LiAlH_4$	HOBn-aPP-BnOH (***a*-Vb**)	>99	13.7	1.11	−7	
I-iPP-Ph (***i*-IIb**)	PhMgBr	Ph-iPP-Ph (***i*-IIIb**)	61	9.8	1.30	−10	98
Ph-iPP-Ph (***i*-IIIb**)	$AcCl/AlCl_3$	AcPh-iPP-PhAc (***i*-IVb**)	>99	6.9	1.43	−10	101
AcPh-iPP-PhAc (***i*-IVb**)	$LiAlH_4$	HOBn-iPP-BnOH (***i*-Vb**)	>99	7.6	1.45	−7	102
I-iPP-Ph (***i*-IIb′**)	PhMgBr	Ph-iPP-Ph (***i*-IIIb′**)	76	5.1	1.21	−16	72
Ph-iPP-Ph (***i*-IIIb′**)	$AcCl/AlCl_3$	AcPh-iPP-PhAc (***i*-IVb′**)	>99	4.2	1.27	−12	65
AcPh-iPP-PhAc (***i*-IVb′**)	$LiAlH_4$	HOBn-iPP-BnOH (***i*-Vb′**)	98	4.0	1.64	−9	73
I-aPMP-Ph (***a*-IIc**)	PhMgBr	Ph-aPMP-Ph (***a*-IIIc**)	88	5.5	1.20	28	
I-iPMP-Ph (***i*-IIc**)	PhMgBr	Ph-iPMP-Ph (***i*-IIIc**)	81	12.7	3.84	19	219
I-PE-Ph (**IIa**)	$AcCl/AlCl_3$	I-PE-PhAc (**VIa**)	97	0.9	1.23	nd	105
I-aPP-Ph (***a*-IIb**)	″	I-aPP-PhAc (***a*-VIb**)	96	14.5	1.07	−7	
I-iPP-Ph (***i*-IIb**)	″	I-iPP-PhAc (***i*-VIb**)	98	8.9	1.33	−9	96
I-iPP-Ph (***i*-IIb′**)	″	I-iPP-PhAc (***i*-VIb′**)	>99	4.0	1.30	−18	70
I-aPMP-Ph (***a*-IIc**)	″	I-aPMP-PhAc (***a*-VIc**)	>99	5.9	1.10	14	
I-iPMP-Ph (***i*-IIc**)	″	I-iPMP-PhAc (***i*-VIc**)	97	12.1	2.28	21	218
I-aPMP-PhAc (***a*-VIc**)	$LiAlH_4$	aPMP-BnOH (***a*-VII**)	>99	6.3	1.20	26	

[a]For experimental details of each transformation, see the SI. [b]AcPh = *p*-C_6H_4−C(O)CH_3, BnOH = *p*-C_6H_4−CH(OH)CH_3. [c]Determined by SEC using polystyrene standards (1,2,4-trichlorobenzene, 135 °C for **IIa** and **IIc**, THF, 40 °C for **IIb**. [d]Determined by DSC.†

scattering (SAXS) at variable temperatures, BCC is observed as well with a q/q^* = 1, 2 , and 3 (q^* = 0.056 Å−1) for a domain spacing of 11.1 nm at 100 °C. In contrast, in BCP material **IX** there is a slightly larger f_{PCL} domain value, the ps-Tm AFM of the sample, annealed to 200 °C for 18 hours and then rapidly quenched with liquid nitrogen, revealed a "fingerprint" surface morphology for ultrathin films consistent with either a lamellar (LAM) mesophase where the LAM is oriented perpendicular to the surface,[43] or *C* phase where cylinders are aligned parallel to the surface. For more evidence of the morphology arising within BCP material **IX** variable temperature SAXS confirmed the existence of LAM phase appearing below 100 °C, with scattering peaks at q/q^* = 1, 2, 3, and 4 (q^* = 0.033 Å−1) that correspond to a domain spacing of 19 nm. In contrast, temperature above 150 °C revealed a *C* phase with a new set of

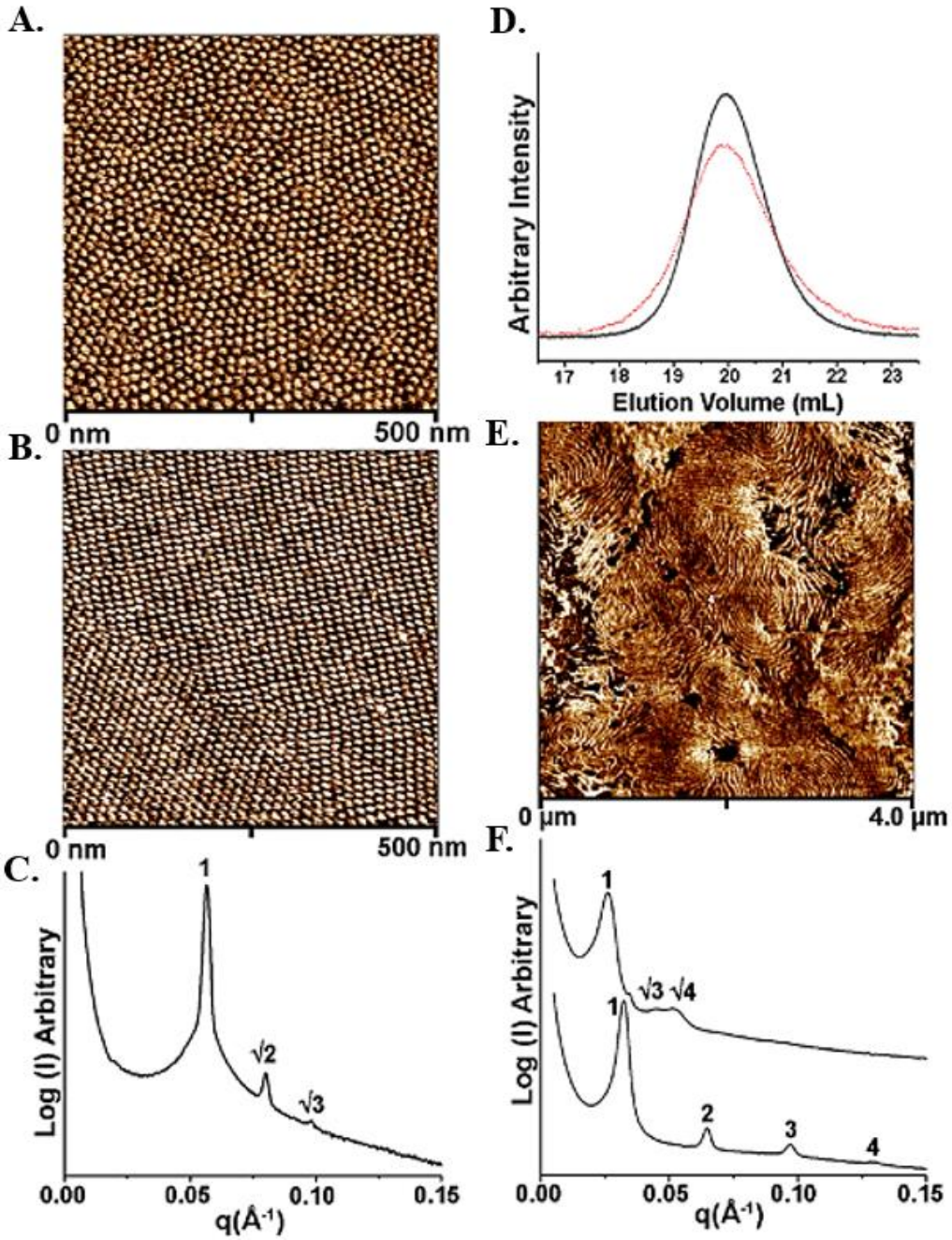

Figure 5.5 (A) ps-tm AFM phase map of "as-cast" from toluene of a 60 nm thick film of aPMP-PCL diblock **VIII** on a carbon-coated SI (c-SI) substrate. (B) ps-tm AFM phase map of the same sample in (A) after thermal annealing at 100 °C for 18 h. (C) 1D SAXS profile of **VIII** obtained at 100 °C. (D) SEC trace (RI detector = black solid line, UV detector = red dotted line of PCL-aPP-PCL triblock **IX.** (E) ps-tm AFM phase map of a 100 nm thick film of **IX** on c-Si substrate annealed to 200 °C followed by a rapid quench into liquid N_2. (F) 1D SAXS profile of the LAM phase of **IX** obtained at 80 °C (bottom and mixed HEX (major)/ LAM (minor) phase observed upon heating the sample to 200 °C (top).[†]

scattering peaks appearing at q/q* = 1, 3 , and 4 (q* = 0.026 Å−1) that are associated with a cylinder-to-cylinder distance, *dc*, of 23.7 nm at 200 °C. This epitaxial thermotropic LAM → *C* phase order-order transition are well-known for other classes of di- and triblock copolymers.[29,44-48]

Lastly, other factors such as overall molar mass of the BCP can affect the nature of these materials and the PAO domain (aPMP or aPP) plays a key role in the morphologies observed. A more extensive understanding of the phase behavior of these PAO-polyester BCPS are currently in progress by Danyon M. Fischbach.

5.4 Conclusions

Both studies of BCPs made within this chapter are just the beginning of how the polyolefin building blocks made through LCP and LCCTP techniques can be utilized to create distinctive polyolefin materials that have the capability to phase separate. BCP materials are of academic and industrial interest due to their programmable and designable nature of each component within the material. The past studies made herein with stereocontrol or modulation of physical properties within the polyolefin domain allow for methodical studies to be explored and discoveries of phase behavior from PAO domains to be explained. Future work with BCP materials is sure to yield endless possibilities.

5.5 Supporting Experimental Information[†]

5.5.1 Synthetic Procedures

All manipulations with air and moisture sensitive materials were carried out under N2 using standard Schlenk or glovebox techniques. Toluene (Fisher Scientific, 99%) was dried and deoxygenated by passage over activated alumina and activated copper catalyst (GetterMax 135) and collected under N2 prior to use. Chlorobenzene (Acros Organic, 99%) was dried over calcium hydride by refluxing at 130 °C for three days and distilled under N2 prior to use. Dichloromethane and 1,2,2,2-tetrachloroethane were distilled over CaH2 prior to use. Chloroform-*d1* and 1,1,2,2-tetrachloroethane-*d2* were purchased from Cambridge Isotopes and used as received. 4-methyl-1-pentene (>97%) was purchased from TCI Chemicals, dried over Na/K alloy and isolated by vacuum-transfer prior to use. Ethene and propene (polymer grade) were purchased from Matheson Trigas and passed through activated Q5 and molecular sieves (13X). Iodine (99.8%) was purchased from Sigma-Aldrich and used as received. Diphenylzinc (99%) was purchased from Strem Chemicals and used as received. [PhNMe2H][B(C6F5)4] (**B1**) was purchased from Boulder Scientific and used as received. Catalyst **Ia** was synthesized according to published procedures. Catalyst **Ib** was synthesized according to published procedures. Aluminum chloride was used as received and stored under inert atmosphere in a glovebox.

General Procedure LCP of *isotactic* 1-hexene, 4-methyl-1-pentene, 1- hexene di- and tri-block copolymers (*i*PH-PMP, *i*PH-PMP-PH).

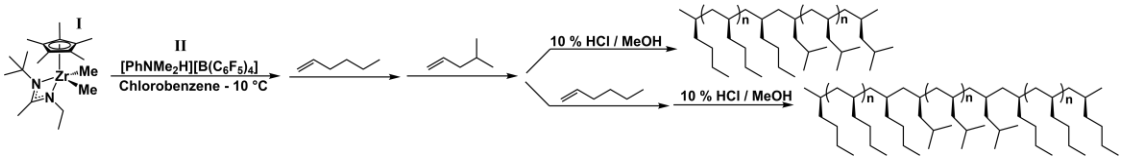

In a 100 mL round bottom flask was filled with 30 mL of chlorobenzene was cooled to – 10 °C. A solution of **I** (0.020 mmol, 7. 96 mg) in 1.0 mL of chlorobenzene was

added to **II** (0.022 mmol, 17.63 mg), at – 10 °C, which was agitated until dissolved, turning yellow, then quickly added to the flask. Then quickly added to the flask was the 1-hexene at targeted equivalence (**x eq**) which was allowed to stir for **x** hours before then next monomer was added, 4-methyl-1-pentene (**x eq**). The reaction would then be removed from the glovebox and quenched with/precipitated in 400 mL acidic methanol (10 % HCl) overnight, to product diblock copolymer iPH-PMP. When synthesizing the triblock poly(1-hexene) (**x eq**)would then be added before the same quenching technique to produce iPH-PMP-PH. The polymer is then purified via a short silica plug with hexane mobile phase and dried under vacuum.

General Procedure LCP of *isotactic* 1-decene, 1,5-hexadiene diblock copolymers.

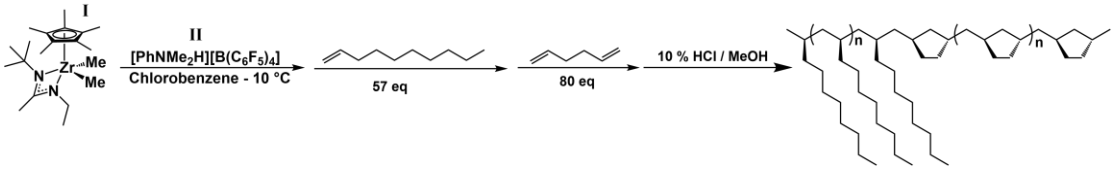

In a 50 mL round bottom flask 10 mL of chlorobenzene was added and cooled to - 10 °C. A solution of **I** (0.05 mmol, 19.88 mg) in 1.0 mL of chlorobenzene was added to **II** (0.055 mmol, 44.07 mg), at – 10 °C, which was agitated until dissolved, turning yellow, and added to flask. Then quickly added was 1-decene monomer (57 eq) which was allowed to stir for 4 h before 1,5-hexadiene monomer (80 eq) was added and stirred for 3 hr. The reaction was removed from the glovebox and quenched/ precipitated with 400 mL acidic methanol (10 % HCl) overnight. The resulting polymer was purified with a silica plug with hexane mobile phase and dried under vacuum.

Synthesis of poly(ε-caprolactone)-polypropene-poly(ε-caprolactone) block copolymer initiated by α,ω-bis(1-hydroxyethylphenyl) atactic polypropene (HOBn-aPP-BnOH, aVb).

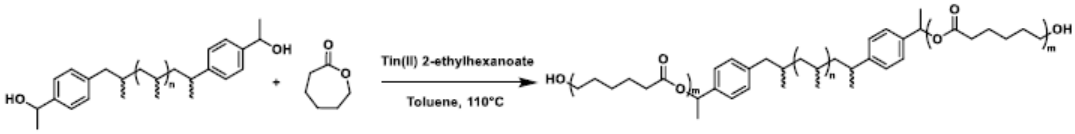

To a 100 mL pressure tube was added **aVb** (229 mg, 0.018 mmol) in 5 mL of toluene followed by ε-caprolactone (272 mg, 2.38 mmol) and tin(II) 2-ethylhexanoate (15 mg, 0.037 mmol). The reaction flask was stirred at 110 °C for 20 hours. The reaction was allowed to cool and precipitated in cold methanol. The resulting block copolymer was isolated via vacuum filtration using MeOH and dried in vacuo yielding 436 mg.

Synthesis of atactic poly(4-methyl-1-pentene)-poly(ε-caprolactone) block copolymer initiated by 1-hydroxyethylphenyl atactic poly(4-methyl-1-pentene) (aPMP-BnOH, aVIIc).

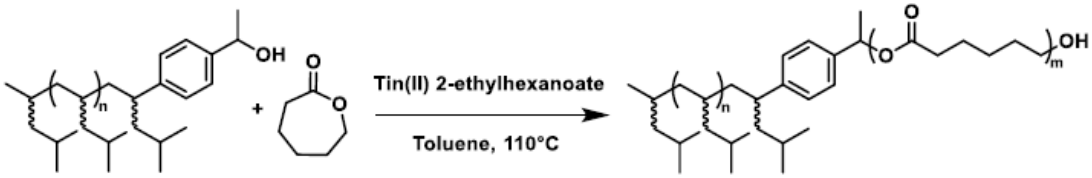

To a 100 mL pressure tube was added **aVIIc** (105 mg, 0.018 mmol) in 5 mL of toluene followed by ε-caprolactone (42 mg, 0.37 mmol) and tin(II) 2-ethylhexanoate (7 mg, 0.02 mmol). The reaction flask was stirred at 110 °C for 36 hours. The reaction was allowed to cool and precipitated in cold methanol. The resulting block copolymer was isolated via vacuum filtration using MeOH and dried in vacuo yielding 125 mg.

5.5.2 Characterization Parameters

Nuclear Magnetic Resonance (NMR). 1H and 13C{1H} NMR spectroscopy were performed on a Bruker AV III 400 MHz or Bruker AVIII-HD 800 spectrometer fitted with a cryo-QCI probe spectrometer. Spectra were referenced to residual solvent peaks (1H: 7.26 ppm for chloroform-*d1* and 6.0 ppm for 1,1,2,2-tetrachloroethane-*d2*; 13C: 77.23 ppm for chloroform-*d1* and 78.8 ppm for 1,1,2,2-tetrachloroethane-*d2*). NMR spectra of polyethene were collected at 90 °C, using 32 scans and a relaxation delay of 10 seconds.

Size Exclusion Chromatography (SEC). High temperature size exclusion chromatography was performed using a Tosoh HT-Eco SEC instrument with differential refractive index detection. Narrow dispersity polystyrene standards were used for calibration. Polyethene and polypropene molar mass was calculated from a polystyrene standard curve and corrected using appropriate Mark-Houwink parameters. Poly(4-methyl-1-pentene) molecular weight calculations were not corrected using Mark-Houwink parameters. Measurements were performed at 135 °C using 1,2,4-trichlorobenzene as the mobile phase (300 mg/kg Irganox 1010 was added as antioxidant to the solvent). The stationary phase was a set of 3 Tosoh HTs columns (2 Tosoh TSKgel GMHhr-H (S) HT2, 13 μm mixed bed, 7.8 mm ID × 30 cm columns and 1 Tosoh TSKgel GMHHR-H (20) HT2, 20 μm, 7.8 mm ID × 30 cm column with an exclusion limit ~4 × 108 g/mol).

Ambient temperature size exclusion chromatography data was obtained on a Tosoh EcoSEC system with differential refractive index (RI) detection coupled to a Wyatt Dawn Heleos II multiangle light scattering detector (18 angles) and a Wyatt Viscostar III differential viscometer. THF was used as mobile phase at 35 °C, and the stationary phase was a set of two Tosoh mixed pore columns (2× TSKgel GMHHR-H). Molar mass was calculated from a polystyrene standard curve.

Differential Scanning Calorimetry (DSC). Differential scanning calorimetry was performed on a TA Instruments Discovery 2500 in aluminum sample pans. Heating and cooling rates are indicated for each sample.

Thermal Gravimetric Analysis (TGA). Thermal gravimetric analysis measurements were performed using a TA Instruments Q500 instrument. Samples were heated from room temperature to 1000 °C at a rate of 40 °C. At 600 °C the sample chamber purge gas was switched from nitrogen to air.

Atomic Force Microscopy (AFM). Atomic force microscopy images were obtained using a Nanoscope IIIa Multimode AFM in tapping mode equipped with Extender Electronics package (Veeco Inc., CA). Height and phase-shift data were recorded simultaneously under ambient conditions with a silicon-etched tip. Thin films were spun cast (2000 RPM) from either 3 wt % (**VIII**) or 15wt % (**IX**) (w/v) solutions prepared in toluene onto a carbon-coated silicon surface. Film thickness was obtained

using a Gaertner optical ellipsometer. When annealed, samples were placed in vacuo overnight (18 hr) at the appropriate temperature.

Small Angle X-ray Scattering (SAXS). Lab-scale small angle X-ray scattering was performed at the University of Maryland with a Xenocs Xeuss SAXS/WAXS/GISAXS system, using CuKα X-rays with a wavelength of 1.5417 Å. Scattering was collected using a photon counting pixel-array detector (Dectris Pilatus 2M, pixel size 172 μm) positioned 1.3 m downstream of the sample. Data were collected at an exposure time of 600 seconds per frame in which 10 frames were compiled for one image. The samples were prepared in washers (1 cm total diameter) sealed with Kapton films. Samples that were thermally annealed were heated in a Linkam Peltier heating stage that encapsulated the wafer.

5.5.3 Supporting Results

A.

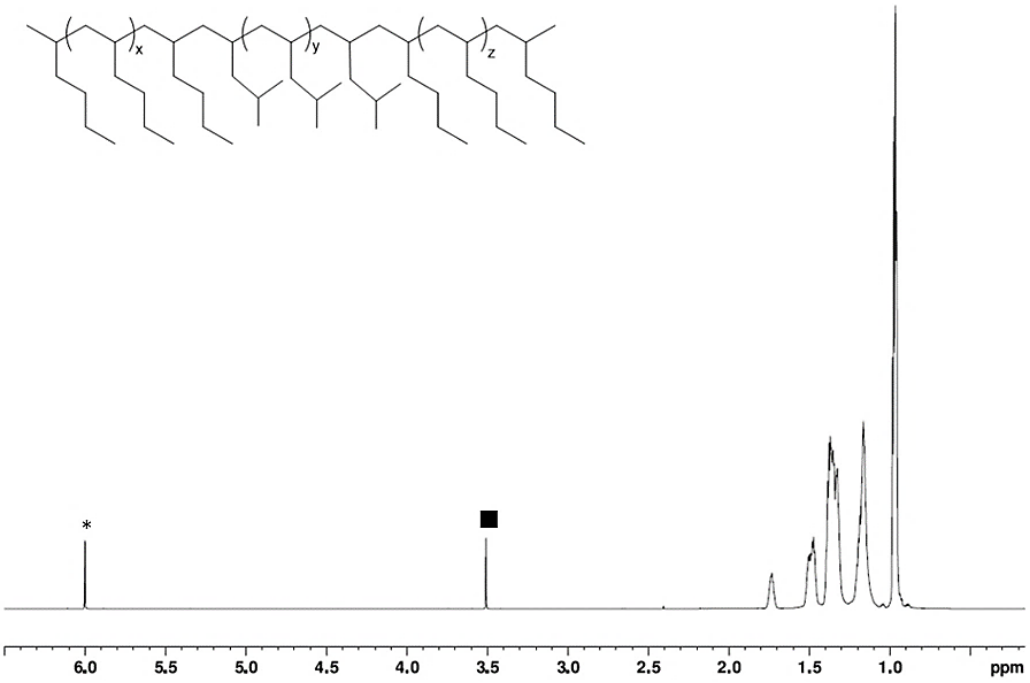

B.

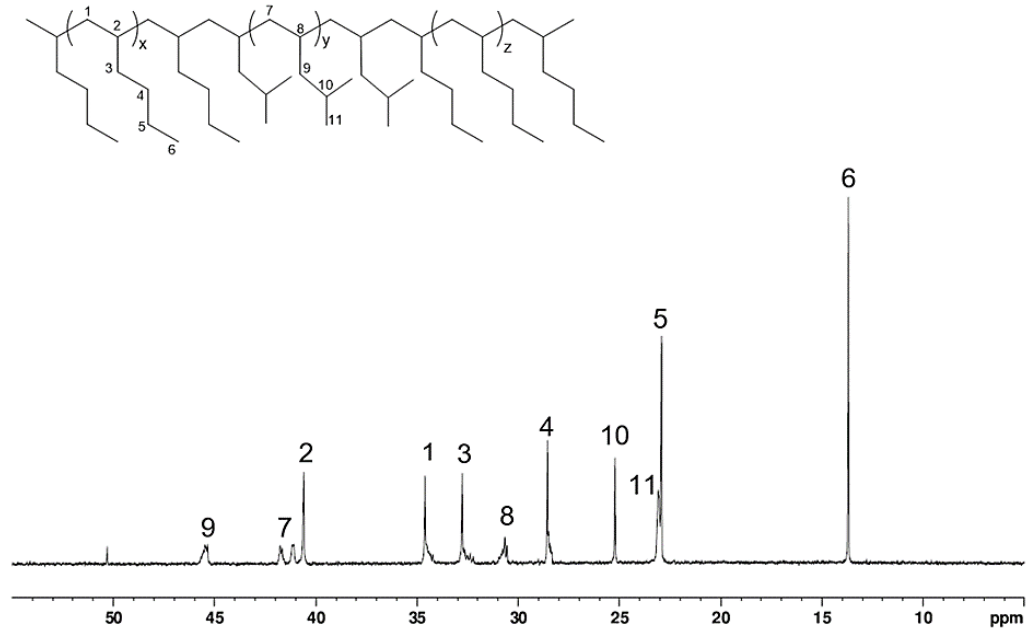

Figure S5.1 (A) ^{1}H-NMR (800 MHz, *1,1,2,2-C_2Cl_4-*d2*, 110 °C after 20 minutes of temperature equilibration, ■ MeOH peak a 3.49 ppm) of **5.1** (iPH-PMP-PH). (B) ^{13}C-NMR (800 MHz, *1,1,2,2-C_2Cl_4-*d2*, 110 °C after 20 minutes of temperature equilibration, MeOH peak seen at 50 ppm) of **5.1** (iPH-PMP-PH).

A.

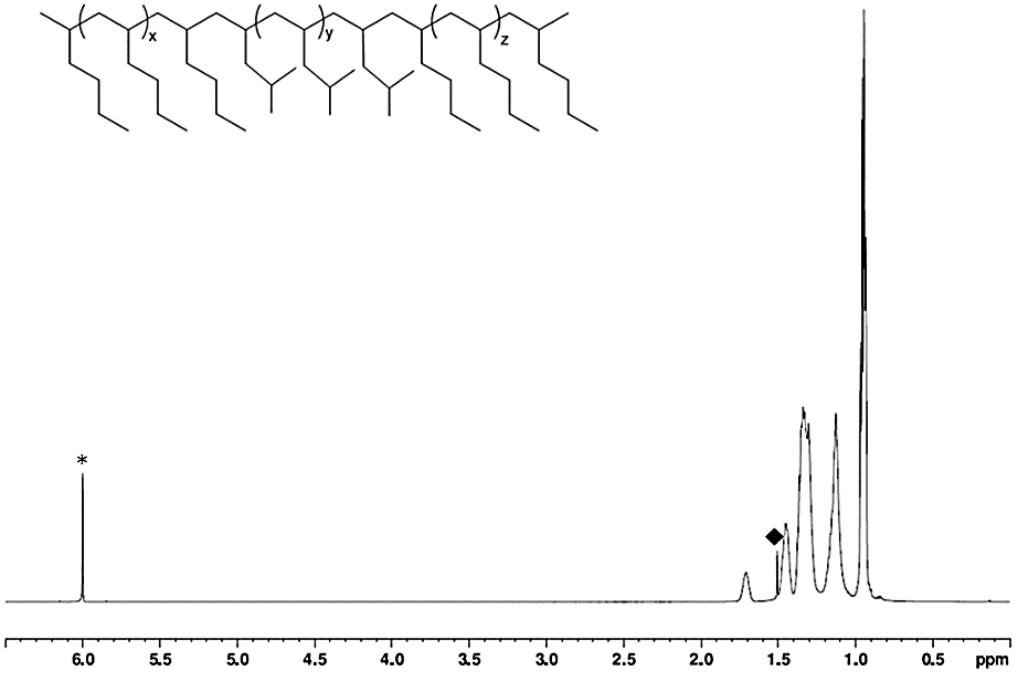

B.

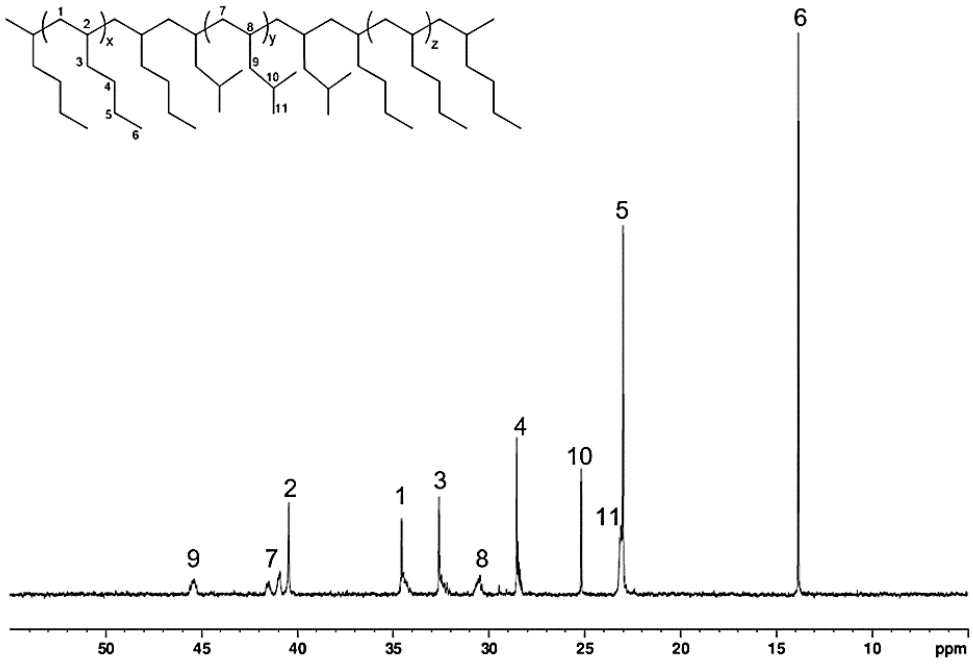

Figure S5.2. (A) ^{1}H-NMR (800 MHz, *1,1,2,2-C_2Cl_4-*d2*, 110 °C after 20 minutes of temperature equilibration, ◆water peak at 1.5 ppm of **5.2** (iPH-PMP-PH). (B) ^{13}C-NMR (800 MHz, *1,1,2,2-C_2Cl_4-*d2*, 110 °C after 20 minutes of temperature equilibration, MeOH peak seen at 50 ppm) of **5.2** (iPH-PMP-PH).

A.

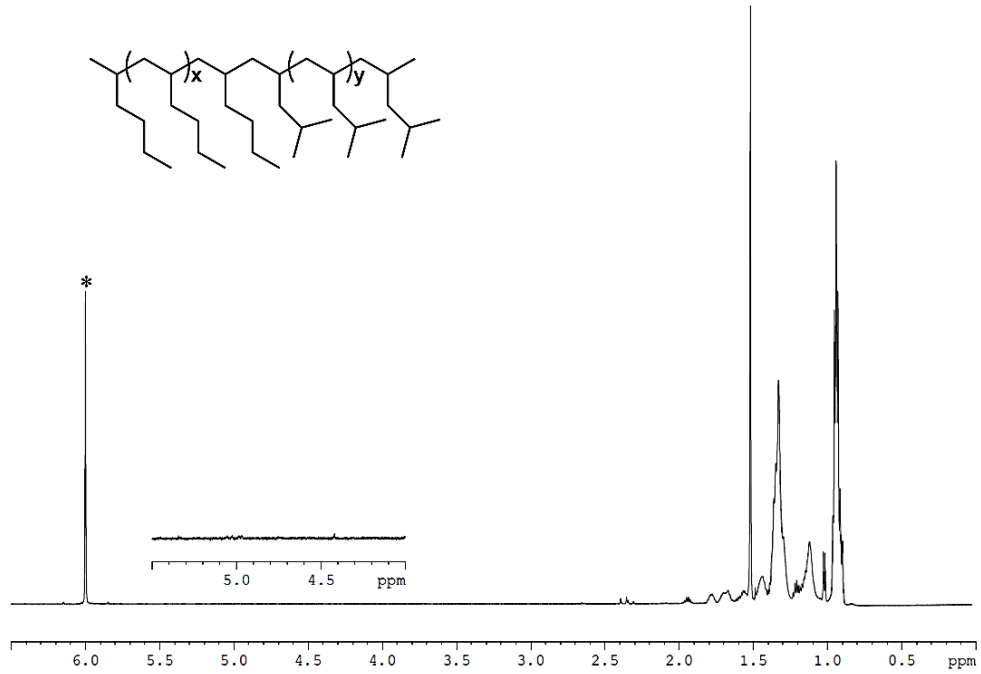

B.

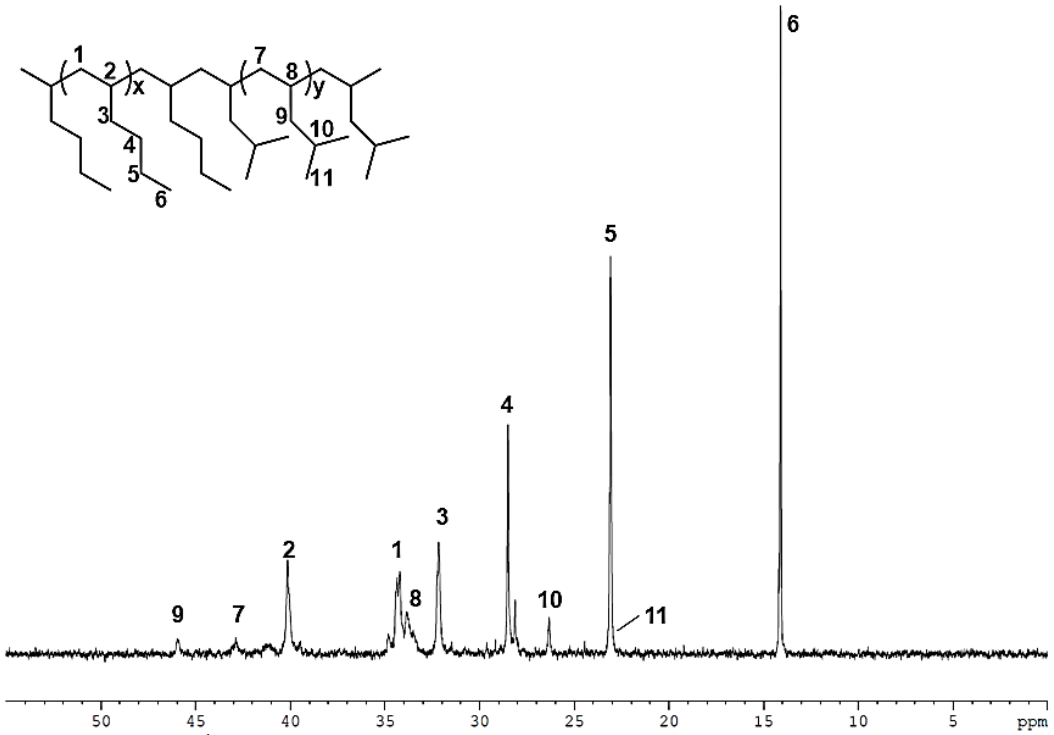

Figure S5.3. (A) ^{1}H-NMR (600 MHz, *1,1,2,2-C_2Cl_4-*d2*, 80 °C after 20 minutes of temperature equilibration, ◆water peak at 1.5 ppm of **5.3** (iPH-PMP). (b) ^{13}C-NMR 600 MHz, *1,1,2,2-C_2Cl_4-*d2*, 80 °C after 20 minutes of temperature equilibration, MeOH peak seen at 50 ppm) of **5.3** (iPH-PMP).

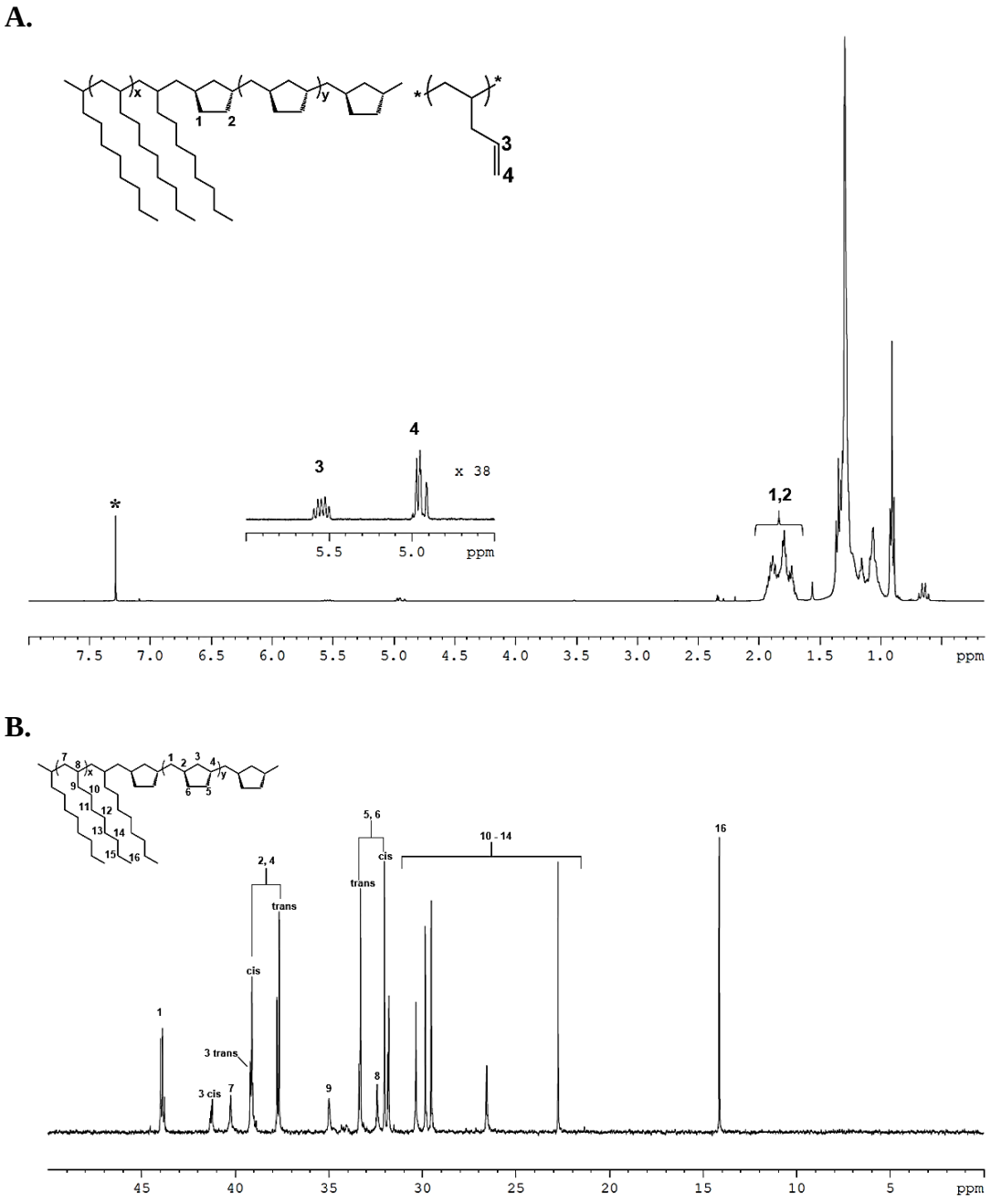

Figure S5.4. (A) ^{1}H-NMR (400 MHz, *1,1,2,2-C_2Cl_4-*d2*, RT) of **5.4** (iPD-PMCP) The protons from pendant group (3,4) and from 5-membered ring (1,2) are displayed. (B) ^{13}C-NMR (400 MHz,RT) of **5.4** (iPD-PMCP).

A.

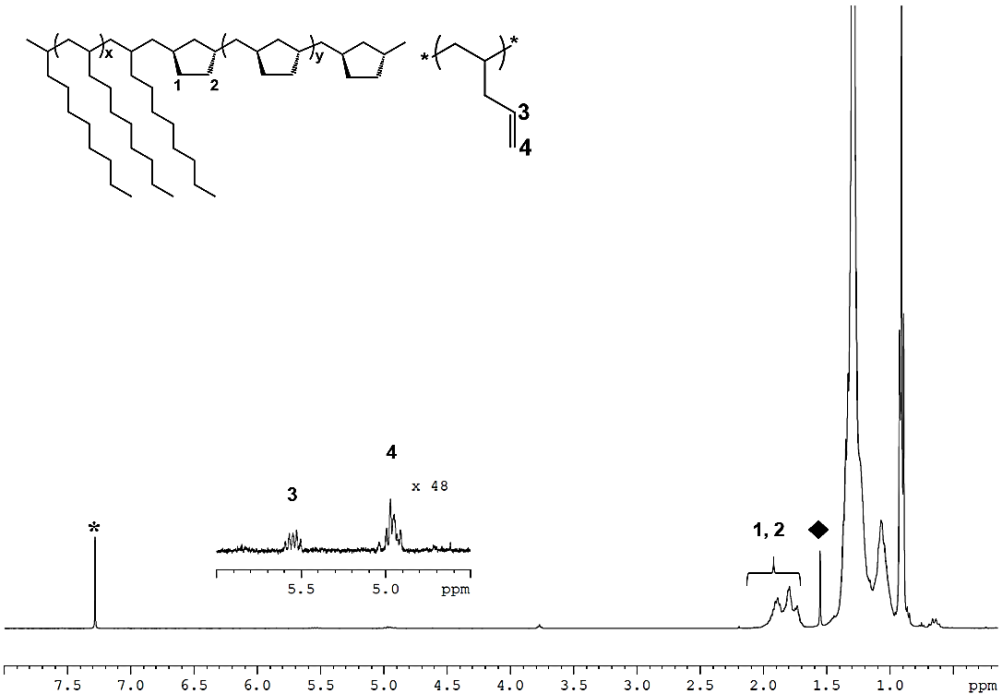

B.

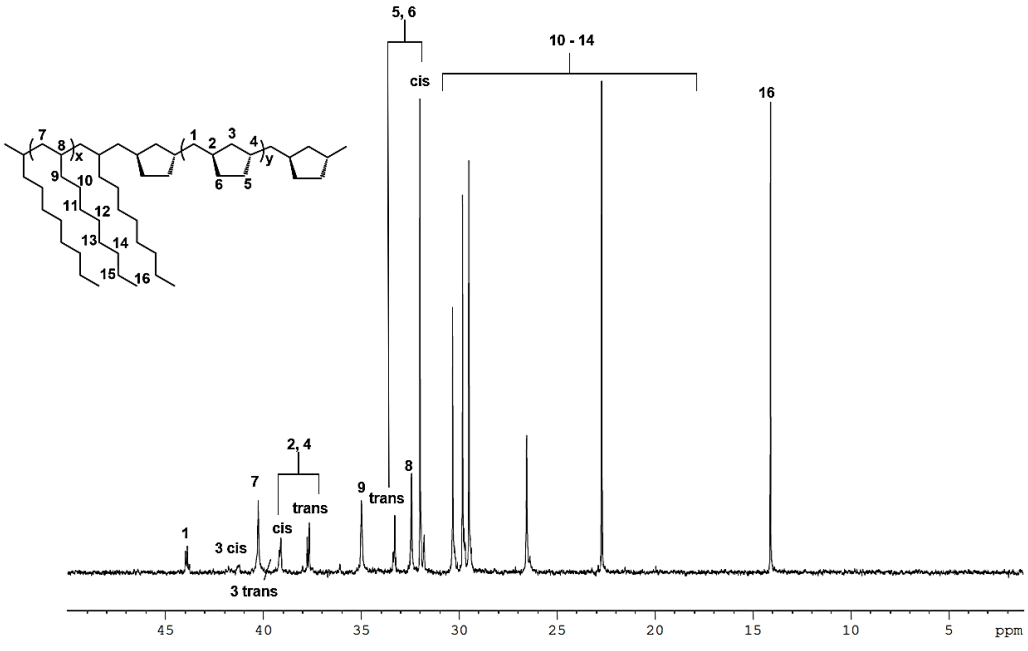

Figure S5.5. (A) ^{1}H-NMR (400 MHz, *1,1,2,2-C_2Cl_4-*d2*, RT, ◆water peak at 1.5 ppm) of **5.5**(iPD-PMCP). The protons from pendant group (3,4) and from 5-membered ring (1,2) are displayed. (B) ^{13}C-NMR (400 MHz, RT) of **5.5** (iPD-PMCP).

A.

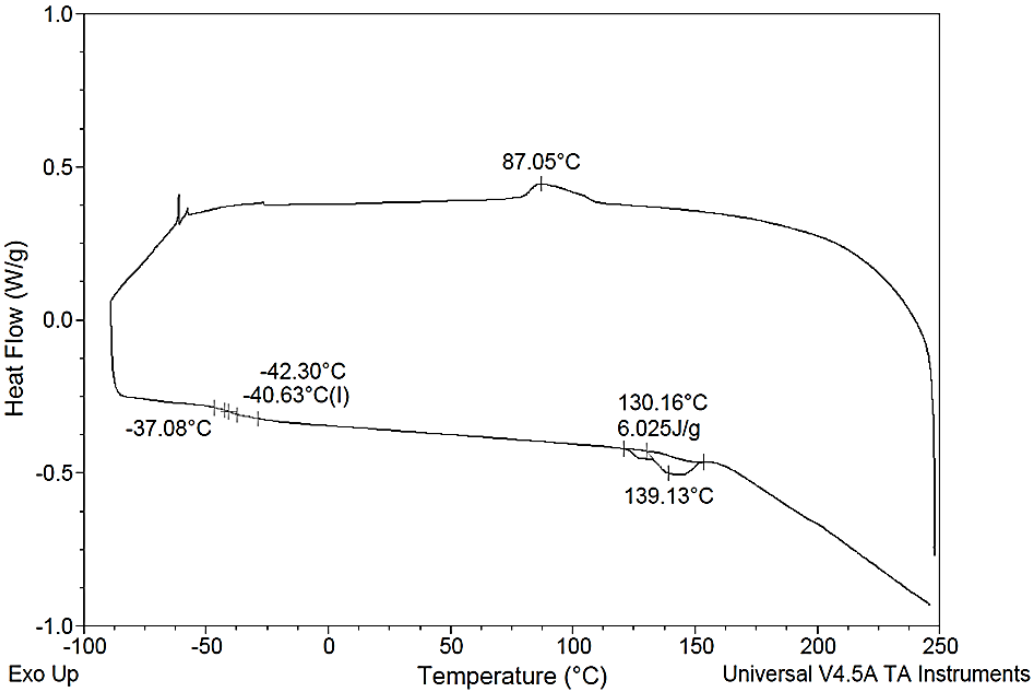
1.0
0.5
0.0
-0.5
-1.0
Heat Flow (W/g)
87.05°C
-42.30°C
-40.63°C(I)
-37.08°C
130.16°C
6.025J/g
139.13°C
-100
-50
0
50
100
150
200
250
Exo Up
Temperature (°C)
Universal V4.5A TA Instruments

B.

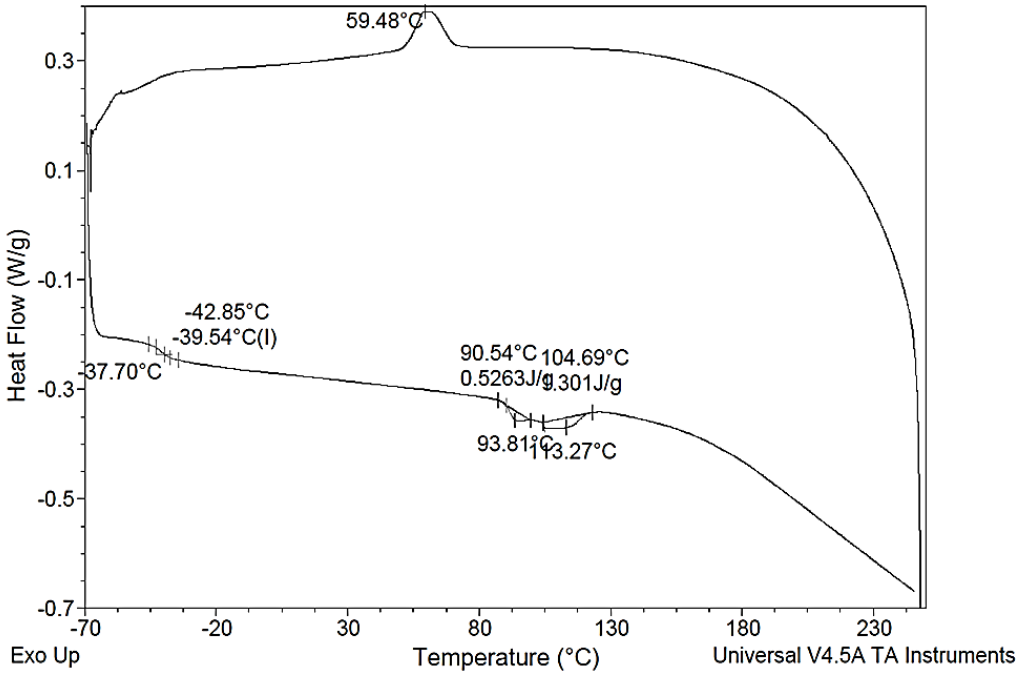
0.3
0.1
-0.1
-0.3
-0.5
-0.7
Heat Flow (W/g)
59.48°C
-42.85°C
-39.54°C(I)
-37.70°C
90.54°C
0.5263J/g
104.69°C
1.301J/g
93.81°C
113.27°C
-70
-20
30
80
130
180
230
Exo Up
Temperature (°C)
Universal V4.5A TA Instruments

C.

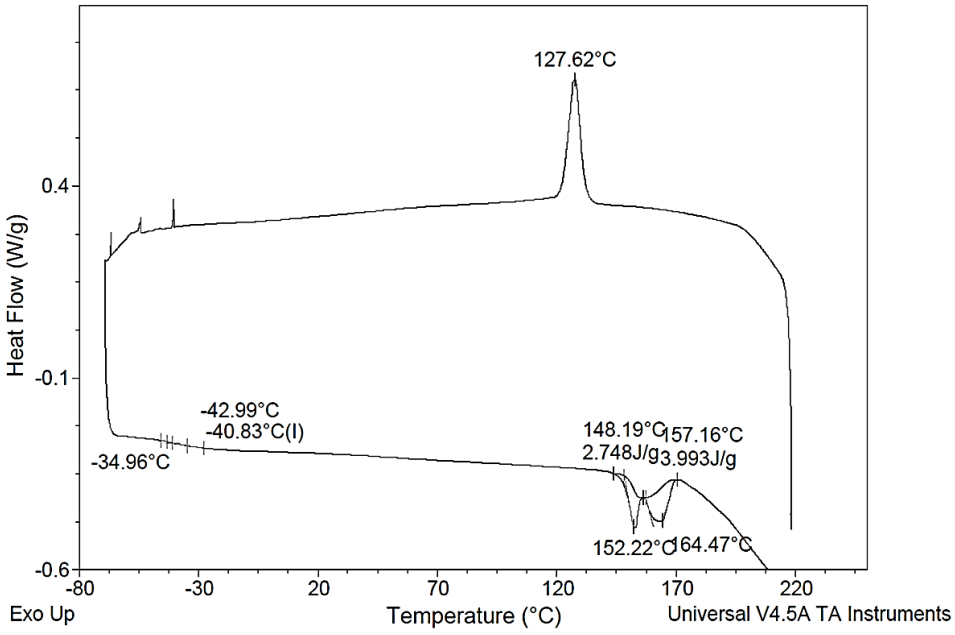

Figure S5.5. (A) DSC trace of **5.1** (iPH-PMP-PH). (B) DSC trace of **5.2** (iPH-PMP-PH). (C) DSC trace of **5.3** (iPH-PMP) were the first heat cycle in heat/cool/heat is removed with a ramp rate of 10 °C/min from -70 – 220 °C.

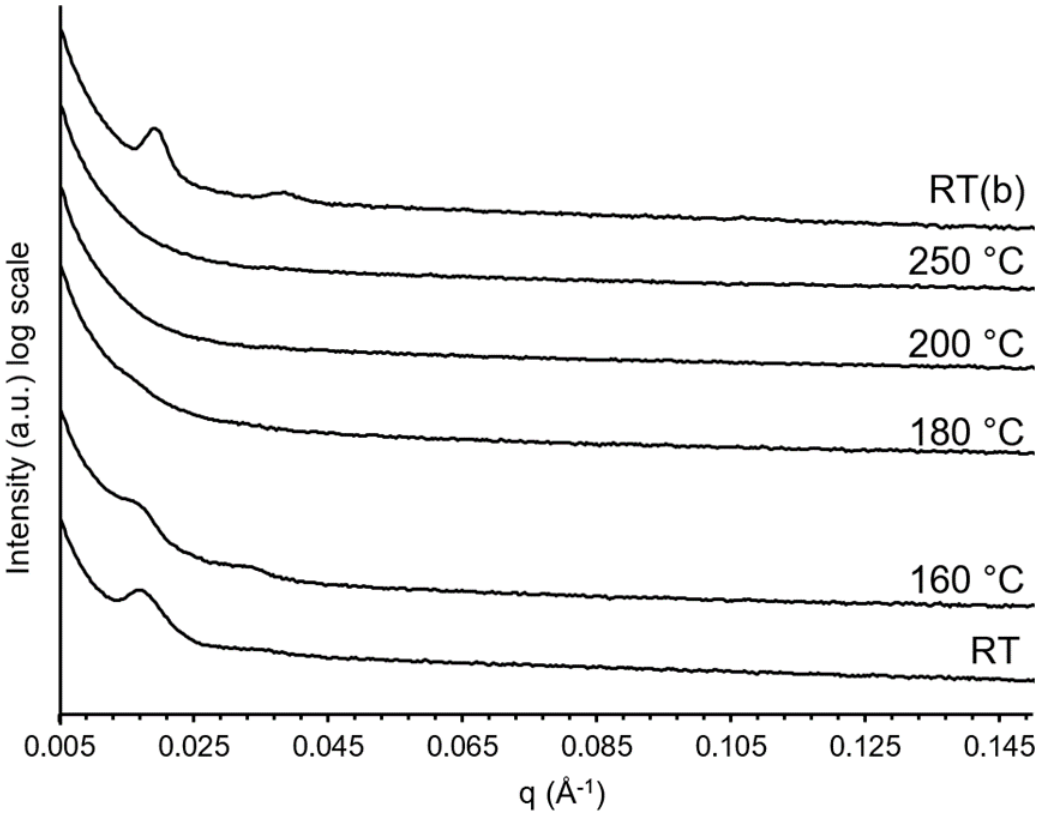

Figure S5.6. SAXS thermal ramp experiment of **5.1** (iPH-PMP-PH), heating at a rate of 1 °C/min from 30-145 °C, with the emergence of lamellae (LAM) at 160 °C, with a domain spacing of 28.5 nm. At 180 °C an order- to-disorder phase is observed continuing to persist all the way to 250 °C. After sample was cooled to room temperature (RT(b)) LAM returned with a domain spacing of 32.6 nm.

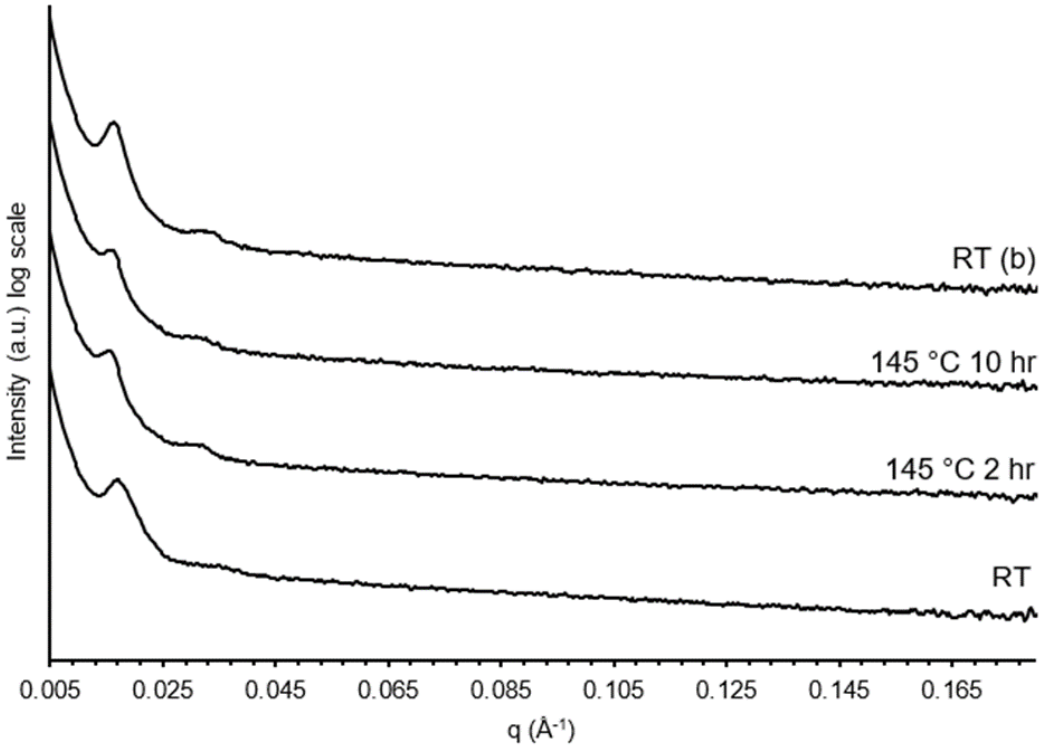

Figure S5.7. Isothermal SAXS profile of **5.1** (iPH-PMP-PH, at 145 °C showing no change in LAM with a domain spacing of 43.4 nm. LAM persisted after thermal ramp at room temperature (RT(b)).

.

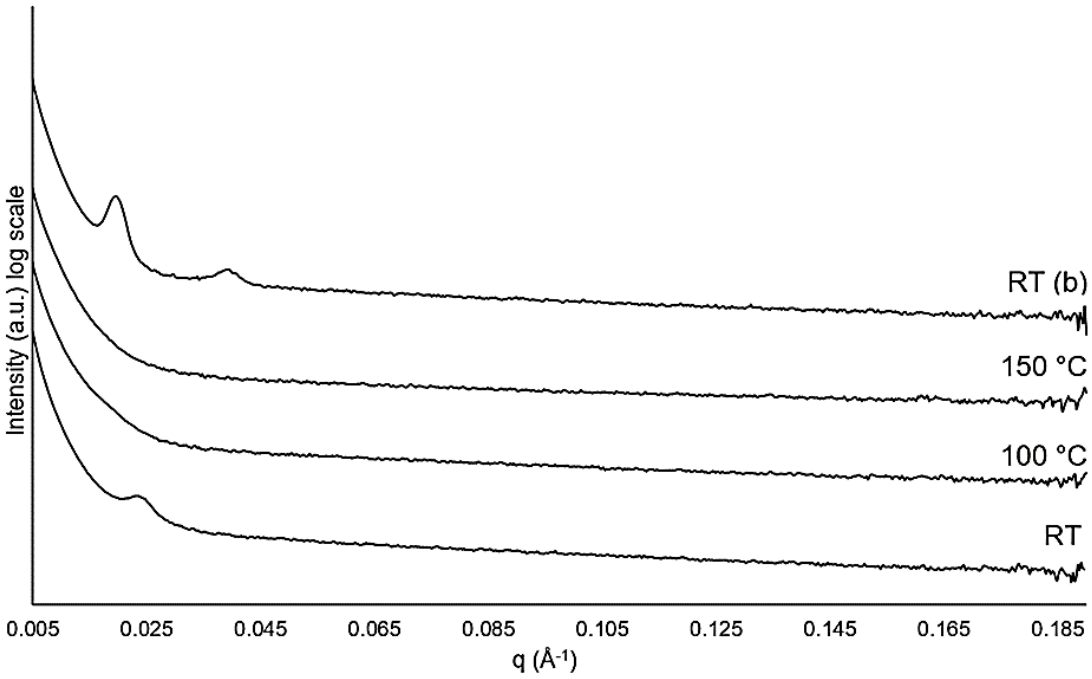

Figure S5.8. SAXS thermal ramp experiment of **5.2** (iPH-PMP-PH), heating at a rate of 1 °C/min from 30 °C – 150 °C, with the emergence of LAM after heating (RT(b)), with a domain spacing of 32.08 nm. Clear disorder phase past 100 °C to 150 °C.

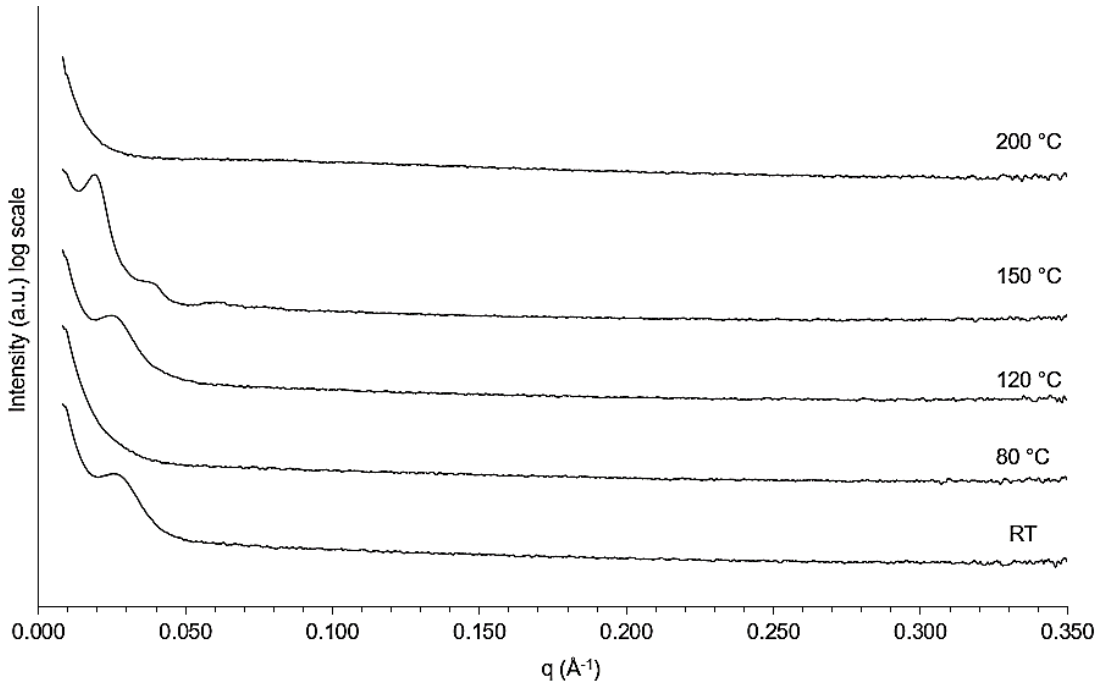

Figure S5.9. SAXS thermal ramp experiment of **5.3**, (iPH-PMP) heating a holding at each temperature for 1 hour, with the emergence of lamellae at 150 °C. Data obtained using Xenocs Xuess Linkam stage

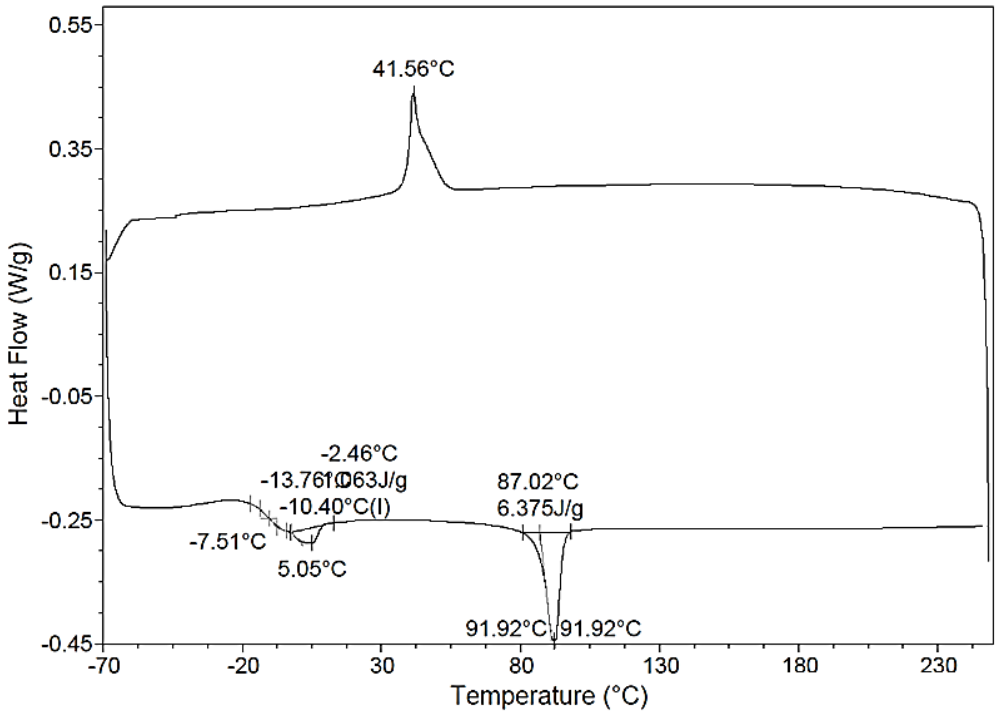

Figure 5.10 DSC trace of **5.4** (iPD-PMCP- were the first heat cycle in heat/cool/heat is removed with a ramp rate of 10 °C/min from -70 – 220 °C.

A.

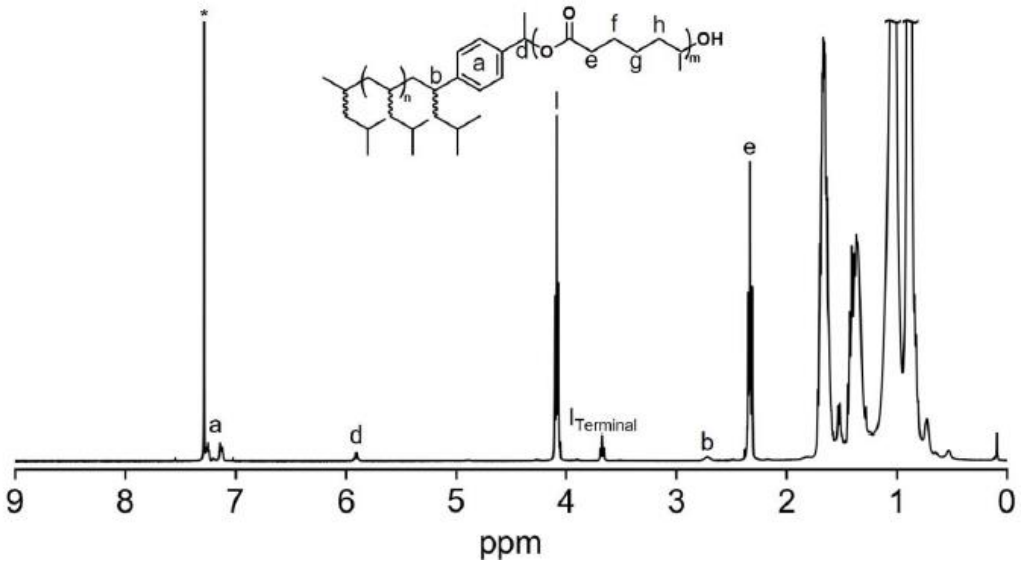

B.

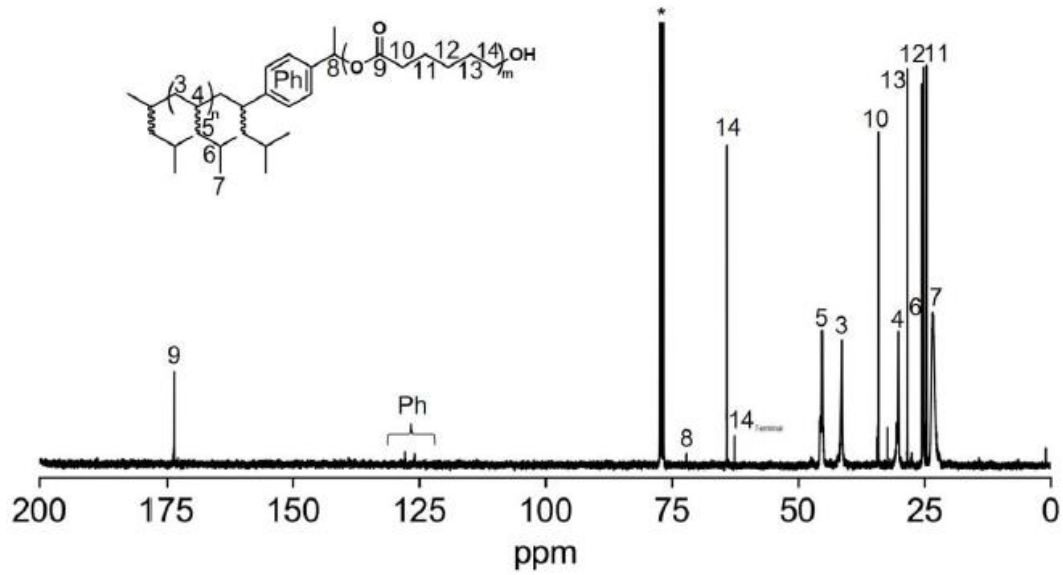

Figure S5.11. (A) ^{1}H NMR spectrum of aPMP-b-PCL, VIII (400 MHz, *Chloroform-*d1*, 25 °C). (B) ^{13}C {^{1}H} NMR spectrum of aPMP-b-PCL, VIII (100 MHz, *Chloroform-*d1*, 25 °C). For all materials in this study please see †.

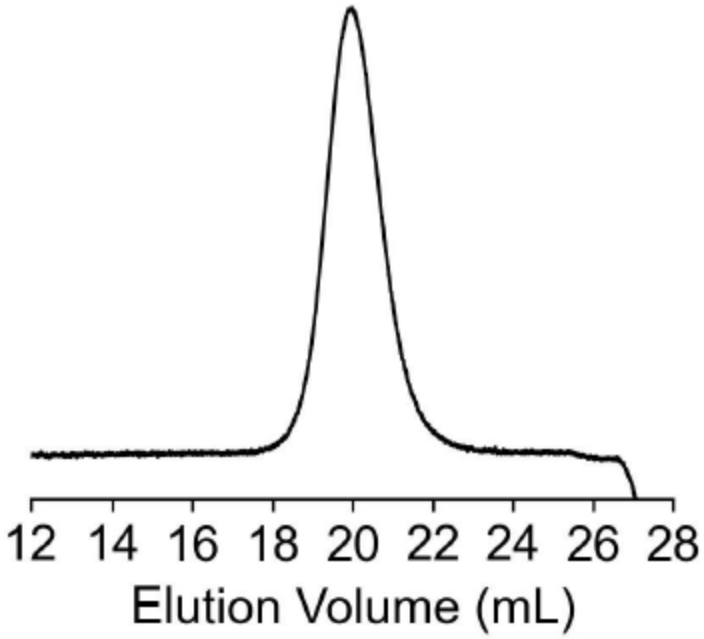

Figure S5.12. SEC differential refractive index trace of **aPMP-*b*-PCL, VIII.** *Mn* = 7.06 kDa, *Đ* = 1.26. For all materials in this study please see †.

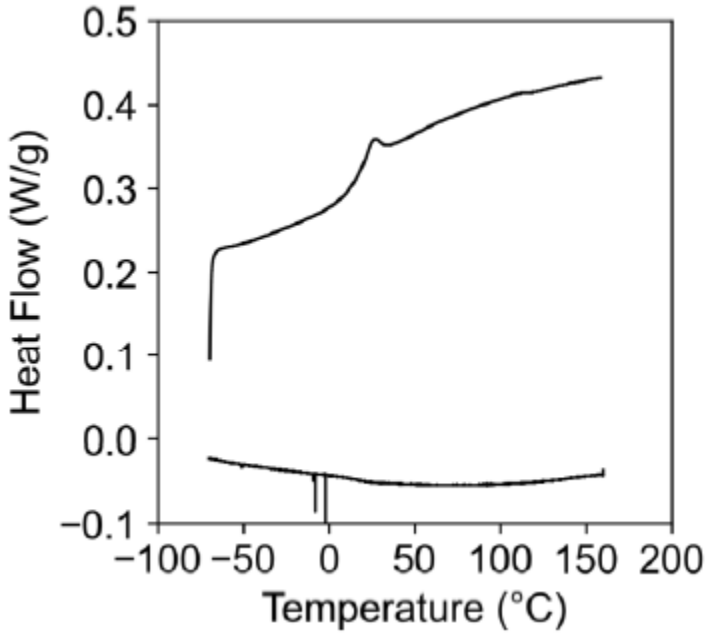

Figure S5.13. DSC trace of **aPMP-*b*-PCL, VIII** (exo down). Heat/cool/heat cycle with a heating ramp rate of 10 °C/min and a cooling ramp rate of 1°C/min from -70 – 160 °C. First cooling cycle (bottom) and second heating cycle (top) shown. *Tg* = 14.2 °C, *Tm* = 87.4 °C. For all materials in this study please see †.

Figure S5.14. *ps-tm* AFM phase map of a 60-nm-thick film of **aPMP-*b*-PCL, VIII** on a c-Si substrate annealed at 100 °C. For all materials in this study please see †.

A.

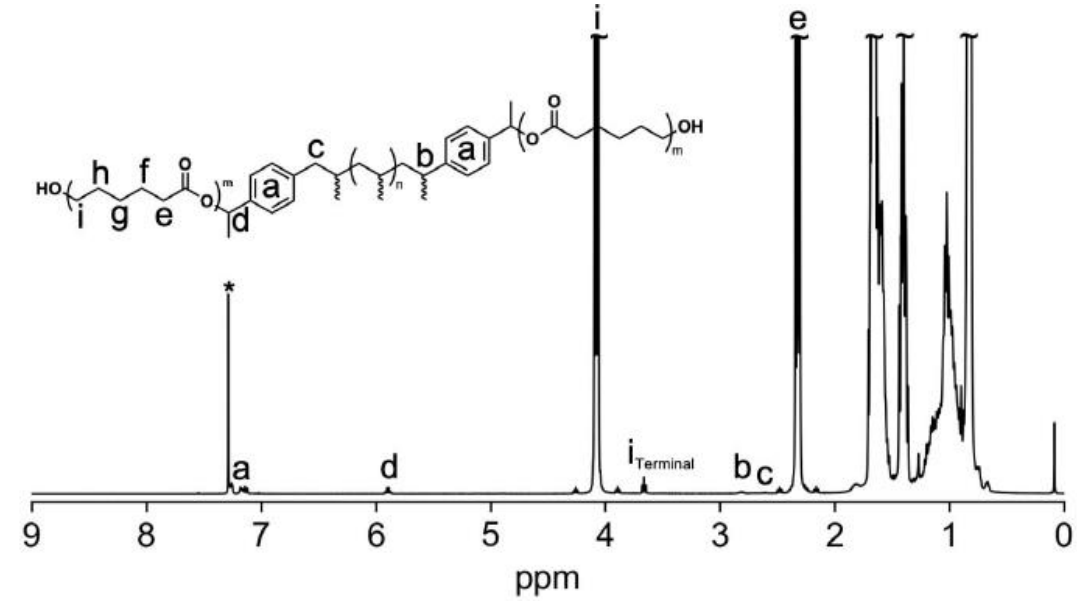

B.

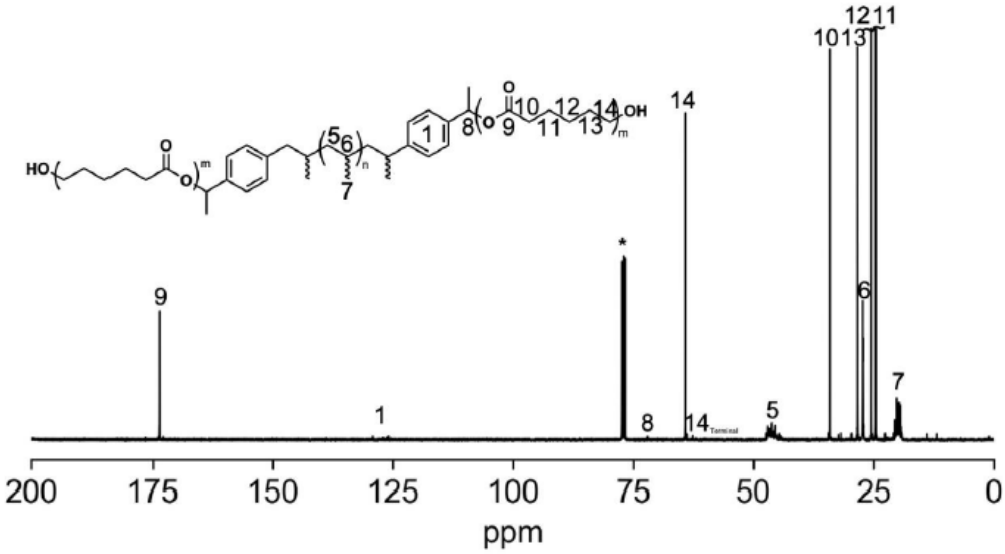

Figure S5.15. (A) ^{1}H NMR spectrum of **PCL-*b*-aPP-*b*-PCL, IX** (400 MHz, *Chloroform-*d1*, 25 °C). (B) ^{13}C{^{1}H} NMR spectrum of **PCL-*b*-aPP-*b*-PCL, IX** (100 MHz, *Chloroform-*d1*, 25 °C).
For all materials in this study please see †.

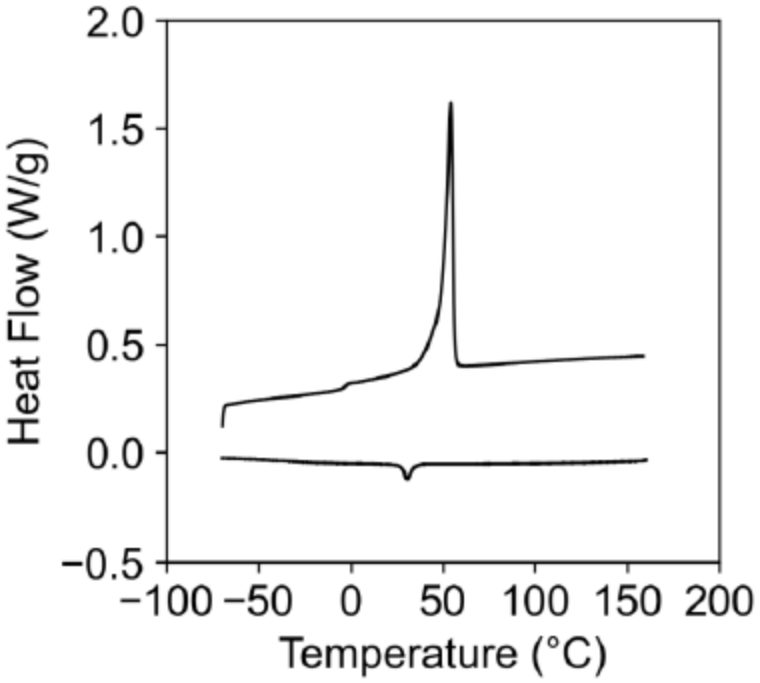

Figure S5.16. DSC trace of **PCL-*b*-aPP-*b*-PCL, IX** (exo down). Heat/cool/heat cycle with a heating ramp rate of 10 °C/min and a cooling ramp rate of 1 °C/min from -70 – 160 °C. First cooling cycle (bottom) and second heating cycle (top) shown. *Tg* = –4 °C. *Tm* = 54 °C. For all materials in this study please see †.

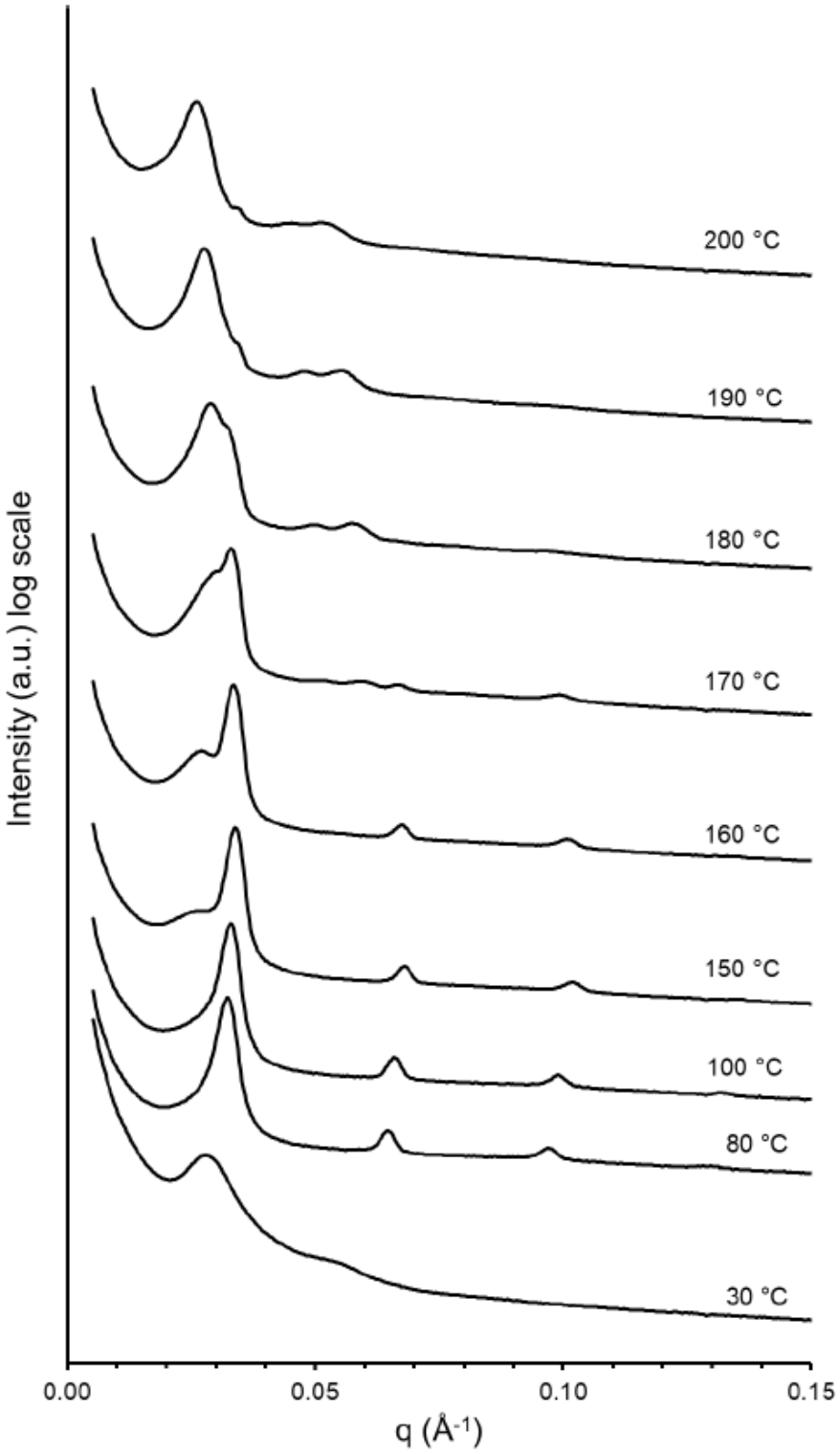

Figure S5.17. 1D SAXS profile of **PCL-*b*-aPP-*b*-PCL, IX.** Heated at 10 °C/min and held at each temperature for 30 minutes. Scanned at 600 sec exposures, then accumulated 10 accumulations. For all materials in this study please see †.

Table S5.1. List of observed peak positions (qobs), domain spacing (d), cylinder-to-cylinder distance (*dc*), and temperatures of **PCL-*b*-aPP-*b*-PCL, IX**, from Figure S120.

Phase	Temperature (°C)	Miller Indices (hkl)	Spacing (nm)	*q*-value ratio	q_{obs} ($Å^{-1}$)
Lamellar	80 °C	(100)	(d) = 19.3 nm	1	0.0325
		(200)		2	0.0648
		(300)		3	0.0971
Lamellar	100 °C	(100)	(d) = 19.0 nm	1	0.0330
		(200)		2	0.0662
		(300)		3	0.0991
Lamellar	150 °C	(100)	(d) = 18.5 nm	1	0.0339
		(200)		2	0.0679
		(300)		3	0.1019
Lamellar	160 °C	(100)	(d) = 18.7 nm	1	0.0336
		(200)		2	0.0673
		(300)		3	0.1013
Hexagonally Packed Cylinder	170 °C	(100)	(d_c) = 23.6 nm	1	0.0305
		(110)		√3	0.0533
		(200)		√4	0.0599
Hexagonally Packed Cylinders	180 °C	(100)	(d_c) = 25.2 nm	1	0.0291
		(110)		√3	0.0499
		(200)		√4	0.0575
Hexagonally Packed Cylinders	200 °C	(100)	(d_c) = 27.6 nm	1	0.0263
		(110)		√3	0.0454
		(200)		√4	0.0518

Chapter 6: Sugar Polyolefin Conjugates†

Lachmayr, K. K.; Wentz, C. M.; Sita, L.R., An exceptionally stable and scalable sugar-polyolefin Frank-Kasper A15 phase. *Angew. Chem. Int. Ed.* **2020**, *59*, 1521-1526.

Author Contributions:
L. R. S. Lead conceptualization, funding, and writing.
C. M. W. Supported writing, reviewing, and editing. Synthesized the new sugar-polyolefin conjugates, while the material was characterized by K. K. L and C. M. W. The collection and analysis of SAXS data was performed and processed by K. K. L., with assistance from C. M. W., of these new materials. L. R. S. wrote the manuscript with contributions from K. K. L and C. M. W. for analysis and implementation of the research that aided in writing of the manuscript. L. R. S. provided the computer-generated graphics and originated the proposed solid-state C → A15 epitaxial order-order transition mechanism. All authors performed the analysis, contributed to discussions and interpretations, and assisted in preparing the manuscript.

Wentz, C. M.; Lachmayr, K. K.; Tsai, E. H. R.; Sita, L. R., Thermotropic Glycolipid Quasicrystal and Frank-Kasper Phases: Unique Mechanism for Rapid Phase Transitions, *(manuscript in preparation).*

Author Contributions:
L. R. S. Lead conceptualization, funding, and writing.
C. M. W. Synthesized the sugar-polyolefin conjugates which formed FK A15 at room temperature. K. K. L. Lead the synthesis and creation of multicomponent sugar-polyolefin blends. All authors performed the analysis, contributed to discussions and interpretations, and assisted in preparing the manuscript. E. H. R. T. Assisted with the collection of SAXS data.

6.1 Background

There are many reasons why sugar polyolefin conjugates have become an essential molecule of exploration given that sugar-based surfactants are a popular class

† The results, figures, schemes, and tables discussed within this chapter have been reused or adapted with permission from Lachmayr, K.K.; Wentz, C. M.; Sita, L.R., An exceptionally stable and scalable sugar-polyolefin Frank-Kasper A15 phase. *Angew. Chem. Int. Ed.* **2020**, *59*, 1521-1526. Copyright 2020 John Wiley and Sons.

of amphiphiles that have a versatile and benign chemical nature, on top of being a way to expand the application range of our groups non-polar building blocks.[1,2] By design, each component is tunable, scalable, and has unprecedented phase behavior with its overall structure seen in Scheme 6.1. The sugar-polyolefins are comprised of a crystalline sugar head group that can be adapted as either a monosaccharide or disaccharide. This selection of head group can change the overall crystallinity and 'shape' of the material. For example, when using a disaccharide head-group the shape is more 'rod-like' than a monosaccharide and can therefore affect the self-assemblies and mechanical stability of the material. The sugar head-groups that have been previously investigated include galactose, cellobiose, melibiose, lactose, and maltose.[1-4] However, alone, many sugar-based surfactants lack the option of programmability. On the other hand, our system has access to tunable structure through a chemical linker that then attaches to an endless selection of polyolefin tails. Linkages previously explored include triazole linkage which is accessed through click-chemistry, and direct ether-linkages both of which have been used in the current studies. Overall, the investigation of sugar polyolefin conjugates began in 2015 by Thomas *et al.* which has then been used to direct Nowak *et al.*, 2017, and Lachmayr *et al.*, 2020, research in discovering desirable and rare phases such as double gyroid and Frank-Kasper (FK) phases.[2-6]

The self-assembling behavior of amphiphiles has been well studied as previously discussed, however the sugar polyolefins conjugates were engineered to have small dimensions using low molecular weight polyolefin domains for the purpose of accessing smaller dimensionalities to be utilized in nanoscale applications.[7]

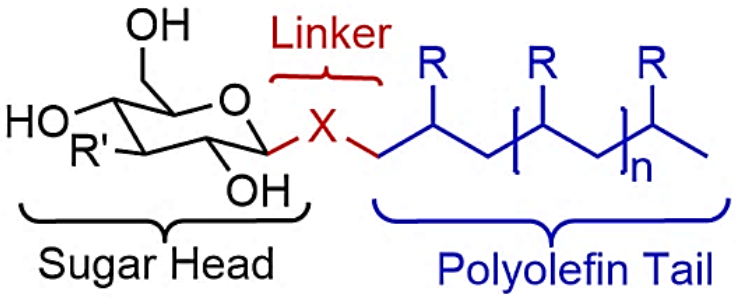

Scheme 6.1 Chemical layout structure of sugar polyolefin conjugates.

Moreover, selection and synthesis of atactic, amorphous, and low molecular weight polyolefin tails allow for conjugates to undergo rapid order-to-order (order-order) phase transitions through the low glass transition temperatures of these domains (Tg). The best strategy to access these sub-10-nm domain morphologies with a limit to chain lengths, requires the access to large Flory-Huggins interaction parameter, χ, to ensure this microphase separation occurs, and domain spacing is a direct result of this parameter, *d*, according to Equation 6.1. In these sugar polyolefins the self-assembly arises due to the incompatibility between a crystallin hydrophilic sugar head-group and a hydrophobic amorphous polyolefin tail, even at low chain lengths, *N*. This incompatibility is large enough that the χ parameter is large and can observe rich phase behavior for both classical and nonclassical morphologies.

Equation 6.1 $$d \approx N^{\frac{2}{3}} \chi^{\frac{1}{6}}$$

Herein, the use of modified polyolefin tails as a building block for sugar polyolefin conjugates have been investigated. The polymer domains that are carefully controlled and design to have specific; (1) occupied volume of the domain, (2) length of the chain, (3) bulk of pendant side groups, (4) overall stereo engineering of the

material, all for the purpose of directing self-assembly. The tunable nature of our non-polar domains help directs the orientation and overall nature of the sugar polyolefin material which leads to the larger goal of this work, which was to not only expand the library of materials, but to use precise polyolefin tails never explored before. This was all done in hopes to access complex, rare, and not well understood phases to expand the knowledge of materials and applications of amphiphilic polyolefin conjugates. Thus, showing the relevance, versatility, and necessity of our group's polyolefin building blocks.

6.2 Introduction

When it comes to soft matter "one-component" Frank-Kasper (FK) phases, they are an intriguing structural form that arises from the close packing of deformable or squishy spheres that are classified as size- or shape-distinct sets of particles. These FK phases have been documented in amphiphilic liquid crystals, dendrons, block copolymers, giant molecules, surfactants, nanoparticles, and sugar polyolefins conjugates.[6,8-22] That being known, Frank and Kasper originally developed the concept of topological close packing (TCP) of these sphere-shaped particles through complex crystal structures of intermetallic alloys. They proposed that FK phases arise through the packing of asymmetric polyhedra and are associated with different sets of atoms with coordination numbers, CNx, where x = 12, 14, 15, or 16. Figure 6.1A can be helpful when visualizing the unit cell of cubic FK A15 ($Pm\bar{3}n$). When found in bimetallic allows with A_3B stoichiometry, such as, Nb_3Sn, it arises from two

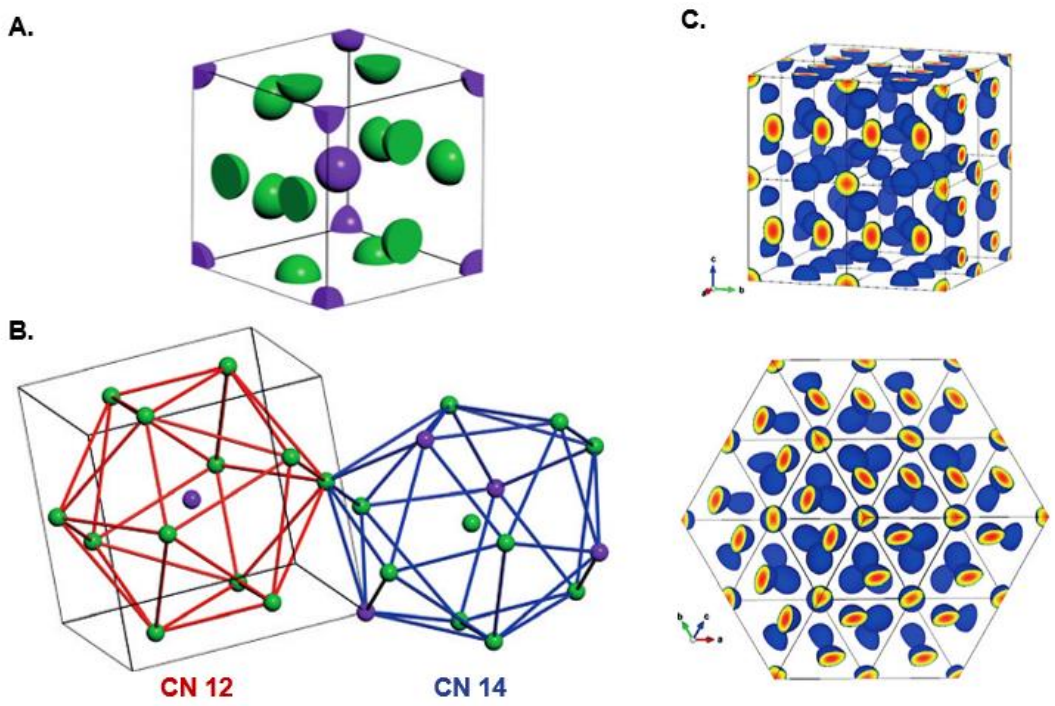

Figure 6.1 (A) Frank Kasper unit cell with stoichiometry A_3B, where crystallographic equivalent corner and center positions are in purple for the B-atoms and face center site are in green for the A-atoms. (B) FK distorted polythedra with coordination numbers (CN) 12 and 14 on the A-atoms. (C) Electron density maps, derived from SAXS data of CB-aPMP (**6.1**) at 212 °C of different orientations of a 4x2 lattice of eight-unit cells. †

crystallographically equivalent B sites and reside within CN12 distorted icosahedra, while six equivalent face-shared A sites are associated with CN14 polyhedra, this can be visualized with Figure 6.1B. There has been great success with 'hard' sphere FK phases which have been utilized in super-conducting materials.[38] Due to this, one of the primary objectives have been to discover one-component soft matter material that can access FK phases. This is desirable so that new underlying principles and mechanisms can be discovered, and potentially new physical properties and applications arise. The concept of one molecule not only self-assembling but self-assembling in a way that requires two distinct shapes or sizes may seem

counterintuitive, but as seen herein and by many others is in fact possible. There are many difficulties when it comes to designing, predicting, and accesses FK phases, since there are few examples of thermotropic soft matter molecules that access FK phases easily it is of great interest to target these phases and discover more. Additionally, there are few examples where the FK A15 is stable for an extended period, or that the material is made through scalable syntheses. Furthermore, there are limited proposed mechanisms by which these phases are observed. For the discovery of new materials to be made and technological innovations that benefit society to occur, we must address all these concerns and seek exploration with the purpose of designing an FK forming material. It is not only about finding an FK forming material but to realistically one day use the FK forming material to do so it must have improved thermodynamic and kinetic stability. The materials must be made in scalable and practical quantities through simple synthetic routes. Lastly, these phases need to be accessed through short to no annealing process. All these relevant concerns and goals represent the scope at which the studies talk about in this work cover.

6.3 Exceptionally Stable One-Component FK A15 Phase

From the original goal to utilize our precisely designed *atactic* polyolefins as a building block for sugar polyolefin materials for new applications, serendipitously the discovery of an FK A15 phase was made. This was done by using an one-component sugar polyolefin conjugate which contained a cellobiose head-group and a 1 kDa molecular weight atatctic poly(4-methyl-1-pentene) (aPMP) tail, CB-aPMP **6.1**, seen

chemical structure in Scheme 6.3. This led to the development of a mechanism that elucidated how an initially identical set of sphere-shaped particles can self-sort into two or more different sets of spheres thus having different sizes or shaped to lead to FK A15 phase. Furthermore, this initial discovery while unexpected has allowed further exploration to be guided through the understandings made with this material.

The sugar polyolefin conjugates **6.1**, CB-aPMP, was obtained through copper mediated click chemistry with a general outlined synthetic scheme for all sugar conjugates shown in Scheme 6.3. The cellobiose sugar head group utilized in **6.1,** CB-aPMP, is first propargylized to allow an azido terminated PMP tail to chemically link. The PMP tail utilized in this study was synthesized through easily scalable LCCTP

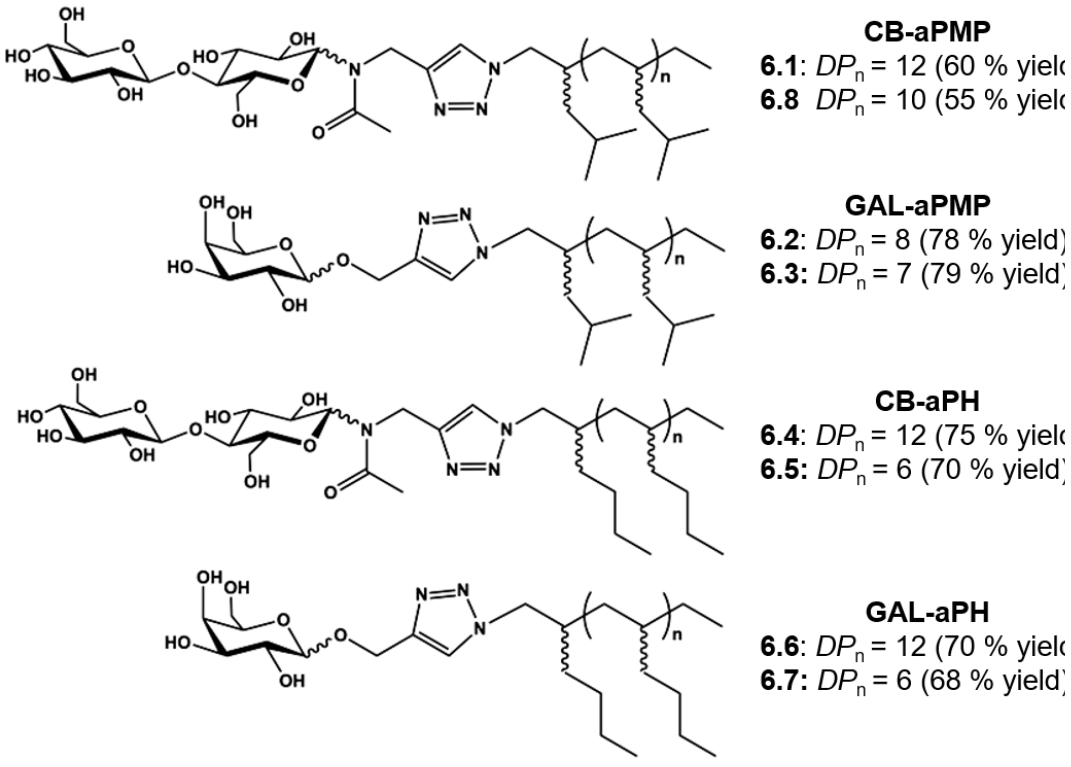

Scheme 6.2 List of structures of sugar polyolefin conjugates with abbreviations, DP_n which corresponds to the polyolefin tail, and yield for the bulk conjugate, for conjugates **6.1 - 6.8.**

technique to form an ultra-low molecular weight of 1 kDa which possesses a narrow PDI. The azido terminated polyolefin is first quenched with elemental iodine to end-group iodo-functionalize and then through simple substitution reaction with sodium azide one can obtain the aPMP polyolefin domain. The overall conjugates can be analyzed with ^{1}H NMR, revealing a successful synthesis with the appearance of rotamer-proton resonances, Figure 6.2, confirms that the triazole linkage between the two domains are formed. The molecular weight of the polyolefin tail is determined before it is attached to the sugar head group through gel permeation chromatography (GPC) but once attached to the sugar head-group can be reexamined through matrix-assisted laser desorption/ionization time-of-flight (MALDI-TOF) mass spectrometry

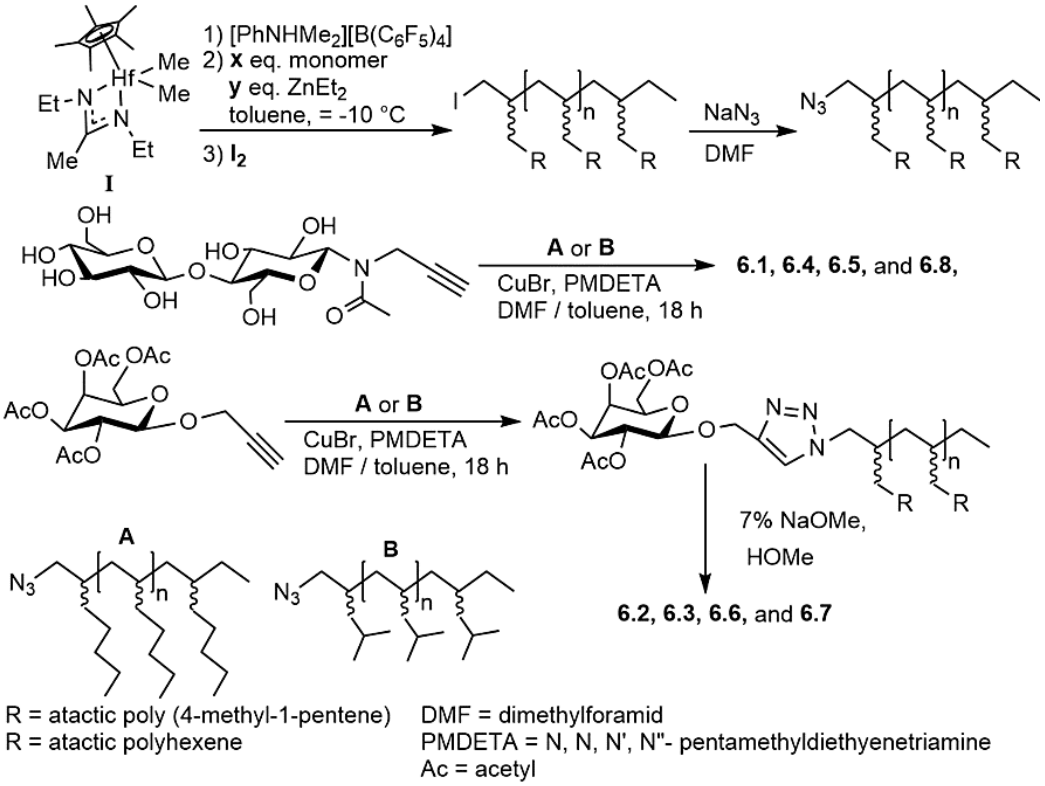

Scheme 6.3 Structure and synthesis of sugar-polyolefin conjugates.[†]

(MALDI-TOF), found in the supporting experimental information (SI). Specifically, the PMP tail has an Mn = 1.0 kDa and $Đ$ = 1.05. To understand the physical properties of the polyolefin domain thermal analysis with differential scanning calorimetry (DSC) is utilized. The instrument is run over the range of -70 to 200 °C, which shows two glass transitions, one at 19 °C which corresponds to the aPMP building block domain, and the other at 80 °C which relates to the sugar head-group. To understand when the CB-aPMP material degrades, and overall thermal stability, TGA was applied and thus determined the onset of thermal decomposition above 250 °C, see SI. The absence of significant weight loss before 250 °C indicated that the material is not hygroscopic, nor does it retain water or other solvents, this is commonly seen with polar hydrophilic head-groups. Based on all the information gathered with the intention of avoiding

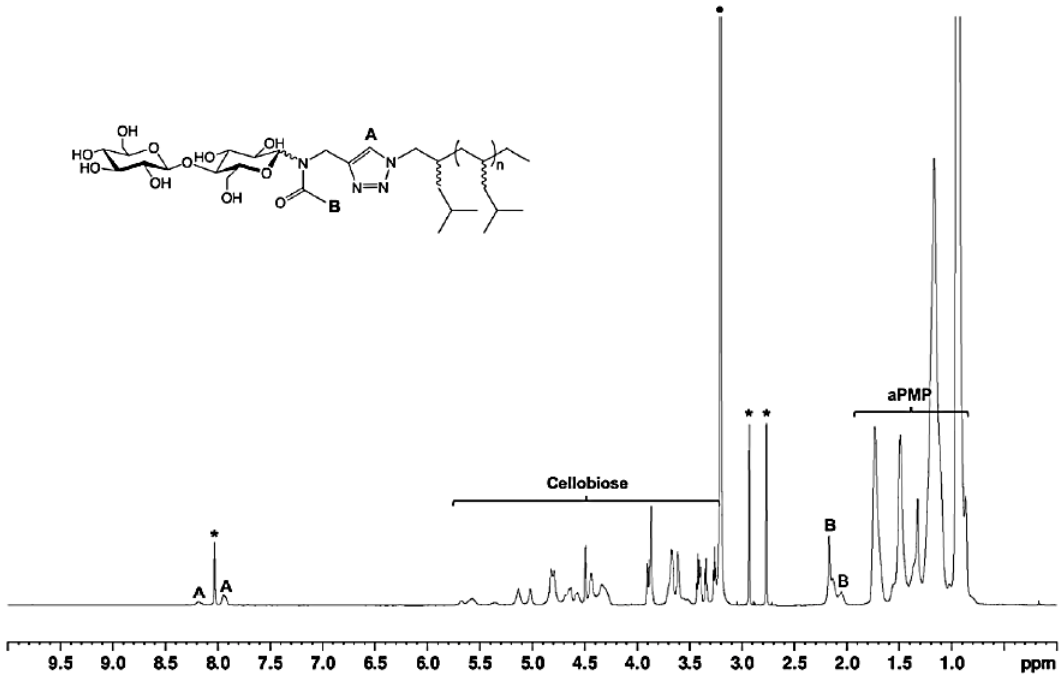

Figure 6.2 ^{1}H NMR of the CB-aPMP conjugate (**6.1**), *DMF-d7, 70 °C, calibrated at 8.03 (COH) ppm), where A marks the appearance of the triazole linkage with two rotamer proton resonances.[†]

thermal decomposition the materials were thermal annealing always under 220 °C and thermal studies would focus on temperatures before and after the 80 °C Tg observed. However, it must be noted that the materials undergo significant color change, white to yellow-brown, after the annealing studies are conducted.

The first attempt to study the self-assembly of the CB-aPMP involved tapping mode AFM results (ps-tm AFM), with both unannealed and annealed samples, but no remarkable features were seen despite previous success with other sugar polyolefin conjugates. With the assistance of Kätchen K. Lachmayr small angle x-ray scattering (SAXS) was needed to study the self-assembling behavior. Given no previous background with this technique this became a major contribution made by my mentor. Using synchrotron x-ray source at Brookhaven National Lab, a routine variable temperature (VT) SAXS experiment was run. On the very last run of the trip the CB-aPMP **6.1** conjugate was placed on the thermal heating stage. The sample was packed

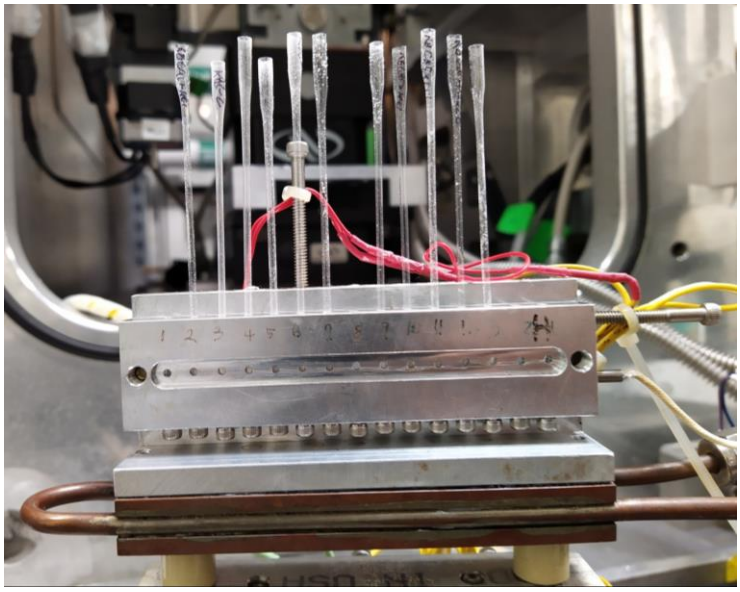

Figure 6.3 Thermal heating stage at Brookhaven National Lab (BNL) where samples are loaded into capillaries, wax sealed, and within the stage.

into a capillary, sealed with melted wax, and placed on the thermal stage seen in Figure 6.3. A heating rate of 1 °C/min from 30 °C to 220 °C was implemented to see any quick order-order transitions as well as capture the whole temperature range. The material is exposed for 10 seconds at a time while the holder is rastered by 0.05 nm increments to avoid beam damage when collecting the data. In figure 6.4 selected VT SAXS images are chosen out of the ramp and highlighted is the initial self-assembly seen which was a hexagonally packed cylinder (*C)* phase .

Remarkably the CB-aPMP conjugate, **6.1**, undergoes an irreversible order-order phase transition from an initial *C* phase to FK A15 phase, Figure 6.4. This is observed with short duration of thermal annealing, and upon cooling to room temperature the FK A15 phase can be seen up to three months, hence the name exceptionally stable. Moreover, the material can withstand thermal cycling to 180 °C

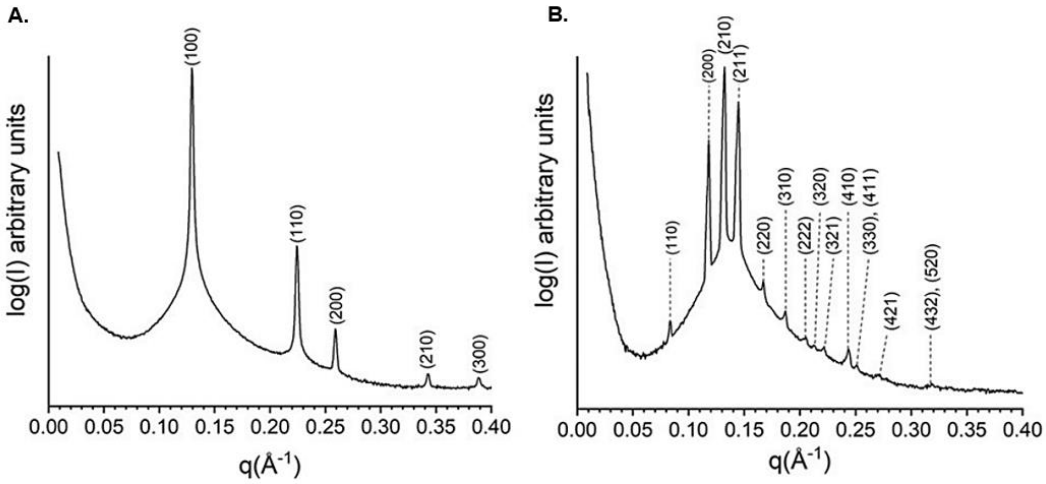

Figure 6.4 (A) SAXS data from selected synchrotron data for a solid sample of CB-aPMP (**6.1**) obtained at fixed time intervals during a heating rate 1 °C/ min at 136 °C with *hkl* Miller indices assigned for a hexagonal cylindrical (*C*) phase. (B) Additional selected SAXS data obtained in the same manner as (A) but at 212 °C with *hkl* Miller indices assigned for the FK $A15_e$ phase. †

and measurements redone in-house on UMD SAXS instrument. The initial *C* phase can be observed at ambient temperatures, Figure 6.4A, and the *C* phase persists until 136 °C, q/q^* = 1, √3, √4, √7, and √9 where q* = 0.1294 $Å^{-1}$, which correspond to the *hkl* miller planes (100), (110), (200), and (300) respectively. After 136 °C five new scattering peaks start to become visible thus representing an order-order transition were the data gathered contained both the original *C* phase and the next phase. The cylinder-to-cylinder domain spacing, d_c, was determined from equation 6.2, and was seen to decrease linearly in d_c for a total of 4.1 %. With an initial d_c = 5.84 nm at 31 °C and only 5.61 nm at 136 °C. This trend is still seen at temperatures were the A15 phase occurs.

Equation 6.2 $d_c = 2\,(d_{110})$ where $d_{110} = 2\pi/q_{110}$

Upon heating to 145 °C the FK A15 scattering peaks grow in through order-order phase transition. These specific peaks continue to increase in intensity until 181 °C, where they diminish, therefore being labeled as a transient phase, FK $A15_t$, Figure 6.5A. At this temperature, a third set of peaks become visible through another order-order transition, which then becomes the only phase dominating at 212 °C, therefore labeled as equilibrium phase, FK A15e, Figure 6.5B. Most notably, between ranges 195 °C to 205 °C, all three-phases coexist which is a highly rare phenomenon for thermotropic phase behaving soft materials.[23] These FK phases were indexed by matching number, pattern, and position of scattering peaks to already documented indices of FK A15 phases in other materials. For each FK A15 phase there was thirteen peaks documented. At 212 °C for the transient A15 q/q^* = √2, √4, √5, √6, √8, √10, √12, √13, √14, √17, √18, √21, and √ 24, where q* = 0.0805 $Å^{-1}$. At 195 °C for the

equilibrium A15, q* = 0.0823 Å^{-1}, all corresponding *hkl* Miller planes are indexed as well.

Equation 6.3 $$\frac{1}{d_{hkl}^2} = \frac{1}{a_{A15}^2}(h^2 + k^2 + l^2)$$

The lattice parameter, *a*, was extracted from the A15 transient and equilibrium phases and calculated using Equation 6.2 which is the scattering wave vector modulus for cubic lattices.[24] Where $d_{hkl} = 2\pi/q_{hkl}$, q is the position of each peak (Å^{-1}). The equation is solved graphically using $y = mx + b$ form, where b is approximately equal to zero, and the slope m, was used to determine a. Once a was calculated, specific temperature points were determined individually, were $A15_t$ a_t = 11.10 nm and $A15_e$ a_e = 10.81 nm, at 195 °C. Notably, a large difference was observed at 212 °C, with the a_e now calculated to be 10.58 nm, which represents a 4.7 % decrease relative to the measurement before.

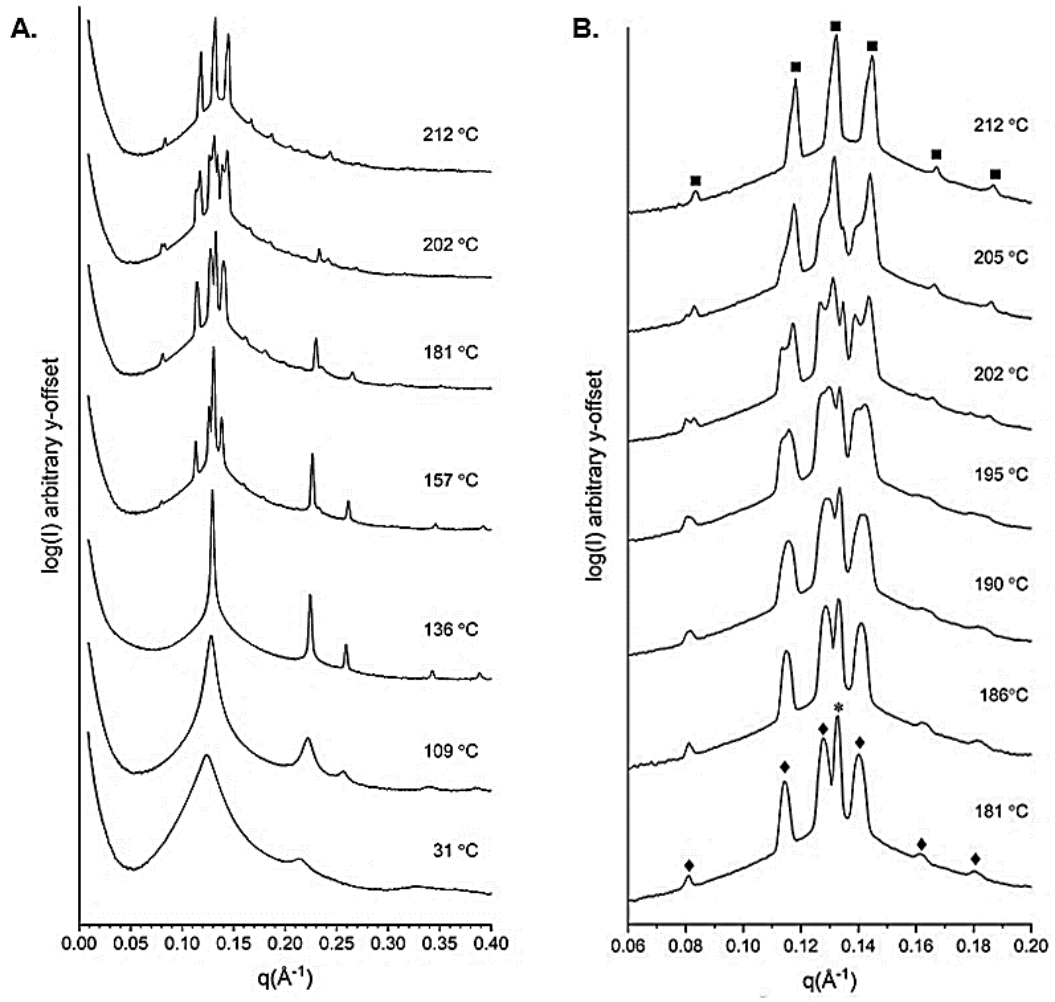

Figure 6.5 (A) Variable temperature (VT) SAXS data from selected synchrotron data for a solid sample of CB-aPMP (**6.1**) obtained at fixed time intervals during a heating rate 1 °C/ min starting from an initial temperature of 30 °C and up to a final temperature of 220 °C. (B) Additional selected SAXS data obtained in (A) with expanded x-axis showing coexistence of *C* (*), a transient FK A15$_t$ phase (◆) and a final equilibrium FK A15$_e$ (■).[†]

6.3.1 Mechanism

To obtain more structural information, Dr. Lawrence R. Sita, used the synchrotron SAXS data from the FK A15$_e$, at 212 °C with JANA2006 program to

generate electron density maps, Figure 6.1C. This was done by first performing *a le* Bail refinement to calculate sets of *hkl* reflections and intensities that were then inputted into SUPERFLIP computational reconstruction. In keeping with similar analyses of soft matter FK A15 phases, the high electron density regions are associated with the sugar domains of core-shell micelles while the colorless space is occupied by the aPMP hydrocarbon chains. From these calculations the A face-centered sites were determined to have a more elongated shape comparative to the more spherical B corner and center positions, which match the nature of an A15 structure since it originates from different crystallographically distinct A and B sites by shape or size. The SUPERFLIP calculation yielded that the A sites are 0 to 25% larger than the B sites. Specifically chosen in Figure 6.1C is a 4x2 lattice of eight A15 unit cells, where the bottom electron density map is oriented on a 3-fold proper rotation axis along the B sites, thus allowing a visual of 3_1-screw axis about the A sites in alternating clockwise and counter-clockwise fashion, this becomes key in our proposed mechanism from a *C* phase to FK A15 phase through a symmetry allowed transition.

Before divulging more about the mechanism, it is important to note that low-level molecular mechanic simulations showed that the aPMP tail can adopt both wedge- and cone-shaped space-filling conformation, with the cone shape favored at elevated temperatures. This is not unheard of as others have seen transitions between an initial *C* phase and A15 phase, such as Percec's dendrimer model. In this model the highly branched dendrimer self-assembles into the *C* phase due to the wedge-shaped molecular units. Upon heating these dendrons convert to cone-shaped filling that drive conversion of cylinder domains into spherical particles. Yet this proposed mechanism

suggests that mass-exchange takes place so as to access the FK A15 phase.[39] This hypothesis does not make sense with our system as these order-order transition take place in a matter of minutes.

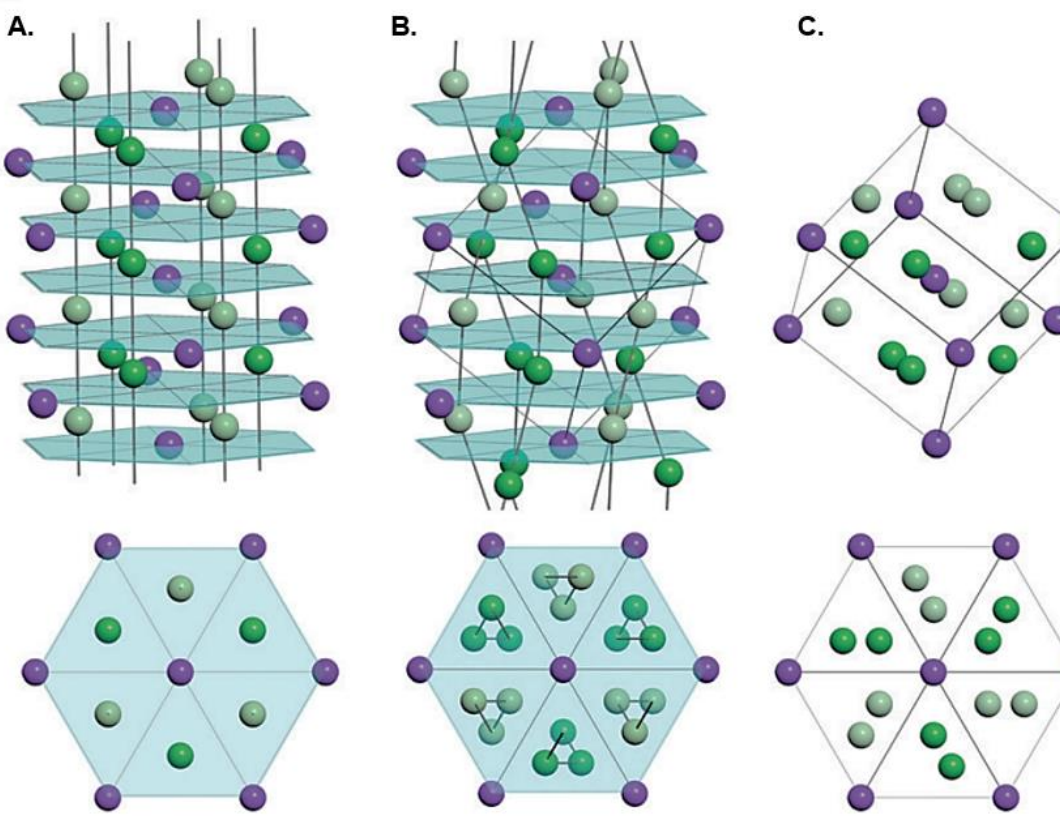

Figure 6.6 Proposed mechanism for solid-state epitaxial order-order transition between rhombohedral to cubic A15 phases via structural displacement of linear chains of spherical particles shown in the oblique (upper) and top (lower) views of (A) to form alternation 3_1 (light green) and 3_2 (dark green) helical chains in the corresponding oblique and top views of (B). In (C), removal of all features lying outside the boundaries of a cube with sided of length, a_{A15}, serves to generate the unit cell of the A15 phase.[†]

Never has a symmetry-allowed mechanisms been proposed that explains an irreversible transition between *C* phase and FK A15 phase. To adapt from Percec's dendrimer model, we agree that the cone to wedge shape transition is occurring within the aPMP tails which is supported through simulations and the supported decreased

cylinder-to-cylinder domain spacing previously discussed. We proposed that as temperatures increase these cylinders elongate before pinching-off into stacked spherical particles. Thus, these spheres undergo an inter- and intra-later displacement, from and initial AAA stacking to a rhombohedral ABC stacking arrangement, therefore having a direct conversion from hexagonal to cubic structures through a symmetry allowed rhombohedral transition. This idea of hexagonal to rhombohedral conversion have been previously observed within Au nanoparticles by a symmetry-allowed pathway.[25,26] As can be seen in the top views of Figure 6.5A-C the micelles shuffle along alternating 3_1 helical screw axis to occupy the transient A15 phase. We speculate that the significant amount of lattice parameter contraction occurs in the $C \rightarrow A15_t \rightarrow A15_e$ transition path which proves to have a high energy barrier thus making it irreversible and have a high kinetic stability. A potential driving force for this simple displacement from linear to helical arrangement can be due to maximization of spheres within a hexagonal array.

A unique feature of this proposed mechanism is that it avoids any large-scale structural reorganization of sphere, such as a translocation between different columns, to establish distinct sets of different sizes that then can undergo formation into various FK phases. Thus, making it a novel mechanism.

6.3.2 Conclusions

Others have proposed mechanism where FK phases are achieved through the melted or disordered states within block copolymers or computational block copolymer

models where it requires large structural reorganizations of sphere to spatial translocation of columns to spheres. These other materials such as dendrimers, large molecules, and block copolymers require multistep complex synthesis with long annealing times of days to weeks where the prediction of the phases cannot be described at programmed but more so as opportune. These materials are often brought into the melt, and then fall into an FK phase rather than through a predicted transition. Thus, making CB-aPMP **6.1** the first FK A15 forming soft-matter material to have this unique proposed mechanism. Others benefits of CB-aPMP compared to other soft-matter FK forming materials is that it was synthesized under shorter and scalable techniques. Furthermore, one can access the phase faster and obtain the phase for longer. Overall, the discovery of CB-aPMP significantly lowers the barrier for further FK phase research and further scientific and technological developments to take place. Lastly, though FK A15 was serendipitous the use of aPMP as a building block to effect self-assembly was proven useful and the shape, length, and dispersity of the material was used to further understand and drive the research that follows.

6.4 Background on Soft Matter Multi-Component FK Phases

There are many complex FK phases such as C14, C15, Z, and σ phase, which is represented in Figure 6.7, and all depend on the need for two or more distinct spherical sets. To date, thermotropic quasicrystalline and FK mesophases have been discovered and characterized in many soft matter material two- or three-component systems.[27-29] This logical next step to access complex FK phases by creating a material

blend makes sense because it encourages the existence of varied sizes and shaped particles to coexist. An example of this blended technique in action includes a recent study involving two-component block copolymer systems were Yamamoto *et al.* used the combination of linear diblock of polybutadiene-poly(ε-caprolactone) with varying

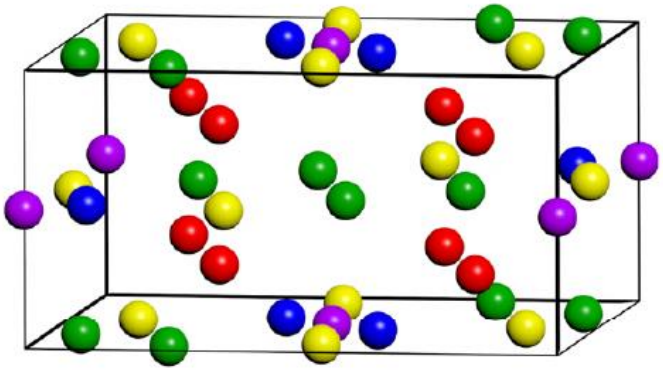

Figure 6.7 Unit cell of FK σ phase. †

molecular weights and weight percentages of homopolymer and polybutadiene. Through various combinations they were able to observe the formation of dodecagonal quasicrystalline (DDQC) and FK σ phase.[30,31] Yet another example of a blended system includes Bates *et al.* were on the other hand they used a high degree of conformational asymmetry within the diblock blends to stabilize a FK σ phase.[32] In these polystyrene-*b*-1,4-polybutadiene blends where the styrene block length remained the same, FK A15, σ, and DDQC phases were captured.[14] Even though these discoveries offer more answers and open doors for new soft-matter thermotropic material systems that lead to complex FK phases, they still do so under elevated temperatures for prolonged amounts of time. The complex blended systems additionally make it difficult to apply to a more general design or simulations to predict future phases.

To explore the sugar polyolefin conjugates as a two-component system it was important to do so while avoiding increasing the complexity of the system or introducing a whole new synthetic species. Additionally, it was of great importance that the material we decided to blend would provide added functionality to the system, thus choosing the bioactive antioxidant vitamin E made sense for many reasons; (1) Vitamin E is a readily available, cheap, and an easy-to-handle liquid material; (2) the chemical structure of vitamin E contains a highly active hydroxyl group on the end of a carbon chain. Therefore, mimicking the hydrophilic head-group and hydrophobic tail such as the sugar polyolefin conjugate, with an expected result of the material packing into the polymer domain while the hydroxyl groups orient near the sugar head; (3) vitamin E has applications in biological membranes.[33]

Lachmayr *et al.* first experimented with the blending of vitamin E using an CB-aPMP conjugate derivative. Upon increasing amounts of vitamin E, the original FK A15 phase now became observable at a lower temperature of 150 °C, rather than 180 °C. Most significantly, for the first time in our systems an FK σ phase was observed when 1% and 3% vitamin E was blended. The FK A15 phase and body centered cubic (BCC) phase still coexisted alongside the σ phase and no pure σ phase was observed. This work provided a methodology to lower the thermal barrier it takes to access new phases without the need for complex blends to be made. It was also a welcomed discovery that our sugar polyolefin could reach more complex FK phases through the loading of a small molecule modulator. [6]

6.5 Room Temperature FK A15 [2†]

In the present work new sugar-polyolefin conjugates were synthesized to investigate the following unknows and objectives:

(1) Can new designs be developed that provide access to QC and FK mesophases at much lower temperatures, such as ambient conditions?

(2) Can increasing the complexity of micelles through a mixture of sugar polyolefin conjugates lead to new mesophases and a clearer picture of a phase map that can be used to establish relative stability

(3) Can new evidence be obtained that can further support or undermine our proposed mechanism for the thermotropic phase transitions of sugar polyolefins, and perhaps glycolipids, that involves micellar in-plane repositioning and reshaping?

In line with the first objective, to promote the formation of a 'spherical' micelle of a sugar polyolefin conjugate at lower temperatures, the strategy presented by Ungar and Percec can be implemented. The strategy involves increasing the lateral width and shortening the longitudinal length of the hydrophobic domain.[34] This was done by replacing the aPMP 'tail' of **6.1** with an atactic poly(1-hexene) (aPH) domain to create CB-aPH conjugates **6.4** and **6.5**. In addition, the GAL-aPH conjugates **6.6** and **6.7** were

2† The results, figures, schemes, and tables discussed within this chapter have been reused or adapted from Wentz, C. M.; Lachmayr, K. K.; Tsai, E. H. R.; Sita, L. R., Thermotropic Glycolipid Quasicrystal and Frank-Kasper Phases: Unique Mechanism for Rapid Phase Transitions, *Science* 2022 (*in the process of being submitted*).

prepared were the cellobiose 'head' group was replaced by the monosaccharide β-D-galactose. In both these designs, the targeted degree of polymerization (DP_n) for the aPH domain was based on the previously made CB-aPMP conjugate as well as to create a 'mini-me' conjugate of half size for both domains, GAL-aPH. The 'mini-me' concept was inspired by the need to increase complexity within the system to reach new mesophases but to do so in a designed and programable way rather than thoughtlessly mixing multiple polyolefin tail lengthen conjugates. Since the A_3B stoichiometry and understanding of size differences between A and B sites already was fully understood in FK systems the logical step would be to have spherical micelles designed to fit this size distribution. More specifically, two series of new sugar polyolefin conjugates were synthesized to have slightly different M_n and $Đ$ values for the aPH 'tail'. For **6.4** and **6.6** the polymer domain contained a DP_n = 12, M_n = 1 kDa, Đ = 1.02, and for the **6.5** and **6.7** series: DPn = 6, Mn = 500 Da, $Đ$ = 1.04. Thus creating a sugar polyolefin conjugate that could be fit into the role of an A site and the other the B site was the originial idea.

Synchrotron variable-temperture small-angle x-ray scattering (VT SAXS) was ubtained for the bulk samples of all four new sugar polyolefins. As Figure 6.8A confirms, the replacement of aPMP tail for aPH of similar molar mass provided a suitable substitute for obtaining highly ordered FK A15 phase but now was observed at 150 °C, for conjugate CB-aPH **6.4**. The twenty-one Bragg peaks were successfully matched for the q/q^* values expected for A15 structure, Figure 6.8B, were q* = 0.0804 $Å^{-1}$ and all *hkl* Miller planes are indexed at 150 °C, were the unit cell length, a_{A15}, of 11.05 nm. For comparison, the CB-aPMP **6.1** conjugate had a_{A15} = 10.88 nm at 180 °C.

Simple first-order estimates for the corresponding spherical particle diameter of **6.4,** $D_{sphere,}$ and volume, V_{sphere} at 150 °C: D_{sphere} = 6.85 nm; V_{sphere} = 168 nm^3, and for **6.1** at 180 ° C: D_{sphere} = 6.75 nm; V_{sphere} = 161 nm^3. The volume-occupied-per-spherical-particle (v_i) can be determined from Equation 6.4

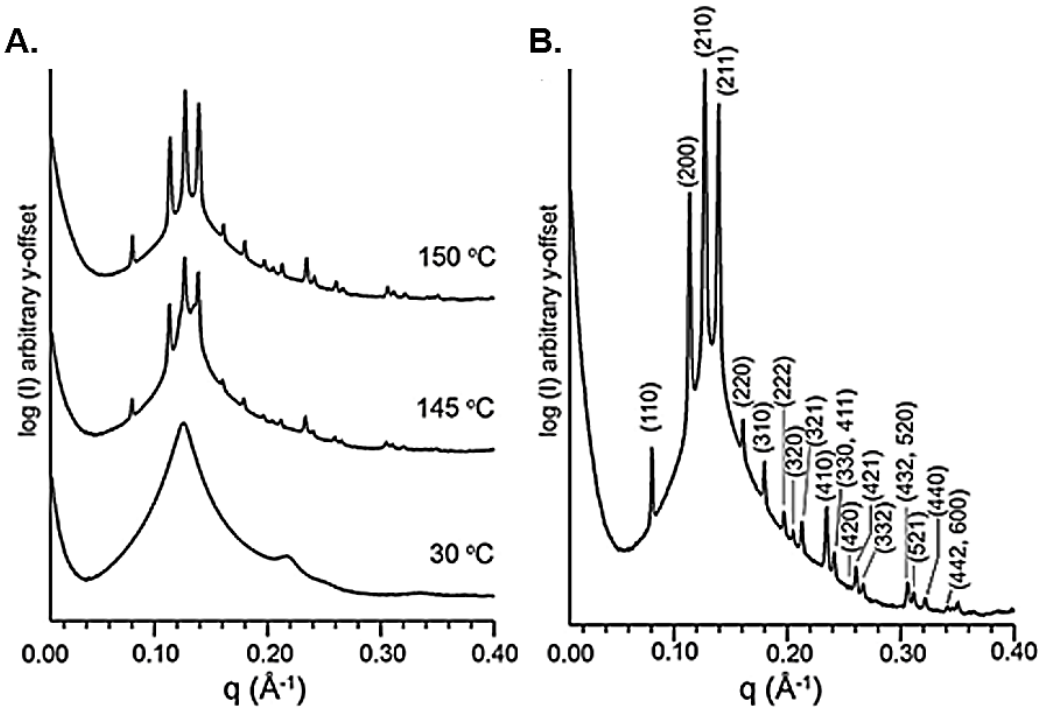

Figure 6.8 Selected synchrotron variable temperature 1D SAXS data for: (A) **6.4**, (B) the data in (A) at 150 °C that is indexed to the A15 phase. [2†]

for cubic lattices and Equation 6.5 tetragonal lattices, for FK A15 (8 particles), and σ phase (30 particles), and BCC (2 particles). Where *a* and *c* are lattice parameters, and *n* is the number *n* particles per unit cell. These observations strongly suggest that the aPH domain of **6.4** does indeed have a slightly greater lateral expansion at a lower temperature than its aPMP domain counterpart with 5% increases in $V_{sphere.}$ It is also important to note that, in contrast to CB-aPMP conjugate **6.1**, the complete VT SAXS data for conjugate CB-aPH **6.4** only shows evidence of very poorly ordered

hexagonally packed cylinder (*C*) morphology prior to FK A15 phase. For the other conjugate, CB-aPH **6.4**, the FK A15 phase within the bulk solid-state persists highly ordered up to the temperature limit of the experiment at 200 °C. For the 'shortened' aPH domain in CB-aPH **6.5** conjugate the *C* phase emerges above 100 °C and remains as the only phase to appear up to 200 °C. This result is also within keeping of Ungar and Percec model due to the much shorter aPH domain.

Equation 6.4 $$v_i = \frac{a^3}{n}$$

Equation 6.5 $$\frac{1}{d_{hkl}^2} = \frac{1}{a_{A15}^2}\,(h^2 + k^2 + l^2)$$

The successful observation of a highly ordered FK A15 phase for CB-aPH **6.4** conjugate was followed by a disappointing lack of FK phase in the monosaccharaide-polyolefin conjugates **6.6** and **6.7**. Where **6.7** was observed in VT SAXS to have only a *C* phase. However, on the brighter side, it was the first time we observed a disordered (DIS) state for these materials, and it was reached at a much lower temperatures than other soft-matter FK forming materials. Thus, providing evidence that upon the decrease of DP_n of aPH there is potential to access phases at possible ambient conditions. For the GAL-aPH **6.6** conjugate of doubled aPH domain size the DIS state was reached at 182 °C rather than for the GAL-aPH **6.7** conjugate of ~ 500 Da aPH domain size the DIS state was observed at 132 °C, see SI for VT SAXS.

As previous discussed and reported it made sense to incorporate vitamin E into these unsuccessful FK forming materials as we know that the small molecule can have a dramatic effect on the thermotropic phase behavior of sugar polyolefin conjugates by swelling the hydrophobic domain in such a way that supports the formation of spherical

micelles at a lower temperture.[6] Employing this same strategy with **6.7** ('mini-me to **6.4**) and anywhere from 20-30 % blends with

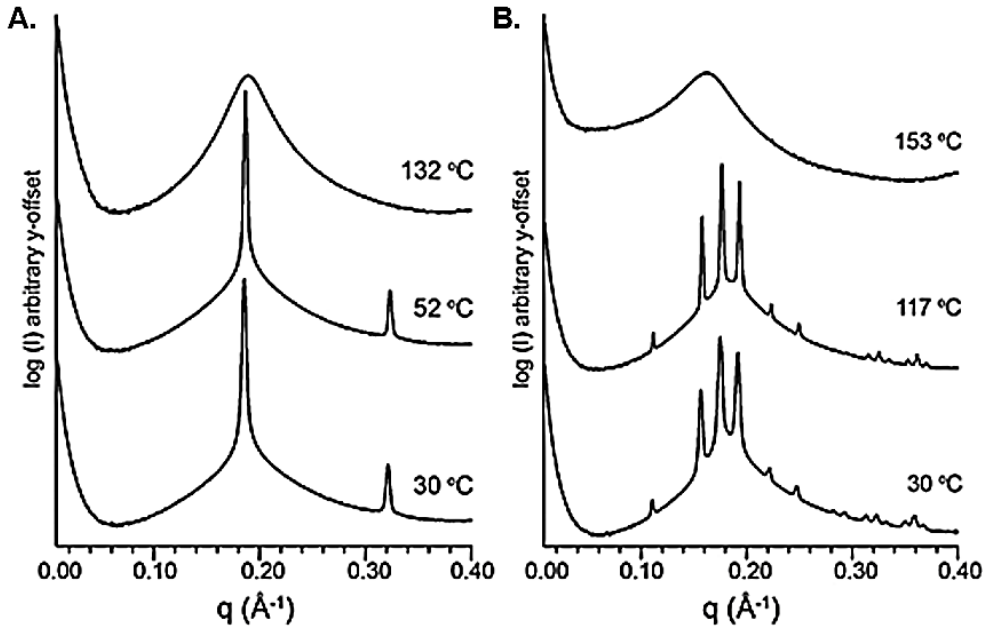

Figure 6.9 Selected synchrotron variable temperature 1D SAXS data for: (A) **6.7**, (B) a blend of **6.7** with 20% vitamin E. [2†]

vitamin E gratifyingly lead to answering the desired objectives (1) and (2) presented in at the beginning of this work. For the first documented time, FK A15 phase was now obtained without thermal annealing and at the ambient temperature of 30 °C. Specifically, when conjugate GAL-aPH **6.7** was blended with, 20% by weight, vitamin E. Quite surprisingly, this FK A15 phase becomes even more well defined at higher temperatures, such as at 117 °C in Figure 6.9B. The FK A15 phase only persists up to 150 °C before the material becomes fully disordered by 153 °C. Further structural analysis through Bragg peak indexing q/q* values for the 117 °C data set, q* = 0.116 $Å^{-1}$ with an a_{A15} = 7.786 nm. This was used to determine D_{sphere} = 4.834 nm and V_{sphere} = 59 nm^3. This value has a 63% decrease in volume to the A15 micelle for the blend of

the monosaccharide-aPH (500 Da) conjugate **6.7** with 20% vitamin E relative to that for the disaccharide CB-aPH **6.4** conjugate. Lastly, very similar results were also obtained for a blend of **6.7** and vitamin E with 30% by weight blend, where in this case the FK A15 was still formed at ambient temperatures with a unit cell parameter only slight larger at a_{A15} = 7.99 nm for the VT SAXS data collected at 120 °C. Expected, the DIS state for this 30% blend was now reached at the lower temperature of 140 °C, for more detailed VT SAXS see SI.

6.6 Two- and Three-Component σ Phase

The results of the 'mini-me' and vitamin E blend discussed above suggested that, in principle, the paradigm of Figure 6.10 could now be put to the test. Thus, changing the original idea that the 'mini-me' and original conjugate would take the role of an A site or a B site we now propose that they for a hybrid combination of the two where A sites and B sites still have distinctly different sizes and shapes. This hybrid theory makes more sense in terms of entropy of the system as the want to keep all 'mini-me' together verses all original conjugates together has no driving force since both contain chemical equivalent components. We choose to combine original FK forming conjugates with 'mini-me' FK forming conjugates first without vitamin E. It was important to do so as to avoid the need for vitamin E as a phase modulator to obtain a 'mini-me' analog of the FK A15 phase of CB-aPMP **6.8** conjugate. Kätchen L. Lachmayr synthesized and characterized conjugates and resulting blends made, **6.8, 6.2, and 6.3**. Fortuitously, a re-investigation of our monosaccharide-polyolefin

conjugate, galactose-O-triazole-linked atactic poly(4-methyl-1-pentene) (GAL-aPMP) (**6.2** and **6.3**) shown in Scheme 6.2, provided a quick solution. More specifically, a synchrotron VT SAXS investigation of a bulk sample of **6.2** (Đ = 1.02) revealed that a thermotropic FK A15 phase rapidly forms at 63 °C from a poorly ordered *C* phase, see Figure 6.11A in comparison to Figure 6.11B. The structural analysis for this 'mini-me' A15 phase to provide the unit cell parameters: a_{A15} = 7.99 nm, D_{sphere} = 4.99 and V_{sphere} = 65 nm^3. The existence of these two 'mini-me's' enabled us to make an important

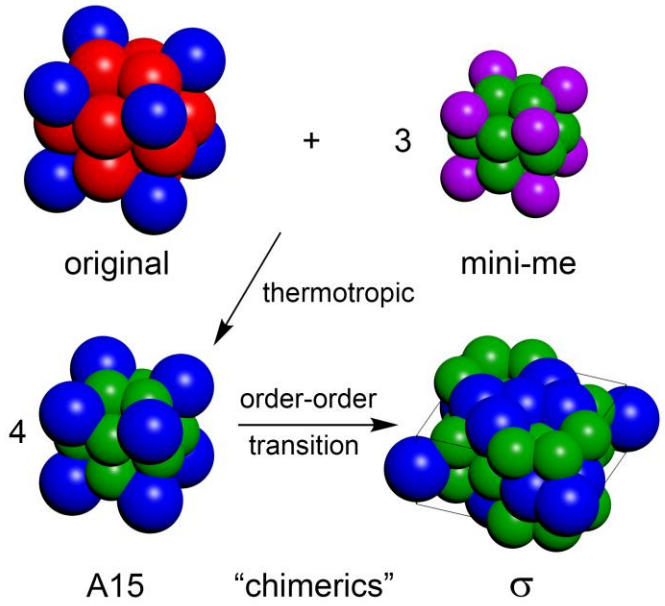

Figure 6.10 Model to produce chimeric and hybrid A15 structures from a 3:1 stoichiometric ratio blend of GAL-aPMP with CB-aPMP.

discovery of how one-unit *DPn* makes on the outcome of a two-component blend. The first, **6.2**, 'mini-me' SAXS data observe a disordered state before forming FK A15 instead transition to an FK A15 from *C*. These differences in behavior are noted to show the great importance of the tails design and influence on the packing of the 'squishy' spheres which lead to our next design decision.

Given the large difference in onset temperature for formation of the original and 'mini-me' A15 phases from the respective sugar-polyolefin conjugates, it was reasoned that two discrete populations of spherical micelles of 'large' and 'small' size, and that are further differentiated with respect to disaccharide vs monosaccharide head group and difference in DPn, could be generated within blends of **6.1** or **6.8** (CB-aPMP) and **6.2 o**r **6.3** (GAL-aPMP). According to Figure 6.10, it was also reasoned that formation of a two-component chimera A15 phase would be best achieved with a 3:1 blend ratio of CB-aPMP conjugates (**6.1, 6.8**) to GAL-aPMP conjugates (**6.2, 6.3**) because of the well-established A_3B stoichiometry for bimetallic FK A15 phases. These hypotheses were reinforced when the two-component system, at a 3:1 ratio (**6.3**:**6.8**) gave floriation for the first time in our system a standalone σ phase. Thus, answering objective (3) proposed at the beginning of this work. The documentation of the FK σ phase from an initial FK A15 phase has only been documented within a few soft matter materials as a function of volume fraction citation needed and has not been previously documented as a thermotropic phase transition. There is considerable theoretical support for this existence of this thermotropic phase transition within soft matter under the premises of the methodology

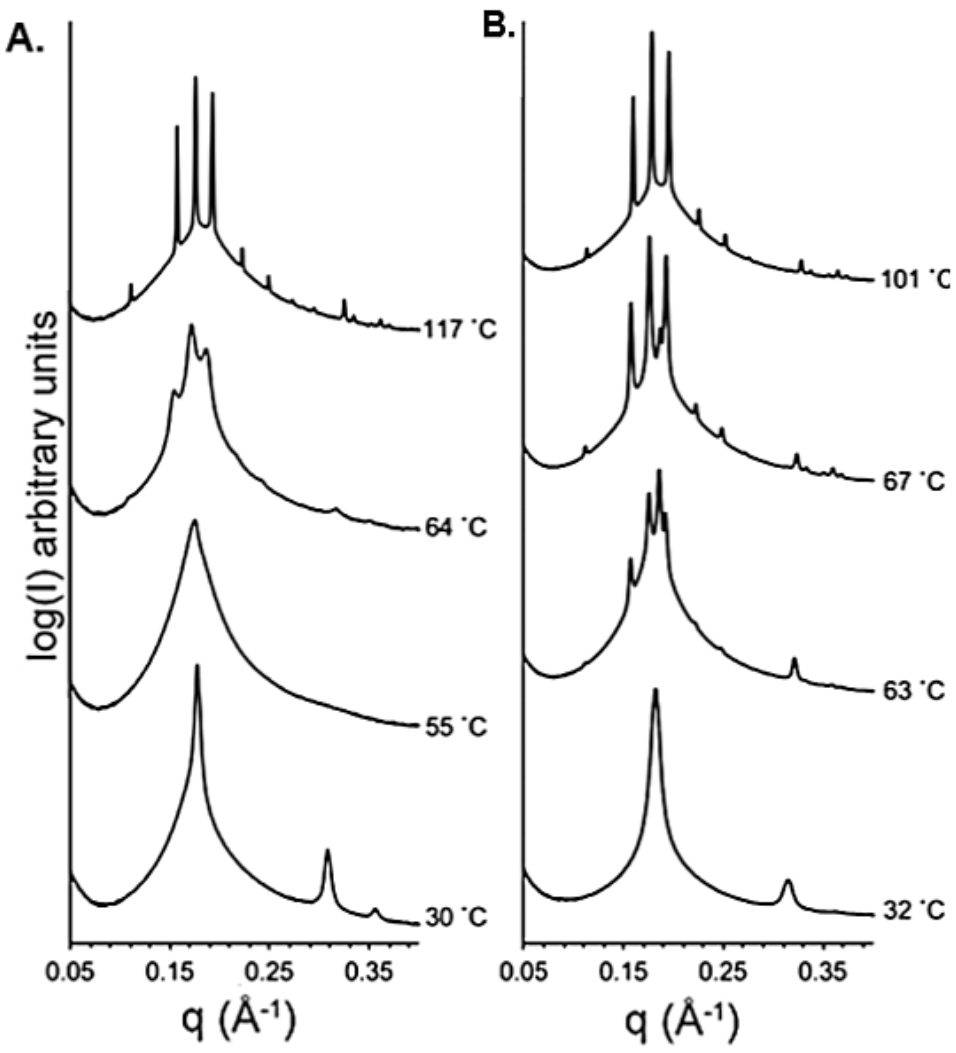

Figure 6.11 (A) Selected 1D VT SAXS of **6.2. (**B) **6.3**, showing important thermal transition for 0.5 and 0.2 °C/min thermal ramps. [2†]

undergoing mass transfer, but due to the rapidity of our system we contradict this hypothesis.[23, 35] The methodology we propose is spoken about more in depth shortly. For the σ phase lattice parameter Equation 6.6 for tetragonal unit cells can be applied.

Equation 6.6 $$q^2 = (2\pi)^2 \left[\frac{h^2k^2}{a^2} + \left(\frac{l^2}{c^2}\right)\right]$$

For the two-component 3:1 (**6.3**:**6.8**) blend, Figure 6.11 shows the order-order transition from FK A15 into a combined phase of FK A15/ σ then at 158 °C the σ phase is pure. Documenting a transition between the two phases where both coexist further proving the speed of the phase changes. The FK A15 phase produced from the 3:1 blend has a lattice parameter of a_{A15} = 8.84 nm, at 158 °C. Capturing the pure σ phase is a first for glycolipids. To better understand how low of a thermal annealing temperature is needed to access this phase an isothermal SAXS experiment was conducted, Figure 6.11. The experiment was conducted by holding at 140 °C for 6.6 hr to produce a pure σ phase at this lowered temperature without the presence of FK A15 phase, with 29 scattering peaks where q* = 0.08036 Å-1, and a lattice parameter a_σ = 16.69 nm and c_σ = 8.77 nm. The results of this blend logically lead us to question if this hypothesis of a 3:1 was just opportune or purposefully followed our theory. This question was answered by trying a variety of two-component blends; 2:1, 1:2, 1:1, and 3:1 with the varied 'mini-me'. Table 6.1 summarizes the data collected from these other blends and the phase transitions observed, see supporting information for more synthetic details. These additional blends solidified our testament that the 3:1 blend was deliberate and match our theory as no other blend compared or produced a σ phase and instead reach disordered phase at higher temperatures. Reinvestigating the disparity between 'mini-me's' previously mentioned fortunately lead to more evidence that could support the newly proposed methodology.

Table 6.1. Correlation between a neat(top) material or two- (middle), three-component (bottom) blends with phase transitions and temperatures where a phase is initially seen. a_{15} and d_c documented for the temperature listen with FK A15 and *C* phases. ◆a_{A15} lattice parameter calculate with the coexistence of σ. ◊ materials highlighted in more detail in the main text. [2†]

Material or Blend	Phase Transitions	a_{A15} (nm)	d_C (nm)
6.2	C → Dis (55 °C) → A15 (64 °C) → Dis (126 °C)	7.96	4.07
6.3	C → A15 (63 °C) → Dis (110 °C)	7.90	4.00
3:1 (**6.2**:**6.8**)	Dis → A15 (100 °C) → σ/A15 (153 °C) → σ (158 °C) → Dis (166 °C)	8.84	-
◊ 3:1 (**6.3**:**6.8**)	Dis → DDQC (83 °C) → A15 (91 °C) → Dis (138 °C)	8.84	-
2:1 (**6.3**:**6.8**)	Dis → DDQC (86 °C) → A15 (97 °C) → Dis (142 °C)	9.13	-
1:2 (**6.2**:**6.8**)	Dis → C (85 °C) → A15 (176 °C) → Dis (183 °C)	9.41	4.95
1:1 (**6.2**:**6.8**)	C → A15 (103 °C) → Dis (180 °C)	9.49	5.00
3:1 [3% vitamin E (**6.3**:**6.8**)]	Dis → DDQC (75 C) → A15 (89 °C) → A15/σ (126 °C) → Dis (127 °C)	8.76	-
◊ 2:1 [10% vitamin E (**6.3**:**6.8**)]	Dis → DDQC (80 °C) → A15/σ (101 °C) → σ (118 °C) → Dis (134 °C)	◆8.91	-

In order to compensate for the *DPn* disparity between **6.2** and **6.3** the conjugate **6.3** was blended with vitamin E, with the intent of swelling the polyolefin domain. Consequently, now creating a three-component system, described as a 2:1 (**6.3**:**6.8**) blend with 10 % vitamin E. This three-component system first formed DDQC phase at 82 °C, which then developed into a mixed phase of DDQC/FK A15/ σ phases at 97 °C, until at 101 °C the FK A15 and σ peaks coexists until 117 °C were only the σ phase persists. Presence of all three phases existing simultaneously and visually being able to see, Figure 6.12, how rapid these phases transitions undoubtedly proves that mass transfer is not a methodology that makes sense for sugar polyolefin materials. Seeing multiple phases coexists has been previously noted however in this case the peaks transition from one to the other with neat phases also being observed. The lattice parameters of FK A15 to σ only fluctuate at 0.03 $Å^{-1}$ amount importantly showing that the lattice is not shifting in size, this can be observed by the dotted lines in Figure

6.12A, and in the supporting information where the lattice parameters are graphed as a function of temperature.

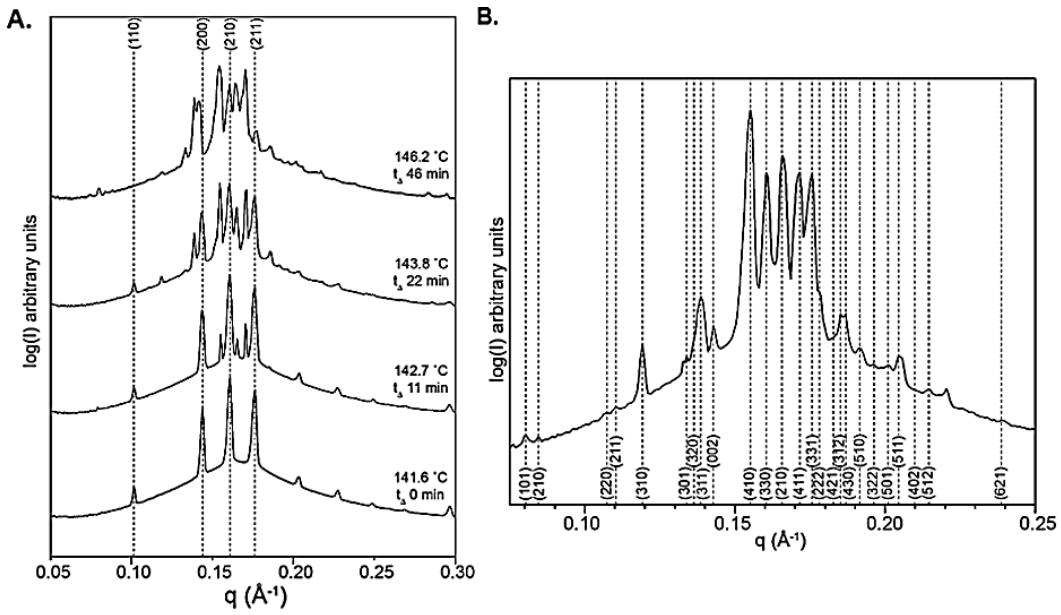

Figure 6.12 (A) Selected 1D SAXS data 0.2 °C/min thermal ramp of the 3:1 (**6.2**:**6.8**) blend. Dotted lined correspond to *hkl* Miller planes on the FK A15 phase, showing the full disappearance of the peaks with increase in temperature. (B) 1D SAXS data of the σ phase from the 3:1 (**6.2**:**6.8**) blend from an isothermal experiment, at 140 °C, where dotted line correlate peaks with corresponding *hkl* Miller phases. [2†]

The 2:1 (**6.3**:**6.8**) blend with 10% vitamin E undergoes an order-disorder transition at 135 °C. Figure 6.13 shows back-to-back SAXS of all these transitions occurring in a matter of only minutes for the full VT-SAXS run conducted at Brookhaven National Labs (BNL). The initial FK A15, though a mixed phase, was indexed to have a lattice parameter a_{A15} = 8.91 nm. The pure σ phase, had a q* = 0.08335 Å-1, with a lattice parameter a_σ = 16.90 nm and c_σ = 8.94 nm, at 117 °C. Note the small lattice parameter increase can be due to FK A15 calculations being done on a mix phase rather than a pure phase.

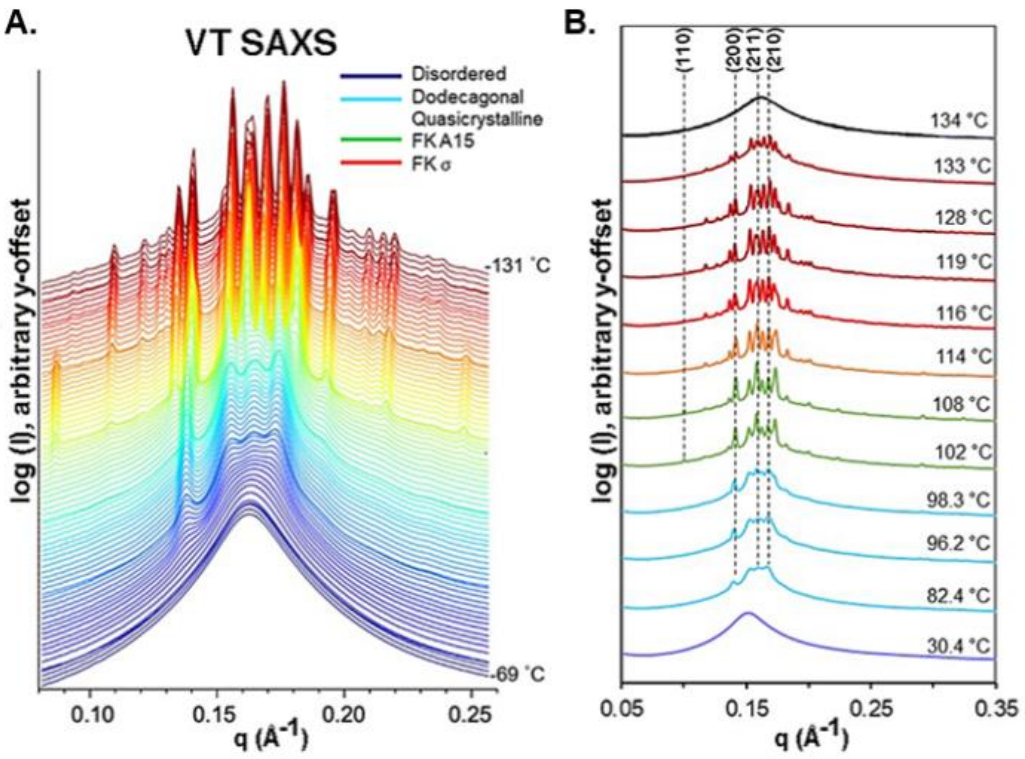

Figure 6.13 (A) Selected 1D SAXS data from 0.2 °C/min thermal ramp showing phase transition sequenced for the 2:1 blend (**6.3:6.8**) with 10% vitamin E, 3-compnent blend from 69 °C – 131 °C with a measurment ~ 179 seconds apart. (B) Selected 1 D SAXS data from (A) with RT before and after heating displayed along with the OD transition of σ → dis. [2†]

With the purpose of estimating the phase composition as a function of normalized intensity at each temperature and time interval, the data was remodeled by BNL staff scientists, Dr. Esther Tsai, for the 0.2 °C/min SAXS thermal ramp, Figure 6.14A. The normalized peak intensities were used to generate composition graphs depicting the amount of each phase present at any given time, only 'pure' phases were chosen within the data set. The green line in Figure 6.14A represents an FK A15 'pure' phase produced from modelling since in the 2:1 (**6.3**:**6.8**) 10 % blend with vitamin E produced only a mixed phase. Figure 6.14A documents clearly the DIS → DDQC → FK A15 → σ phase order-order transition. These normalized peak intenstities were then

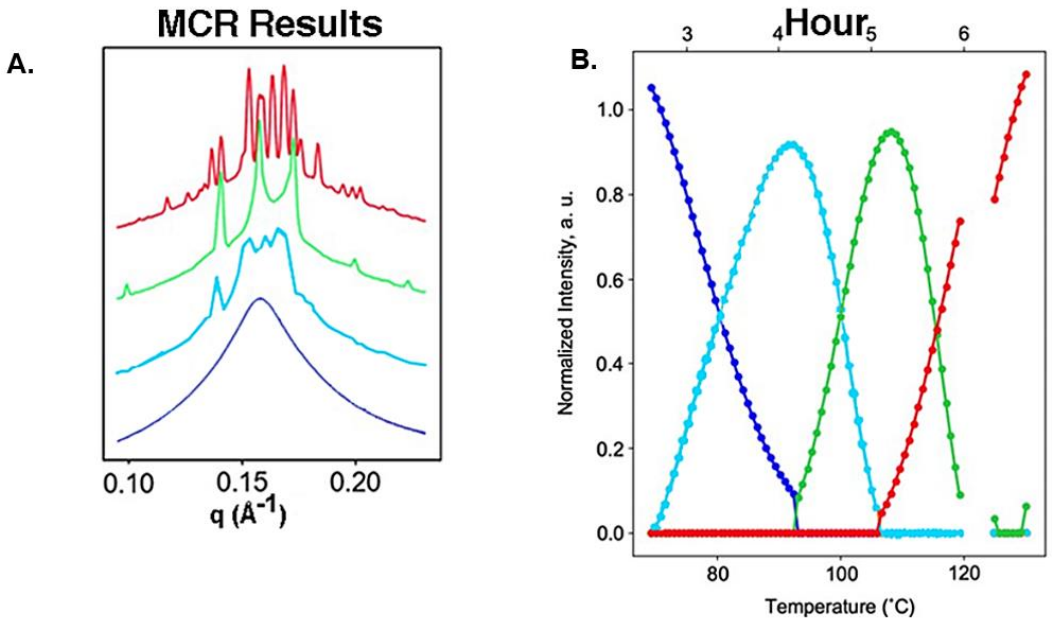

Figure 6.14 (A) Fitting model (MCR) assumes 4 pure phases and solve their ratios during transition while only allowing two phases at a time. (B) An approximation of phase compositions at each data point as a function of normalized peak intensity, where data collection halted for a period of 5.65 C from 119 to 124 C as indicated bu the line-breaks. [2†]

used to generate composition graphs, Figure 6.14B, depecting the amount of time each phase was present. The red lines corrosponds to only the pure σ phase. The model produced provided a good approximation of the data which then allows for estimation of the phase transtion kinetics to be done.

6.6.1 Mechanism FK A15 to σ Phase

The appearance of FK σ phase, from an initial A15 phase, has only been documented a hand-full of times within soft matter materials as a function of volume fraction in thermotropic phase transition.[18] There has been a lot of theoretical support for the existence of this thermotropic phase transition within solid-state soft matter,[40-

[43] but none experimentally observed, until now. To review, the FK σ phase has been conventionally considered the thermodynamically stable state for DDQC forming materials and systems.[36] Within Ni-Cr alloy systems the FK A15 to σ phase has been documented with the displacement vector < 7/8, ½, 0> a_{A15}. With the aim of producing the σ phase, two planar defects along the (100) plane need to be introduced onto the A15 structure at twice the distance of the A15 lattice parameter, then followed by an additional defect into the (010) plane.[37] The resulting displacements generate the σ phase with unit cell dimensions that double the original A15 structure, Figure 6.15. Important to note, the σ phase can also be produced from faulted sequences, where the

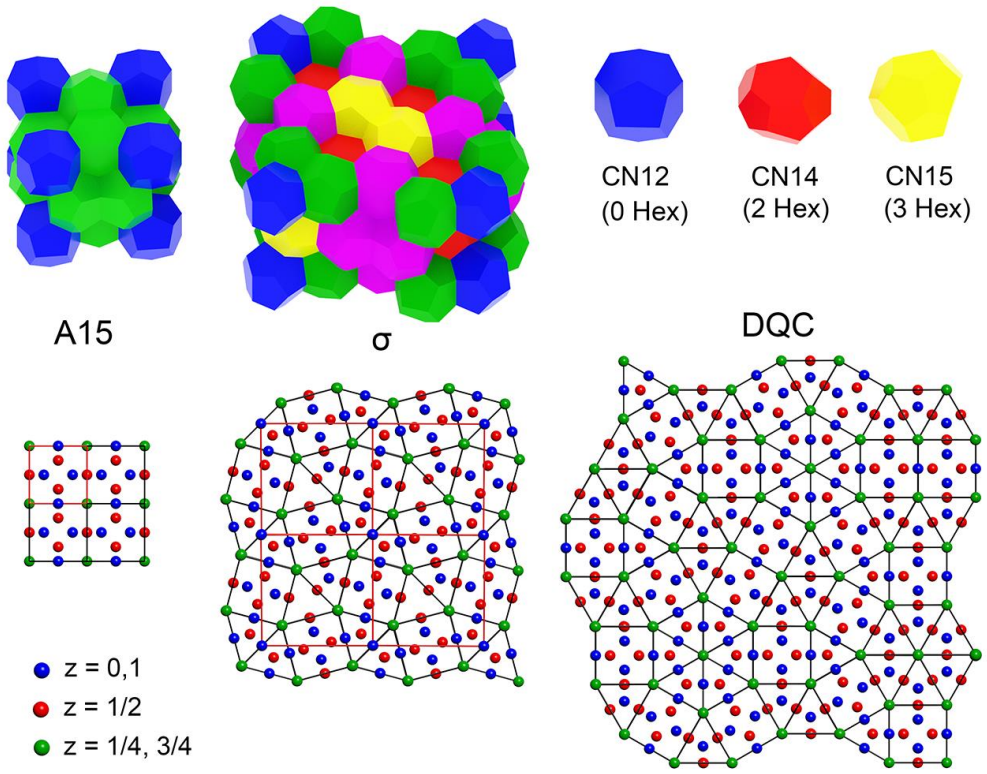

Figure 6.15 Transformation from the FK A15 to σ phase, where the arrows represent the displacement vectors of each planar defect, from a top-down view of the lattice. [2†]

½ value within the displacement vector can be positive or negative, producing a mirrored twin σ phase structure.

This trend was in fact observed from the comparison of the FK A15 to σ phase lattice parameters, see in Figure S6.45. The dislocation within the x and y planes can therefore explain the doubling seen of the a_σ in relation to the a_{A15}, this produced the lattice parameter relationship $a_\sigma = 2\ (a_{A15})$, which is supported from the results. The z direction contains no lattice distortion there for the relationship is $c_\sigma = a_{A15}$.

6.6.2 Conclusions

In addition to capturing an FK A15 to σ phase order-order phase transition, never documented in two- and three-blended systems, this work has provided access to a range of different FK A15 structures of varying sizes. The three objectives originally sought after were answered through the development of swapping out the aPMP domain for aPH thus accessing FK A15 at ambient temperatures for and infinite amount of time. Or achieved by creating 'mini-me' conjugates that when blended with their original counterparts access complex DDQC and FK σ phase.

6.7 Overall Sugar Polyolefin Conjugates Conclusions

Successfully, the expansion of the sugar polyolefin library has been made in a programmable fashion, providing access to a tunable molecule through reasonable

mechanisms for the solid-state self-assembly and re-organization of these phases in rapid time frames. This is done through the simple synthesis of an end-group functionalized polyolefin domain chemically linked to a sugar head-group. These materials have been the first in their class to observe FK phase in one-, two-, and three-component systems. The discoveries made have allowed new methodologies to be considered and further advancements to gain a better understanding. Delineating the rules that dictate the design and rapid fabrication of soft matter QC and FK mesophases can have far-reaching implications for life, science, and technology. These range from question regarding the abiotic origins of protocells with nascent capabilities for complex hierarchical function, to the development of reconfigurable smart materials for shape-shifting photonic applications or other technological advancements. It was important that for these goals to become fully realized through new paradigms that require an accelerated rate at which new structural categories of soft matter QC and FK phases are conceived and validated. Through viable mechanisms for kinetically fast phase transitions that occur in the bulk are identified and exploited to provide thermodynamically stable or long-term metastable states.

6.8 Supporting Experimental Information

6.8.1 Synthetic Procedures

All manipulations of air and moisture sensitive compounds were carried out under N_2 atmospheres with standard Schlenk line or glovebox techniques. N,N-dimethylformamide (DMF) was dried over molecular sieves and collected by fractional distillation before use. Toluene (ReagentPlus, 99%) was dried and deoxygenated by passage over activated alumina and GetterMax® 135 catalyst (purchased from Research Catalysts, Inc.) and collected prior to use. Chlorobenzene (ReagentPlus, 99%) was dried over potassium hydride, refluxed at 130 ˚C for three days, and collected prior to use. All other solvents and reagents were used as received unless otherwise noted. Precatalyst (I) was synthesized as previously described by our group. N,N-dimethylaniliniumtetrakis(pentafluorophenyl)borate ($[PhNMe_2H][B(C_6F_5)_4]$ (II) was purchased from Boulder Scientific.

Synthesis of azido-terminated atactic poly(4-methyl-1-pentenet), N_3-aPMP.[2†]

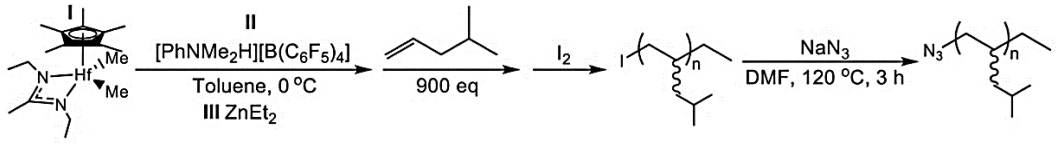

In a 100 mL round bottom flask, 20.0 ml of toluene was cooled to -5 °C. The 4-methyl-1-pentene monomer (1.89 g, 22.5 mmol) was added to the flask. A solution of (**I**) (11.4 mg, 0.0250 mmol) in -5 °C 1.0 mL chlorobenzene was added to (**II**) (22.0 mg, 0.0275 mmol) which was vigorously agitated until dissolved and activated, whereupon it was added to the flask. Then 92.6 mg (0.75 mmol) of chain transfer agent (**III**), was quickly added to the flask. The flask was stirred for 18 hours at -5 °C and quenched with excess iodine (464 mg, 0.0250 mmol) until a pink color persisted. The resulting I-aPMP was

purified using a silica column with a chloroform mobile phase, precipitated in acetone to remove excess iodine, and evacuated to dryness. The resulting polymer (82% yield, 1.55 g) was characterized by ^{1}H NMR ($CDCl_3$) δ 3.24, 2.15, 1.61, 1.32, 1.00, 0.84. I-aPMP was dissolved in minimal toluene (2-3mL) and added to a 50 mL Schlenk flask. NaN_3 (1.2 eq) dissolved in 10 ml of DMF was added to the solution. The solution was then refluxed for 2 hours at 120 °C. The resulting product was purified using a silica plug and dried. To yield 1.15 g of N_3-aPMP (74%). The polymer was characterized by GPC, DSC, ^{1}H NMR and ^{13}C NMR. ^{1}H NMR ($CDCl_3$) δ 3.20, 1.61, 1.32, 1.23, 0.99, 0.84. ^{13}C δ 45.48, 41.61, 30.37, 25.42, 23.51.

Synthesis of N-Acetal-propargyl D-(+)-cellobiose. [2†]

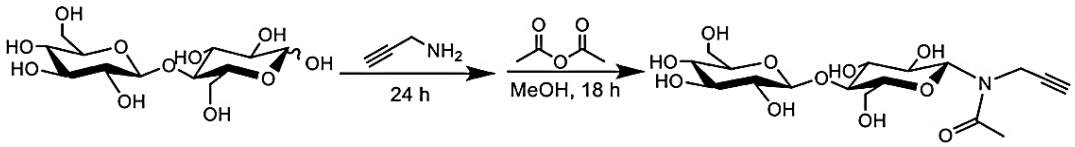

D-(+)-Cellobiose was dried under reduced pressure for 24 h (1.80 g, 5.84 mmol) in a Schlenk flask. Neat propargyl amine (6 mL 5.84 mmol) was added to the flask using air free technique and the mixture stirred for 24 hours. The excess propargyl amine was removed under reduced pressure at 35 °C co-evaporated with a 9:1 toluene:methanol mixture (v/v). The yellow solid was dissolved in methanol and precipitated in cold dichloromethane (DCM). The precipitate was collected by vacuum filtration, resulting in a white solid which was the dried for 2 h under vacuum. For acetylation of the secondary amine, 5:1 mixture of methanol (dried over magnesium sulfate) and acetic anhydride, was added to the flask. The reaction stirred at room temperature for 18 h. Solvent and acetic anhydride were co-evaporated to dryness with a 1:1 mixture of

methanol:toluene (v/v) followed by precipitation in cold DCM, then dried, to yield 2.24 g of white solid (76.0%). The product was dried under vacuum and characterized by ^{1}H and ^{13}C NMR.

Synthesis of cellobiose atactic poly(1-methyl-4-pentene), CB-aPMP 6.1 sugar polyolefin conjugate. [2†]

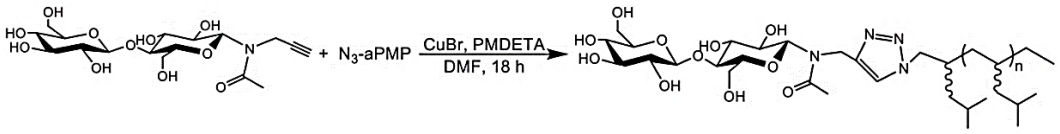

The N-acetyl-propargyl cellobiose (0.299 mmol, 128 mg) was dissolved in 5 mL DMF. The N_3-aPMP (0.299 mmol, 564 mg) was dissolved in minimal toluene (3-5 mL), and N,N,N',N",N"-pentamethyldiethylenetriamine (0.299 mmol, 25.9 mg) was added to a 50 mL heart-shaped flask. While stirring, copper (I) bromide (0.299 mmol, 21.4 mg) in 5 mL of DMF was added to the flask drop-wise, to create an aqua blue solution. The reaction stirred for 18 h and was quenched with methanol, turning navy blue. Solvents were removed under reduced pressure at 40 °C and the product was purified by flash column chromatography using a chloroform:methanol gradient from 100:1 to 9:1 mixture to yield a white powder dried for 3 days and characterized by SAXS, DSC, TGA, MALDI-TOF, ^{1}H NMR, and ^{13}C NMR (415 g, 60.0%).

Synthesis of Sugar Polyolefin Conjugates 6.2-6.7. [2†]

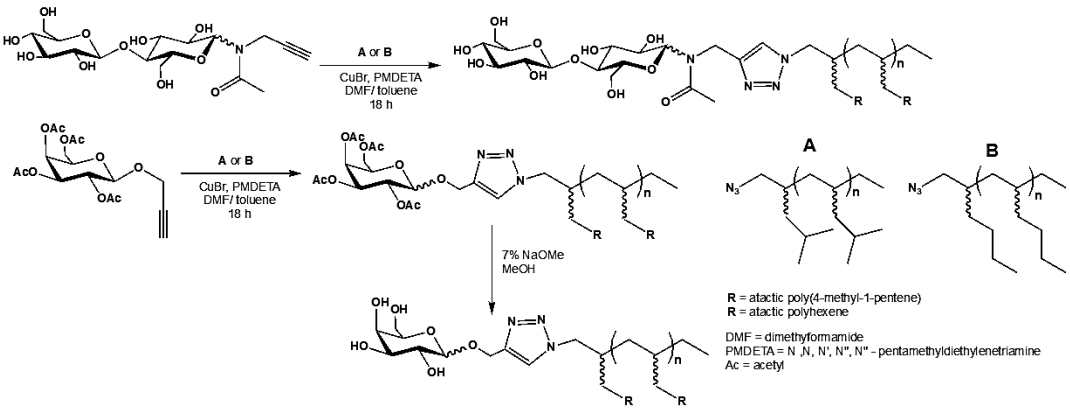

In a N_2 glovebox, the ß-D-galactose tetraacetate O-propargyl galactose was dissolved in 5-7 mL DMF, **A** or **B** was dissolved in minimal toluene (3-5 mL), and N,N,N',N",N"-Pentamethyldiethylenetriamine (0.5 eqv.) was added to a 50 mL heart-shaped flask. While stirring, copper (I) bromide (0.5 eqv.) in 0.5 mL of DMF was added to the flask drop-wise, to create an aqua blue solution. The reaction stirred for 18 h and was quenched with methanol, turning navy blue. Solvents were removed in vacuo at 40 °C and the product was purified by flash column chromatography using a chloroform:methanol gradient from 100:1 to 9:1 mixture to yield a white. For the deprotection of the sugar, in a 100 mL Schlenk flask, 15 mL of methanol was added. Sodium methoxide (NaOMe) was dissolved in 2 mL methanol (2mmol, 14 mg) and the dry acetylated GAL-aPMP conjugate was added to Schlenk flash. A minimal amount of dry toluene (less than 2 mL) was used to transfer polymer-sugar conjugate into the flask. Solution was stirred for under N_2 overnight, color will have changed from cloudy white to transparent pale yellow. Two drops of acetic acid were added to quench reaction. Solvents were removed in vacuo at 40 °C and the product was purified by flash column chromatography using a chloroform:methanol gradient from 100:1 to

9:1 mixture to yield a light-yellow solid. The conjugates were characterized with ^{1}H and ^{13}C NMR, and MALDI, before X-ray analysis.

Preparation of Sugar Polyolefin Conjugates and Vitamin E blends

The sugar polyolefin-vitamin E weight percent blends were prepared using (±)-alpha-tocopherol 95% synthetic, from Acros Organics, as the vitamin E additive. First, the predetermined amount of the sugar polyolefin conjugate was dispensed into a glass vial, using a Mettler Toledo analytical balance, followed by vitamin E into a separate vial. Then sugar polyolefin conjugate was dissolved in 0.3 mL of chloroform and added to the vial containing the vitamin E. The vial containing the sugar polyolefin conjugate was then rinsed three times with 0.3 mL aliquots of chloroform and added to blend solution. The solution was then homogenized for 1 h at room temperature with frequent agitation. The blend was then concentration under high vacuum for 18 h, until no trace solvent remained. The blended samples were then loaded into a washers or thin wall capillary tubes for VT SAXS analysis.

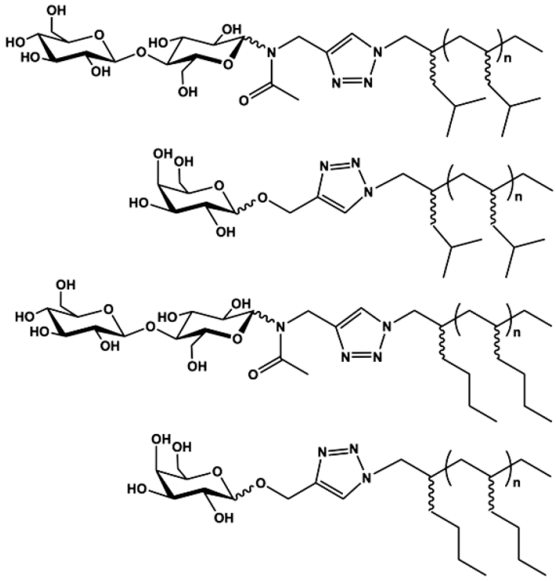

CB-aPMP
6.1: DP_n = 12 (60 % yield)
6.8 DP_n = 10 (55 % yield)

GAL-aPMP
6.2: DP_n = 8 (78 % yield)
6.3: DP_n = 7 (79 % yield)

CB-aPH
6.4: DP_n = 12 (75 % yield)
6.5: DP_n = 6 (70 % yield)

GAL-aPH
6.6: DP_n = 12 (70 % yield)
6.7: DP_n = 6 (68 % yield)

Table S6.1. Synthetic details for sugar polyolefin conjugates. [2†]

Material	Polydispersity	Amount of Sugar Head Group (g)	Polyolefin Tail (g)	Yield (g)
1b; 6.8	1.01	3.54	2.64	1.45
2a; 6.2	1.02	1.10	0.82	0.64
2b; 6.3	1.03	1.37	2.06	1.62
3a; 6.4	1.02	0.30	0.70	0.53
3b; 6.5	1.01	0.61	0.70	0.49
4a; 6.6	1.04	0.80	0.65	0.92
4b; 6.7	1.02	0.52	0.21	0.92

Table S6.2. Preparation of sugar polyolefin blends from two-component systems. [2†]

Blend	M_n of GAL-aPMP (g/mol)	Amount of GAL-aPMP (mg)	M_n of CB-aPMP (g/mol)	Amount of CB-aPMP (mg)
3:1 with **2a:1b; 6.2;6.8**	940	83.1	1346	40.3
1:1 with **6.2;6.8**	940	37.0	1346	53.7
1:2 with **6.2;6.8**	940	27.7	1346	80.6
3:1 with **6.2;6.8**	840	202	1346	107.7
2:1 with **6.2;6.8**	840	134	1346	107.7

Table S6.3. Preparation of sugar polyolefin blends from three-component systems. [2†]

Blend	Amount of original blend (mg)	Amount of vitamin E (mg)
3:1, with 3% vitamin E (**2a:1b**; **6.2;6.8)**	63.4	1.9
2:1, with 1% vitamin E (**6.2;6.8**)	64.9	6.5

6.8.2 Characterization Parameters

Gel Permeation Chromatography (GPC). Used to obtain molecular weight (Mn and Mw) and polydispersity index (PDI) of polymers using Viscotek GPCMax equipped with 4 columns (T2500, T3000, T4000, and T5000) in a column oven and differential refractometer (maintained at 40 °C). Tetrahydrofuran (HPLC Grade) was used as the eluent with a flow rate of 1 mL/min). Polystyrene standards (from Polymer Laboratories Inc., 580 Da – 3,150 kDa) were used for calibration. For GPC sample preparation 10 mg of dry polymer sample was dissolved in 1 g of Xylenes then filtered through a 0.2μm Nylon Target2 filter.

Nuclear Magnetic Resonance (NMR) Spectroscopy. ^{1}H and ^{13}C NMR carried out with a Bruker AV 400, Bruker DRX 500, and Bruker AV III 800 MHz Varian spectrometers. Chloroform-*d1* was used as the solvent for polymer samples, water-*d2* used for all sugars and sugar intermediates, and DMF-*d7* used as the solvent for conjugates (all solvents indicated in spectra by asterisks on NMR spectra). All spectra were referenced to tetramethylsilane using residual ^{1}H and ^{13}C chemical shifts of the deuterated solvents.

Differential Scanning Calorimetry (DSC). Was used to detect any thermal transitions with a TA instruments DSC Q1000 system. Samples were run in sealed hermetical aluminum pans with an empty pan as reference. A heat/cool/heat temperature program was used at a flow rate of 10 °C/min from -70 °C – 200 °C to prevent compound decomposition. The initial mass of the sample was 8 mg.

Thermalgravimetric Analysis (TGA). Determined onset of thermal decomposition measures as a function of weight loss and temperature using Shimadzu TGA-50 with a starting weight of material at about 2.5 mg. Material was run in a platinum pan, flow rate of 50 mL/min of N_2 gas, with a temperature range of 30 °C to 500 °C with a 10 °C/min ramp rate.

Matrix-assisted Laser Desorption/Ionization Time-of-Flight (MALDI-TOF) Mass Spectrometry. 10 mg/mL concentrations were used for both the dithranol matrix (> 90% HPLC grade from Milipore sigma) and the conjugate sample, in toluene. A silver trifluoroacetate of 5 mg/mL concentration in toluene was used as the salt in the matrix. The matrix was prepared with 20 uL of conjugate sample, 20 uL of dithranol, and 2 uL of silver trifluoroacetate solutions, which was then spotted onto a steel 384-well target plate and analyzed with a Bruker Autoflex Speed MALDI-TOF. All measurements were performed in the positive mode with the laser at 80% power.

Powder X-ray Diffraction (XRD) Samples were carried out with a D8 Advanced Diffractometer equipped with a LynxEye detector under ambient conditions. On a scatter less sample holder the sample was compacted in a circle with a diameter of 2mm for measurement. X-rays from Cu Kα radiation source with a wavelength of 1.5418 Å was used, and the θ-angle starting at 5° ending at 60° with a 0.05° step. The data profiles were processed using Advanced TOPAS.

Small Angle X-ray Scattering (SAXS). For lab-scale small angle X-ray scattering (SAXS) done at the University of Maryland with Xenocs Xess SAXS/WAXS/GISAXS system, from CuKα X-rays with a wavelength of 1.5417 Å. Scattering was collected using a photon-counting pixel-array detector (Dectris Pilatus 2M, pixel size 172 μm) positioned 2.00 m downstream of the sample. Data was collected at an exposure time of 600 seconds per frame in which the 10 frames are compiled for one image. The samples were prepared in washers (1 cm total diameter) sealed with Kapton films. Samples that were thermally annealed were done so in a Linkam stage that encapsulated the wafer. For the synchrotron X-ray source, at Brookhaven National Lab, through the Center for Functional Nanomaterials (CFN) NSLS-II, BM-11 was used for small angle X-ray scattering (SAXS) analyses with energies ranging from 10-17 keV were delivered by a 3-pole wiggler source, with 10 sec exposure times, and an X-ray wavelength of 0.9184 Å. The samples were prepared in capillary tubes with thin wall borosilicate glass, 0.01 mm. Data was collected using a photon-counting pixel-array detector positioned 2.00 m downstream of the sample. For both systems silver behenate (AgBN) was used as a reference sample to determine beam center and sample to detector distance, and the detector data was converted to reciprocal-space (q) using AgBN the reference.

6.8.3 Supporting Result [†,2†]

A.

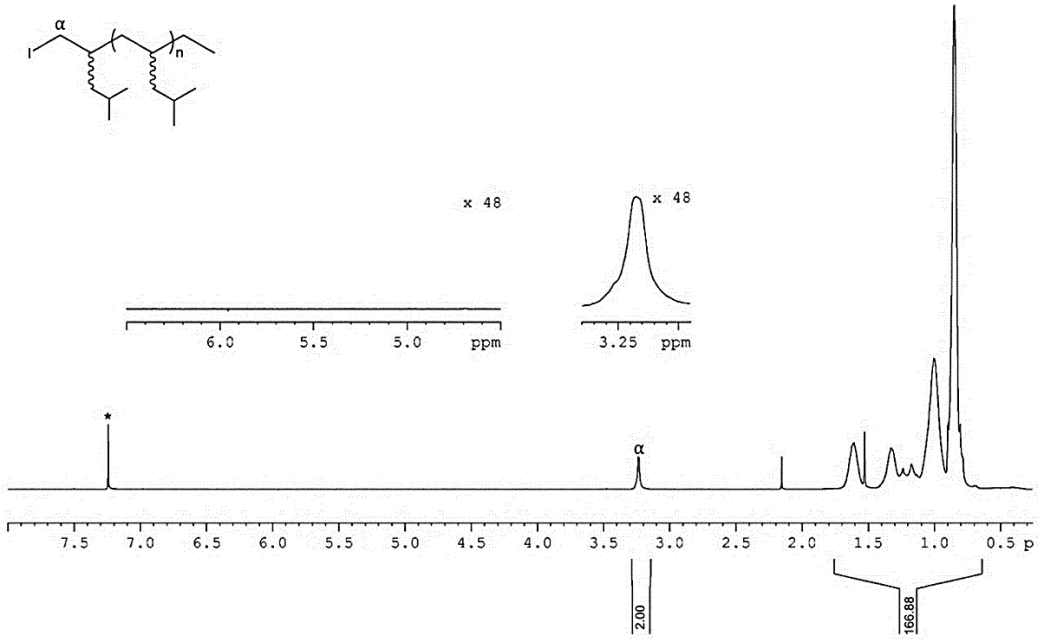

B.

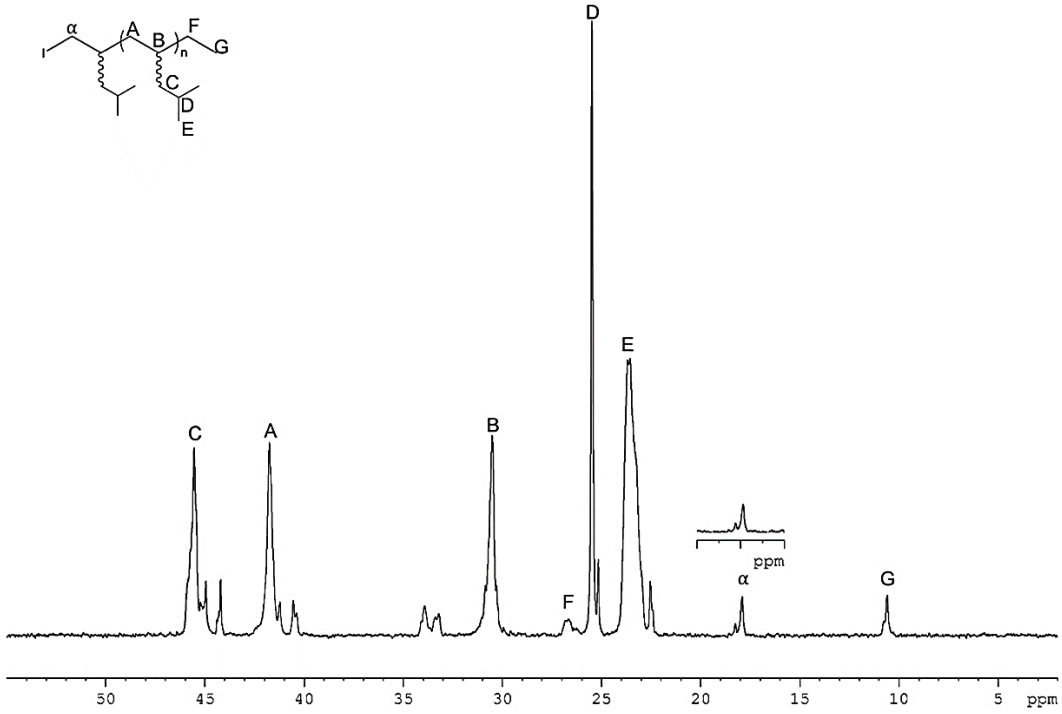

Fig. S6.1 (A) ^{1}H-NMR (400 MHz, *Chloroform-*d1*, RT) of I-aPMP, note the absence of vinylic peaks at 6-5 ppm. (B) ^{13}C-NMR (500 MHz, *Chloroform-*d1*) of I-aPMP. Reproduced with permission from the supporting information of Lachmayr, K. K.; Wentz, C. M.; Sita, L.R., An exceptionally stable and scalable sugar-polyolefin Frank-Kasper A15 phase. *Angew. Chem. Int. Ed.* **2020**, *59*, 1521-1526.

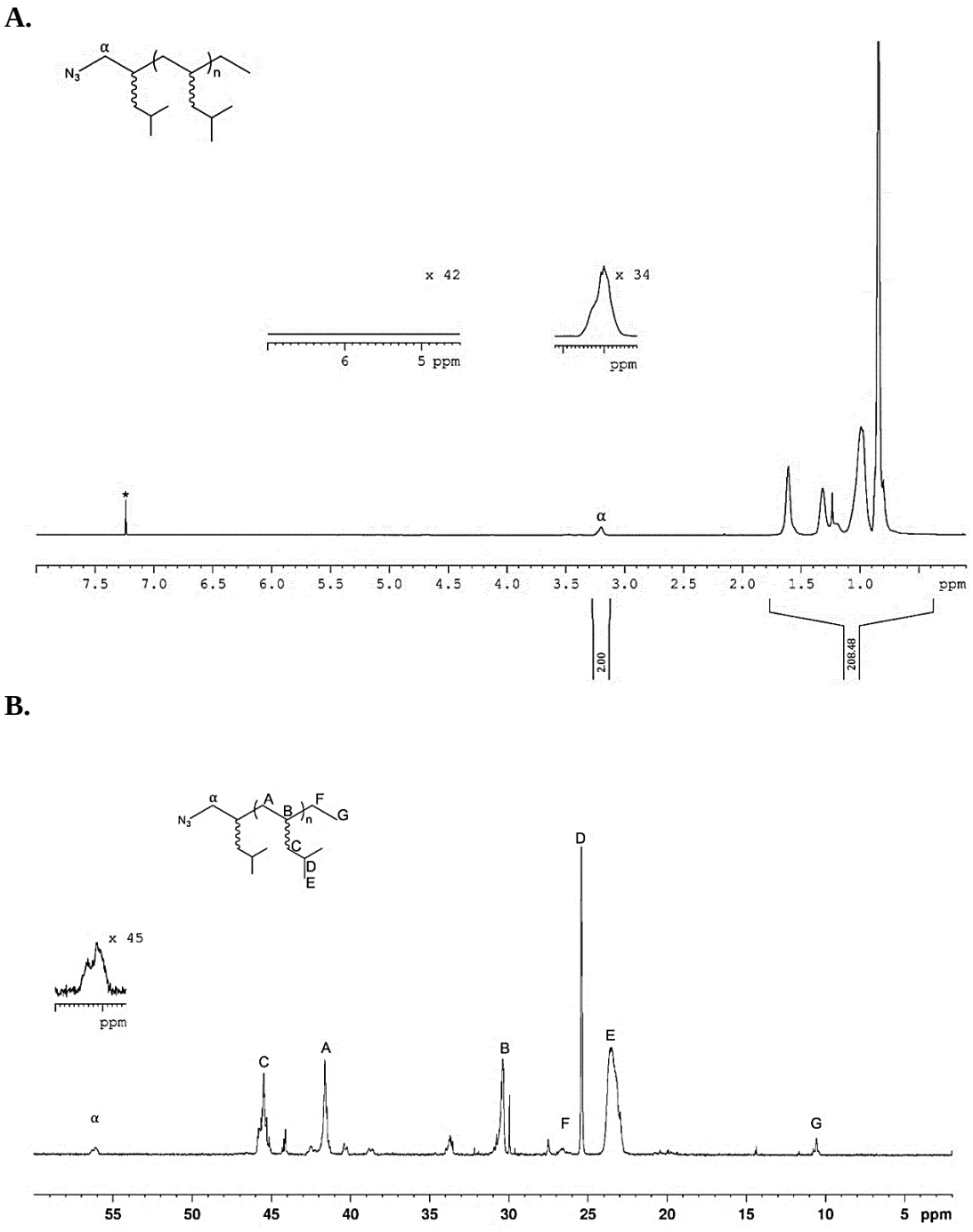

Fig. S.6.2 (A)[1]H-NMR (800 MHz, *Chloroform-*d1*, RT) of N_3-aPMP, note the absence of vinylic peaks at 6-5 ppm. (B) [13]C-NMR (800 MHz, *Chloroform-*d1*, RT) of N_3-aPMP. Reproduced with permission from the supporting information of Lachmayr, K. K.; Wentz, C. M.; Sita, L.R., An exceptionally stable and scalable sugar-polyolefin Frank-Kasper A15 phase. *Angew. Chem. Int. Ed.* **2020**, *59*, 1521-1526.

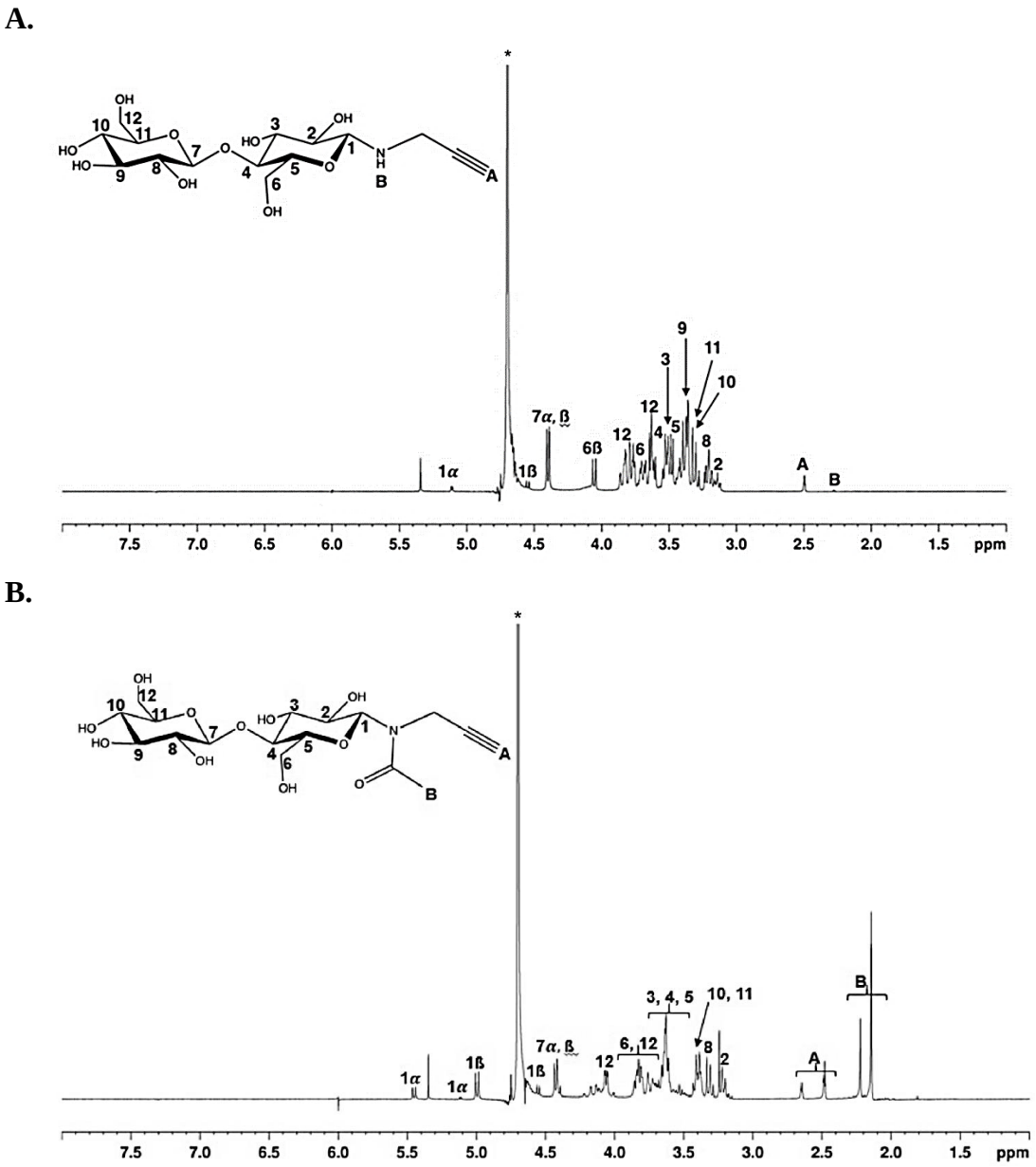

Fig. S6.3 (A) ^{1}H-NMR (400 MHz, *Water-*d2*, RT) of N-propargyl cellobiose intermediate. (B) ^{1}H-NMR (400 MHz, *Water-*d2*, RT) of N-acetyl propargyl cellobiose. Assignments made from HSQC. Reproduced with permission from the supporting information of Lachmayr, K. K.; Wentz, C. M.; Sita, L.R., An exceptionally stable and scalable sugar-polyolefin Frank-Kasper A15 phase. *Angew. Chem. Int. Ed.* **2020**, *59*, 1521-1526.

A.

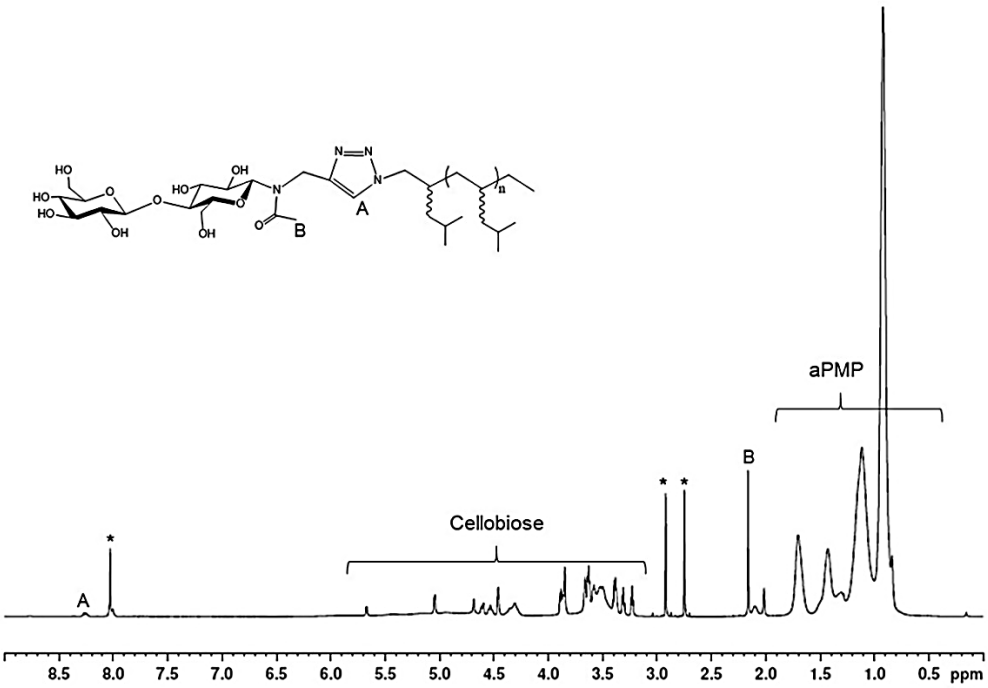

B.

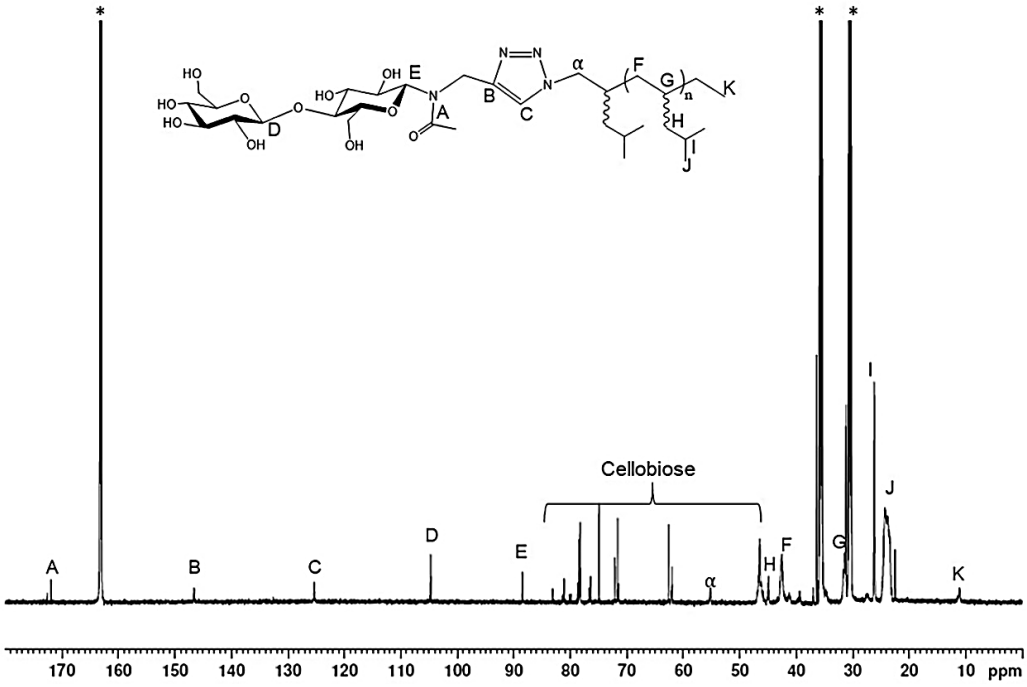

Fig. S6.4. (A)[1]H-NMR (800 MHz, *DMF-*d7*, RT, calibrated at 8.01 (CO*H*) ppm) of CB-aPMP. **(**B) [13]C-NMR (800 MHz, *DMF-*d7*, RT, calibrated at 163 (CO*H*) ppm) of CB-aPMP, Assignments made from HSQC.†

A.

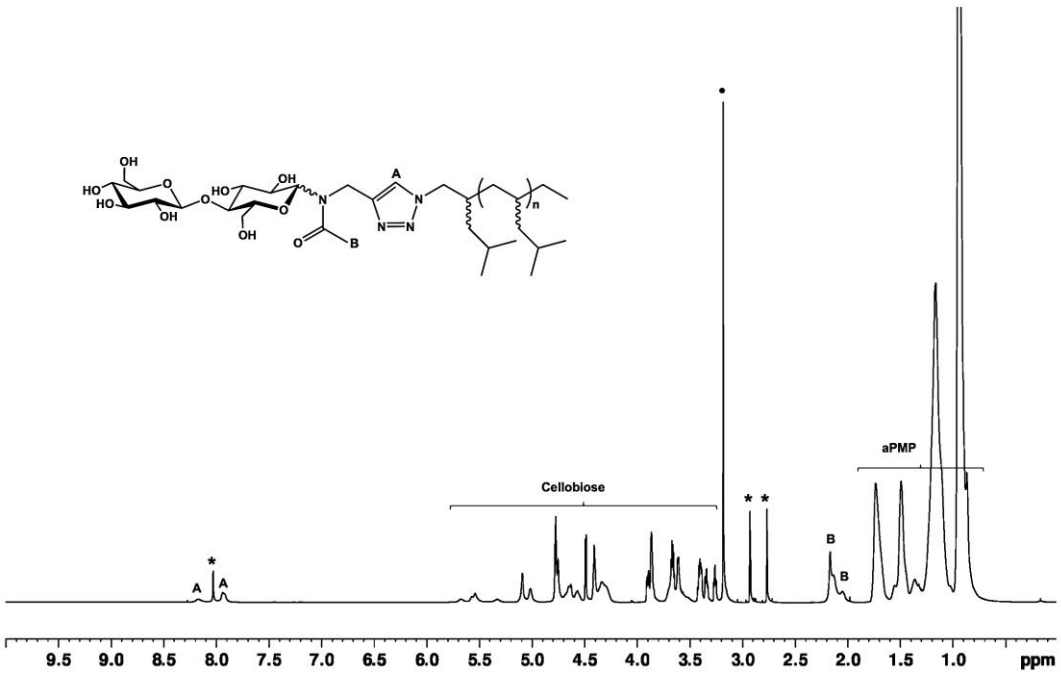

B.

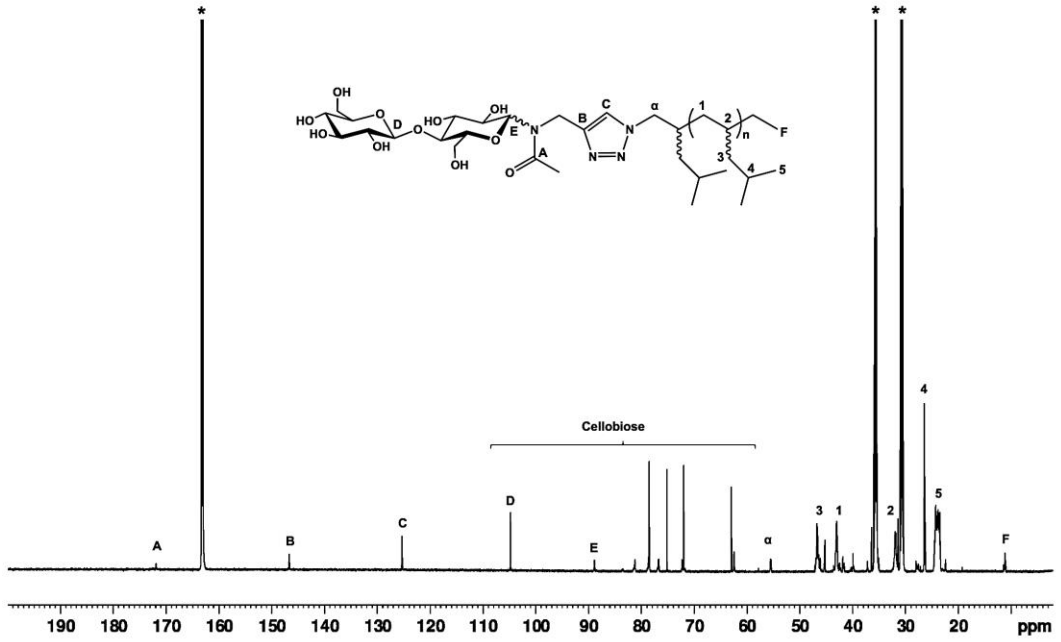

Fig. S6.5. (A)[1]H-NMR (800 MHz, *DMF-*d7*, 70 ˚C, calibrated at 8.03 (CO*H*) ppm) of CB-aPMP. (B) [13]C-NMR (800 MHz, *DMF-*d7*, RT, calibrated at 163 (CO*H*) ppm) of CB-aPMP, assignments made from reference 3 (● denotes methanol).

A.

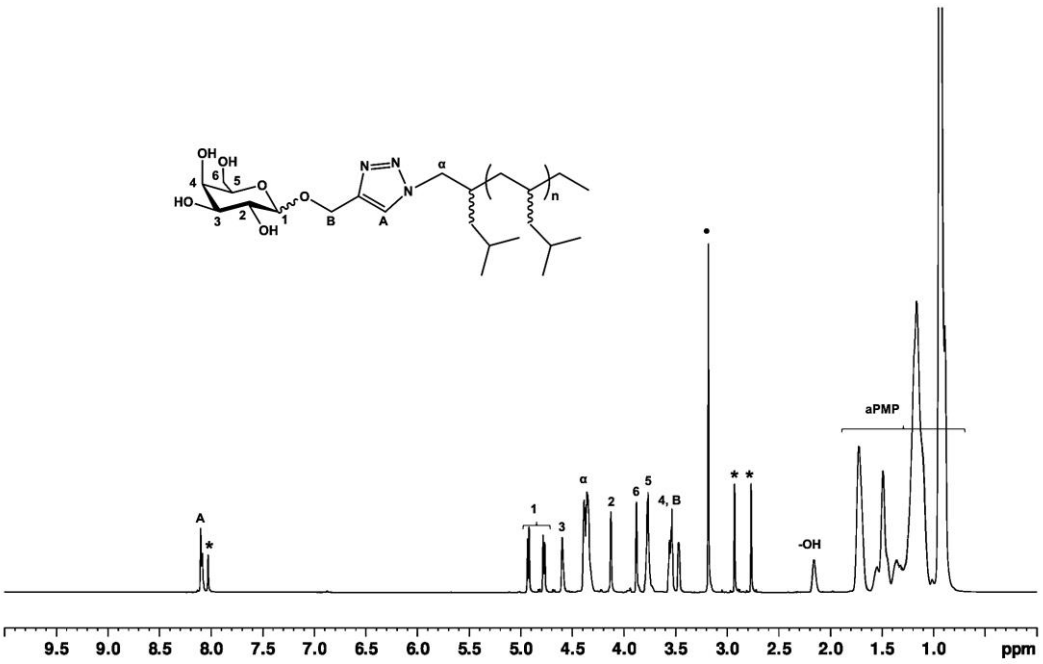

B.

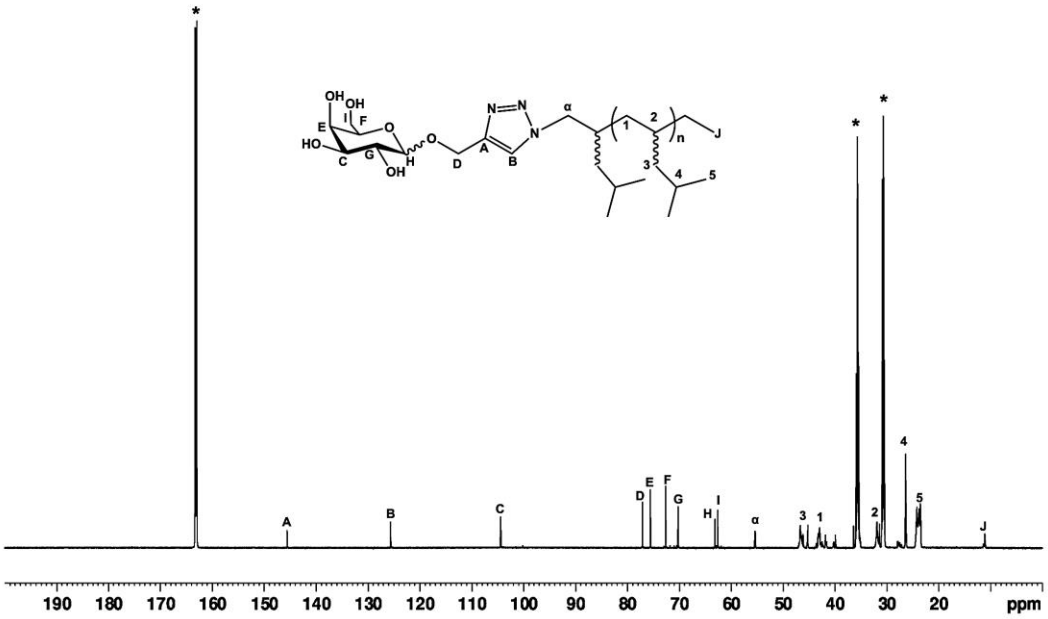

Fig. S6.6. (A)[1]H-NMR (800 MHz, *DMF-*d7*, 70 ˚C, calibrated at 8.03 (CO*H*) ppm) of GAL-aPMP, **6.2**. (B) [13]C-NMR (800 MHz, *DMF-*d7*, RT, calibrated at 163 (CO*H*) ppm) of GAL-aPMP, **6.2**, assignments made from reference 4 (● denotes methanol).

A.

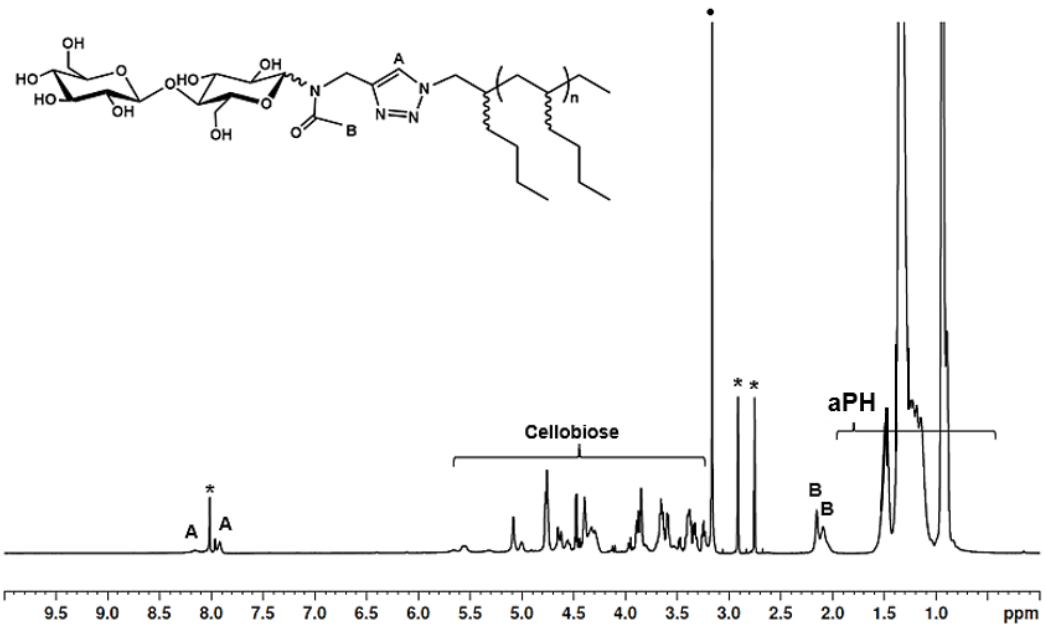

B.

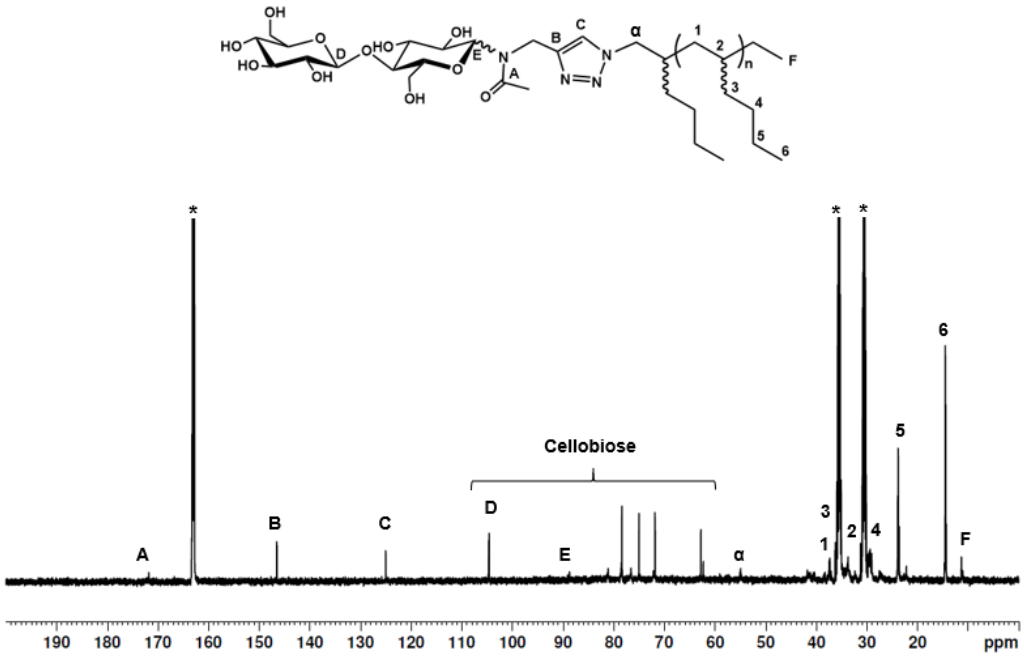

Fig. S6.7. (A)[1]H-NMR (800 MHz, *DMF-*d7*, 70 ˚C, calibrated at 8.03 (CO*H*) ppm) of CB-aPH. (B) [13]C-NMR (800 MHz, *DMF-*d7*, RT, calibrated at 163 (CO*H*) ppm) of CB-aPH (denotes methanol).

A.

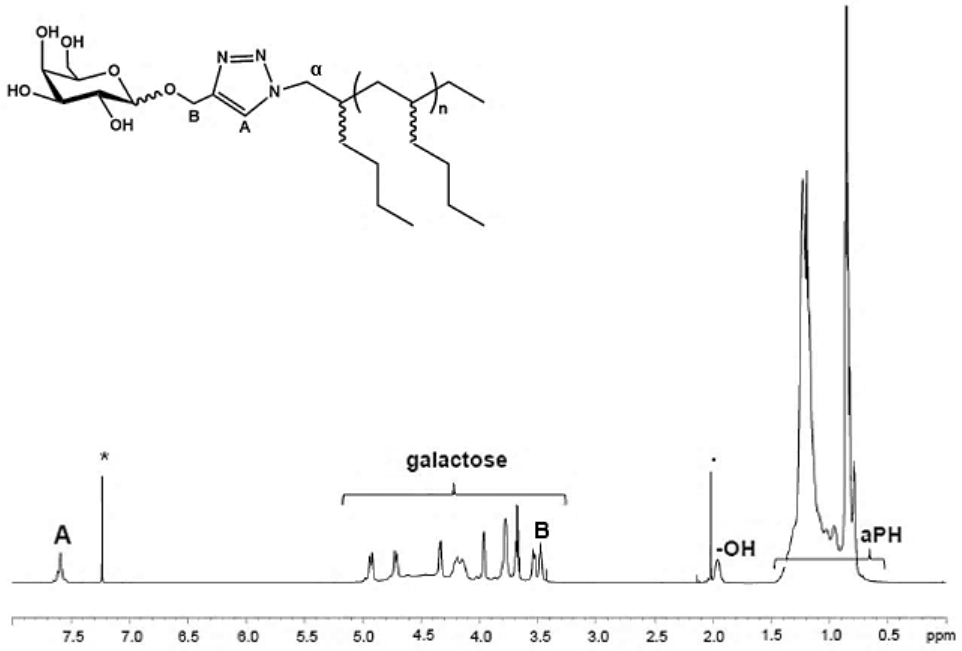

B.

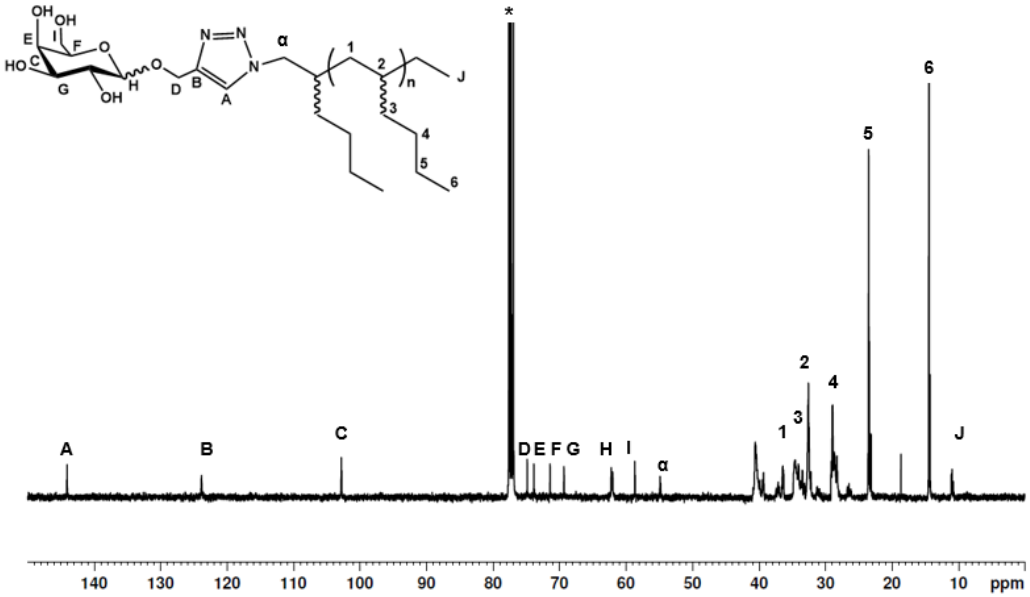

Fig. S6.8. (A)^{1}H-NMR (800 MHz, *CDCl3-*d1*, RT, calibrated at 7.26 ppm) of GAL-aPH. (B) ^{13}C-NMR (800 MHz, *CDCl3 -*d1*, RT, calibrated at 77.26 ppm of GAL-aPH (● denotes methanol).

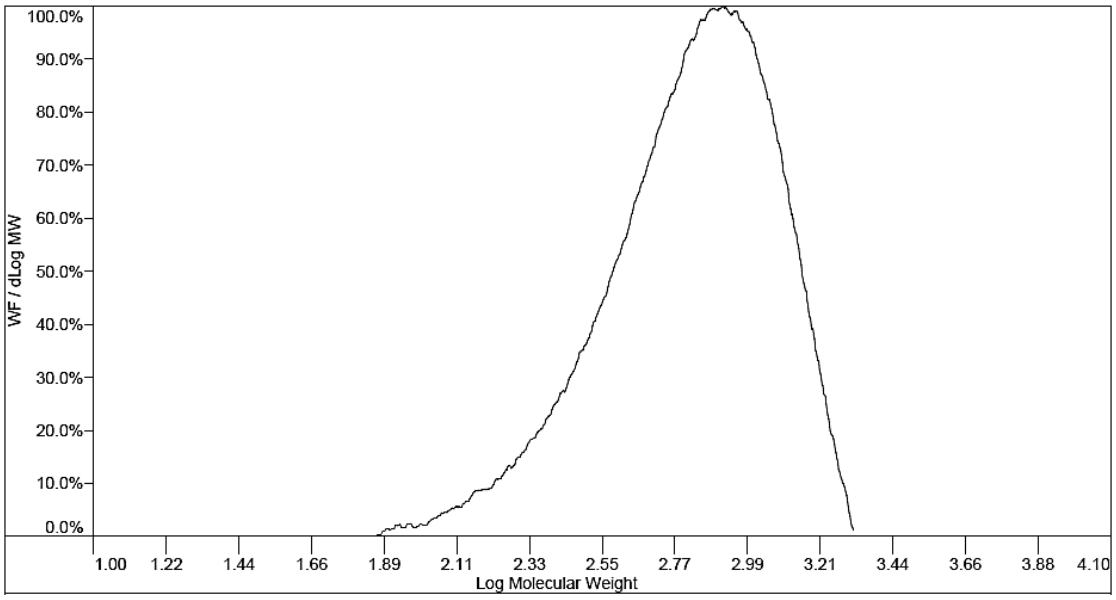

Fig. S6.9. GPC trace of N_3-aPMP. Reproduced with permission from the supporting information of Lachmayr, K. K.; Wentz, C. M.; Sita, L.R., An exceptionally stable and scalable sugar-polyolefin Frank-Kasper A15 phase. *Angew. Chem. Int. Ed.* **2020**, *59*, 1521-1526.

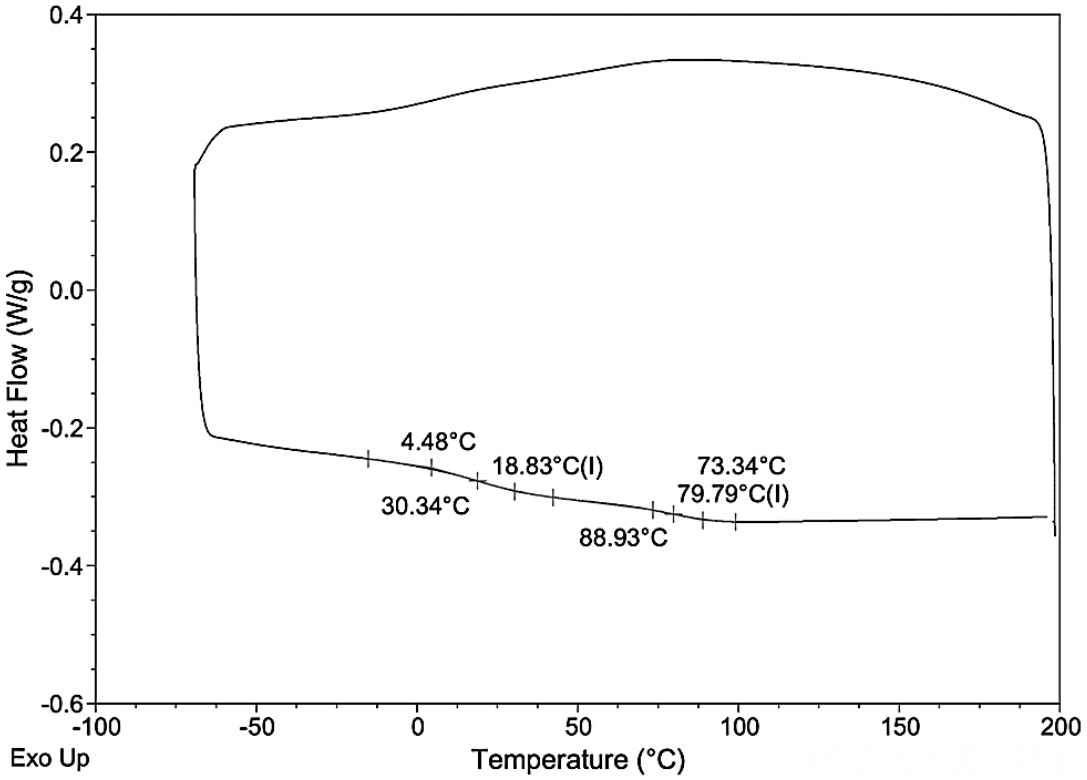

Fig. S6.10. DSC trace of CB-aPMP **6.1.** Two glass transitions labeled on second heating cycle, with first heating cycle removed. Reproduced with permission from the supporting information of Lachmayr, K. K.; Wentz, C. M.; Sita, L.R., An exceptionally stable and scalable sugar-polyolefin Frank-Kasper A15 phase. *Angew. Chem. Int. Ed.* **2020**, *59*, 1521-1526.

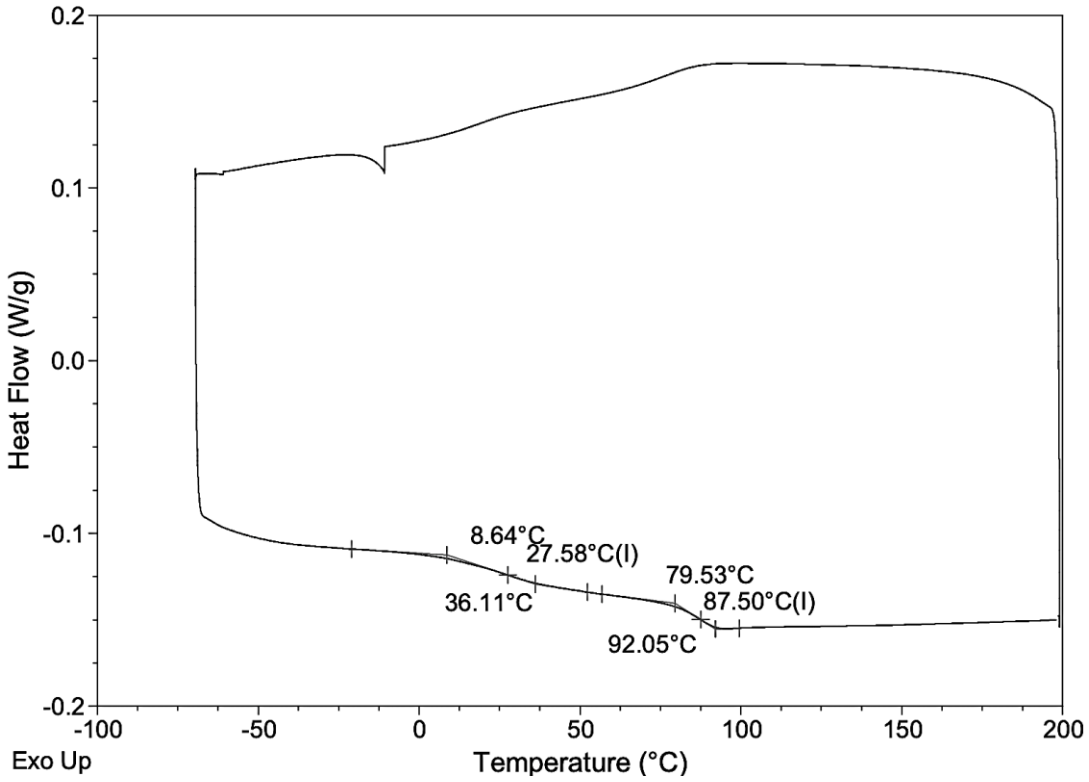

Fig. S6.11. DSC trace of CB-aPMP, **6.8**, two glass transitions labeled on second heating cycle, with first heating cycle removed.

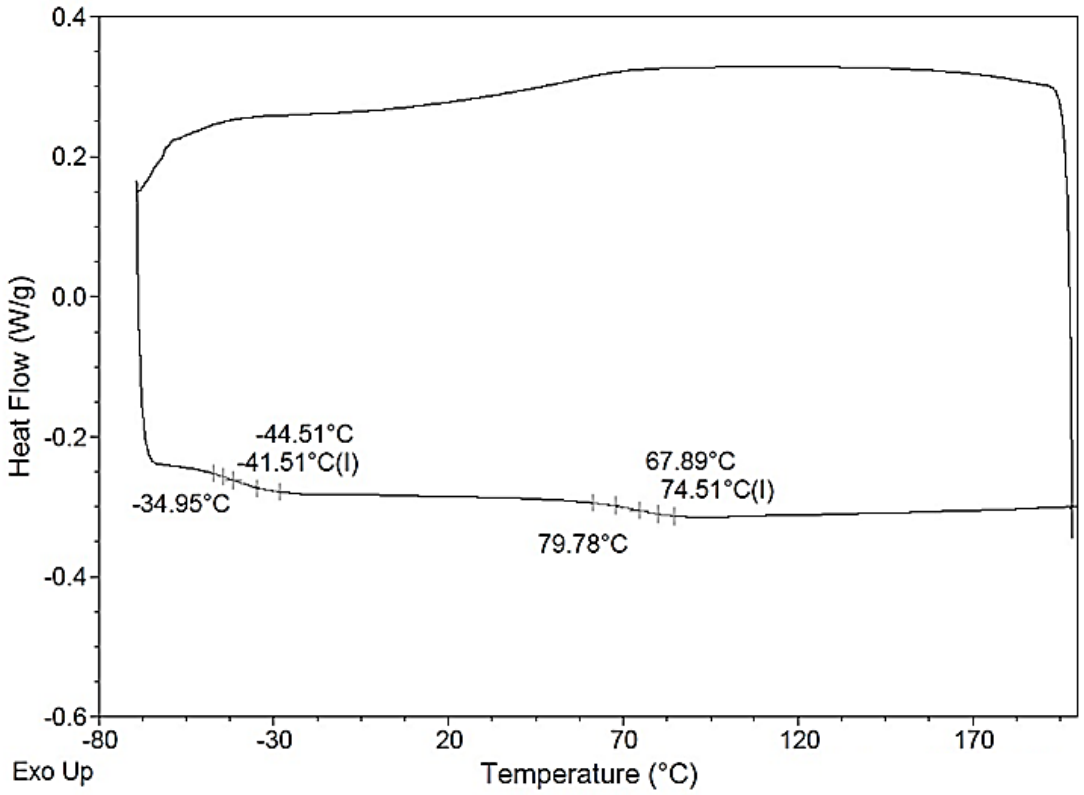

Fig. S6.12. DSC trace of CB-aPH, **6.4**, two glass transitions labeled on second heating cycle, with first heating cycle removed.

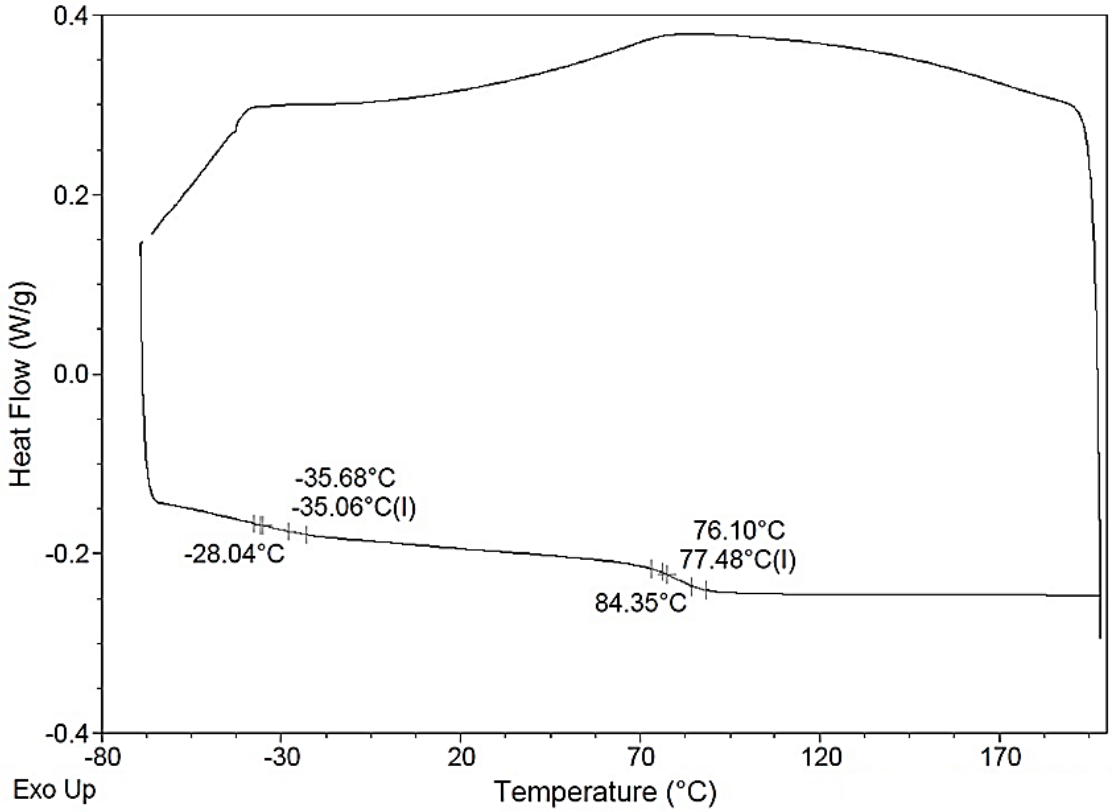

Fig. S6.13. DSC trace of CB-aPH, **6.5**, two glass transitions labeled on second heating cycle, with first heating cycle removed**.**

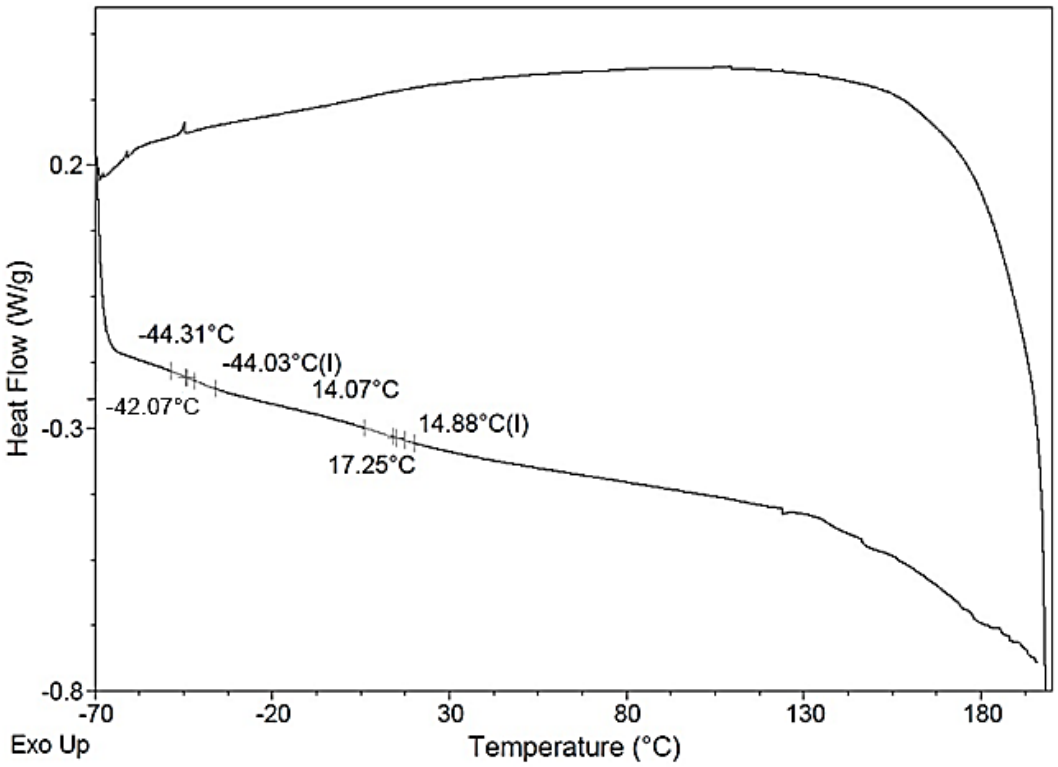

Fig. S6.14. DSC trace of GAL-aPH, **6.6**, two glass transitions labeled on second heating cycle, with first heating cycle removed**.**

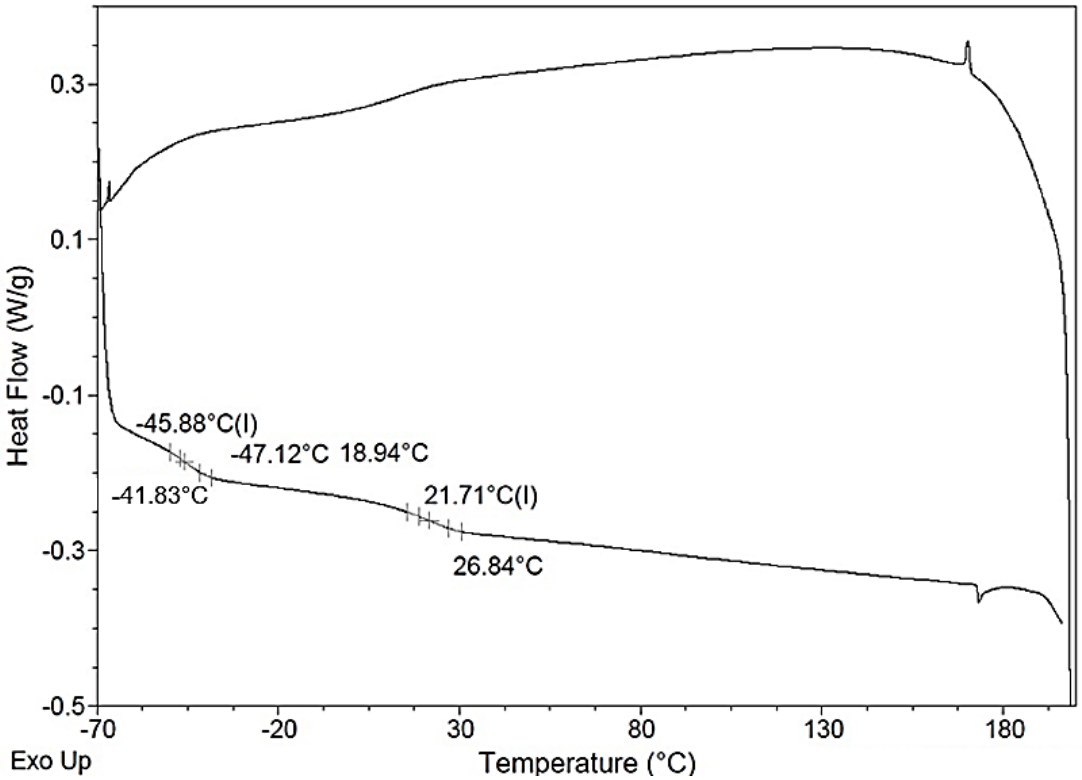

Fig. S6.15. DSC trace of GAL-aPH, **6.7**, two glass transitions labeled on second heating cycle, with first heating cycle removed**.**

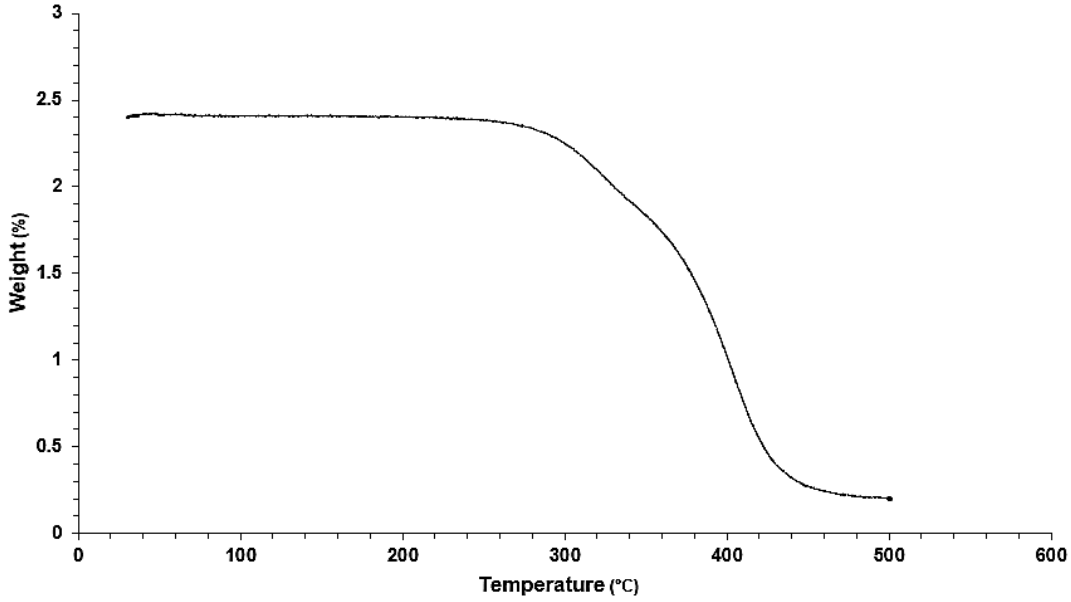

Fig. S6.16. TGA of the CB-aPMP conjugate over a temperature range 30 °C - 500 °C, with a 10 ˚C/min ramp rate starting mass 2.407mg at 30 ˚C. Reproduced with permission from the supporting information of Lachmayr, K. K.; Wentz, C. M.; Sita, L.R., An exceptionally stable and scalable sugar-polyolefin Frank-Kasper A15 phase. *Angew. Chem. Int. Ed.* **2020**, *59*, 1521-1526.

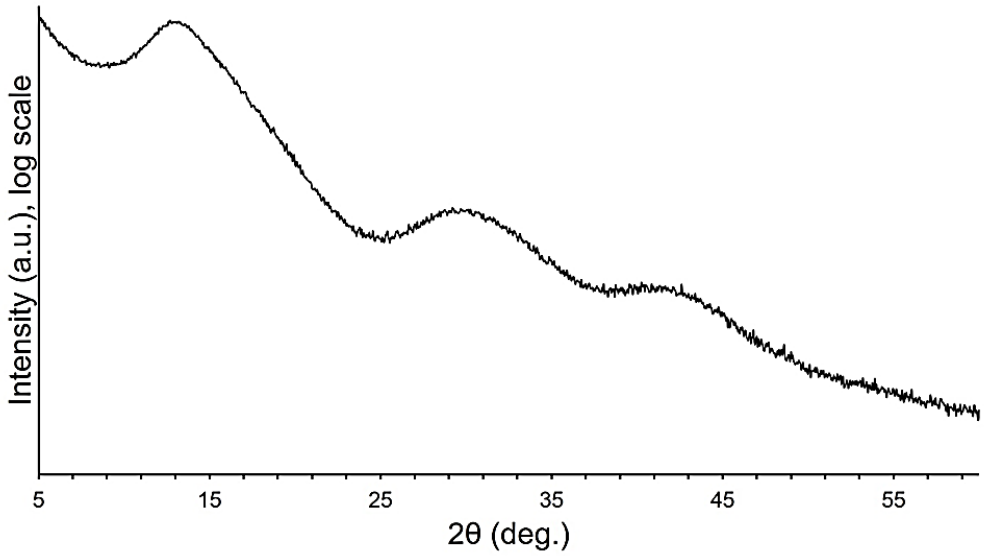

Figure S6.17. Powder x-ray diffraction (XRD) spectrum of N_3-aPMP. Reproduced with permission from the supporting information of Lachmayr, K. K.; Wentz, C. M.; Sita, L.R., An exceptionally stable and scalable sugar-polyolefin Frank-Kasper A15 phase. *Angew. Chem. Int. Ed.* **2020**, *59*, 1521-1526.

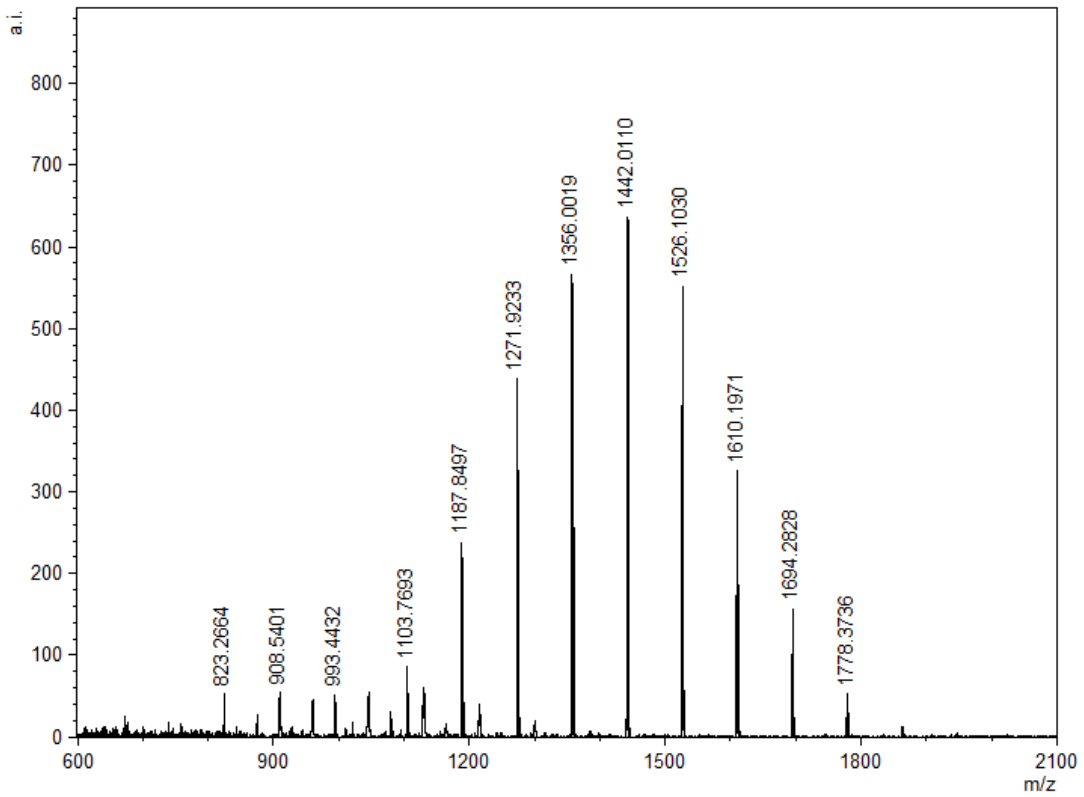

Fig. S6.18. MALDI-TOF of CB-aPMP conjugate PDI = 1.02, Mn = 1400 g/mol, and Mw = 1420 g/mol, with some lower molecule weight fragments observed from polymer tail cleaved from the sugar head-group, **6.1**. Reproduced with permission from the supporting information of Lachmayr, K. K.; Wentz, C. M.; Sita, L.R., An exceptionally stable and scalable sugar-polyolefin Frank-Kasper A15 phase. *Angew. Chem. Int. Ed.* **2020**, *59*, 1521-1526.

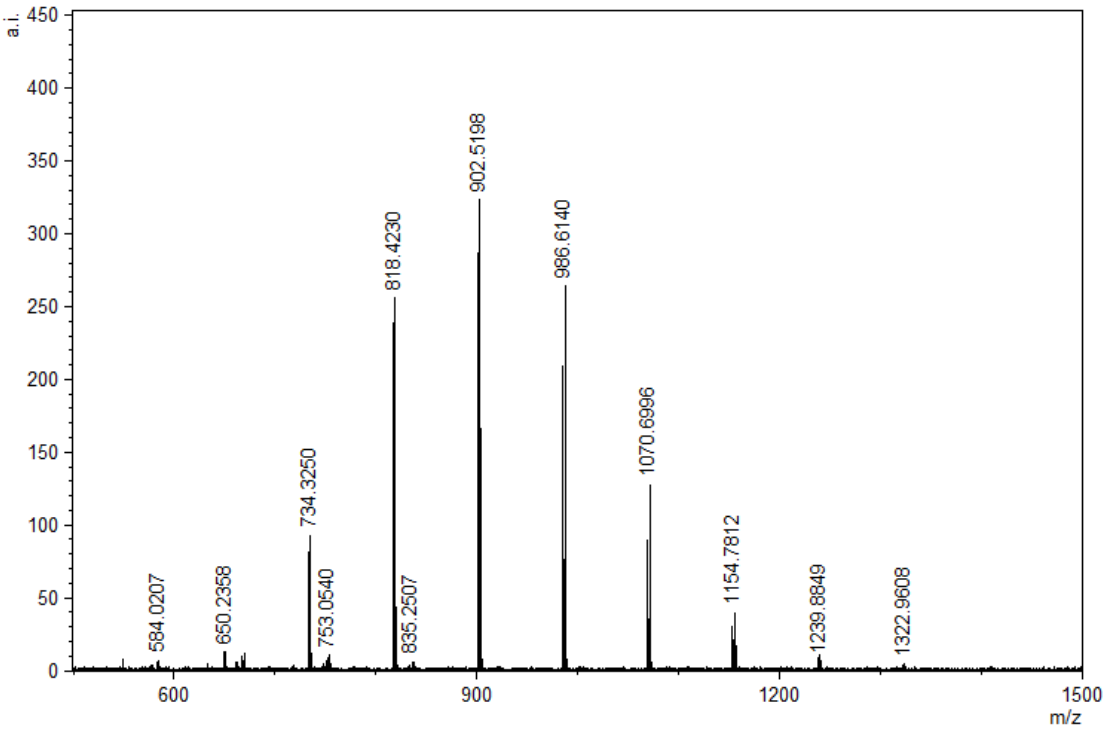

Fig. S6.19. MALDI-TOF of GAL-aPMP conjugate PDI = 1.02, Mn = 0.92 KDa, and Mw = 0.94 kDa, **6.2**, with some lower molecule weight fragments observed from polymer tail cleaved from the sugar head-group.

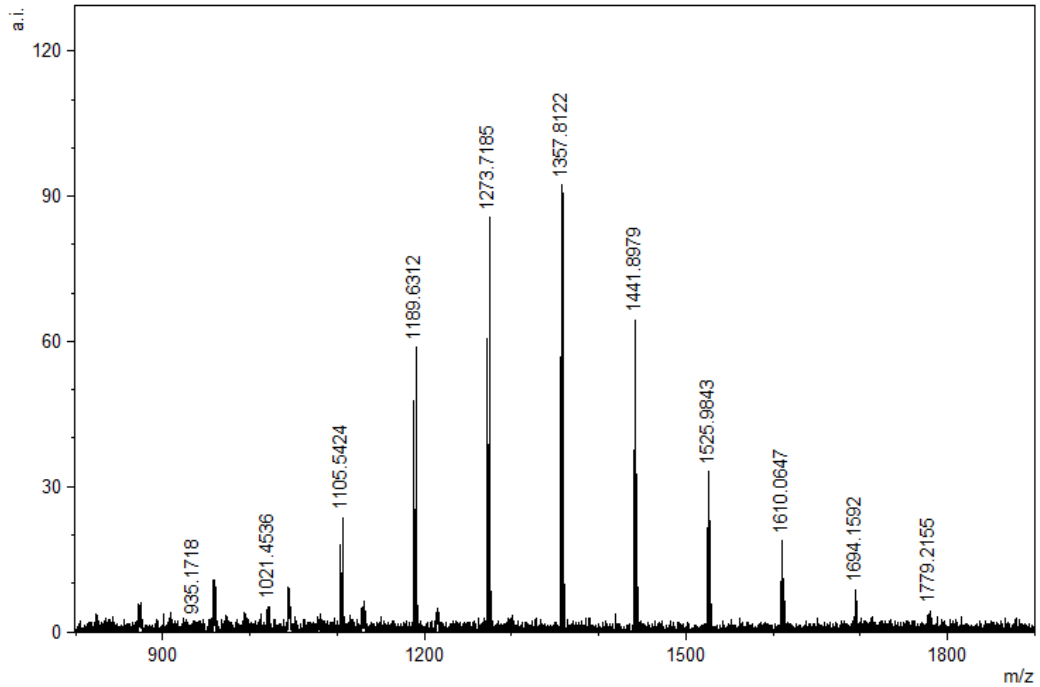

Fig. S6.20. MALDI-TOF of CB-aPMP conjugate PDI = 1.01, Mn = 1.34 kDa, and Mw = 1.36 kDa, **6.8**, with some lower molecule weight fragments observed from polymer tail cleaved from the sugar head-group.

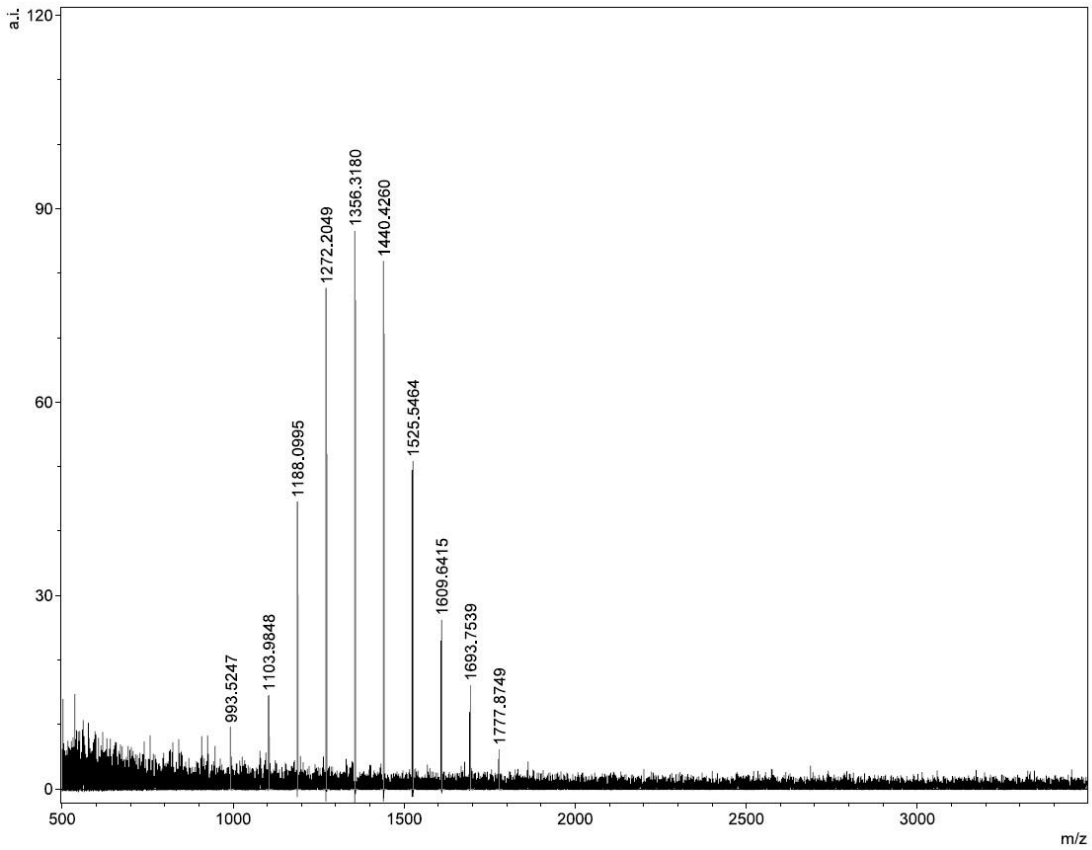

Fig. S6.21. MALDI-TOF of CB-aPH conjugate, **6.4**, PDI = 1.02, Mn = 1.39 KDa, and Mw = 1.41 kDa, with some lower molecule weight fragments observed from polymer tail cleaved from the sugar head-group.

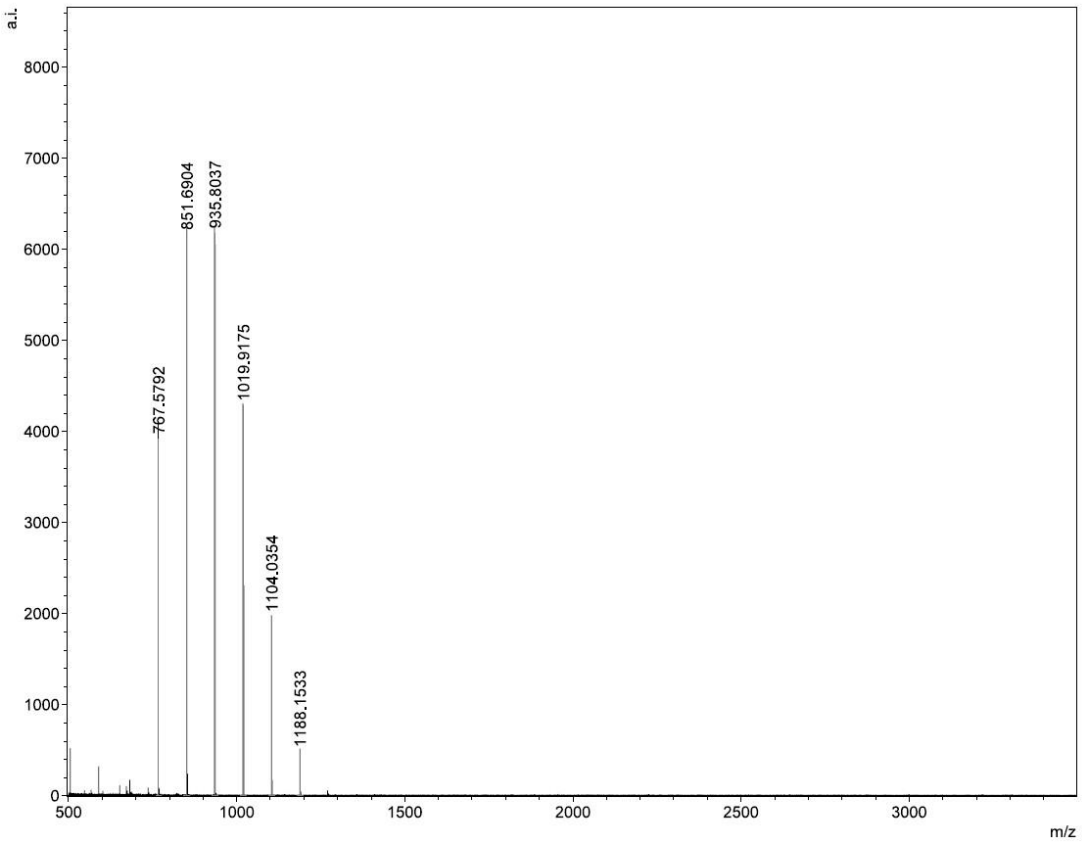

Fig. S6.22. MALDI-TOF of CB-aPH conjugate, **6.5**, PDI = 1.01, Mn = 925 Da, and Mw = 938 Da, with some lower molecule weight fragments observed from polymer tail cleaved from the sugar head-group.

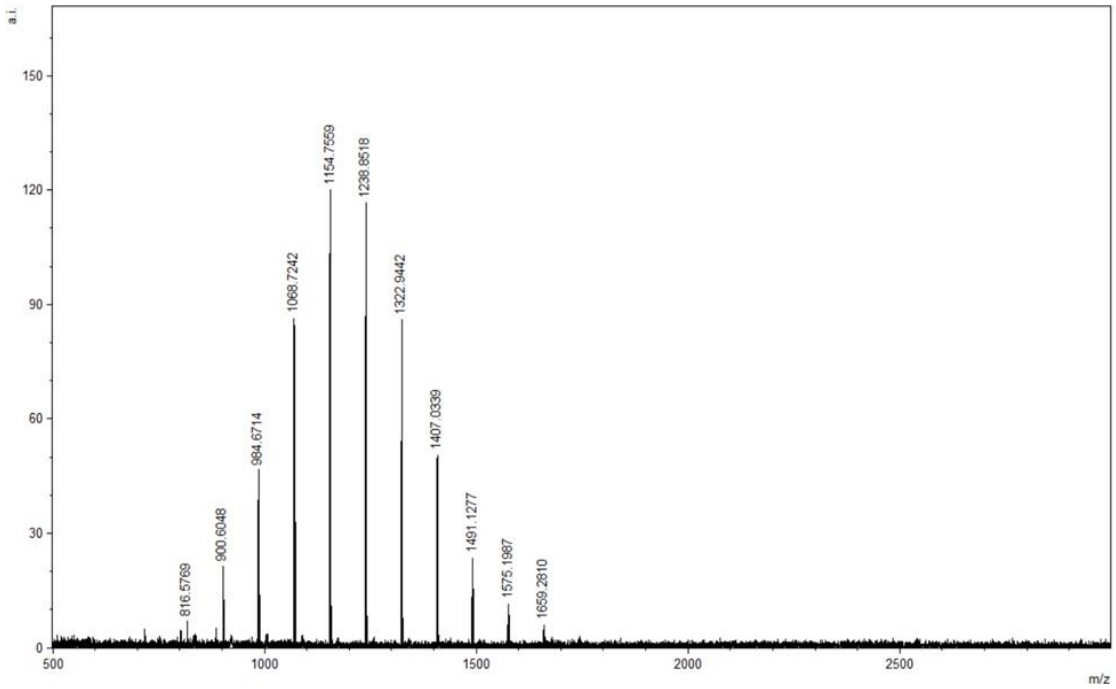

Fig. S6.23. MALDI-TOF of GAL-aPH conjugate, **6.6**, PDI = 1.02, Mn = 1.21 kDa, and Mw = 1.23 kDa, with some lower molecule weight fragments observed from polymer tail cleaved from the sugar head-group.

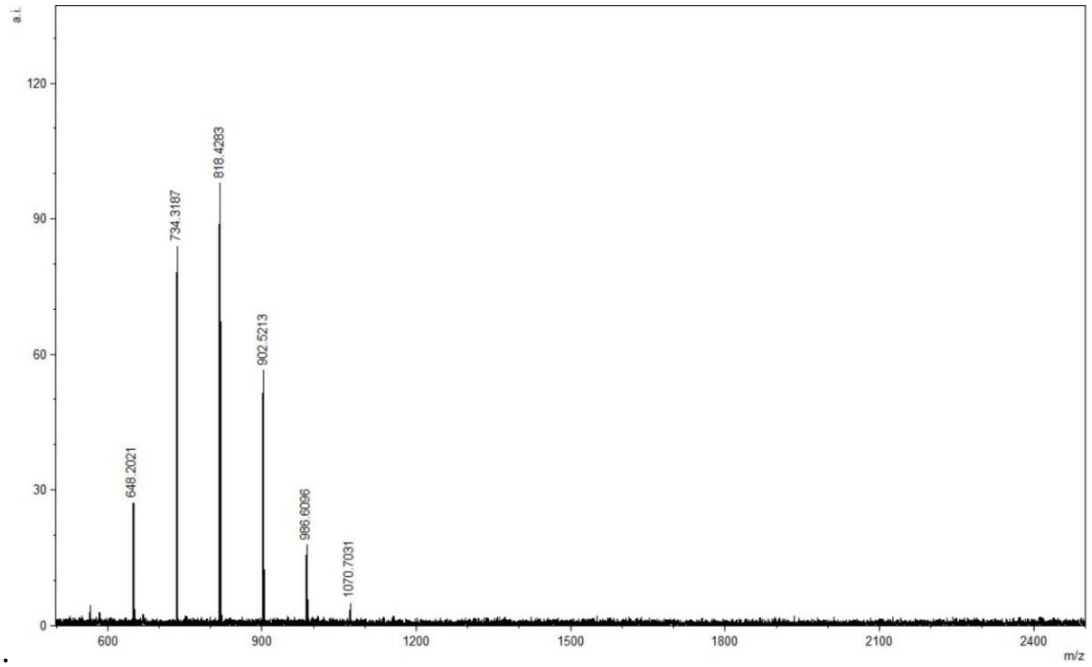

.

Fig. S6.24. MALDI-TOF of GAL-aPH conjugate, **6.7**, PDI = 1.04, Mn = 788 Da, and Mw = 816 Da, with some lower molecule weight fragments observed from polymer tail cleaved from the sugar head-group

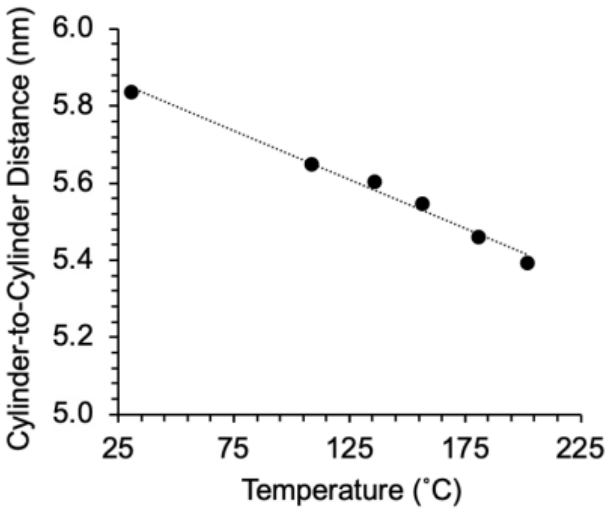

Fig. S6.25. Cylinder-to-cylinder distance, of the *C* phases as function of temperature. Collected from a SAXS thermal ramp experiment conducted using a synchrotron x-ray source and thermal stage, heating at a rate of 1 °C/min from 30-220 °C Reproduced with permission from the supporting information of Lachmayr, K. K.; Wentz, C. M.; Sita, L.R., An exceptionally stable and scalable sugar-polyolefin Frank-Kasper A15 phase. *Angew. Chem. Int. Ed.* **2020**, *59*, 1521-1526.

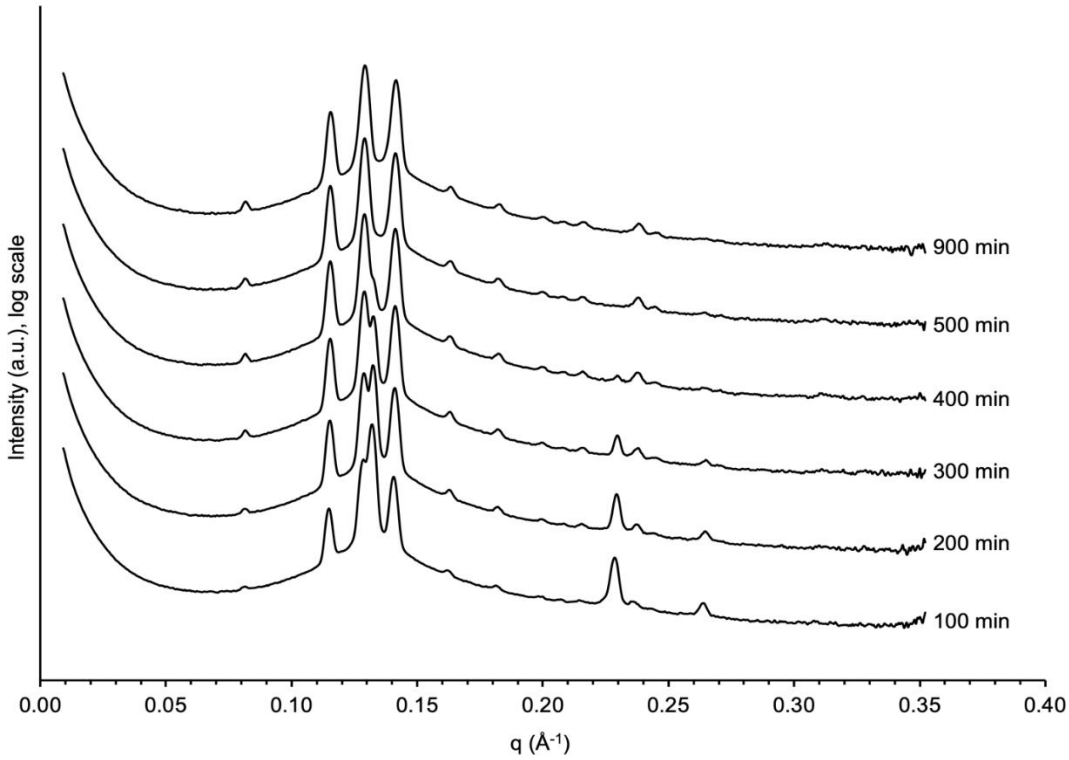

Fig. S6.26. Isothermal SAXS profile of CB-aPMP at 180 ˚C, recording the order-order phase transition of a mixed C/FK A15 phase to pure FK A15 phase over 900 minutes (min), with the phase transition complete at 500 min. Data was collected using a Xenocs Xess SAXS system. Each time is y-offset by a factor of ten. Reproduced with permission from the supporting information of Lachmayr, K. K.; Wentz, C. M.; Sita, L.R., An exceptionally stable and scalable sugar-polyolefin Frank-Kasper A15 phase. *Angew. Chem. Int. Ed.* **2020**, *59*, 1521-1526.

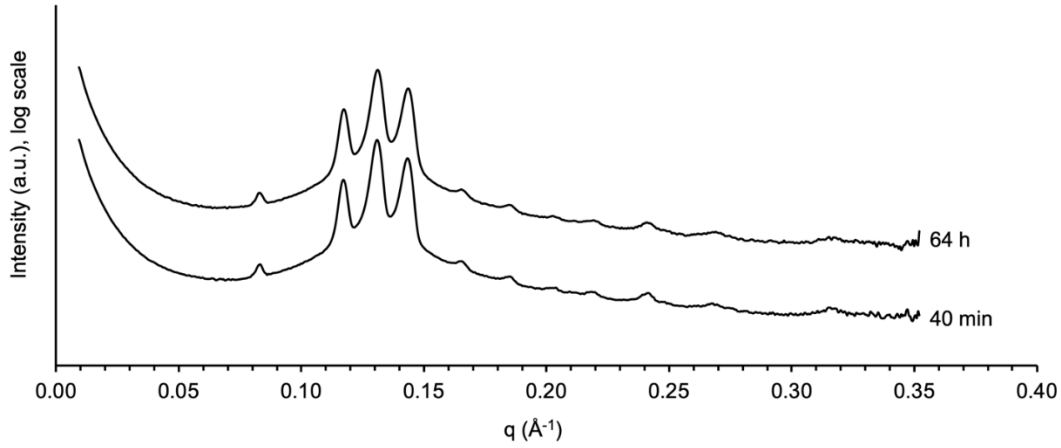

Fig. S6.27. SAXS profile of CB-aPMP at 23 ˚C, recorded no order-order phase transition or order-disorder phase transition of the FK A15 phase after 40 min and 64 h at room temperature (23 ˚C) data taken immediately after the isothermal transition at 180 ˚C. Sample remained *in vacuo* for duration of 23 ˚C data collection period. Data was collected using Xenocs Xess SAXS system. Each time is y-offset by a factor of ten. Reproduced with permission from the supporting information of Lachmayr, K. K.; Wentz, C. M.; Sita, L.R., An exceptionally stable and scalable sugar-polyolefin Frank-Kasper A15 phase. *Angew. Chem. Int. Ed.* **2020**, *59*, 1521-1526.

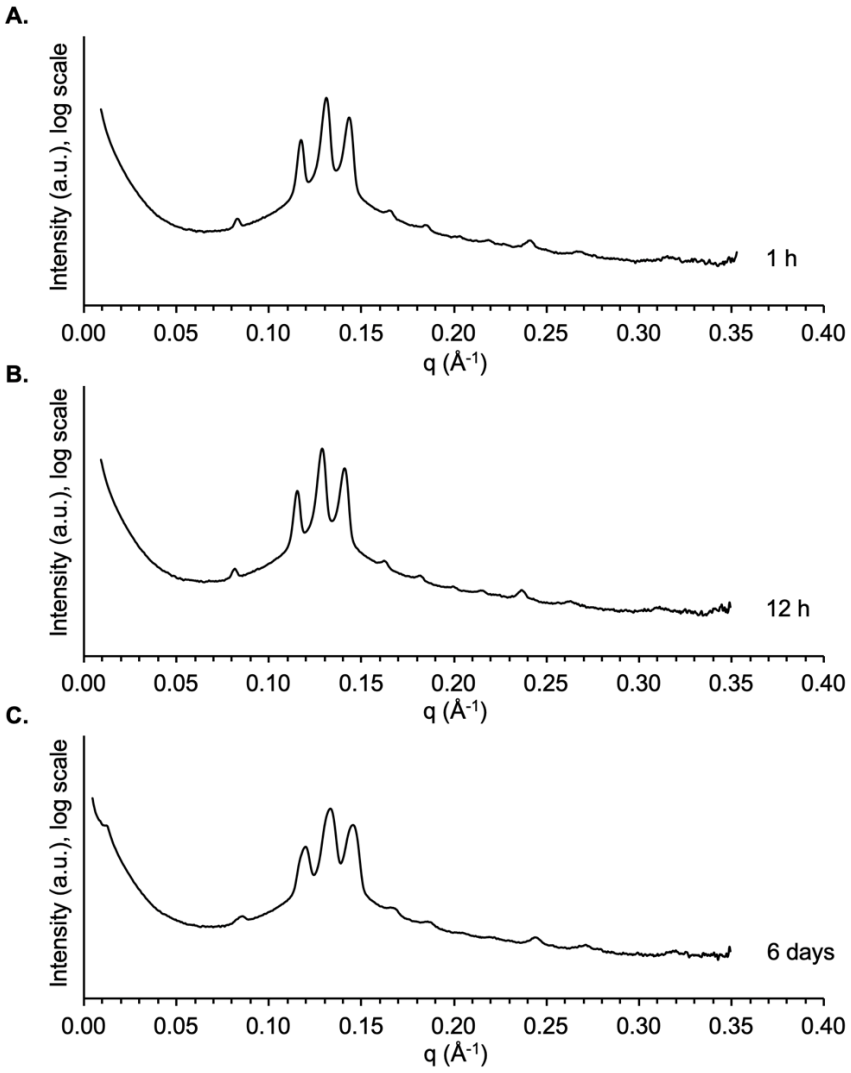

Fig. S6.28. SAXS profile of CB-aPMP at 23 ˚C at 1 h (A), 12 h (B), and 6 days (C) to determine stability of the FK A15 phase, recorded no order-order phase transition or order-disorder phase transition of the FK A15 phase after annealing at 180 ˚C for 23 h was complete. Sample was annealed and remained on Linkam stage *in vacuo* for first 12 h. After 12 h, was removed from SAXS stage and exposed to ambient conditions for remaining length of experiment (6 days). Data was collected using Xenocs Xess SAXS system. Reproduced with permission from the supporting information of Lachmayr, K. K.; Wentz, C. M.; Sita, L.R., An exceptionally stable and scalable sugar-polyolefin Frank-Kasper A15 phase. *Angew. Chem. Int. Ed.* **2020**, *59*, 1521-1526.

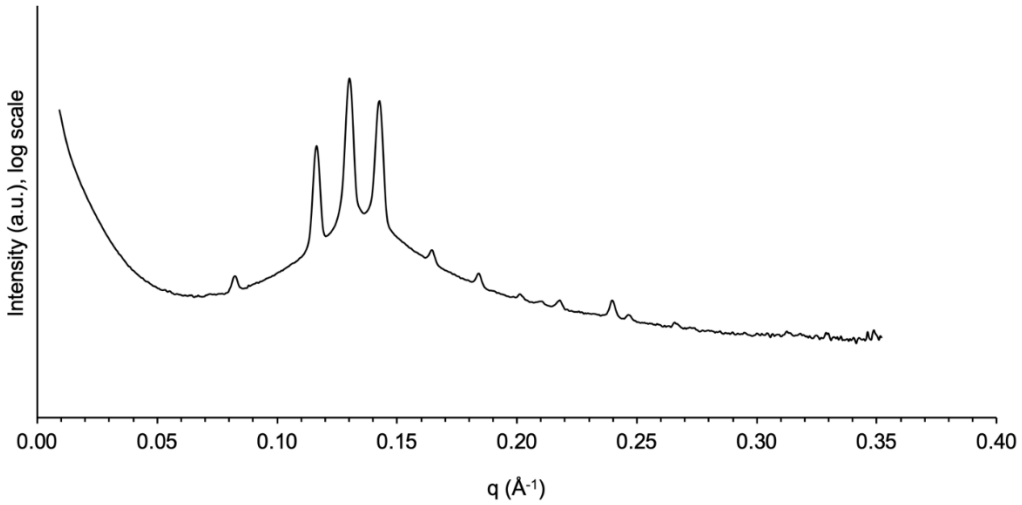

Fig. S6.29. SAXS profile of CB-aPMP re-heated to 180 ˚C for 2 h after 7 day in ambient conditions (post-annealing to FK A15 at 180 ˚C 7 days prior), which resulted in sharpening of broadened peaks of the FK A15 phase from Fig. S28C. Data was collected using Xenocs Xess SAXS system. Reproduced with permission from the supporting information of Lachmayr, K. K.; Wentz, C. M.; Sita, L.R., An exceptionally stable and scalable sugar-polyolefin Frank-Kasper A15 phase. *Angew. Chem. Int. Ed.* **2020**, *59*, 1521-1526.

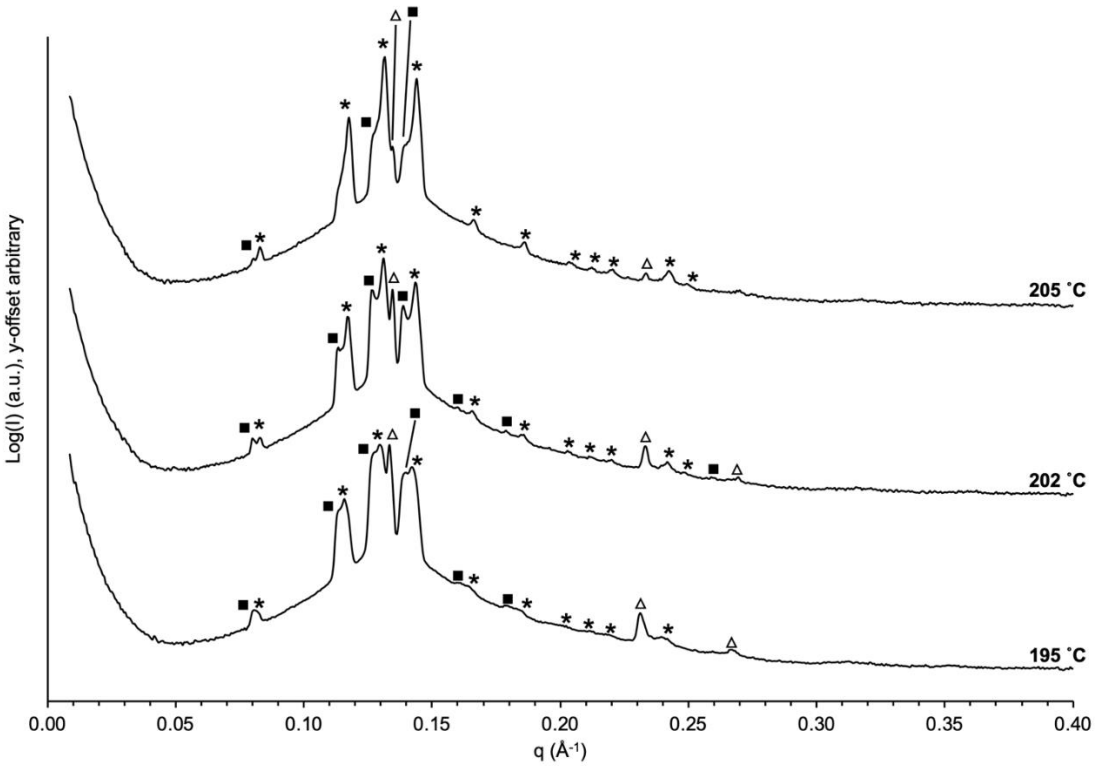

Fig. S6.30. SAXS thermal ramp experiment was conducted using a synchrotron x-ray source and thermal sample stage, heating at a rate of 1 ˚C/min from 30 – 220 ˚C, with the three phases coexisting, HEX and two FK A15 phases. The transient FK A15 phase marked with ■, second equilibrium FK A15 phase *, and HEX △. Each time is y-offset by a factor of one hundred. Reproduced with permission from the supporting information of Lachmayr, K. K.; Wentz, C. M.; Sita, L.R., An exceptionally stable and scalable sugar-polyolefin Frank-Kasper A15 phase. *Angew. Chem. Int. Ed.* **2020**, *59*, 1521-1526.

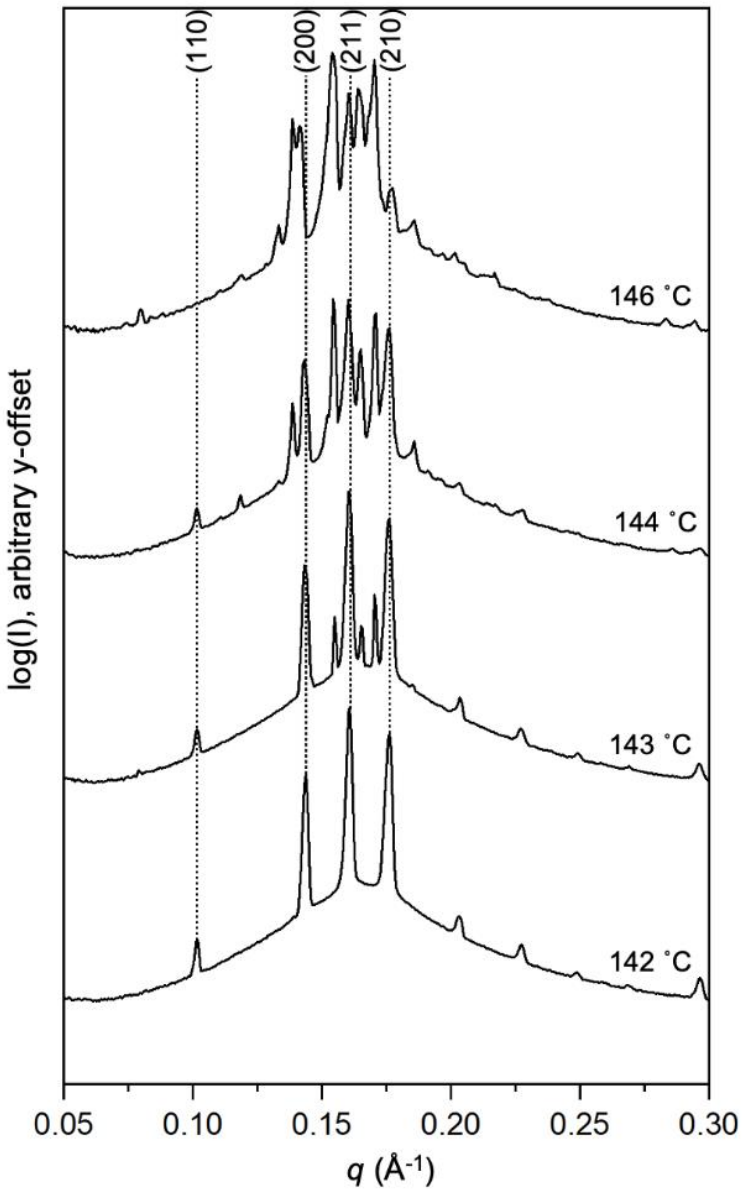

Fig. S6.31 Selected 1D SAXS data 0.2 ˚C/min thermal ramp of the 3:1 blend with **6.2** and **6.8**. Dotted lines correspond to *hkl* Miller planes on the FK A15 phase, showing the full disappearance of the peaks with increase in temperature.

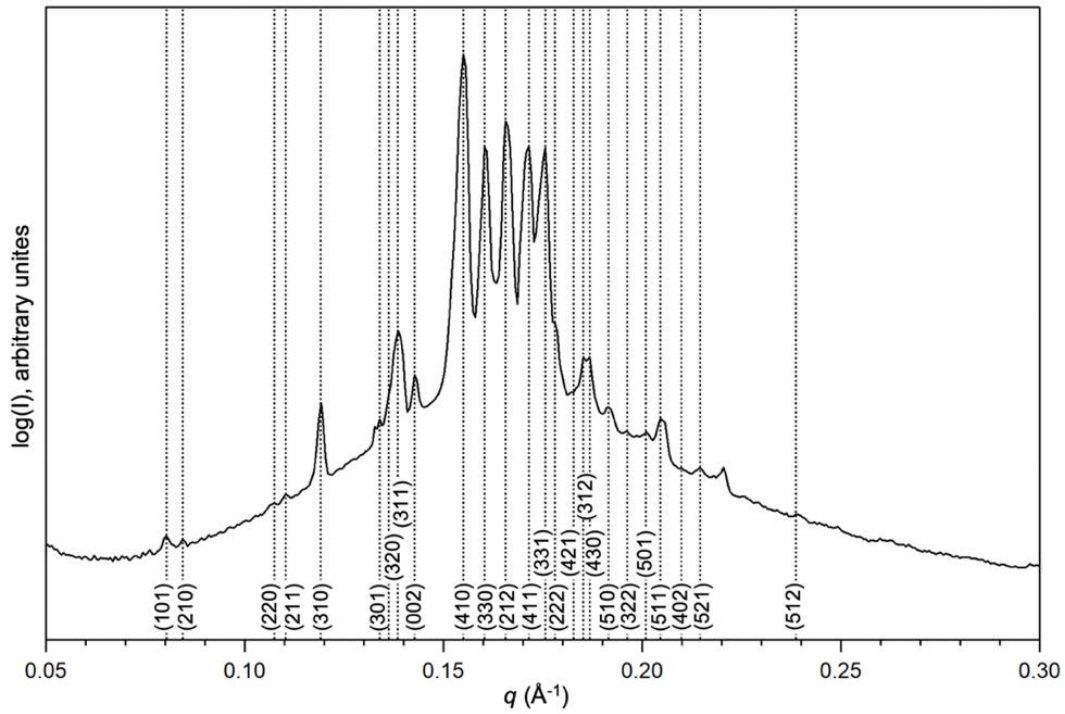

Fig. S6.32. 1D SAXS data of the FK σ phase from the 3:1 blend of **6.2** and **6.8** from an isothermal experiment after 6.6 h at 140 ˚C, where dotted line correlate peaks with corresponding *hkl* Miller planes.

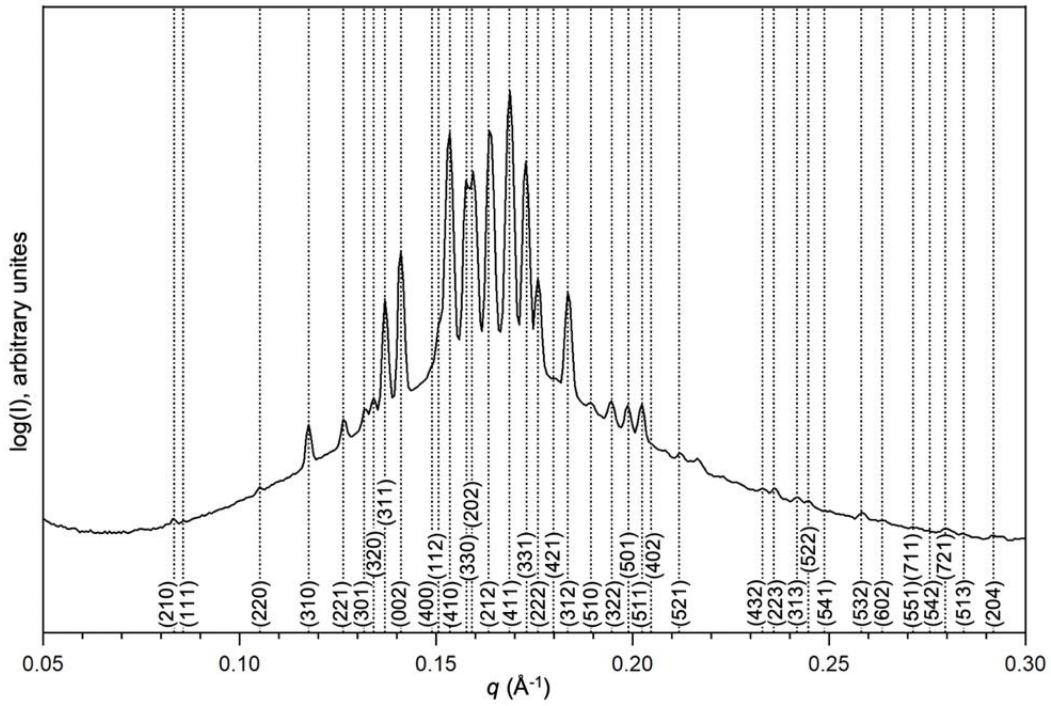

Fig. S.6.33. 1D SAXS data of the σ phase with 2:1 blend of **6.3** and **6.8** from an 0.2 ˚C/min thermal ramp at 127 ˚C.

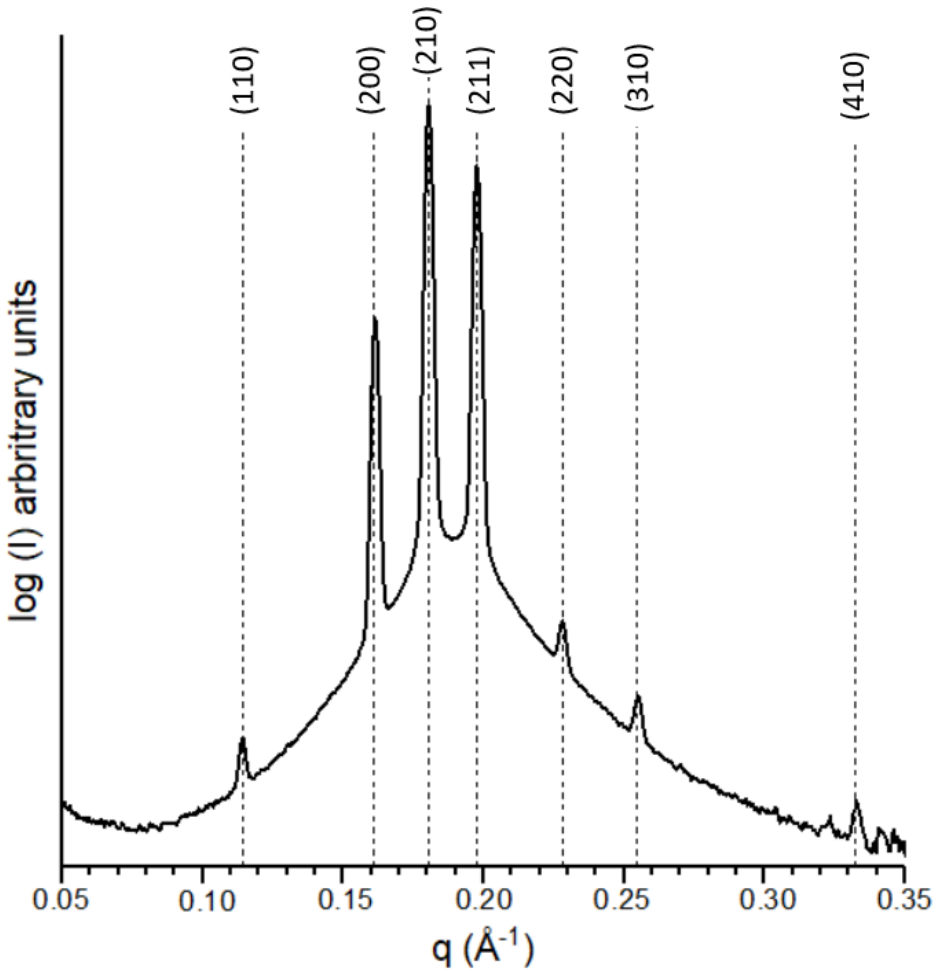

Fig. S.6.34. 1D SAXS data of the FK A15 phase from the GAL-aPH sugar-polyolefin conjugate, **6.6**, blended with vitamin E at 10 % at 80 °C, were the dotted line correlate peaks with corresponding *hkl* Miller planes.

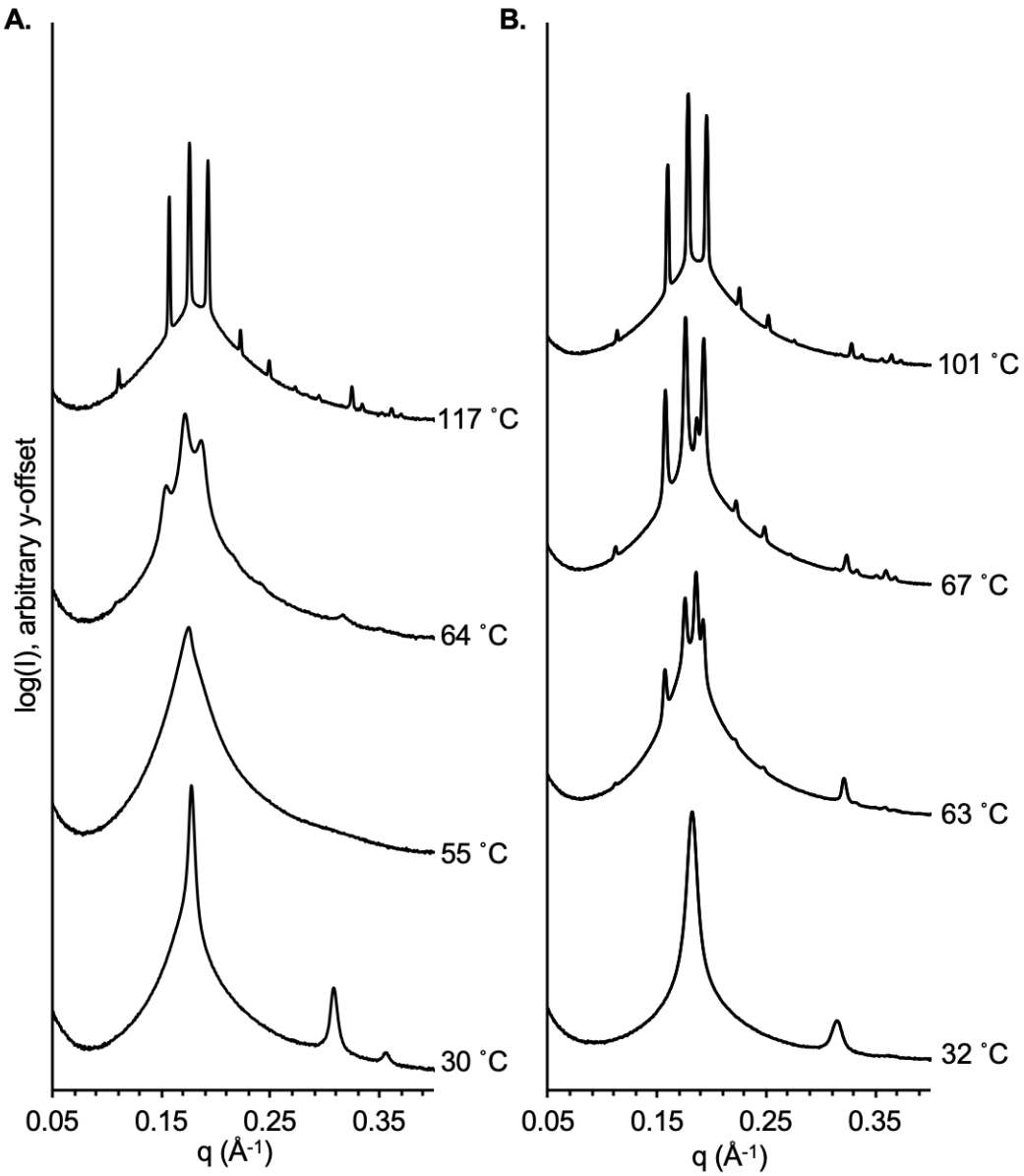

Fig. S.6.35. Selected 1D SAXS of GAL-aPMP, **6.2** (A), and **6.3** (B), showing important thermal transition for 0.5 and 0.2 ˚C/min thermal ramps.

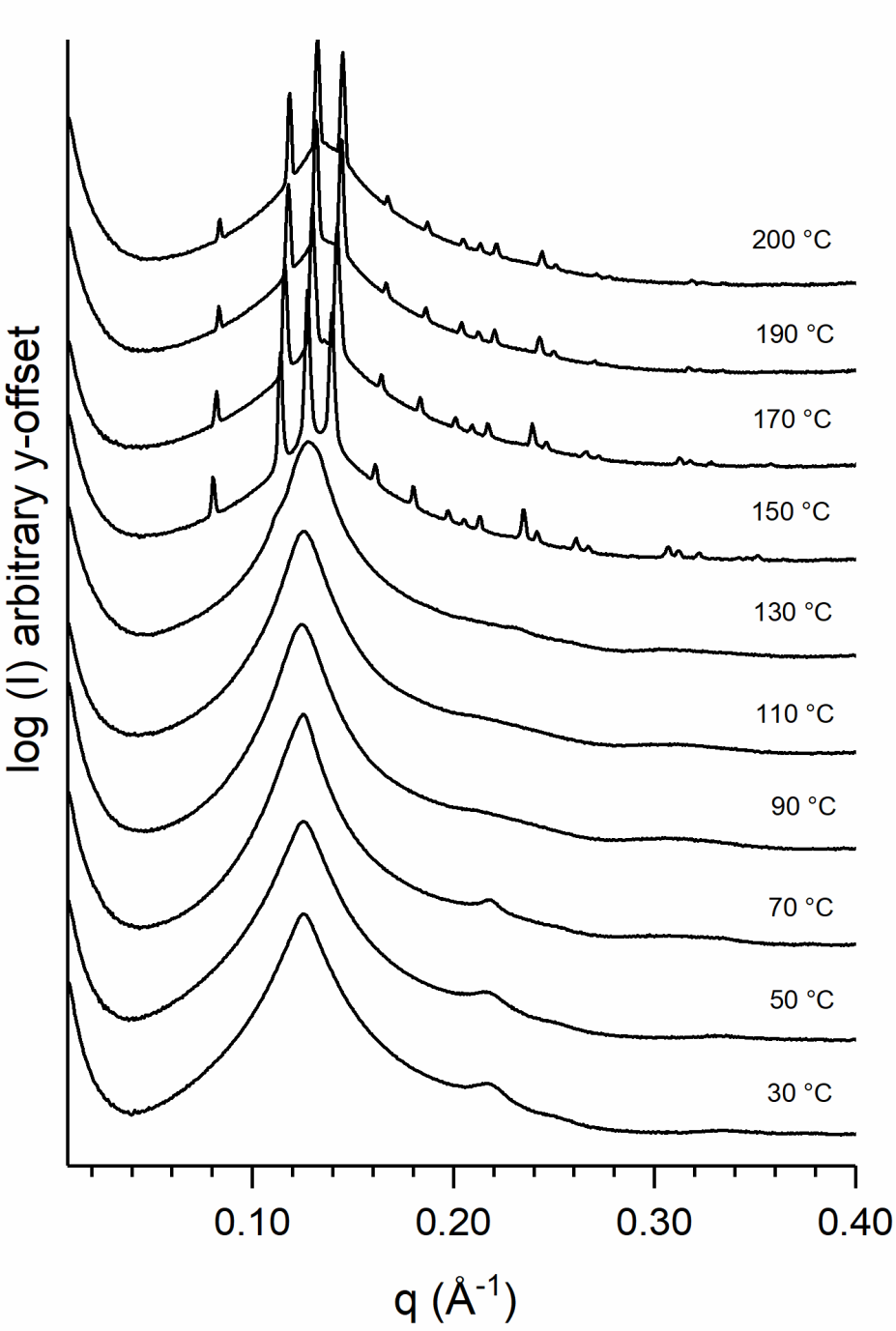

Fig. S.6.36. VT SAXS was conducted using a synchrotron x-ray source and thermal sample stage, heating at a rate of 0.5 °C/min from 30 °C – 200 °C of the CB-aPH sugar-polyolefin conjugate, **6.4**, cylindrical phase is observed at lower temperatures, and at higher temperatures FK A15 is observed.

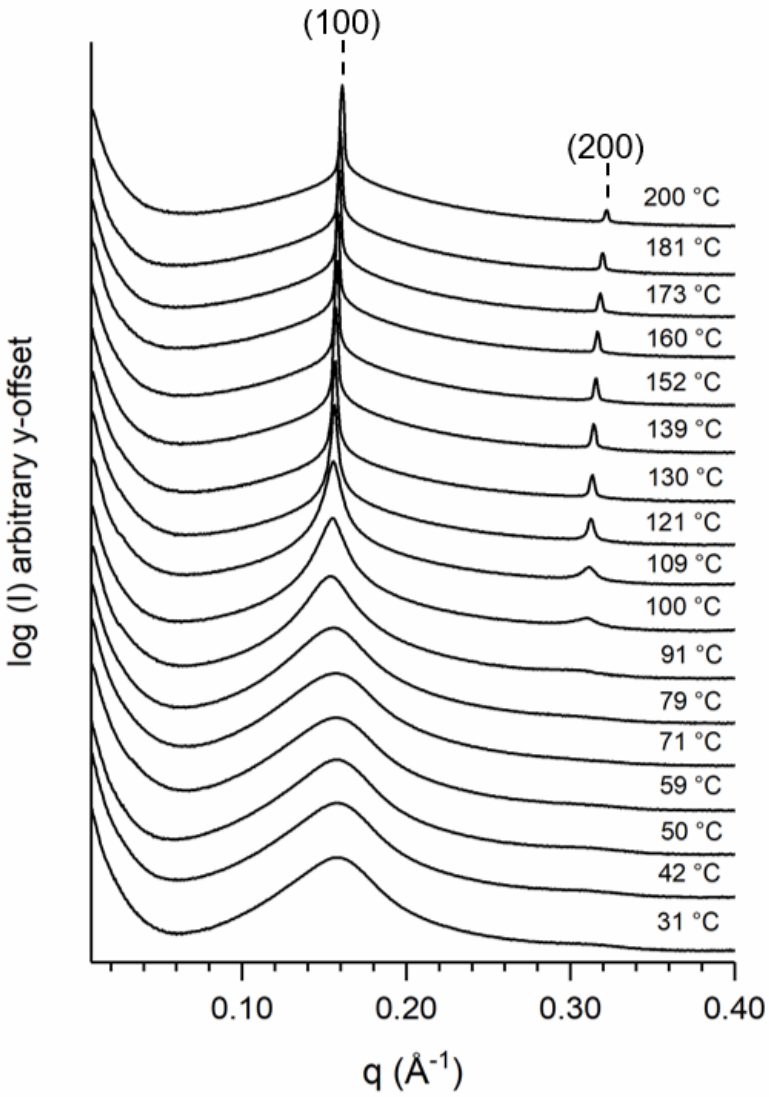

Fig. S.6.37. VT SAXS was conducted using a synchrotron x-ray source and thermal sample stage, heating at a rate of 0.5 °C/min from 30 °C – 200 °C of the CB-aPH sugar-polyolefin conjugate, **6.5**, cylindrical phase is observed at higher temperatures.

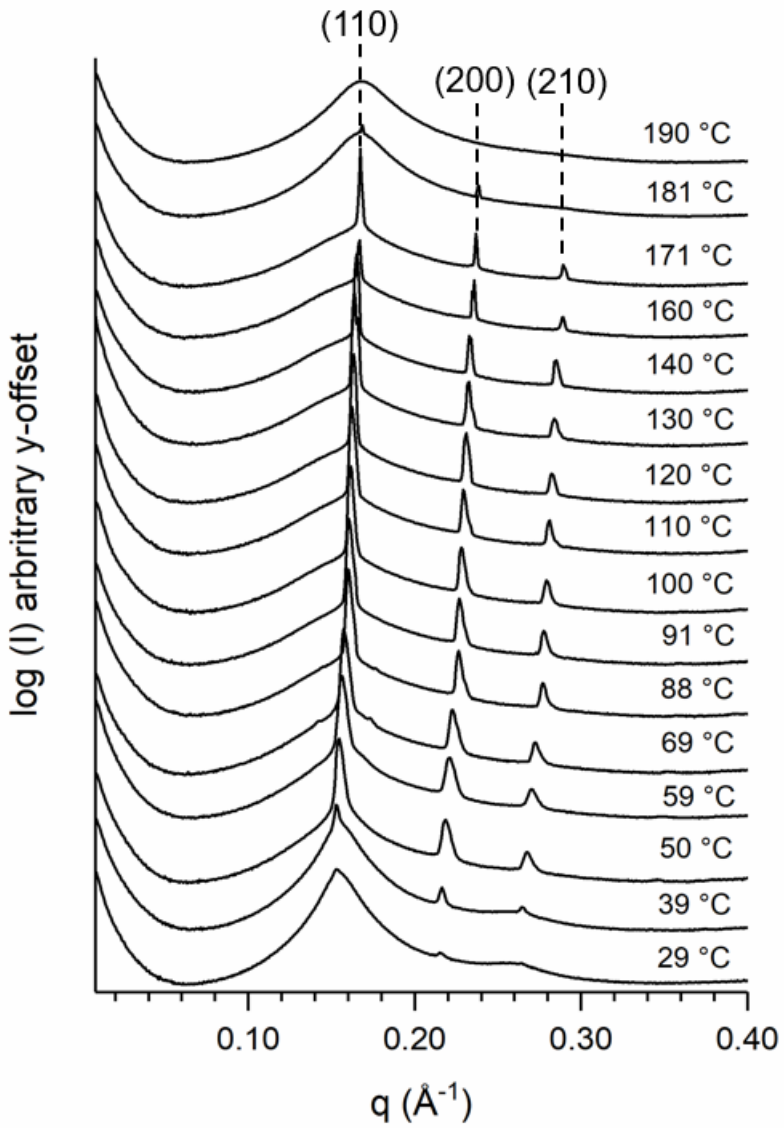

Fig. S6.38. VT SAXS was conducted using a synchrotron x-ray source and thermal sample stage, heating at a rate of 0.5 °C/min from 30 °C – 190 °C. of the GAL-aPH sugar-polyolefin conjugate, **6.6**, body centered cubic (BCC) phase was observed.

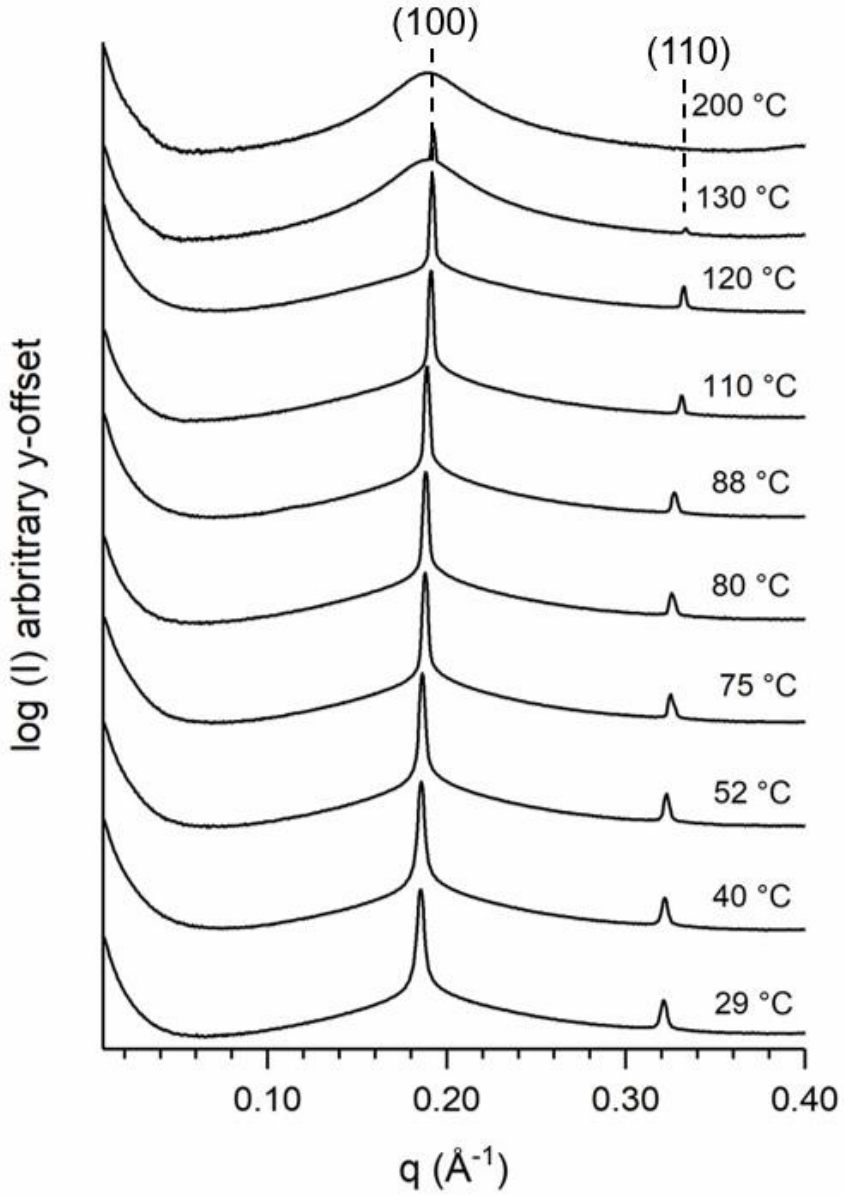

Fig. S6.39 VT SAXS was conducted using a synchrotron x-ray source and thermal sample stage, heating at a rate of 0.5 °C/min from 30 °C – 200 °C. of the GAL-aPH sugar-polyolefin conjugate, **6.7**, cylindrical phase is observed.

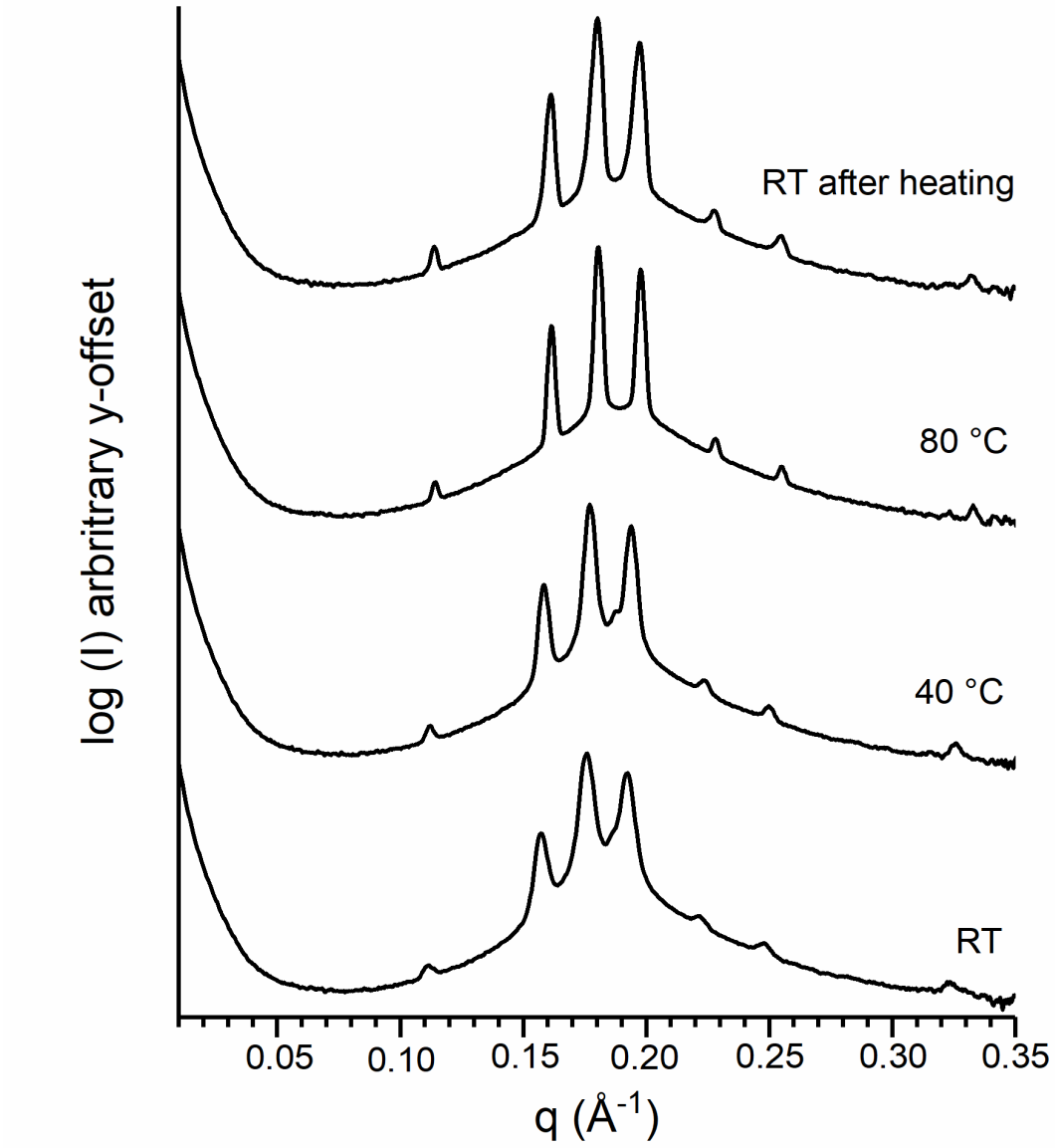

Fig. S.6.40. VT was conducted using Xenocs Xess SAXS system heating from RT to 40 °C, to 80 °C, and then slow cooled back to RT for a final measurement of Gal-aPH sugar-polyolefin conjugate, **6.7**, blended with vitamin E at 10 %.

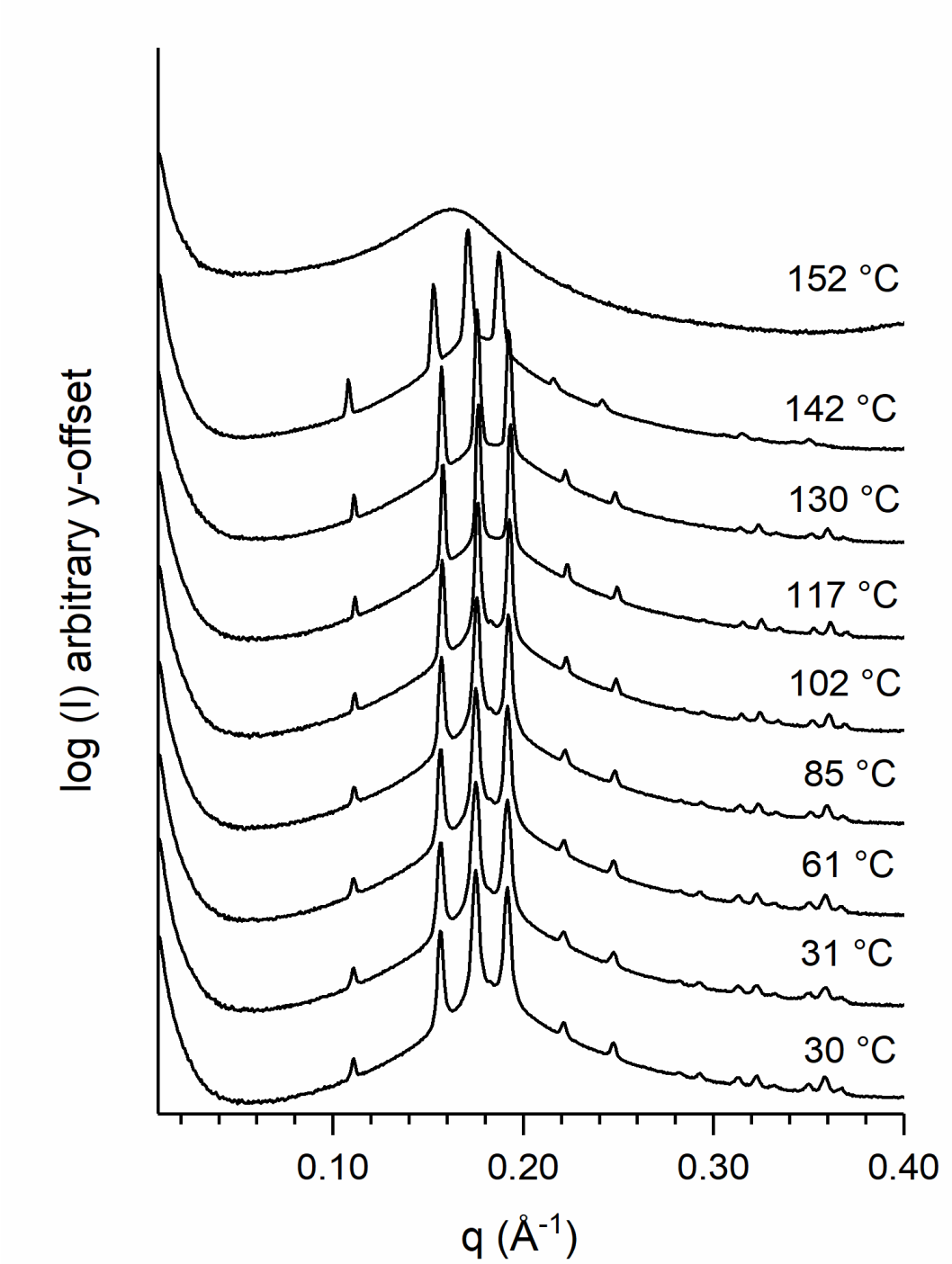

Fig. S.6.41. VT was conducted using Xenocs Xess SAXS system heating from RT to 152 °C of Gal-aPH sugar-polyolefin conjugate, **6.7**, blended with vitamin E at 20 %.

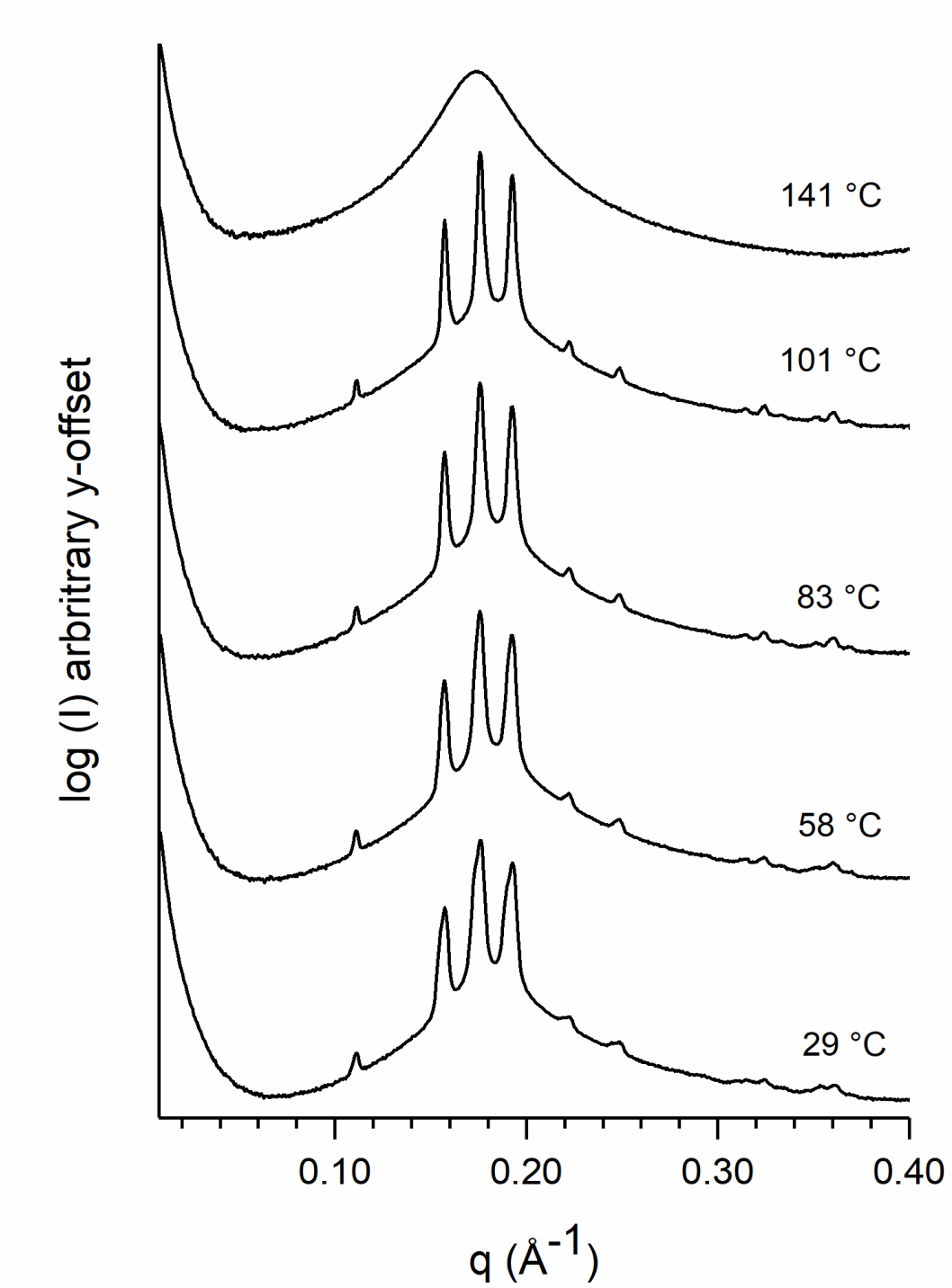

Fig. S.6.42. VT was conducted using Xenocs Xess SAXS system heating from 29 °C to 141 °C, Gal-aPH sugar-polyolefin conjugate, **6.7**, blended with vitamin E at 30 %.

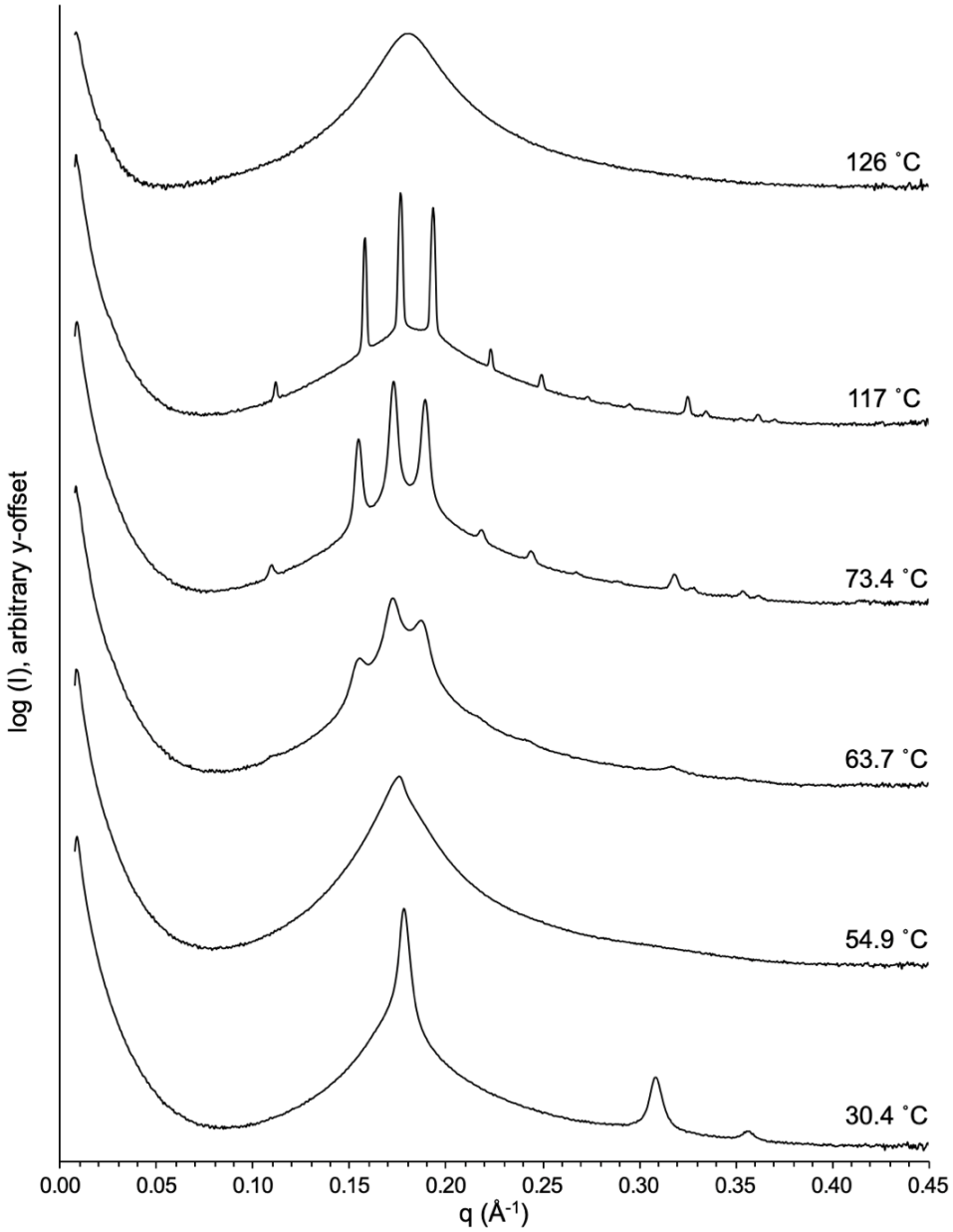

Fig. S.6.43. Variable temperature, synchrotron SAXS of GA-aPMP 0.5 ˚C/min thermal ramp from 30 to 126 ˚C.

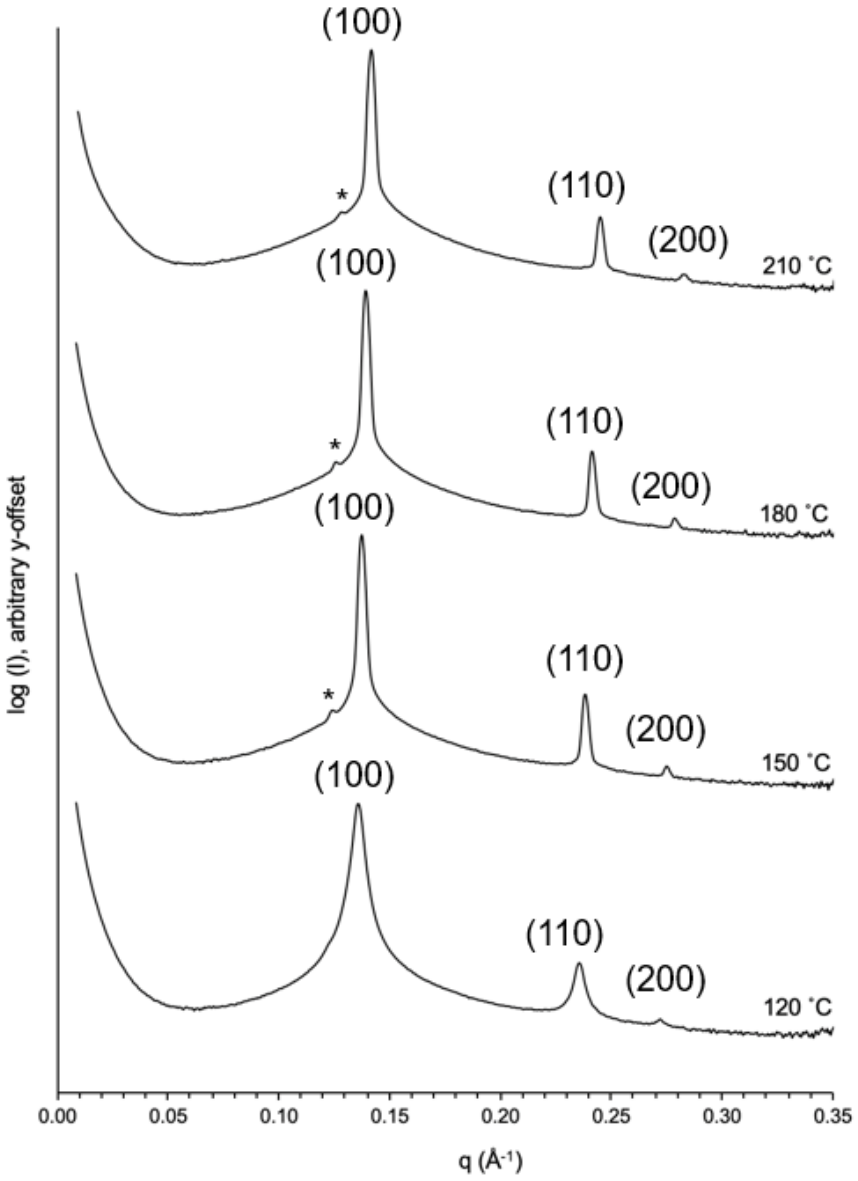

Fig. S.6.44. Variable temperature, SAXS of CB-aPMP, **6.8**, held at each temperature for 2 h, comprised of a 40-minute equilibration period, and 100-minute measurement period, all temperature revealed a cylindrical phase, * represents artifact.

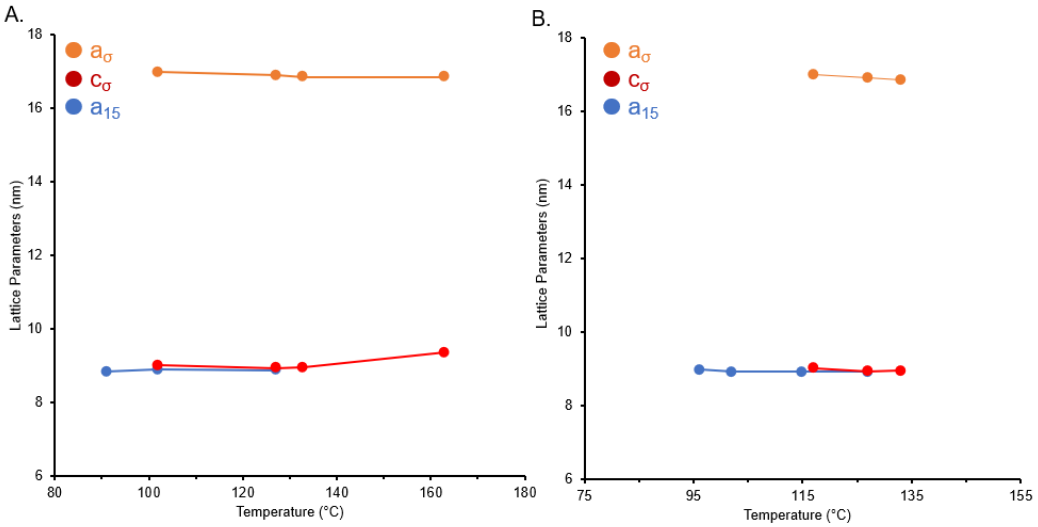

Fig. S.6.45. Correlation between temperature of phase with lattice parameters of FK A15 and FK σ phases. (A) 3:1 blend of **6.2** and **6.8**. (B) 2:1 blend with 10 % vitamin E of **6.3** and **6.8.**

Table S.6.4. Data from Figure 6.4A-B cylinder domain spacing, lattice parameters for the transient and equilibrium A15 phase over 157 °C to 212 °C thermal range. Reproduced with permission from the supporting information of Lachmayr, K. K.; Wentz, C. M.; Sita, L.R., An exceptionally stable and scalable sugar-polyolefin Frank-Kasper A15 phase. *Angew. Chem. Int. Ed.* **2020**, *59*, 1521-1526.

Temperature (˚C)	Cylinder Domain Spacing, d_C (nm)	Transient FK A15 Phase Lattice Parameter, a_t (nm)	Equilibrium FK A15 Phase Lattice Parameter, a_e (nm)
157	4.81	10.76	--
181	4.73	11.01	--
186	4.73	10.99	--
190	4.71	10.88	--
195	4.71	11.10	10.81
202	4.66	11.21	10.73
205	4.66	11.16	10.68
212	--	--	10.58

Table S6.5. Data from Figure S6.26. (A) Cylinder domain spacing (d_C), observed peak positions (q_{obs}) and corresponding Miller Indices to the *C* phase during annealing at 180 ˚C for 100 – 400 min. (B) Lattice parameters (a), q_{obs} and q_{calc} with corresponding Miller Indices to the FK A15 phase during annealing at 180 ˚C for 100 – 400 min. Reproduced with permission from the supporting information of Lachmayr, K. K.; Wentz, C. M.; Sita, L.R., An exceptionally stable and scalable sugar-polyolefin Frank-Kasper A15 phase. *Angew. Chem. Int. Ed.* **2020**, *59*, 1521-1526.

A.

	100 min, d_C = 4.75 nm	**200 min**, d_C = 4.75 nm	**300 min**, d_C = 4.73 nm	**400 min**, d_C = 4.73 nm
Miller Indices (hkl)	q_{obs} (Å^{-1})	q_{obs} (Å^{-1})	q_{obs} (Å^{-1})	q_{obs} (Å^{-1})
(100)	0.1323	0.1323	0.1328	0.1328
(110)	0.2285	0.2296	0.2296	0.2296
(200)	0.2637	0.2643	0.2648	0.2632

B.

	100 min, a = 10.98 nm		**200 min**, a = 10.93 nm		**300 min,** a = 10.93 nm		**400 min,** a = 10.95 nm	
Miller Indices (hkl)	q_{calc} (Å^{-1})	q_{obs} (Å^{-1})	q_{calc} (Å^{-1})	q_{obs} (Å^{-1})	q_{calc} (Å^{-1})	q_{obs} (Å^{-1})	q_{calc} (Å^{-1})	q_{obs} (Å^{-1})
(110)	0.0810	0.0813	0.0813	0.0813	0.0813	0.0818	0.0811	0.0818
(200)	0.1145	0.1149	0.1150	0.1154	0.1150	0.1154	0.1148	0.1154
(210)	0.1280	0.1286	0.1286	0.1286	0.1286	0.1291	0.1283	0.1291
(211)	0.1402	0.1407	0.1409	0.1412	0.1409	0.1412	0.1406	0.1412
(220)	0.1619	0.1617	0.1627	0.1617	0.1627	0.1617	0.1623	0.1617
(310)	0.1810	0.1812	0.1819	0.1822	0.1819	0.1822	0.1815	0.1822
(222)	0.1983	0.1996	0.1992	0.1991	0.1992	0.1991	0.1988	0.1991
(320)	0.2064	0.2069	0.2073	0.2080	0.2074	0.2075	0.2069	0.2075
(321)	0.2142	0.2148	0.2152	0.2154	0.2152	0.2159	0.2147	0.2159
(400)	0.2290	0.2285	0.2300	--	0.2301	--	0.2295	--
(410)	0.2360	0.2359	0.2371	0.2374	0.2371	0.2380	0.2366	0.2374
(330)	0.2429	0.2432	0.2440	0.2438	0.2440	0.2438	0.2434	0.2432
(411)	0.2429	0.2432	0.2440	0.2438	0.2440	0.2438	0.2434	0.2432

Table S6.6. Data from Figure S6.26. Lattice parameters (a), q_{obs}, and q_{calc} for FK A15 phase during annealing at 180 ˚C for 500 and 900 min. Reproduced with permission from the supporting information of Lachmayr, K. K.; Wentz, C. M.; Sita, L.R., An exceptionally stable and scalable sugar-polyolefin Frank-Kasper A15 phase. *Angew. Chem. Int. Ed.* **2020**, *59*, 1521-1526.

	500 min, a = 10.90 nm		**900 min**, a = 10.88 nm	
Miller Indices (hkl)	q_{calc} (Å^{-1})	q_{obs} (Å^{-1})	q_{calc} (Å^{-1})	q_{obs} (Å^{-1})
(110)	0.0815	0.0818	0.0816	0.0818
(200)	0.1152	0.1154	0.1154	0.1154
(210)	0.1288	0.1291	0.1291	0.1291
(211)	0.1411	0.1412	0.1414	0.1417
(220)	0.1630	0.1633	0.1633	0.1633
(310)	0.1822	0.1817	0.1825	0.1817
(222)	0.1996	0.1996	0.2000	0.1996
(320)	0.2078	0.2080	0.2081	0.2080
(321)	0.2156	0.2159	0.2160	0.2159
(400)	0.2305	--	0.2309	--
(410)	0.2376	0.2380	0.2380	0.2380
(330)	0.2445	0.2443	0.2449	0.2448
(411)	0.2445	0.2443	0.2449	0.2448
(420)	0.2577	--	0.2582	--
(421)	0.2641	0.2643	0.2645	0.2648

Table S6.7. Data from Fig. S6.27. Lattice parameters (a), q_{obs}, and q_{calc} for FK A15 phase at room temperature (23 ˚C) for 40 min and 64 h, prior to annealing at 180 ˚C for 900 min. Reproduced with permission from the supporting information of Lachmayr, K. K.; Wentz, C. M.; Sita, L.R., An exceptionally stable and scalable sugar-polyolefin Frank-Kasper A15 phase. *Angew. Chem. Int. Ed.* **2020**, *59*, 1521-1526.

	40 min, a = 10.89 nm		**64 h**, a = 10.82 nm	
Miller Indices (hkl)	q_{calc} (Å^{-1})	q_{obs} (Å^{-1})	q_{calc} (Å^{-1})	q_{obs} (Å^{-1})
(110)	0.0816	0.0823	0.0821	0.0823
(200)	0.1154	0.1170	0.1162	0.1170
(210)	0.1290	0.1307	0.1299	0.1312
(211)	0.1413	0.1433	0.1423	0.1433
(220)	0.1632	0.1654	0.1643	0.1654
(310)	0.1825	0.1843	0.1837	0.1843
(222)	0.1999	0.2022	0.2012	0.2022
(320)	0.2081	0.2096	0.2094	0.2112
(321)	0.2159	0.2185	0.2173	0.2185
(400)	0.2308	--	0.2323	--
(410)	0.2379	0.2411	0.2395	0.2411
(330)	0.2448	0.2469	0.2464	0.2474
(411)	0.2448	0.2469	0.2464	0.2474
(420)	0.2581	--	0.2597	--
(421)	0.2644	0.2674	0.2661	0.2680
(432)	0.3107	0.3105	0.3128	0.3127
(520)	0.3107	0.3105	0.3128	0.3127

Table S6.8. From Figure 6.4A thermal ramp over temperature range 30 – 220 ˚C at a heating rate of 1 ˚C/min, list of d_C and q_{obs} with corresponding Miller Indices to the *C* phase at 31 ˚C (A), 109 ˚C (B), and 136 ˚C (C). Reproduced with permission from the supporting information of Lachmayr, K. K.; Wentz, C. M.; Sita, L.R., An exceptionally stable and scalable sugar-polyolefin Frank-Kasper A15 phase. *Angew. Chem. Int. Ed.* **2020**, *59*, 1521-1526.

A.

31 ˚C, d_C = 5.09 nm	
Miller Indices (hkl)	q_{obs} (Å^{-1})
(100)	0.1235
(110)	0.2154

B.

109 ˚C, d_C = 4.90 nm	
Miller Indices (hkl)	q_{obs} (Å^{-1})
(100)	0.1282
(110)	0.2224
(200)	0.2566
(210)	0.3413
(300)	0.3843

C.

136 ˚C, d_C = 4.86 nm	
Miller Indices (hkl)	q_{obs} (Å^{-1})
(100)	0.1294
(110)	0.2242
(200)	0.2589
(210)	0.3461
(300)	0.3884

Table S6.9. From Figure 6.4A thermal ramp over temperature range 30 – 220 ˚C at a heating rate of 1 ˚C/min, list of d_C and q_{obs} with corresponding Miller Indices and lattice parameter for transient (a_t) and equilibrium (a_e) FK A15 phases, q_{obs}, and q_{calc} with corresponding Miller Indices for 157 ˚C (A), 181 ˚C (B), 186 ˚C (C), and 190 ˚C (D). Reproduced with permission from the supporting information of Lachmayr, K. K.; Wentz, C. M.; Sita, L.R., An exceptionally stable and scalable sugar-polyolefin Frank-Kasper A15 phase. *Angew. Chem. Int. Ed.* **2020**, *59*, 1521-1526.

A.

	157 ˚C, a_t = 10.76 nm			**157 ˚C**, d_C = 4.81 nm
Miller Indices (hkl)	q_{calc} (Å^{-1})	q_{obs} (Å^{-1})	Miller Indices (hkl)	q_{obs} (Å^{-1})
(110)	0.0826	0.0800	(100)	0.1306
(200)	0.1168	0.1129	(110)	0.2265
(210)	0.1306	0.1265	(200)	0.2613
(211)	0.1430	0.1382	(210)	0.3455
(220)	0.1652	0.1635	(300)	0.3926
(310)	0.1846	0.1789		
(222)	0.2023	0.1995		
(320)	0.2105	--		
(321)	0.2185	0.2177		
(400)	0.2336	--		
(410)	0.2407	0.2460		
(330)	0.2477	0.2460		
(411)	0.2477	0.2460		

B.

181 ˚C, a_t = 11.01 nm			**181 ˚C**, d_C = 4.73 nm	
Miller Indices (hkl)	q_{calc} (Å^{-1})	q_{obs} (Å^{-1})	Miller Indices (hkl)	q_{obs} (Å^{-1})
(110)	0.0807	0.0811	(100)	0.1329
(200)	0.1141	0.1141	(110)	0.2301
(210)	0.1276	0.1276	(200)	0.2654
(211)	0.1398	0.1400	(210)	--
(220)	0.1614	0.1612	(300)	--
(310)	0.1805	0.1806		
(222)	0.1977	0.1977		
(320)	0.2058	--		
(321)	0.2135	0.2118		
(400)	0.2283	--		
(410)	0.2353	0.2354		
(330)	0.2421	0.2430		
(411)	0.2421	0.2430		
(420)	0.2552	--		
(421)	0.2615	--		
(432)	0.3073	0.3072		
(520)	0.3073	0.3072		

C.

186 ˚C, a_t = 10.99 nm			**186 ˚C**, d_C = 4.73 nm	
Miller Indices (hkl)	q_{calc} (Å^{-1})	q_{obs} (Å^{-1})	Miller Indices (hkl)	q_{obs} (Å^{-1})
(110)	0.0808	0.0811	(100)	0.1329
(200)	0.1143	0.1147	(110)	0.2307
(210)	0.1278	0.1288	(200)	0.2660
(211)	0.1400	0.1412	(210)	--
(220)	0.1617	0.1618	(300)	--
(310)	0.1808	0.1812		
(222)	0.1980	0.1977		
(320)	0.2061	--		
(321)	0.2139	0.2142		
(400)	0.2286	--		
(410)	0.2357	0.2365		
(330)	0.2425	0.2442		
(411)	0.2425	0.2442		
(420)	0.2556	0.2536		

D.

	190 ˚C, a_t = 10.88 nm		**190 ˚C**, d_C = 4.71 nm	
Miller Indices (hkl)	q_{calc} (Å^{-1})	q_{obs} (Å^{-1})	Miller Indices (hkl)	q_{obs} (Å^{-1})
(110)	0.0817	0.0817	(100)	0.1335
(200)	0.1155	0.1159	(110)	0.2312
(210)	0.1291	0.1288	(200)	0.2660
(211)	0.1414	0.1406	(210)	--
(220)	0.1633	0.1618	(300)	--
(310)	0.1826	0.1818		
(222)	0.2000	0.1983		
(320)	0.2082	--		
(321)	0.2160	0.2142		
(400)	0.2309	--		
(410)	0.2381	0.2365		

Table S6.10. From Figure 6.5B and Fig. S6.30. thermal ramp over temperature range 30 – 220 ˚C at a heating rate of 1 ˚C/min. List of d_C and q_{obs} with corresponding Miller Indices and lattice parameter for transient (a_t) and equilibrium (a_e) FK A15 phases, q_{obs}, and q_{calc} with corresponding Miller Indices for 195 ˚C (A), 202 ˚C (B), and 205 ˚C (C). Reproduced with permission from the supporting information of Lachmayr, K. K.; Wentz, C. M.; Sita, L.R., An exceptionally stable and scalable sugar-polyolefin Frank-Kasper A15 phase. *Angew. Chem. Int. Ed.* **2020**, *59*, 1521-1526.

A.

	195 ˚C, a_t = 11.10 nm		**195 ˚C**, a_e = 10.81 nm		**195 ˚C**, d_C = 4.71 nm	
Miller Indices (hkl)	q_{calc} (Å^{-1})	q_{obs} (Å^{-1})	q_{calc} (Å^{-1})	q_{obs} (Å^{-1})	Miller Indices (hkl)	q_{obs} (Å^{-1})
(110)	0.0800	0.0805	0.0822	0.0823	(100)	0.1335
(200)	0.1132	0.1135	0.1162	0.1159	(110)	0.2312
(210)	0.1265	0.1265	0.1299	0.1300	(200)	0.2666
(211)	0.1386	0.1388	0.1423	0.1424	(210)	--
(220)	0.1600	0.1600	0.1643	0.1641	(300)	--
(310)	0.1789	0.1783	0.1837	0.1830		
(222)	0.1960	--	0.2013	0.2012		
(320)	0.2040	--	0.2095	0.2112		
(321)	0.2117	--	0.2174	0.2177		
(400)	0.2263	--	0.2324	--		
(410)	0.2333	--	0.2396	0.2395		
(330)	0.2401	--	0.2465	--		
(411)	0.2401	--	0.2465	--		
(420)	0.2531	--	0.2599	--		
(421)	0.2593	0.2595	0.2663	--		

B.

	202 ˚C, a_t = 11.21 nm		**202 ˚C**, a_e = 10.73 nm		**202 ˚C**, d_C = 4.66 nm	
Miller Indices (hkl)	q_{calc} (Å^{-1})	q_{obs} (Å^{-1})	q_{calc} (Å^{-1})	q_{obs} (Å^{-1})	Miller Indices (hkl)	q_{obs} (Å^{-1})
(110)	0.0799	0.0800	0.0828	0.0829	(100)	0.1347
(200)	0.1131	0.1135	0.1172	0.1170	(110)	0.2330
(210)	0.1264	0.1265	0.1310	0.1312	(200)	0.2695
(211)	0.1385	0.1388	0.1435	0.1435	(210)	--
(220)	0.1599	0.1600	0.1657	0.1659	(300)	--
(310)	0.1788	0.1789	0.1853	0.1859		
(222)	0.1958	0.1959	0.2029	0.2030		
(320)	0.2038	--	0.2112	0.2112		
(321)	0.2115	--	0.2192	0.2201		
(400)	0.2261	--	0.2343	--		
(410)	0.2331	--	0.2415	0.2418		
(330)	0.2398	--	0.2485	0.2483		
(411)	0.2398	--	0.2485	0.2483		
(420)	0.2528	--	0.2620	--		
(421)	0.2590	0.2625	0.2685	--		

C.

	205 ˚C, a_t = 11.16 nm		**205 ˚C**, a_e = 10.68 nm		**205 ˚C**, d_C = 4.66 nm	
Miller Indices (hkl)	q_{calc} (Å^{-1})	q_{obs} (Å^{-1})	q_{calc} (Å^{-1})	q_{obs} (Å^{-1})	Miller Indices (hkl)	q_{obs} (Å^{-1})
(110)	0.0796	0.0829	0.0831	0.0829	(100)	0.1347
(200)	0.1126	--	0.1175	0.1176	(110)	0.2336
(210)	0.1259	0.1276	0.1313	0.1318	(200)	--
(211)	0.1379	0.1400	0.1439	0.1441	(210)	--
(220)	0.1593	--	0.1661	0.1665	(300)	--
(310)	0.1781	--	0.1857	0.1859		
(222)	0.1951	--	0.2035	0.2036		
(320)	0.2031	--	0.2118	0.2124		
(321)	0.2107	--	0.2198	0.2207		
(400)	0.2253	--	0.2349	--		
(410)	0.2322	--	0.2422	0.2424		
(330)	0.2389	--	0.2492	0.2495		
(411)	0.2389	--	0.2492	0.2495		

Table S6.11. Data from Figure 6.5A-B thermal ramp over temperature range 30 – 220 ˚C at a heating rate of 1 ˚C/min. List lattice parameter for the equilibrium (a_e) FK A15 phase, q_{obs}, and q_{calc} with corresponding Miller Indices for 212 ˚C. Reproduced with permission from the supporting information of Lachmayr, K. K.; Wentz, C. M.; Sita, L.R., An exceptionally stable and scalable sugar-polyolefin Frank-Kasper A15 phase. *Angew. Chem. Int. Ed.* **2020**, *59*, 1521-1526.

212 ˚C, a_e = 10.58 nm		
Miller Indices (hkl)	q_{calc} (Å^{-1})	q_{obs} (Å^{-1})
(110)	0.0840	0.0835
(200)	0.1187	0.1182
(210)	0.1327	0.1324
(211)	0.1454	0.1447
(220)	0.1679	0.1671
(310)	0.1877	0.1871
(222)	0.2057	0.2053
(320)	0.2140	0.2124
(321)	0.2221	0.2218
(400)	0.2375	--
(410)	0.2448	0.2436
(330)	0.2519	0.2513
(411)	0.2519	0.2513
(420)	0.2655	--
(421)	0.2721	0.2719
(432)	0.3197	0.3196
(520)	0.3197	0.3196

Table S.6.12. FK A15 and FK σ phase lattice parameters at select temperatures for the (A) 3:1 blend and (B) 2:1 with 10% vitamin E blend, corresponds to Fig. S.6.45**..**

A.

Temperature (°C)	A15 lattice parameters (a_{A15}) (nm)	σ lattice parameters (a_σ) (nm)	σ lattice parameters (c_σ) (nm)
91	8.84	-	-
102	8.91	16.99	9.01
127	8.88	16.89	8.94
133	-	16.85	8.95
163	-	16.84	9.36

B.

Temperature (°C)	A15 lattice parameters (a_{A15}) (nm)	σ lattice parameters (a_σ) (nm)	σ lattice parameters (c_σ) (nm)
96	8.99	-	-
102	8.92	-	-
115	8.92	16.99	9.01
127	8.91	16.89	8.94
133	-	16.85	8.95

Table S6.13. FK A15 lattice parameters from **6.2** and **6.3**, in addition to two- and three-component blended systems with **6.8** and vitamin E for the production of A15 structures with tunable size; and corresponding temperature of the FK A15 phase.

Material or Blend	A15 lattice parameters (a_{A15}) (nm)	Temperature (˚C)
6.3	7.90	101
6.2	7.96	117
3:1 blend (**6.2:6.8**)	8.84	117
2:1 blend (**6.3:6.8**) with 10% vitamin E	*8.91	102
2:1 blend (**6.3:6.8**)	9.13	101

* indicates mixed A15/ σ phase

Table S6.14. List of the observed (q_{obs}) and calculated (q_{calc}) peak positions for the FK σ phase at 127 ˚C for the 2:1 blend of **6.3** and **6.8** with 10% vitamin E.

h	*k*	*l*	q_{obs} (Å^{-1})	q_{calc} (Å^{-1})	% Residual
2	1	0	0.0833	0.0831	-0.24
1	1	1	0.0857	0.0878	2.39
2	2	0	0.1051	0.1052	0.10
3	1	0	0.1175	0.1176	0.09
2	2	1	0.1264	0.1265	0.08
3	0	1	0.1317	0.1319	0.15
3	2	0	0.1340	0.1341	0.07
3	1	1	0.1370	0.1370	0.00
0	0	2	0.1411	0.1406	-0.36
4	0	0	0.1487	0.1487	0.00
1	1	2	0.1505	0.1501	-0.27
4	1	0	0.1535	0.1533	-0.13
3	3	0	0.1576	0.1577	0.06
2	0	2	0.1593	0.1591	-0.13
2	1	2	0.1635	0.1634	-0.06
4	1	1	0.1688	0.1687	-0.06
3	3	1	0.1729	0.1727	-0.12
2	2	2	0.1758	0.1756	-0.11
4	2	1	0.1799	0.1805	0.33
3	1	2	0.1835	0.1833	-0.11
5	1	0	0.1894	0.1896	0.11
3	2	2	0.1947	0.1943	-0.21
5	0	1	0.1988	0.1988	0.00
5	1	1	0.2023	0.2022	-0.05
4	0	2	0.2046	0.2047	0.05
5	2	1	0.2118	0.2122	0.19
4	3	2	0.2330	0.2331	0.04
2	2	3	0.2359	0.2357	-0.08
3	1	3	0.2418	0.2415	-0.12
5	2	2	0.2447	0.2447	0.00
5	4	1	0.2489	0.2482	-0.28
5	3	2	0.2583	0.2584	0.04
6	0	2	0.2636	0.2637	0.04
7	1	1	0.2712	0.2722	0.37
5	5	1	0.2712	0.2722	0.37
5	4	2	0.2754	0.2765	0.40
7	2	1	0.2795	0.2797	0.07
5	1	3	0.2842	0.2836	-0.21

2	0	4	0.2919	0.2909	-0.34

Table S6.15. List of the observed (q_{obs}) and calculated (q_{calc}) peak positions for the FK σ phase for 3:1 blend of **6.2** and **6.8** from an isothermal experiment after 6.6 h at 140 ˚C.

h	*k*	*l*	q_{obs} (Å^{-1})	q_{calc} (Å^{-1})	% Residual
1	0	1	0.0804	0.0809	0.62
2	1	0	0.0845	0.0842	-0.36
2	2	0	0.1075	0.1065	-0.94
2	1	1	0.1104	0.1105	0.09
3	1	0	0.1192	0.1190	-0.17
3	0	1	0.1340	0.1337	-0.22
3	2	0	0.1363	0.1357	-0.44
3	1	1	0.1386	0.1389	0.22
0	0	2	0.1428	0.1432	0.28
4	1	0	0.1551	0.1552	0.06
3	3	0	0.1604	0.1597	-0.44
2	1	2	0.1657	0.1661	0.24
4	1	1	0.1716	0.1709	-0.41
3	3	1	0.1757	0.1750	-0.40
2	2	2	0.1781	0.1785	0.22
4	2	1	0.1828	0.1829	0.05
3	1	2	0.1851	0.1862	0.59
4	3	0	0.1869	0.1882	0.69
5	1	0	0.1916	0.1919	0.16
3	2	2	0.1963	0.1973	0.51
5	0	1	0.2010	0.2014	0.20
5	1	1	0.2046	0.2049	0.15
4	0	2	0.2099	0.2078	-1.01
5	2	1	0.2146	0.2150	0.19
5	1	2	0.2387	0.2395	0.33
6	2	1	0.2493	0.2486	-0.28
2	1	4	0.2976	0.2985	0.30
8	1	0	0.3034	0.3035	0.03
7	4	0	0.3034	0.3035	0.03

Table S6.16. List of the observed (q_{obs}) and calculated (q_{calc}) peak positions for the FK A15 phase of **6.2** at 117 ˚C.

h	*k*	*l*	q_{obs} (Å^{-1})	q_{calc} (Å^{-1})	% Residual
1	1	0	0.1116	0.1116	0.00
2	0	0	0.1578	0.1581	0.19
2	1	0	0.1765	0.1763	-0.11
2	1	1	0.1933	0.1934	0.05
2	2	0	0.2232	0.2234	0.09
3	1	0	0.2496	0.2493	-0.12
2	2	2	0.2734	0.2734	0.00
3	2	0	0.2845	0.2817	-0.99
3	2	1	0.2953	0.2952	-0.03
4	0	0	--	--	--
4	1	0	0.3254	0.3252	-0.06
3	3	0	0.3348	0.3346	-0.06
4	1	1	0.3348	0.3346	-0.06
4	2	0	0.3529	0.3529	0.00
4	2	1	0.3616	0.3617	0.03
3	3	2	0.3702	0.3705	0.08

Table S6.17. List of the observed (q_{obs}) and calculated (q_{calc}) peak positions for the FK A15 phase of **6.3** at 101 ˚C.

h	*k*	*l*	q_{obs} (Å^{-1})	q_{calc} (Å^{-1})	% Residual
1	1	0	0.1124	0.1126	0.18
2	0	0	0.1590	0.1591	0.06
2	1	0	0.1777	0.1780	0.17
2	1	1	0.1947	0.1944	-0.15
2	2	0	0.2248	0.2245	-0.13
3	1	0	0.2514	0.2515	0.04
2	2	2	0.2753	0.2798	1.61
3	2	0	--	--	--
3	2	1	--	--	--
4	0	0	0.3179	0.3174	-0.16
4	1	0	0.3277	0.3274	-0.09
3	3	0	0.3372	0.3374	0.06
4	1	1	--	--	--
4	2	0	0.3555	0.3557	0.06
4	2	1	0.3642	0.3645	0.08
3	3	2	0.3728	0.3728	0.00

Table S6.18. Summary of SAXS result for materials and material blend systems. LLP indicate liquid lie packing, 'Dis' is disordered, and * indicate mix of A15 and Sigma phases.

Material or Blend	Phase Sequence	a_{A15} (nm)	d_C (nm)
6.3 with 5% Vit E	A15 → Dis (42 ˚C) →A15 (47 ˚C →Dis (109 ˚C)	7.77	-
6.3 with 3% Vit E	C → Dis (40 ˚C) → A15 (56 ˚C) → Dis (109 ˚C)	7.82	3.97
6.3 with 1% Vit E	C → A15 (60 ˚C) → Dis (106 ˚C)	7.88	3.98
6.3	C → A15 (63 ˚C) → Dis (110 ˚C)	7.90	4.00
6.2	C → Dis (55 ˚C) →A15 (64 ˚C→ Dis (126 ˚C)	7.96	4.07
3:1 blend (**6.2:6.8**)	Dis → A15 (100 ˚C) → Sigma/A15 (153 ˚C) → Sigma (158) → Dis (166˚C)	8.84	-
4:1 blend (**6.3:6.8**)	C → Dis (55 ˚C) → A15 (80 ˚C) → Dis (119 ˚C)	8.65	4.42
3:1 blend (**6.3:6.8**)with 3% Vit E	Dis → DDQC (75 ˚C) →A15 (89 ˚C) → A15/Sigma (126 ˚C) → Dis (127 ˚C)	8.76	-
3:1 blend (**6.3:6.8**)	Dis → DDQC (83 ˚C) → A15 (91 ˚C) → Dis (138 ˚C)	8.84	-
2:1 blend (**6.3:6.8**) with 10% Vit E	Dis → DDQC (80 ˚C) →A15/Sigma (101 ˚C) → Sigma (118 ˚C) → Dis (134 ˚C)	*8.91	-
2:1 blend (**6.3:6.8**)	Dis →DDQC (86 ˚C) → A15 (97 ˚C) → Dis (142 ˚C)	9.13	-
1:2 blend (**6.2:6.8**)	Dis → C (85 ˚C) → A15 (176 ˚C) → Dis (183 ˚C)	9.41	4.95
1:1 blend (**6.2:6.8**)	C →A15 (103˚C) → Dis (180 ˚C)	9.49	5.00

Table S6.19. Comparison of different FK A15 sizes from various one-, two-, and three-component systems.

Material or Blend	A15 lattice parameter (a_{15}) (nm)	Temperature (˚C)
6.3 with 5% Vit E	7.77	100
6.3 with 3% Vit E	7.82	100
6.3 with 1% Vit E	7.88	100
6.3	7.90	101
6.2	7.96	117
3:1 blend (**6.2:6.8**)	8.84	117
4:1 blend (**6.3:6.8**)	8.65	101
3:1 blend **6.3:6.8**, with 3% Vit E	8.76	101
3:1 blend (**6.3:638**)	8.84	101
2:1 blend (**6.3:6.8**) with 10% Vit E	*8.91	102
2:1 blend (**6.3:6.8**)	9.13	101
1:2 blend (**6.2:6.8**)	9.41	187
1:1 blend (**6.2:6.8**)	9.49	144

* indicates mixed A15/Sigma phase

Table S6.20. FK A15 at 150 °C of the CB-aPH sugar-polyolefin conjugate, **6.4**, with lattice parameters a = 11.05 nm, qobs and qcalc with corresponding Miller Indices.

h	*k*	*l*	q_{obs} (Å^{-1})	q_{calc} (Å^{-1})	% Residual
1	1	0	0.0804	0.0804	0.00
2	0	0	0.1139	0.1137	-0.18
2	1	0	0.1269	0.1272	0.24
2	1	1	0.1392	0.1393	0.07
2	2	0	0.1610	0.1609	-0.06
3	1	0	0.1798	0.1799	0.06
2	2	2	0.1969	0.1971	0.10
3	2	0	0.2046	0.2051	0.24
3	2	1	0.2128	0.2129	0.05
4	1	0	0.2346	0.2346	0.00
3	3	0	0.2411	0.2414	0.12
4	1	1	0.2411	0.2414	0.12
4	2	0	0.2546	0.2544	-0.08
4	2	1	0.2605	0.2607	0.08
3	3	2	0.2670	0.2668	-0.08
4	3	2	0.3058	0.3063	0.16
5	2	0	0.3058	0.3063	0.16
5	2	1	0.3111	0.3116	0.16
4	4	0	0.3217	0.3218	0.03
4	4	2	0.3417	0.3413	-0.12
6	0	0	0.3417	0.3413	-0.12

Table S6.21. Data for FK A15 Gal-aPH sugar-polyolefin conjugate, **6.7**, with 10% vitamin E with lattice parameters a, qobs and qcalc with corresponding Miller Indices; (A) RT (no annealing), a = 7.99 nm; (B) 40 °C, a = 7.95 nm; (C) 80 °C, a = 7.79 nm; (D) RT after thermal annealing, a = 7.78 nm.

A.

h	*k*	*l*	q_{obs} (Å^{-1})	q_{calc} (Å^{-1})	% Residual
1	1	0	0.1140	0.1112	-2.52
2	0	0	0.1571	0.1573	0.13
2	1	0	0.1761	0.1759	-0.11
2	1	1	0.1924	0.1926	0.10
2	2	0	0.2213	0.2224	0.49
3	1	0	0.2477	0.2487	0.40
4	1	0	0.3250	0.3243	-0.22

B.

h	*k*	*l*	q_{obs} (Å^{-1})	q_{calc} (Å^{-1})	% Residual
1	1	0	0.1124	0.1118	-0.50
2	0	0	0.1582	0.1581	-0.02
2	1	0	0.1771	0.1768	-0.18
2	1	1	0.1940	0.1937	-0.14
2	2	0	0.2234	0.2236	0.09
3	1	0	0.2498	0.2500	0.12
4	1	0	0.3261	0.3260	-0.02

C.

h	*k*	*l*	q_{obs} (Å^{-1})	q_{calc} (Å^{-1})	% Residual
1	1	0	0.1145	0.1140	-0.40
2	0	0	0.1613	0.1613	-0.05
2	1	0	0.1808	0.1803	-0.29
2	1	1	0.1977	0.1975	-0.10
2	2	0	0.2277	0.2281	0.18
3	1	0	0.2550	0.2550	0.00
4	1	0	0.3324	0.3324	0.00

D.

h	*k*	*l*	q_{obs} (Å^{-1})	q_{calc} (Å^{-1})	% Residual
1	1	0	0.1140	0.1142	0.18
2	0	0	0.1613	0.1615	0.12
2	1	0	0.1803	0.1805	0.11
2	1	1	0.1971	0.1978	0.35
2	2	0	0.2277	0.2284	0.31
3	1	0	0.2550	0.2553	0.12
4	1	0	0.3335	0.3329	-0.18

Table S6.22. FK A15 at 30 °C of the Gal-aPH sugar-polyolefin conjugate, **6.7**, with 20% vitamin E, with lattice parameters a = 8.03 nm, qobs and qcalc with corresponding Miller Indices.

h	*k*	*l*	q_{obs} (Å^{-1})	q_{calc} (Å^{-1})	% Residual
1	1	0	0.1110	0.1107	-0.27
2	0	0	0.1563	0.1565	0.13
2	1	0	0.1751	0.1750	-0.06
2	1	1	0.1916	0.1917	0.05
2	2	0	0.2216	0.2213	-0.14
3	1	0	0.2475	0.2475	0.00
3	2	0	0.2810	0.2821	0.39
3	2	1	0.2928	0.2928	0.00
4	0	0	0.3129	0.3130	-1.00
4	1	0	0.3228	0.3226	-0.06
3	3	0	0.3323	0.3320	-0.09
4	1	1	0.3323	0.3320	-0.09
4	2	0	0.3499	0.3499	0.00
4	2	1	0.3582	0.3586	0.11
3	3	2	0.3676	0.3670	-0.16

Table S6.23. FK A15 at 30 °C of the Gal-aPH sugar-polyolefin conjugate, **6.7**, with 20% vitamin E, with lattice parameters a = 8.03 nm, qobs and qcalc with corresponding Miller Indices.

h	*k*	*l*	q_{obs} (Å^{-1})	q_{calc} (Å^{-1})	% Residual
1	1	0	0.1110	0.1107	-0.27
2	0	0	0.1563	0.1565	0.13
2	1	0	0.1751	0.1750	-0.06
2	1	1	0.1916	0.1917	0.05
2	2	0	0.2216	0.2213	-0.14
3	1	0	0.2475	0.2475	0.00
3	2	0	0.2810	0.2821	0.39
3	2	1	0.2928	0.2928	0.00
4	0	0	0.3129	0.3130	-1.00
4	1	0	0.3228	0.3226	-0.06
3	3	0	0.3323	0.3320	-0.09
4	1	1	0.3323	0.3320	-0.09
4	2	0	0.3499	0.3499	0.00
4	2	1	0.3582	0.3586	0.11
3	3	2	0.3676	0.3670	-0.16

Table S6.24. List of the observed (qobs) peak positions for the cylindrical (C) phase at 30 °C for the CB-aPH sugar-polyolefin conjugate, **6.5**, domain spacing was calculated d=2π/q100 where d= 5.00 nm.

Miller Indices (hkl)	q_{obs} ($Å^{-1}$)
(100)	0.1257
(110)	0.2157
(200)	0.2640
(210)	0.3388

Table S6.25. List of the observed (qobs) peak positions for the cylindrical (C) phase at 130 °C for the CB-aPH sugar-polyolefin conjugate, **6.5**, where d= 4.00 nm.

Miller Indices (hkl)	q_{obs} ($Å^{-1}$)
(100)	0.1569
(200)	0.3140
(210)	0.4153

Table S6.26. List of the observed (qobs) peak positions for the body centered cubic (BCC) phase at 140 °C for the GAL-aPH sugar-polyolefin conjugate, **6.6**, where lattice parameter a = 5.35 nm.

Miller Indices (hkl)	q_{obs} ($Å^{-1}$)
(110)	0.1651
(200)	0.2334
(211)	0.2870

Table S6.27. List of the observed (qobs) peak positions for the cylindrical (C) phase at 110 °C for the GAL-aPH sugar-polyolefin conjugate, **6.7,** where domain spacing was d = 3.38 nm.

Miller Indices (hkl)	q_{obs} ($Å^{-1}$)
(100)	0.1857
(110)	0.3211

Chapter 7: Perylene Bisimide Polyolefin Conjugates

7.1 Background on Perylene Bisimide (PBI)

About a hundred years after their discovery, perylene tetracarboxylic dianhydride (PTCDA) a precursor for perylene-3,4:9,10-bis(dicarboximides)s, commonly abbreviated as PDI or herein PBI, have become one of the most important classes of functional dyes for organic semiconductors. PTCDA falls under a class of molecules known as Rylene dyes which are classified as useful pigments and dyes with a strikingly dark red color.[1,2] However, PTCDA, is a highly crystalline and extremely insoluble even in aromatic solvents. None-the-less PBIs have been utilized not only for their semiconducting properties but also for their easily synthetic modification.

The first several years of research on PBIs focused on variations of the imide substituents[3] which helped control the solubility of the perylene core and the overall packing arrangement in the solid state to try and achieve a pigment of different color or a liquid luminophore.[1,4] Later research on PBI delt with functionalization of the electron-deficient aromatic core to tune the florescence and electronic properties. Scheme 7.1 and Scheme 7.2 display the overall structure of PBI chromophore core were ‘A’ and ‘B’ sites were altered in order to develop new electronics, photovoltaics, and photonics. The popularity of these compounds is due to their excellent functional properties in combination with application-relevant features of photo- and thermal stability and chemical robustness.[12]

One of the main goals of this work was to utilize our polyolefin domains by design and chemically link them to functional counterparts to generate new technologies and applications for our polymer materials. This led us to investigate components that can be chemically modified in combination with end-group functionalized polyolefin domains that have properties useful in nanotechnology since our polyolefin are of low molecular weight and have the bonus of small dimensionalities to create thin films. The PTCDA precursor and resulting PBI materials studied lead us to believe that our polymer domains could serve as a potentially useful component.

Firstly, from a functional point of view, the optical properties, in particular fluorescence, are probably still the most appreciated motivation to work with PBIs. Only a few abbreviations of dyes can match PBIs properties in terms of fluorescence quantum yields.[5] This specific feature makes PBIs interesting for various applications including single molecule spectroscopy,[6-8] biomolecular imaging,[9] controlling light matter interaction in photonic devices,[10] and organic solar cells.[1]

Secondly, PTCDA and PBI based materials were generally of interest due to their electron-poor character with first reduction potential for core-unsubstituted PBIs around -10. *V* in comparison to ferrocenium/ferrocene (Fc^+/Fc) redox couples. This makes PBI equally suited to fullerenes as an electron transport material.[11] However, PBI have the added bonus of being stable at ambient conditions for uses in organic transistor devices that feature high electron mobility that ultimately is controlled through the packing arrangement and adjusting the position of the LUMO level. The LUMO levels adjustments have already been studied and understood thanks to the ease

of synthetic manipulation of the perylene chromophore via substitution at the ortho- or bay-positions of the PBI core.[5,12] However, controlling the arrangement of the perylene cores has still been an ongoing issue as it is highly crystalline and incredible insoluble.

Thirdly, the obstacle of insolubility could easily be overcome through our polyolefin domain in combination to PBI core. Not only are our polyolefin domains

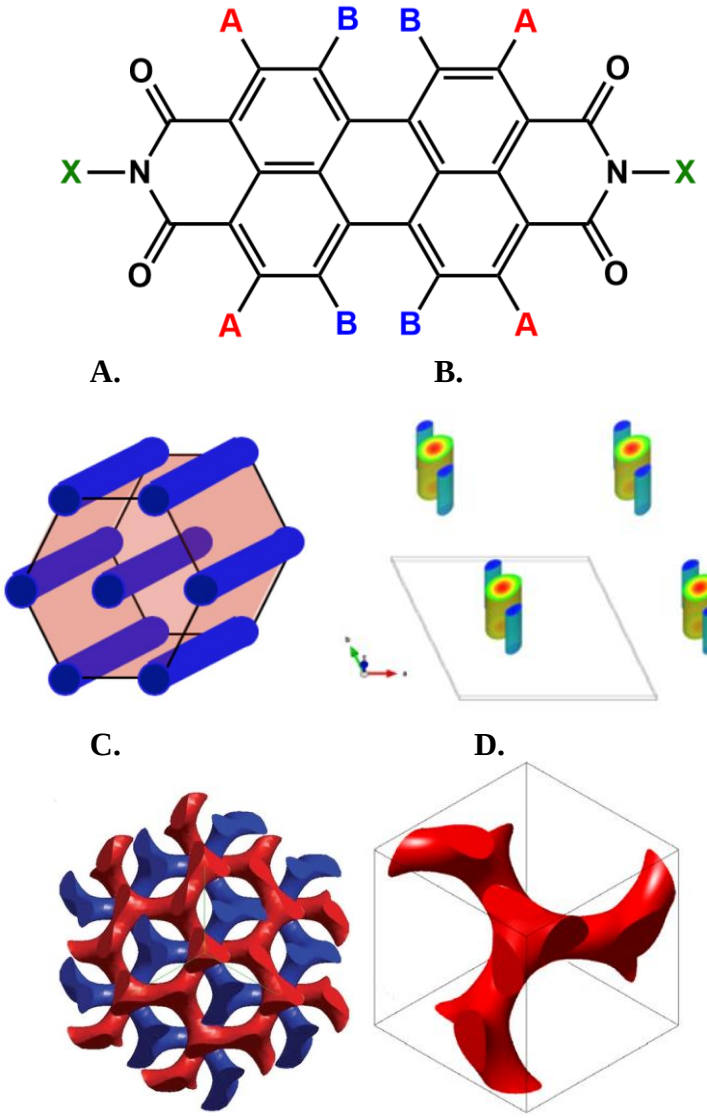

Scheme 7.1 (top) General structure of perylene bisimide (PBI) derivatives and (bottom) unit cells for different mesophases, including columnar hexagonal (Φ_h) (A), columnar oblique (Φ_{ob}) (B), double gyroid (DG) (C), and single gyroid (SG) (D).

endless in possible physical properties but they also are easily soluble, can easily be synthetically functionalized to have amine end-groups to substitute into the core, but also are known and have been proven herein to direct self-assembly. The strong $\pi - \pi$ interactions between PBIs and the possibility for hydrogen-bond-directed self-assembly via the self-complimentary imide functional groups enable a plethora of supramolecular structures with distinct photophysical properties to be achievable. The use of our polyolefin domains to investigate the self-assembly of the PBI polyolefin conjugates can lead to considerable insights into the use of PBIs for supramolecular photosystems as well as organic electronics and photovoltaics. Many recent review articles and studies have shown the relationship between a molecular structure and morphology, and how that impacts the operation of organic transistors and organic photovoltaic devices (OPV).[13,14]

7.2 Mesophase Engineering of Perylene Bisimide Polyolefin Conjugates

Introduction

Wentz, C. M; Tsai, E. H. R.; Yager, K. G.; Gonzalez-Lopez, L.; Diethrich, T. J.; Al-Sheikly, M. I.; Sita, L. R. Mesophase Engineering of Perylene Bisimide Polyolefin Conjugates: From Columnar & Optically Active Single Gyroid Nanostructures of Neutral & Radical Anions to Luminous Liquids & Waxes, (*manuscript in preparation*).

Author Contributions:
L. R. S. Lead conceptualization, funding, and writing.
C. M. W. Synthesized and characterized all perylene bisimide conjugates.
E. H. R. and K. G. Y. are beam-staff scientists at Brookhaven National Labs that assisted with the collection of GISAXS and indexing the diffraction.
L. G. -L. Collected and analyzed EPR data. T. J. D. collected and analyzed SQUID data. M. I. A. Lead conceptualization and analysis of EPR data.

To reach the goal of adding functionality to our precise polyolefin domain PBIs yield great promise to produce many new discoveries, and study if the polymer domains has influence on the self-assembly of the chromophore core. If not only for this broad range of application PBIs encompass it was also chosen to be investigated when in combination with our polyolefin domains because there is an wealth of information known regarding the structure/property relationships for PBI derivatives bearing substituents of varying steric and electronic demand that are placed at different positions within the perylene chromophore, including at the peripheral (A), the 'bay' (B) and the *N*-imide (X) positions according to Scheme 7.1. Potential further synthetic modification on these positions and could open even more technological advancements if the PBI polyolefin conjugates prove successful. Furthermore, aside from swapping out the polyolefin domain there is also a long- and well-established dye and pigment chemistry associated with PBI derivatives which provides access to a range of commercially available starting materials that have proven high yielding synthetic methods that could be adapted and investigated with our polyolefins.[3]

On the topic of self-assembly, the supramolecular organization of PBI derivatives in the condensed phase can also give rise to scientifically interesting and technologically important optoelectronic properties through formation of different short and long-range periodic ordering of nanostructured mesophases in which preferential $\pi - \pi$ stacking and geometric alignment of chromophores can occur.[3] As mentioned before our polyolefin domains have already been studied to influence conjugate materials into unique morphologies. Ultimately utilizing our polyolefins as a building block in combination with perylene can create a system that can easily be

synthetically modified to study structure/ self-assembling properties in a programmable way.

Inspiring contributions have previously been made by the groups of Percec, Würthner, Tschierske, Gunther and others have also established that PBI derivatives with dendritic and dendron-like N-imide substituents based on the tris(alkoxy)phenyl structural motif form a variety of structurally unique thermotropic columnar hexagonal (Φ_h) and oblique (Φ_{ob}) mesophases that are represented by the unit cells **A** and **B**, respectively.[5,16] These studies provide a reference for how structure/ property of PBI based materials can heavily rely upon the 'tails' that attach to the core. The progress that has been made with the synthesis and characterization of canonical and non-canonical thermotropic mesophases of PBI derivatives have now far outpaced the systematic investigation of the corresponding optoelectronic properties of these various nanostructures within both the bulk and within sub-100-nm-thick ultrathin films that are required for device fabrication.

For the goal of utilizing a PBI base material for optoelectronic applications it important to note that many of the targeted organic optoelectronic applications require that blends be made between the n-type PBI derivative serving as an electron-acceptor and an electron-donating p-type organic semiconductor.[1,2] Remembering that the highly crystalline nature of perylene bisimide derivatives in general, a melting point of > 400 °C for the parent compound, N,N-dimethyl-3,4,9,10-perylenetetracarboylic bisimide (A = B = H, X = CH_3 in Scheme 7.1, and a strong tendency for PBI aggregation to occur in solution and the condensed state greatly hampers physical processing of these materials and often leads to macroscopic phase separation of blend

components. This in turn, leads to a significant decrease in charge transport and device efficiency. Strategies for controlling molecular aggregation have included the design and synthesis of 'twisted' PBI cores through introduction of sterically encumbered substituents at the bay (B) positions. However, such structural perturbation also leads to substantial perturbation of the photophysical properties of the PBI chromophore.[1,2]

An attractive alternative strategy that has long been proposed is to develop blends that can undergo thermotropic supramolecular organization to form a bicontinuous mesophase, such as the double gyroid (*DG*) nanostructure of in Scheme 7.1C, in which the two components are held to being microphase segregated on the nanometer length scale within ultrathin films that should now be ideal in providing the highest efficiency for charge generation, separation, and mobility within so-called bulk-heterojunction organic solar cells (BHJ-OSCs).[15] Some validation of this strategy has been achieved through the use of a *DG* mesophase of a block copolymer as a template for formation of a 'hard' titania gyroidal nanostructure that was then successfully incorporated into a hybrid BHJ solar cell.[15] To the best that can be determined, however, no report has yet appeared in which a PBI derivative in either pure form or as a component of a donor-acceptor blend has been shown to form a DG phase, or any other bicontinuous mesophase for that matter. PBI-derivatives can also be electrochemically or chemically reduced to the corresponding p-delocalized radical anions for which an additional set of intriguing photophysical properties now arise, including absorption maxima that are dramatically shifted into the near infrared region (NIR) (i.e. $\lambda > 800$ nm) and radical anion excited states that can participate as powerful photo reducers and photocatalysts. Here too, however, the literature is devoid of any

documented example in which thermotropic supramolecular organization of a PBI-based radical anion soft material into either a canonical or non-canonical highly-ordered nanostructured mesophase has occurred.[16] Further, there is no report of the impact that different thermotropic mesophase ordering and alignment of extended arrays of interacting PBI radical anions has on the manifestation of optoelectronic, and possibly magneto-optoelectronic, properties. Finally, a few investigations of the synthesis and supramolecular organization of optically active PBI-derivatives have been reported, but these reports did not include any mention of the emergence of unique thermotropic mesophase-dependent chiroptical properties, such as circularly polarized luminescence (CPL).[1,4,15,16]

7.3 Mesophase Engineering of Perylene Bisimide–Polyolefin Conjugates: From Columnar and Optically Active Single Gyroid Nanostructures of Neutral and Radical Anions to Luminous Liquids and Waxes

With all that has been investigated with PBI based materials it seemed fitting that our polyolefin domains had a strong possibility of impacting perylene chromophore core properties and self-assembly and thus the current work within this chapter does exactly that. Through the synthesis, properties, and thermotropic structures of neutral and radical anion forms of a new category of PBI-polyolefin conjugates of general structure of **1** in Scheme 7.2, that are of unprecedented nature. Collectively, these results serve to establish **1** as a highly versatile platform for the

further discovery, investigation, and technological development of PBI based materials for organic optoelectronic applications.

Scheme 7.2 presents the simple one-step synthesis of the PBI polyolefin conjugates **7.1** – **7.4** that utilizes the commercially available unsubstituted perylene bis(anhydride) (PTCDA) **2** and two equivalents

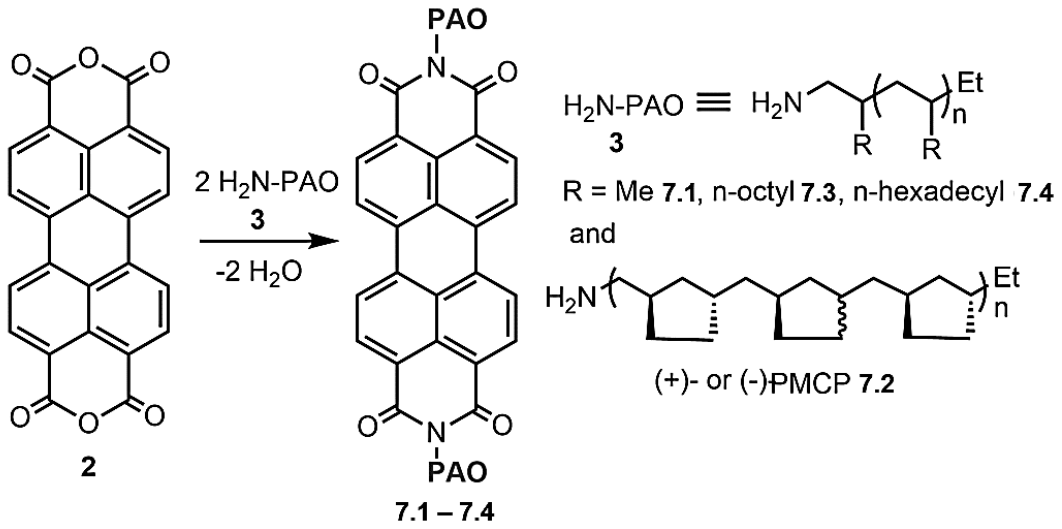

Scheme 7.2 Synthesis of PBI-polyolefin conjugates **7.1 – .7.4**.

of the corresponding amino-terminated poly(α-olefinates) (NH_2-PAOs) (**3**) as the hydrophobic domain precursor.[15] These amino terminated polyolefins are part of a growing number of x-PAO derivatives that the Sita group has previously shown can be obtained in practical and scalable quantities (from grams to kilograms) through the transition-metal-mediated living coordinative chain transfer polymerization (LCCTP) of higher carbon-numbered linear and branched α-olefins and α,ω-non-conjugated dienes that uses a stoichiometric excess of an abundant and relatively inexpensive main group metal alkyl, such as diethylzinc ($ZnEt_2$), as a reversible chain transfer agent (CTA) and the source of a population of surrogate chain growth centers.[19-22] Upon

reactive quenching of LCCTP with molecular iodine (I_2), a quantitative yield of iodo-terminated PAO products can be obtained and that are subsequently used as precursors for a variety of other end-group functionalized PAOs through simple nucleophilic substitution. In this fashion, we have previously reported the synthesis of azido-terminated PAOs through reaction of iodo-terminated PAO with sodium azide (NaN_3) and in the present study,[24,25] is reduced with lithium aluminium hydride ($LiAlH_4$) in diethyl ether (Et_2O) to provide the desired derivatives of **3** with an amino-terminated end-group, that are shown in Scheme 7.2. For these studies, values of DP_n were between 11 - 14 and $Đ$ values were all between 1.1 - 1.3, see SI for specific details of each x-PAO derivative or Table 7.1. Finally, it must be pointed out that use of an achiral C_s-symmetric hafnium initiator for the LCCTP of α-olefin monomers, such as the propene, 1-decene, and 1-octadecene employed here, provides an *atactic* stereochemical microstructure for the x-PAO products that possess a low (sub-ambient) glass transition temperature, *T*g. In addition, the physical nature of all the atactic poly(1-decene) (aPD) materials is as liquids, while those of atactic poly(1-octadecene) (aPOD) are as low melting waxes with a melting temperature, T_m, of about 35 °C, represented as **7.3** and **7.4**, respectively, in Scheme 7.2. Table 7.1 provides a summary of the components of each PBI-polyolefin conjugate. On the other hand, as recently reported, *enantioselective* LCCTP of 1,5-hexadiene using a homochiral C_1-symmetric hafnium initiator can be used to provide optically active (+)- and (-)- *isotactic* 1,3-*cis/trans* poly(methylene-1,3-cyclopentane) (PMCP) and the corresponding iodo-terminated (+)- and (-)-PMCP products (see **7.2** in Scheme 7.1) upon I_2 quench.[22,23]

Table 7.1 Summary of PBI polyolefin conjugates properties and behavior.

Conjugate Label	Polymer Tail	M_n (kDa)[a]	M_w (kDa)[a]	$Đ^a$	T_g (°C)[b]	T_m (°C)[b]	Morphology[c]
7.1	aPP	1.11	1.12	1.11	-24.8	-	*C*
7.2a	(-)-PMCP	1.31	1.70	1.31	-27.1	34.9	Col_{ob}
7.2b	(+)-PMCP	1.14	1.71	1.21	-51.4	24.5	Col_{ob}
7.3	aPD	1.56	1.83	1.18	-	-	-
7.4	aPOD	3.74	4.19	1.12	-	32.5	-

[a]Determined by GPC. [b]Determined by DSC. [c]Determined by SAXS.

Importantly, these NH_2-PMCP materials are semicrystalline with a T_m of 28 - 24 °C. Analytical and spectroscopic data for all the PBI polyolefin conjugates **7.1** – **7.4** are fully consistent with the structure presented in Scheme 7.1 and can be seen in the SI. Generally, all conjugates share the same absorbance and fluorescence profile see in figure 7.1 and are identical to many other PBI based materials in the literature.

Towards the goal of making PBI more easily processable it was hypothesized that our PAO domains would influence solubility and in fact all PAO substituents do render all these PBI materials highly soluble in several common aprotic polar and nonpolar solvents, including toluene, methylcyclohexane (MCH), THF, chloroform, chlorobenzene, and dichloromethane (DCM), and this property greatly facilitates solution characterization and the fabrication of ultra-thin films. In this regard, the parent PBI chromophore (A = B = H in Scheme 7.1) is well known to aggregate in solution through formation of intermolecular $\pi - \pi$ stacking interactions that can greatly affect photophysical properties – but not always in a good way. Indeed, much effort has been made to understand how the structure of the N-substituents can be used to control and direct the supramolecular organization of PBI derivatives in solution and

the condensed state.[1-7] Figure 7.1 presents the partial electronic absorption (UV-vis) and fluorescence emission spectra of the PBI-polyolefin **7.1** with PAO = atactic polypropylene (aPP). These measurements are recorded at room temperature using MCH as solvent. Most importantly, both spectra display the vibronic

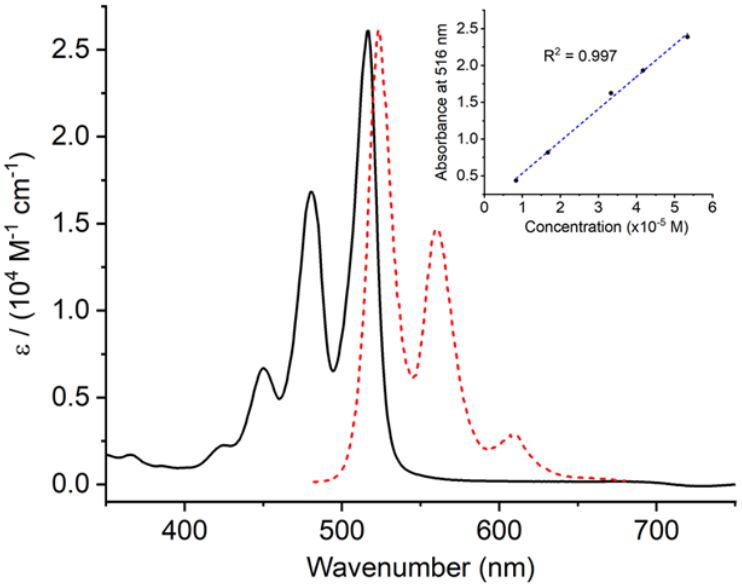

Figure 7.1 Partial electronic absorption (black line) and fluorescence (l_{ex} = 265 nm) (red dotted line) spectra for **7.1** recorded at room temperature in MCH (c = 0.053 mM). Inset shows the dependence of the absorption l_{max} = 516 nm as a function of concentration.

progression of electronic transitions that is a defining hallmark of the PBI chromophore, and a linear relationship between the absorption value of l_{max} at 516 nm with concentration strongly suggests that no aggregation through $\pi - \pi$ stacking is occurring in solution. Virtually identical data were obtained for all the other derivatives **7.1** – **7.4** under the same conditions.[15] It is important to note that when the concentration in solution of the PBI conjugates is drastically affected there is a color change from most concentrated to least concentrated: red – orange – yellow- green, seen in Figure S7.90. This suggests that the molecule does aggregate at high concentrations as the

deep red color is associated with $\pi - \pi$ stacking co-facial interactions among perylene nuclei.[26]

Quite unexpectedly, electronic circular dichroism (ECD) spectra of these PBI polyolefin conjugates now provided a very strong chiroptical signal that is associated with the PBI chromophore as shown in Figure 7.2A. ECD is a method that closely resembles UV-vis but makes use of circular polarized light instead of 'regular' unpolarized light and helps identify supramolecular organization within chiral compounds in solution. Based on the reports of other optically active PBI derivatives and observation that the nature of these ECD spectra for (+)- and (-)-**7.2a or 7.2b** are highly concentration dependent, it can be concluded that while not strongly affecting the electronic absorption and emission spectra, a sufficient degree of $\pi - \pi$ stacking of the PBI cores must still be occurring to provide a helical supramolecular organization in solution that is responsible for the ECD signal. From the ECD and UV-vis spectra that are collected simultaneously a *g*-factor can be calculated for the PBI polyolefin conjugate, Figure 7.2B, were only positive *g*-values are shown. The ratio between the CD signal and absorption intensity is

Equation 7.1 $$g = \frac{\Delta\epsilon}{\epsilon} = \frac{\boldsymbol{CD}}{\boldsymbol{Abs}}$$

defined through this anisotropy or dissymmetry *g*-factor, equation 7.1. This g-factor is a pure number independent of concentration or path length. Generally speaking, *g*-values are in the 10^{-5} – 10^{-3} range. The dissymmetry factor *g* is in principle larger for inherent symmetric chromophores. Furthermore, it can be seen that the ECD signal strength is influenced by the concentration of PBI polyolefin conjugate in solution, Figure 7.2C, and this trend can be seen as a linear regression of peak intensity. The

A.

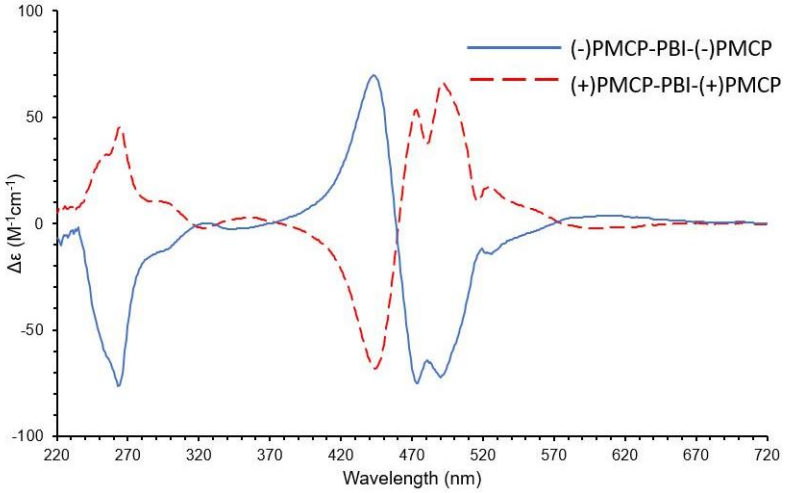

B.

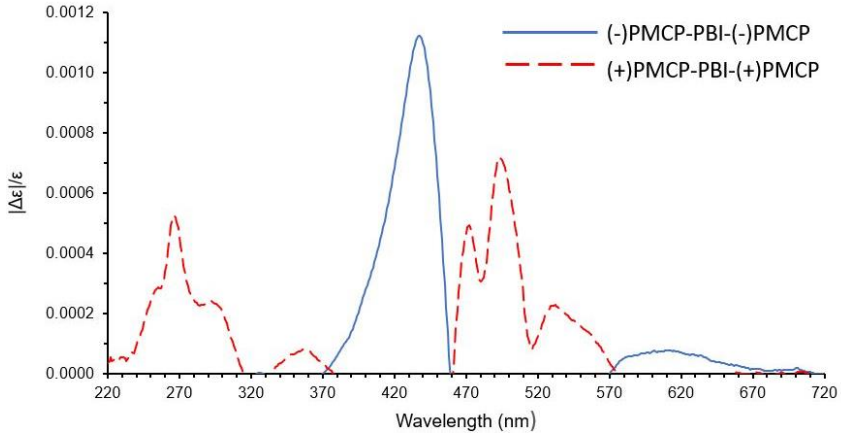

C.

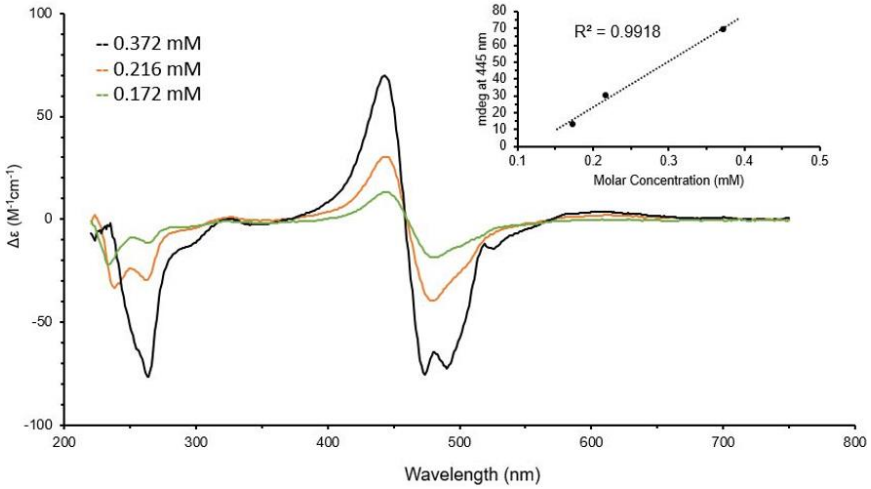

Figure 7.2 (A) Electronic circular dichroism of (+)- and (-)-**7.2ab** recorded at room temperature in MCH (c = 0.372 mM). (B) Positive values only for g-factor of (+)- and (-)-**7.2ab** values are calculated from the ECD run simultaneously. (C) Concentration study of (-)-PMCP.

dissymmetry *g*-factor was measured to be 0.11 x 10^{-3} $M^{-1}cm^{-1}$ which indicates high supramolecular helical formation in solution.

The high degree of solubility of **7.1** – **7.4** permits facile formation of ultrathin films on a variety of substrates through spin casting. Figure 7.3 presents images obtained from the phase-sensitive, tapping mode atomic force microscopy (ps-tm AFM) of a 180 nm-thick film of **7.1** that is supported on a carbon-coated polycrystalline silicon (cc-Si) substrate at low annealing and after thermal annealing at 110 °C in vacuo. For highly ordered graphene (HOPG) the material has similar phase separation which can be seen in the SI. Seen in phase mapping of Figure 7.3A is the as-cast of conjugates **7.1** which appears to form hexagonal packed cylinders parallel to the surface of the chip. At first glance the thin films did appear to look like a typical lamellae morphology but utilizing SAXS and GISAXS it confirmed instead a columnar hexagonal phased. Interestingly, as the thin film is annealed to 110 °C these cylinders appear to organize and orient themselves into neat long-range ordering 'rods' parallel to the surface. This long-range ordering of the material can potentially be useful in thin-film electronics due to its parallel organized of the hexagonal cylinders.

Furthermore, in Figure 7.3C and 7.3D, for conjugate **7.2a,** there are signs of phase separation at 110 °C of a 76 nm-thick film on cc-Si that once annealed higher to 240 °C becomes resolved into a similar appearing columnar rods as seen previously. However, there is a stark difference in periodicity within these thin-films as it appears columns can orient parallel and perpendicular to the surface as small circular dots appear throughout the thin-film. At room temperature conjugate **7.2a** does not have a well-defined phase separation, but does have hard crystallin fibrils present, seen in SI.

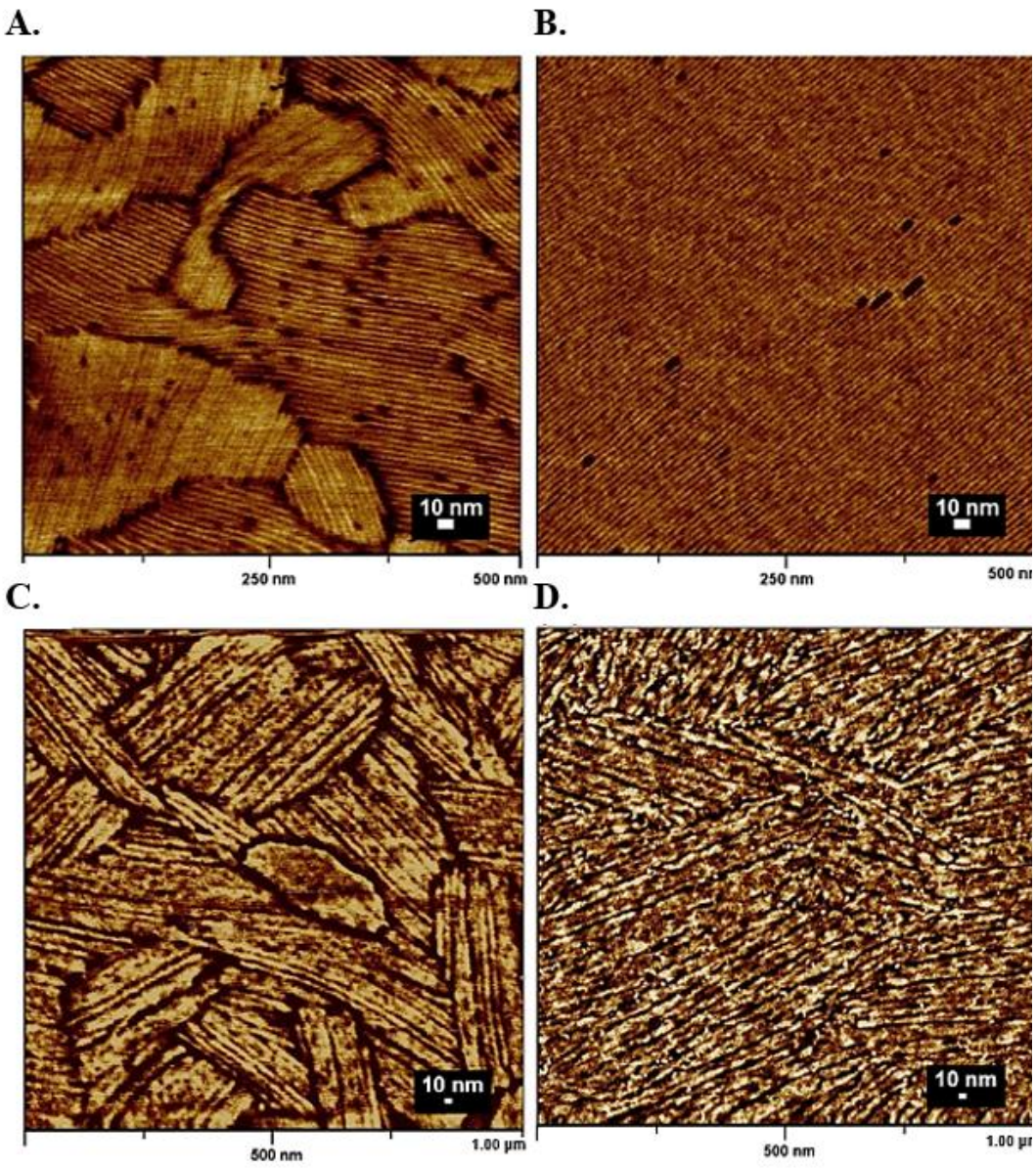

Figure 7.3 Atomic force microscopy phase map of (A) **7.1** at 50 °C with a 180 nm-thickness, (B) **7.1** at 110 °C with a 180 nm-thickness recording long-ranged order columnar, (C) **7.2a** at 110 °C, and (D) **7.2a** at 240 °C recording a similar looking columnar phase.

To better determine and clarify the morphology in these thin films these materials were studied using synchrotron x-ray source through GISAXS which provided clear evidence. Figure 7.4B and 7.4D are diffraction images collected through GISAXS of similarly thickness of thin films. These studies enabled the definite

understanding that conjugate **7.1** is forming hexagonal packed cylinders parallel to the chip rather than lamellae. These diffraction patterns also lead to the understanding that conjugate **7.2a** has unique phase separation of a cubic columnar oblique and is phase indexed as such by *hkl* Miller Indicies.[17-19] The columnar oblique mesophase (Col_{ob}) consists of molecular columns arranged in an oblique manner in which the columns are tilted, this can be seen in Scheme 7.1B. This specific phase is uncommon since it demands relatively strong core-core interactions within the columns.[27-29]

Self-organized columnar mesophases are obtained utilizing both an aPP and (+)- or (-)-PMCP PAO domain with a perylene core. It has been predicted that these columnar phases are observed because of the disc shaped perylene core that organizes into columns and these columns possess long-rang 2D order in the condensed phase which is observable through GISAXS and SAXS collected both utilizing the on-site SAXS and Brookhaven National Labs (BNL) synchrotron x-ray source. We propose that the polyolefin domain rigidity and physical properties dictate bulk properties of the PBI conjugate and help orient the perylene core alongside the natural drive to π-π stacking. Between the two materials they adapt different columnar phases with **7.1** being columnar hexagonal (Col_h) and **7.2a** at higher temperatures adopts a columnar oblique (Col_{ob}) stacking. Through selected variable temperatures utilizing heating stages, Figure 7.4 displays the Col_h of **7.1** at 90 °C. The Col_h arises even at room temperature, for full temperature ramp see SI. GISAXS data collected at 100 °C shows that the hexagonal cylinders do in fact exist parallel to the chip at high periodicity with large grain size. For the conjugate **7.2a** the ordering begins with lamellae phase with an observable order-to-order transitions into Col_{ob} as early as 135 °C, and in Figure 7.4

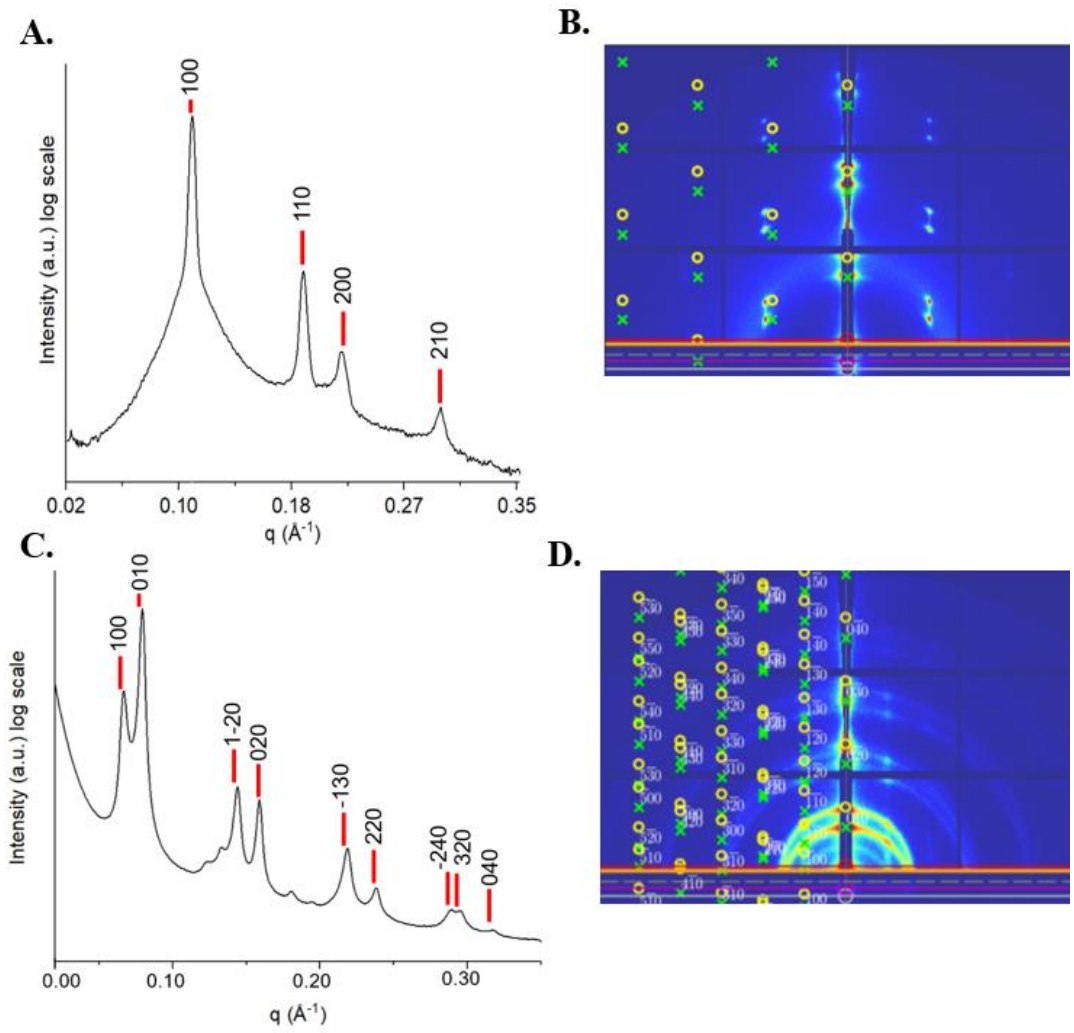

Figure 7.4 (A) On-site x-ray source 1D SAXS for **7.1** obtained at a fixed temperature of 90 °C. (B) GISAXS collected at BNL of **7.1** at 100 °C with film-thickness 190 nm, hkl Miller indices assigned for Col_h. (C) 1D SAXS data collected at BNL for **7.2a** obtained at 175 °C during heating ramp, *hkl* Miller indices assigned for Col_{ob}. (D) GISAXS collected at BNL of **7.2a** at 160 °C with film-thickness 160 nm.

selected temperature 175 °C displays the Col_{ob} with calculated a = 10.4 nm, b = 8.55 nm, and gamma = 111.16 ° utilizing GISAXS measurements made at BNL, at 160 °C, with film-thickness of 160 nm. It is hypothesized that the chiral nature of the PMCP creates a unique packing where each PMCP crystallinity and packing nature forces the core to have strong $\pi - \pi$ stacking forcing it into the uncommon Col_{ob} phase. The

perylene cores must be twisting in a helical fashion with a slight distortion in order to fit the Col_{ob} phase which is caused by the optical nature of the PAO domain whereas in aPP-PBI-aPP conjugate **7.1** the aPP domain does not influence the twisting of the core so a more common *Colh* phase can be observed. It is clear that the physical property difference of a T_m and structural difference in PMCP plays a large role in the self-assembly of the bulk conjugate.

Throughout making these PBI materials obstacles of aggregation were never seen because of the design and solubility of the polyolefin domain. Even when using the optically active, rigid, and crystalline x-PAOs such as in **7.2a** and **7.4** successfully completing the hypothesis that the bulk properties of these materials can be dictated by the polyolefin domain. While a goal was to influence the self-assembly and organization in condensed phase by the DP_n, molecular weight, and type of x-PAOs there was a more important and long-lasting goals of creating a partnership of n-type and p-type system that allowed us to continue to access the organized assembly while making use of functionality. This was achieved by blending **7.1** with cobaltocene under inert atmosphere with distilled dried DCM by weight percentage (25 wt% **7.1** and cobaltocene). Cobaltocene was chosen for its ability to be a one radical electron donor, as well as its small size to incorporate into the blend without disrupting any condensed phase separation. By UV-vis a dramatic change in profile was observed from the neat. More significantly, overtime the peak profile changed, Figure 7.5. It is important to note that the solution of PBI polyolefin conjugate

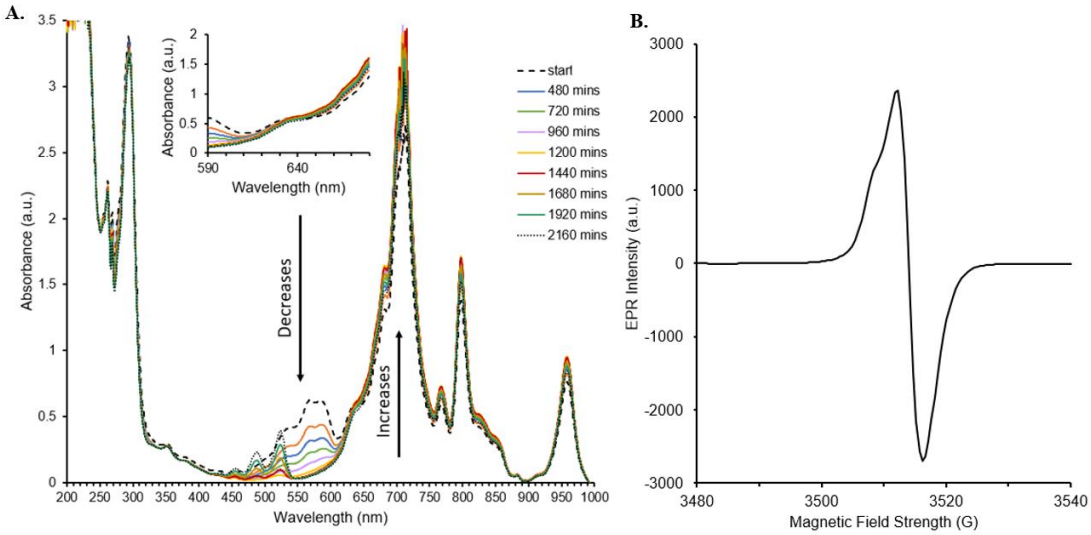

Figure 7.5 For (A-B) **7.1** cobaltocenium radical complex were 25 wt% of cobaltocene was blended with **7.1** with dry DCM. (A) UV-vis spectra of the **7.1** blend, in dry DCM, over a time lapse showing the decrease of the dianion and an increase of the radical anion pair as well as the neutral peaks. (B) EPR spectrum of solid film of **7.1** cobaltocenium radical complex.

and cobaltocene were prepared in a glove box, sealed in an airtight cuvette, and then measured in the UV-vis. Initially one can see that the one radical electron does donate to create a dianion, peaks that span 600 - 500 nm, however these peaks begin to decrease over time. Then as the dianion redistributes to equilibrate to a radical anion on the perylene, signals span 1000 - 600 nm, can be witnessed and these specific signals increase over time. Once the solution has reached over 12 hours of measurement in the UV-vis there becomes an inhomogeneity of both neutral species, spans 518 - 450 nm, and radical anion. The resulting neutral species is believed to exist due to an incorrect stoichiometric necessity between the cobaltocene and the perylene core. To avoid this inhomogeneity, one would have to have the correct blended amount of cobaltocene to the perylene chromophore present to create a completely balanced radical species and

cobaltocenium species. There is an isosbestic point at 640 nm which is noticeable at 1440 minutes from T_0 (start).

When these radical species are examined in the condensed phase, employing electron paramagnetic resonance (EPR), there is further evidence of the radical anion presence indicated by the broad peak in Figure 7.5B. EPR spectroscopic method assists in obtaining information on the structure and dynamics of systems with unpaired electrons. The broadness and intensity of the peak is speculated to be because of the solid films contact with air which subsequently quenches the radical anion over time. Figure 7.5B further confirms the ability to make robust solutions and free-standing films of the radical anion forms of conjugate **7.1** via chemical reduction with decamethyl cobaltocene and provides further proof of the stable open-spin nature of isolated free-standing films of [**7.1**]$^{-\bullet}$. In summary, the combination of cobaltocene creates a partnership that over time results in the non-homogeneity of a radical anion pair and neutral compound because which is observable through a color change from blue/purplish to yellow green as well as the profile seen in UV-vis and EPR. These same features can be seen when **7.2a** or **7.2b** is reduced by cobaltocene at 30 wt% blend by both UV-vis and EPR, with the main differences being the length of time to observe the isosbestic point and location and broadness of EPR signal, see SI. Conjugate **7.2** PMCP polyolefin domains contain more rigidity thus creating a more stable environment for this radical species to exist. EPR was conducted by Lorelis Gonzalez-Lopez from Dr. Mohamad Al-Sheikhly group at University of Maryland. The material was measure in solution and measured in the condense phase. Due to the decomposition of cobaltocene in air the solid-state measurements by EPR yielded the results observed

and discussed about previously. Dr. Al-Sheikhly and Lorelis proposed the hypothesis that the radical species can be existing on the PBI conjugate material in many locations including the carbonyl, chromophore itself, or the nitrogen in the amide. Based on stability it makes most sense that the radical species is located on the pi-conjugated chromophore core or the carbonyl directly off the chromophore.

Most satisfyingly the use of the cobaltocene as a radical donor does not prevent phase separation but instead in both in conjugate **7.1** and **7.2** the reduction and inclusion of cobaltocenium drives the self-assembly into new phases. For conjugate **7.1** radical species with cobaltocenium, on-site x-ray at selected temperatures elucidated the nanostructure seen within the material. Seen in Figure 7.6, starting at room temperature what was hexagonally packed cylinders, also referred to as columnar hex. (Col_h), in the neat conjugate now has other peaks emerging that do not have a strong presence but loosely fits columnar oblique phase (Col_{ob}). Once annealed at higher temperatures of 150 °C the Col_h starts to have an order-disorder transition. Then at 180 °C a broadened peaks at 0.15 Å begins to emerge to finally at 200 °C emerge into a well-defined Col_{ob} phase. The Col_{ob} phase has a slight presence of melt hump as seen before during the thermal ramp. When the radical species **7.1** with cobaltocenium is cooled back to room temperature the Col_{ob} phase persists, see supporting information. Due to the nature of the radical species that exists on the perylene core it is believed to influence the $\pi - \pi$ stacking in a way that causes this uncommon phase to emerge at elevated temperatures. Logically, two radical species do not want to be in close proximity to one another due to electronic interactions therefore it is hypothesized that the cobaltocenium sandwiches itself between the cores causing them to have an oblique shifting of the

disks due to the interruption in the cores stacking consequently leading to this new phase.

For conjugate **7.2a** blended with cobaltocene thus creating a radical species, x-ray synchrotron data of the material starts off with loose ordering lamellae, this was observed before in the neat conjugate, but as the material is annealed there are new peaks emerging. An order-order phase transition is seen at 180 °C during heating, and 103 °C during cooling, of a single gyroid (SG) phase ($I4_132$). Using on-site x-ray source, one can observe SG as well at elevated temperatures including the important presence of $\sqrt{2}$ but due to the low intensity of the beam source the peaks are too broad to directly fit to a SG utilizing electron density programming but does confirm it is a cubic phase. Temperature ramp of on-site data can be seen in the SI as well as additional analysis of collected BNL 1D SAXS of the SG. One must note that this PBI conjugate blend incorporates the chiral (+) PMCP domains and that single gyroid (SG) itself is chiral. Could this be coincidental or is it necessary to have a chiral rigid domain in order to access this phase, this is under further investigation. The PMCP rigidity as well as the high crystallinity of the perylene chromophore core can be used to validate why higher temperatures are needed to allow for the reassembly into other ordered phases, as seen in the neat, so understandably when at higher temperatures the radical anion partnered cobaltocenium with the perylene core can create such a rarely seen phase such as the SG. There are many ways in which one can envision cobaltocenium' s place amongst the perylene within the SG with one hypothesis being that the perylene makes up the main interconnected domains of the SG, forced to be SG instead of alternating double gyroid because of the chirality of the PMCP that makes up the other domain.

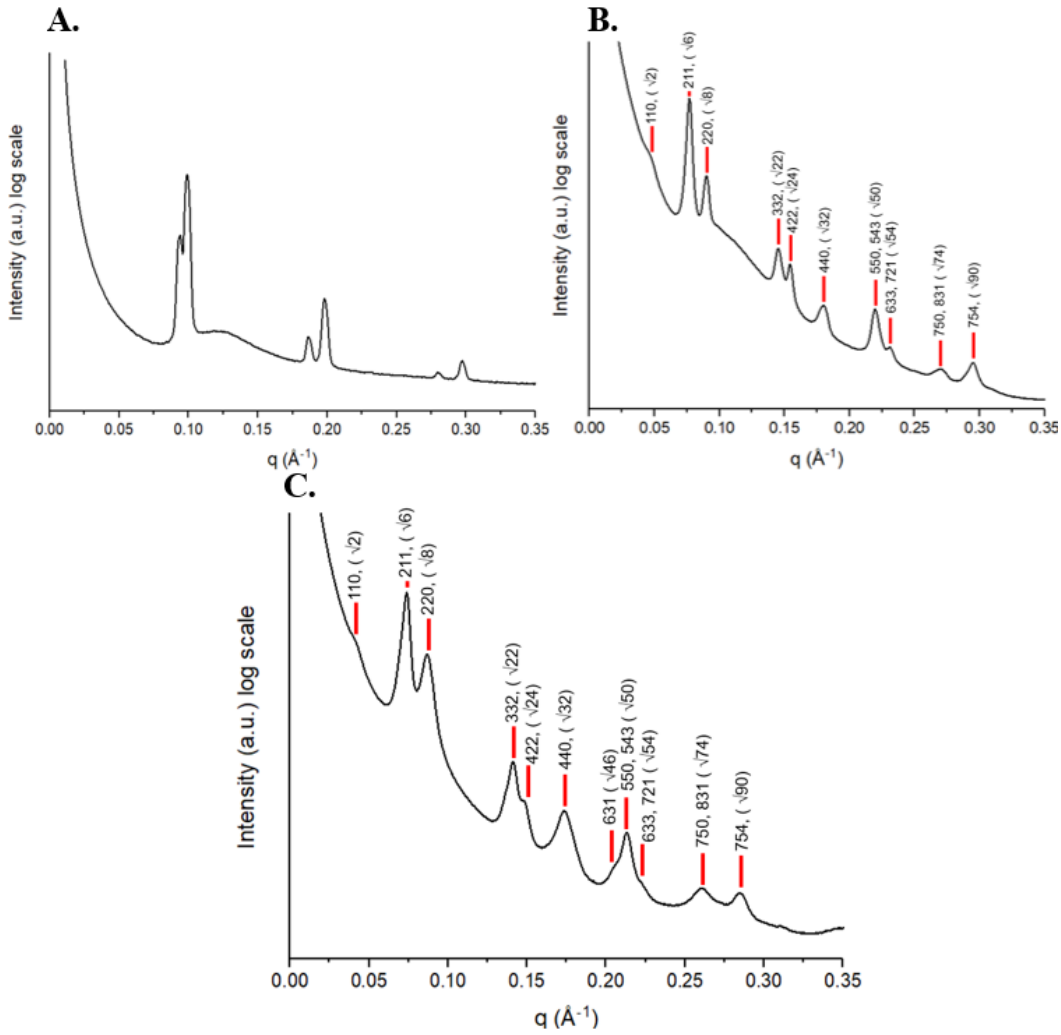

Figure 7.6 (A) Selected 1D SAXS was collected using on-site x-ray source observed Col_{ob}, at 200 °C when **7.1** and cobaltocene are blended at 25 wt%. (B) 1D SAXS was collected using BNL synchrotron source with *hkl* Miller Indices and sqrt ratios of observed single gyroid (SG), at 180 °C, when **7.2a** and cobaltocene are blended at 30 wt% (C) 1D SAXS was collected using BNL synchrotron source with *hkl* Miller indices and sqrt ratios of observed SG, at 103 °C, when **7.2a** and cobaltocene are blended at 30 wt%.

Or the cobaltocenium coats the outside of the perylene. While another hypothesis of cobaltocenium's location could be that the cobaltocenium is incorporated in between the radical perylene chromophore core within the SG in a stacking sandwich manner between each chromophore.

Due to the air-sensitivity as well as polyolefin make-up of the material SEM and TEM has not been used to locate the cobaltocene's relationship to the PBI-polyolefin conjugate. To further clarify the structure to be SG one can see in the SAXS that peaks do not conform to the predictions for alternative cubic by the complete absence of predicted √16 and √19 peak positions and simply does not support the assignment of the single diamond space group, see in SI. Single gyroid morphology has been seen in elements of nature from bird feather,[30] to butterfly wings,[31] and gyroid structures generally have better ion conductivity within materials.[32] To the best of our knowledge, however, a single gyroid morphology has never been documented in a PBI polyolefin-based material. This serendipitous discovery of such a phase within this material hopefully will provide suitable for technological applications.

Conducted by Timothy Diethrich, temperature dependent magnetic susceptibility was performed on both the (+)PMCP-PBI-(+)PMCP radical reduction by cobaltocene blend and the aPP-PB1-aPP radical reduction by cobaltocene blend (Figure S7.71 - S7.72). Both samples demonstrated a positive magnetic susceptibility magnitude indicating the presence of unpaired electrons. A purely diamagnetic response would have given a negative value of χ. Magnetization (M) vs. field (H) measurements were performed on the aPP-PB1-aPP: Cobaltocenium species resulting in a slight hysteresis which would indicate ferromagnetism at both temperatures recorded. The positive slope also confirms that this blend is not diamagnetic.

In summary, the organized assembly of the n- and p-type partnership in conjugates 7.1 or **7.2** with cobaltocene present important for the field of organic optoelectronics, and it is anticipated that through different guests one can manipulate

the self-assembly of these PBI-polyolefin conjugate and it can be expected that varied degrees of conductivity can be seen based on the dopant.

Lastly, when xPAOs are obtained from long-chain liner α-olefins, such as 1-decene (conjugate **7.3**) and 1-octadecene (conjugate **7.4**) it can be used to produce completely amorphous PBI polyolefin conjugates. In both forms they are highly luminous and in conjugate aPD-PBI-aPD **7.3** at room temperature is a liquid. Figure 7.7A shows the PBI conjugate being pipetted onto a glass slide. While conjugate aPOD-PBI-aPOD **7.4** is a mouldable wax. Figure 7.7B shows the material as a turtle, which was made by filling the mould with the conjugate then using a vacuum oven to

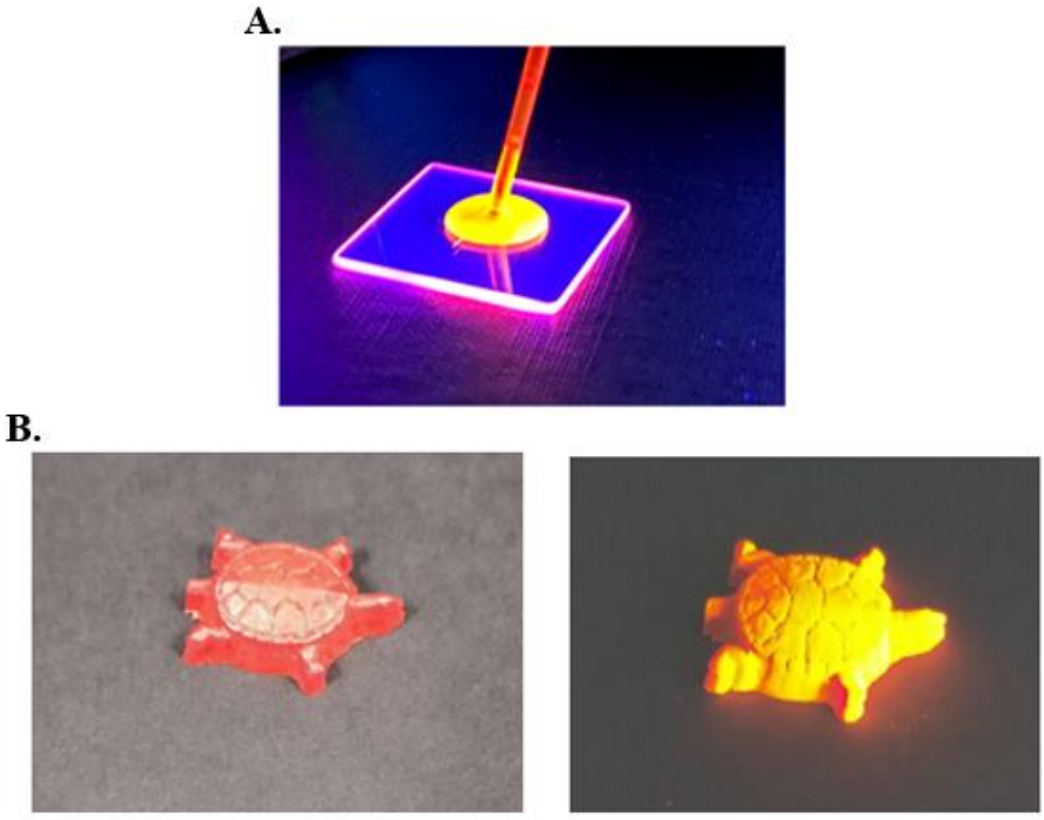

Figure 7.7 (A) Luminous liquid of **7.3** at room temperature under UV-lighting. (B) molded wax of **7.4** (left) under lab lighting and (right) under UV-vis lighting.

melt the conjugate into the mould and popping it out of the mould at room temperature, thus creating a free-standing wax that is luminescent. By completely isolating the chromophore within a rigidified polyolefin wax matrix one can facilitate sing-triplet intersystem crossing to produce scientifically novel and technological interesting room-temperature phosphorescence. Furthermore, the amorphous nature and isolation of perylene chromophores within liquid and wax PBI-polyolefin conjugate can provide new test beds for probing and quantifying the manifestation of new photophysical and optoelectronic properties. Here, it can be restated that LCCTP is particularly well-suited for the production of low-to ultra-low molecular weight x-PAOs for which small DP_n values of between 5 and 30 can be routinely obtained and with extremely narrow dispersity's (e.g. $Đ = M_w / M_n \leq 1.15$). The benefit of these demonstrated abilities of LCCTP is that xPAOs can be obtained for which molar mass remains under the minimum chain entanglement molecular weight (M_e) threshold. In turn, keeping $M_n < M_e$ for the PAO domains of molecular-polyolefin conjugates can translate into the observation of rapid thermotropic order-order phase transitions that would not normally be possible on such short time scales with either higher DP_n or broader $Đ$ values. The conjugates **7.3** and **7.4** truly show that the bulk like properties of the conjugate materials is influenced by the design xPAO domain made possible by this developed system.

To determine the energy levels of the PBI polyolefin conjugates cyclic voltammetry (CV) were investigates and results can be seen in SI (Figure S7.67 – S7.70). Within the cyclic voltammetry scanning range of -2.0 to + 2.0 V measure, oxidation and reduction waves were observed. The profiles of each conjugate similarly matched with a slight discretion when it came to wave intensity and location. Future

investigations involve utilizing the PBI polyolefin conjugates as an electron transporting layer within an organic solar cell device or within thin films. Due to PBIs electron-deficient core they are a classified as a n-type organic semiconductor which show considerable promise as (photo)conductive materials for a range of optoelectronic applications.

7.4 Blends

7.4.1 Poly(3-hexylthiophene) (P3HT)

Another prospective guest that was investigated was p-type donor poly(3-hexylpolythiophene) (P3HT) with the optically active PMCP-PBI-PMCP conjugate **7.2b**. Were P3HT, purchased at sigma Aldrich, was blended at a 1:1 by weight with dried DCM. Upon removal of solvent, a bronze-colored free-standing film with a metallic luster was created, seen in Figure 7.8A, and can be isolated. EPR reveals that there is a radical species existing between the PBI polyolefin conjugate and P3HT in the condensed phase, Figure 7.8B, which over time and exposure to air decreases in intensity. This air-sensitivity and decrease in intensity is also noticeable in **7.1** however **7.2b** has a less drastic intensity to start and loses intensity faster than the **7.1** PBI-polyolefin conjugate, see SI. UV-vis shows that the presence of P3HT does change the profile, range, and intensity of the typical three peaks seen in the neat, Figure 7.8C. Moreover, the on-site 1D SAXS shows loose ordering that is non-typical and

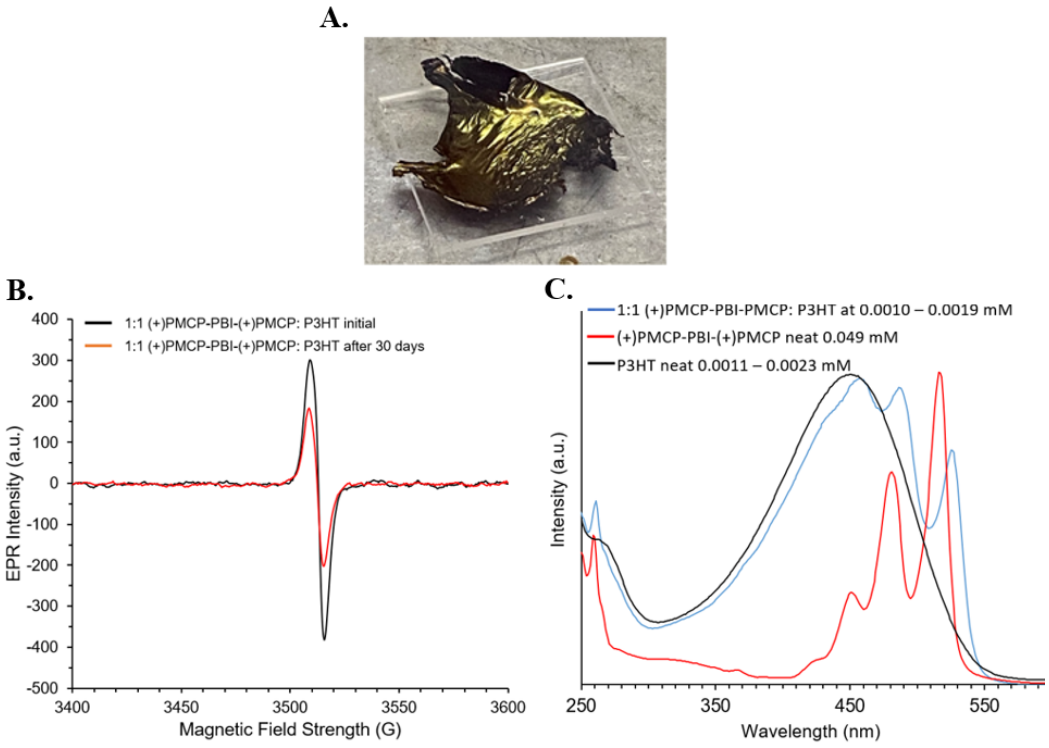

Figure 7.8 (A) Metallic luster of free-standing film 1:1 blend by weight of **7.1** and P3HT under lab lighting. (B) EPR signal 1:1 blend by weight of **7.2b**: P3HT initial measurement in condensed phase, initial measurement (black) and after 30 days exposed to air (orange). (C) UV-vis spectra of 1:1 blend by weight of **7.2b**: P3HT at 0.0010 mM – 0.0019 mM in MCH (blue), neat **7.2b** at 0.049 mM in MCH (red), and P3HT at 0.0011 – 0.0023 mM in chloroform (black).

is not indexable to any know phase. These results are similar when **7.1** is blended with P3HT at a 1:1 weight, see SI. The thiophene molecules can be useful guest due to their donating ability and due to the high molecular weight and dispersity of the P3HT molecular weight we utilized (50 kDa – 100 kDa) it causes the disruption of self-assembly as well as could be a distinguishing factor in the UV-vis profile. Future studies will incorporate oligomeric amounts of thiophene to mimic results seen with cobaltocene and not disrupt the already phase separating PBI polyolefin conjugates.

7.4.2. Dye 254 Conjugate

It was of interest to try different dye cores with the same polyolefin domains. Another dye of interest was Pigment Red 254 (DPP), Figure 7.9 shows overall structure. DPP structure has phenyl branching off the core structure with para positioned chlorines for further ease of modification. DPP are ideal for their high resistance to photodegradation and bioimaging

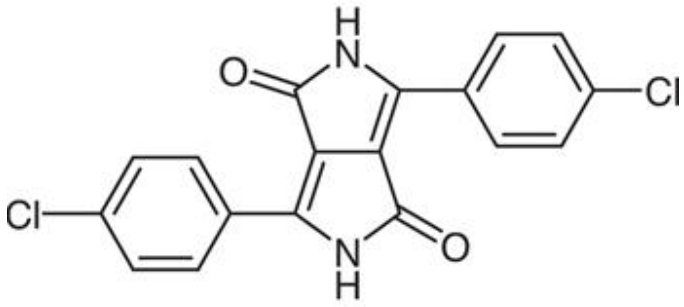

Figure 7.9 Pigment Red 254 (DPP).

applications,[33] as well as components of materials for use in organic electronics[34-39] Through faster synthetic routes Pigment red 254 was easily purchased and in a solution of K_2CO_3 and DMF the pigment was stirred at 65 °C for 30 minutes before iodo-terminated atactic polypropylene, in toluene, was dropwise added to the reaction mixture. The reaction was cooled to room temperature and stirred for 24 hours before quenched with water and thoroughly washed with DCM and finally precipitated in methanol and collected through vacuum filtration. Just like in the perylene based conjugate the aPP domain broke up crystallinity within the materials and made it soluble in organic solvents. The aPP-DPP-aPP conjugate was then blended with aPP-

PBI-aPP conjugate **7.1** by 15 wt % and measure in-house SAXS at selected temperatures, Figure 7.10.

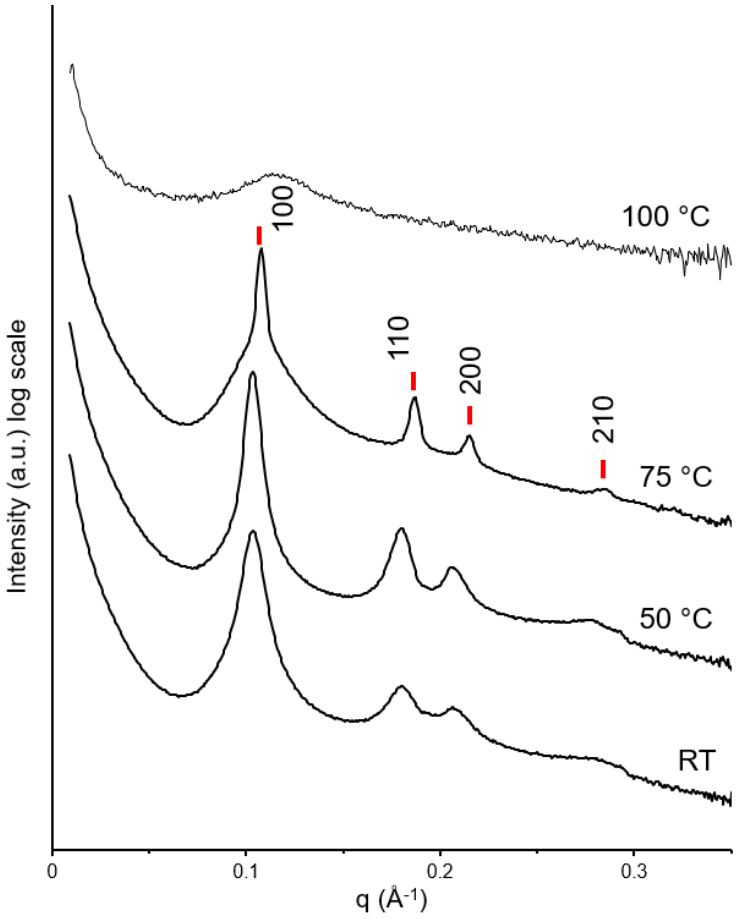

Figure 7.10 VT 1D SAXS was collected using on-site x-ray source were selected temperatures were ramped to and held for 20 minutes before collection of data of blended aPP-DPP-aPP and aPP-PBI-aPP conjugates. Hexagonal packed cylinder (*C or* Col_h*)* phase seen and *hkl* Miller indices added.

The aPP-PBI-aPP conjugate **7.1** original morphology was hexagonal packed cylinders and at 15 wt% blend with aPP-DPP-aPP there is no change in morphology. Ironically, the material flows so easily that collecting SAXS data above 100 °C became close to impossible as the sample would leak from its wafer during annealing. Future

work with DPP-aPP involves synthetically modifying the side groups attached to the core in order to influence the overall properties of the material and potentially create a system within one material that contains both n- and p-type characteristics.

7.5 Conclusions

In conclusion a library of PBI polyolefin conjugates were synthesized to enable bulk property changes based on the xPAO domain. Through these efforts conjugates containing aPP PAO domain and (+)- or (-)-PMCP PAO domain were observed to have unique self-assembly. The design and successful demonstration of a highly versatile new strategy for manipulating perylene chromophores through the simple and scalable addition of xPAOs with a breath of physical properties resulting in PBI-polyolefin conjugates that range from liquid luminophores, to oils, and hard waxes. Most notably when utilizing a chiral (+)- or (-)PMCP domain blended with a p-type dopant cobaltocene it gives rise to single gyroid in the bulk observable through synchrotron small angle x-ray scattering. When utilizing an aPP oil, it allows for columnar phases both in the neat and when blended with cobaltocene. When aPP-PBI-polyolefin conjugate is spun-cast into thin films it displays long-range ordering across microns of hexagonal cylinder parallel to the carbon-coated silicon which can provide useful for optoelectronics. All PBI-polyolefin conjugate synthesized possess luminescence behaviour and the ability to blend easily with p-type guests which ultimately shows considerable promise that these materials can be valuable as (photo)conductive

materials for a range of optoelectronic applications, such as organic field effect transistors, organic light emitting diodes and organic solar cells.

7.6 Supporting Experimental Information

7.6.1 Synthetic Procedures

All manipulations of air and moisture sensitive compounds were carried out under N_2 atmospheres with standard Schlenk line or glovebox techniques. Toluene (ReagentPlus, 99%) was dried and deoxygenated by passage over activated alumina and GetterMax® 135 catalyst (purchased from Research Catalysts, Inc.) and collected prior to use. Chlorobenzene (ReagentPlus, 99%) was dried over potassium hydride, refluxed at 130 ˚C for three days, and collected under N_2 prior to use. Diethyl ether was dried using a sodium/ benzophenone still. All other solvents were used as received unless otherwise noted. Precatalyst (I) was synthesized as previously described by our group.[1] $[PhNMe_2H][B(C_6F_5)_4]$ was purchased from Boulder Scientific and used as received. Perylene-3, 4, 9, 10-tetracarboxylic dianhydride, imidazole, and poly(3-hexylthiophene-2,5-diyl) were purchased from Sigma Aldrich.

Preparation of Blends

The P3HT blends were prepared in a glove box, where equal amounts of the P3HT and PBI conjugate were weighed out in separate vial (30 mg:30 mg), then using minimal amounts of dried chloroform they were mixed together and homogenized for 1 hour at room temperature (RT) with frequent agitation, then the blended sample was evacuated to dryness for 12 hours.

The aPP-PBI-aPP:Cobaltocene (25 wt%) blends were prepared in a glove box, where 80 mg of aPP-PBI-aPP conjugate was weighed out in separate vial, and 20 mg of cobaltocene was weighed out in a separate vial, then using minimal amounts of dried dichloromethane (DCM) they were mixed together and homogenized for 1 hour

at RT with frequent agitation, then the blended sample was evacuated to dryness for 12 hours.

The aPP-PBI-aPP: Cobaltocenium (25 wt%) radical species were prepared in a glove box, where 80 mg of aPP-PBI-aPP conjugate was weighed out in separate vial, and 20 mg of cobaltocene was weighed out in a separate vial, then using minimal amounts of dried dichloromethane (DCM) they were mixed together and homogenized for 1 hour at room temperature (RT) with frequent agitation, then the blended sample was evacuated to dryness for 12 hours inside the glove box. The radical species when in solution was a purple color and once dried appeared purple/black and glossy.

The (+)PMCP-PBI-(+)PMCP: Cobaltocenium (30 wt%) radical species were prepared in a glove box, where 30 mg of (+)PMCP-PBI-(+)PMCP conjugate was weighed out in separate vial, and 9 mg of cobaltocene was weighed out in a separate vial, then using minimal amounts dried DCM they were mixed together and homogenized for 1 hour at RT with frequent agitation, then the blended sample was evacuated to dryness for 12 hours. The radical species was a blue color when in solutions and purple/black when dry.

The aPP-DPP-aPP and aPP-PBI-aPP conjugate **7.1** were measured in separate vials to be 45.2 mg of aPP-PBI-aPP **7.1** and 6.78 mg of aPP-DPP-aPP. Chloroform was used to transfer aPP-DPP-aPP into the vial containing the aPP-PBI-aPP conjugate and agitated continuously over the course of 30 minutes before vacuuming to dryness. The blend was a glossy red color.

General synthesis of amino-terminated atatctic polypropene (NH_2-aPP).

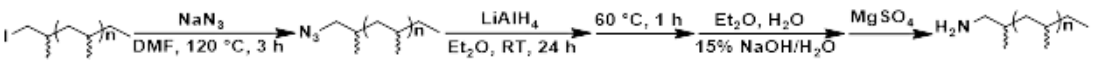

Iodo-terminated polypropene (1 kDa) was provided by PPL (3.00 g) was dissolved in minimal toluene and added to a 100 mL Schlenk flask under air sensitive technique. NaN_3 (1.2 eq) was dissolved in 10 mL of DMF and added to the solution. The solution was then refluxed for 3 h at 120 °C. The resulting product was purified using a silica plug and dried (2.353, 78.4 %) then characterized by GPC, ^{1}H NMR and ^{13}C NMR. The resulting azido-terminated polymer (1.017 g) was then dissolved in 15 mL of diethyl ether (Et_2O) and transferred into a round bottom flask under air sensitive techniques. A 3-neck round bottom flask was prepared with a condenser, addition funnel, and a septum for addition of LiAlH4 and 10 mL of Et_2O at 0 °C under air sensitive technique. The polymer was then cannula transferred into the addition funnel and drop-wise added to the solution of $LiAlH_4$ and Et_2O at 0 °C. The reaction was then allowed to stir for 24 h then refluxed at 60 °C for 1 h before quenching. The reaction was quenched with addition of diethyl ether, then H_2O, then 15 % NaOH/ H_2O solution, and additional H_2O all at 0 °C. Finally, MgSO4 was added, and the reaction was brough back to RT before running the solution through a celite plug using excess THF. The resulting filtered liquid was then pump down to dryness and run through a silica column and dried. To yield the amino terminated polypropene (838 mg, 84 %).

General synthesis of amino-terminated poly(methylene-1,3-cyclopentane) (NH_2-(-)PMCP)

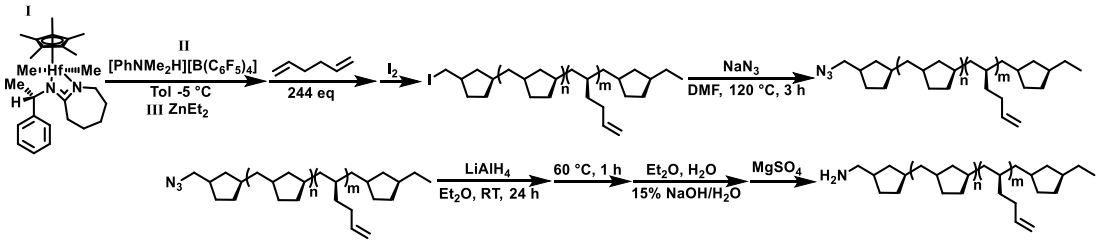

In a 25 mL round bottom, to a 5 mL toluene solution of 38.8 mg (0.048 mmols) of **II** chilled to -5 °C was added to **I,** 24.6 mg (0.044 mmols) of (Sc, SHf)-1, in 1 mL of chlorobenzene prechilled to -5 °C. In the flask 882 mg (244 eq) of 1,5-hexadiene was cooled, then 54.3 mg of **III** was added to the flask immediately followed by activated **I** and **II** turning a pale-yellow color. The reaction mixture was stirred for 24 hours at –5 °C before quenching with excess I_2 (280 mg). Solvent was removed in vacuo and passed through a silica column using hexanes. The solvent was then removed, and the isolated polymer was dried overnight (612 mg, 70.0 %) characterized by 1H NMR and ^{13}C NMR. The iodo-terminated (-)PMCP (577 mg) was then dissolved in minimal toluene (Tol) and added to a 50 mL Schlenk flask. NaN_3 (44.4 mg, 1.2 eq) was dissolved in 5 mL of DMF and added to the solution. The solution was then refluxed for 3 h at 120 °C. The resulting product was purified using a silica plug and dried (576 mg, 99.7 %) characterized by GPC, DSC, ^{1}H NMR and ^{13}C NMR. The resulting azido-terminated polymer (451 mg) was then dissolved in 15 mL of Et_2O and transferred into a round bottom flask under air sensitive techniques. A 3-neck round bottom flask was prepared with a condenser, addition funnel, and a septum for addition of $LiAlH_4$ and 10 mL of Et_2O at 0 °C under air sensitive technique. The polymer was then cannula transferred into the addition funnel and drop-wise added to the solution of $LiAlH_4$ and

Et_2O at 0 °C. The reaction was then allowed to stir for 24 h then refluxed at 60 °C for 1 h before quenching. The reaction was quenched with addition of Et_2O, then H_2O, then 15 % NaOH/ H_2O solution, and additional H_2O all at 0 °C. Finally, $MgSO_4$ was added, and the reaction was brough back to RT before running the solution through a vacuum filter using excess diethyl ether. The resulting filtered liquid was then pump down to dryness and run through a silica column and dried. To yield the amino terminated poly(methylene-1,3-cyclopentane) (389 mg, 86.3 %), $[\alpha]_D$ = -12.23.

General synthesis of amino-terminated poly(methylene-1,3-cyclopentane) (NH_2-(+)PMCP)

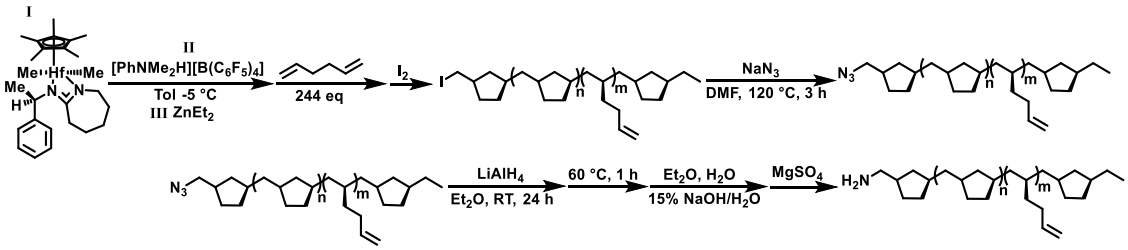

In a 25 mL round bottom, to a 5 mL toluene solution of 38.7 mg (0.048 mmols) of **II** chilled to -5 °C was added to **I**, 24.6 mg (0.044 mmols) of (Rc, RHf)-1, in 1 mL of chlorobenzene prechilled to -5 °C. In the flask 882 mg of 1,5-hexadiene was cooled, then 54.4 mg of **III** was added to the flask immediately followed by activated **I** and **II** turning a pale-yellow color. The reaction mixture was stirred for 24 h at – 5 °C before quenching with excess I_2 (282 mg) characterized by 1H NMR and 13C NMR. Solvent was removed in vacuo and passed through a silica column using hexanes. The solvent was then removed and the isolated polymer (606 mg, 68.7 %) was dried overnight. The iodo-terminated (+)PMCP (450 mg) was then dissolved in minimal toluene and added to a 50 mL Schlenk flask. NaN_3 (1.2 eq) was dissolved in 5 mL of DMF and added to

the solution. The solution was then refluxed for 3 h at 120 °C. The resulting product was purified using a silica plug and dried (431 mg, 96 %) characterized by GPC, DSC, and ^{1}H NMR and ^{13}C NMR. The resulting azido-terminated polymer (380 mg) was then dissolved in 15 mL of diethyl ether and transferred into a round bottom flask using air sensitive techniques. A 3-neck round bottom flask was prepared with a condenser, addition funnel, and a septum for addition of $LiAlH_4$ and 10 mL of Et_2O at 0 °C under air sensitive technique. The polymer was then cannula transferred into the addition funnel and drop-wise added to the solution of $LiAlH_4$ and Et2O at 0 °C. The reaction was then allowed to stir for 24 h then refluxed at 60 °C for 1 h before quenching. The reaction was quenched with addition ofEt_2O, then H_2O, then 15 % NaOH/ H_2O solution, and additional H_2O all at 0 °C. Finally, $MgSO_4$ was added, and the reaction was brough back to RT before running the solution through a filter paper rinsing with hexane and chloroform. The resulting filtered liquid was then pump down to dryness and run through a silica column and dried. To yield the amino terminated poly(methylene-1,3-cyclopentane) (334 mg, 88.0 %), $[\alpha]_D$ =+ 10.98.

General synthesis of amino-terminated *atactic* polydecene (NH_2-aPD)

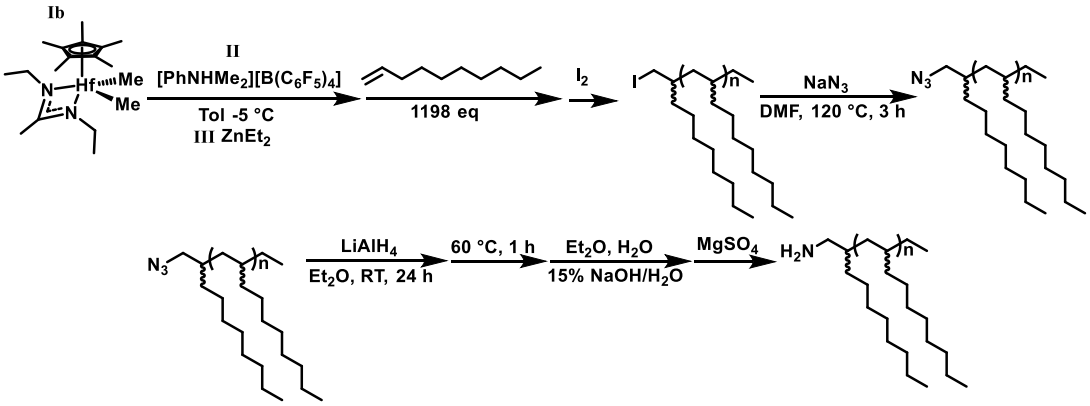

In a 100 mL round bottom, to a 40 mL toluene solution of 35.25 mg (0.044 mmols) of **II** chilled to 0 °C was added to **Ib**, 18.28 mg (0.04 mmols), in 1 mL of chlorobenzene prechilled to 0 °C. In the flask 6.7 g of 1-decene was cooled, then 296 mg of **III** was added to the flask immediately followed by activated **I** and **II** turning a yellow color. The reaction mixture was stirred for 24 h at 0 °C before quenching with excess I_2 (1.48 g) characterized by ^{1}H NMR and ^{13}C NMR. Solvent was removed in vacuo and passed through a silica column using hexanes. The solvent was then removed and the isolated polymer (5.06 g, 76 %) was dried overnight. The iodo-terminated aPD was then dissolved in minimal toluene and added to a 100 mL Schlenk flask. NaN_3 (1.2 eq) was dissolved in 5 mL of DMF and added to the solution. The solution was then refluxed for 3 h at 120 °C. The resulting product was purified using a silica plug and dried (3.38 g, 68 %) characterized by 1H NMR and 13C NMR. The resulting azido-terminated polymer (3.30 g) was then dissolved in 15 mL of diethyl ether and transferred into a round bottom flask using air sensitive techniques. A 3-neck round bottom flask was prepared with a condenser, addition funnel, and a septum for addition of $LiAlH_4$ and 10 mL of ET_2O at 0 °C under air sensitive technique. The polymer was then cannula

transferred into the addition funnel and drop-wise added to the solution of $LiAlH_4$ and Et_2O at 0 °C. The reaction was then allowed to stir for 24 h then refluxed at 60 °C for 1 h before quenching. The reaction was quenched with addition of Et_2O, then H_2O, then 15 % NaOH/ H_2O solution, and additional H_2O all at 0 °C. Finally, $MgSO_4$ was added, and the reaction was brough back to RT before running the solution through a filter paper rinsing with hexane and chloroform. The resulting filtered liquid was then pump down to dryness and run through a silica column and dried. To yield the amino terminated polydecene (2.24 g, 68 %).

General synthesis of amino-terminated *atactic* poly(1-octadecene) (NH_2-aPOD)

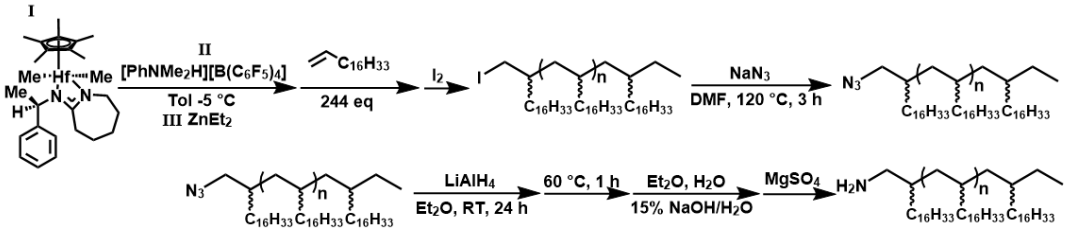

In a 100 mL round bottom, to a 20 mL toluene solution of 9.13 mg (0.02 mmols) of **II** chilled to 0 °C was added to **Ib**, 17.63 mg (0.022 mmols), in 1 mL of chlorobenzene prechilled to 0 °C. In the flask 5.2 g of 1-octadecene was cooled, then 160.55 mg of **III** was added to the flask immediately followed by activated **I** and **II** turning a yellow color. The reaction mixture was stirred for 24 h at 0 °C before quenching with excess I_2 (1.48 g) characterized by ^1H NMR and ^{13}C NMR. Solvent was removed in vacuo and passed through a silica column using hexanes. The solvent was then removed and the isolated polymer (5.2 g, 100 %) was dried overnight. The iodo-terminated aPOD was then dissolved in minimal toluene and added to a 100 mL Schlenk flask. NaN_3 (1.2 eq) was dissolved in 5 mL of DMF and added to the solution. The solution was then

refluxed for 3 h at 120 °C. The resulting product was purified using a silica plug and dried (5.1 g 98 %) characterized by ^{1}H NMR and ^{13}C NMR. The resulting azido-terminated polymer (4.5 g) was then dissolved in 15 mL of diethyl ether and transferred into a round bottom flask using air sensitive techniques. A 3-neck round bottom flask was prepared with a condenser, addition funnel, and a septum for addition of $LiAlH_4$ and 10 mL of Et_2O at 0 °C under air sensitive technique. The polymer was then cannula transferred into the addition funnel and drop-wise added to the solution of $LiAlH_4$ and Et_2O at 0 °C. The reaction was then allowed to stir for 24 h then refluxed at 60 °C for 1 h before quenching. The reaction was quenched with addition ofEt_2O, then H_2O, then 15 % NaOH/ H_2O solution, and additional H_2O all at 0 °C. Finally, $MgSO_4$ was added, and the reaction was brough back to RT before running the solution through a filter paper rinsing with hexane and chloroform. The resulting filtered liquid was then pump down to dryness and run through a silica column and dried. To yield the amino terminated poly(1-octadecene) (4.2 g, 68 %).

General procedure for perylene bisimide atactic polypropylene conjugate (aPP-PBI-aPP).

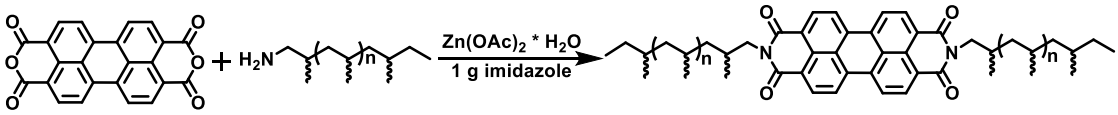

In 50 mL Schlenk flask amino-terminated atatctic polypropylene (267mg 0.267 mmol) was added with hexane then pumped down overnight. Using air sensitive technique Perylene-3,4,9,10-tetracarboxylic dianhydride (50.46 mg, 0.127 mmol) was added to the flask, then zinc acetate (23.2 mg, 0.127 mmol), then 1 gram of imidazole. The reaction mixture was brought to reflux at 160 °C for 24 hr. The reaction was then cooled

to RT and dissolved in minimal THF to poor into MeOH. The resulting red precipitate was filtered and washed with water and MeOH through vacuum filtration. The resulting product was dried then run through combi flash with 100 % dichloromethane (DCM) mobile phase (280 mg, 88.2 %).

General procedure for perylene bisimides (-) poly(methylene-1,3-cyclopentane) conjugate ((-)PMCP-PBI-(-)PMCP).

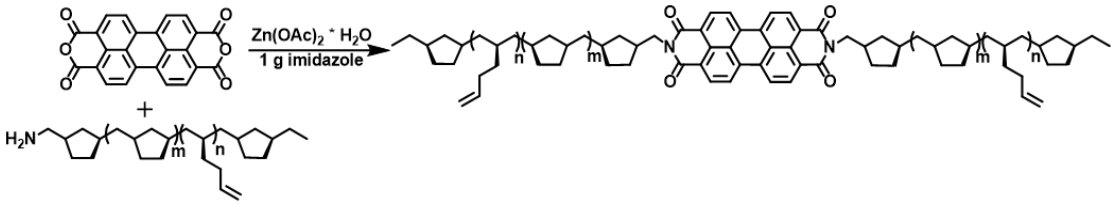

In 50 mL schlenk flask amino-terminated (-) poly(methylene-1, 3-cyclopentane) (170 mg, 0.170 mmol) was added with hexane then pumped down overnight. Using air sensitive technique Perylene-3,4,9,10-tetracarboxylic dianhydride (33.77 mg, 0.085 mmol) was added to the flask, then zinc acetate (16.6 mg, 0.085 mmol), then 1 gram of imidazole. The reaction mixture was brought to reflux at 160 °C for 24 hr. The reaction was then cooled to RT and dissolved in minimal THF to pore into MeOH. The resulting red precipitate was filtered and washed with water and MeOH. The resulting product was dried then run through combi flash with 100 % dichloromethane (DCM) mobile phase (178 mg, 87.3 %).

General procedure for perylene bisimides (+) poly(methylene-1,3-cyclopentane) (PBI-(+)PMCP).

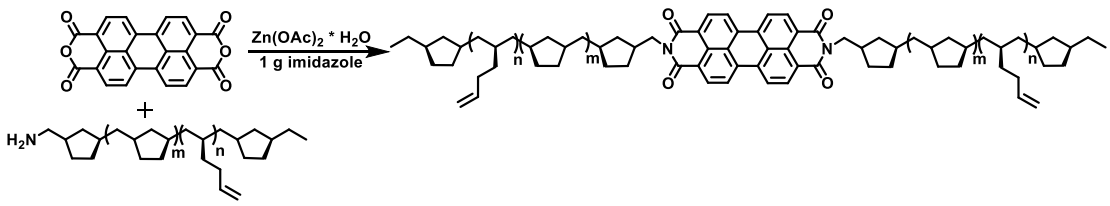

In 50 mL Schlenk flask amino-terminated (+) poly(methylene-1,3-cyclopentane) (280 mg 0.262 mmol) was added with hexane then pumped down for 6 h. Using air sensitive technique perylene-3,4,9,10-tetracarboxylic dianhydride (52.1 mg, 0.0131 mmol) was added to the flask, then zinc acetate (24.0 mg, 0.0131 mmol), then 1.20 gram of imidazole. The reaction mixture was brought to reflux at 130 °C for 24 h. The reaction was then cooled to RT and dissolved in minimal THF and hexane to pore into MeOH. The resulting red precipitate was filtered and washed with water and MeOH. The resulting product was dried then run through combi flash with 100 % dichloromethane (DCM) mobile phase (284 mg, 85.5 %).

General procedure for perylene bisimide atactic polydecene conjugate (aPD-PBI-aPD).

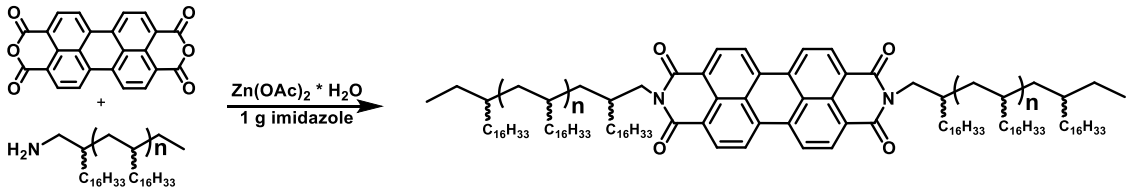

In 50 mL Schlenk tube amino-terminated polydecene (1.15 g, 0.700 mmol) was added with hexane then pumped down overnight. Using air sensitive technique Perylene-3,4,9,10-tetracarboxylic dianhydride (140 mg, 0.035 mmol) was added to the flask, then zinc acetate (64 mg, 0.035 mmol), then 1 gram of imidazole. The reaction mixture

was brought to reflux at 160 °C for 24 hr. The reaction was then cooled to RT and dissolved in minimal THF to pore into MeOH. The resulting red precipitate was filtered and washed with water and MeOH. The resulting product was dried then run through combi flash with 100 % dichloromethane (DCM) mobile phase. The resulting product was then dried and characterized by UV-vis, DSC, SAXS and ^{1}H NMR and ^{13}C NMR (958 mg, 87 %).

General procedure for perylene bisimide atactic poly(1-octadecene) conjugate (aPOD-PBI-aPOD).

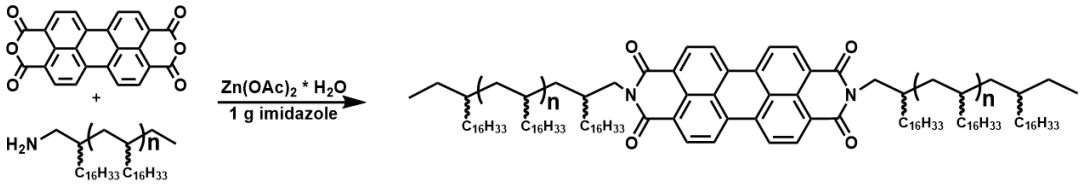

In 50 mL Schlenk tube amino-terminated polydecene (1.15 g, 0.700 mmol) was added with hexane then pumped down overnight. Using air sensitive technique Perylene-3,4,9,10-tetracarboxylic dianhydride (140 mg, 0.035 mmol) was added to the flask, then zinc acetate (64 mg, 0.035 mmol), then 1 gram of imidazole. The reaction mixture was brought to reflux at 160 °C for 24 hr. The reaction was then cooled to RT and dissolved in minimal THF to pore into MeOH. The resulting red precipitate was filtered and washed with water and MeOH. The resulting product was dried then run through combi flash with 100 % dichloromethane (DCM) mobile phase. The resulting product was then dried and characterized by UV-Vis, DSC, SAXS and ^{1}H NMR and ^{13}C NMR (958 mg, 87 %).

7.6.2 Characterization Parameters

Nuclear Magnetic Resonance (NMR) Spectroscopy of ^{1}H and ^{13}C nuclei was carried out with a Bruker AV 400 and Bruker DRX 600. Chloroform-*d1* was used as the solvent for samples. All spectra were referenced to tetramethyl silane using residual ^{1}H and ^{13}C chemical shifts of the deuterated solvents. $^{13}C\{^{1}H\}$ NMR assignments for the microstructures of poly(methylene-1,3-cyclopentance) (PMCP) were made according to previously reported assignments 1-2.

Gel Permeation Chromatography (GPC) was used to obtain molecular weight (Mn and Mw) and polydispersity index (PDI) of polymers using Viscotek GPCMax equipped with three columns (Styragel HR-4, HR-3, and HR-1) in a column oven and differential refractometer (maintained at 40 °C). Tetrahydrofuran (HPLC Grade) was used as the eluent with a flow rate of 1 mL/min. Polystyrene standards (from Polymer Laboratories Inc., 580 Da – 3,039 kDa) were used for calibration. For GPC sample preparation, 2 mg of dry polymer sample was dissolved in 1 mL of THF (HPLC Grade).

Differential scanning calorimetry (DSC) was used to obtain thermal transition (Tg and Mp) values using TA instruments DSC Q1000 system. Samples were run in sealed hermetical aluminum pans with an empty pan as reference. A heat/cool/heat temperature program was used at a flow rate of 10 °C/min at different specified temperature ranges. The initial mass of the sample was between 5 -10 mg.

UV-vis absorption (UV-vis) of samples were carried out with Agilent Technologies Cary 60 UV-vis in solution of methylcyclohexane or chloroform: methanol using volumetric glassware. The material was then put into a 1 cm cuvette and run-on fast speed with a baseline correction and a wavelength range of 200 nm – 1000 nm.

Fluorimeter was carried out on an Edinburgh FS-5 fluorimeter at 25 ± 1 °C. Materials were prepared in a volumetric flask and dissolved into methylcyclohexane solution and transferred into a 0.1 cm cuvette. Data collection was on fast speed with a baseline correction. All conjugates were excited at a λ_{exc} = 280 nm using 0.5 – 2.0 nm slit size using a low-pressure mercury lamp.

Circular Dichroism (CD) was carried out in-house Jasco J-810 spectropolarimeter with a wavelength range or 190-900nm, provided by a 150 W xenon arc lamp and a monochromator. Sample cell had a 1 cm path length. The instrument was equipped with a water bath to maintain a constant and uniform temperature of 23 °C.

Grazing Incident Small Angle X-ray Scattering (GISAXS) SAXS experiments were performed at the Complex Materials Scattering (CMS) 11-BM beamline of the National Synchrotron Light Source II at Brookhaven National Laboratory. The x-ray energy was set to 13.5 keV (x-ray wavelength 0.9184 Å) using a double multilayer monochromator. Beam size was adjusted to 200 µm horizontal by 50 µm vertical using a two-slit system. Beam flux at the sample position was approximately 5×1010 photons/s. Small-angle scattering was collected using a photo-counting pixel-array detector (Dectris Pilatus

2M, pixel size 172 μm) positioned 2.012 m downstream of the sample. Detector data was converted to reciprocal-space (q) by calibrating using measurements of a standard sample (silver behenate). We define qz to be the vertical (film normal) direction, and qx to be the orthogonal horizontal (in-plane) direction. Samples were measured under vacuum, using a typical exposure time of 10 s. GISAXS data was collected across a range of incident angles (0.08 ° to 0.20 °), with measurements both below and above the film critical angle. The critical angle was estimated to be 0.10 ° based on material makeup and density, which is consistent with the experimental position of the Yoneda scattering at small incident angle. A selection of samples was measured in grazing-incidence transmission (GTSAXS) geometry, where the beam is aligned with the downstream edge of the sample at a large incident angle (0.80°), allowing undistorted subhorizon scattering to exit from the substrate. Sample preparation of the conjugates were spun cast (2000 RPM) from toluene solution on carbon-coated silicon SI(100) chips. Film thickness were determined using Gaertner optical ellipsometer. Indexing of GISAXS data was performed by computing the 3D reciprocal-space positions of peaks for a candidate unit cell (at a candidate orientation), rotating peaks about the vertical (qz) to account for in-plane isotropy (in-plane powder), projecting these peaks onto the detector (accounting for Ewald sphere curvature, and applying GISAXS refraction corrections to shift the q peak positions.

Electron Paramagnetic Resonance (EPR) measurements were performed on a Bruker EMX EPR spectrometer at X-band frequency. The spectra were acquired at a modulation frequency of 100 kHz with a modulation amplitude of 1 G. Field-swept

spectra represent 4 scan averages collected over a 500 G sweep width centered at 3448 G, with receiver gain of 63 dB, time constant of 40.86 s, and sweep time of 10.486 s. Liquid samples were transferred to 1 mm OD glass capillary tubes. Film samples were transferred to 5 mm glass EPR tubes. These experiments were conducted by Lorelis Gonzalez-Lopez.

Small Angle X-ray Scattering (SAXS) For the synchrotron X-ray source, at Brookhaven National Lab, through the Center for Functional Nanomaterials (CFN) NSLS-II, BM-11 was used for SAX) analyses with energies ranging from 10-17 keV were delivered by a 3-pole wiggler source, with 10 sec exposure times, and an X-ray wavelength of 0.9184 Å. The samples were prepared in washers (1 cm total diameter) sealed with Kapton films. Data was collected using a photon-counting pixel-array detector positioned 2.00 m downstream of the sample.

Lab-scale small angle X-ray scattering (SAXS) was performed at the University of Maryland with Xenocs Xeuss SAXS/WAXS/GISAXS system, using CuKα X-rays with a wavelength of 1.5417 Å. Scattering was collected using a photoncounting pixel-array detector (Dectris Pilatus 2M, pixel size 172 μm) positioned 1.3 m downstream of the sample. Data were collected at an exposure time of 600 seconds per frame in which 10 frames were compiled for one image. The samples were prepared in washers (1 cm total diameter) sealed with Kapton films. Samples that were thermally annealed were done so in a Linkam stage that encapsulated the wafer. For both systems silver behenate (AgBN) was used as a reference sample to determine beam center and sample to

detector distance, and the detector data was converted to reciprocal-space (q) using AgBN the reference.

Atomic force microscopy (AFM) images were obtained using a Nanoscope IIIa Multimode AFM in tapping mode (ps-tm-AFM) equipped with silicon etched tip (Nanosensors: spring constant = 25-55 N/m, resonance frequency = 292 – 377 kHz) used in conjunction with Extender Electronics package (Veeco Inc., CA). Height and phase-shift data were recorded in parallel under ambient conditions. Thin films of the PBI conjugates were spun cast (2000 RPM) in toluene onto highly order graphite or silicon surface that was carbon coated. Film thickness was obtained using a Gaertner optical ellipsometer. The thin films were placed in vacuo at varied temperatures if annealed.

Electrochemically characterized by **cyclic voltammetry** (CV) and **differential pulse voltammetry** (DPV) in dichloromethane with tetrabutylammonium hexafluorophosphate (TBAHFP, 0.1 M) as supporting electrolyte on an *EC epsilon* potentiostat connected to a three-electrode single-compartment cell always degassed with argon. A glassy carbon disc electrode was used as working electrode, a platinum wire as counter electrode and Ag/AgCl reference electrode. The Ag/Ag^{+} reference electrode had a potential of – 0.051 V in DCM vs ferrocene/ferrocenium (Fc/Fc+) couple as an internal standard set to 0.00. The spectra were referenced using the ferrocene redox couple as an internal standard. All experiments were carried out under argon at 25 °C.

A 7 Tesla Quantum Design **Superconducting Quantum Interference Device** (SQUID) MPMS3 was used for all magnetometry data collection. Approximately 4.4 mg of (+)PMCP-PBI-(+)PMCP:Cobaltocene blend and 7.6 mg of aPP-PB1-aPP:Cobaltocene blend powder were added to small capsules. These capsules were then inserted into the MPMS for both susceptibility and field dependent measurements. Susceptibility measurements were performed from base temperature (2 K) to room temperature and then back down to base all at an applied field of 10,000 Oe. Field sweeps were performed from 0 T to 7 T, from 7 T to – 7 T, and then from -7 T back to 0 T. All magnetometry experiments were performed at the Quantum Materials Center at the University of Maryland. These measurements were conducted by Timothy J. Diethrich.

7.6.3 Supporting Results

A.

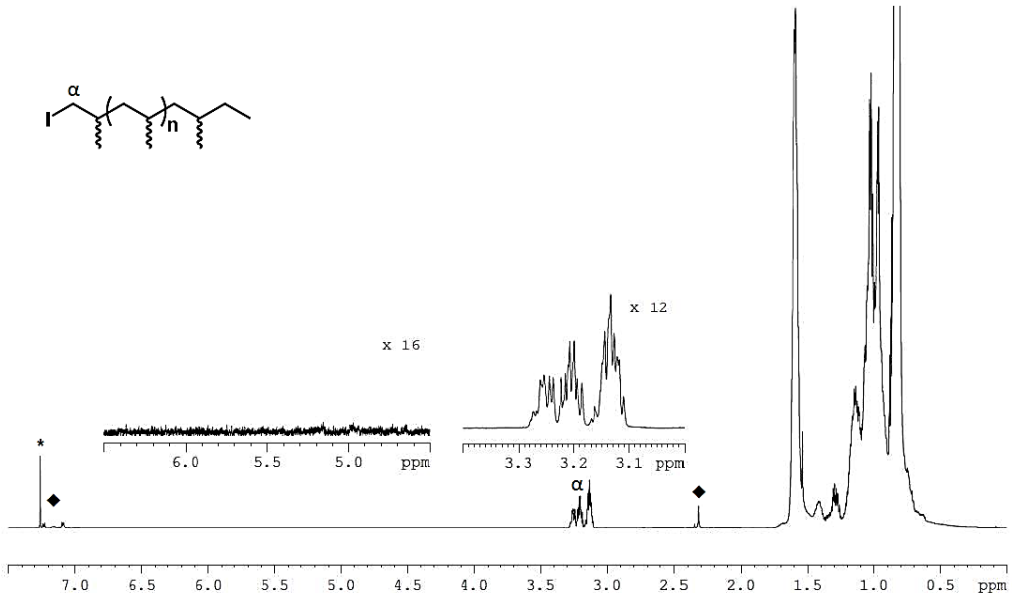

B.

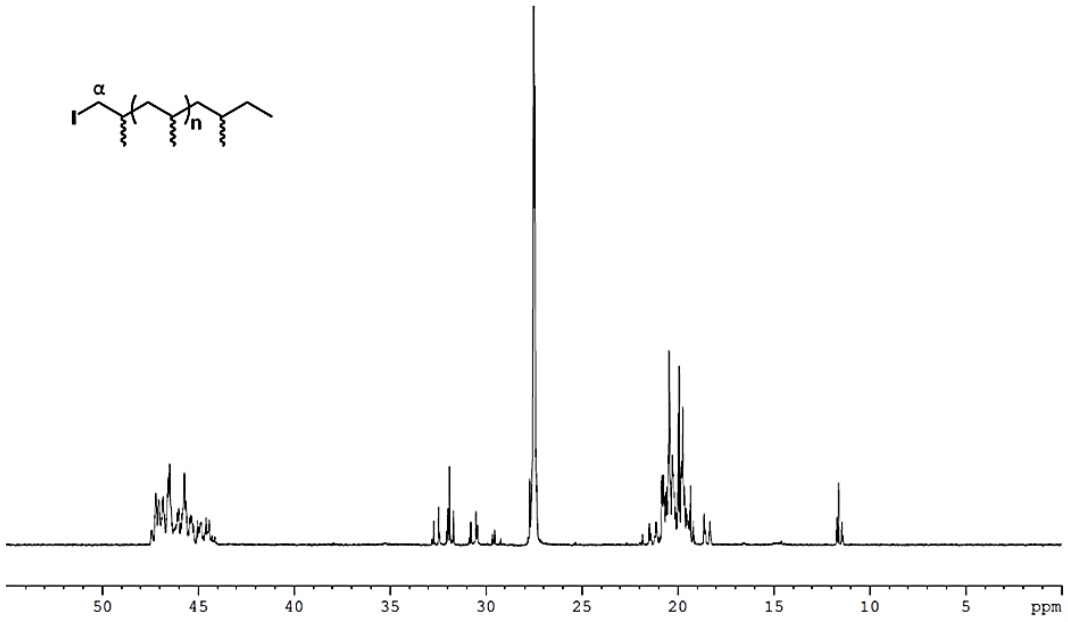

Figure S7.1. (**A**)^{1}H-NMR (600 MHz, *Chloroform-*d1*, ◆ toluene, RT) of I-aPP, donated from PPL, note the absence of vinylic peaks at 6-5 ppm. (**B)** partial ^{13}C-NMR (150 MHz, RT) of I-aPP.

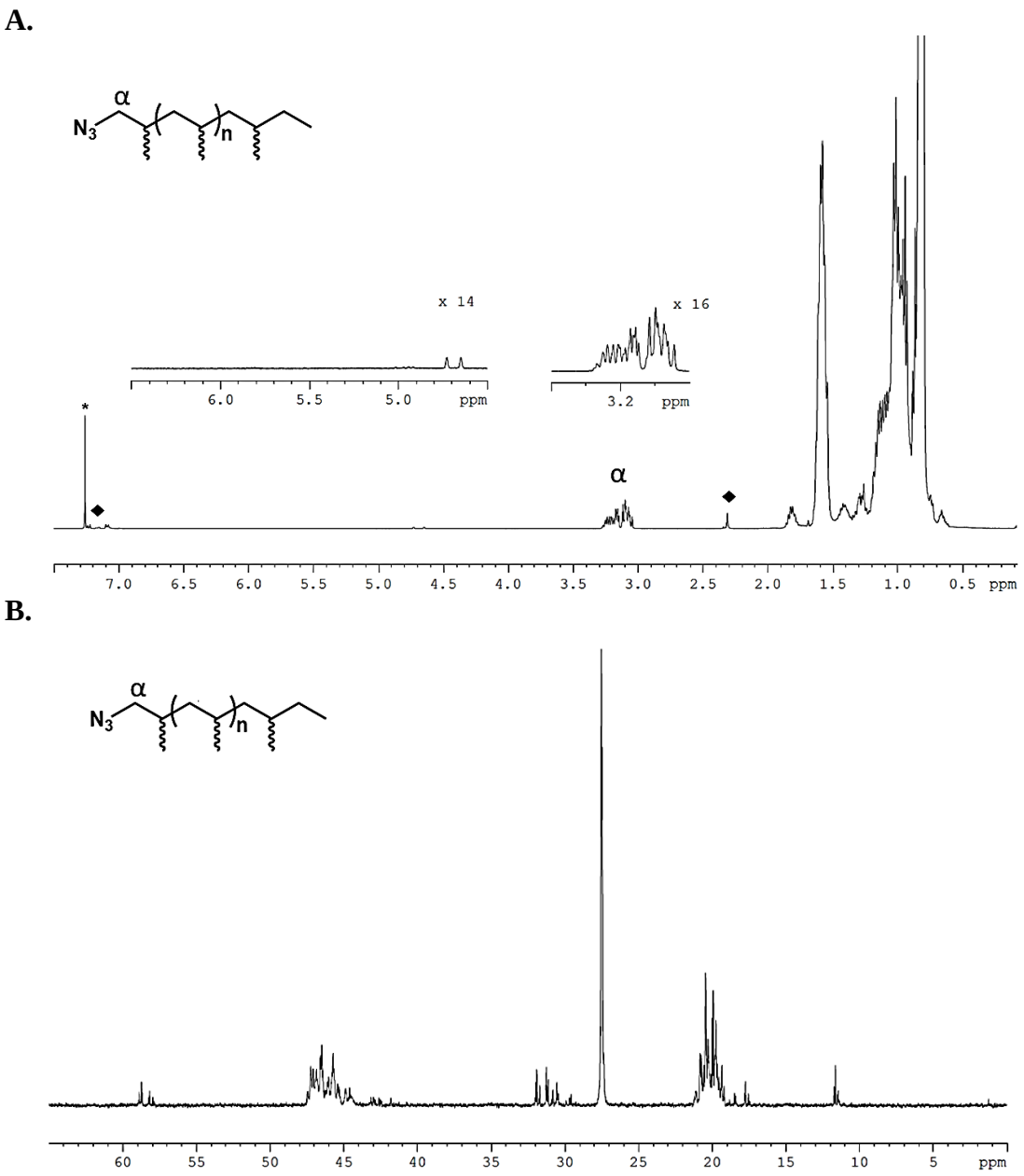

Figure S7.2. (A)^{1}H-NMR (600 MHz, *Chloroform-*d1*, ◆ toluene, RT) of N_3-aPP, note the presence of vinylic peaks for the elimination product. (B) partial ^{13}C-NMR (150 MHz, RT) of N_3-aPP.

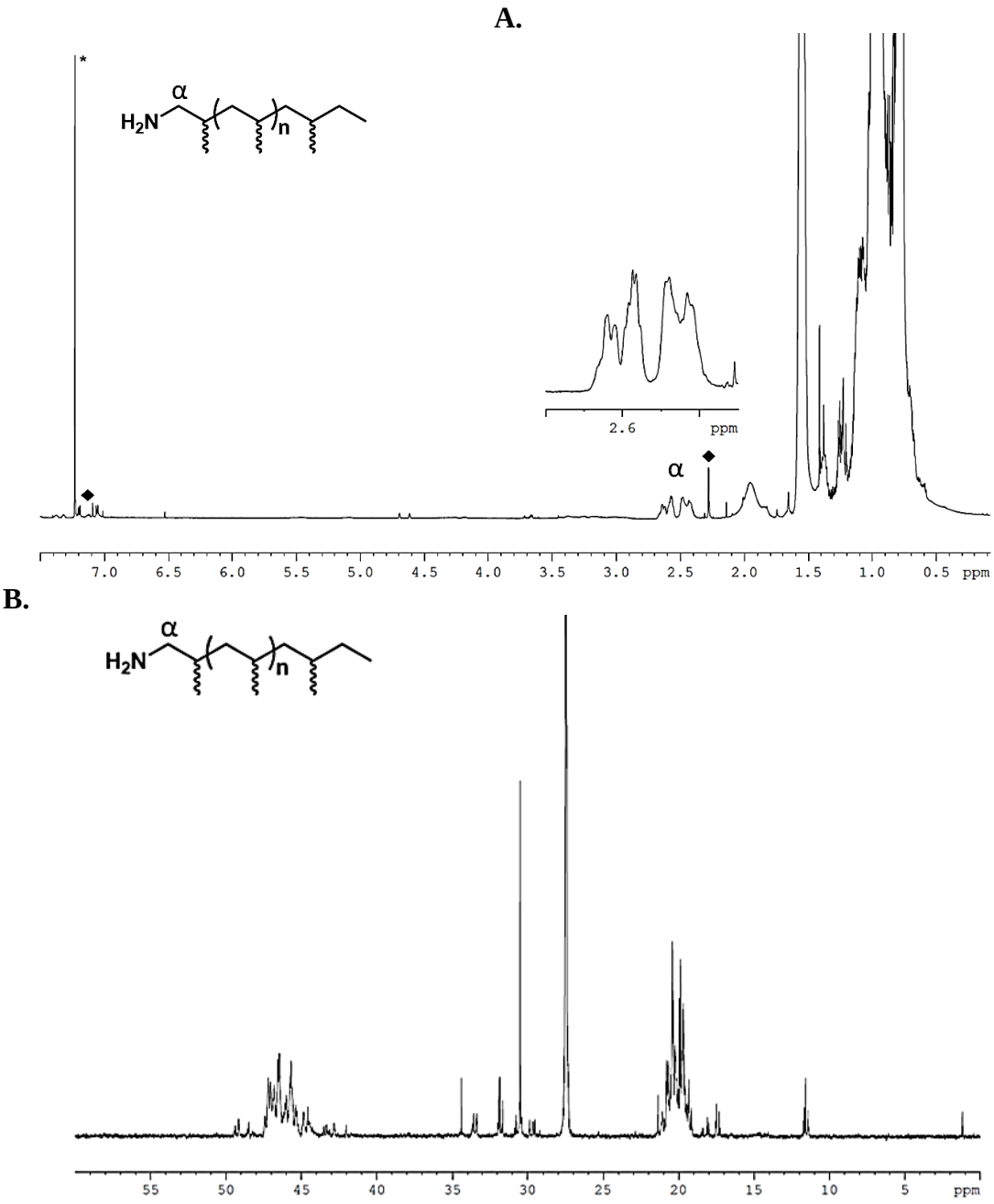

Figure. S7.3. (A)^{1}H-NMR (600 MHz, *Chloroform-*d1*, ◆ toluene, RT) of NH_2-aPP. (B) partial ^{13}C-NMR (150 MHz, *Chloroform-*d1*, RT) of NH_2-aPP.

A.

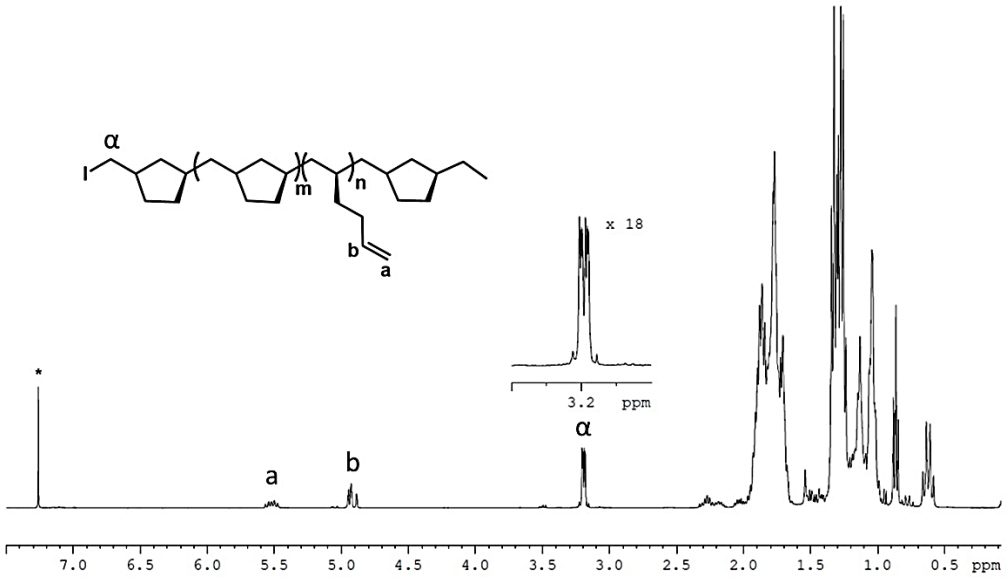

B.

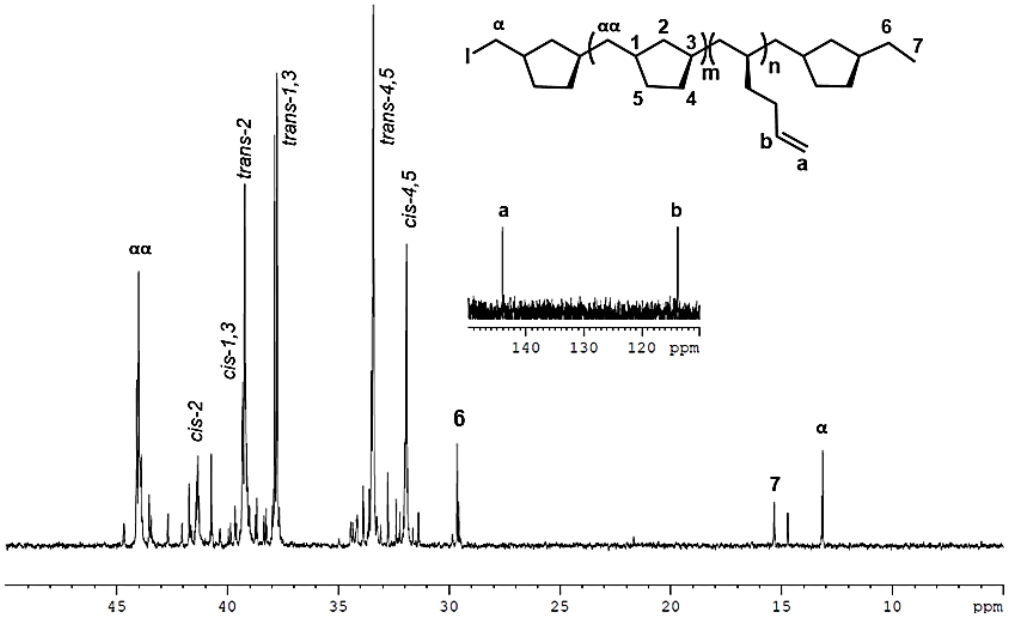

Figure S7.4. (A)^{1}H-NMR (400 MHz, *Chloroform-*d1*, RT) of I-(-)PMCP. (B) partial ^{13}C-NMR (100 MHz, *Chloroform-*d1*, RT) of I-(-)PMCP.

A.

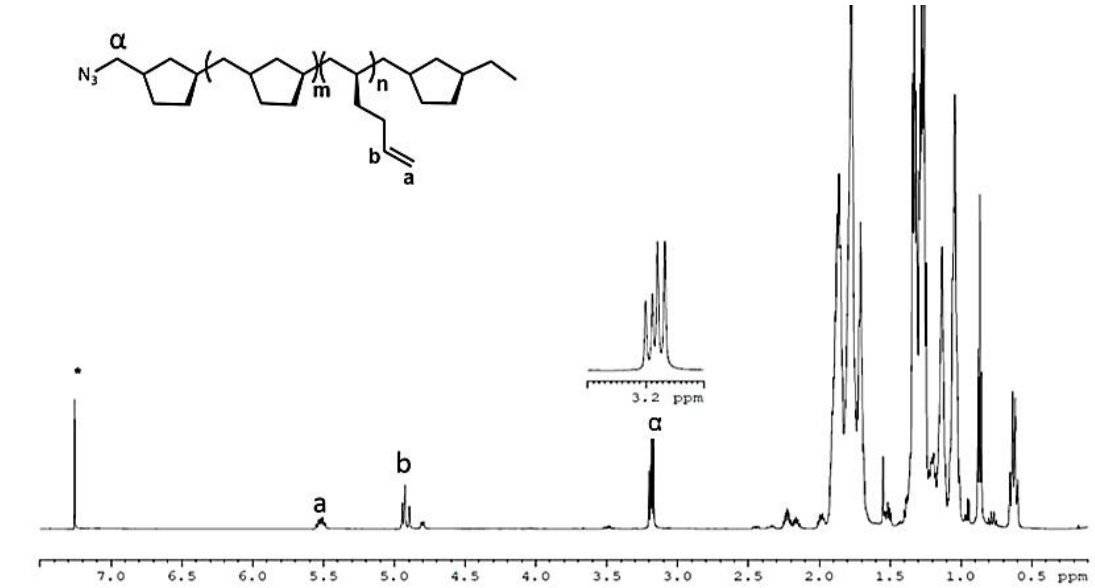

B.

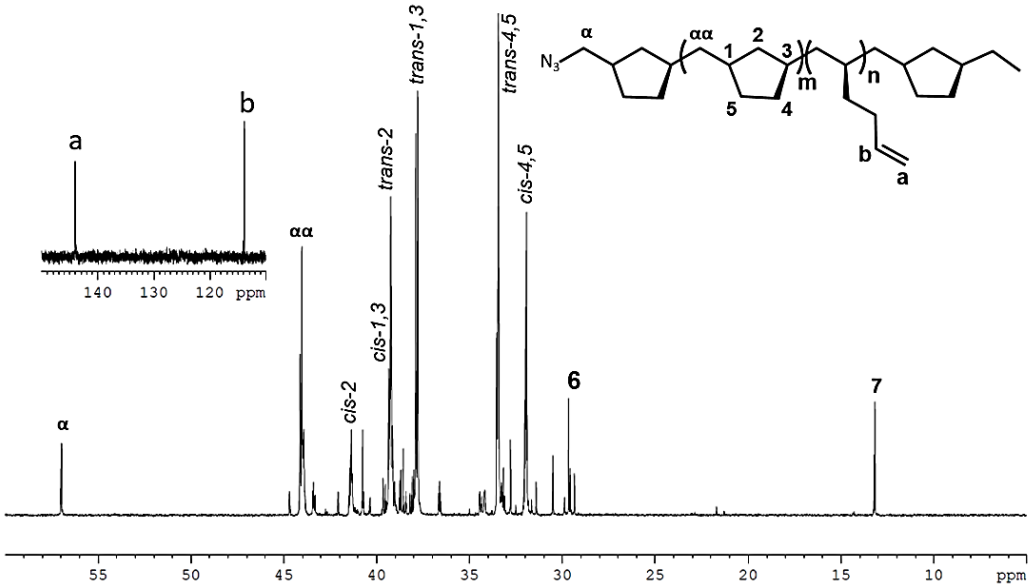

Figure S7.5. (A) ^{1}H-NMR (600 MHz, *Chloroform-*d1*, RT) of N_3-(-)PMCP. (B) partial ^{13}C-NMR (150 MHz, *Chloroform-*d1*, RT) of N_3-(-)PMCP.

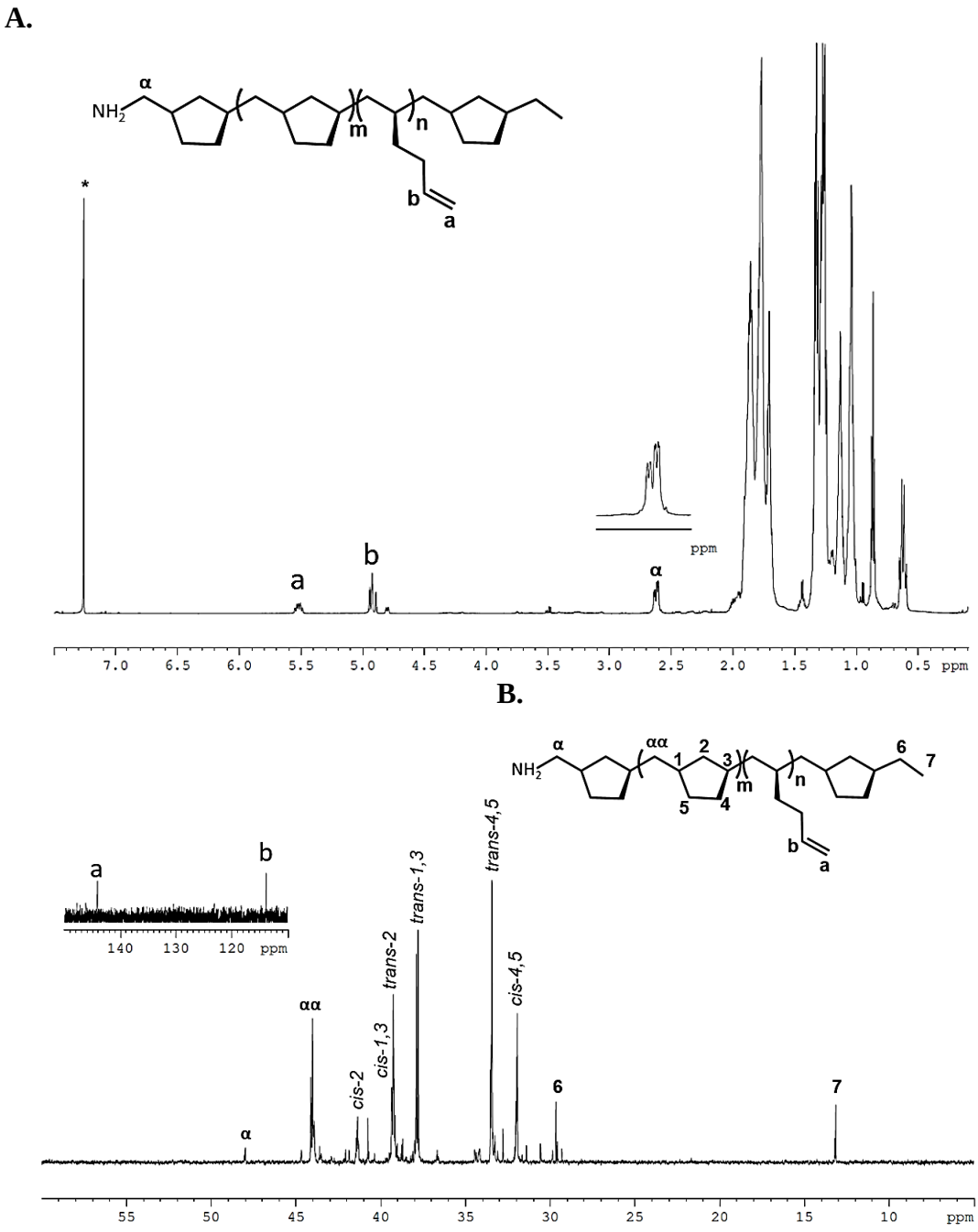

Figure S7.6. (A)^{1}H-NMR (600 MHz, *Chloroform-*d1*, RT) of NH_2-(-)PMCP. (B) partial ^{13}C-NMR (150 MHz, *Chloroform-*d1*, RT) of NH_2-(-)PMCP.

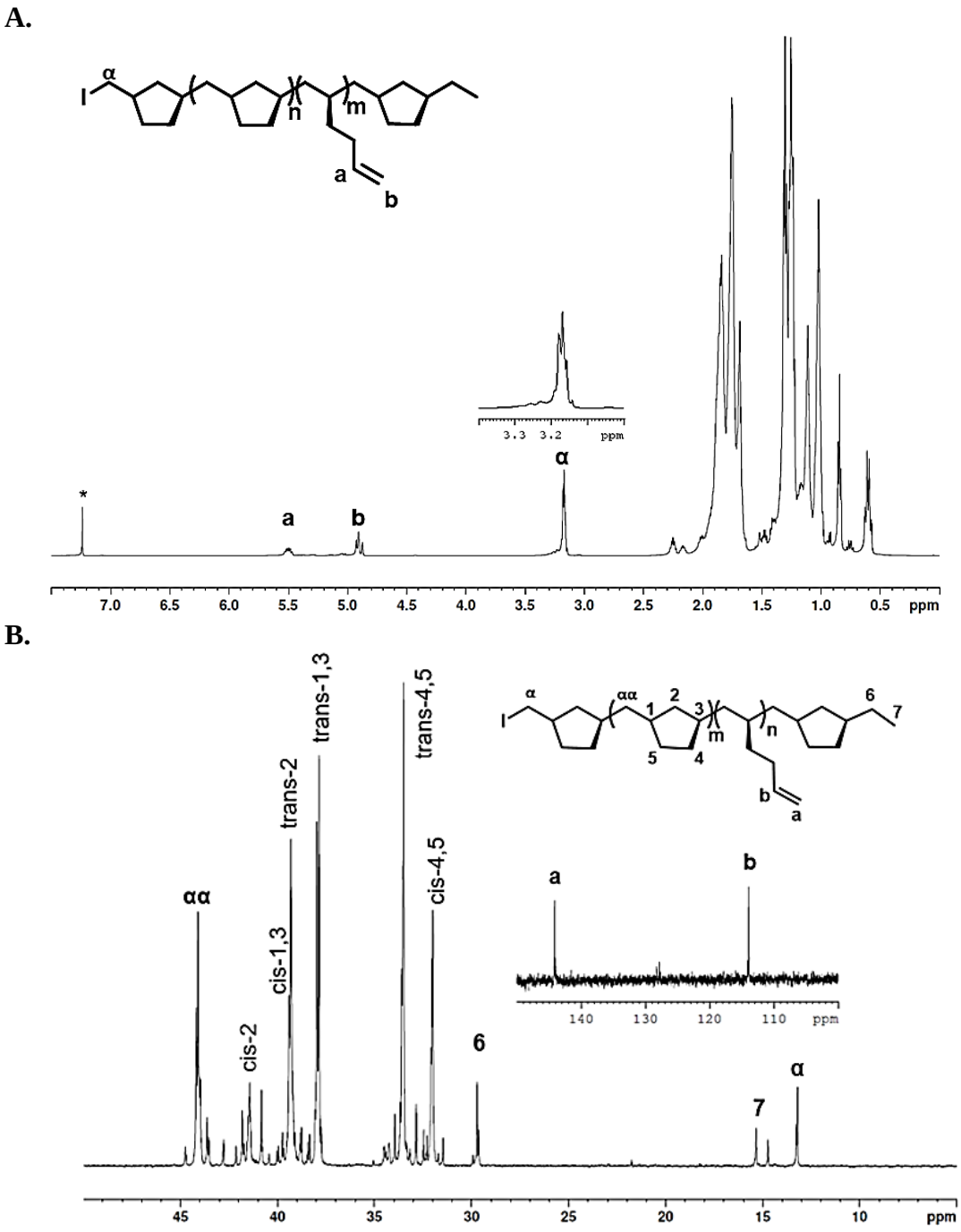

Figure S7.7. (**A**)[1]H-NMR (600 MHz, *Chloroform-*d1*, RT) of I-(+)PMCP. (**B**) partial [13]C-NMR (150 MHz, *Chloroform-*d1*, RT) of I-(+)PMCP.

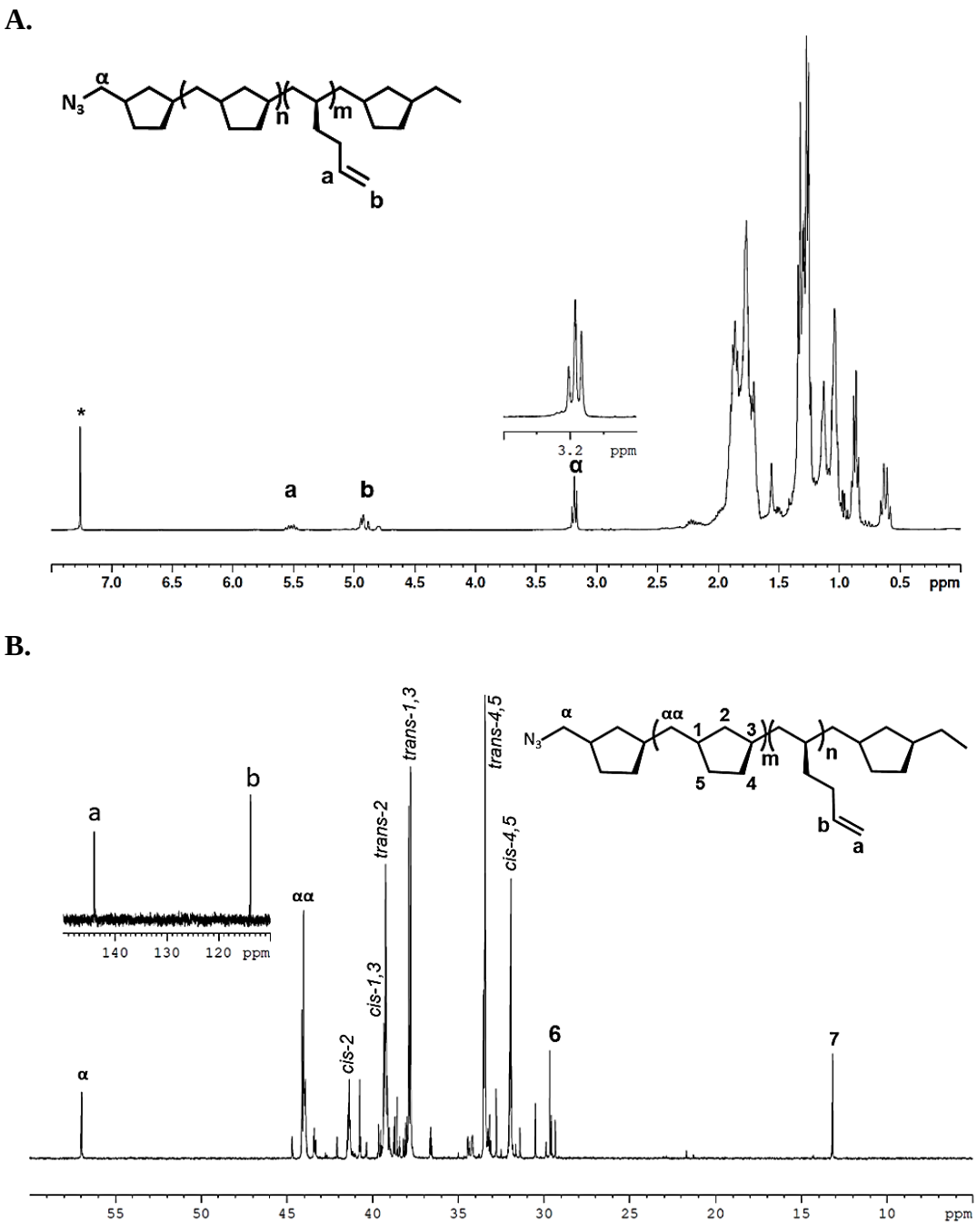

Figure S7.8. (A) ^{1}H-NMR (600 MHz, *Chloroform-*d1*, RT) of N_3-(+)PMCP. (B) partial ^{13}C-NMR (150 MHz, *Chloroform-*d1*, RT) of N_3-(+)PMCP.

A.

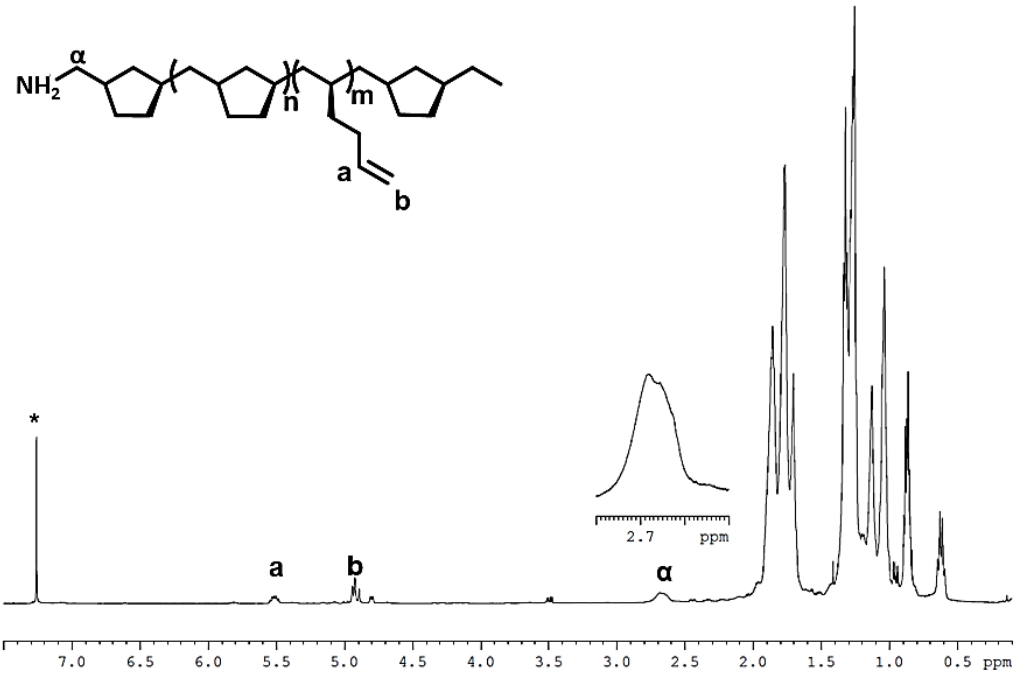

B.

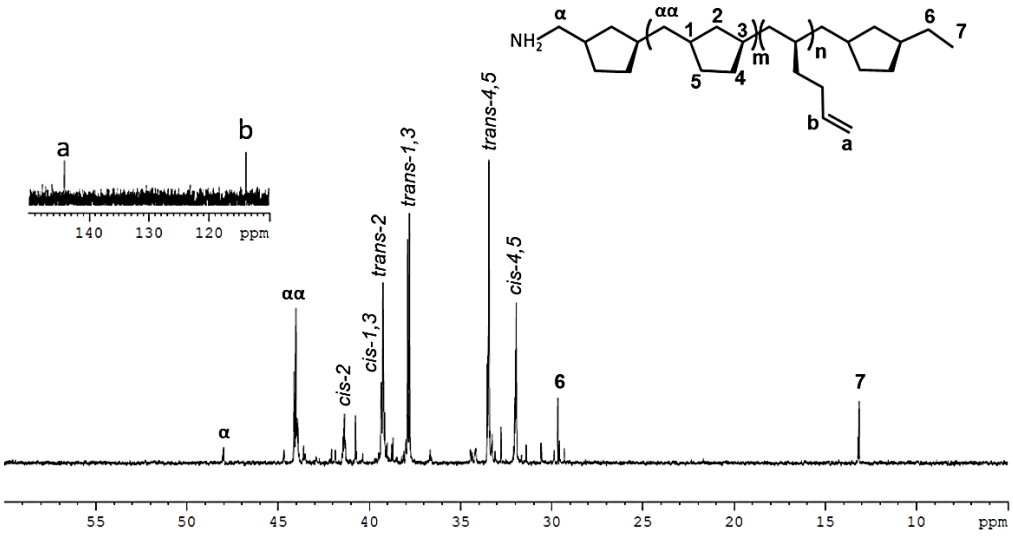

Figure S7.9. (A)^{1}H-NMR (600 MHz, *Chloroform-*d1*, RT) of NH_2-(+)PMCP. (B) partial ^{13}C-NMR (150 MHz, *Chloroform-*d1*, RT) of NH_2-(+)PMCP.

A.

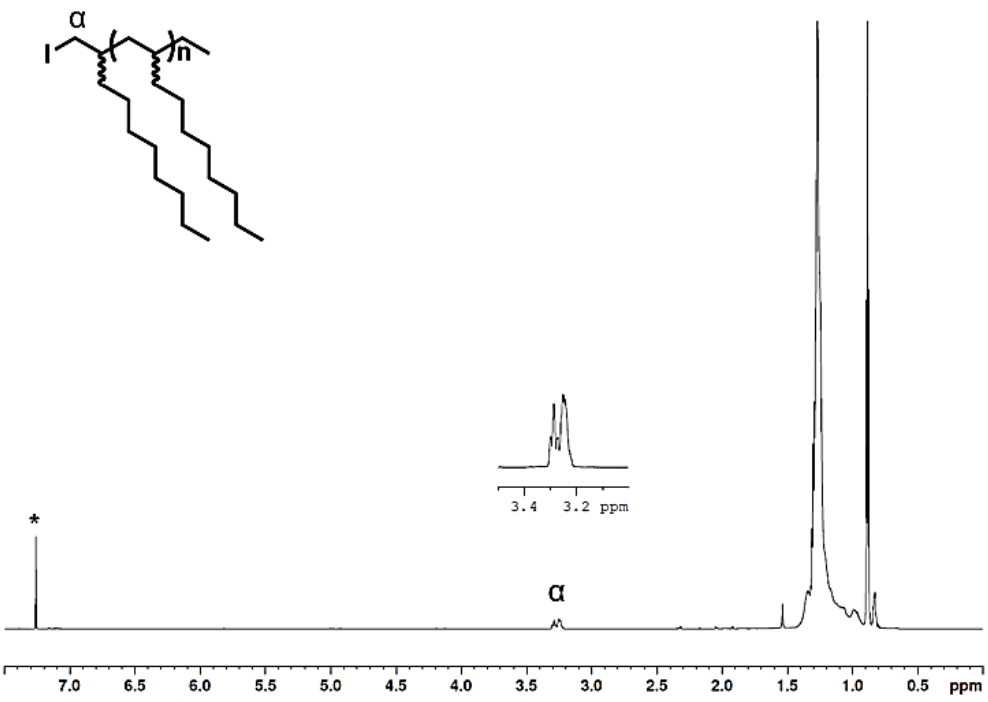

B.

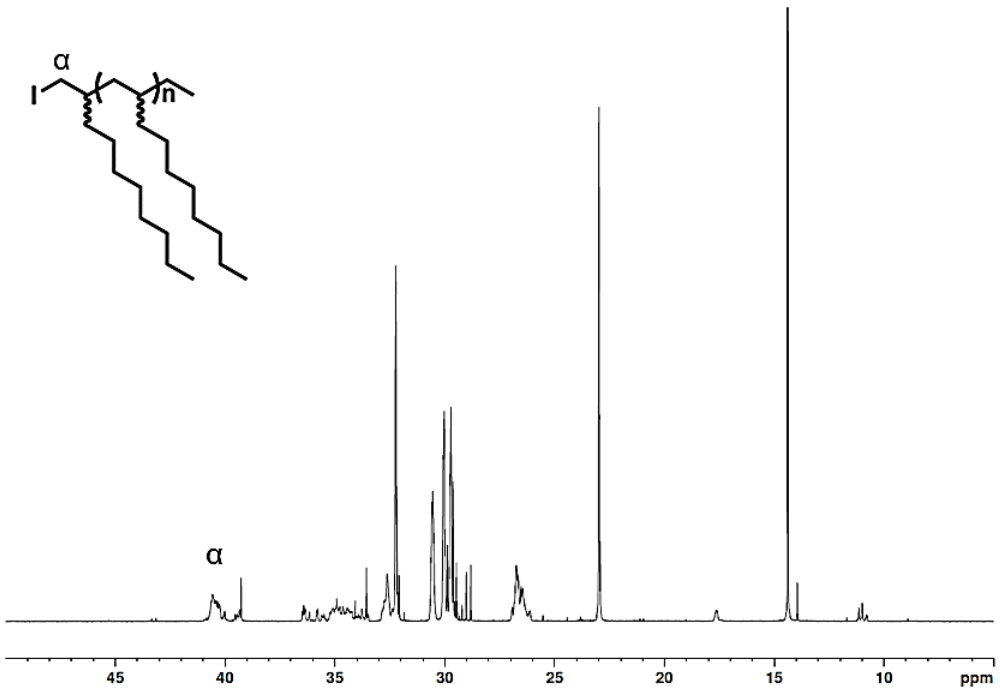

Figure S7.10. (A)^{1}H-NMR (600 MHz, *Chloroform-*d1*, RT) of I-aPD**.** (B) partial ^{13}C-NMR (150 MHz, *Chloroform-*d1*, RT) of I-aPD.

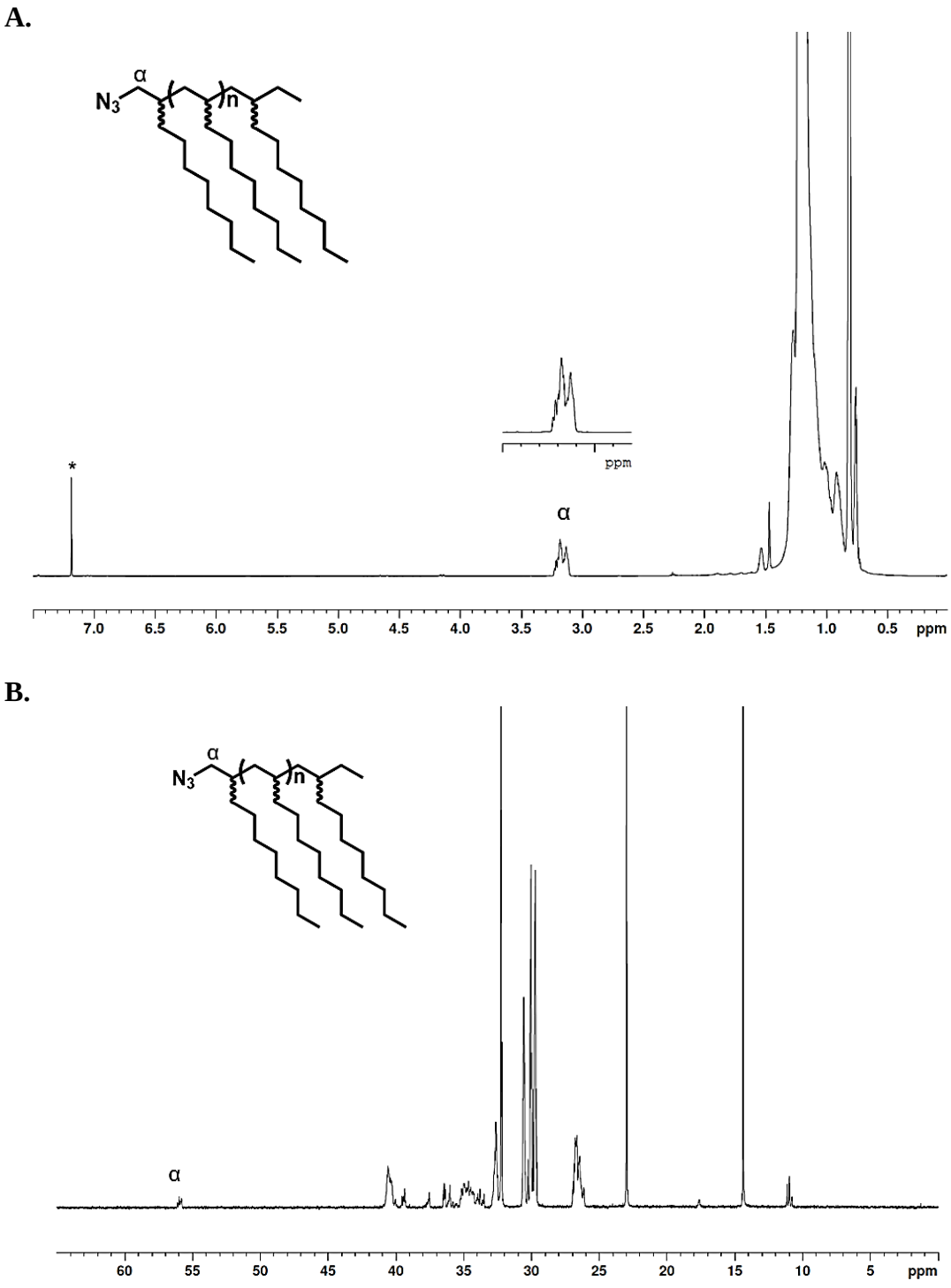

Figure S7.11. (A)^{1}H-NMR (800 MHz, *Chloroform-*d1*, RT) of N_3-aPD. (B) partial ^{13}C-NMR (200 MHz, *Chloroform-*d1*, RT) of N_3-aPD.

A.

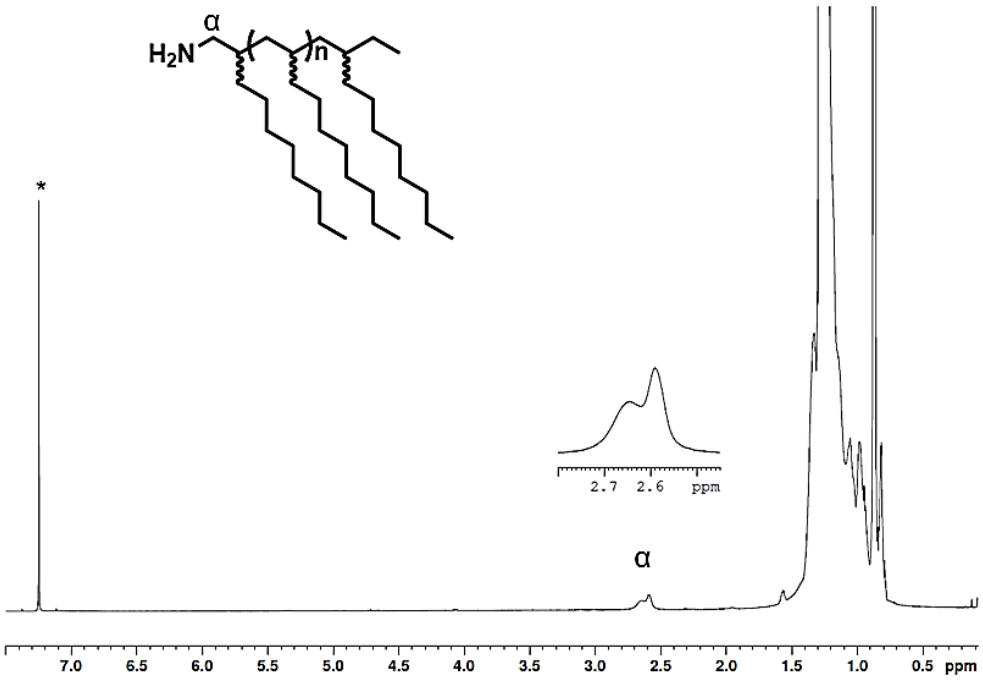

B.

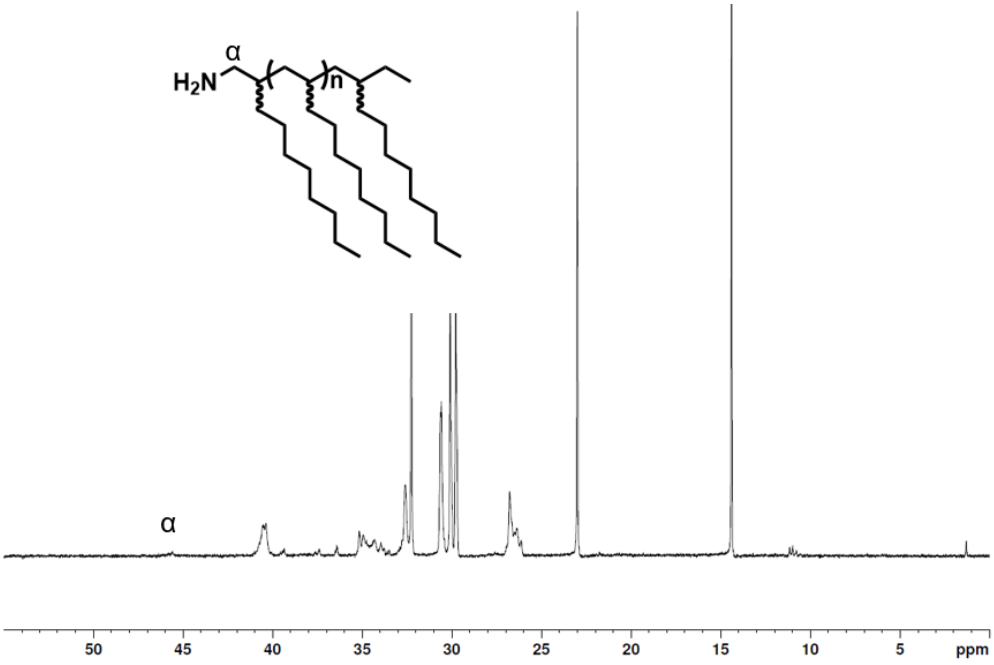

Figure S7.12. (A)^{1}H-NMR (800 MHz, *Chloroform-*d1*, RT) of NH_2-aPD**.** (B) partial ^{13}C-NMR (200 MHz, *Chloroform-*d1*, RT) of NH_2-aPD.

A.

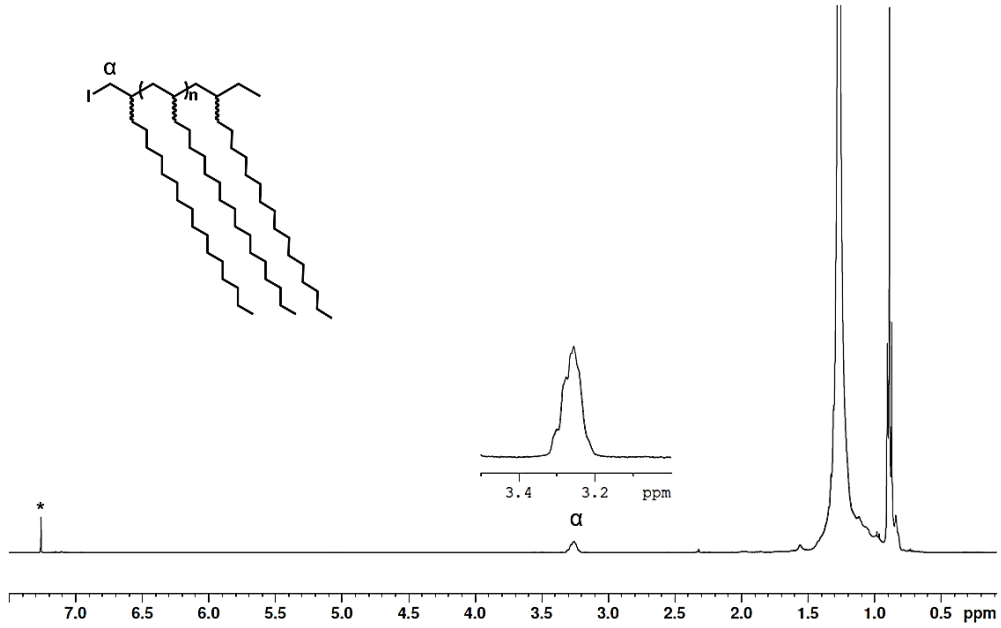

B.

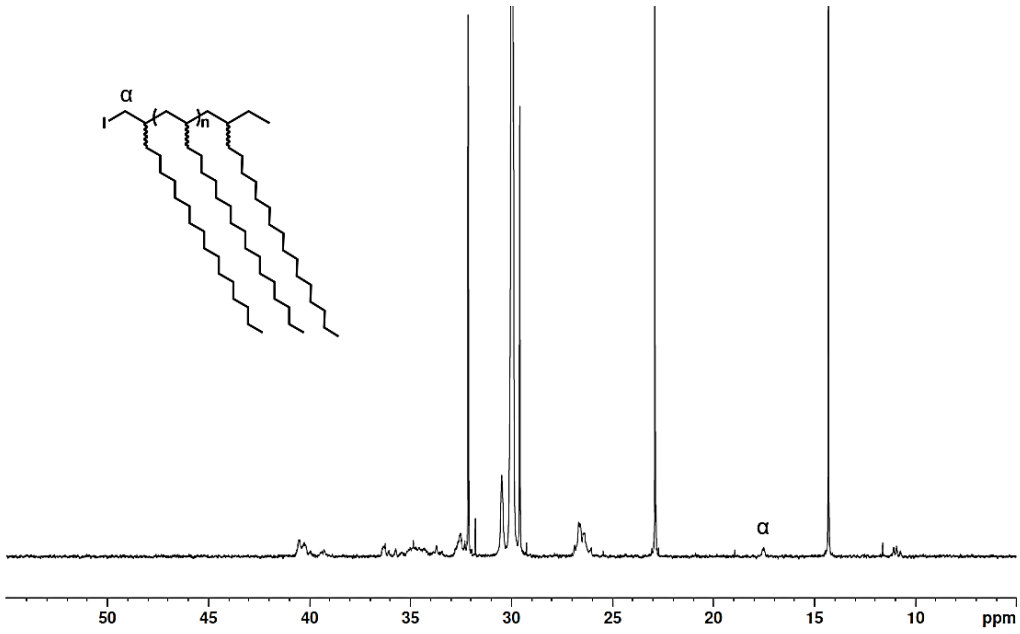

Figure S7.13. (A)^{1}H-NMR (600 MHz, *Chloroform-*d1*, RT) of I-aPOD. (B) partial ^{13}C-NMR (150 MHz, *Chloroform-*d1*, RT) of I-aPOD.

A.

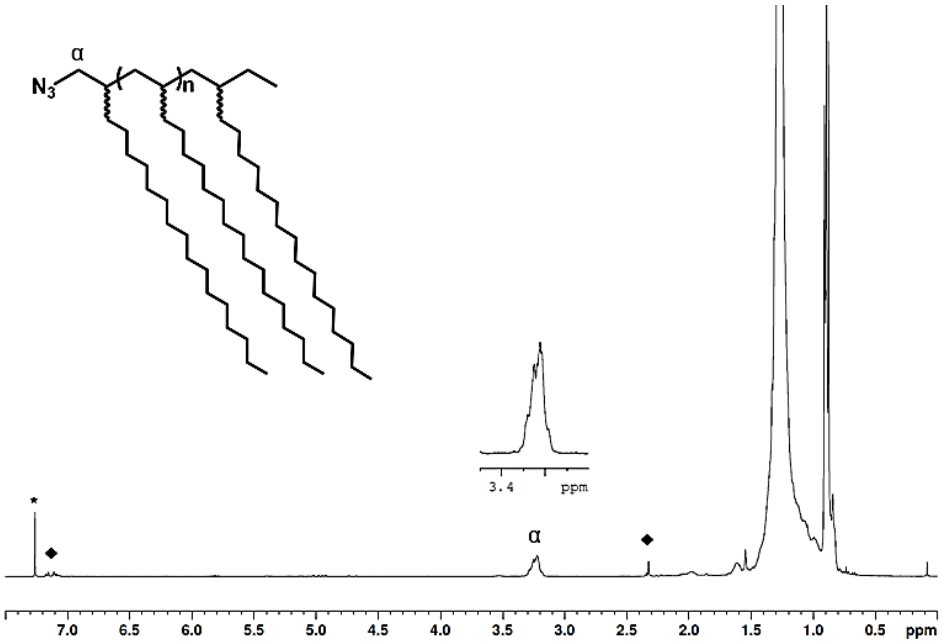

B.

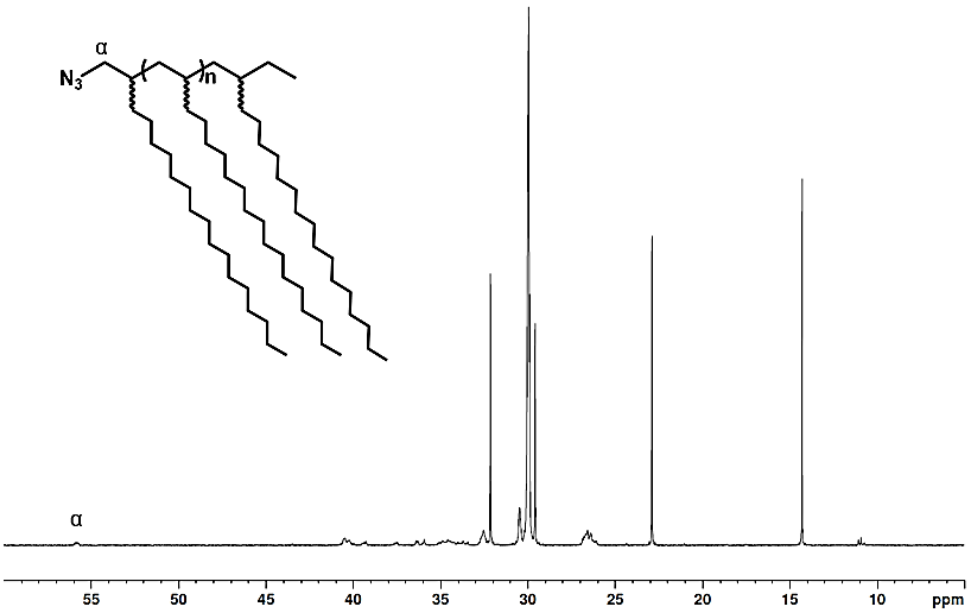

Figure S7.14. (A)^{1}H-NMR (600 MHz, *Chloroform-*d1*, ◆ toluene, RT) of N_3-aPOD (B) partial ^{13}C-NMR (150 MHz, *Chloroform-*d1*, RT) of N_3-aPOD.

A.

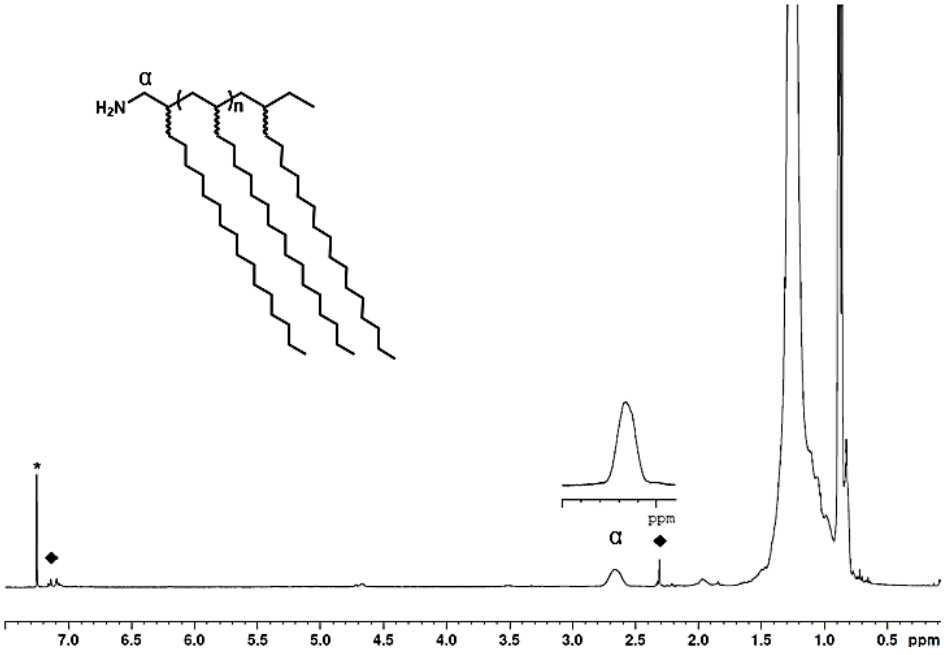

B.

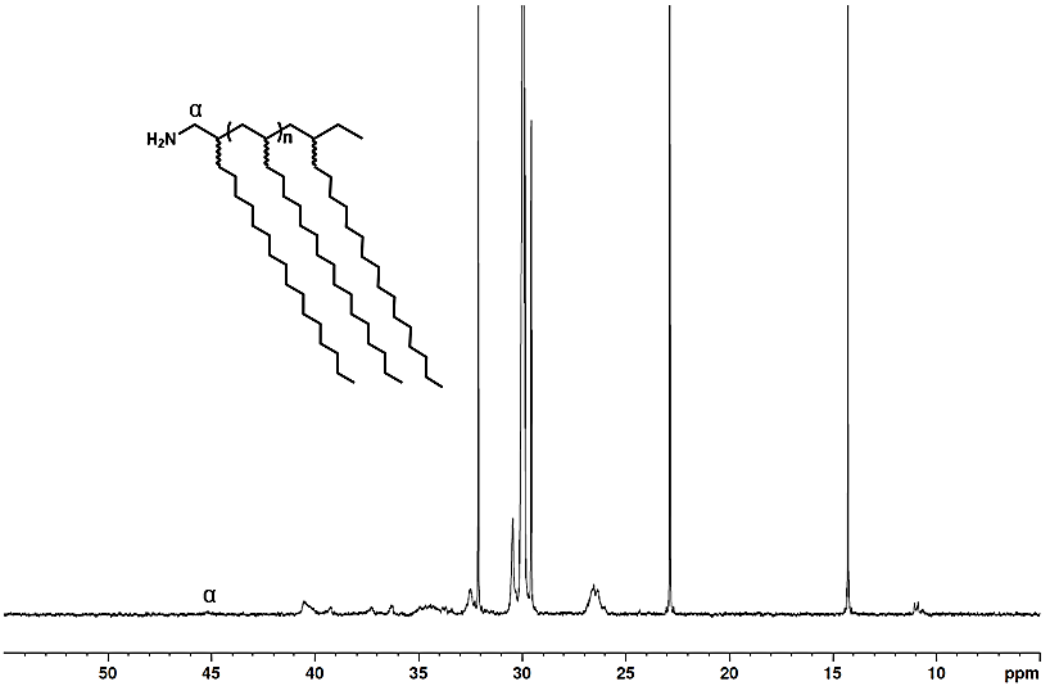

Figure S7.15. (A)^{1}H-NMR (600 MHz, *Chloroform-*d1*, ◆ toluene, RT) of NH_2-aPOD**.** (B) partial ^{13}C-NMR (150 MHz, *Chloroform-*d1*, RT) of NH_2-aPOD.

A.

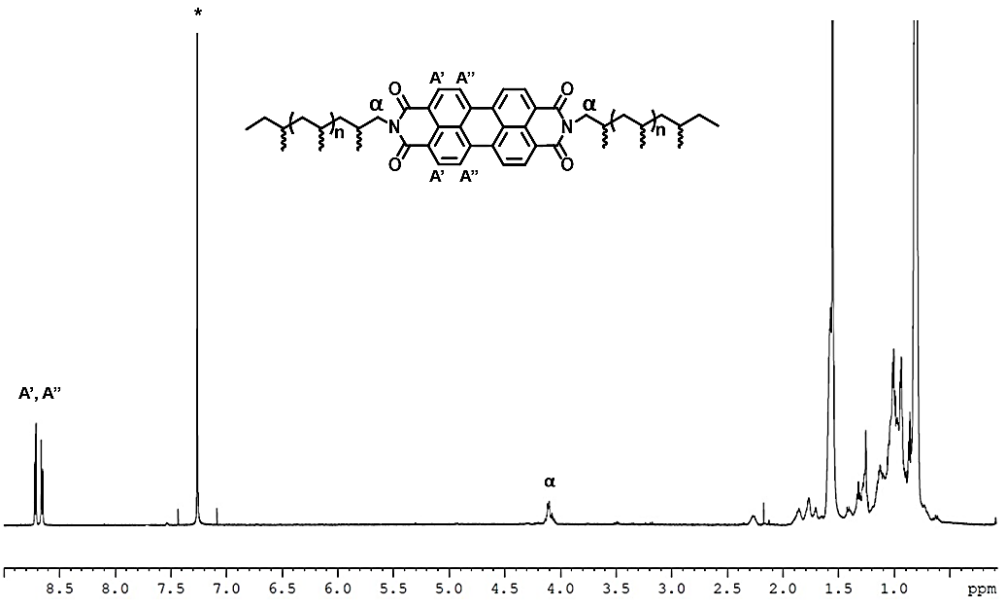

B.

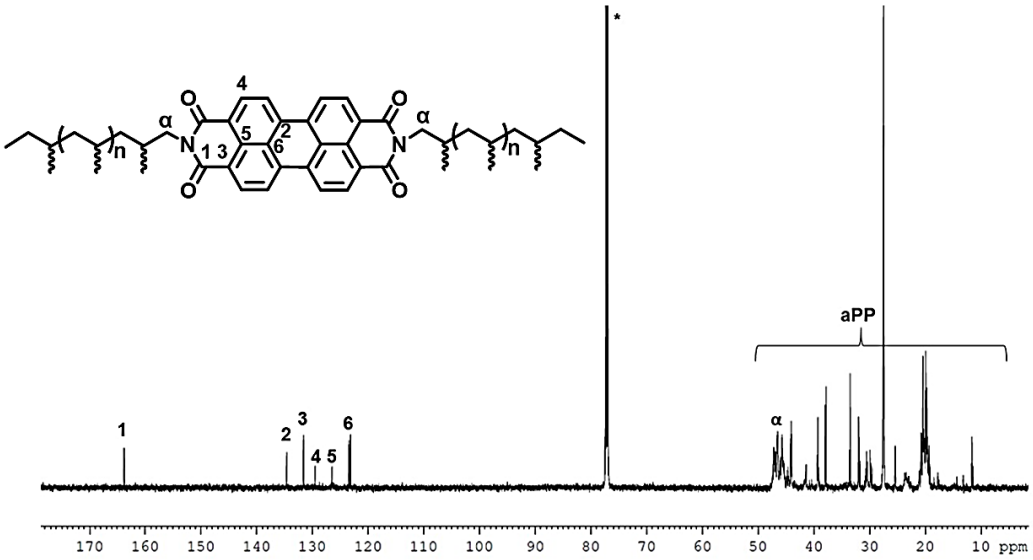

Figure S7.16. (A) ^{1}H NMR (600 MHz. *Chloroform-*d1*, RT) of aPP-PBI-aPP. (B) Partial ^{13}C-NMR (600 MHz, *Chloroform-*d1*) of aPP-PBI-aPP.

A.

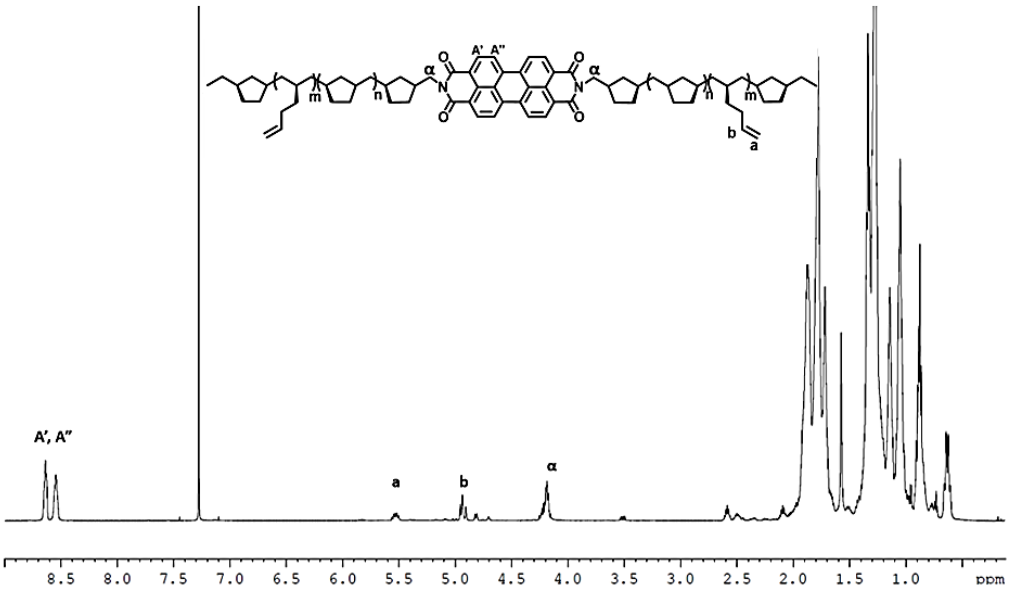

B.

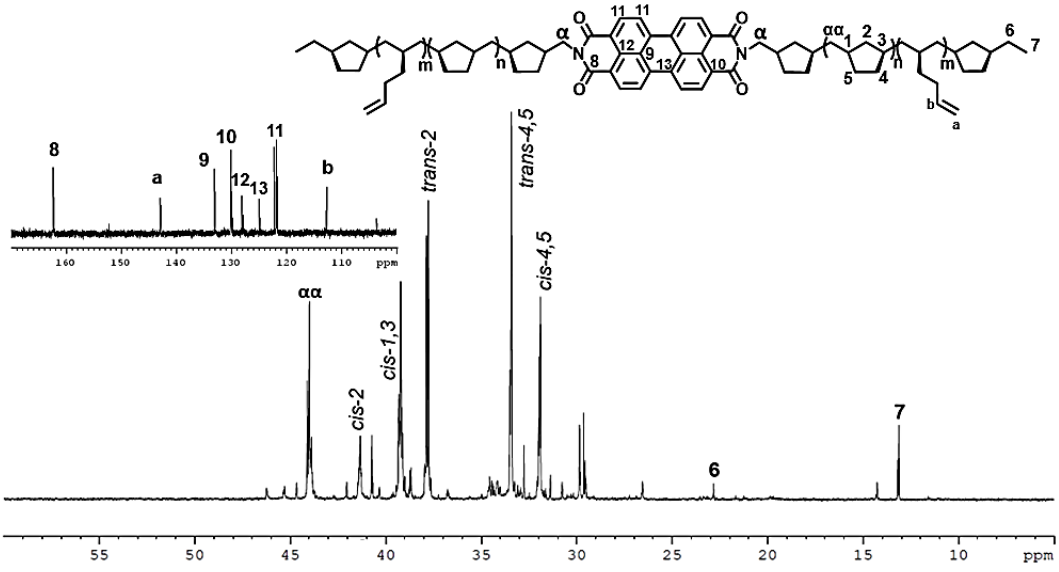

Figure S7.17. (A) ^{1}H NMR (600 MHz. *Chloroform-*d1*, RT) of (+)PMCP-PBI-(+)PMCP. (B) Partial ^{13}C-NMR (600 MHz, *Chloroform-*d1*) of (+)PMCP-PBI-(+)PMCP.

A.

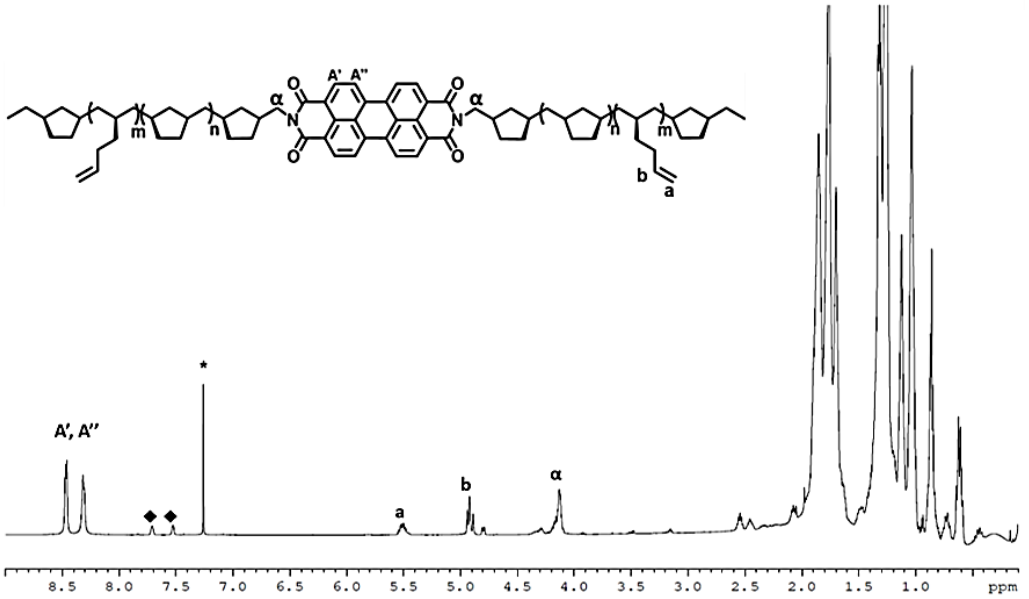

B.

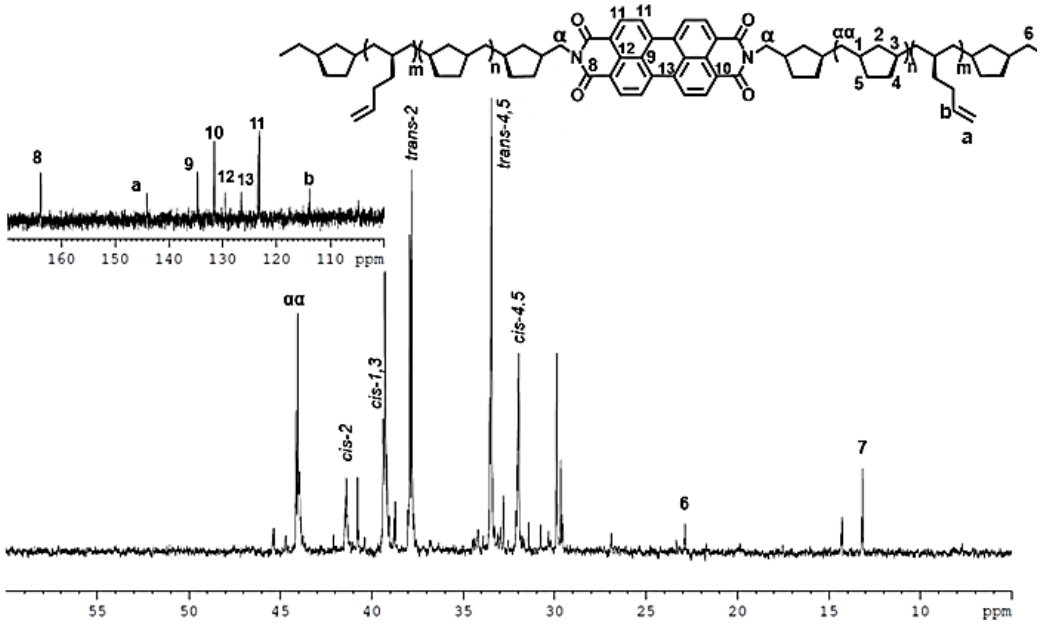

Figure S7.18. (A) ^{1}H NMR (600 MHz. *Chloroform- *d1*, ◆ show degradation peaks due to light exposure, RT) of (-)PMCP-PBI-(-)PMCP. (B) Partial ^{13}C-NMR (150 MHz, *Chloroform- *d1*) of (-)PMCP-PBI-(-)PMCP.

Molecular Weight (Da)

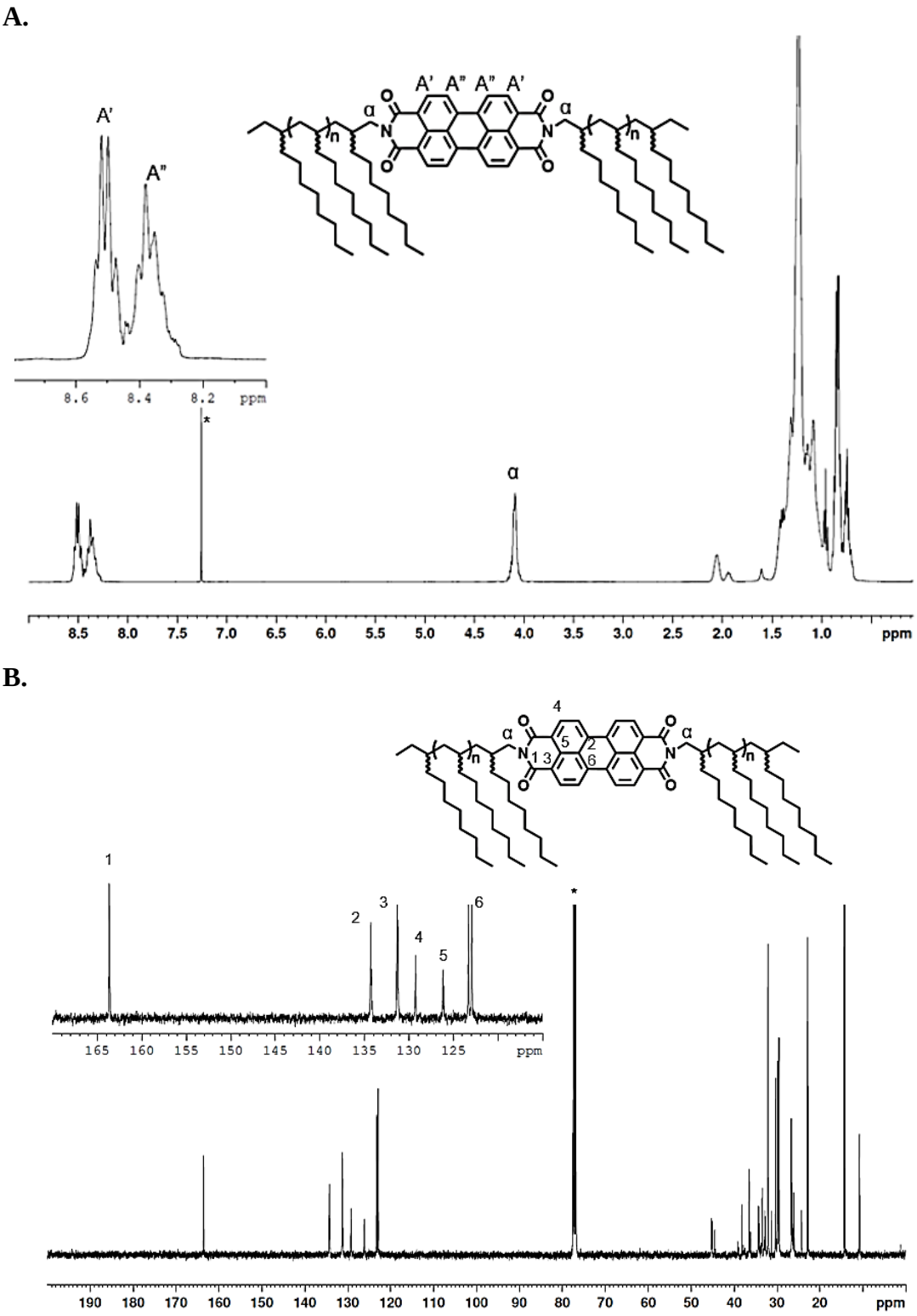

Figure S7.19. (A) ^{1}H NMR (600 MHz. *Chloroform- *d1*, RT) of aPD-PBI-aPD. (B) Partial ^{13}C-NMR (150 MHz, *Chloroform- *d1*) of aPD-PBI-aPD.

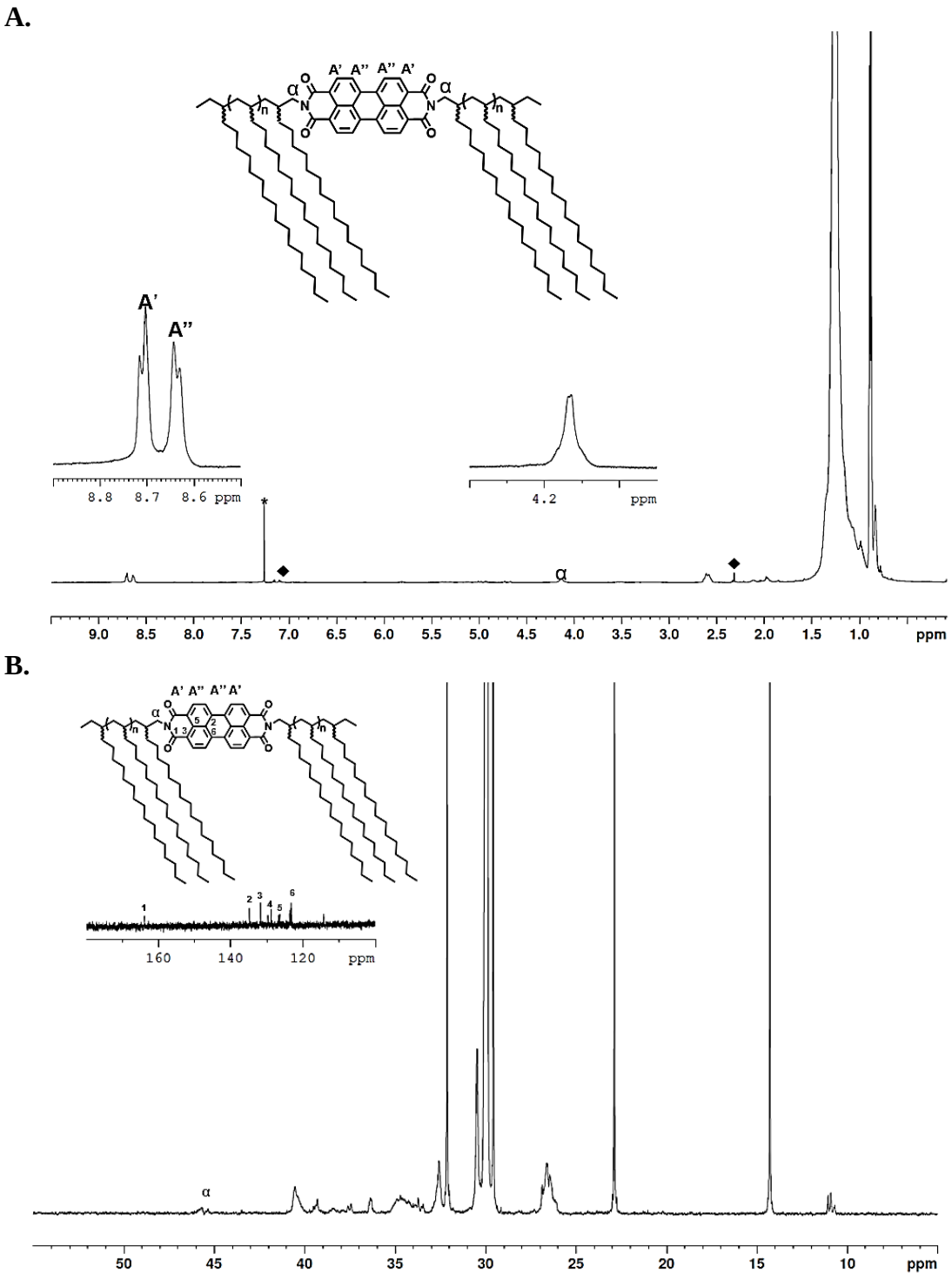

Figure S7.20. (A) ^{1}H NMR (600 MHz. *Chloroform-*d1*, RT) of aPOD-PBI-aPOD. (B) Partial ^{13}C-NMR (150 MHz, *Chloroform-*d1*) of aPOD-PBI-aPOD.

A.

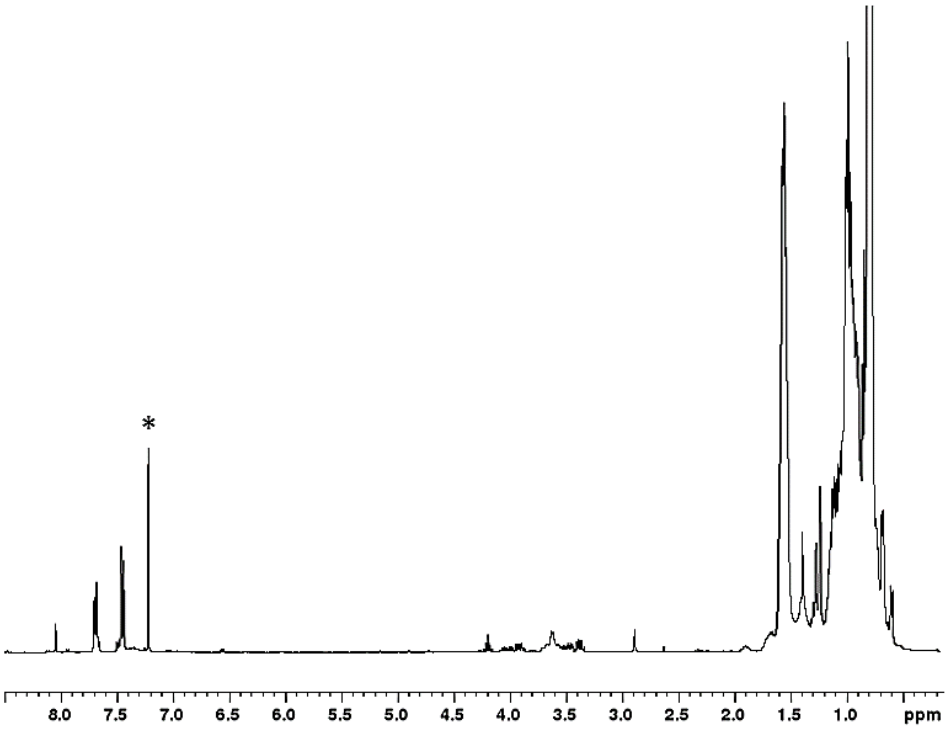

B.

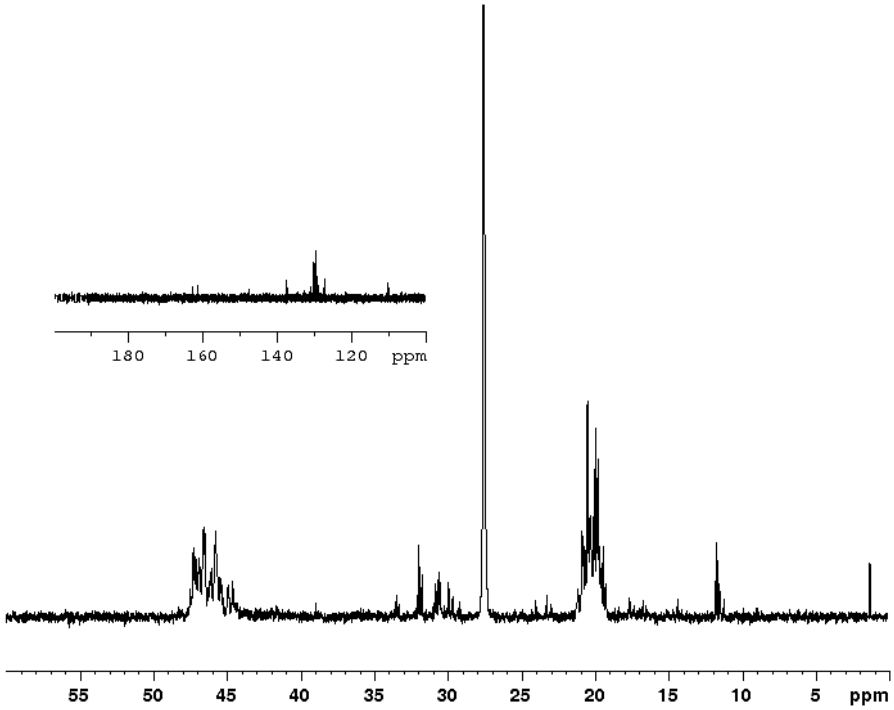

Figure S7.21. (A) ^{1}H NMR (600 MHz. *Chloroform-*d1*, RT) of red dye 254 (DPP) of aPP-DPP-aPP. (B) Partial ^{13}C-NMR (150 MHz, *Chloroform-*d1*) of aPP-DPP-aPP.

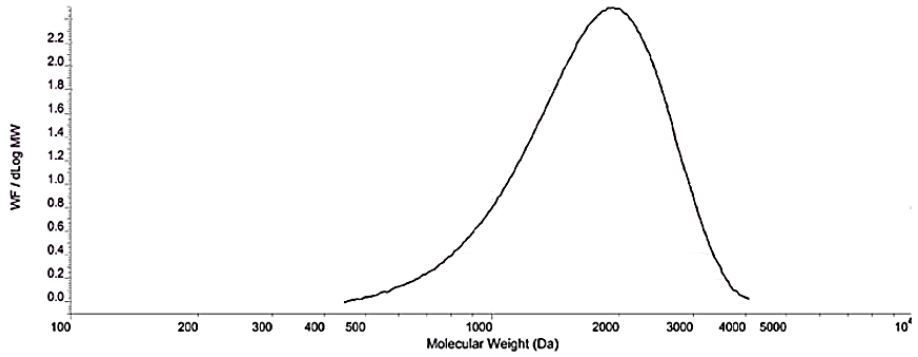

Figure S7.22. GPC trace of I-aPP provided by PPL Mn: 1,105 Da, Mw: 1,115 Da, PDI: 1.109.

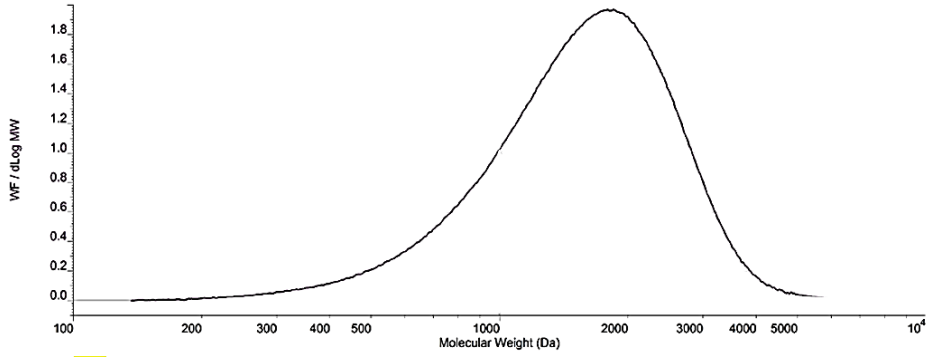

Figure S7.23. GPC trace of N_3-(-)PMCP Mn: 1,305 Da, Mw: 1,703 Da, PDI: 1.305.

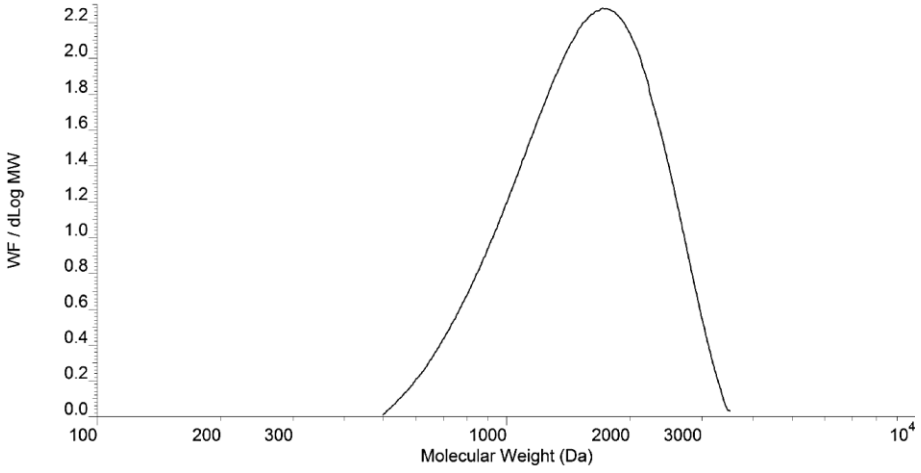

Figure S7.24. GPC trace of I-(+)PMCP Mn: 1,139 Da, Mw: 1,709, PDI: 1.205.

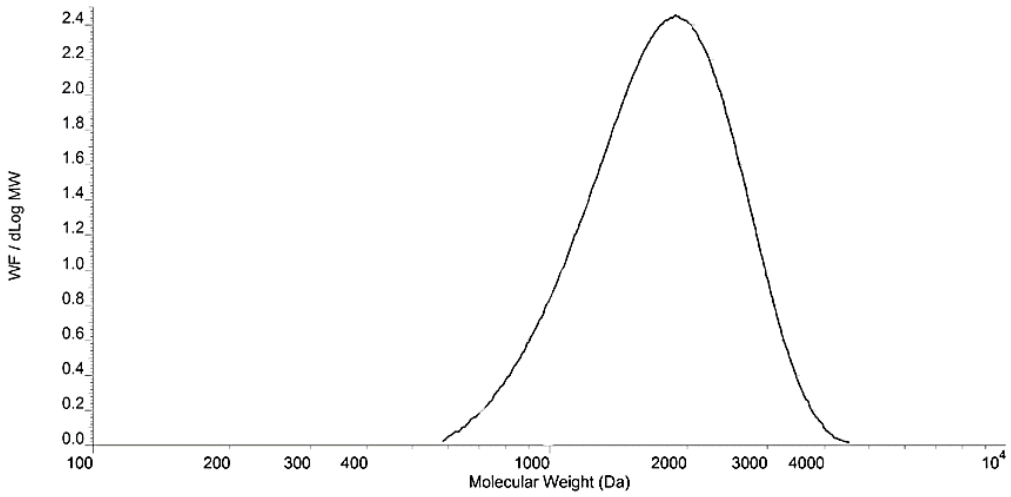

Figure S7.25. GPC trace of I-aPD Mn: 1,555 Da, Mw: 1,833, PDI: 1.18.

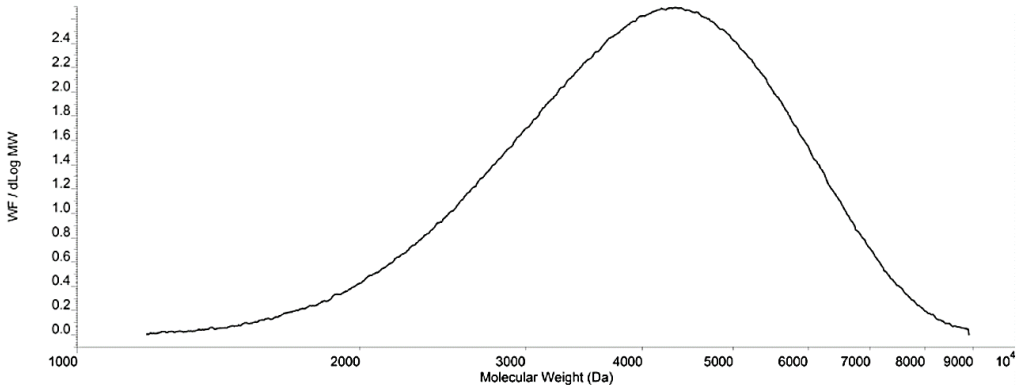

Figure S7.26. GPC trace of I-aPOD Mn: 3,735 Da, Mw: 4187 PDI: 1.12.

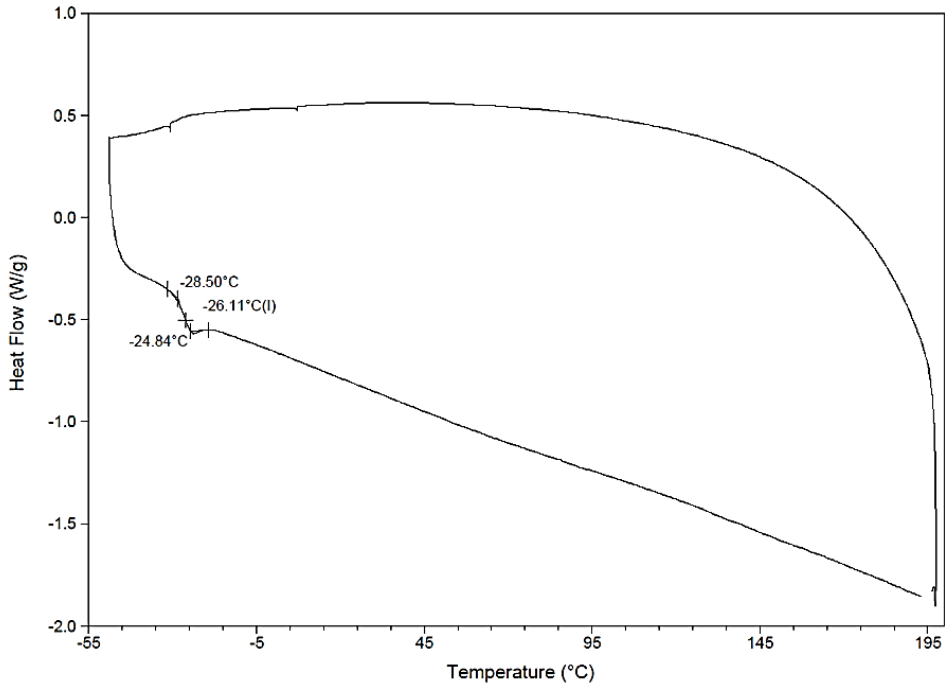

Figure S7.27. DSC trace of NH_2-aPP ramp rate of 10 °C/min from -50 °C – 195 °C, 1st heat cycle removed.

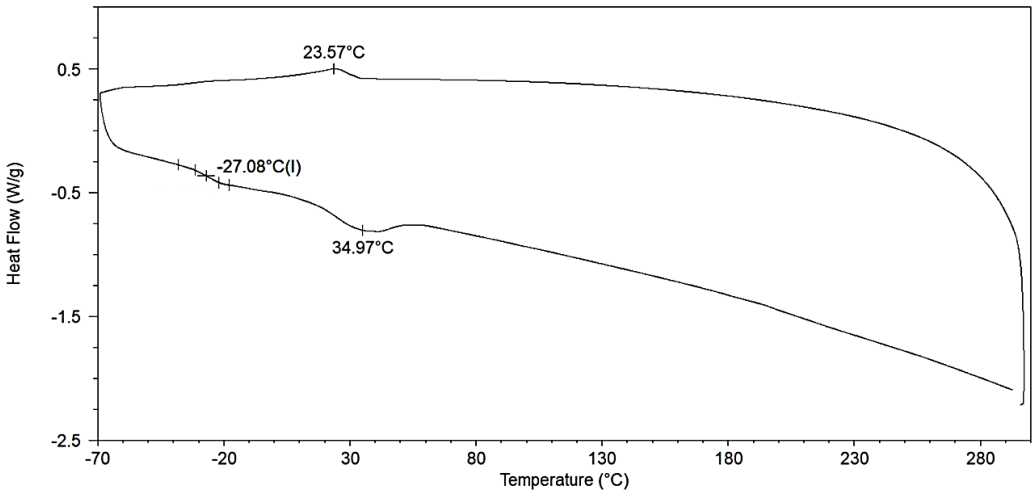

Figure S7.28. DSC trace of N_3-(-)PMCP ramp rate of 10 °C/min from -70 °C – 300 °C, 1st heat cycle removed.

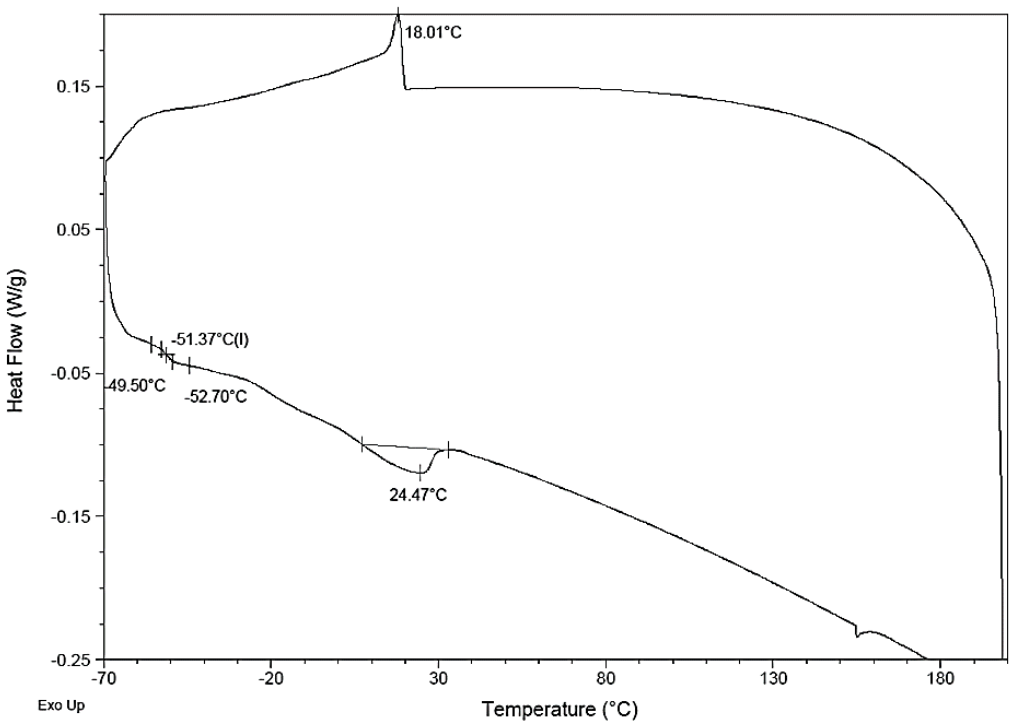

Figure S7.29. DSC trace of I-(+)PMCP ramp rate of 10 °C/min from -70 °C – 200 °C, 1st heat cycle removed.

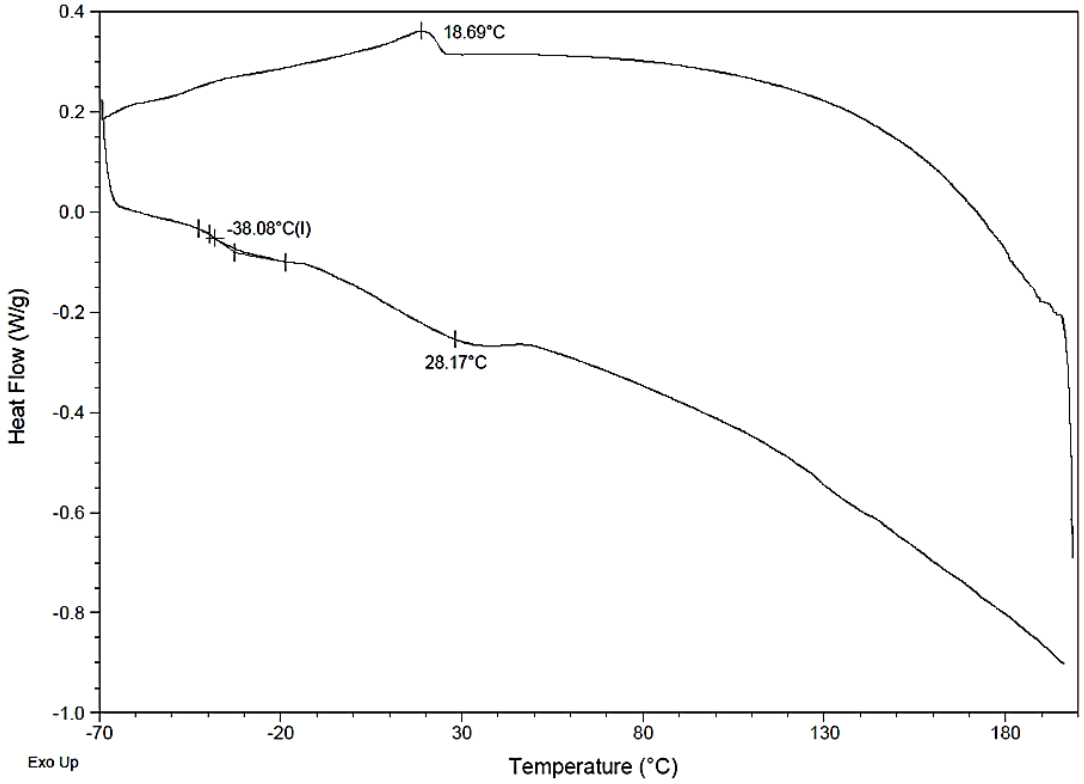

Figure S7.30. DSC trace of N_3-(+)PMCP ramp rate of 10 °C/min from -70 °C – 200 °C, 1st heat cycle removed.

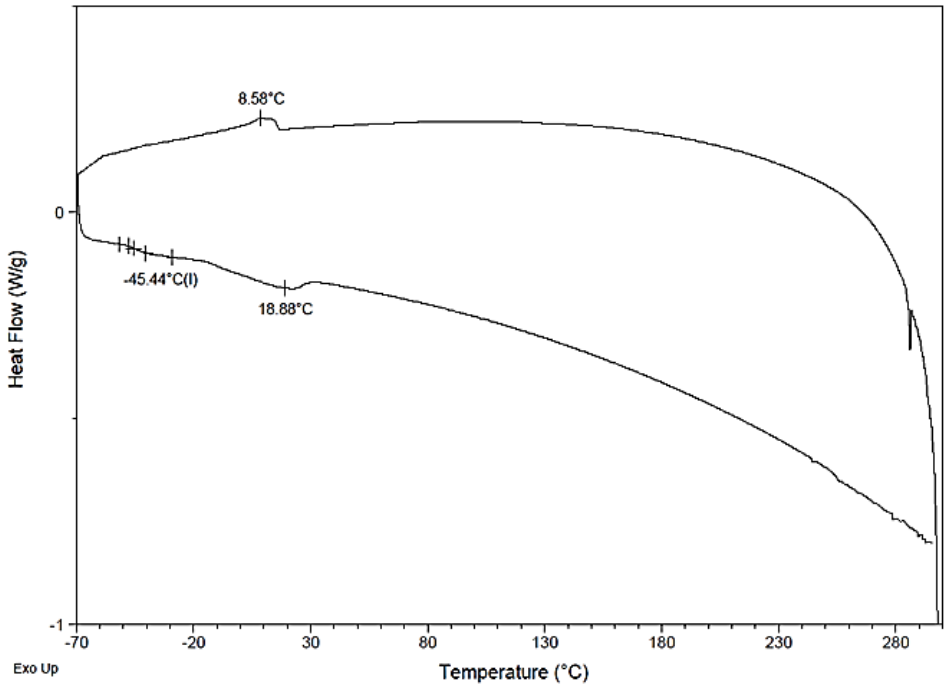

Figure S7.31. DSC trace of NH_2-(+)PMCP ramp rate of 10 °C/min from -70 °C – 200 °C, 1st heat cycle removed.

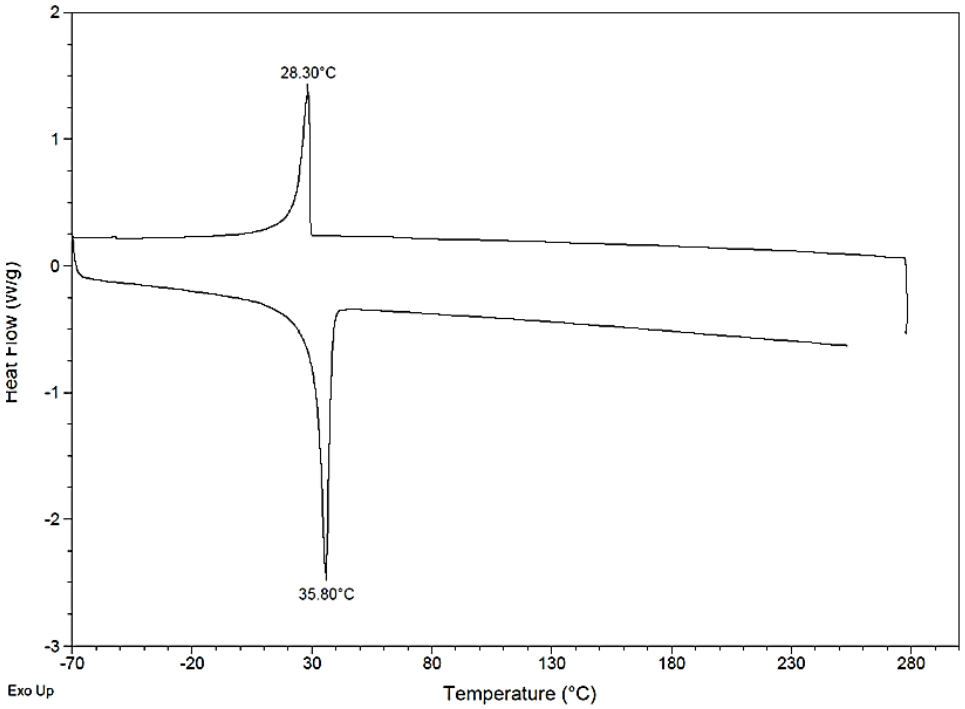

Figure S7.32. DSC trace of N3-POD ramp rate of 10 °C/min from -70 °C – 200 °C, 1st heat cycle removed.

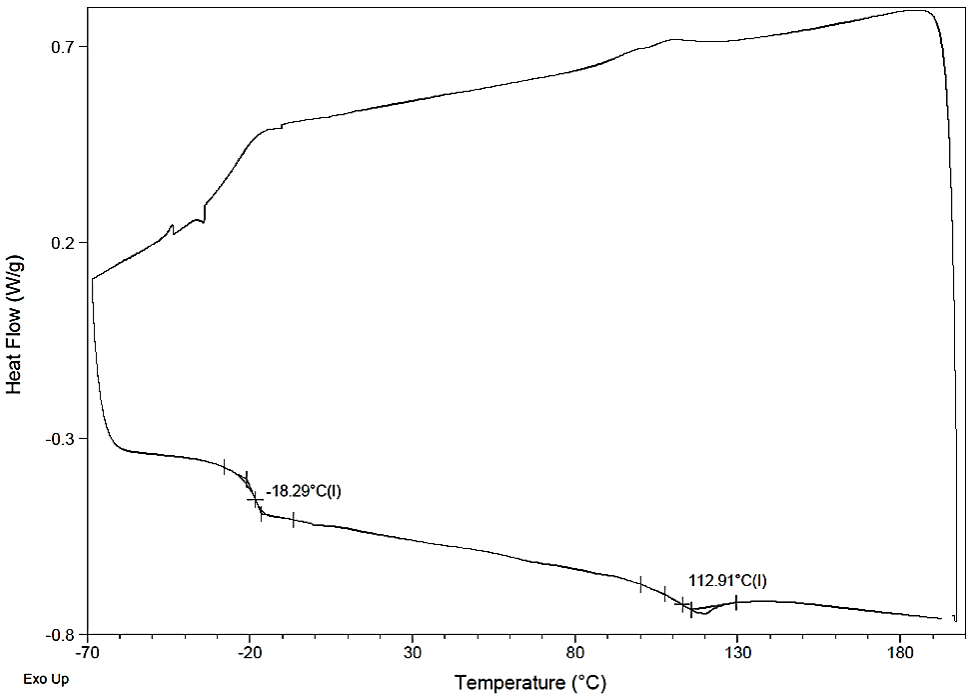

Figure S7.33. DSC trace of sample aPP-PBI-aPP with a ramp rate of 10 °C/min from -70 °C- 280 °C, 1st heat cycle removed.

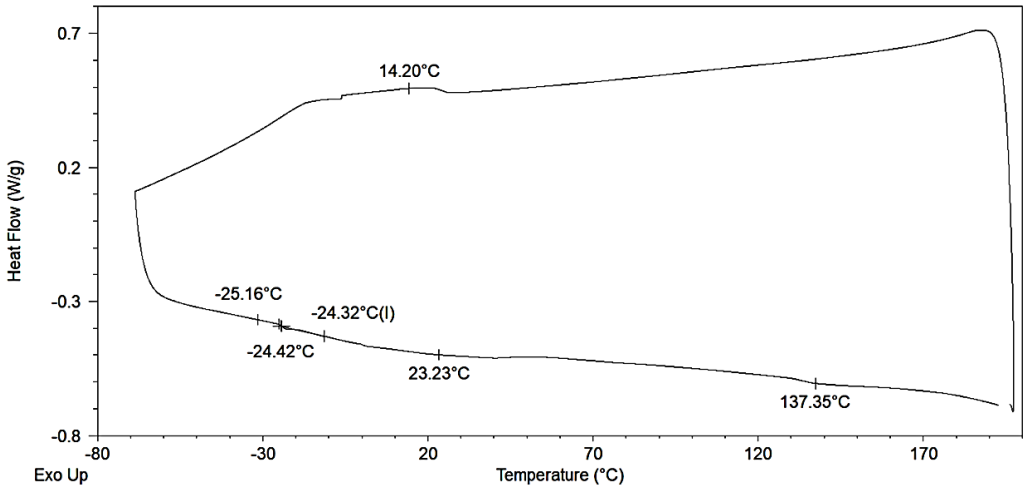

Figure S7.34. DSC trace of sample (+)PMCP-PBI-(+)PMCP with a ramp rate of 10 °C/min from -70 °C- 280 °C, 1st heat cycle removed.

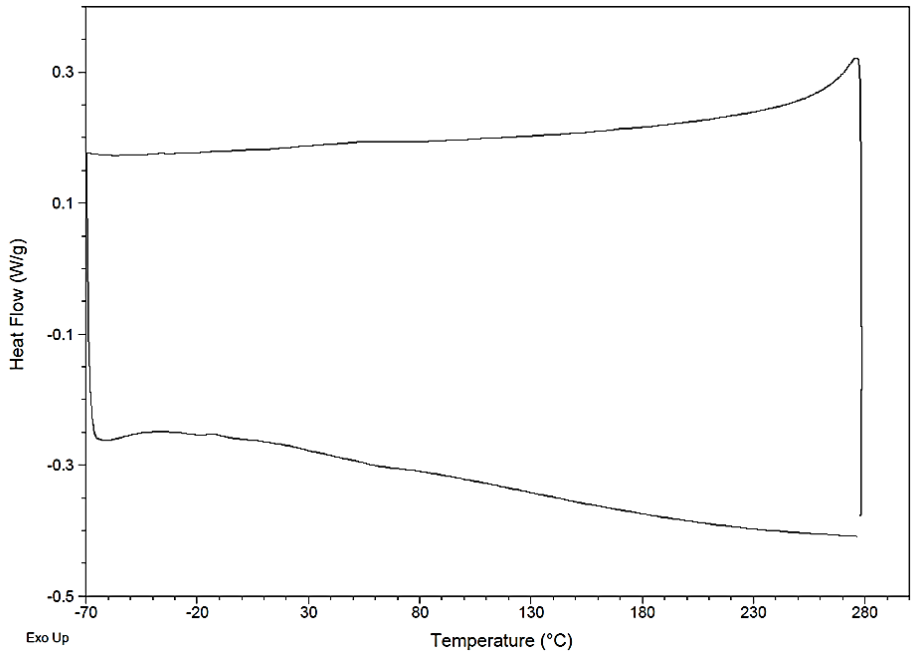

Figure S7.35. DSC trace of sample aPD-PBI-aPD with a ramp rate of 10 °C/min from -70 °C- 280 °C, 1st heat cycle removed.

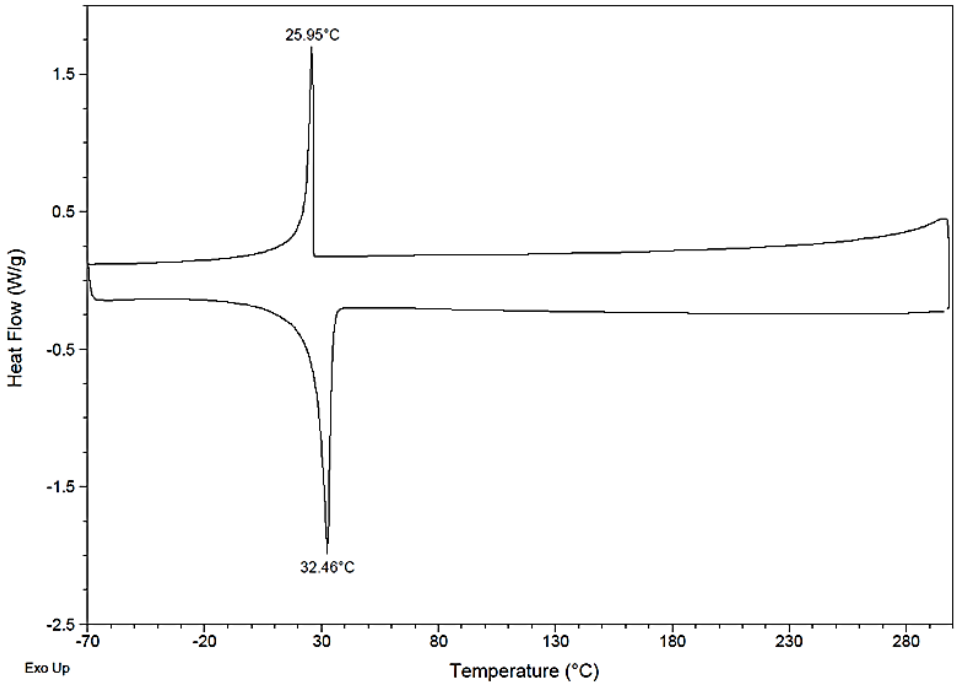

Figure S7.36. DSC trace of sample aPOD-PBI-aPOD with a ramp rate of 10 °C/min from -70 °C- 280 °C, 1st heat cycle removed.

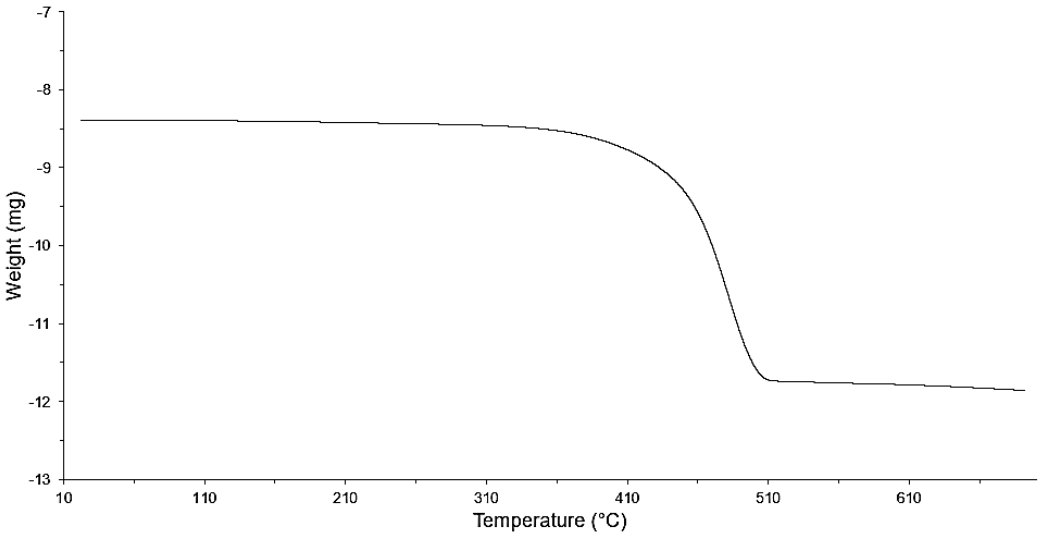

Figure S7.37. TGA trace of sample aPP-PBI-aPP with a ramp rate of 10 °C/min from 22 °C- 700 °C.

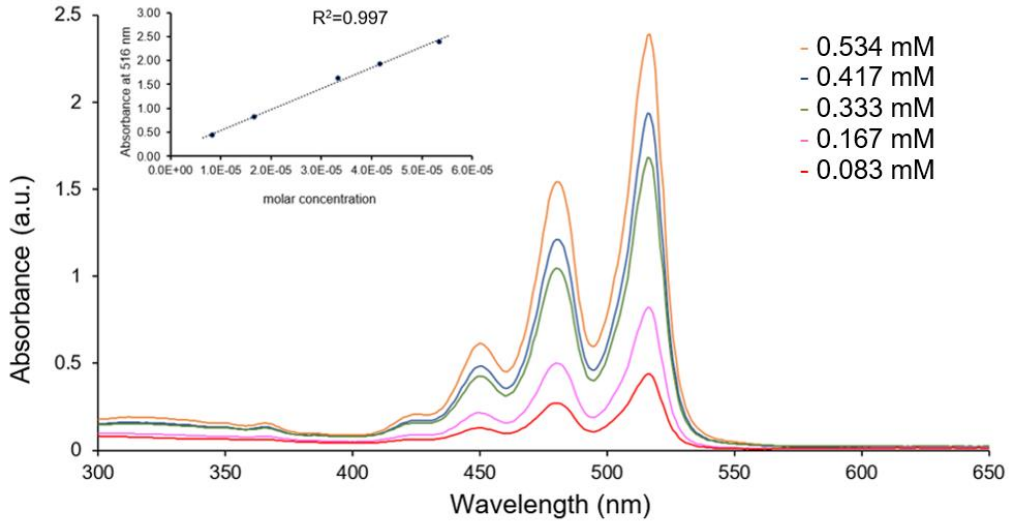

Figure S7.38. UV-vis concentration study of aPP-PBI-aPP in methylcyclohexane.

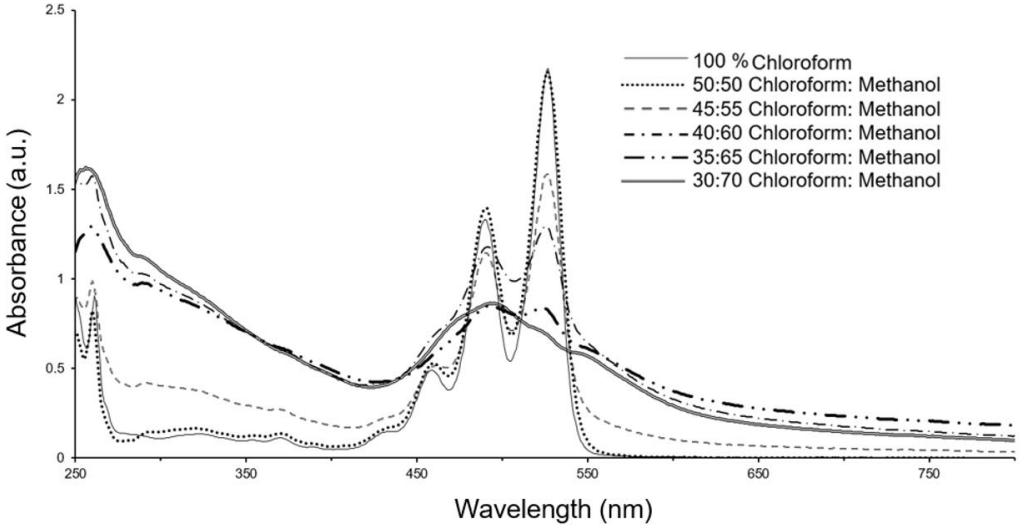

Figure S7.39. Solubility study with differing ratios of chloroform to methanol of aPP-PBI-aPP at 0.534 mM.

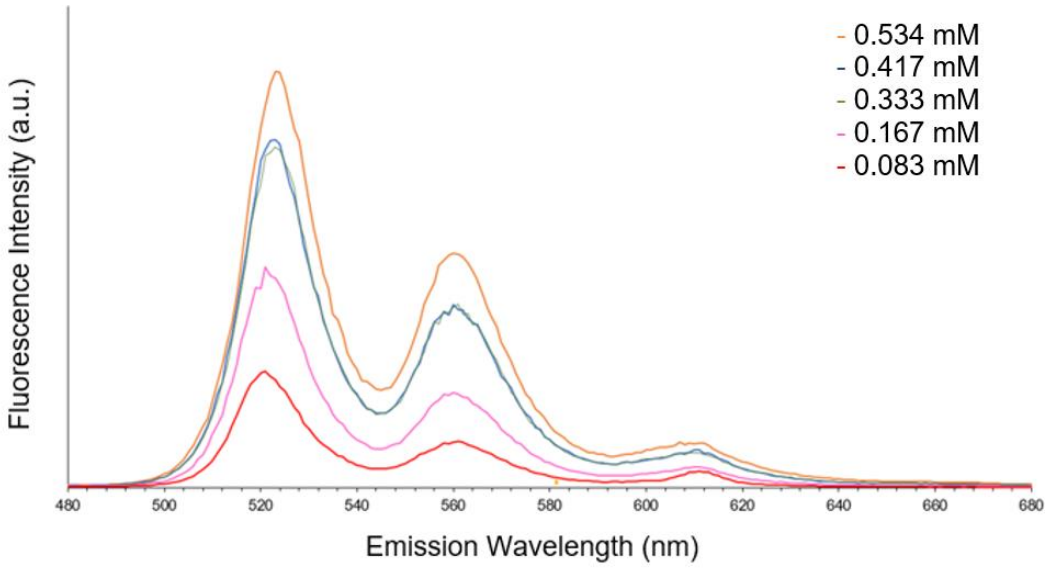

Figure S7.40. Fluorescence spectra of aPP-PBI-aPP (λ_{exc} = 280 nm) in methylcyclohexane at different concentrations and dependence of absorption maximum at 480 nm.

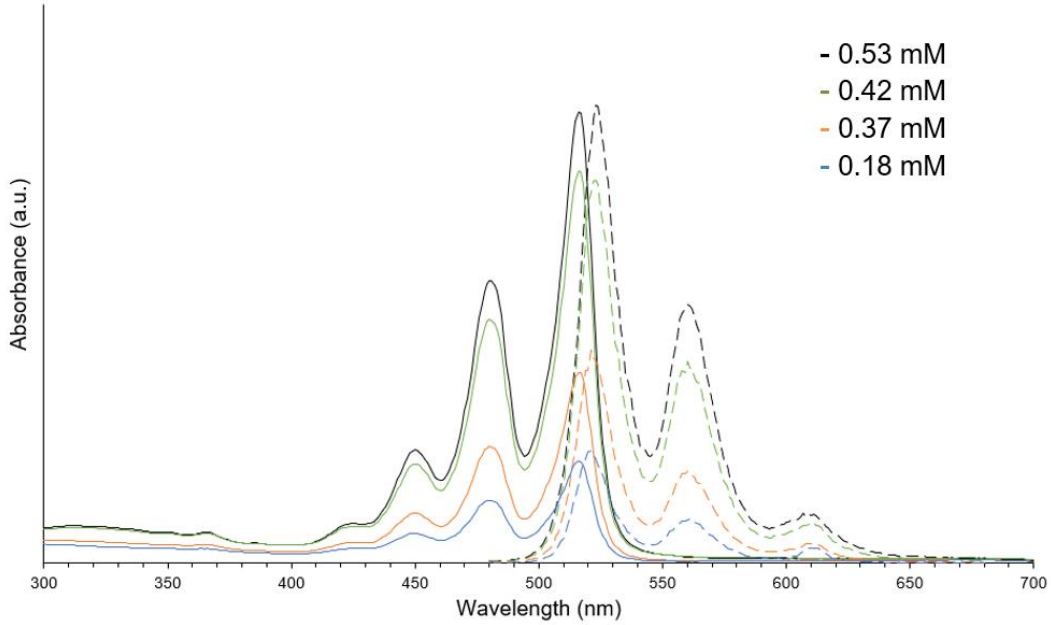

Figure S7.41. Absorbance spectra solid lines and fluorescence spectra dashed lines of aPP-PBI-aPP (λ_{exc} = 280 nm) in methylcyclohexane at different concentrations and dependence of absorption maximum at 480 nm.

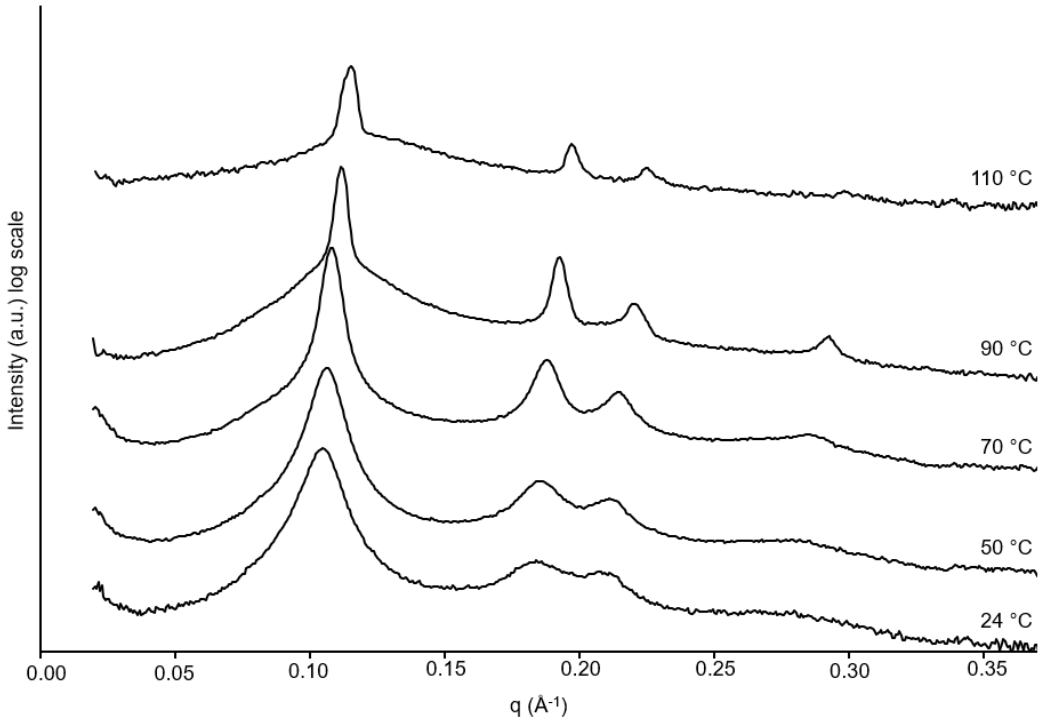

Figure S7.42. VT SAXS was conducted using on-sight synchrotron x-ray source and linkam heating stage heating at targeted temperature and holding for 30 minutes before measurement of the aPP-PBI-aPP.

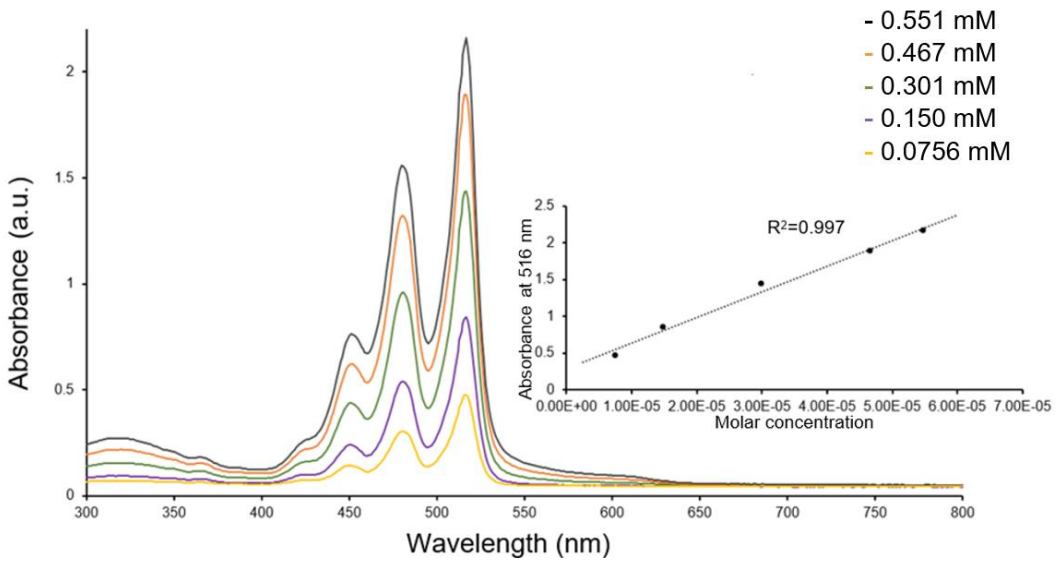

Figure S7.43. UV-vis concentration study of (-)PMCP-PBI-(-)PMCP in methylcyclohexane.

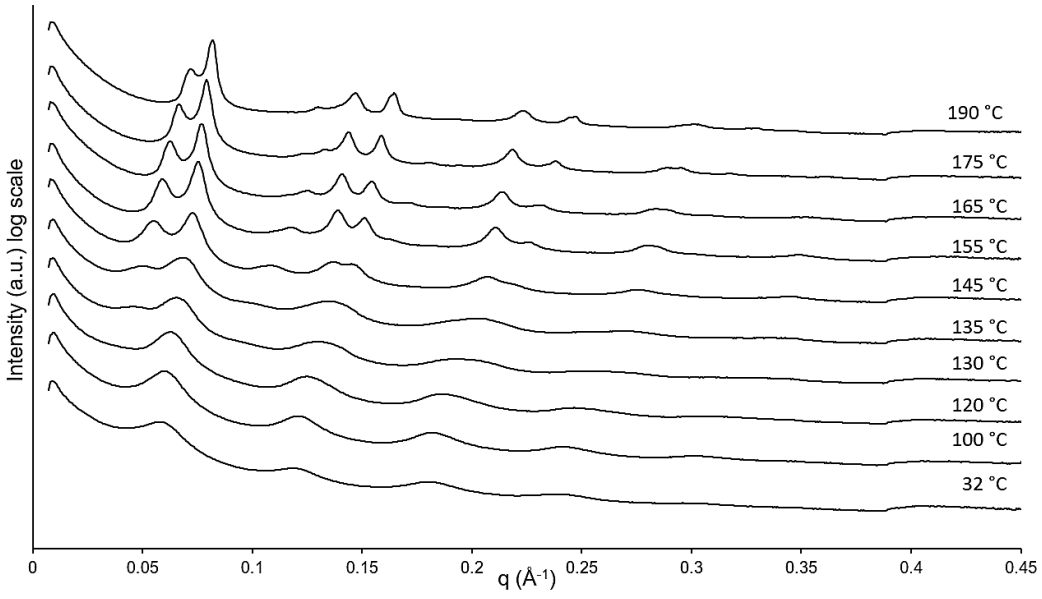

Figure S7.44. VT SAXS was conducted using a synchrotron x-ray source and thermal sample stage, heating at a rate of 0.5 °C/min from 30 °C – 200 °C of the (-)PMCP-PBI-(-)PMCP. Observed was columnar oblique at higher temperatures.

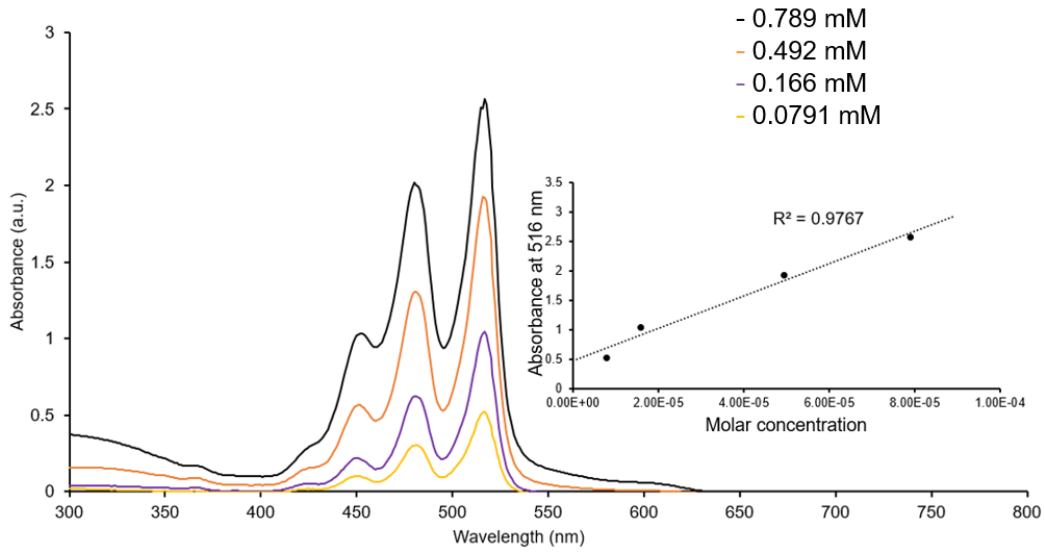

Figure S7.45. UV-vis concentration study of (+)PMCP-PBI-(+)PMCP in methylcyclohexane.

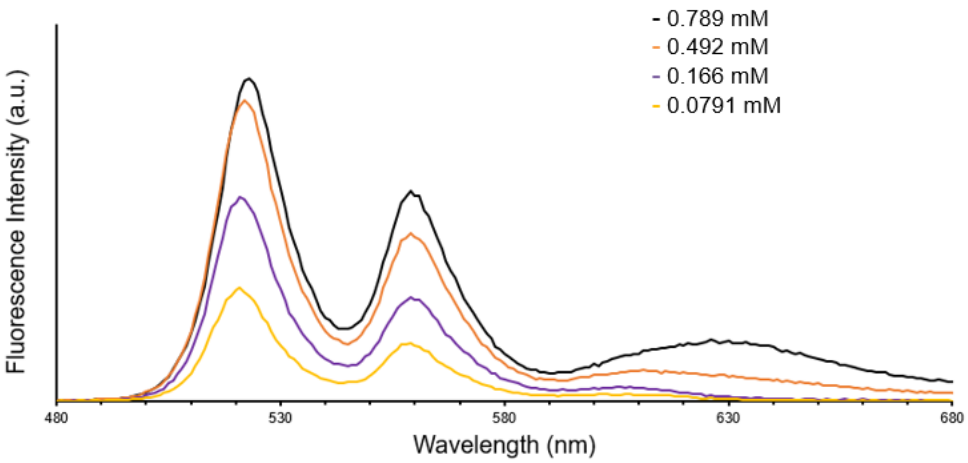

Figure S7.46. Fluorescence spectra of (+)PMCP-PBI-(+)PMCP (λ_{exc} = 280 nm) in methylcyclohexane at different concentrations and dependence of absorption maximum at 480 nm.

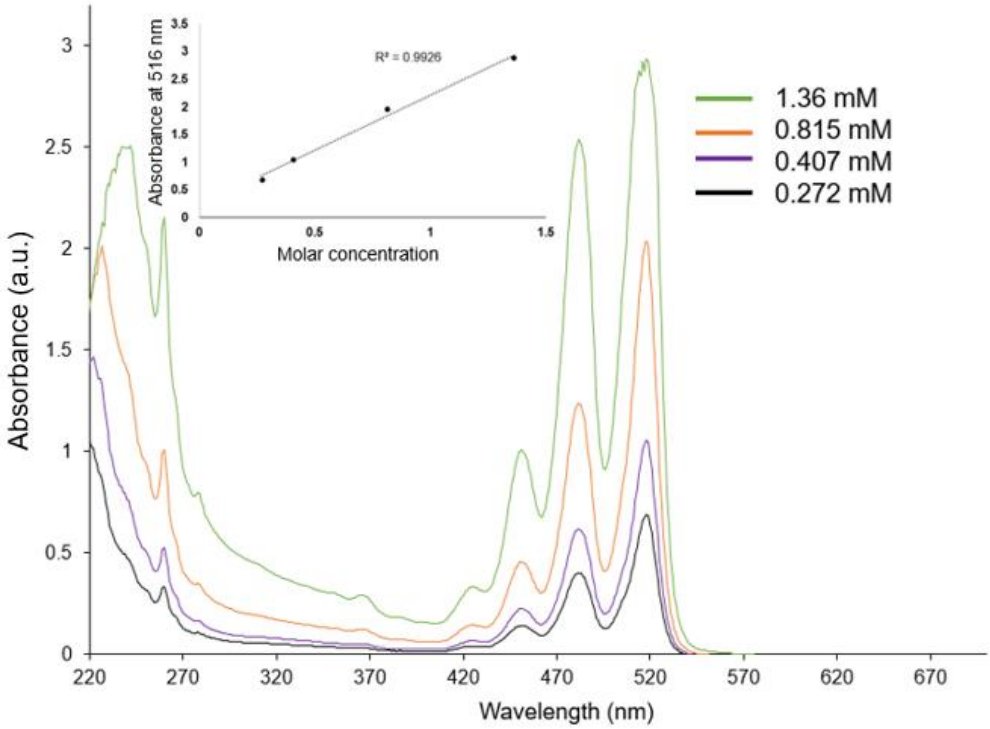

Figure S7.47. UV-vis concentration study of aPD-PBI-aPD in methylcyclohexane.

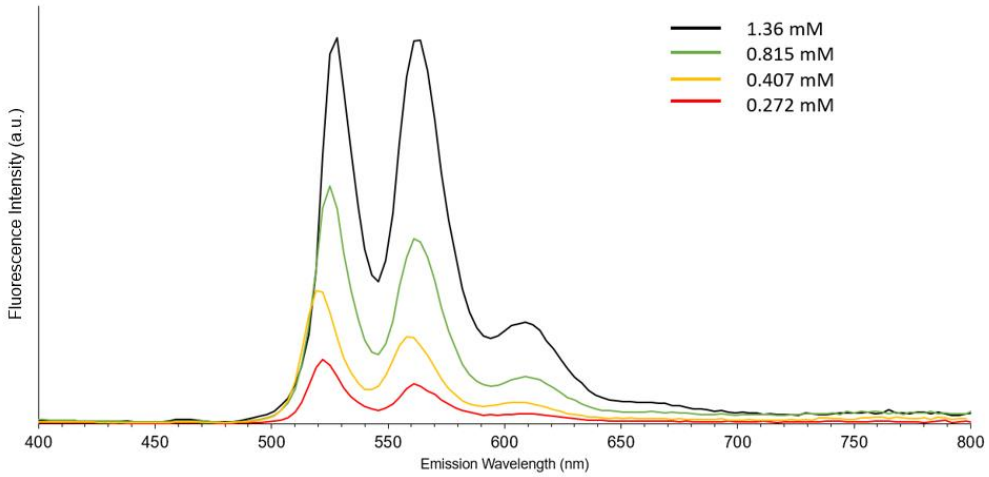

Figure S7.48. Fluorescence spectra of aPD-PBI-aPD (λ_{exc} = 280 nm) in methylcyclohexane at different concentrations and dependence of absorption maximum at 480 nm.

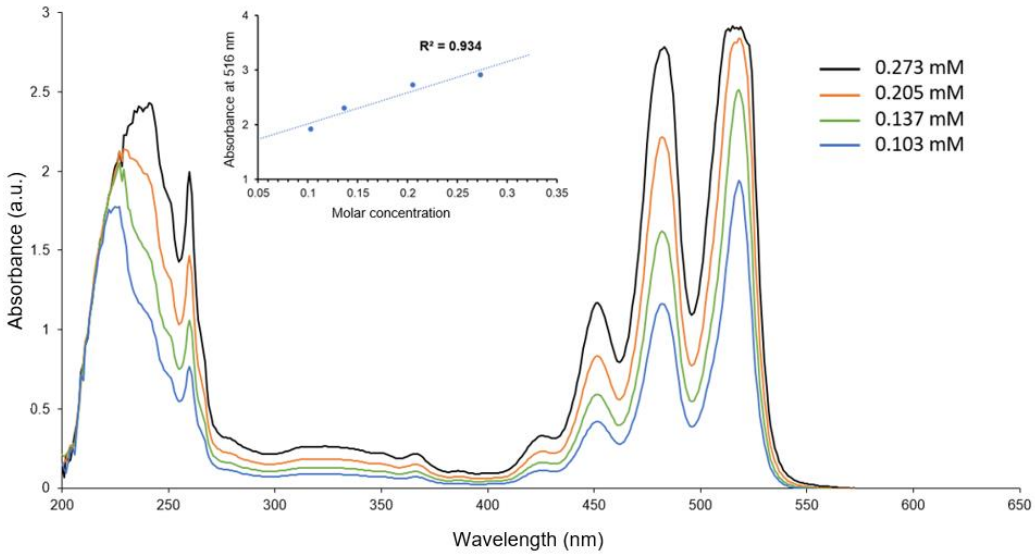

Figure S7.49. UV-vis concentration study of aPOD-PBI-aPOD in methylcyclohexane.

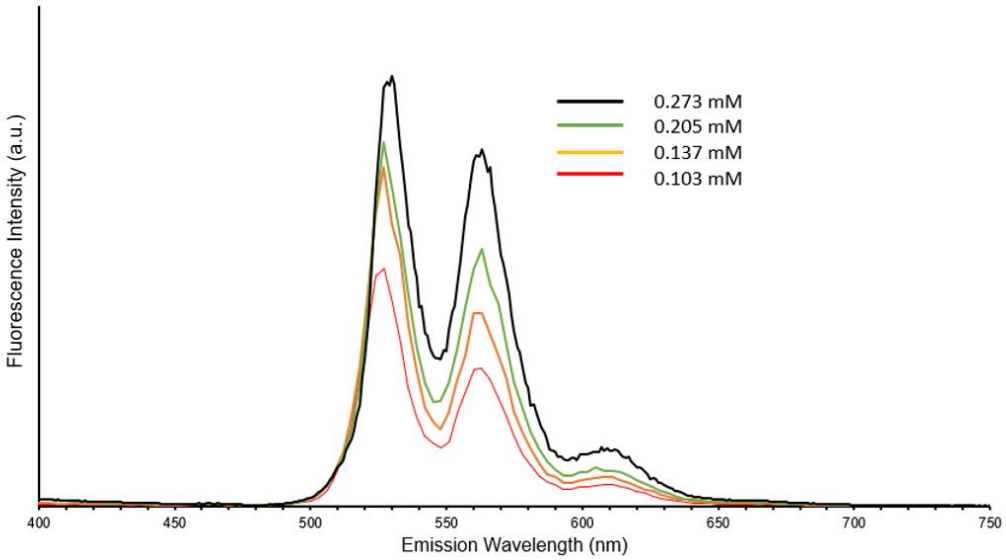

Figure S7.50. Fluorescence spectra of aPOD-PBI-aPOD (λ_{exc} = 280 nm) in methylcyclohexane at different concentrations and dependence of absorption maximum at 480 nm.

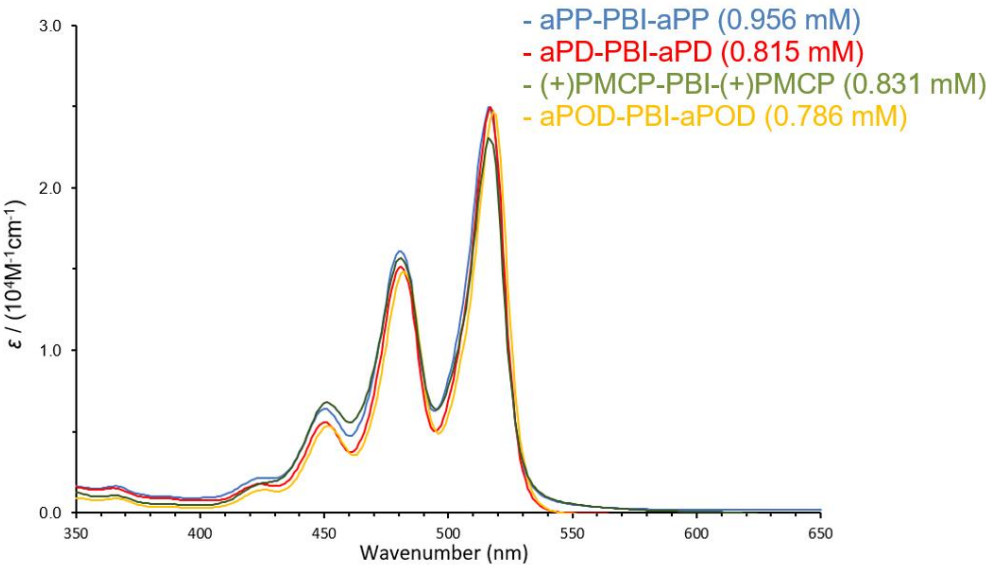

Figure S7.51. Absorbance spectra for all PBI conjugates in methylcyclohexane in relation to the ε.

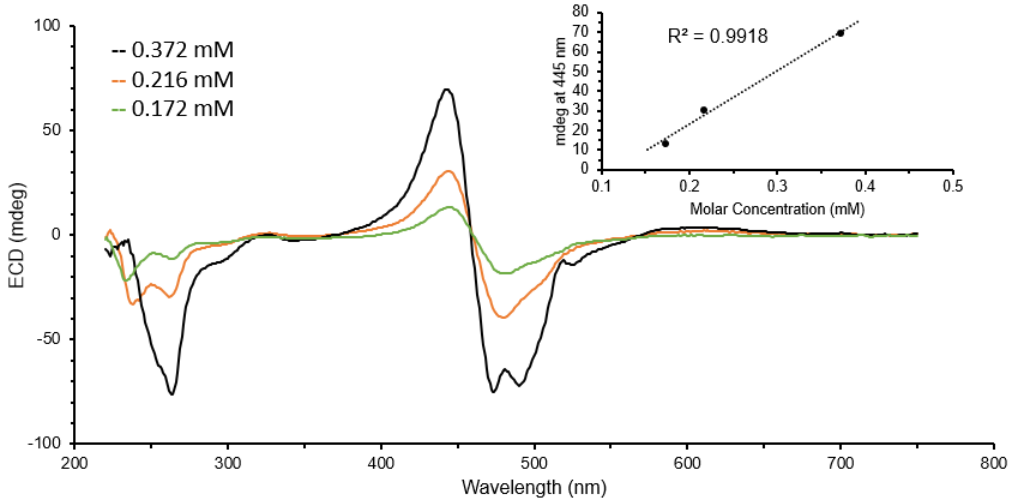

Figure S7.52. ECD traces of (-)PMCP-PBI-(-)PMCP at varied concentrations in methylcyclohexane, 10 mm cuvette, all measurements were below 700 voltage.

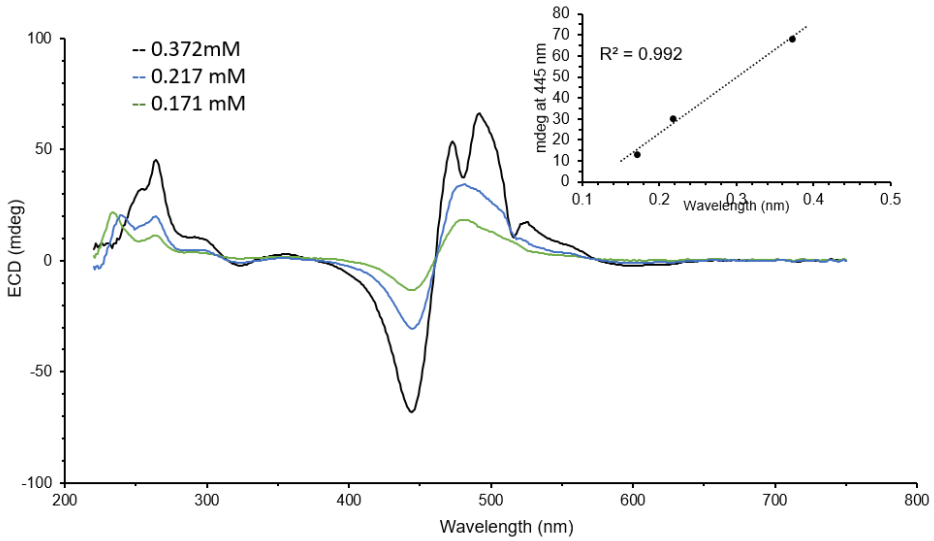

Figure S7.53. ECD traces of (+)PMCP-PBI-(+)PMCP at varied concentrations in methylcyclohexane, 10 mm cuvette, all measurements were below 700 voltage.

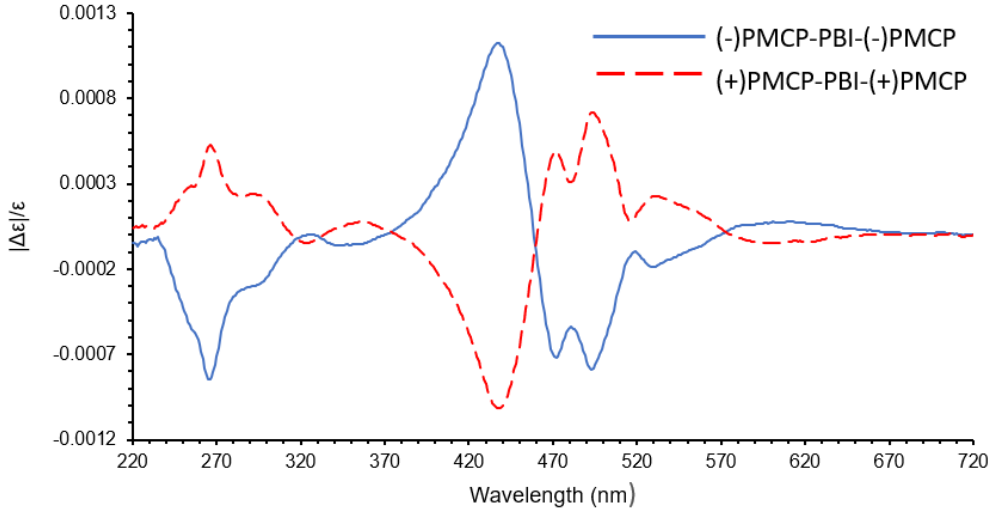

Figure S7.54. ECD g-factor traces of (-)PMCP-PBI-(-)PMCP (solid lines) and (+)PMCP-PBI-(+)PMCP (dashed lines) at 0.372 mM in methylcyclohexane, 10 mm cuvette, all measurements were below 700 volts.

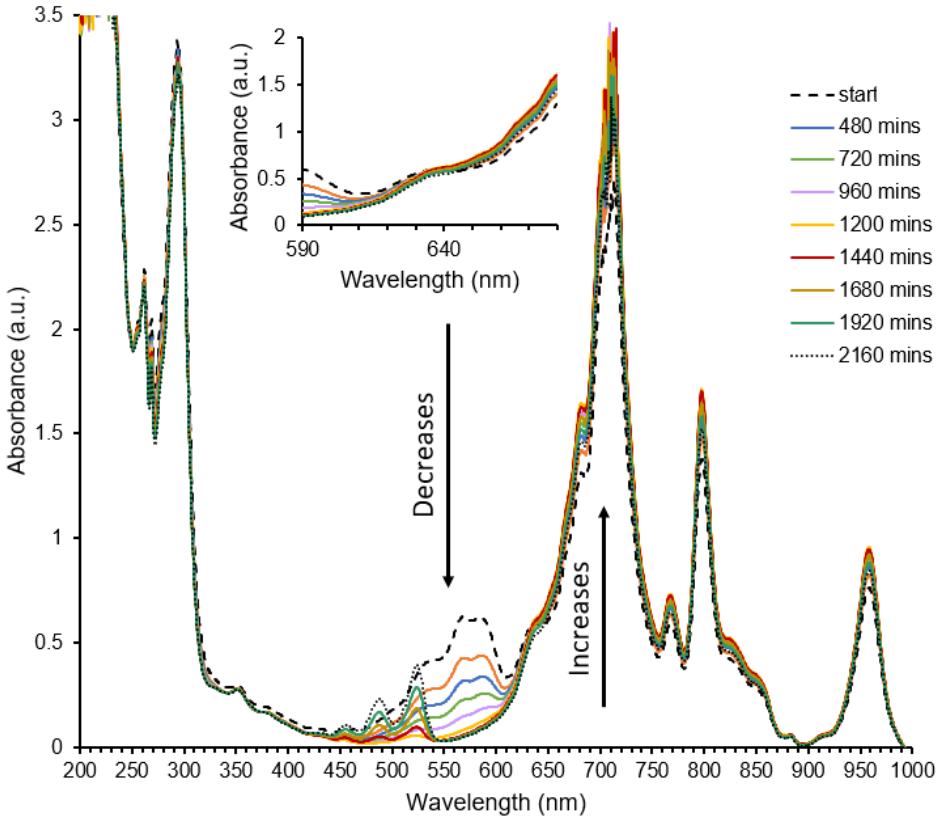

Figure S7.55. UV-vis time-lapse study of radical anion formation of aPP-PBI-aPP:Cobaltocene (25 wt%) blends in dichloromethane.

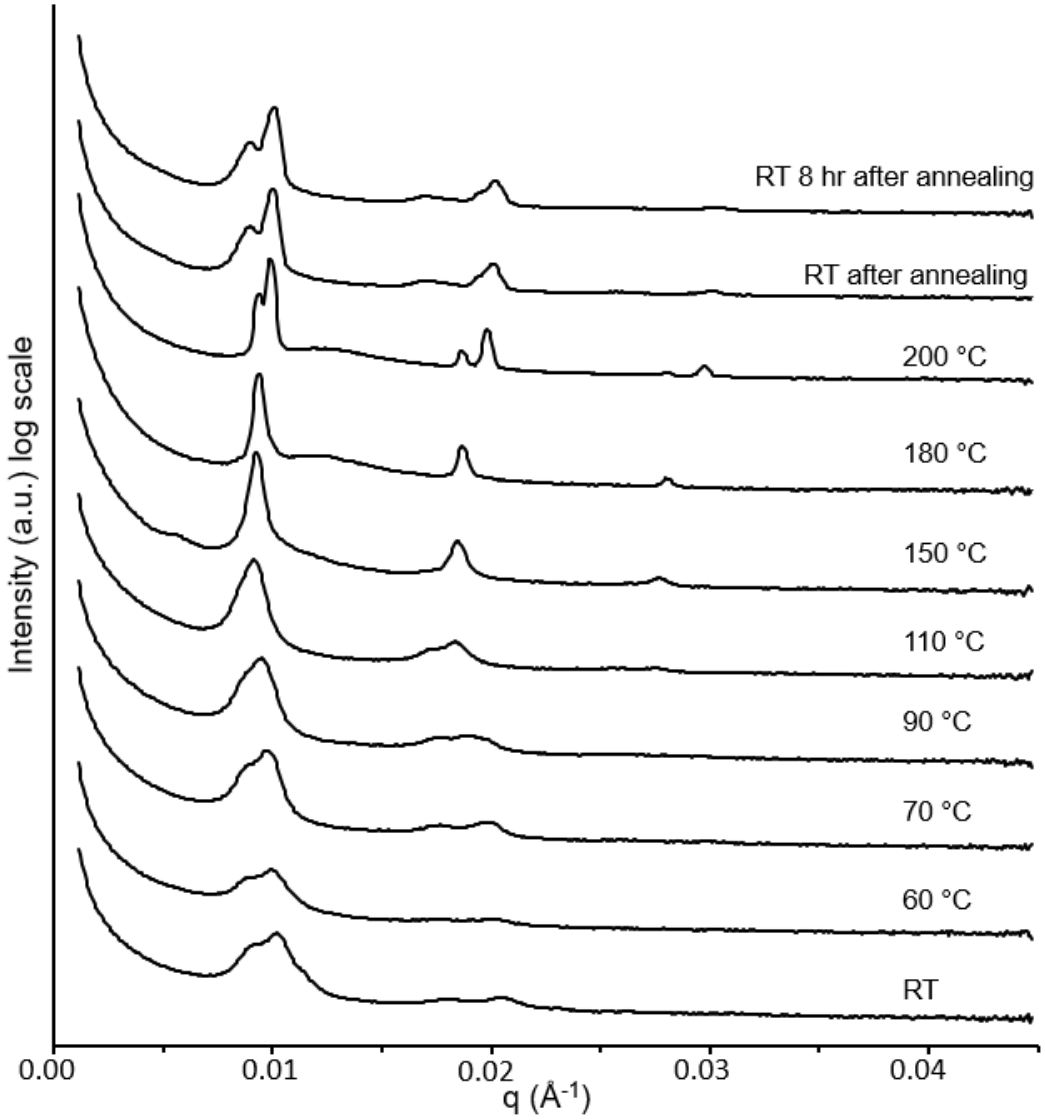

Figure S7.56. VT SAXS was conducted using on-sight x-ray source and thermal sample stage, heating to specific set temperatures, holding for 30 minutes, before measurement of the aPP-PBI-aPP:Cobaltocene blends (25 wt%), columnar oblique was observed.

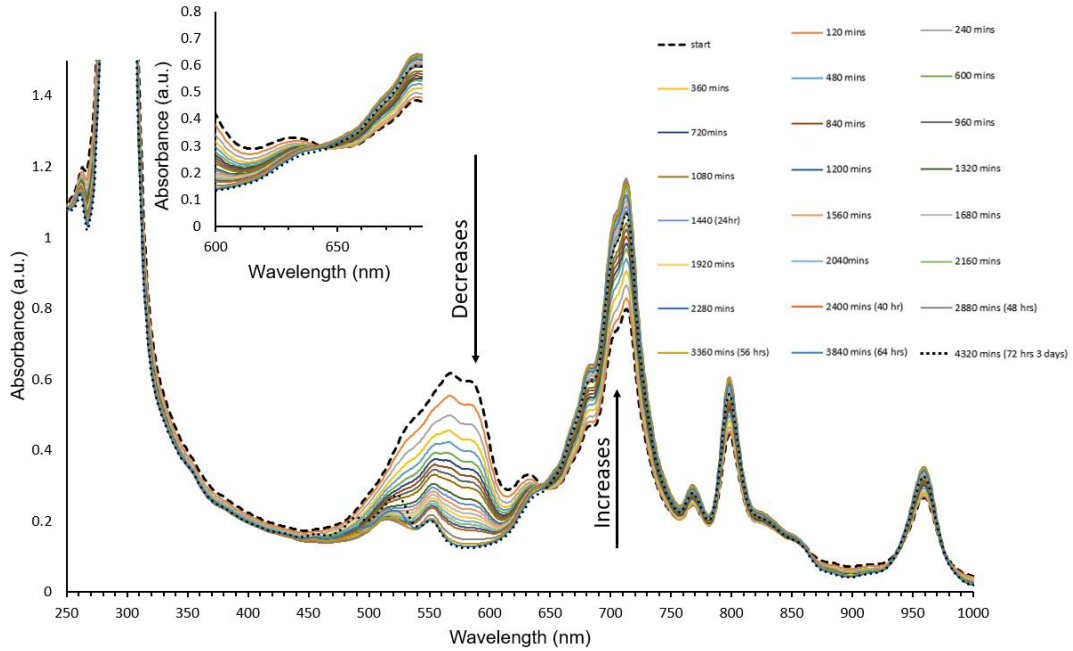

Figure S7.57. UV-vis time-lapse study of radical anion formation of (+)PMCP-PBI-(+)PMCP:Cobaltocene (30 wt%) blends in dichloromethane.

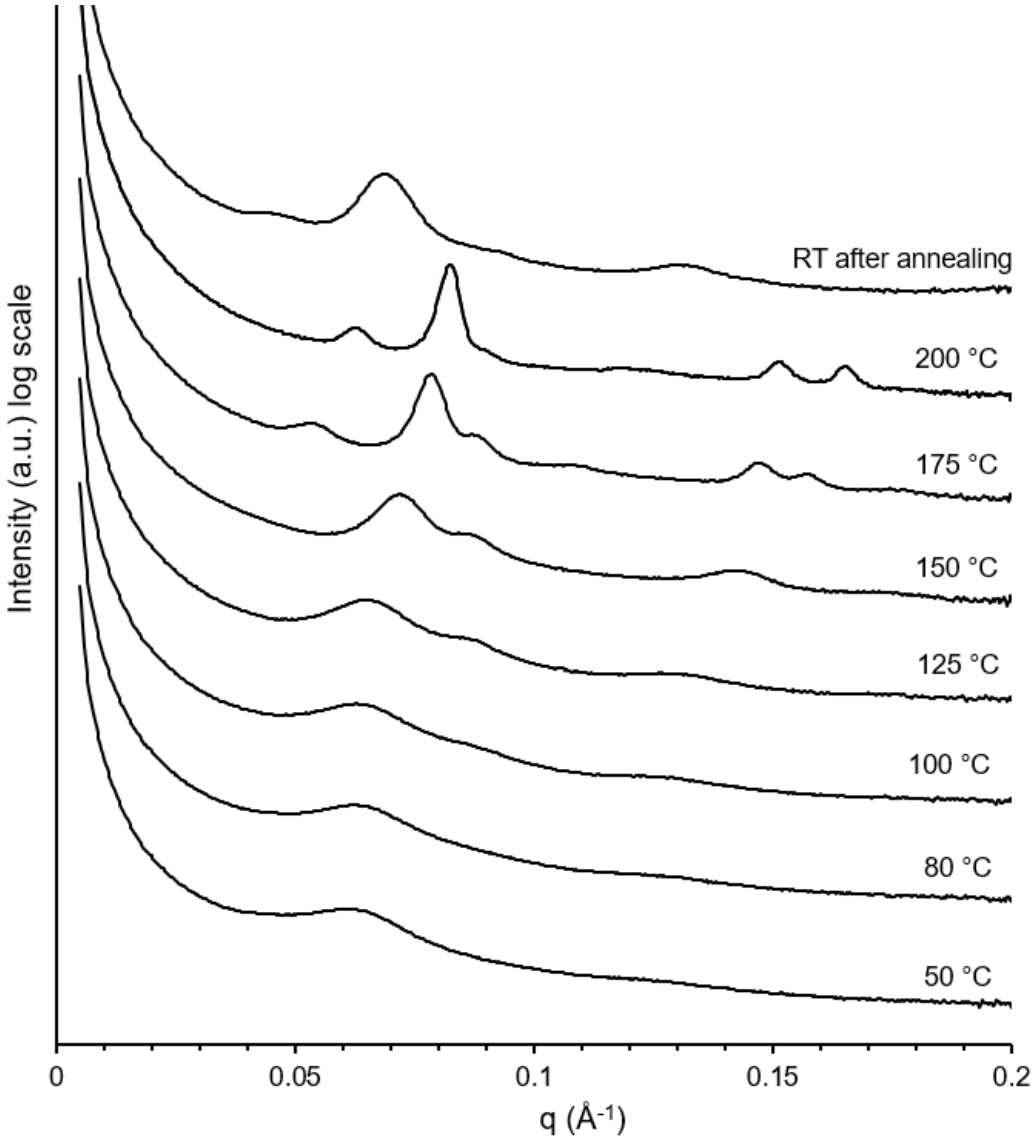

Figure S7.58. VT SAXS was conducted using on-sight x-ray source and thermal sample stage, heating to specific set temperatures, holding for 30 minutes, before measurement of the (+)PMCP-PBI-(+)PMCP:Cobaltocene blends (30 wt%).

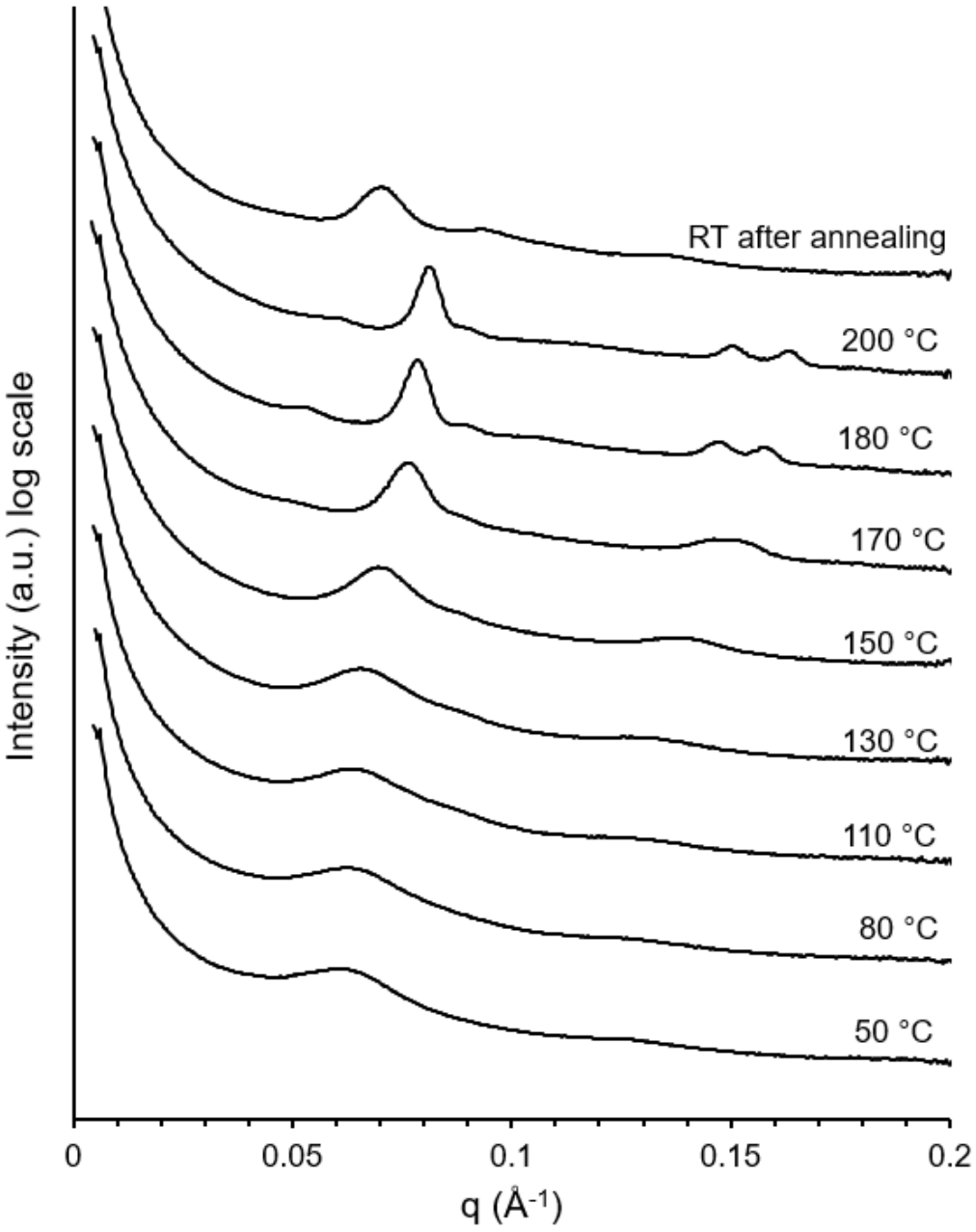

Figure S7.59. VT SAXS was conducted using on-sight x-ray source and thermal sample stage, heating to specific set temperatures, holding for 30 minutes, before measurement of a repeated newly made blend and sample of (+)PMCP-PBI-(+)PMCP:Cobaltocene (30 wt%).

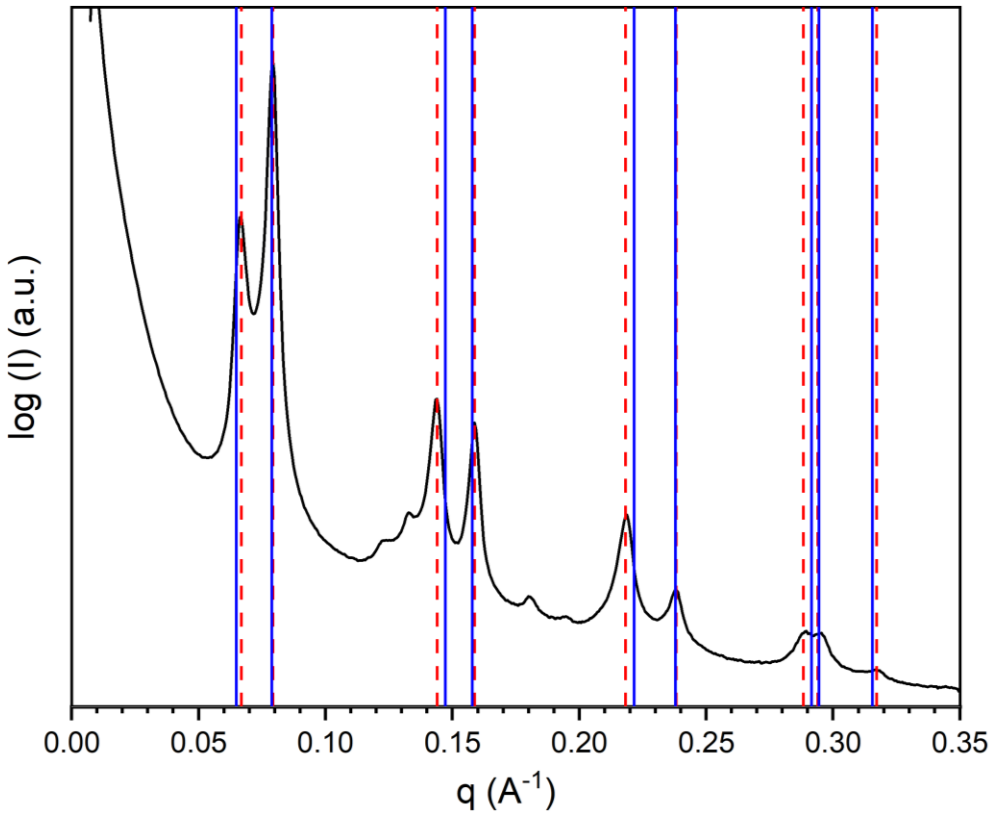

Figure S7.60. VT SAXS was conducted using on-sight x-ray source and thermal sample stage, heating to 175 °C, holding for 30 minutes, before measurement, same data as Fig. S43. Dotted red line is q_{obs} and solid blue line is q_{calc} for columnar oblique phase.

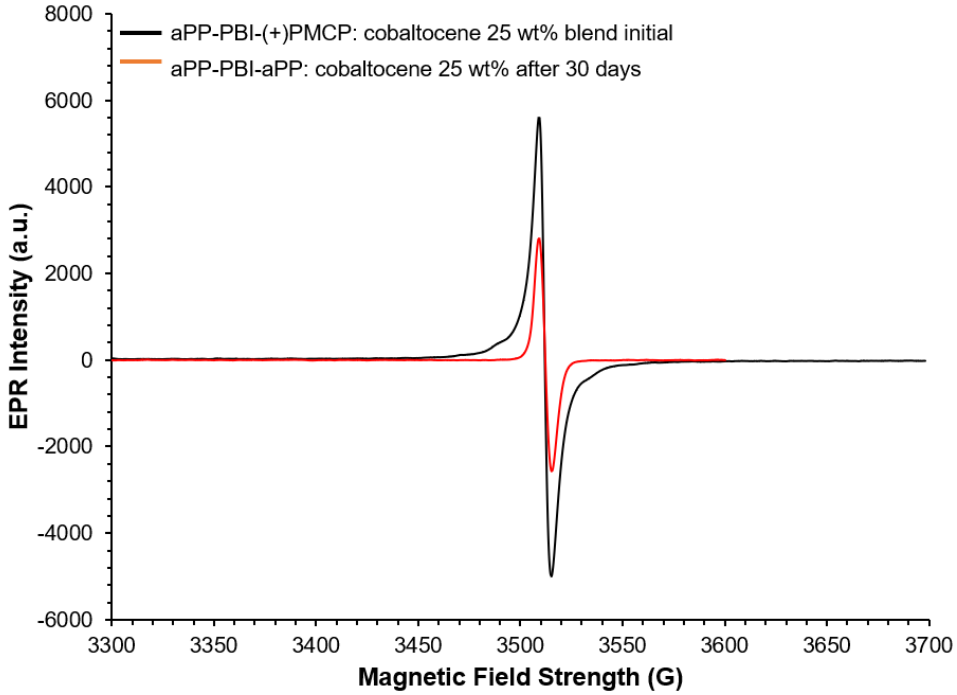

Figure S7.61. EPR spectrum of isolated solid film of the aPP-PBI-aPP:Cobaltocene (25 wt% blend) radical anion.

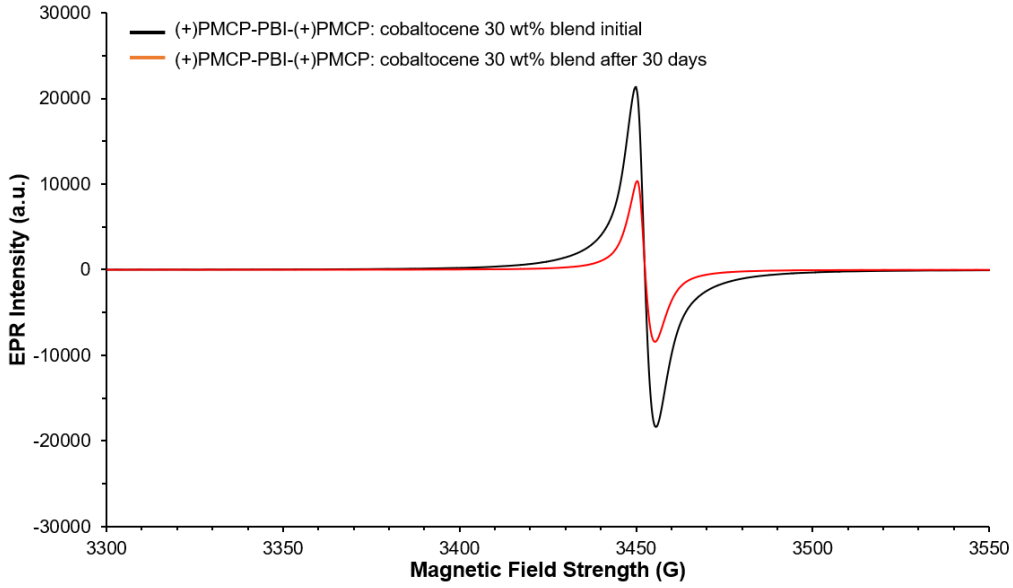

Figure S7.62. EPR spectrum of isolated solid film of the (+)PMCP-PBI-(+)PMCP:Cobaltocene (30 wt% blend) radical anion.

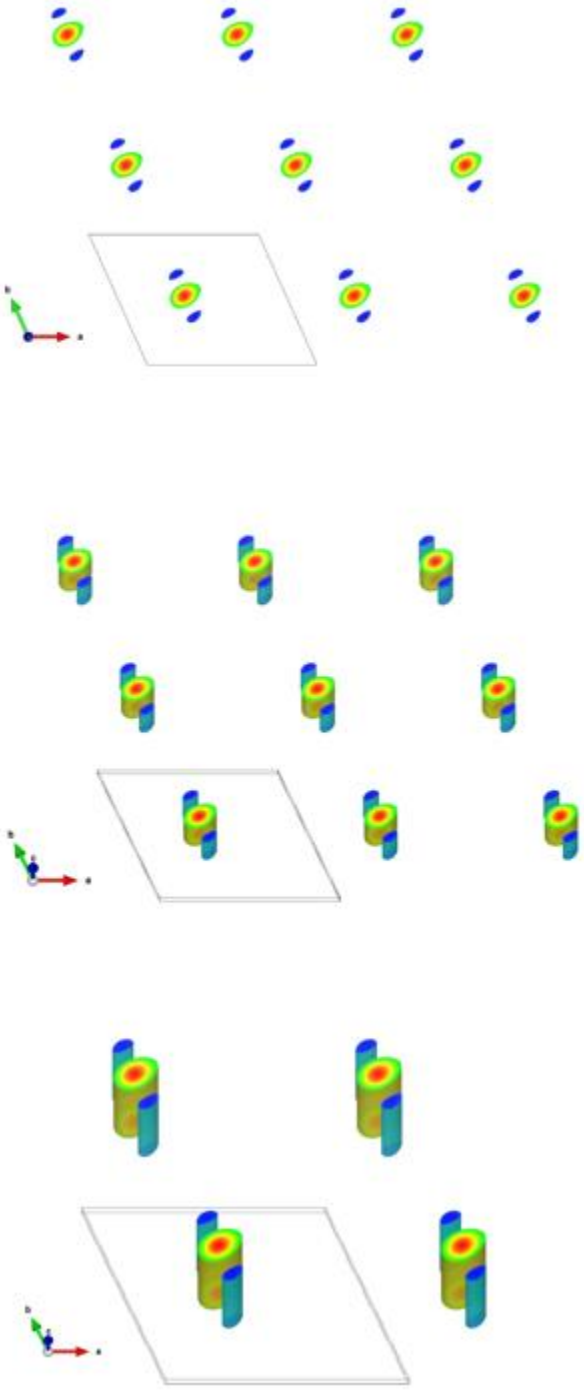

Figure S7.63. Electron density mapping fit to Col(ob) for the 175 °C SAXS data in Fig. S43.

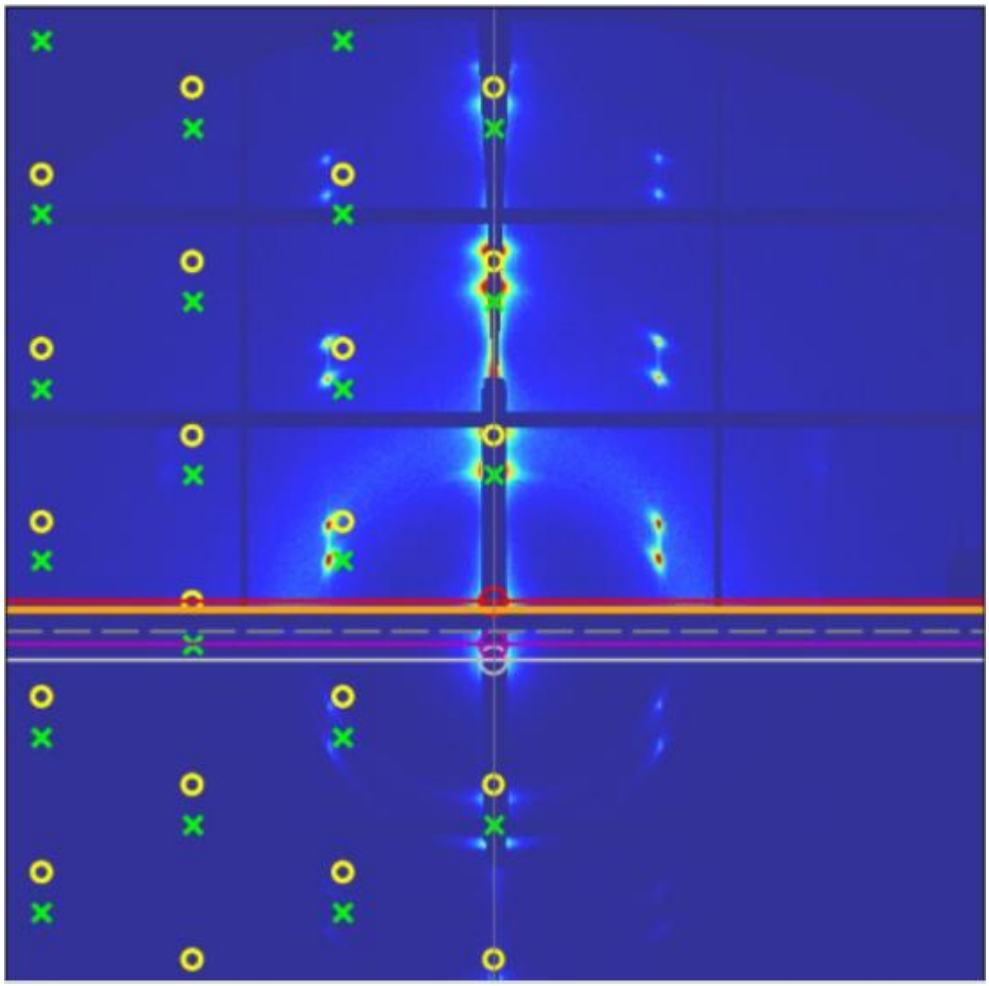

Figure S7.64. Indexed 2D GISAXS data of the hexagonally packed cylinders of aPP-PBI-aPP, recorded at 100.7 °C, with a film-thickness 190 nm, calculated grain size > 4 um. Indexed within the image are green ‘x’ represents peak diffraction and yellow ‘o’ which represents the mirrored scattering Bragg peaks. Fig. S41 represents on-site SAXS reinforcing hexagonally packed cylinder observation in bulk.

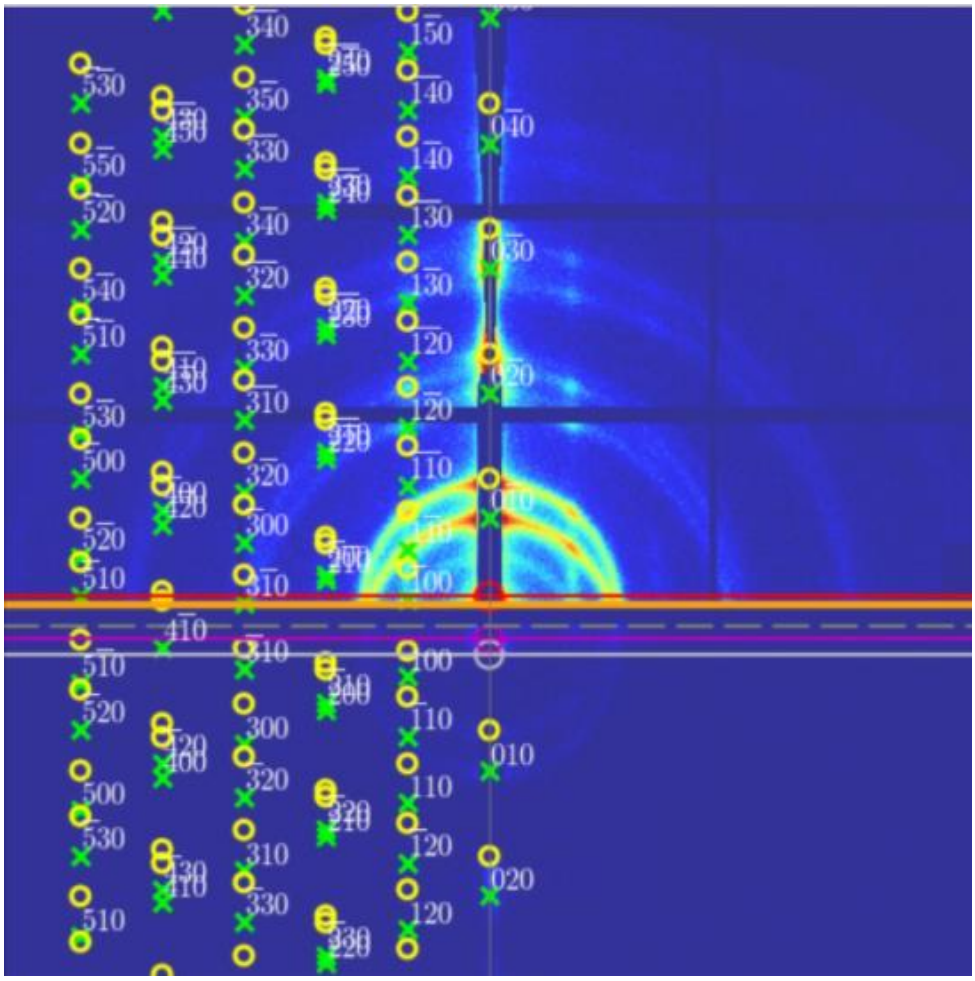

Figure S7.65. Indexed 2D GISAXS data of best fit oblique for (+)PMCP-PBI-(+)PMCP, recorded at 160.2 °C, with a film-thickness 160 nm. Indexed within the image are green ‘x’ represents peak diffraction and yellow ‘o’ which represents the mirrored scattering Bragg peaks. Fig. S43 represents synchrotron SAXS reinforcing columnar oblique observation in bulk.

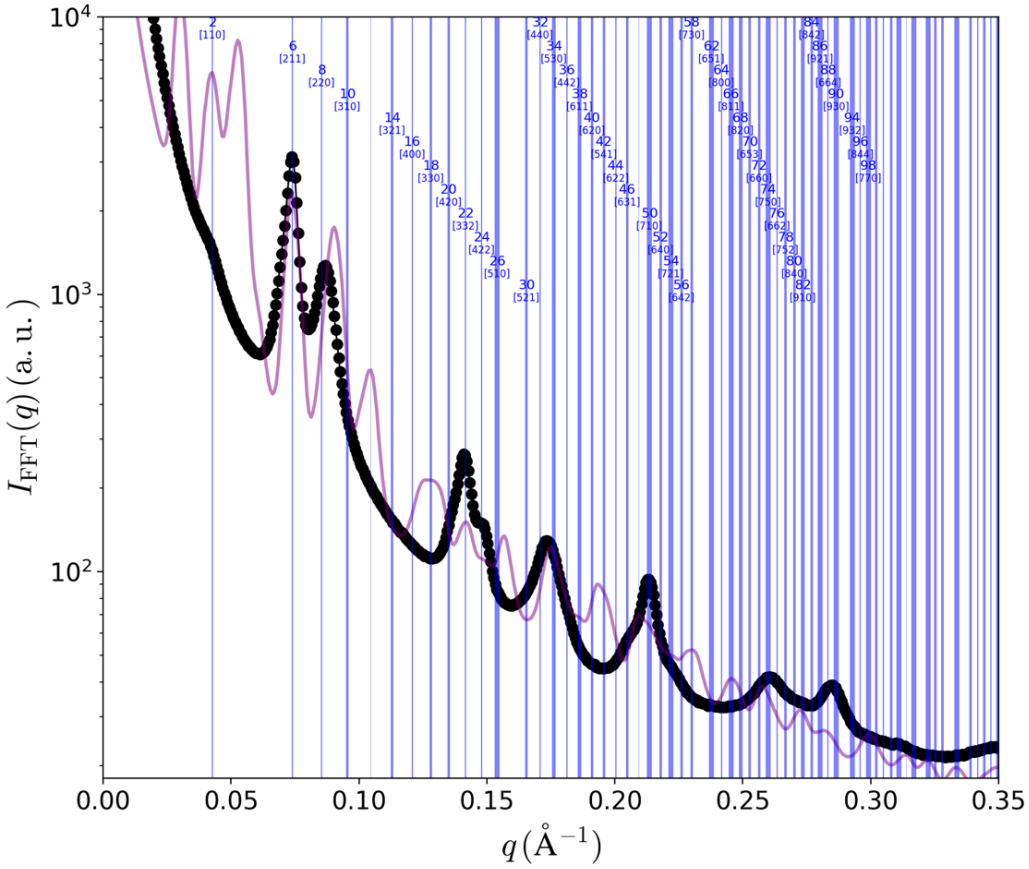

Figure S7.66. Indexed SAXS data of best fit for (+)PMCP-PBI-(+)PMCP:Cobaltocene blend experimentally seen single gyroid (black curve), recorded at 103 °C, Brookhaven National Labs synchrotron x-ray source. Simulation of scattering for a lattice parameter a = 19.6 nm (purple curve). Blue lines represent all possible Miller Indices that could be present for single gyroid.

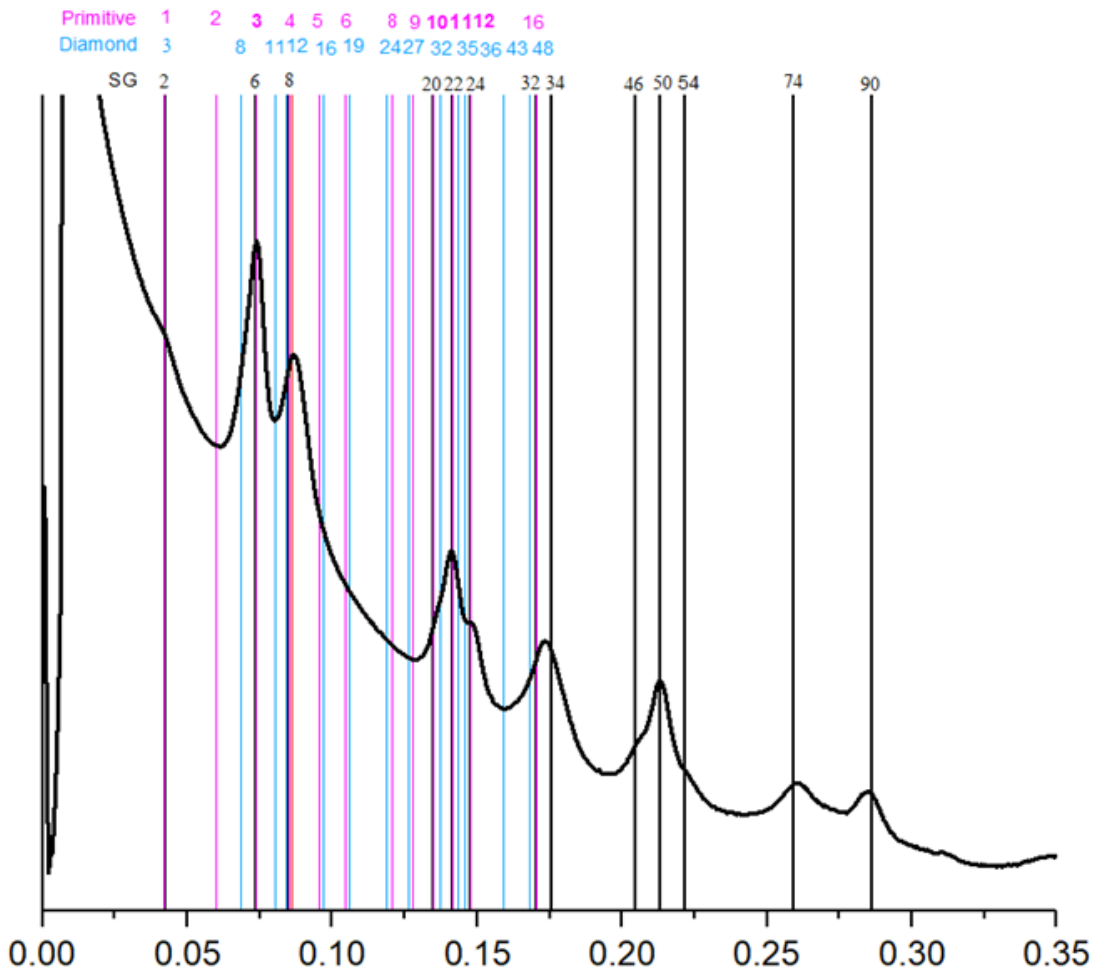

Figure S7.67. Indexed SAXS data of best fit for (+)PMCP-PBI-(+)PMCP:Cobaltocene blend experimentally seen single gyroid (black curve), recorded at 103 °C, Brookhaven National Labs synchrotron x-ray source. Other fits such as primitive and diamond are compared to the observed peaks.

A.

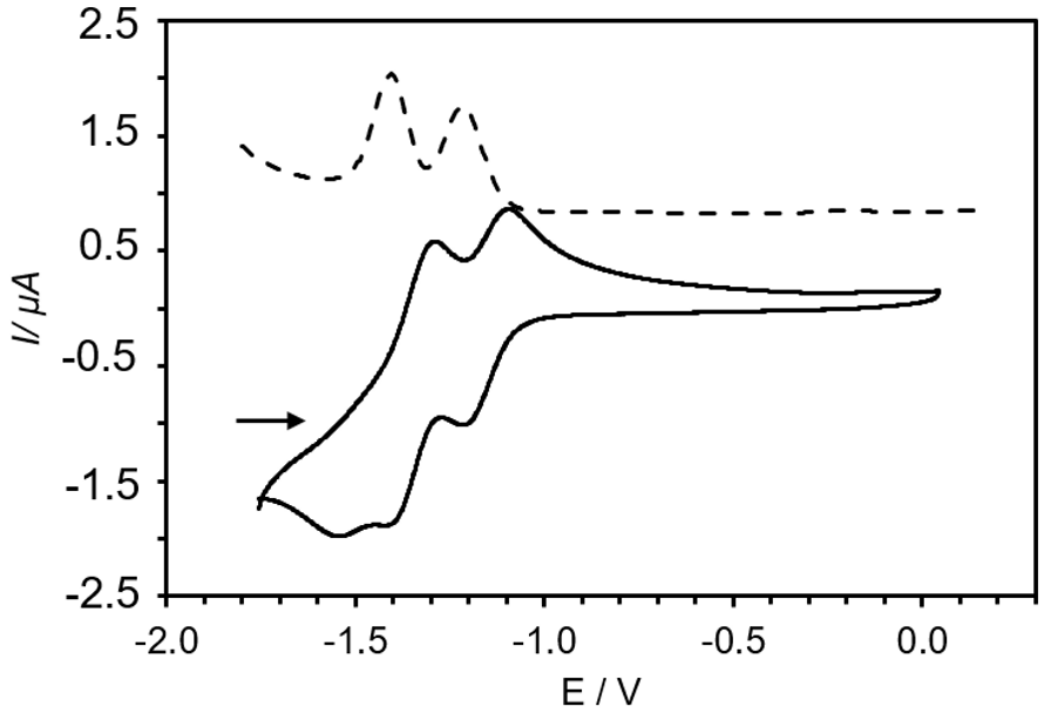

B.

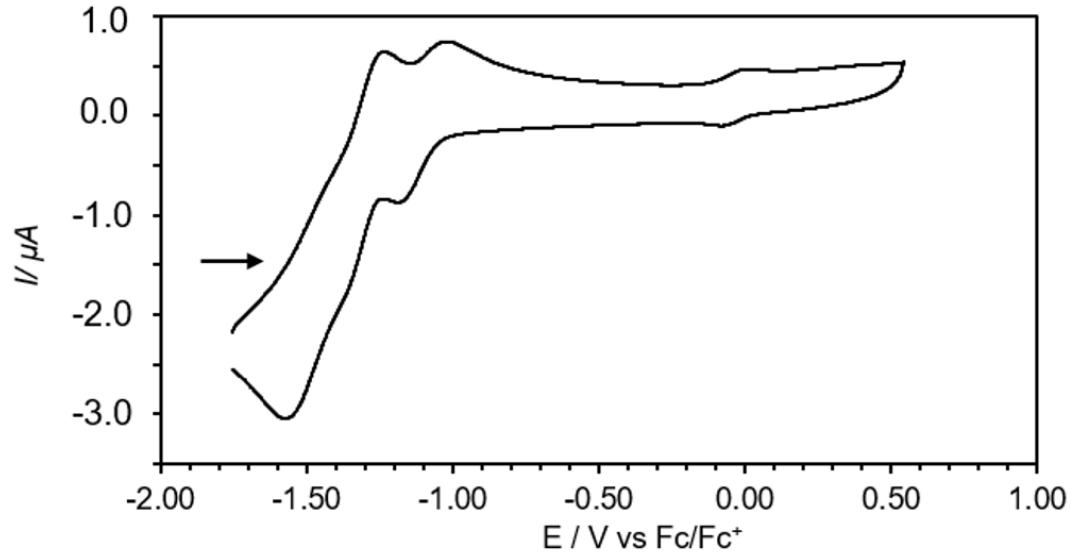

Figure S7.68. (A) CV (solid line) of aPP-PBI-aPP, 200 scan rate (SR), square wave voltammograms (dashed line), 200 SR, arbitrary intensity shift so lines did not overlap. Measurements were performed in DCM solutions (0.45 mM, 293 K), using TBAHFP (0.1 M) as electrolyte without ferrocene internal (calibrated to internal standard as done in (B), arrow indicates direction of the run. (B) CV (Solid line), 200 SR, shift with ferrocene internal standard present and calibrated to 0.0.

A.

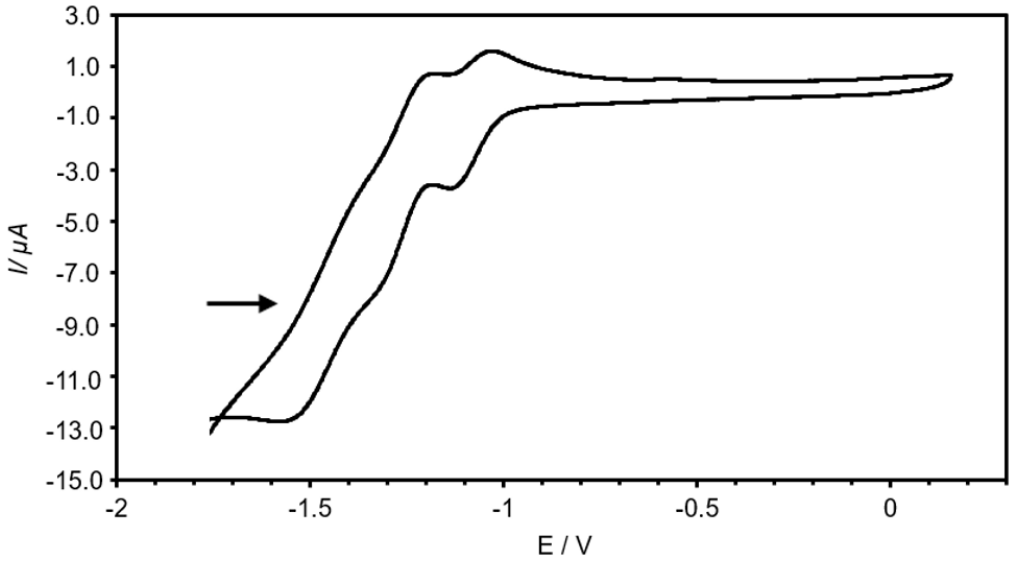

B.

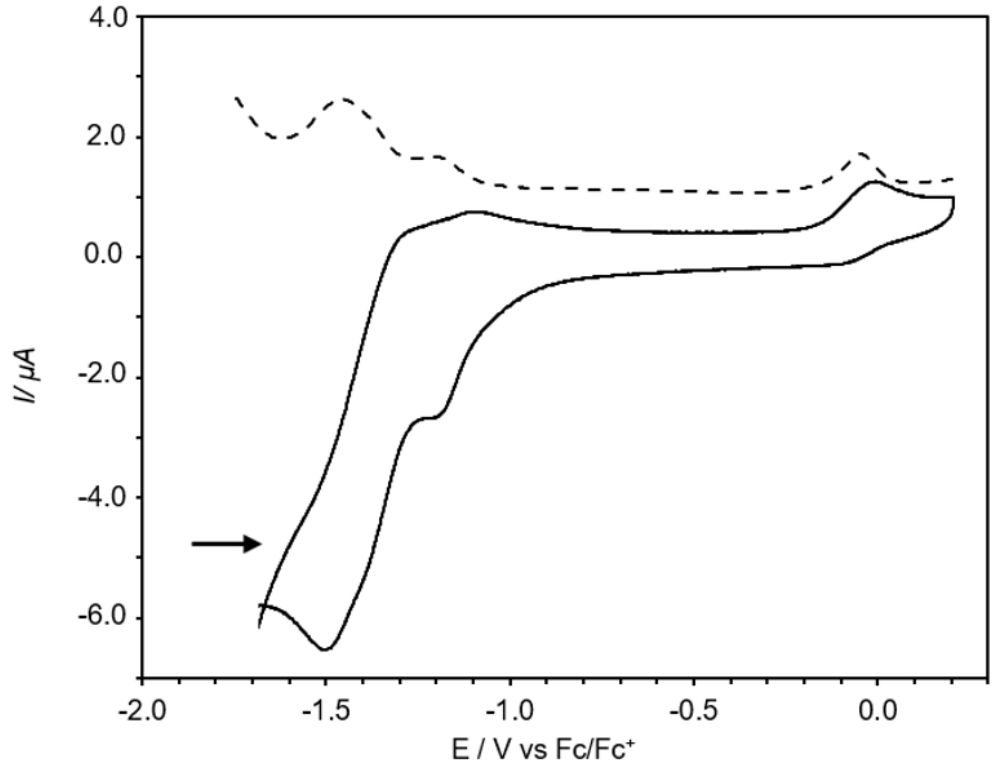

Figure S7.69. (A) CV (Solid line) of (+)PMCP-PBI-(+)PMCP, 50 SR, without ferrocene internal standard (calibrated to internal standard as done in (B)), arrow indicated direction of run. (B) CV (solid line), 50 SR, square wave voltammograms (dashed line), 50 SR, arbitrary intensity shift so lines did not overlap of (+)PMCP-PBI-(+)PMCP. Measurements were performed in DCM solutions (0.54 mM, 293 K), using

TBAHFP (0.1 M) as electrolyte with ferrocene internal standard, calibrated to 0.0, arrow indicates direction of the run.

A.

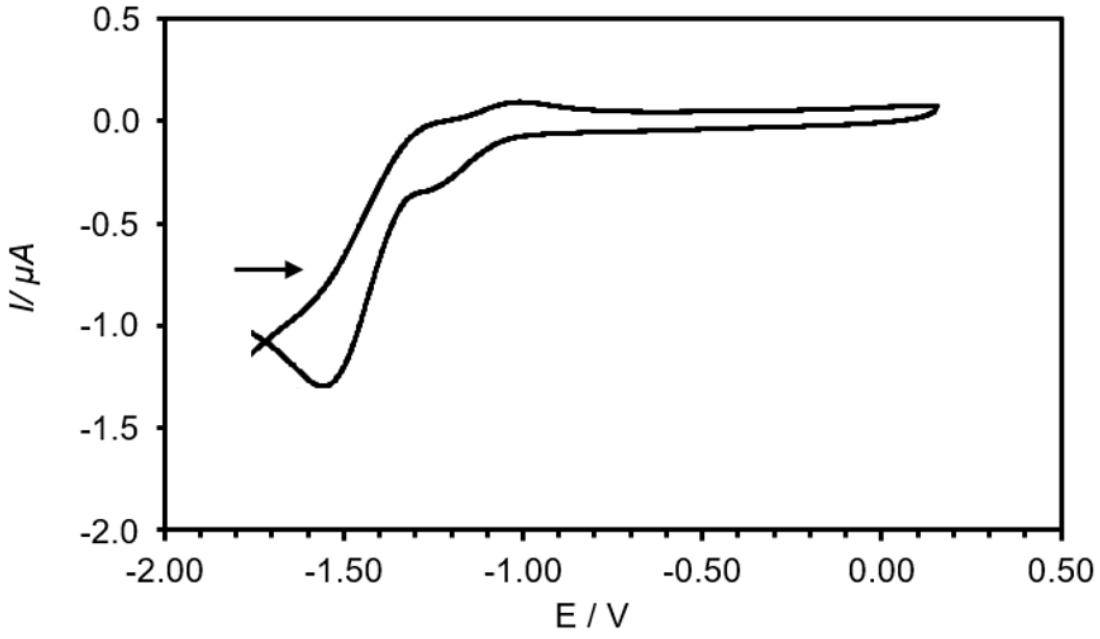

B.

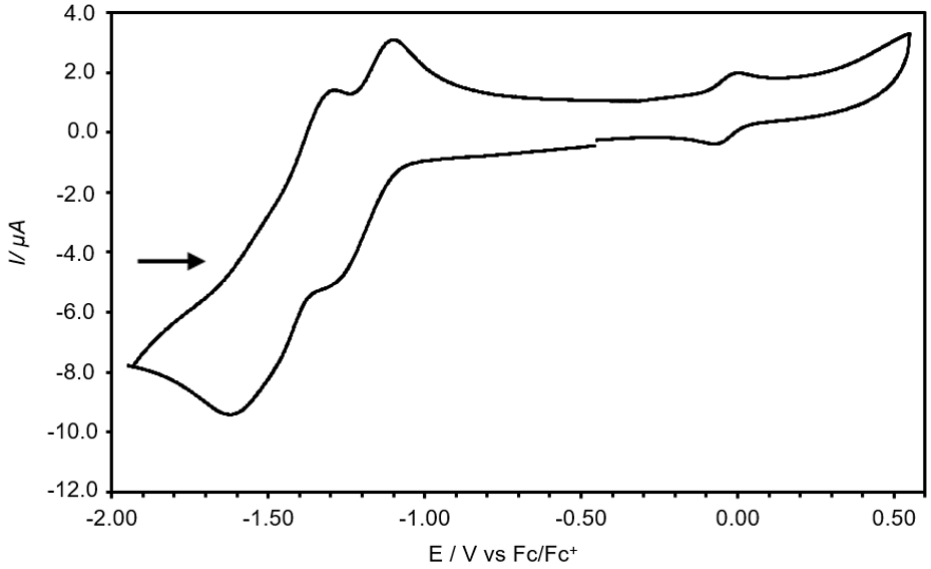

Figure S7.70. (A) CV (Solid line) of aPD-PBI-aPD, 100 SR, without ferrocene internal standard (calibrated to internal standard as done in (B)), arrow indicated direction of run. (B) CV (solid line), 100 SR, square wave voltammograms (dashed line), 100 SR, arbitrary intensity shift so lines did not over, or aPD-PBI-aPD. Measurements were performed in DCM solutions (0.54 mM, 293 K), using TBAHFP (0.1 M) as electrolyte with ferrocene internal standard, calibrated to 0.0, arrow indicates direction of the run.

A.

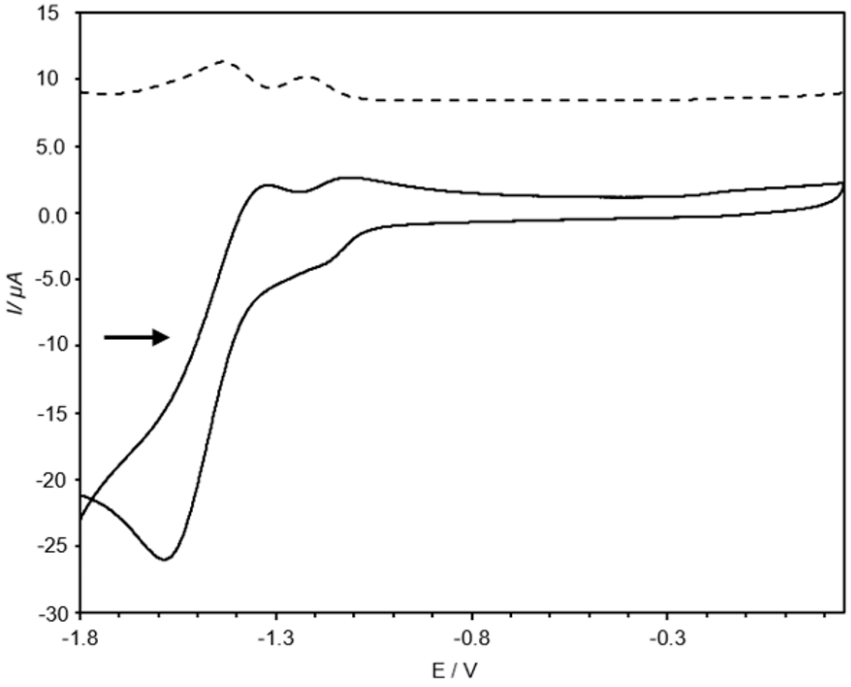

B.

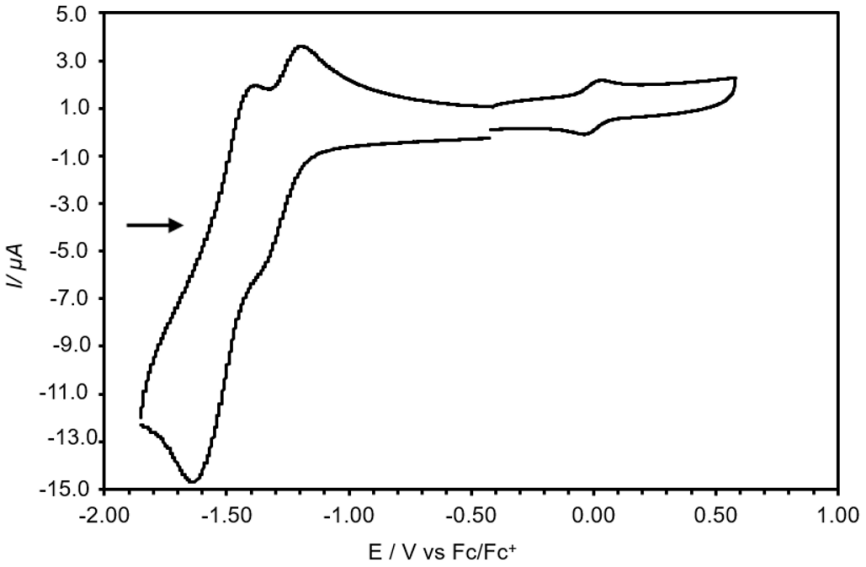

Figure S7.71. (A) CV (solid line) of aPOD-PBI-aPOD, 100 scan rate (SR), square wave voltammograms (dashed line), 100 SR, arbitrary intensity shift so lines did not overlap. Measurements were performed in DCM solutions (0.45 mM, 293 K), using TBAHFP (0.1 M) as electrolyte without ferrocene internal (calibrated to internal standard as done in (B), arrow indicates direction of the run. (B) CV (Solid line), 100 SR, shift with ferrocene internal standard present and calibrated to 0.0.

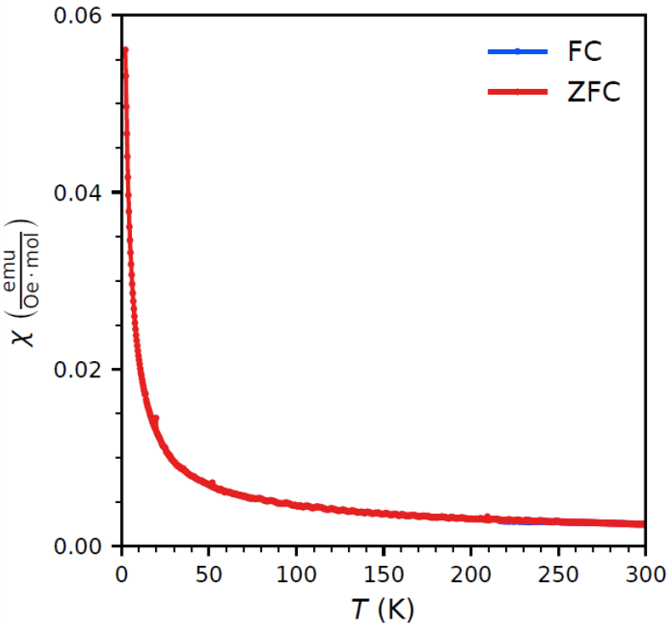

Figure S7.72. Temperature dependent susceptibility scan of the aPP-PBI-aPP:Cobaltocene blend. Positive χ values indicate unpaired electrons and therefore a paramagnetic response. The rapid increase in susceptibility at low temperatures also confirms paramagnetic behavior and does not suggest any long-range magnetic order.

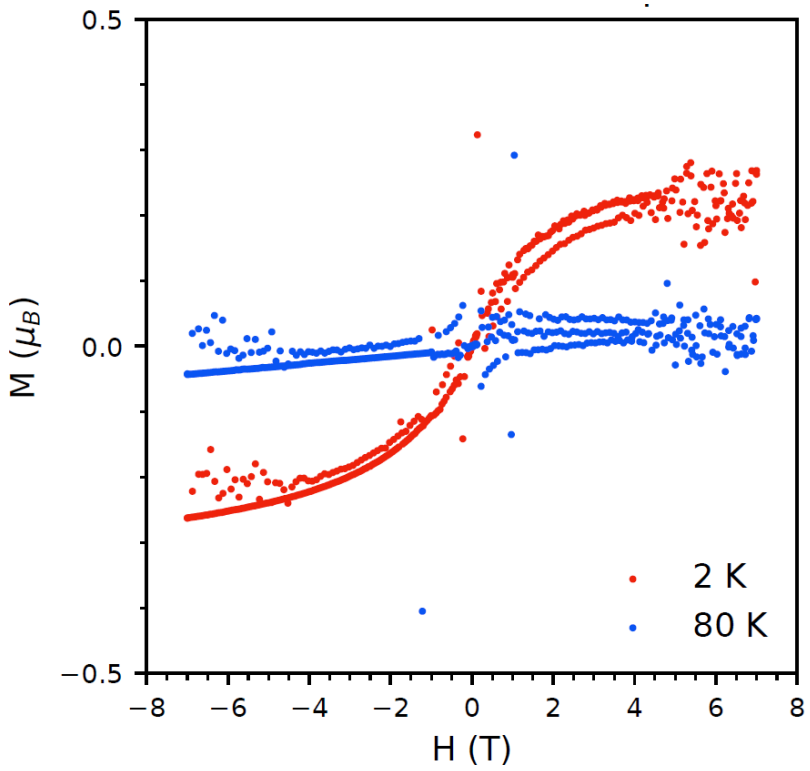

Figure S7.73. Magnetization (M) versus field (H) measurements from – 7 T to 7 T of the aPP-PBI-aPP:Cobaltocene blend. A small amount of separation of the curves results in hysteresis that could indicate ferromagnetic order. To confirm the results seen in the susceptibility, the positive slopes in the field dependent scan indicate unpaired electrons. The noise seen in the curves are due to instrument background at low and high fields.

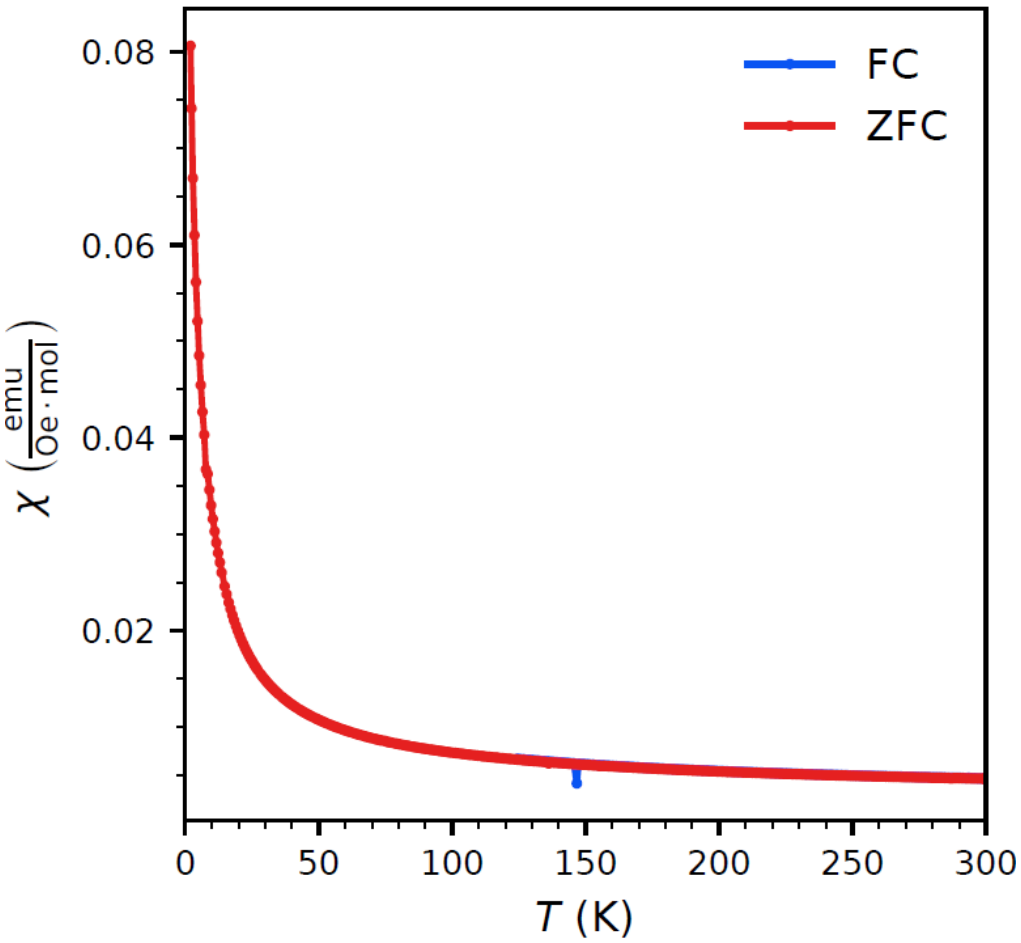

Figure S7.74. Temperature dependent susceptibility scan of the (+)PMCP-PBI-(+)PMCP:Cobaltocene blend. Positive χ values indicate unpaired electrons and therefore a paramagnetic response. The rapid increase in susceptibility at low temperatures also confirms paramagnetic behavior and does not suggest any long-range magnetic order.

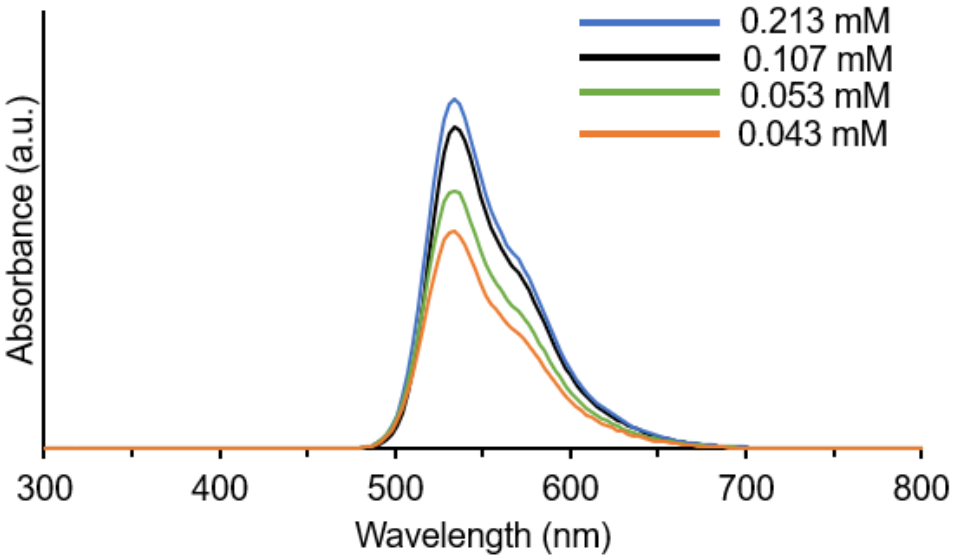

Figure S7.75. UV-vis of aPP-DPP-aPP conjugate at varied concentrations.

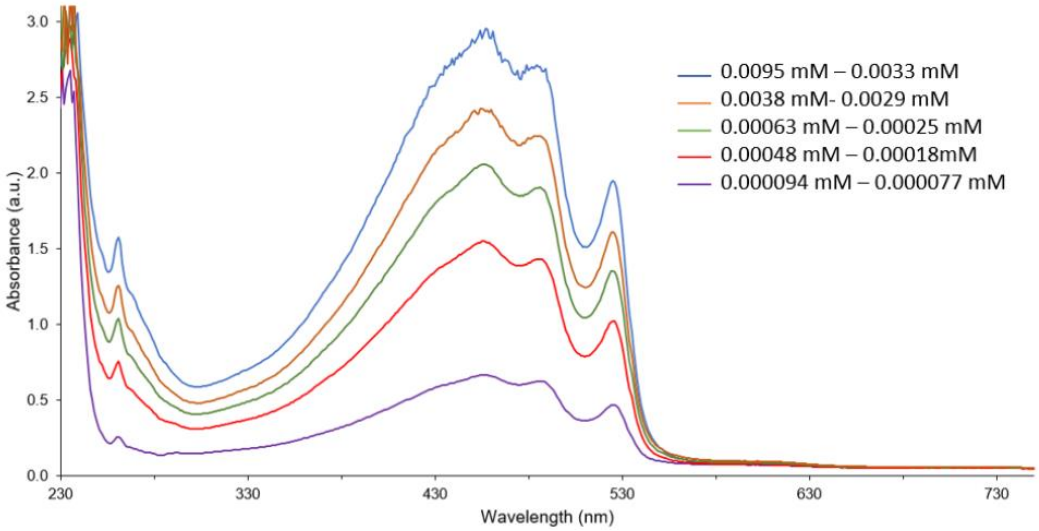

Figure S7.76. UV-vis concentration study of aPP-PBI-aPP:P3HT (1:1 by mass) blend in methylcyclohexane. The range of mM is due to the P3HT ranging molecular weight.

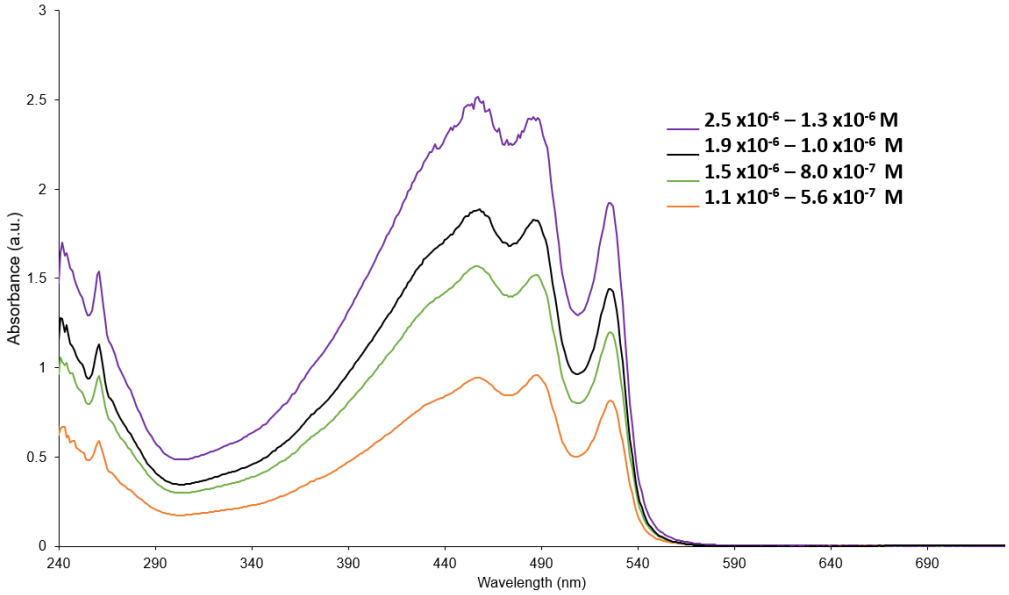

Figure S7.77. UV-vis concentration study of (+)PMCP-PBI-(+)PMCP:P3HT (1:1 by mass) blend in methylcyclohexane. The range of mM is due to the P3HT ranging molecular weight.

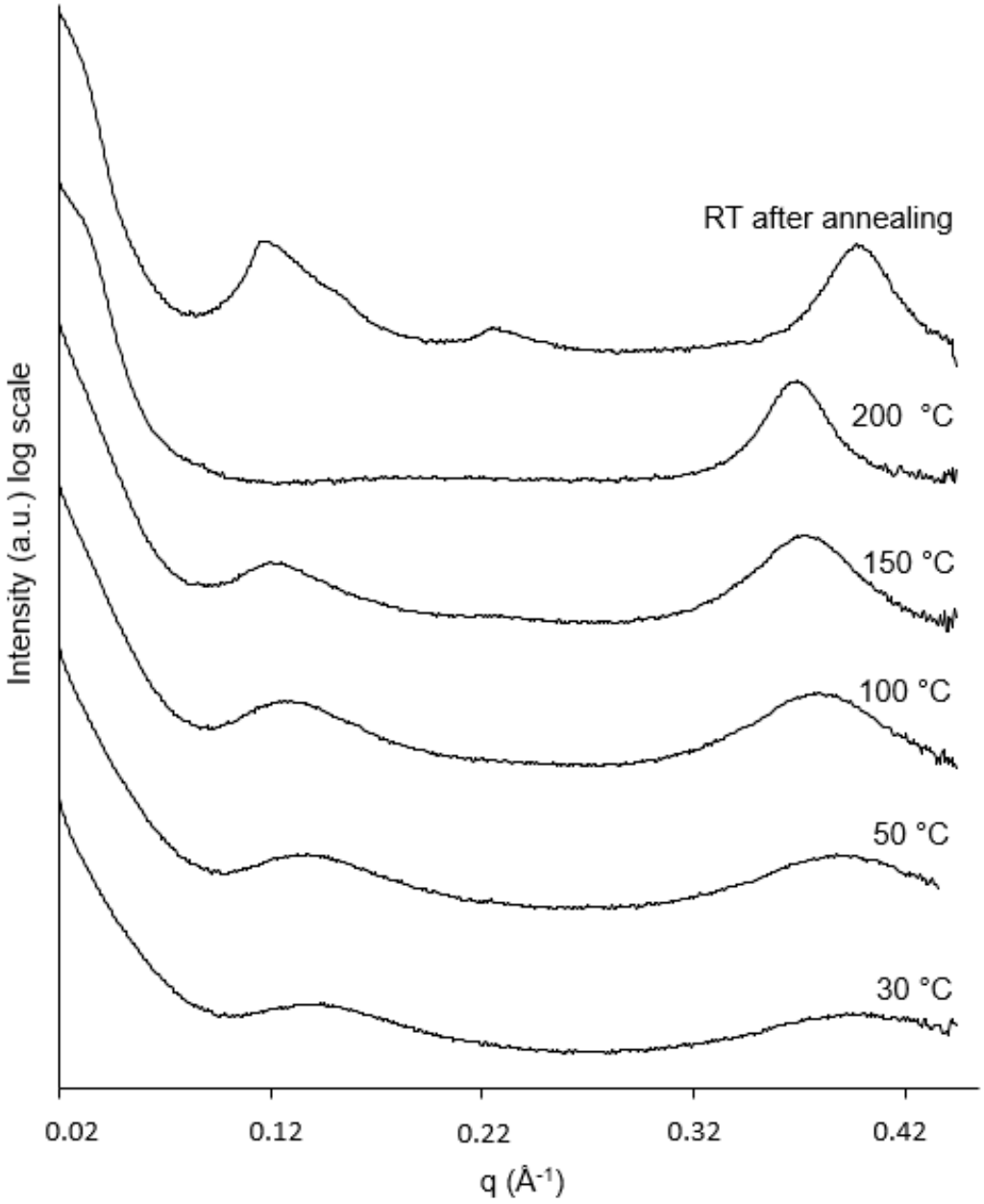

Figure S7.78. VT SAXS was conducted using on-sight x-ray source and thermal sample stage, heating to specific set temperatures, holding for 30 minutes, before measurement of the aPP-PBI-aPP:P3HT blends (1:1 by mass).

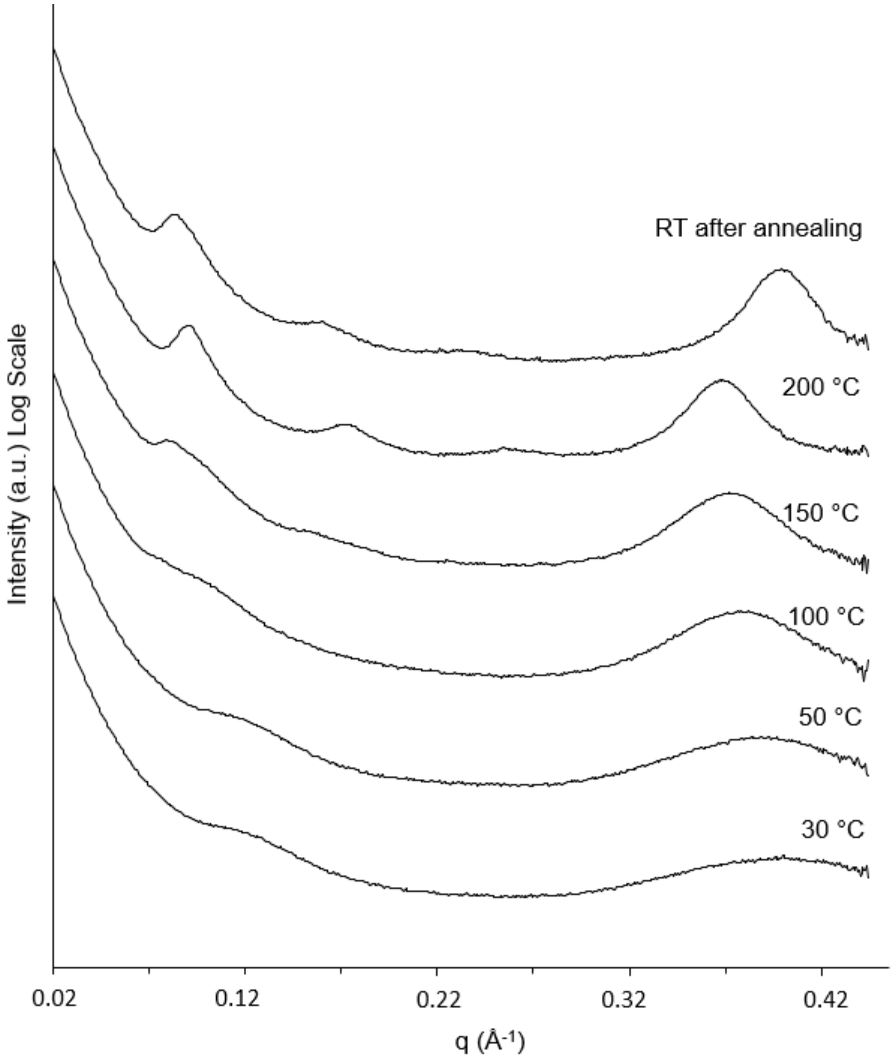

Figure S7.79. VT SAXS was conducted using on-sight x-ray source and thermal sample stage, heating to specific set temperatures, holding for 30 minutes, before measurement of the (+)PMCP-PBI-(+)PMCP:P3HT blends (1:1 by mass).

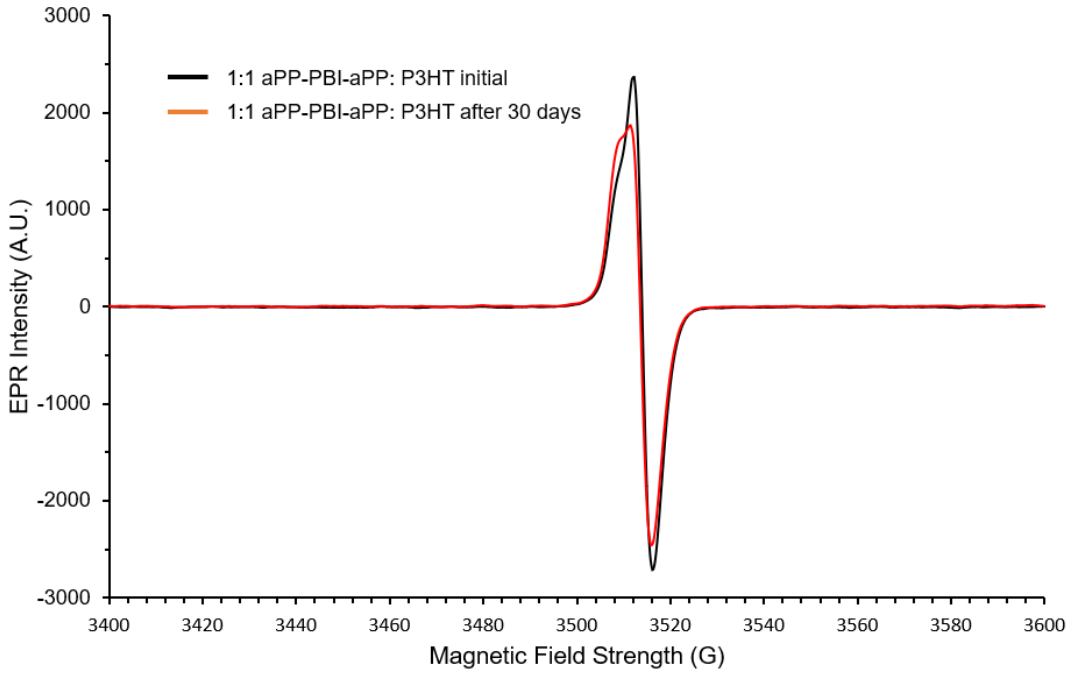

Figure S7.80. EPR spectrum of isolated solid film of the aPP-PBI-aPP:P3HT (1:1 by mass blend) radical anion before and after exposure to air.

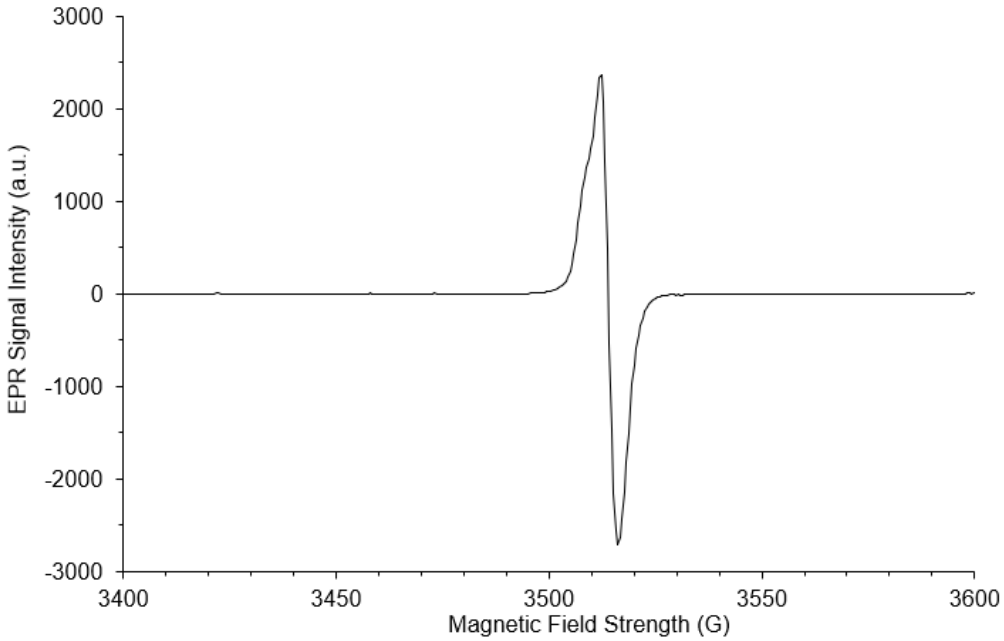

Figure S7.81. EPR spectrum of isolated solid film of the (+)PMCP-PBI-(+)PMCP:P3HT (1:1 by mass blend) radical anion.

Figure S7.82. Image of free-standing metallic luster film of (+)PMCP-PBI-(+)PMCP:P3HT blend (1:1 by mass).

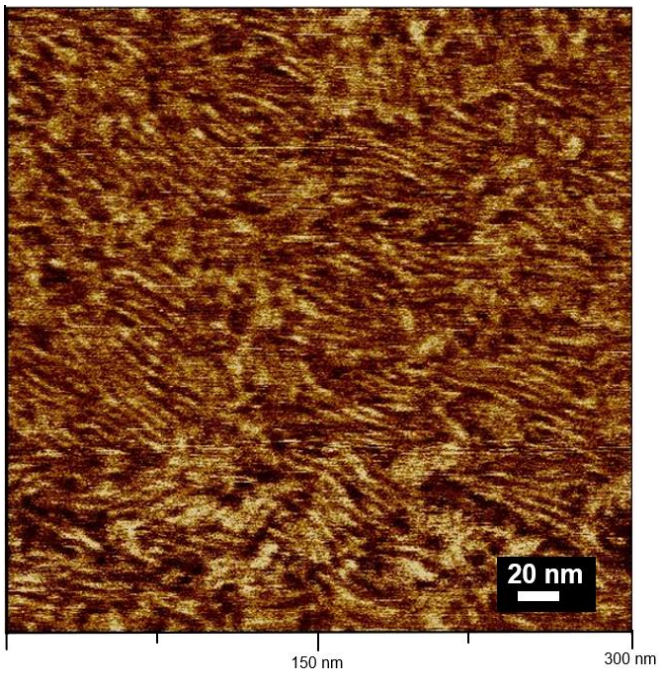

Figure S7.83. AFM phase map 300 nm scan of aPP-PBI-aPP on graphite substrate, unannealed, 76.1 nm thick, from a 2 wt% (w/v) in toluene solution.

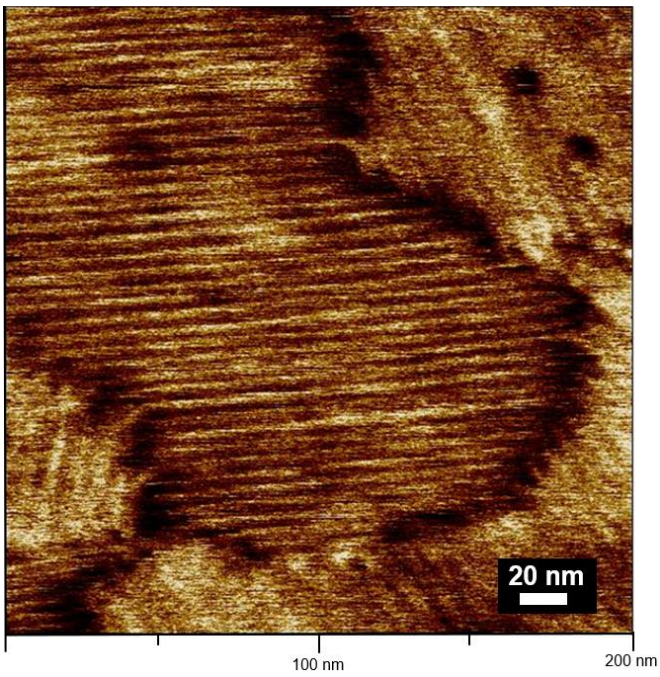

Figure S7.84. AFM phase map 200 nm scan of aPP-PBI-aPP on graphite substrate, annealed at 50 °C for 16 h, 76.1 nm thick, from a 2 wt% (w/v) in toluene solution

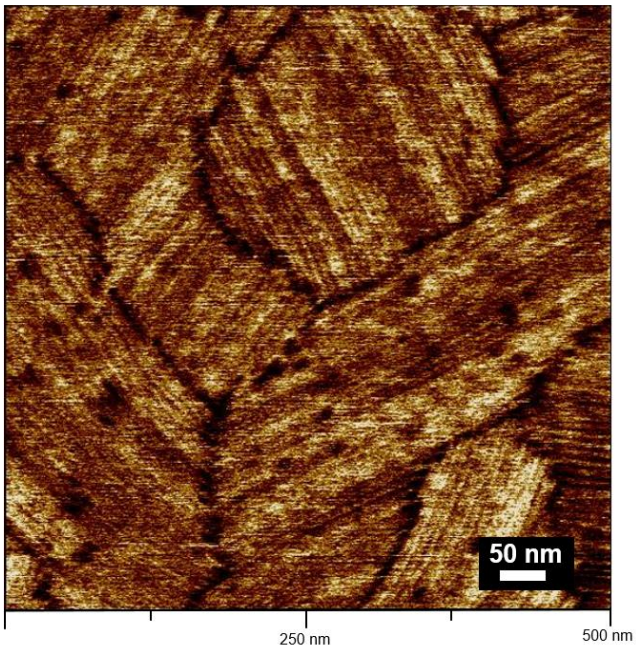

Figure S7.85. AFM phase map 500 nm scan of aPP-PBI-aPP on graphite substrate, annealed at 50 °C for 16 h, 76.1 nm thick, from a 2 wt% (w/v) in toluene solution.

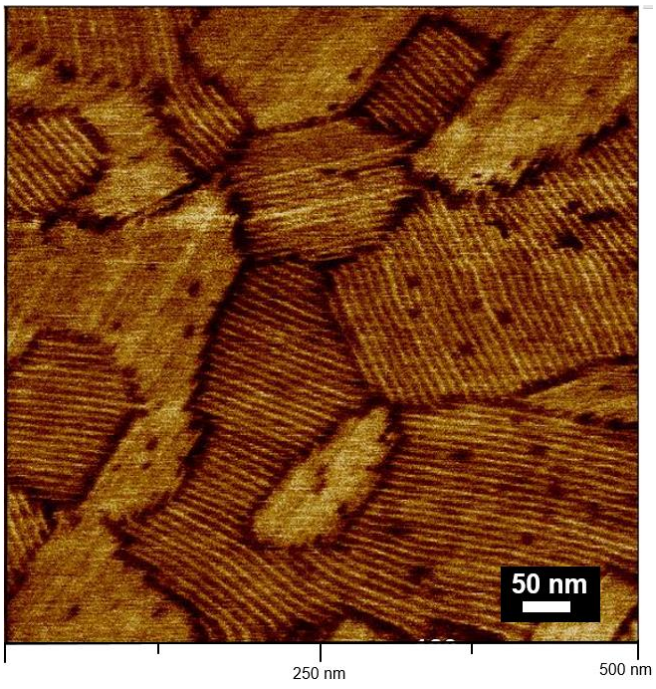

Figure S7.86. AFM phase map 500 nm scan of aPP-PBI-aPP on carbon coated silicon substrate, annealed at 50 °C for 16 h, 76.1 nm thick, from a 2 wt% (w/v) in toluene solution.

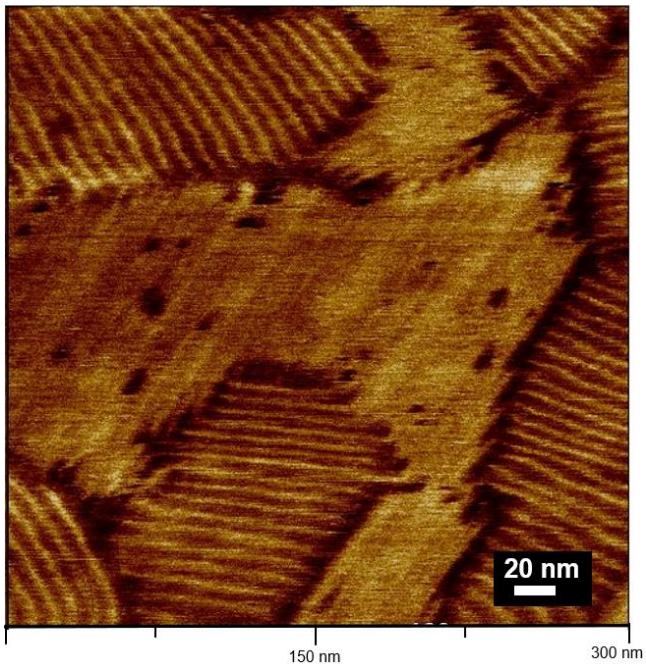

Figure S7.87. AFM phase map 300 nm scan of aPP-PBI-aPP on carbon coated silicon substrate, annealed at 50 °C for 16 h, 76.1 nm thick, from a 2 wt% (w/v) in toluene solution

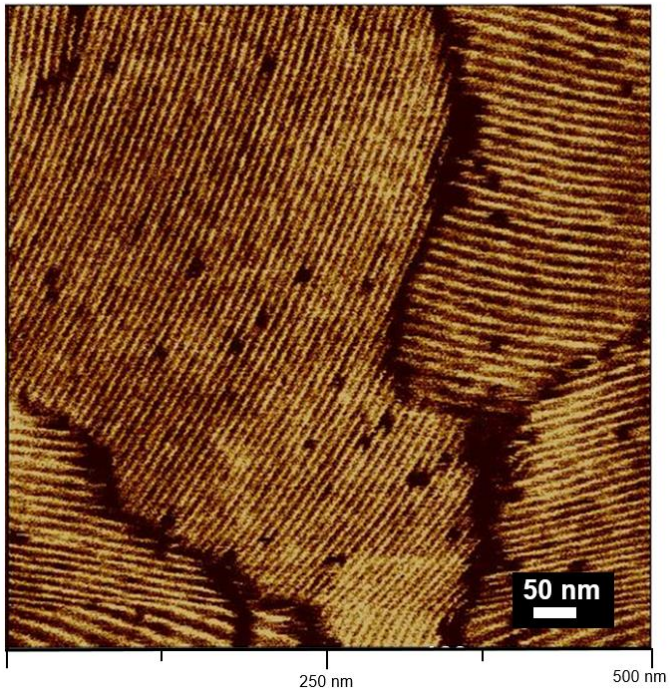

Figure S7.88. AFM phase map 180 nm scan of aPP-PBI-aPP on carbon coated silicon substrate, annealed at 55 °C for 16 h, 180 nm thick, from a 4.7 wt% (w/v) in toluene solution.

Figure S7.89. AFM phase map 180 nm scan of aPP-PBI-aPP on carbon coated silicon substrate, annealed at 110 °C for 16 h, 180 nm thick, from a 4.7 wt% (w/v) in toluene solution.

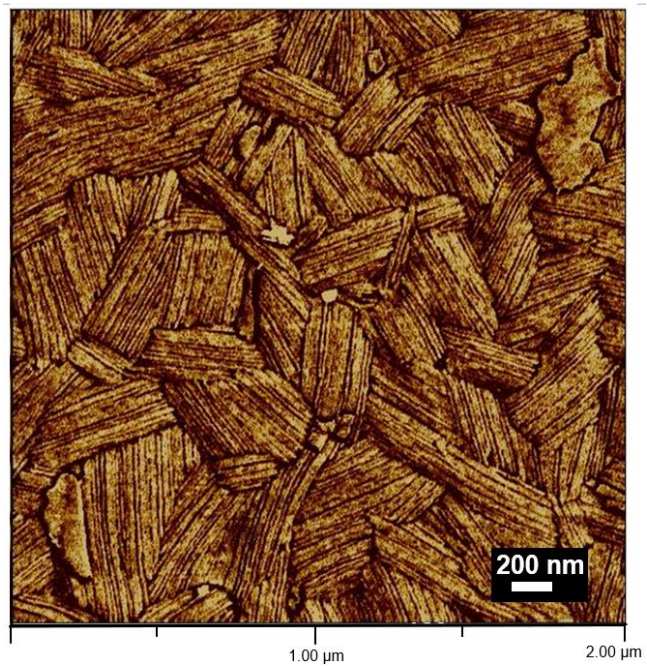

Figure S7.90. AFM phase map 2.00 µm scan of (+)PMCP-PBI-(+)PMCP on carbon-coated silicon, annealed at 110 °C for 18 hr, 78 nm thick, from a 2.8 wt% (w/v) in toluene solution**.**

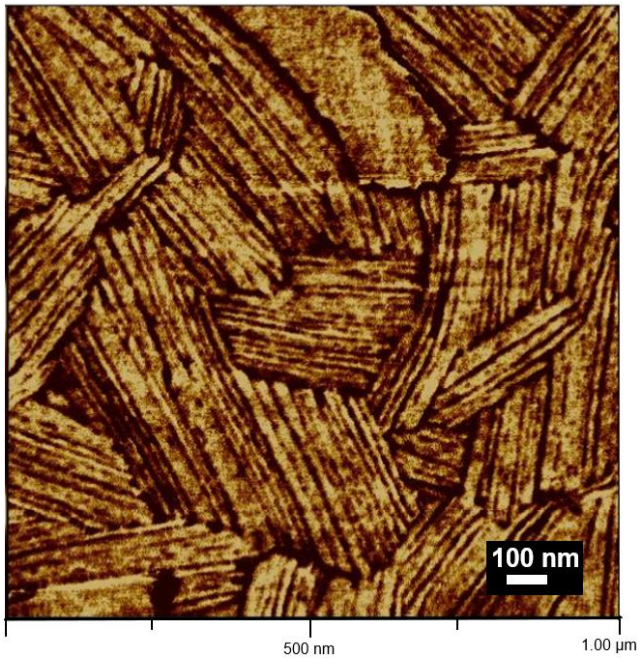

Figure S7.91. AFM phase map 1.00 µm scan of (+)PMCP-PBI-(+)PMCP on carbon-coated silicon, annealed at 110 °C for 18 hr, 78 nm thick, from a 2.8 wt% (w/v) in toluene solution.

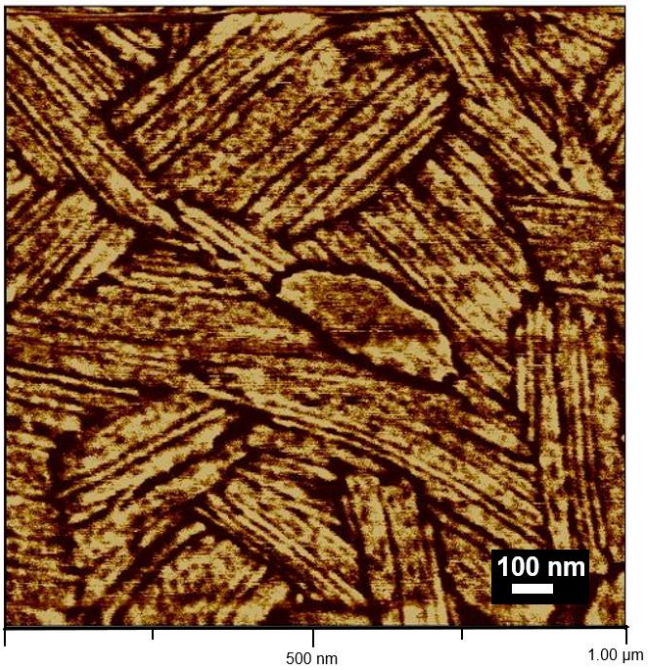

Figure S7.92. AFM phase map 1.00 µm scan of (+)PMCP-PBI-(+)PMCP on carbon-coated silicon, annealed at 150 °C for 18 hr, 78 nm thick, from a 2.8 wt% (w/v) in toluene solution.

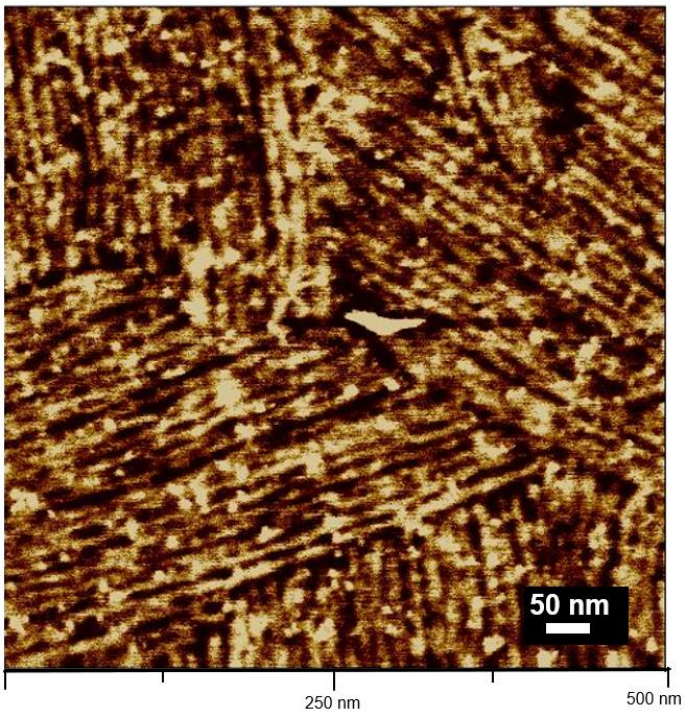

Figure S7.93. AFM phase map 500 nm scan of (+)PMCP-PBI-(+)PMCP on carbon-coated silicon, annealed at 200 °C for 18 hr, 78 nm thick, from a 2.8 wt% (w/v) in toluene solution.

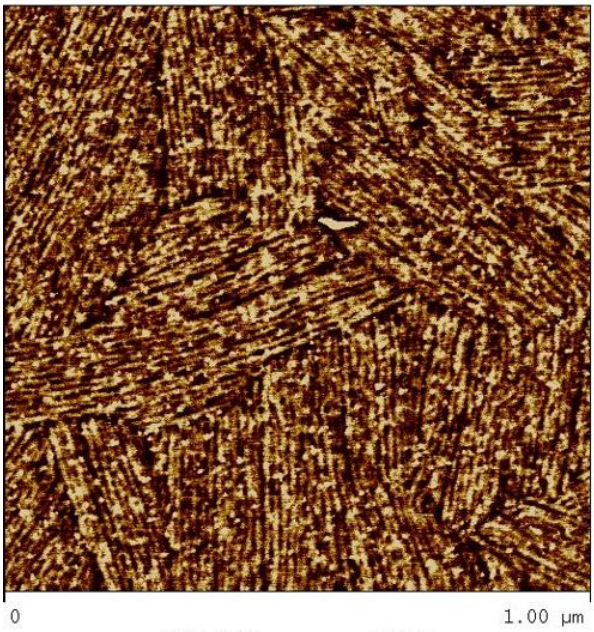

Figure S7.94. AFM phase map 1.00 µm scan of (+)PMCP-PBI-(+)PMCP on carbon-coated silicon, annealed at 200 °C for 18 hr, 78 nm thick, from a 2.8 wt% (w/v) in toluene solution.

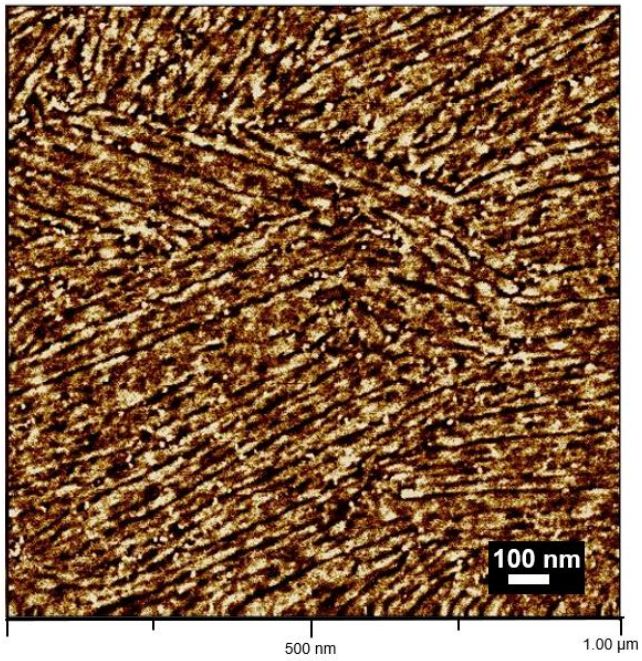

Figure S7.95. AFM phase map 1.00 µm scan of (+)PMCP-PBI-(+)PMCP on carbon-coated silicon, annealed at 240 °C for 18 hr, 78 nm thick, from a 2.8 wt% (w/v) in toluene solution.

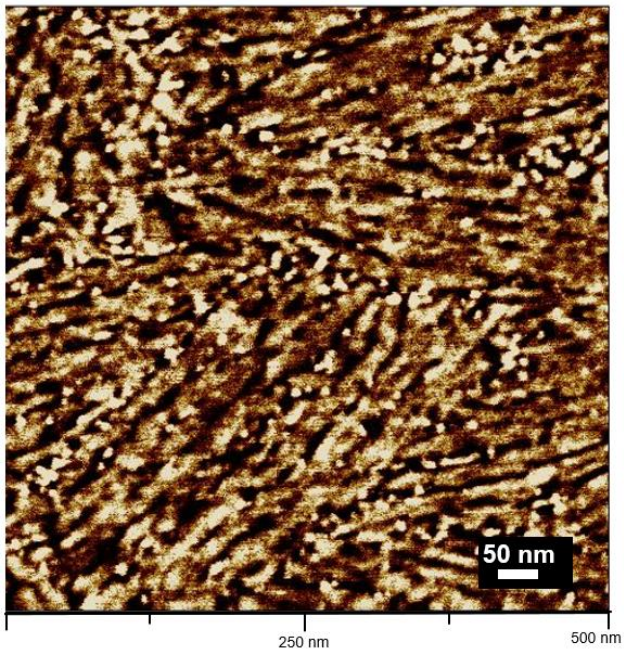

Figure S7.96. AFM phase map 500 nm scan of (+)PMCP-PBI-(+)PMCP on carbon-coated silicon, annealed at 240 °C for 18 hr, 78 nm thick, from a 2.8 wt% (w/v) in toluene solution.

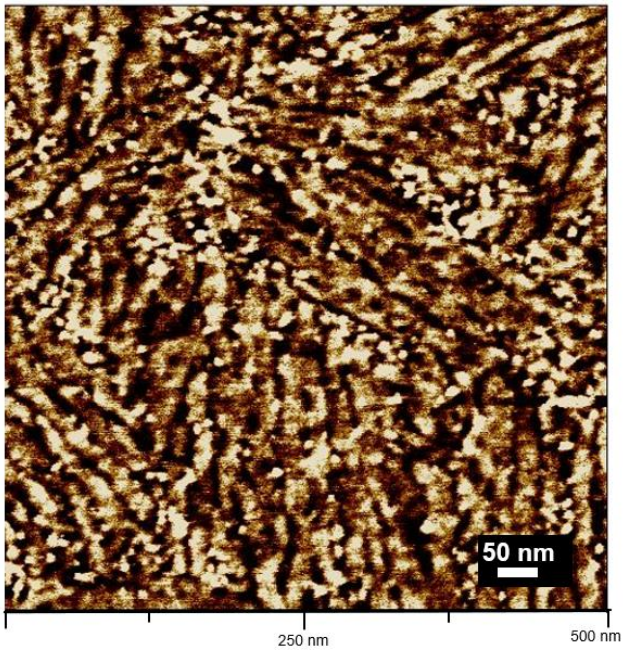

Figure S7.97. AFM phase map 500 nm scan of (+)PMCP-PBI-(+)PMCP on carbon-coated silicon, annealed at 240 °C for 18 hr, 78 nm thick, from a 2.8 wt% (w/v) in toluene solution.

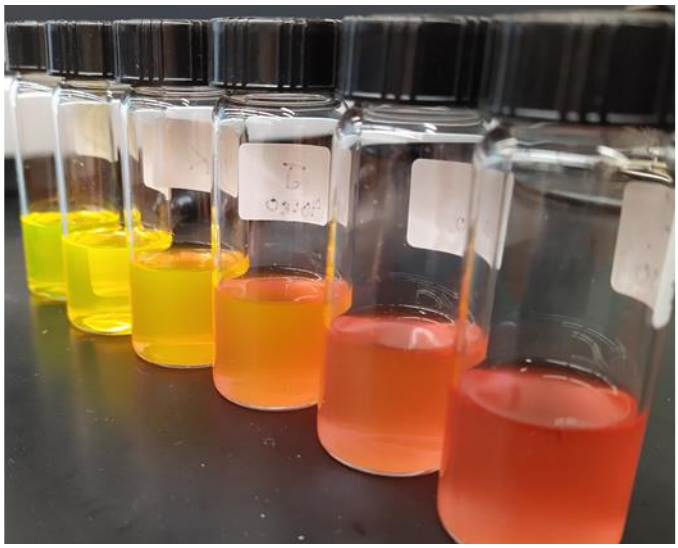

Figure S7.98. PBI conjugate aPP-PBI-aPP (**7.1**) at varied concentration in MCH.

Table S7.1 List of extinction coefficients for absorbance maximums in perylene bisiimde conjugates . Graph of the absorbance of these comparisons shown in Figure S7.51.

PBI conjugates	ε ($M^{-1}cm^{-1}$) at 516 nm	ε ($M^{-1}cm^{-1}$) at 482 nm	ε ($M^{-1}cm^{-1}$) at 452 nm
aPP-PBI-aPP	2.5 $x10^4$	1.6 $x10^4$	0.6 $x10^4$
(+)PMCP-PBI-(+)PMCP	2.3 $x10^4$	1.6 $x10^4$	0.7 $x10^4$
aPD-PBI-aPD	2.5 $x10^4$	1.5 $x10^4$	0.6 $x10^4$
aPOD-PBI-aPOD	2.4 $x10^4$	1.5 $x10^4$	0.5 $x10^4$

Table S7.2. List of observed peak positions (q_{obs}), domain spacing (d), and temperatures for hexagonal cylinders from Figure S7.42.

	23 ˚C d = 5.98 nm	**50 ˚C**, d = 5.87 nm	**70 ˚C**, d = 5.82 nm	**90 ˚C**, d = 5.61 nm	**110 °C** d = 5.44 nm
Miller Indices (hkl)	q_{obs} ($Å^{-1}$)	q_{obs} ($Å^{-1}$)	q_{obs} ($Å^{-1}$)	q_{obs} ($Å^{-1}$)	q_{obs} ($Å^{-1}$)
(100)	0.105	0.107	0.108	0.112	0.154
(110)	0.182	0.185	0.188	0.193	0.197
(200)	0.208	0.211	0.214	0.221	0.229
(210)	-	0.286	0.283	0.293	0.298

Table S7.3. List of observed peak positions (q_{obs}), calculated peak positions (q_{calc}) for single gyroid phase at 200 °C during heating ramp, Figure S7.58, and 103 °C during cooling ramp from Figure S7.65.

	200 ˚C a= 15.62 nm		**103 ˚C** a = 19.61 nm	
Miller Indices (hkl)	q_{calc} ($Å^{-1}$)	q_{obs} ($Å^{-1}$)	q_{calc} ($Å^{-1}$)	q_{obs} ($Å^{-1}$)
(110)	0.640	0.629	1.414	1.395
(211)	0.826	0.804	2.449	2.449
(220)	0.881	0.886	2.828	2.858
(420)	-	-	4.472	4.460
(332)	-	-	4.690	4.677
(422)	1.513	1.542	4.899	4.870
(440)	1.650	1.620	5.657	5.748
(530)	-	-	5.831	5.750
(631)	-	-	6.782	6.783
(710)	-	-	7.071	7.075
(640)	-	-	7.211	7.348
(750)	-	-	8.602	8.599
(664)	-	-	9.381	9.496

Table S7.4. List of observed peak positions (q_{obs}), calculated peak positions (q_{calc}) for columnar oblique at 175 °C from Fig. S7.44 for the (+)PMCP-PBI-(+)PMCP.

alpha = 104 nm	beta = 85.5 nm	gamma = 111.16
Miller Indices (hkl)	q_{calc} ($Å^{-1}$)	q_{obs} ($Å^{-1}$)
(100)	0.065	0.067
(010)	0.079	0.079
(1-20)	0.147	0.144
(020)	0.158	0.158
(-130)	0.222	0.18
(220)	0.238	0.238
(-240)	0.294	0.288
(320)	0.292	0.294
(040)	0.316	0.317

Table S7.5. Summary of the redox properties of PBI-conjugates 1a-1d, for runs with Ferrocene internal standard present. Half-wave potentials were determined by cyclic or square wave voltammetry measure in DCM (0.1 M TBAHFP) vs. Fc/Fc^+ at 293 k. Calculated according to known procedure using the experimentally determined redox potentials (E_{HOMO} = -[E_{ox1} + -4.8eV] and E_{LUMO} = -[E_{red1} + -4.8 eV]) and the energy level of Fc/ Fc^+ with respect to the atmospheric level.

PBI-conjugate	E_{ox1} (V)	E_{ox2} (V)	E_{red1} (V)	E_{red2} (V)
aPP-PBI-aPP	-1.10	-1.58	-1.22	-1.04
(+)PMCP-PBI-(+)PMCP	-1.20	-1.50	-1.29	-1.11
aPD-PBI-aPD	-1.24	-1.56	-1.27	-1.03
aPOD-PBI-aPOD	-1.29	-1.61	-1.27	-1.07

Chapter 8: Conclusions and Future Work

The research discussed within this dissertation originated from the desire to increase the scope of polyolefin products and utilized functionalized polyolefins as a designable building block to study self-assembly of conjugate materials. At the foundation of this work LCP and LCCTP techniques are scalable, versatile, and are a controlled process that allows for designable polymer materials creating a toolbox of techniques and methods that create an endless library of materials. This work is just a small piece of the large scope of materials possible with xPAO building blocks where block copolymers, sugar polyolefin conjugates, and perylene bisimide polyolefin conjugates were investigated for their rich and unique self-assembling behaviors.

Future work relies on the endless building blocks of xPAO as every type of polyolefin tail imaginable can be paired with a variety of sugar heads, or a selection of chromophores, or used in a living system to create a range of block copolymers. This work sets a precedent for future reactions and designs to be guided by the discoveries made herein. One of the major goals that still exist is tacking our stereomodulated PMP materials and utilizing them as compatibilizers to help in the reachability of plastics. This would require one to take each ‘grade’ of PMP and blend with a variety of PP and PE at differing ratios. Another possible avenue of pursuit that this research opens is access FK phases such as σ phase at ambient conditions, and with the correct sugar and polyolefin domain this can be achievable. Lastly, within the perylene bisimide polyolefin conjugates it would of great interest to see the material neat or blended with a dopant in an organic solar cell. Though these routes of research still should be

investigated, and are of great interest, the materials made throughout this work are of great value in those pursuits.

In the end, the main goals of this research were achieved: (1) the toolbox of living polymerization techniques allowed for a better understanding of many neglected olefins, (2) sugar polyolefin conjugates were able to access a variety of rich phase behaviors including rare FK phases, (3) PBI polyolefin conjugates allowed for novel phases to be observed with our xPAO building blocks and a rare single gyroid phase to be observed opening the possibilities of applications with polymer, and (4) self-assembly was influenced by the design of the polymer domains within conjugates in a programmable way. The versatility of xPAO building blocks is indisputable and versatility within a variety of materials which will shape and influence the future of scientific community, today's technologies, and the possibilities of polymer-based materials.

References

Chapter 1:

1. Jubinville, D.; Esmizadeh, E.; Saikrishnan, S.; Tzoganakis, C.; Mekonnen, T. A comprehensive review of global production and recycling methods of polyolefin (PO) based products and their postrecycling application. *Sustainable Mater. Technol*. **2020**, *25*, No. e00188.

2. Albizzati, E.; Galimberti, M. Catalysts for olefins polymerization. *Catal. Today* **1998,** *41*, 415–421.

3. Ziegler, K. Organometallic Chemistry; Zeiss, H., Ed.; ACS Monograph 147; Reinhold Publishing Corp.: New York, NY, USA, 1960; Volume 194.

4. (a) Natta, G. Kinetic studies of α-olefin polymerization. J. Polym. Sci. 1959, 34, 21– 48.

4. (b) Natta, G.; Pino, P.; Corradini, P.; Danusso, F.; Mantica, E.; Mazzanti, G.; Moraglio, G., Crystalline high polymers of alpha-olefins. *J. Am. Chem. Soc.* **1955,** *77*, 1708-1710.

5. Cossee, P. *J Catal.* **1964**, *3*, 80-88. (b) Arlman, E. J.; Cossee, P. *J Catal.* **1964**, *3*, 89-98.

6. Arlman, E. J., Ziegler-Natta Catalysis II. Surface structure of layer-lattice transitionmetal chlorides. *J. Catal.* **1964,** *3*, 89-98.

7. Collins, R.A., Russell, A.F. & Mountford, P. Group 4 metal complexes for homogeneous olefin polymerisation: a short tutorial review. *Appl Petrochem Res.* **2015**, *5*, 153–171.

8. Thayer, A. M., Metallocene catalysts initiate new era in polymer synthesis *Chem. Eng. News* **1995,** *73*, 15-20.

9. Wilkinson, G.; Pauson, P. L.; Birmingham, J. M.; Cotton, F. A. Biscyclopentadienyl Derivatives of Some Transition Elements. *J. Am. Chem. Soc*. **1953**, *75*, 1011–1012.

10. Resconi, L.; Cavallo, L.; Fait, A.; Piemontesi, F., Selectivity in Propene Polymerization with Metallocene Catalysts. *Chem. Rev.* **2000,** *100*, 1253-1346.

11. Kaminsky, W., The discovery and evolution of metallocene-based olefin polymerization catalysts. *Rendi. Fisc. Acc. Lincei.* **2017,** *28*, 87-95.

12. Resconi, L.; Cavallo, L.; Fait, A.; Piemontesi, F., Selectivity in propene polymerization with metallocene catalysts. *Chem. Rev.* **2000,** *100*, 1253-1345.

13. Natta, G.; Pino, P.; Corradini, P.; Danusso, F.; Mantica, E.; Mazzanti, G.; Moraglio, G. Crystalline High Polymers of α-Olefins. *J. Am. Chem. Soc*. **1955**, *77*, 1708−1710.

14. Natta, G. A New Class of Polymers of α-Olefin Having Exceptional Regularity of Structure. *Atti Acc. Naz. Lincei Mem*. **1955**, *4*, 61.

15. Corradini, P. The Discovery of Isotactic Polypropylene and its Impact on Pure and Applied Science. *J. Polym. Sci., Part A: Polym. Chem*. **2004**, *42*, 391−395.

16. Sivaram, S. Giulio Natta and the origins of stereoregular polymers. *Resonance* **2017**, *22*, 1007−1023.

17. Baugh, L. S., Canich, J. M., Eds.; *Stereoselective Polymerization with Single-Site Catalysts*; CRC Press: Boca Raton, 2008.

18. Ewen, J. A.; Elder, M. J.; Jones, R. L.; Curtis, S.; Cheng, H. N., Syndiospecific propylene polymerizations with iPr[CpFlu]ZrCl2. In *Studies in surface science and catalysis*, Keii, T.; Sogo, K., Eds. Elsevier: 1990; Vol. 56, pp 439-482.

19. Giannetti, E.; Nicoletti, G. M.; Mazzocchi, R., Homogeneous Ziegler-Natta catalysis. II. Ethylene polymerization by IVB transition metal complexes/methyl aluminoxane catalyst systems *J. Polym. Sci. Polym. Chem* **1985,** *23*, 2117.

20. Ewen, J. A., Mechanisms of stereochemical control in propylene polymerizations with soluble group-4B metallocene methylalumoxane catalysts. *J. Am. Chem. Soc.* **1984,** *106*, 6355-6364.

21. Kaminsky, W.; Kulper, K.; Brintzinger, H. H.; Wild, F., Polymerization of propene and butene with a chiral zirconocene and methylaluminoxane as cocatalyst. *Angew. Chem. Int. Ed.* **1985,** *24*, 507-508.

22. De Rosa, C.; Auriemma, F.; Di Capua, A.; Resconi, L.; Guidotti, S.; Camurati, I.; Nifant'ev, I. E.; Laishevtsev, I. P., Structure-Property Correlations in Polypropylene from Metallocene Catalysts: Stereodefective, Regioregular Isotactic Polypropylene. *J. Am. Chem. Soc.* **2004,** *126*, 17040-17049.

23. Flory, P. J., Molecular Size Distribution in Ethylene Oxide Polymers. *J. Am. Chem. Soc.* **1940,** *62*, 1561-1565.

24. Melville, H. W.; Evans, M. G.; Price, W. C.; Bell, R. P.; Schulman, J. H., General and physical chemistry. *Annu. Rep. Prog. Chem.* **1939,** *36*, 33-115.

25. Grubbs, R. B.; Grubbs, R. H. *50th Anniversary Perspective*: Living Polymerization—Emphasizing the *Molecule* in *Macromolecules*. *Macromolecules* **2017**, *50*, 6979–6997.

26. Franta, E.; Hogen-Esch, T.; van Beylen, M.; Smid, J. Fifty years of living polymers. *J. Polym. Sci., Part A: Polym. Chem*. **2007**, *45*, 2576– 2579.

27. Muller, A. H. E.; Matyjaszewski, K., Eds.; Wiley- VCH: Weinheim, 2009

28. Hirao, A.; Goseki, R.; Ishizone, T. Advances in Living Anionic Polymerization: From Functional Monomers, Polymerization Systems, to Macromolecular Architectures. *Macromolecules* **2014**, *47*, 1883– 1905.

29. Hadjichristidis, N.; Iatrou, H.; Pitsikalis, M.; Mays, J. Macromolecular architectures by living and controlled/living polymerizations. *Prog. Polym. Sci*. **2006**, *31*, 1068– 1132.

30. Rubinstein, M.; Colby, R. H., *Polymer Physics*. Oxford University Press: 2003.

31. Gentekos, D. T.; Sifri, R. J.; Fors, B. P., Controlling polymer properties through the shape of the molecular-weight distribution. *Nat. Rev. Mater.* **2019,** *4*, 761-774.

32. Gentekos, D. T.; Sifri, R. J.; Fors, B. P., Controlling polymer properties through the shape of the molecular-weight distribution. *Nat. Rev. Mater.* **2019,** *4*, 761-774.

33. Balani, K.; Verma, V.; Agarwal, A.; Narayan, R., Physical, thermal, and mechanical properties of polymers. In *Biosurfaces: A Materials Science and Engineering Perspective*, John Wiley & Sons, Inc Amer Ceramic Soc, 735 ceramic place, Westerville, OH 43081-8720 USA, 2015; pp 329-344

34. Britovsek, G. J. P.; Cohen, S. A.; Gibson, V. C.; van Meurs, M. Iron Catalyzed Polyethylene Chain Growth on Zinc: A Study of the Factors Delineating Chain Transfer *versus* Catalyzed Chain Growth in Zinc and Related Metal Alkyl Systems. *J. Am. Chem. Soc.* **2004,** *126*, 10701-10712.

35. Hustad, P. D.; Kuhlman, R. L.; Carnahan, E. M.; Wenzel, T. T.; Arriola, D. J., An Exploration of the Effects of Reversibility in Chain Transfer to Metal in Olefin Polymerization. *Macromolecules* **2008,** *41*, 4081-4089.

36. Grubbs, R. H.; Coates, G. W., alpha-Agostic interactions and olefin insertion in metallocene polymerization catalysts. *Acc. Chem. Res* **1996,** *29*, 85-93.

37. Coates, G. W.; Hustad, P. D.; Reinartz, S., Catalysts for the living insertion polymerization of alkenes: Access to new polyolefin architectures using Ziegler-Natta chemistry. *Angew. Chem. Int. Ed.* **2002,** *41*, 2236-2257.

38. Doi, Y.; Ueki, S.; Keii, T. "Living" Coordination Polymerization of Propene Initiated by the Soluble $V(acac)_3$-$Al(C_2H_5)_2Cl$ System. *Macromolecules* **1979**, *12*, 814 - 819.

39. Doi, Y.; Ueki, S.; Keii, T. Preparation of "living" polypropylenes by a soluble vanadium-based Ziegler catalyst. *Makromol. Chem. Macromol. Chem. Phys*. **1979**, *180*, 1359-1361.

40. Scollard, J. D.; McConville, D. H.; Payne, N. C.; Vittal, J. J., Polymerization of r-Olefins by Chelating Diamide Complexes of Titanium. *Macromolecules* **1996,** *29*.

41. Scollard, J. D.; McConville, D. H., Living Polymerization of alpha-Olefins by Chelating Diamide Complexes of Titanium. *J. Am. Chem. Soc.* **1996,** *118*, 10008-10009.

42. Tshuva, E. Y.; Goldberg, I.; Kol, M., Isospecific Living Polymerization of 1-Hexene by a Readily Available Nonmetallocene C_2-Symmetrical Zirconium Catalyst. **2000**, *122*, 10706 10707.

43. Baumann, R.; Davis, W.; Schrock, R. R., Synthesis of Titanium and Zirconium Complexes That Contain the Tridetate Diamido Ligand, $[((t\text{-}Bu\text{-}d_6)N\text{-}o\text{-}C_6H_4)_2O]^{2-}$ ($[NON]^{2-}$) and the Living Polymerization of 1-Hexene by Activated $[NON]ZrMe_2$. *J. Am. Chem. Soc.* **1997**, 3830-3831.

44. Matsui, S.; Tohi, Y.; Mitani, M.; Saito, J.; Makio, H.; Tanaka, H.; Nitabaru, M.; Nakano, T.; Fujita, T., New bis(salicylaldiminato) titanium complexes for ethylenepolymerization. *Chem. Lett.* **1999**, 1065-1066.

45. Jayaratne, K. C.; Sita, L. R., Stereospecific living Ziegler-Natta polymerization of 1-hexene. *J. Am. Chem. Soc.* **2000,** *122*, 958-959.

46. Jayaratne, K. C.; Keaton, R. J.; Henningsen, D. A.; Sita, L. R., Living Ziegler-Natta cyclopolymerization of nonconjugated dienes: New classes of microphaseseparated polyolefin block copolymers via a tandem polymerization/cyclopolymerization strategy. *J. Am. Chem. Soc.* **2000,** *122*, 10490-10491.

47. Keaton, R. J.; Jayaratne, K. C.; Henningsen, D. A.; Koterwas, L. A.; Sita, L. R., Dramatic enhancement of activities for living Ziegler-Natta polymerizations mediated by "exposed" zirconium acetamidinate initiators: The isospecific living polymerization of vinylcyclohexane. *J. Am. Chem. Soc.* **2001,** *123*, 6197-6198.

48. Giller, C.; Gururajan, G.; Wei, J.; Zhang, W.; Hwang, W.; Chase, D. B.; Rabolt,; J. F.; Sita, L. R. Synthesis, Characterization, and Electrospinning of Architecturally-Discrete Isotactic-Atactic-Isotactic Triblock Stereoblock Polypropene Elastomers. *Macromolecules* **2011**, *44*, 471−482.

49. Crawford, K. E.; Sita, L. R. De Novo Design of a New Class of “Hard-Soft” Amorphous, Microphase-Separated, Polyolefin

50. Zhang, Y.; Keaton, R. J.; Sita, L. R. Degenerative Transfer Living Ziegler-Natta Polymerization: Application to the Synthesis of Monomodal Stereoblock Polyolefins of Narrow Polydispersity and Tunable Block Length. *J. Am. Chem. Soc*. **2003**, *125*, 9062−9069.

51. Zhang, Y.; Sita, L. R. Stereospecific Living Ziegler-Natta Polymerization via Rapid and Reversible Chloride Degenerative Transfer between Active and Dormant Sites. *J. Am. Chem. Soc*. **2004**, *126*, 7776−7777

52. Kissounko, D. A.; Zhang, Y.; Harney, M. B.; Sita, L. R. Evaluation of (η5-C_5Me_5)Hf$(R)_2$[N(Et)C(Me)N(t-Bu)] (R = Me and i-Bu) for the Stereospecific Living and Degenerative Transfer Living ZieglerNatta Polymerization of α- Olefins. *Adv. Synth. Catal*. **2005**, *347*, 426− 432.

53. Harney, M. B.; Zhang, Y.; Sita, L. R. Bimolecular Control over Polypropene Stereochemical Microstructure in a Well-Defined Two-State System and a New Fundamental Form: Stereogradient Polypropene. *Angew. Chem., Int. Ed*. **2006**, *45*,6140−6144.

54. Harney, M. B.; Zhang, Y.; Sita, L. R. Discrete, Multiblock Isotactic-Atactic Stereoblock Polypropene Microstructures of Differing Block Architectures through Programmable Stereomodulated Living Ziegler-Natta Polymerization. *Angew. Chem., Int. Ed*. **2006**, *45*, 2400−2404.

55. Zhang, W.; Sita, L. R. Investigation of Dynamic Intra- and Intermolecular Processes within a Tether-Length Dependent Series of Group 4 Bimetallic Initiators

for Stereomodulated Degenerative Transfer Living Ziegler-Natta Propene Polymerization. *Adv. Synth. Catal*. **2008**, *350*, 439−447.

56. Crawford, K. E.; Sita, L. R. Stereoengineering of Poly(1,3-methylenecyclohexane) via Two-State Living Coordination Polymerization of 1,6-Heptadiene. *J. Am. Chem. Soc*. **2013**, *135*, 8778−8781.

57. Crawford, K. E.; Sita, L. R. Regio- and Stereospecific Cyclopolymerization of Bis(2-propenyl)diorganosilanes and the Two-State Stereoengineering of 3,5-Cis, Isotactic Poly(3,5- methylene-1-silacyclohexane)s. *ACS Macro Lett*. **2014**, *3*, 506−509.

58 . Zhang, W.; Sita, L. R., Highly Efficient, Living Coordinative Chain-Transfer Polymerization of Propene with ZnEt2: Practical Production of Ultrahigh to Very LowMolecular Weight Amorphous Atactic Polypropenes of Extremely Narrow Polydispersity. *J. Am. Chem. Soc.* **2008,** *130*, 442-443.

59. Zhang, W.; Wei, J.; Sita, L. R., Living Coordinative Chain-Transfer Polymerization and Copolymerization of Ethene, R-Olefins, and R,ω-Nonconjugated Dienes using Dialkylzinc as "Surrogate" Chain-Growth Sites. *Macromolecules* **2008,***41*, 7829-7833.

60. Wei, J.; Wickham, R.; Sita, L. R., Scalable Production of End-Group Functionalized Precision Polyolefins. *Poly. Prepr.* **2010,** *51*, 370-371.

61. Thomas, T. S.; Hwang, W.; Sita, L. R., End-Group-Functionalized Poly(alphaolefinates) as Non-Polar Building Blocks: Self-Assembly of Polyolefin Hybrid Conjugates. *Angew. Chem. Int. Ed.* **2016,** *55*, 4683-4687.

62. Nowak, S. R.; Hwang, W.; Sita, L. R. Dynamic Sub-10-nm Nanostructured Ultrathin Films of Sugar-Polyolefin Conjugates Thermoresponsive at Physiological Temperatures. *J. Am. Chem. Soc*. **2017**, *139*, 5281−5284.

63. Lachmayr, K. K.; Wentz, C. M.; Sita, L. R. An Exceptionally Stable and Scalable Sugar-Polyolefin Frank-Kasper A15 Phase. *Angew. Chem., Int. Ed*. **2020**, *59*, 1521−1526.

64. Lachmayr, K. K.; Sita, L. R. Small Molecule Modulation of Soft Matter Frank-Kasper Phases: A New Paradigm for Adding Function to Form. *Angew. Chem., Int. Ed*. **2020**, *59*, 3563−3567.

65. Nowak, S. R.; Lachmayr, K. K.; Yager, K. G.; Sita, L. R. Stable Thermotropic 3D and 2D Double Gyroid Nanostructures with Sub-2-nm Feature Size for Scalable Sugar-Polyolefin Conjugates. *Angew. Chem., Int. Ed*. **2021**, *60*, 8710−8716.

66. Wallace, M. A.; Burkey, A. A.; Sita, L. R. Phenyl-Terminated Polyolefins via Living Coordinative Chain Transfer Polymerization with $ZnPh_2$ as a Chain Transfer Agent. *ACS Catal.* **2021**, *11*, 10170-10178.

67. Su, W.-F. *Principles of Polymer Design and Synthesis,* Springer-Verlag Berlin Heidelberg, 2013.

68. Service, R. F.; Szuromi, P.; Uppenbrink, J., Supramolecular Chemistry and Self-Assembly: Strength in Numbers. *Science* **2002,** *295*, 2395.

69. Rosler, A.; Vandermeulen, G. W. M.; Klok, H., Advanced drug delivery devices via self-assembly of amphiphilic block copolymers. *Adv. Drug Deliv. Rev.* **2001,** (53), 95-108.

70. Kunitake, T., Synthetic Bilayer Membranes: Molecular Design, Self-Organization, and Application. *Angew. Chem. Int. Ed.* **1992,** (31), 709-726.

71. (a) Alexandridis, P.; Lindman, B., *Amphiphilic Block Copolymers: Self-Assembly and Applications*. Elsevier Science B.V.: 2000.

71. (b) Keyes, A.; Alhan, H. E. B.; Ordonez, E.; Ha, U.; Beezer, D. B.; Dau, H.; Liu, Y. S.; Tsogtgerel, E.; Jones, G. R.; Harth, E., Olefins and Vinyl Polar Monomers: Bridging the Gap for Next Generation Materials. *Angew. Chem. Int. Ed.* **2019,** *58*,12370-12391.

72. Zhang, X.; Wang, C., Supramolecular amphiphiles. *Chem. Soc. Rev.* **2011,** (40), 94-101.

73. Park, M.; Harrison, C.; Chaikin, P. M., Block Copolymer Lithography: Periodic Arrays of ~1011 Holes in 1 Square Centimeter. *Science* **1997,** (5317), 1401-1404.

74. Kato, T.; Mizoshita, N.; Kishimoto, K., Functional liquid-crystalline assemblies: self-organized soft materials. *Angew. Chem. Int. Ed.* **2006,** (45), 1401-1404.

75. Israelachvili, J.; Mitchell, D. J.; Ninham, B. W., *J. Chem. Soc., Faraday Trans. 2* **1976,** (72), 1525-1568.

76. Su, Z. B.; *et al.* The role of architectural engineering in macromolecular self-assemblies via non-covalent interactions: A molecular LEGO approach. *Prog. Polym. Sci.* **2020,** *103*.

77. Jungwirth, P.; Zahradnfk, R., The entropy driven hydrophobic effect as a function of solute-solvent interactions. A molecular dynamics study. *Chem. Phys. Lett.* **1994,** *217*, 319-324.

78. Rodriguez-Hernandez, J.; Checot, F.; Gnanou, Y.; Lecommandoux, S., Toward 'smart' nano-objects by self-assembly of block copolymers in solution. *Prog. Polym. Sci.* **2005,** *30*, 691-724.

79. Lombardo, D.; Kiselev, M. A.; Magazu, S.; Calandra, P., Amphiphiles Self-Assembly: Basic Concepts and Future Perspectives of Supramolecular Approaches. *Adv. Cond. Matter Phys.* **2015,** 151683f.

80. Rosen, M. J.; Kunjappu, J. T., *Surfactants and Interfacial Phenomena* John Wiley & Sons: 2012.

81. Danov, K. D.; Kralchevsky, P. A.; Stoyanov, S. D.; Cook, J. L.; Stott, I. P.; Pelan, E. G., Growth of wormlike micelles in nonionic surfactant solutions: Quantitative theory vs. experiment. *Adv. Colloid Interface Sci.* **2018,** *256*, 1-22.

82. Nicolas-Morgantini, L., *Giant Micelles and Shampoo*. CRC Press: 2077.

83. Tanford, C., Micelle Shape and Size. *J. Phys. Chem.* **1972,** *76*, 3020-3024.

84. Tanford, C., Thermodynamics of micelle formation: prediction of micelle size and size distribution. *Proc. Natl. Acad. Sci. USA* **1974,** *71*, 1811.

85. Tanford, C., The hydrophobic effect and the organization of living matter. *Science* **1978,** *200*, 1012-1018.

86. Nagarajan, R., Molecular Parking Parameter and Surfactant Self-Assembly: The Neglected Role of the Surfactant Tail. *Langmuir* **2002,** *18*, 31-38.

87. Hashim, R.; Zahid, N. I.; Velayutham, T. S.; Aripin, N. F. K.; Ogawa, S.; Sugimura, A., Dry Thermotropic Glycolipid Self-Assembly: A Review. *J. Oleo. Sci.* **2018,** *67*, 651-668.

88. Tschierske, C., Non-conventional liquid crystals - the importance of microsegregation for self-organisation. *J. Mater. Chem.* **1998,** *8*, 1485-1508.

89. Hadziioannou, G.; Malliaras, G. C., *Semiconducting Polymers: Chemistry, Physics and Engineering*. John Wiley & Sons: 2006.

90. Darling, S. B., Directing the self-assembly of block copolymers. *Prog. Polym. Sci.* **2007,** *32*, 1152-1204.

91. Bates, F. S.; Fredrickson, G. H., Block Copolymers—Designer Soft Materials *Physics Today* **1999,** *52*.

92. Leibler, L., Theory of Microphase Separations in Block Copolymers *Macromolecules* **1980,** *13*, 1602-1617.

93. Matsen, M. W.; Schick, M., Stable and Unstable Phases of a Diblock Copolymer Melt. *Phys. Rev. Lett.* **1994,** *72*, 2660-2663.

94. Matsen, M. W.; Bates, F. S., Unifying weak- and strong-segregation block copolymer theories. *Macromolecules* **1996,** *29*, 1091-1098.

95. Bates, F. S., Polymer-Polymer Phase Behavior. *Science* **1991,** *251*, 898-905.

96. Sinturel, C.; Bates, F. S.; Hillmyer, M. A., High *X*-Low *N* Block Polymer: How Far Can We Go? *ACS Macro Lett.* **2015,** *4*, 1044-1050.

97. Frank, F. C.; Kasper, J. S., Complex alloy structures regarded as sphere packing. I. Definitions and basic principles. *Acta Crystallogr.* **1958,** *11*.

98. Frank, F. C.; Kasper, J. S., Complex Alloy Structures Regarded as Sphere Packings. II. Analysis and Classification of Representative Structures. *Acta Crystallogr.* **1959,** *12*, 483-499.

99. Graef, M. D.; McHenry, M. E., *Structure of Materials: An Introduction to Crystallography, Diffraction and Symmetry*. 2nd ed.; Cambridge Univ. Press: Cambridge, UK, 2012; p 466-496.

100. Steward, G. R., Superconductivity in the A15 structure. *Phys. C.* **2015,** *514*, 25-28.

101. Borisch, K.; Diele, S.; Goring, P.; Tschierske, C., Molecular design of

amphitropic liquid crystalline carbohydrates-amphiphilic N-methyl-glucamides

exhibiting lamellar, columnar or cubic mesophases. *Chem. Commun.* **1996**, 237-238.

102. Borisch, K.; Diele, S.; Goring, P.; Muller, H.; Tschierske, C., Amphiphilic Nbenzpyl-1-amino-1-deoxy-D-glucitol derivatives forming thermotropic lamellar,columnar and different types of cubic mesophases. *Liq. Cryst.* **1997,** *22*, 427-443.

103. Balagurusamy, V. S. K.; Ungar, G.; Percec, V.; Johansson, G., Rational design of the first spherical supramolecular dendrimers self-organized in a novel thermotropic cubic liquid-crystalline phase and the determination of their shape by X-ray analysis. *J. Am. Chem. Soc.* **1997,** *119*, 1539-1555.

104. Yue, K.; Huang, M. J.; Marson, R. L.; He, J. L.; Huang, J. H.; Zhou, Z.; Wang, J.; Liu, C.; Yan, X. S.; Wu, K.; Guo, Z. H.; Liu, H.; Zhang, W.; Ni, P. H.; Wesdemiotis, C.; Zhang, W. B.; Glotzer, S. C.; Cheng, S. Z. D., Geometry induced sequence of nanoscale Frank-Kasper and quasicrystal mesophases in giant surfactants. *Proc. Natl. Acad. Sci. USA* **2016,** *113*, 14195-14200.

105. Su, Z.; Hsu, C.-H.; Gong, Z.; Feng, X.; Huang, J.; Zhang, R.; Wang, Y.; Mao, J.; Wesdemiotis, C.; Li, T.; Seifert, S.; Zhang, W.; Aida, T.; Huang, M.; Cheng, S. Z. D., Identification of a Frank-Kasper Z phase from shape amphiphile self-assembly. *Nat. Chem.* **2019,** *11*, 899-905.

106. Lee, S.; Bluemle, M. J.; Bates, F. S., Discovery of a Frank-Kasper sigma Phase in Sphere-Forming Block Copolymer Melts. *Science* **2010,** *330*, 349-353.

107. Yue, K.; Huang, M. J.; Marson, R. L.; He, J. L.; Huang, J. H.; Zhou, Z.; Wang, J.; Liu, C.; Yan, X. S.; Wu, K.; Guo, Z. H.; Liu, H.; Zhang, W.; Ni, P. H.; Wesdemiotis, C.; Zhang, W. B.; Glotzer, S. C.; Cheng, S. Z. D., Geometry induced sequence of nanoscale Frank-Kasper and quasicrystal mesophases in giant surfactants. *Proc. Natl. Acad. Sci. USA* **2016,** *113*, 14195-14200.

108. Su, Z.; Hsu, C.-H.; Gong, Z.; Feng, X.; Huang, J.; Zhang, R.; Wang, Y.; Mao, J.; Wesdemiotis, C.; Li, T.; Seifert, S.; Zhang, W.; Aida, T.; Huang, M.; Cheng, S. Z. D., Identification of a Frank-Kasper Z phase from shape amphiphile selfassembly. *Nat. Chem.* **2019,** *11*, 899-905.

109. Vargas, R.; Mariani, P.; Gulik, A.; Luzzati, V., Cubic Phase of Lipid containing Systems The Structure of Phase Q223 (Space Group Pm3n). An X-ray Scattering Study. *J. Mol. Biol.* **1992,** *225*, 137-145.

110. Hajiw, S.; Pansu, B.; Sadoc, J.-F., Evidence for a C14 Frank-Kasper Phase in one-size gold nanoparticles superlattices *ACS Nano* **2015,** *9*, 8116-8121.

111. Levine, D.; Steinhardt, P. J., Quasicrystals: A new class of ordered structures. *Phys. Rev. Lett.* **1984,** *53*, 2477-2480.

112. Shechtman, D.; Blech, I.; Gratias, D.; Cahn, J. W., Metallic phase with long range orientational order and no translational symmetry. *Phys. Rev. Lett.* **1984,** *53*, 1951-1953.

113. Ungar, G.; Zeng, X., Frank-Kasper, quasicrystalline and related phases in liquid crystals. *Soft Matter* **2005,** *1*, 95-106.

114. Hudson, S. D.; Jung, H.-T.; Percec, V.; Cho, W.-D.; Johansson, G.; Ungar, G.; Balagurusamy, V. S. K., Direct Visualization of Individual Cylindrical and Spherical Supramolecular Dendrimers. *Science* **1997,** *278*, 449-452.

115. Percec, V.; Ahn, C.-H.; Barboiu, B., Self-Encapsulation, Acceleration and Control in the Radical Polymerization of Monodendritic Monomers vis Self Assembly.*J. Am. Chem. Soc.* **1997,** *199*, 12978-12979.

116. Kumar S. *Chemistry of discotic liquid crystals : from monomers to polymers*. Boca Raton: CRC Press; 2011.

117. Laschat, S.; Baro, A.; Steinke, N.; Giesselmann, F.; Hägele, C.; Scalia, G.; Judele, R.; Kapatsina, E.; Sauer, S.; Schreivogel, A.; Tosoni, M., Discotic liquid crystals: From tailormade synthesis to plastic electronics. *Angew Chem Int Ed.* **2007**, *46*, 4832-4887.

118. Chandrasekhar, S.; Sadashiva, B. K.; Suresh, K. A., Liquid crystals of disc-like molecules. *Pramana.* **1977**, *9*, 471-480

119. Bisoyi, H. K.; Kumar, S., Microwave-assisted facile synthesis of liquid crystalline non-symmetrical hexaalkoxytriphenylenes containing a branched chain and their characterization. *J. Phys. Org. Chem.* **2008**, *21*, 47-52.

120. Krishna Prasad, S.; Shankar Rao D. S.; Chandrasekhar, S.; Kumar, S., X-ray studies on the columnar structures of discotic liquid crystals. *Mol Cryst Liq Cryst.* **2003**, *396*, 121- 139.

121. Destrade, C.; Foucher, P.; Gasparoux, H.; Huu Tinh, N.; Levelut, A. M.; Malthete. J., Disclike mesogen polymorphism. *Mol. Cryst. Liq. Cryst.* **1984**, *106*, 121-146.

122. Destrade, C.; Tinh, N. H.; Mamlok, L.; Malthete, J., Trioxatruxenes - a new family of disc-like mesogens with a complex polymorphism. *Mol. Cryst. Liq. Cryst.* **1984**, *114*, 139- 150.

123. Donnio, B.; Heinrich, B.; Allouchi, H.; Kain, J.; Diele, S.; Guillon, D.; Bruce, D. W., A generalized model for the molecular arrangement in the columnar mesophases of polycatenar mesogens. Crystal and molecular structure of two hexacatenar mesogens. *J. Am. Chem. Soc.* **2004**, *126*, 15258-15268.

124. Kumar, S., Triphenylene-based discotic liquid crystal dimers, oligomers and polymers. *Liq Cryst.* **2005**, *32*, 1089-1113.

125. Kumar, S., Recent developments in the chemistry of triphenylene-based discotic liquid crystals. *Liq Cryst.* **2004**, *31*, 1037-1059.

126. Kaafarani, B. R., Discotic liquid crystals for opto-electronic applications. *Chem. Mater.* **2011**, *23*, 378-396.

127. Pal, S. K.; Setia, S.; Avinash, B. S.; Kumar, S., Triphenylene-based discotic liquid crystals: recent advances. *Liq. Cryst.* **2013**, *40*, 1769-1816.

128. Sergeyev, S.; Pisula, W.; Geerts, Y. H., Discotic liquid crystals: A new generation of organic semiconductors. *Chem. Soc. Rev.* **2007**, *36*, 1902-1929.

129. Martinez, C. R.; Iverson, B. L., Rethinking the term “pi-stacking”. *Chem. Sci.* **2012**, *3*, 2191-2201

130. Hecht, M.; Wurther, F., Supramolecularly Enginnered J-Aggregates Based on Perylene Bisimide Dyes. *Acc. Chem. Res.* **2021**, *54*, 642-653.

131. Würthner, F.; Saha-Möller, C. R.; Fimmel, B.; Ogi, S.; Leowanawat, P.; Schmidt, D., Perylene Bisimide Dye Assemblies as Archetype Functional Supramolecular Materials. *Chem. Rev.* **2016**, *116*, 962-1052

Chapter 2:

1. Jubinville, D.; Esmizadeh, E.; Saikrishnan, D.; Tzoganakis, C.; Mekonnen, T. A., Comprehensice review of global production and recycling methods of polyolefin (PO) based products and their posy-recycling applications. *Sustain. Mater. Tech.* **2020**, e00188.

2. Geyer, R.; Jambeck, J. R.; Law, K. L., Production, Use, and Fate of All Plastics Ever Made. *Sci. Adv.* **2017**, *3* (7), 19-24.

3. Tolinski, M Additives for Polyolefins, 2nd ed.; Elsevier 2015.

4. Arriola, D. J.; Carnahan, E. M.; Hustad, P. D.; Kuhlman, R. L.; Wenzel, T. T., Catalytic Production of Olefin Block Copolymers via Chain Shuttling Polymerization. *Science* **2006**, *312*, 714-719.

5. Sita, L. R., *Ex Uno plures* (“out of one, many”): new paradigms of expanding the range of polyolefins through reversible group transfers. *Angew. Chem. Int. Ed.* **2009**, *48*, 2464-2472.

6. Hustad, P. D., Frontiers in Olefin Polymerization: Reinventing the World’s Most Common Synthetic Polymers. *Science* **2009**, *325*, 704-707.

7. Stürzel, M.; Mihan, S.; Mülhaupt, R., From Multisite Polymerization Catalysis to Sustainable Materials and All-Polyolefin Composites. *Chem Rev.* **2016**, *116*, 1398-1433.

8. Kida, T.; Tanaka, R.; Hiejima, Y.; Nitta, K.; Shiono, T., *Polymer* **2021,** *218*, 123526.

9. Tran, T. V.; Doi, L. H., Tunable modalities in polyolefin synthesis via coordination insertion catalysis. *Eur. Polym. J.* **2021**, *142*, 110100.

10. Zanchin, G.; Leone, G., Polyolefin thermoplastic elastomers from polymerization catalysis: advantages, pitfalls and future challenges. *Prog. Polym. Sci.* **2021**, *113*, 101342.

11. Miyoshi, T.; Pascui, O.; Reichert, D., Slow Chain Dynamics in *Isotactic*-poly(4-methyl-1-pentene) Crystallites near the Glass Transition Temperature Characterized by Solid-State ^{13}C MAS Exchange NMR. *Macromolecules* **2004**, *37*, 6460-6471.

12. Nickl, J.; Schick, H.; Mueller-Tamm, H. Manufacture of homopolymers of 4-methylpentene-1. US3969335 A, July 13, 1976.

13. Kashiwa, N.; Fukui, K Process for production of 4-methyl-1-pentene polymer or copolymer. US EP0125910 A1, November 21, 1984.

14. Vasile, C. (ed.) *Handbook of Polyolefins.* Marcel Dekker, Inc.: New York, 2000.

15. Kaminsky (ed.), Polyolefins: 50 years after Ziegler and Natta I: Polyethylene and Polypropylene. *Adv. Polym. Sci. Vol. 258* Springer-Verlag: Heidelberg, 2013.

16. Al-AliAlNa'adeed, M.; Krupa, I., (eds) *Polyolefin Compounds and Materials.* Springer: Heidelberg, 2016.

17. Kots, P. A.; Vance, B. C.; Vlachos, D. G., Polyolefin plastic waste hydroconversion to fuels, lubricants, and waxes: a comparative study. *React. Chem. Eng.* **2022**, *7*, 41-45.

18. Natta, G.; Pino, P.; Corradini, P.; Danusso, F.; Mantica, E.; Mazzanti, G.; Moraglio, G., Crystalline High Polymers of α-Olefins. *J. Am. Chem. Soc.* **1955**, *77*, 1708-1710.

19. Natta. G., A New Class of Polymers of α-Olefins Having Exceptional Regularity of Structure. *Atti. Acc. Naz. Lincei Mem.* **1955**, *4*, 61.

20. Corradini, P., The Discovery of Isotactic Polypropylene and its Impact on Pure and Applied Science. *J. Am. Polym. Sci. Part A: Polym. Chem.* **2004**, *42*, 391

21. Sivaram, S., Giulio Natta and the origins of stereoregular polymers. *Resonance* **2017**, *22*, 1007-1023.

22. Baugh, L. S.; Canich, J. M. (eds.) *Stereoselective Polymerization with Single-Site Catalysts.* CRC Press: Boca Raton, 2008.

23. De Rosa, C.; Auriemma, F.; Di Capua, A.; Resonci, L.; Guidotti, S.; Camurati, I.l Nifant'ew I. E.; Laishevtsev, I., Structure-Property Correlations in Polypropylene from Metallocene Catalysis: Stereodefective, Regioregular Isotactic Polypropylene. *J. AM. Chem. Soc.* **2004**, *126*, 17040-17049.

24. (a) Jayaratne, K. C. ; Sita, L. R., Stereospecific Living Ziegler-Natta Polymerization of 1-Hexene. *J. Am. Chem. Soc.* **2000**, *122*, 958-959.

24. (b) Zhang, Y.; Keaton, R. J. ; Sita, L. R., Degenerative Transfer Living Ziegler-Natta Polymerization: Application to the Synthesis of Monomodal Stereoblock Polyolefins of Narrow Polydispersity and Tunable Block Length. *J. Am. Chem. Soc.* **2003**, *125*, 9062-9069.

25. (a) Jayaratne, K. C.; Sita, L. R., Direct Methyl Group Exchange between Cationic Zirconium Ziegler-Natta Initiators and Their Living Polymers: Ramifications for the Production of Stereoblock Polyolefins. *J. Am. Chem. Soc.* **2001**, *123*, 10754-10755.

25. (b) Zhang, Y.; Sita, L. R., Stereospecific Living Ziegler-Natta Polymerization via Rapid and Reversible Chloride Degenerative Transfer between Active and Dormant Sites. *J. Am. Chem. Soc.* **2004**, *126*, 7776-7777.

26. Harney, M. B.; Zhang, Y.; Sita, L. R., Bimolecular Control over Polypropene Stereochemical Microstructure in a Well-Defined Two-State System and a New Fundamental Form: Stereogradient Polypropene. *Angew. Chem. Int. Ed.* **2006**, *45*, 6140-6144.

27. Harney, B.; Zhang, Y.; Sita, L. R., Discrete, Multiblock Isotactic-Atactic Stereoblock Polypropene Microstructures of Differing Block Architectures through Programmable Stereomodulated Living Ziegler-Natta Polymerization. *Angew. Chem. Int. Ed.* **2006**, *45*, 6140-6144.

28. Zhang, W.; Sita, L. R., Investigation of Dynamic Intra- and Intermolecular Processes within a Tether-Length Dependent Series of Group 4 Bimetallic Initiators for Stereomodulated Degenerative Transfer Living Ziegler-Natta Propene Polymerization. *Adv. Synth Catal.* **2008**, *350*, 439-447.

29. Giller, C.; Gururajan, G. ; Wei, J.; Zhang, W.; Hwang, W.; Chase, D. B.; Rabolt, J. F.; Sita, L. R., Synthesis, Characterization, and Electrospinning of Architecturally Discrete Isotactic-Atactic Triblock Stereoblock Polypropene Elastomers. *Macromolecules* **2011**, *44*, 471-482.

30. Crawford, K. E. ; Sita, L. R., Stereoengineering of Poly(1,3-methylenecyclohexane) via Two-State Living Coordination Polymerization of 1,6-Heptadiene. *J. Am. Chem. Soc.* **2013**, *135*, 8778-8781.

31. W. Zhang, L. R. Sita, Highly Efficient Living Coordinative Chain-Transfer Polymerization of Propene with ZnEt2: Practical Production of Ultrahigh to Very Low Molecular Weight Amorphous Atactic Polypropene of Extremely Narrow Polydispersity. J. Am. Chem. Soc. 2008, 130, 442-443.

32. Zhang, W.; Wei, J.; Sita, L. R., Living Coordinative Chain-Transfer Polymerization and Copolymerization of Ethene, α-Olefins, and α,ω-Nonconjugated Dienes using Dialkylzinc as "Surrogate" Chain-Growth Sites. *Macromolecules* **2008**, *41*, 7829-7833.

33. Wei, J.; Zhang, W. ; Sita, L. R., Aufbaureaktion Redux: Scalable Production of Precision Hydrocarbons from AlR3 (R = Et or iBu) by Dialkyl Zinc Mediated Ternary Living Coordinative Chain-Transfer Polymerization. *Angew. Chem. Int. Ed.* **2010**, *49*, 1768-1772.

34. Wei, W. Zhang, R. Wickham, L. R. Sita, Programmable Modulation of Co-monomer Relative Reactivities for Living Coordination Polymerization through Reversible Chain Transfer between "Tight" and "Loose" Ion Pairs. *Angew. Chem.Int. Ed*. 2**010**, *49*, 9140-9144.

35. Wei, J.; Hwang, W. ; Zhang, W.; Sita, L. R., Dinuclear Bis-Propagators for the Stereoselective Living Coordinative Chain Transfer Polymerization of Propene. *J. Am. Chem. Soc.* **2013**, *135*, 2132-2135.

36. Wei, J.; Duman, L. M.; Redman, D. W.; Yonke, B. L.; Zavalij, P. Y.; Sita, L. R., N-Substituted Iminocaprolactams as Versatile and Low Cost Ligands in Group 4 Metal Initiators for the Living Coordinative Chain Transfer Polymerization of α-Olefins. *Organometallics* **2017**, *36*, 4202-4207.

37. Wallace, M. A.; Zavalij, P. Y.; Sita, L. R., Enantioselective Living Coordinative Chain Transfer Polymerization: Production of Optically Active End-Group-Functionalized (+) or (-)-Poly(methylene-1,3-cyclopentane) via a Homochiral C1-Symmetric Caproamidinate Hafnium Initiator. *ACS Catal.* **2020**, *10*, 8496-8502.

39. Cuney, E. S.; Sita, L. R.; Landis. C. R., Quantitative Validation of the Living Coordinative Chain-Transfer Polymerization of 1-Hexene using Chromophore Quench Labeling. *Macromolecules* **2020**, *53*, 5816-5825.

40. Wallace, M. A.; Wentz, C. M.; Sita, L. R., Optical Purity as a Programmable Variable for Controlling Polyolefin Tacticity in Living Coordinative Chain Transfer Polymerization: Application to the Stereomodulated LCCTP of α, ω-Nonconjugated Dienes. *ACS Catal.* **2021**, *11*, 4583-4592.

41. Wallace, M. A.; Sita, L. R., Multi-state Living Degenerative and Chain Transfer Coordinative Polymerization of α-Olefins via Sub-Stoichiometric Activation. *ACS Catal.* **2021**, *11*, 9754-9760.

42. Wallace, M. A.; Sita, L. R., Temporal Control over Two- and Three-State Living Coordinative Chain Transfer Polymerization for Modulating the Molecular Weight Distribution Profile for Polyolefins. *Angew. Chem. Int. Ed.* **2021**, *60*, 19671-19678.

43. Wallace, M. A.; Burkey, A. A.; Sita, L. R., Phenyl-terminated Polyolefins via Living Coordinative Chain-Transfer Polymerization with ZnPh2 as a Chain Transfer Agent. *ACS Catal.* **2021**, *11*, 10170-10178.

44. Burkey, A. A.; Fischbach, D. M.; Wentz, C. M.; Beers, K. L.; Sita, L. R., Highly Versatile Strategy for the Production of Telechelic Polyolefins. *ACS Macro Lett.* **2022**, *11*, 402-409.

45. Lopez, L. C.; Wilkes, G. L.; Stricklen, P. M.; White, S. A., Synthesis, Structure, and Properties of Poly(4-methyl-1-pentene). *J. Macromol. Sci. Part C* **1992**, *32*, 301-406.

46. Forni, L.; Invernizzi, R., Kinetics and Mechanism of Propylene to 4-methyl-1-pentene catalytic dimerization. *Ind. Eng. Chem. Process Des. Develop.* **1973**, *12*, 455-459.

47. Jin, H.; Jiang, H.; Yang, S.; Guo., G. He, X., The catalytic characteristic and synthesis technique for 4-methyl-1-pentene over a potassium-supported superbase catalyst. *Chem. Eng. Commun.* **2019**, *206*, 346-354.

48. Griffith, J. H.; Rånby, B. G.; Dilatometric measurements on poly(4-methyl-1-pentene) glass and melt transition temperatures, crystallization rates, and unusual density behavior. *J. Polym. Sci.* **1960**, *45*, 509-518.

49. Miao, Z.; Pal, D.; Niu, W.; Kubo, T.; Sumerlin, B. S.; Veige. A. S., Cyclic poly(4-methyl-1-pentene): Efficient catalytic synthesis of a transparent cyclic polymer. *Macromolecules* **2020**, *53*, 7774-7782.

50. Szwarc, M.; Van Beylen, M.; *Ionic and Living Polymers.* Chapman & Hall, Inc: New York, 1993.

51. Descour, C.; Duchateau, R.; Mosia, M. R.; Gruter, G. -J. M.; Severn, J. R.; Rastogi, J. R., Catalyst behavior for 1-pentene and 4-methyl-1-pentene polymerization for C2-, Cs-, and C1-symmetric zirconocenes. *Polym. Chem.* **2011**, *2*, 2261-2272.

52. Fox, T.; Flory. P. J., The glass temperture and related properties of polystyrene. Influence of molecular weight. *J. Polym. Sci*. **1954**, *14*, 315-319.

53. Ueberreiter, K.; Kanig, G., Self-Plasticization of Polymers *J. Colloid Sci.* **1952**, *7*, 569-583.

54. Agapov, A. L.; Sokolov, A. P., Does the Molecular Weight Dependence of Tg Correlate to Me? *Macromolecules* **2009**, *42*, 2877-2878.

55. Keaton, R. J.; Jayaratne, K. C.; Henningsen, D. A.; Koterwas, L. A.; Sita, L. R., Dramatic Enhancement of Activities for Living Ziegler-Natta Polymerizations Mediated by "Exposed" Zirconium Acetamidinate Initiators: The Isospecific Living Polymerization of Vinylcyclohexane. *J. Am. Chem. Soc.* **2001**, *123*, 6197-6198.

Chapter 3:

1. Jubinville, D.; Esmizadeh, E.; Saikrishnan, S.; Tzoganakis, C.; Mekonnen, T. A., Comprehensive review of global production and recycling methods of polyolefin (PO) based products and their post-recycling applications *Sustain. Mater. Tech.* **2020**, e00188.

2. Geyer, R.; Jambeck, J. R.; Law, K. L., Production, Use, and Fate of All Plastics Ever Made. **Sci. Adv. 2017**, *3*(7), 19–24.

3. Lieber, S.; Brintzinger, H. Propene Polymerization with Catalyst Mixtures Containing Different *ansa*-Zirconocenes: Chain Transfer to Alkylaluminum Cocatalysts and Formation of Stereoblock Polymers. *Macromolecules* **2000**, *33*, 9192-9199.

4. Legge, N. R.; Holden, G.; Schroeder, H. E.: Thermoplastic Elastomers: *A Comprehensive Review*; Hanser Gardner Publications: New York, New York, 1987.

5. White, J. L.; Choi, D. D.: *Polyolefins: Processing, Structure Development, and Properties*; Hanser Gardner Publications: Cincinnati, Ohio, 2004.

6. Baugh, L. S.; Canich, J. A. M.: Stereoselective Polymerization with Single-Site Catalysts; CRC Press: Boca Raton, Florida, 2007.

7. Lin, S.; Waymouth, R. M.: 2-Arylindene Metallocenes: Conformationally Dynamic Catalysts to Control the Structure and Properties of Polypropylenes. *Accounts of Chemical Research* **2002**, *35*, 765-773.

8. Schonherr, H.; Wiyatno, W.; Pople, J.; Frank, C. W.; Fuller, G. G.; Gast, A. P.; Waymouth, R. M.: Morphology of Thermoplastic Elastomers: Elastomeric Polypropylene. *Macromolecules* **2002**, *35*, 2654-2666.

9. Collette, J. W.; Ovenall, D. W.; Buck, W. H.; Ferguson, R. C.: Elastomeric Polypropylenes from Alumina-Supported Tetraalkyl Group-Ivb Catalysts .2. Chain Microstructure, Crystallinity, and Morphology. *Macromolecules* **1989**, *22*, 3858-3866.

10. Collette, J. W.; Tullock, C. W.; Macdonald, R. N.; Buck, W. H.; Su, A. C. L.; Harrell, J. R.; Mulhaupt, R.; Anderson, B. C.: Elastomeric Polypropylenes from Alumina-Supported Tetraalkyl Group-IVB Catalysts .1. Synthesis and Properties of High Molecular-Weight Stereoblock Homopolymers. *Macromolecules* **1989**, *22*, 3851-3858.

11. Xu, J. T.; Feng, L. X.; Yang, S. L.: Formation Mechanism of Stereoblocks in Polypropylene Produced by Supported Ziegler-Natta Catalysts. *Macromolecules* **1997**, *30*, 2539-2541.

12. De Rosa, C.; Auriemma, F.; Perretta, C.: Structure and Properties of Elastomeric Polypropylene from C-2 and C-2v Symmetric Zirconocenes. The Origin of Crystallinity and Elastic Properties in Poorly Isotactic Polypropylene. *Macromolecules* **2004**, *37*, 6843-6855.

13. Resconi, L.; Cavallo, L.; Fait, A.; Piemontesi, F.: Selectivity in Propene Polymerization with Metallocene Catalysts. *Chemical Reviews* **2000**, *100*, 1253-1346.

14. Brintzinger, H. H.; Fischer, D.; Mulhaupt, R.; Rieger, B.; Waymouth, R. M.: Stereospecific Olefin Polymerization with Chiral Metallocene Catalysts. *Angewandte Chemie-International Edition* **1995**, *34*, 1143-1170.

15. Chien, J. C. W.; Llinas, G. H.; Rausch, M. D.; Lin, Y. G.; Winter, H. H.; Atwood, J. L.; Bott, S. G.: Metallocene Catalysts for Olefin Polymerizations .24. Stereoblock Propylene Polymerization Catalyzed by Rac-[Anti-Ethylidene(1-Eta-5-Tetramethylcyclopentadienyl) (1-Eta-5-Indenyl)Dimethyltitanium - a 2-State Propagation. *Journal of Polymer Science Part a-Polymer Chemistry* **1992**, *30*, 2601-2617.

16. Llinas, G. H.; Dong, S. H.; Mallin, D. T.; Rausch, M. D.; Lin, Y. G.; Winter, H. H.; Chien, J. C. W.: Crystalline Amorphous Block Polypropylene and Nonsymmetric Ansa-Metallocene Catalyzed Polymerization. *Macromolecules* **1992**, *25*, 1242-1253.

17. Kravchenko, R.; Masood, A.; Waymouth, R. M.; Myers, C. L.: Strategies for Synthesis of Elastomeric Polypropylene: Fluxional Metallocenes with C-1 Symmetry. *Journal of the American Chemical Society* **1998**, *120*, 2039-2046.

Chapter 4:

1. Sita, L. R., Ex Uno Plures ("Out of One, Many): New Paradigms for Expanding the Range of Polyolefins through Reversible Group Transfers. *Angew. Chem., Int. Ed.* **2009**, *48*, 2464−2472.

2. Wenzel, T. T.; Arriola, D. J.; Carnahan, E. M.; Hustad, P. D.; Kuhlman, R. L., Chain Shuttling Catalysis and Olefin Block Copolymers (OBCs). *Top. Organomet. Chem.* **2009**, *26*, 65−104.

3. Chen, C. Designing Catalysts for Olefin Polymerization and Copolymerizations: Beyond Electronic and Steric Tuning. *Nat. Rev. Chem*. 2018, *2*, 6−14.

4. Coates, G. W.; Waymouth, R. M., Enantioselective Cyclopolymerization: Optically Active Poly(methylene-1,3-cyclopentane). *J. Am. Chem. Soc.* **1991**, *113*, 6270−6271. (b) Coates, G. W.;

5. Waymouth, R. M., Enantioselective Cyclopolymerization of 1,5-Hexadiene Catalyzed by Chiral Zirconocenes: A Novel Strategy for the Synthesis of Optically Active Polymers with Chirality in the Main Chain. *J. Am. Chem. Soc.* **1993**, *115*, 91−98.

6. Wallace, M. A.; Zavalij, P. Y.; Sita, L. R., Enantioselective Living Coordinative Chain Transfer Polymerization: Production of Optically Active End-Group-Functionalized (+) or (-)-Poly(methylene-1,3-cyclopentane) via a Homochiral C1-Symmetric Caproamidinate Hafnium Initiator. *ACS Catal.* **2020**, *10*, 8496−8502.

7. Wallace, M. A.; Wentz, C. M.; Sita, L. R., Optical Purity as a Programmable Variable for Controlling Polyolefin Tacticity in Living Coordinative Chain Transfer Polymerization: Application to the Stereomodulated LCCTP of α,ω- Nonconjugated Dienes. ACS Catal. **2021**, *11*, 4583−4592.

8. Shi, X.; Wang, Y.; Liu, J.; Cui, D.; Men, Y.; Li, Y., Stereospecific Cyclopolymerization of α-Diolefins by Pyridylamidohafnium Catalyst with the Highest Activity. *Macromolecules* **2011**, *44*, 1062−1065.

9. Crawford, K. E.; Sita, L. R., Stereoengineering of Poly(1,3-methylenecyclohexane) via Two-State Living Coordination Polymerization of 1,6-Heptadiene. *J. Am. Chem. Soc*. **2013**, *135*, 8778−8781.

10. Wei, J.; Duman, L. M.; Redman, D. W.; Yonke, B. L.; Zavalij, P. Y.; Sita, L. R. N Substituted Iminocaprolactams as Versatile and Low Cost Ligands in Group 4 Metal Initiators for the Living Coordinative Chain Transfer Polymerization of α-Olefins. *Organometallics* **2017**, *36*, 4202−4207.

11. Zhang, Y.; Keaton, R. J.; Sita, L. R., Degenerative Transfer Living Ziegler-Natta Polymerization: Application to the Synthesis of Monomodal Stereoblock Polyolefins of Narrow Polydispersity and Tunable Block Length. *J. Am. Chem. Soc*. **2003**, *125*, 9062−9069.

12. Ballesteros, O. R.; Venditto, V.; Auriemma, F.; Guerra, G. Thermal and Structural Characterization of Poly(methylene-1,3-cyclopentane) Samples of Different Microstructures. *Macromolecules* **1995**, *28*, 2383-2388.

13. Guo, F.; Nishiura, M.; Li, Y.; Huo, Z. Cyclocopolymerization of 1,6-heptadiene with ethylene by half-sandwich scandi-um catalyst *Sci China Chem.* **2014**, *57*, 1150-1156.

14. Guo, F. Nishiura, M.; Koshino, H.; Hou, Z. Cycloterpolymerization of 1,6-Heptadiene with Ethylene and Styrene Catalyzed by a THF-Free-Hald-Sandwich Scandium Complex. *Macromolecules* **2011,** *44*, 2400-2403.

15. Guo, F.; Nishiura, M.; Li, Y.; Huo, Z. Cyclocopolymerization of 1,6-heptadiene with styrene catalyzed by a half-sandwich scandium dialkyl complex bearing a phosphine oxide side arm *Chem. Asian J.* **2013**, *52,* 1509-1513.

16. Takeuchi, D.; Matsuura, R.; Park, S.; Osakada, K. Cyclopolymerization of 1,6-heptadienes Catalyzed by Iron and Cobalt Complexes: Synthesis of Polymers with Trans- or Cis-Fused 1,2-Cyclopentanediyl Groups Depending on the Catalyst *J. Am. Chem. Soc.* **2007**, *129*, 7002-7003.

17. Guo, F.; Nishiura, M.; Li, Y.; Hou, Z.. Copolymerization of Isoprene and Nonconjugated σ, ω-dienes by Hald-sandwich Scandium Catalyst with and without a Coordinative Side Arm *Chem. Asian J.* **2013**, 8*,* 2471-2482.

18. Takeuchi, D.; Matsuura, R.; Park, S.; Osakada, K. Cyclopolymerization of 1,6-heptadienes Catalyzed by Iron and Cobalt Complexes: Synthesis of Polymers with Trans- or Cis-Fused 1,2-Cyclopentanediyl Groups Depending on the Catalyst *J. Am. Chem. Soc.* **2007**, *129*, 7002-7003.

19. Hustad, P. D.; Tian, J.; Coates, G. W. Mechanisum of Proylene Insertion Using Bic(phenoxyimine)-Based Titanium Catalysts: An Unusual Secondary Insertion of Propylene in a Croup IV Catalyst System *J. Am. Chem. Soc.* **2002**, *124*, 3614-3621.

20. Worch, J.C.; Prydderch, H.; Jimaja, S.; Bexis, P.; Becker, M. L.; Dove, A. P. Stereochemical enhancement of polymer properties *Nature Reviews* **2019**, *3*, 514-535.

21. Geyer, R.; Jambeck, J. R.; Law, K. L. Production, Use, and Fate of All Plastics Ever Made.*SciAdv* **2017**, *3* (7), e1700782.

22. Zeng, M.; Lee, Y.-H.; Strong, G.; LaPointe, A. M.; Kocen, A. L.; Qu, Z.; Coates, G. W.; Scott, S. L.; Abu-Omar, M. M. Chemical Upcycling of Polyethylene to Value-Added α,ω-Divinyl-Functionalized Oligomers. *ACS Sustainable Chem. Eng.* **2021,** *9* (41), 13926–13936.

23. Wentz, C. M.; Fischbach, D. M.; Sita, L. R., Stereomodulation of Poly(4-methyl-1-pentene): Adoption of a Neglected and Misunderstood Commercial Polyolefin. *Angew. Chem. Int. ed.* **2022**, e202211992

Chapter 5:

1. Hong, S.; MacKnight, W. J.; Russell, T. P.; Gido, S. P.: Structural evolution of multilayered, crystalline-amorphous diblock copolymer thin films. *Macromolecules* **2001**, *34*, 2876-2883.

2. Hong, S.; Yang, L. Z.; MacKnight, W. J.; Gido, S. P.: Morphology of a crystalline/amorphous diblock copolymer: Poly((ethylene oxide)-b-butadiene). *Macromolecules* **2001**, *34*, 7009-7016.

3. Chen, J. T.; Thomas, E. L.; Ober, C. K.; Mao, G.: Self-Assembled Smectic Phases in Rod-Coil Block Copolymers. *Science* **1996**, *273*, 343-346.

4. Park, J. W.; Thomas, E. L.: Frustrated crystallization of a rod-coil block copolymer from its liquid crystalline state. *Macromolecules* **2006**, *39*, 4650-4653.

5. Hentschel, J.; Kushnew, A. M.; Ziller, J.; Guan, Z., Self-Healing Supramolecular Block Copolymers. *Angew. Chem.* **2012**, *124*, 10713-10717.

6. Zhang, H.; Cui, Z.; Brinson, L. C., Mechanical Properties of Hard-Soft Block Copolymers Calculated from Coarse-Grained Molecular Dynamics Models. *Journal of Polymer Science, Part B: Polymer Physics* **2018**, *56*, 1552-1566.

7. Abetz, V.: *Block Copolymers II*; Springer: Berlin Heidelberg, 2005.

8. Hamley, I. W.: *The Physics of Block Copolymers*; Oxford Science Publications: New York, New York, 1998.

9. Cohen, R. E.; Cheng, P. L.; Douzinas, K.; Kofinas, P.; Berney, C. V.: Path-Dependent Morphologies of a Diblock Copolymer of Polystyrene Hydrogenated Polybutadiene. *Macromolecules* **1990**, *23*, 324-327.

10. Cohen, R. E.; Cheng, P. L.; Douzinas, K.; Kofinas, P.; Berney, C. V.: Path-Dependent Morphologies of a Diblock Copolymer of Polystyrene Hydrogenated Polybutadiene. *Macromolecules* **1990**, *23*, 324-327.

11. Hamley, I. W.; Fairclough, J. P. A.; Ryan, A. J.; Bates, F. S.; TownsAndrews, E.: Crystallization of nanoscale-confined diblock copolymer chains. *Polymer* **1996**, *37*, 4425-4429.

12. Weimann, P. A.; Hajduk, D. A.; Chu, C.; Chaffin, K. A.; Brodil, J. C.; Bates, F. S.: Crystallization of tethered polyethylene in confined geometries. *Journal of Polymer Science Part B-Polymer Physics* **1999**, *37*, 2053-2068.

13. Loo, Y. L.; Register, R. A.; Adamson, D. H.: Direct imaging of polyethylene crystallites within block copolymer microdomains. *Journal of Polymer Science Part B-Polymer Physics* **2000**, *38*, 2564-2570.

14. Zhu, L.; Calhoun, B. H.; Ge, Q.; Quirk, R. P.; Cheng, S. Z. D.; Thomas, E. L.; Hsiao, B. S.; Yeh, F.; Liu, L. Z.; Lotz, B.: Initial-stage growth controlled crystal orientations in nanoconfined lamellae of a self-assembled crystalline-amorphous diblock copolymer. *Macromolecules* **2001**, *34*, 1244-1251.

15. Zhu, L.; Cheng, S. Z. D.; Calhoun, B. H.; Ge, Q.; Quirk, R. P.; Thomas, E. L.; Hsiao, B. S.; Yeh, F.; Lotz, B.: Phase structures and morphologies determined by self-organization, vitrification, and crystallization: confined crystallization in an ordered lamellar phase of PEO-b-PS diblock copolymer. *Polymer* **2001**, *42*, 5829-5839.

16. Loo, Y. L.; Register, R. A.; Ryan, A. J.; Dee, G. T.: Polymer Crystallization Confined in One, Two, or Three Dimensions. *Macromolecules* **2001**, *34*, 8968-8977.

17. Dimarzio, E. A.; Guttman, C. M.; Hoffman, J. D.: Calculation of Lamellar Thickness in a Diblock Copolymer, One of Whose Components Is Crystalline. *Macromolecules* **1980**, *13*, 1194-1198.

18. Whitmore, M. D.; Noolandi, J.: Theory of Crystallizable Block Copolymer Blends. *Macromolecules* **1988**, *21*, 1482-1496.

19. Vilgis, T.; Halperin, A.: Aggregation of Coil Crystalline Block Copolymers - Equilibrium Crystallization. *Macromolecules* **1991**, *24*, 2090-2095.

20. Nojima, S.; Kato, K.; Yamamoto, S.; Ashida, T.: Crystallization of Block Copolymers .1. Small-Angle X-Ray-Scattering Study of an Epsilon-Caprolactone Butadiene Diblock Copolymer. *Macromolecules* **1992**, *25*, 2237-2242.

21. Rohadi, A.; Endo, R.; Tanimoto, S.; Sasaki, S.; Nojima, S.: Effects of Molecular Weight and Crystallization Temperature on the Morphology Formation in Asymmetric Diblock Copolymers with a Highly Crystalline Block. *Polymer Journal* **2000**, *32*, 602-609.

22. Nojima, S.; Toei, M.; Hara, S.; Tanimoto, S.; Sasaki, S.: Size dependence of crystallization within spherical microdomain structures. *Polymer* **2002**, *43*, 4087-4090.

23. Quiram, D. J.; Register, R. A.; Marchand, G. R.: Crystallization of Asymmetric Diblock Copolymers from Microphase-Separated Melts. *Macromolecules* **1997**, *30*, 4551-4558.

24. Zhao, J.; Majumdar, B.; Schulz, M. F.; Bates, F. S.; Almdal, K.; Mortensen, K.; Hajduk, D. A.; Gruner, S. M.: Phase Behavior of Pure Diblocks and Binary Diblock Blends of Poly(ethylene)-Poly(ethylethylene). *Macromolecules* **1996**, *29*, 1204-1215.

25. Rangarajan, P.; Register, R. A.; Fetters, L. J.: Morphology of Semicrystalline Block-Copolymers of Ethylene-(Ethylene-Alt-Propylene). *Macromolecules* **1993**, *26*, 4640-4645.

26. Quiram, D. J.; Register, R. A.; Marchand, G. R.; Ryan, A. J.: Dynamics of Structure Formation and Crystallization in Asymmetric Diblock Copolymers. *Macromolecules* **1997**, *30*, 8338-8343.

27. Quiram, D. J.; Register, R. A.; Marchand, G. R.; Adamson, D. H.: Chain Orientation in Block Copolymers Exhibiting Cylindrically Confined Crystallization. *Macromolecules* **1998**, *31*, 4891-4898.

28. Rangarajan, P.; Register, R. A.; Fetters, L. J.; Bras, W.; Naylor, S.; Ryan, A. J.: Crystallization of a Weakly Segregated Polyolefin Diblock Copolymer. *Macromolecules* **1995**, *28*, 4932-4938.

29. Hamley, I. W.; Fairclough, J. P. A.; Terrill, N. J.; Ryan, A. J.; Lipic, P. M.; Bates, F. S.; TownsAndrews, E.: Crystallization in oriented semicrystalline diblock copolymers. *Macromolecules* **1996**, *29*, 8835-8843.

30. Hobbs, J. K.; Register, R. A.: Imaging block copolymer crystallization in real time with the atomic force microscope. *Macromolecules* **2006**, *39*, 703-710.

31. Reiter, G.; Castelein, G.; Sommer, J. U.; Rottele, A.; Thurn-Albrecht, T.: Direct Visualization of Random Crystallization and Melting in Arrays of Nanometer-Size Polymer Crystals. *Physical Review Letters* **2001**, *87*, 226101-226104.

32. Ueda, M.; Sakurai, K.; Okamoto, S.; Lohse, D. J.; MacKnight, W. J.; Shinkai, S.; Sakurai, S.; Nomura, S.: Spherulite formation from microphase-separated lamellae in semi-crystalline diblock copolymer comprising polyethylene and atactic polypropylene blocks. *Polymer* **2003**, *44*, 6995-7005.

33. Seto, C. T.; Whitesides, G. M. Molecular self-assembly through hydrogen bonding: supramolecular aggregates based on the cyanuric acid-melamine lattice. *J. Am. Chem. Soc.* **1993**, *115*, 905-916.

34. Stupp S. I.; LeBonheur V.; Walker K.; Li L. S.; Huggins K. E.; Keser M.; Amstutz A. Supramolecular Materials: Self-Organized Nanostructures. *Science* **1997**, *276*, 384.

35. Wang H.; Wang H. H.; Urban V. S.; Litterell K. C.; Thiyagarajan P.; Yu L. Synthesis of amphiphilic diblock copolymers containing a conjugated block and their self-assembling properties. *J. Am. Chem. Soc*. **2000**, *122*, 6855.

36. Leclère P.; Calderone A.; MArsitzky D.; francke V.; Geerts Y.; Müllen K.; Brédas J. L.; Lazzaroni R. Highly Regular Organization of Conjugated Polymer Chains via Block Copolymer Self-Assembly *Adv. Mater*. **2000**, *12*, 1042.

37. Halperin A. Rod-coil copolymers: their aggregation behavior. *Macromolecules*, **1990**, *23*, 2724.

38. Raez J.; Manners I.; Winnik M. A. Nanotubes from the Self-Assembly of Asymmetric Crystallin-Coil Poly(ferrocenylsilane-siloxane) Block Copolymers. *J. Am. Chem. Soc*. **2002**, *124*, 10381 and references cited therein.

39. Rastogi S.; Hohne G. W. H.; Keller A. Unusual Pressure-Induced Phae Behavior in Crystalline Poly(4-methylpentene-1):Calorimetric and Spectroscopic results and Further Implications. *Macromolecules* **1999**, *32*, 8897 and references cited therein.

40. Kim M. H.; Londono J. D.; Habenschuss A. Structure of molten stereoregular polyolefins with different side-chain sizes: Linear polyethylene, polypropylene, poly(1-butene), and poly(4-methyl-1-pentene). *J. Polym. Sci. Part B: Polym. Phys.* **2000**, *38*, 2480.

41. Brandrup J.; Immergut E. H.; Grulke E. A. *Polymer Handbook*, Fourth Ed., John Wiley and Sons, Inc.: New York, 1999.

42. Giller C.; Gururajan G.; Wei J.; Zhang W.; Hwang W.; Chase D. B.; Rabolt J. F.; Sita L. R. Synthesis, Characterization, and Electrospinning of Architecturally-Discrete Isotactic-Atactic-Isotactic Triblock Stereoblock Polypropene Elastomers. *Macromolecules* **2011**, *44*, 471-482.

43. Nowak, S. R.; Hwang, W.; Sita, L. R. Dynamic Sub-10-nm Nanostructured Ultrathin Films of Sugar Polyolefin Conjugates Thermoresponsive at Physiological Temperatures. *J. Am. Chem. Soc.* **2017**, *139*, 5281−5284.

44. Almdal, K.; Koppi, K. A.; Bates, F. S.; Mortensen, K. Multiple ordered phases in a block copolymer melt. *Macromolecules* **1992**, *25*, 1743−1751.

45. Hamley, I. W.; Koppi, K. A.; Rosedale, J. H.; Bates, F. S.; Almdal, K.; Mortensen, K. Hexagonal mesophases between lamellae and cylinders in a diblock copolymer melt. *Macromolecules* 1**993**, *26*, 5959−5970.

46. Sakurai, S.; Momii, T.; Taie, K.; Shibayama, M.; Nomura, S.; Hashimoto, T. Morphology transition from cylindrical to lamellar microdomains of block copolymers. *Macromolecules* **1993**, *26*, 485−491.

47. Hajduk, D. A.; Gruner, S. M.; Rangarajan, P.; Register, R. A.; Fetters, L. J.; Honeker, C.; Albalak, R. J.; Thomas, E. L. Observation of a reversible thermotropic order-order transition in a diblock copolymer. *Macromolecules* **1994**, *27*, 490−501.

48. Liu, Y.; Li, M.; Bansil, R.; Steinhart, M. Kinetics of Phase Transition from Lamellar to Hexagonally Packed Cylinders for a Triblock Copolymer in a Selective Solvent. *Macromolecules* **2007**, *40*, 9482−9490.

49. Higuchi, T., Microphase-seperated structures under spherical 3D confinement. *Polymer Jornal* **2017**, *49*, 467-475.

50. Hamley, I., Developments in Block Copolymer Science and Technology, (John Wiley & Sons Ltd, Chichester, 2004).

51. Bates, S. F.; Fredrickson, H. G., Block copolymer thermodynamics: theory and experiment. *Annu. Rev. Phys. Chem.* **1990**, *41*, 525–557.

52. Park, M., Harrison, C., Chaikin, P. M., Register, R. A. & Adamson, D. H. Block copolymer lithography: periodic arrays of ~ 1011 holes in 1 square centimeter. *Science* **1997**, *276*, 1401–1404

53. Kang, C., Kim, E., Baek, H., Hwang, K., Kwak, D., Kang, Y. & Thomas, E. L. Full color stop bands in hybrid organic/inorganic block copolymer photonic gels by swelling freezing. *J. Am. Chem. Soc.* **2009**, *131*, 7538–7539.

54. Yoon, J., Lee, W. & Thomas, E. L. Optically pumped surface-emitting lasing using self-assembled block-copolymer-distributed Bragg reflectors. *Nano Lett.* **2006**, *6*, 2211–2214.

55. Yang, S., Ryu, I., Kim, H., Kim, J., Jang, S. & Russell, T. P. Nanoporous membranes

with ultrahigh selectivity and flux for the filtration of viruses. *Adv. Mater.* 2006, *18*,

709–712.

56. Johnson, K., Huang, Y. S., Huettner, S., Sommer, M., Brinkmann, M., Mulherin, R.,

57. Niedzialek, D., Beljonne, D., Clark, J., Huck, W. T. & Friend, R. H. Control of intrachain charge transfer in model systems for block copolymer photovoltaic materials. *J. Am. Chem. Soc.* **2013**, *135*, 5074–5083.

Chapter 6:

1. Thomas, T. S.; Hwang, W.; Sita, L.R., End-Group Functioalized Poly(alphaolefinates) as Non-Polar Building Blocks: Self-Assembly of Polyolefin Hybrid Conjugates. *Angew. Chem. Int. ed.* **2016**, *55*, 4683-4687.

2. Nowak, S. R.; Whang, W.; Sita, L.R., Dynamic Sub-10-nm Nanostructured Ultrathin Films of Sugar-Polyolefin Conjugates Thermoresponsive at Physiological Temperatures. *J. Am. Chem. Soc.* **2017**, *139*, 5281-5284.

3. Thomas, T. S. End-group functionalized poly(α - olefinates) as modular building blocks. University of Maryland, College Park, 2016.

4. Nowak, S. R. Self-assembly of precession polyolefin block copolymers and sugar-polyolefin conjugates University of Maryland, College Park, 2018.

5. Lachmayr, K. K.; Wentz, C. M.; Sita, L. R., An exceptionally stable and scalable sugar-polyolefin Frank-Kasper A15 phase. *Angew. Chem. Int. Ed*. **2020**, *59*, 1521-1526.

6. Lachmayr, K. K.; Sita, L. R., Small-Molecule modulation of soft-matter Frank-Kasper phases: a method for adding function to form. *Angew. Chem. Int. Ed.* **2020**, *59*, 3563-3567.

7. Sinturel, C.; Bates, F. S.; Hillmyer, M. A., High *X* Low *N* Block Polymer: How Far Can We Go? *ACS Macro Lett.* **2015**, *4*, 1044-1050.

8. Borisch, K.; Diele, S.; Goring, P.; Muller, H.; Tschierske, C., Amphiphilic Nbenzpyl-1-amino-1-deoxy-D-glucitol derivatives forming thermotropic lamellar, columnar and different types of cubic mesophases. *Liq. Cryst.* **1997,** *22*, 427-443.

9. Balagurusamy, V. S. K.; Ungar, G.; Percec, V.; Johansson, G., Rational design of the first spherical supramolecular dendrimers self-organized in a novel thermotropic cubic liquid-crystalline phase and the determination of their shape by X-ray analysis. *J. Am. Chem. Soc.* **1997,** *119*, 1539-1555.

10. Lee, S.; Bluemle, M. J.; Bates, F. S., Discovery of a Frank-Kasper sigma Phase in Sphere-Forming Block Copolymer Melts. *Science* **2010,** *330*, 349-353.

11. Yue, K.; Huang, M. J.; Marson, R. L.; He, J. L.; Huang, J. H.; Zhou, Z.; Wang, J.; Liu, C.; Yan, X. S.; Wu, K.; Guo, Z. H.; Liu, H.; Zhang, W.; Ni, P. H.; Wesdemiotis, C.; Zhang, W. B.; Glotzer, S. C.; Cheng, S. Z. D., Geometry induced sequence of nanoscale Frank-Kasper and quasicrystal mesophases in giant surfactants. *Proc. Natl. Acad. Sci. USA* **2016,** *113*, 14195-14200.

12. Su, Z.; Hsu, C.-H.; Gong, Z.; Feng, X.; Huang, J.; Zhang, R.; Wang, Y.; Mao, J.; Wesdemiotis, C.; Li, T.; Seifert, S.; Zhang, W.; Aida, T.; Huang, M.; Cheng, S. Z. D., Identification of a Frank-Kasper Z phase from shape amphiphile self-assembly. *Nat. Chem.* **2019,** *11*, 899-905.

13. Hajiw, S.; Pansu, B.; Sadoc, J.-F., Evidence for a C14 Frank-Kasper Phase in one-size gold nanoparticles superlattices *ACS Nano* **2015,** *9*, 8116-8121.

14. Lindsay, A. P.; Lewis, R. M. I.; Lee, B.; Peterson, A. J.; Lodge, T. P.; Bates, F. S., A15, σ, and quasicrystal: access to complex particle packings via bidisperse diblock copolymer blends. *ACS Macro Lett.* **2020,** *9*, 197-203.

15. Jeon, S.; Jun, T.; Jo, S.; Ahn, H.; Lee, S.; Lee, B.; Ryu, D. Y., Frank-Kasper phases identified in PDMS-*b*-PTFEA copolymers with high conformational asymmetry. *Macromol. Rapid. Commun.* **2019,** *40*, 190025.

16. Xie, N.; Li, W.; Qiu, F.; Shi, A.-C., Sigma phase formed in conformationally asymmetric AB-type block copolymers. *ACS Macro Lett.* **2014,** *3*, 906-910.

17. Percec, V.; Ahn, C.-H.; Barboiu, B., Self-Encapsulation, Acceleration and Control in the Radical Polymerization of Monodendritic Monomers vis Self-Assembly. *J. Am. Chem. Soc.* **1997,** *199*, 12978-12979.

18. Ungar, G.; Liu, Y.; Zeng, X.; Percec, V.; Cho, W.-D., Giant Supramolecular Liquid Crystal Lattice. *Science* **2003,** *299*, 1208-1211.

19. Zhang, W.-B.; Yu, X.; Wang, C.-L.; Sun, H.-J.; Hsieh, I.-F.; Li, Y.; Dong, X.-H.; Yue, K.; Horn, R. V.; Cheng, S. Z. D., Molecular Nanoparticles Are Unique 274 Elements for Macromolecular Science: From "Nanoatoms" to Giant Molecules *Macromolecules* **2014,** *47*, 1221-1239.

20. Huang, M.; Hsu, C.-H.; Wang, J.; Mei, S.; Dong, X.; Li, Y.; Li, M.; Liu, H.; Zhang, W.; Aida, T.; Xhang, W.-B.; Yue, K.; Cheng, S. Z. D., Selective assemblies of giant tetrahedra via precisely controlled positional interactions. *Science* **2015,** *348*, 424-428.

21. Cho, B. K.; Gruner, S. M.; Wiesner, U., Mesophase Structure-Mechanical and Ionic Transport Correlations in Extended Amphiphilic Dendrons. *Science* **2004**, 1598-1601.

22. Borisch, K.; Diele, S.; Goring, P.; Kresse, H.; Tschierske, C., Tailoring thermotropic cubic mesophases: amphiphilic polyhydroxy derivatives. *J. Mater. Chem.* **1998,** *8*, 529-543.

23. Park, M. J.; Bang, J.; Harada, T.; Char, K.; Lodge, T. P., *Macromolecules* **2004**, *37*, 9064-9075.

24. Imai, M.; Sakai, K.; Kikuchi, M.; Nakaya, K.; Saeki, A.; Teramoto, T., Kinetic pathway to double-gyroid structure. *J. Chem. Phys.* **2005,** *122*.

25. Zeng, X. B.; Liu, F.; Fowler, A. G.; Ungar, G.; Cseh, L.; Mehl, G. H.; Macdonald, J. E., 3D Ordered Gold Strings by Coating Nanoparticles with Mesogens. *Adv. Mater.* **2009,** *21*, 1746.

26. Kanie, K.; Matsubara, M.; Zeng, X. B.; Liu, F.; Ungar, G.; Nakamura, H.; Muramatsu, A., Simple Cubic Packing of Gold Nanoparticles through Rational Design of Their Dendrimeric Corona. *J. Am. Chem. Soc.* **2012,** *134*, 808-811.

27. Ungar, G.; Percec, V.; Zeng, C.; Leowanawat,, P., Liquid Quasicrystals. *Isr. J. Chem.* **2011**, *51*, 1206-1215.

28. Dorfman, K. D., frank-Kasper Phases in Block Polymers. *Macromolecules* **2021**, *54*, 10251-10270.

29. Goodby, J. W.; Gortz, V.; Cowling, S. J.; Mackenzie, G.; Martin, P.; Plusquellec D.; Benvegnu, T.; Boullanger, P.; Lafont, D.; Queneau, Y.; Chambert, S.; Fitremann, J., Thermotropic liquid crystalline glycolipids. *Chem. Soc. Rev.* **2007**, *36*. 1971-2012

30. Takagi, H.; Yamamoto, K., Phase Boundary of Frank-Kasper sigma Phase in Phase Diagrams of Binary Mixtures of Block Copolymers and Homopolymers. *Macromolecules* **2019,** *52*, 2007-2014.

31. Takagi, H.; Hashimoto, R.; Igarashi, N.; Kishimoto, S.; Yamamoto, K., Frank-Kasper sigma-phase in polybutadiene-poly(e-caprolactone)diblock copolymer/polybiutadiene blends. *J. Phys.: Condens. Matter* **2017,** *29*, 1-6.

32. Schulze, M. W.; Lewis III, R. M.; Lettow, J. H.; Hickey, R. J.; Gillard, T. M.; Hillmyer, M. A.; Bates, F. S., Conformational asymmetry and quasicrystal approximates in linear diblock copolymers. *Phys. Rev. Lett.* **2017,** *118*, 207801.

33. Niki, E.; Abe, K., *Vitamin E: Chemistry and Nutritional Benefits*. Royal Society of Chemistry: 2019; p 1-11.

34. G. K. Cheong, F. S. Bates, K. D. Dorfman. Symmetry breaking in particle-forming diblock polymer/homopolymer blends. *Proc. Natl. Acad. Sci. USA*. **2020**, *117*, 16764-16769.

35. Huang, Y. -Y.; Hsu, J. -H.; Chem, H. -L.; Hashimoto, T., Block Copolymers: Long-Term Growth with Added Value. *Macromolecules* **2007**, *40*, 406-409.

36. Iacovella, C. R.; Keys, A. S.; Glotzer, S. C., Self-assembly of soft-matter quasicrystals and their approximants. *Proc. Nat. Acad. Sci. USA* **2011,** *108*, 19935-19940.

37. Ishimasa, T.; Fukano, Y., Crystal Structure and Morphology of Ni-Cr Fine Particles. *Surf. Sci.* **1985**, *156*, 241-248.

38. Steward, G. R., Superconductivity in the A15 structure. *Phys. C.* **2015,** *514*, 25-28.

39. Ungar, G.; Percec, V.; Holerca, M. N.; Johansson, G.; Heck, J. A., Heatshrinking spherical and columnar supramolecular dendrimers: their interconversion and dependence of their shape on molecular taper angle. *Chem. Eur. J.* **2000,** *6*, 1258-1266.

40. Yue, K.; Huang, M. J.; Marson, R. L.; He, J. L.; Huang, J. H.; Zhou, Z.; Wang, J.; Liu, C.; Yan, X. S.; Wu, K.; Guo, Z. H.; Liu, H.; Zhang, W.; Ni, P. H.; Wesdemiotis, C.; Zhang, W. B.; Glotzer, S. C.; Cheng, S. Z. D., Geometry induced sequence of nanoscale Frank-Kasper and quasicrystal mesophases in giant surfactants. *Proc. Natl. Acad. Sci. USA* **2016,** *113*, 14195-14200.

41. Bates, M. W.; Barbon, S. M.; Levi, A. E.; Lewis, R. M. I.; Beech, H. K.; Vonk, K. M.; Zhang, C.; Fredrickson, G. H.; Hawker, C. J.; Bates, C. M., Synthesis and self-assembly of ABn Miktoarm star polymers. *ACS Macro Lett.* **2020,** *9*, 396-403.

42. Feng, X.; Xhang, R.; Li, Y.; Hong, Y.-L.; Guo, D.; Lang, K.; Wu, K.-Y.; Huang, M.; Mao, J.; Wedemiotis, C.; Nishiyama, Y.; Zhang, W.; Zhang, W.; Miyoshi, T.; Li, T.; Cheng, S. Z. D., Hierarchical Self-Organization of ABn Dendron like Molecules into a Supramolecular Lattice Sequence. *ACS Cent. Sci.* **2017,** *3*, 860-867.

43. Feng, X.; Liu, G.; Guo, D.; Lang, K.; Zhang, R.; Huang, J.; Su, Z.; Li, Y.; Huang, M.; Li, T.; Cheng, S. Z. D., Transition kinetics of self-assembled supramolecular dodecagonal quasicrystal and Frank-Kasper σ phase in ABn dendron like giant molecules. *ACS Marco Lett.* **2019,** *8*, 875-881.

Chapter 7:

1. Nowak-Król, A.; Würthner, F., Progress in the synthesis of perylene bisimide dyes. *Org. Chem. Front.* **2019**, *6*, 1272-1318

2. Herbstm W.; Hunger, K., *Industrial Organic Pigments*, Wiley-VCH, Weinheim, 2004.

3. Langhals, H., Cyclic carboxylic imide structures as structure elements of high stability. Novel developments in perylene dye chemistry. *Heterocycles* **1995**, *40*, 477.

4. Lu, F.; Nakanishi, T., Solvent-Free Luminous Molecular Liquids. *Adv. Optical Mater.* **2019**, *7*, 1900176.

5. Würthner, F., Perylene bisimide dyes as versatile building blocks for functional supramolecular architectures. *Chem. Commun.* **2004**, *14*, 1564-1579

6. Gronheid, R.; Stefan, A,; Cotlet, M.; Hofkens, J.; Qu, J.; Müllen, K.; Auweraer, M. Van der, Verhoeven, J. W.; De Schryver, F. C., Reversible Intramolecular Electron Transfer and the Single-Molecular Level. *Angew. Chem. Int. Ed.* **2003**, *42*, 4209.

7. Tinnefeld, T.; Hofkens, J.; Herten, D.-P.; Masuo, S.; Vosch, T.; Cotlet, M.; Habuchi, S.; Müllen, K.; De Schryver, F. C.; Sauer, M., Higher-excited-state photophysical pathways in multichromophoric systems revealed by single-molecule fluorescence spectroscopy. *ChemPhysChem* **2004**, *5*, 1786 – 1790.

8. Weil, T.; Vosch, T.; Hofkens, J.; Peneva, K.; Müllen, K., The Rylene Colorant Family – Tailored Nanoemitters for Photonics Research and Applications. *Angew. Chem. Int. Ed.* **2010**, *49*, 9068-9093.

9. Sun, M.; Müllen, K.; Yin, M. Water-soluble perylenediimides: design concepts and biological applocations. *Chem. Soc. Rev.* **2016**, *45*, 1513-1528.

10. Betzold, S.; Herbst, S.; Trichet, A. A. P.; Smith, J. M.; Würthner, F.; Höfling, S.; Dietrich, C. P., Tunable Light-Matter Hybridization in Open Organic Microcavities. *ACS Photonics* **2018**, *5*, 90-94.

11. Nowak- Król, A.; Shoyama, K.; Stolte, M.; Würthner, F., Napthalene and perylene diimides – better alternatives to fullerenes for organic electronics? *Chem. Commun.* **2018**, *54*, 13763-13772.

12. Huang, C.; Barlow, S.; Marder, S. R., Perylene-3,4,9,10-tetracarboxylic Acid Diimides: Synthesis, Physical Properties, and Use in Organic Electronics. *J. Org. Chem.* **2011**, *76*, 2386-2407.

13. Zhang, G.; Zhao, J.; Chow, P. C. Y.; Jiang, J.; Zhu, Z.; Zhang, J.; Huang, F.; Yan, H., Norfullerene Acceptor Molecules for Bulk Heterojunction Organic Solar Cells. *Nat. Rev. Mater.* **2018**, *118*, 3447-3507.

14. Yan, C.; Barlow, S.; Wang, Z.; Yan, H.; Jen, A. K. -Y.; Marder, S. R.; Zhan, X. Non-fullerene acceptors for organic solar cells. *Nature Reviews* **2018**, *3*, 1-19.

15. Crossland, E. J. W.; Kamperman, M.; Nedelcu, M.; Ducati, C.; Wiesner, U.; Smilgies, D.-M.; Toombes, G. E. S.; Hillmyer, M. A.; Ludwigs, S.; Steiner, U.; Snaith, H. J., A Bicontinuous Double Gyroid Hybrid Solar Cell. *Nano. Lett.* **2009**, *9*, 2807-2812.

16. Wang, L.; Partridge, B. E.; Huang, N.; Olsen, J. T.; Sahoo, D.; Zeng, X.; Ungar, G.; Graf, R.; Spiess, H. W.; Percec, V., Extraordinary Acceleration of Cogwheel Helical Self-Organization Dendronized Perylene Bisimides by the Dendron Sequence Encoding Their Tertiary Structure. *J. Am. Chem. Soc.* **2020**, *142*, 9525-9536.

17. Kumar S. *Chemistry of discotic liquid crystals : from monomers to polymers.* Boca Raton: CRC Press; 2011.

18. Safinya, C. R.; Liang, K. S.; Varady, W.A.; Clark, N. A.; Andersson, G., Synchrotron x-ray study of the orientational ordering D 2-D 1 structural phase transition of freely suspended discotic strands in triphenylene hexa-n-dodecanoate. *Phys Rev Lett.* **1984**, *53*, 1172-1175.

19. Sita, L. R., *Ex Uno plures* ("out of one, many"): new paradigms of expanding the range of polyolefins through reversible group transfers. *Angew. Chem. Int. Ed.* **2009**, *48*, 2464-2472.

20. Wei, W. Zhang, R. Wickham, L. R. Sita, Programmable Modulation of Co-monomer Relative Reactivities for Living Coordination Polymerization through Reversible Chain Transfer between "Tight" and "Loose" Ion Pairs. *Angew. Chem.Int. Ed.* 2**010**, *49*, 9140-9144.

21. Wallace, M. A.; Wentz, C. M.; Sita, L. R., Optical Purity as a Programmable Variable for Controlling Polyolefin Tacticity in Living Coordinative Chain Transfer Polymerization: Application to the Stereomodulated LCCTP of α, ω-Nonconjugated Dienes. *ACS Catal.* **2021**, *11*, 4583-4592.

22. Wallace, M. A.; Sita, L. R., Multi-state Living Degenerative and Chain Transfer Coordinative Polymerization of α-Olefins via Sub-Stoichiometric Activation. *ACS Catal.* **2021**, *11*, 9754-9760.

23. M. A. Wallace, P. Y. Zavalij, L. R. Sita, *ACS Catal.* **2020**, *10*, 8496-8502. (i) M. A. Wallace, C. M. Wentz, L. R. Sita, *ACS Catal*. **2021**, *11*, 4583-4592.

24. Thomas, T. S.; Hwang, W.; Sita, L.R., End-Group Functioalized Poly(alphaolefinates) as Non-Polar Building Blocks: Self-Assembly of Polyolefin Hybrid Conjugates. *Angew. Chem. Int. ed.* **2016**, *55*, 4683-4687.

25. Thomas, T. S. End-group functionalized poly(α - olefinates) as modular building blocks. University of Maryland, College Park, 2016.

26. Donati, F.; Pucci, A.; Cappelli, C.; Mennucci, B.; Ruggeri, G., Modulation of the Optical Response of Polyethylene Films Containing Luminescent Perylene Chromophores. *J. Phys. Chem B* **2008**, *112*, 3668-3679.

27. Destrade, C.; Foucher, P.; Gasparoux, H.; Huu Tinh, N.; Levelut, A. M.; Malthete, J., Disclike mesogen polymorphism. *Mol Cryst Liq Cryst.* **1984**, *106*, 121-146.

28. Destrade, C.; Tinh, N. H.; Mamlok, L.; Malthete, J., Trioxatruxenes - a new family of disc-like mesogens with a complex polymorphism. *Mol Cryst Liq Cryst.* **1984**, *114*, 139- 150. 19.

29. Donnio, B.; Heinrich, B.; Allouchi, H.; Kain, J.; Diele, S.; Guillon, D.; Bruce, D. W., A generalized model for the molecular arrangement in the columnar mesophases of polycatenar mesogens. Crystal and molecular structure of two hexacatenar mesogens. *J Am Chem Soc.* **2004**, *126*, 15258-15268.

30. Saranathan, V.; Narayanan, S.; Sandy, A., Evolution of single gyroid photonic crystals in bird feathers. **2021**, *118*, e2101357118.

31. Saranathan, V.; Osuji, C. O.; Mochrie, S. G. J.; Noh, H.; Narayanan, S.; Sandy, A.; Dufrensne, E. R.; Prum, R. O., Structure, function, self-assembly of single network gyroid ($I4_132$) photonic crystals in butterfly wing scales. *PNAS* **2010**, *107*, 11676 – 11681.

32. Yan, L.; Rank, C.; Mecking, S.; Winey, K. I., Gyroid and Other Ordered Morphologies in Single-Ion Conducting Polymers and Their Impact on Ion Conductivity. *J. Am. Chem. Soc.* **2020**, *142*, 857-866.

33. Choi, D. H.; Matinder, K., Diketopyrrolopyrrole: brilliant red pigment dye-based fluorescent probes and their applications. *Chemical Society Reviews*. **2014**, *44*, 58–77.

34. Khan, F.; Jang, Y.; Patil, Y.; Misra, R.; D'Souza, F., Photoinduced Charge Separation Prompted Intervalence Charge Transfer in a Bis(thienyl)diketopyrrolopyrrole Bridged Donor-TCBD Push-Pull System. *Angew. Chem. Int. Ed.* **2021**, *60*, 20519 – 20527.

35. Popli, C.; Jang, Y.; Patil, Y.; Misra, R. D'Souza, F., Formation of Highly Efficient, Long-Lived Charge Separated States in Star-Shaped Ferrocene-Diketopyrrolopyrrole-Triphenylamine Donor-Acceptor-Donor Conjugates. *Chem. Eur. J.* **2020**, *26*, 15109-15115.

36. Patil, Y.; Popli, C.; Misra, R., Near-Infrared absorbing tetracyanobutadiene bridged diketopyrrolopyrroles. *J. Chem.* **2018**, *42*, 3892-3899.

37. Popli, C.; Patil, Y.; Misra, R., Design and Synthesis of *N*-Phenylcarbazole-substituted Diketopyrrolopyrrole-Based Monomers and Dimers: A Comparative Study. *Eur. J. Org. Chem.* **2018**, 46, 6474-6481

38. Patil, Y.; Jadhav, T.; Dhokale, B.; Misra, R., Tuning of the HOMO-LUMO Gap of Symmetrical and Unsymmetrical Ferrocenyl-Substituted Diketopyrrolopyrroles. *Eur. J. Org. Chem.* **2016**, *4*, 733 – 738.

39. Patil, Y.; Jadhav, T.; Dhokale, B.; Misra, R., Design and Synthesis of Low HOMO-LUMO Gap *N*-Phenylcarbazole-Substituted Diketopyrrolopyrroles. *Asian J. Org. Chem.* **2016**, *5*, 1008-1014.